MATH MODEL RESEARCH GROUP
DEPARTMENT OF MATHEMATICS
FEDERAL UNIVERSITY OF TECHNOLOGY (FUT)
GIDAN KWANO CAMPUS MINNA, NIGERIA

BOOK OF PROCEEDINGS

2nd INTERNATIONAL CONFERENCE ON MATHEMATICAL MODELING, OPTIMIZTICAL AND ANALYSIS OF DISEASE DYNAMICS [ICMMOADD 2025]

HYBRID (VIRTUAL & PHYSICAL)

THEME:

MATHEMATICAL MODELLING AND APPLICATION TO CLIMATE CHANGE AND ENVIRONMENTAL ISSUES

DATE: FEBRUARY 18TH - 21ST, 2025 TIME: 10:00AM PROMPT
VENUE: DEPARTMENT OF MATHEMATICS, FUT MINNA, NIGERIA

PROFESSOR N.I AKINWANDE FNMS
CONVENER

MATH MODEL RESEARCH GROUP
DEPARTMENT OF MATHEMATICS
FEDERAL UNIVERSITY OF TECHNOLOGY, MINNA, NIGERIA

BOOK OF PROCEEDINGS

for the

2ND INTERNATIONAL CONFERENCE ON MATHEMATICAL MODELLING, OPTIMIZATION AND ANALYSIS OF DISEASE DYNAMICS (ICMMOADD) 2025

HYBRID (VIRTUAL & PHYSICAL)

Theme:

MATHEMATICAL MODELLING AND APPLICATION TO CLIMATE CHANGE AND ENVIRONMENTAL ISSUES

DATE: 18th to 21st February, 2025 **TIME:** 10.00am Prompt
VENUE: Department of Mathematics, Federal University of Technology, Minna, Nigeria

PROFESSOR N. I. AKINWANDE FNMS
Convener

ISBN: 978-978-789-930-4

EDITORIAL BOARD

CENTRAL ORGANIZING COMMITTEE

NAME	STATUS	INSTITUTION
Prof. N. I. Akinwande	Convener	Dept. of Mathematics, F. U. T., Minna
Dr. S. A. Somma	Secretary	Dept. of Mathematics, F. U. T., Minna
Dr. N. O. Abdurrahman	Ass. Secretary	Dept. of Mathematics, F. U. T., Minna
Prof. R. O. Olayiwola	Member	Dept. of Mathematics, F. U. T., Minna
Prof. F. A. Kuta	Member	Dept. of Microbiology, F. U. T., Minna
Prof. A. I. Enagi	Member	Dept. of Mathematics, F. U. T., Minna
Prof. S. Abdulrahman	Member	Dept. of Mathematics, F. U. Birnin Kebbi
Prof. M. D. Shehu	Member	Dept. of Mathematics, F. U. T., Minna
Prof. G. A. Bolarin	Member	Dept. of Mathematics, F. U. T., Minna
Dr. A. Usman	Member	Dept. of Statistics, F. U. T., Minna
Dr. T. T. Ashezua	Member	Dept. of Mathematics, JSTU, Makurdi
Dr. O. M. Adetutu	Member	Dept. of Statistics, F. U. T., Minna
Dr. F. A. Oguntolu	Member	Dept. of Mathematics, F. U. T., Minna
Dr. R. I. Gweryina	Member	Dept. of Mathematics, JSTU, Makurdi
Dr. P. T. Adajime	Member	Dept. of Epidemiology, BSU, Makurdi

LOCAL ORGANIZING COMMITTEE

Prof. N. I. Akinwande	Chaiman	Dr. R. Muhammad	Member
Dr. S. A. Somma	Secretary	Dr. N. Nyor	Member
Dr. N. O. Abdurrahman	Ass. Secretary	Dr. S. I. Yusuf	Member
Prof. Y. M. Aiyesimi	Member	Dr. O. R. Jimoh	Member
Prof. Y. A. Yahaya	Member	Dr. F. A. Oguntolu	Member
Prof. U. Y. Abubakar	Member	Dr. A. Lawal	Member
Prof. M. Jiya	Member	Dr. A. Yusuf	Member
Prof. D. Hakimi	Member	Dr. K. J. Audu	Member
Prof. A. A. Muhammed	Member	Dr. (Mrs) Deborah Bako	Member
Prof. R. O. Olayiwola	Member	Dr. N. O. Salihu	Member
Prof. A. Ndanusa	Member	Mr. A. B. Zhiri	Member
Prof. A. I. Enagi	Member	Mr. C. U. Ugwu	Member
Prof. M.D. Shehu	Member	Mr. J. A. Jiddah	Member
Prof. G. A. Bolarin	Member	Mr. A. Gana	Member
Prof. (Mrs) A. T. Cole	Member	Mr. B. D. Bako	Member
Dr. U. Mohammed	Member		

KEYNOTE AND PLENARY SPEAKERS

Keynote Speaker,
Mr. Jubril Adeniji,
The Regional Managing Director,
Guaranty Trust Bank, East Africa

Plenary Speaker I,
Prof. Samuel Segun Okoya of the Department of Mathematics, Obafemi Awolowo University, Ile – Ife, Nigeria

Plenary Speaker II,
Dr. Olawale Oladeji,
Metropolitan Water Reclamation District of Greater Chicago, Chicago, USA

TABLE OF CONTENTS

ARTICLES

SPEECH FROM KEYNOTE SPEAKER

AT THE 2ND INTERNATIONAL CONFERENCE ON MATHEMATICAL MODELLING, OPTIMISATION AND ANALYSIS OF DISEASE DYNAMICS (ICMMOADD 2025)

Mr. Jubril Adeniji jubrilnbs@gmail.com
Regional Managing Director, Guaranty Trust Bank, East Africa, Nairobi, Kenya.

From Equations to Action: Using Mathematical Models for Climate Change Predictions

Good morning, everyone.

It's truly a great pleasure to be here with you today. I know that when most people hear mathematical modelling, their first instinct might be to tune out, thinking, Oh no, not more numbers and equations! But don't worry, I promise this won't be a lecture filled with complex formulas. Instead, I would like us to talk about something that affects all of us: our planet, our future, and how we can use data and science to make better decisions.

Mathematical modelling is a hidden superpower that quietly shapes our world using concepts, equations, graphs, algorithms, and numbers to represent real- world phenomena, helping us understand, predict, and make informed decisions about complex systems. I'm sure we'd all agree. Practical mathematical modelling applications are vast, ranging from weather forecasting, where data and equations simulate atmospheric changes, to personal finance, health and fitness tracking, and investment planning, where models help visualise and optimise decisions. Simply put, these models help us make sense of the chaos around us and prepare for what's ahead.

No where is this more critical than in tackling climate change. The challenges we face: rising sea levels, unpredictable weather, and extreme heat can all feel overwhelming. But thanks to mathematical models, we have gained an understanding of how to address these global issues. We're not just guessing what might happen next; we have real tools through these models that provide valuable insights that guide policy-making and strategic planning by simulating distinctive scenarios and predicting outcomes. As we continue to face the challenges posed by climate change, the role of mathematical modelling in developing

effective solutions and strategies cannot be overemphasised.

Mathematical models are vital for understanding and addressing the complex challenges of climate change and environmental issues. Equations and algorithms are used to simulate interactions within the Earth's climate system, and these models provide critical insights into how various factors influence climate patterns and environmental processes. They help predict future climate scenarios by incorporating data on greenhouse gas emissions, ocean currents, and atmospheric conditions, enabling meteorologists to forecast changes in temperature, sea levels, and weather patterns.

These models also inform policy decisions by predicting the outcomes of different emission reduction strategies, aiding governments and organisations in choosing effective actions to combat climate change. Additionally, they help us understand environmental interactions, manage natural resources sustainably, and prepare for extreme weather events. By forecasting events like hurricanes, storms, floods, and droughts, mathematical models enable communities to respond more effectively, reducing potential damage and saving lives.

In today's world, predictions are vital tools that help communities prepare for disasters, prevent loss of life, and protect the environment. Advanced climate and environmental models predict everything from hurricanes to air pollution, transforming how cities and people respond to challenges. For example:

- ✓ **2012 Hurricane Sandy:** Advanced models predicted Sandy's path, leading to early evacuations and pre-planned disaster relief, saving thousands of lives.
- ✓ **2014 Jakarta Giant Sea Wall:** Flood models guided the development of a sea wall to protect against coastal flooding, aiming to safeguard 10 million people.
- ✓ **2019 London's ULEZ:** Air quality models identified pollution hotspots, leading to the implementation of the Ultra-Low Emission Zone, which significantly reduced nitrogen dioxide (NO_2) levels.
- ✓ **2019–2020 Australian Bushfires:** Models forecasted extreme fire conditions, enabling warnings and resource mobilisation that reduced casualties.
- ✓ **2021 European Floods:** Flood models predicted extreme rainfall, prompting early

warnings and evacuations, giving people time to prepare, reducing damage and loss of lives.

- ✓ **2022–2023 Horn of Africa Drought:** Early warnings from climate models led to pre-emptive aid efforts, reducing malnutrition and displacement.

While predictive models are invaluable in mitigating disasters and improving public health, they face significant challenges. The unpredictable nature of climate and environmental systems, influenced by numerous variables, makes accurate predictions difficult. Additionally, data gaps, especially in remote areas, can impact the reliability of these models. Due to insufficient and up-to-date data, predictions for local events like flash floods or droughts become less accurate.

Moreover, the effectiveness of predictive models depends on human action. Even the most advanced models cannot compel people to act. The information provided by these models must be communicated clearly and trusted by local authorities, leaders, and communities. Human decision-making is crucial in turning predictions into actionable steps to reduce risks and save lives.

As we look to the future, innovation offers hope through, more innovative and more accurate predictive models. Integrating new technologies like **satellites**, **artificial intelligence (AI)**, and **Geographic Information Systems (GIS)** is revolutionising data collection and analysis. Satellites now give us a real-time view of the planet's changes, artificial intelligence helps us analyse massive data sets to detect patterns faster than ever, and GIS lets us visualise and interpret spatial data. These advancements enable more precise and timely predictions, especially in remote areas, enhancing our ability to prepare for and respond to natural events globally.

The future of predictive modelling also lies in the hands of young individuals, innovators, and everyday citizens. Empowering youth through **STEM (science, technology, engineering, and mathematics)** programs fosters the next generation of leaders and innovators, bringing fresh perspectives and creative solutions. Collaboration between scientists, governments, local communities, and individuals is therefore crucial for

success. By working together and sharing knowledge and resources, we can create more effective and inclusive models that benefit everyone, ensuring a more resilient and prepared society.

As we look toward a future that leverages predictive models for better environmental outcomes, it's crucial to remember that while mathematical models may not plant trees, they guide us on where to plant them for the biggest environmental impact. These models provide the critical data needed to make informed decisions, but it's up to all of us to put that knowledge into action. **Hence, mathematical models aren't just numbers on a screen; they are real-life applications that make a difference, turning equations into action.**

Therefore, we all have a role to play, advocating for policies prioritising climate resilience and data collection, spreading awareness about the importance of predictive modelling, and making eco-friendly choices in our daily lives. Every small action counts in reducing environmental strain and making the planet safer for future generations. Together, we can turn predictions into meaningful action that makes a real difference.

So today, as we reflect on how to move equations to action, let's remember: **mathematical models don't just belong in research labs, they belong in boardrooms, government policies, classrooms and everyday decisions.**

And to those who might not love math, I get it. But this isn't just about numbers, it's about the future we want to create. When we use data wisely, we are not just solving equations; we're solving real-world problems.

Thank you for being part of this conversation. Let's take what we learn today and turn it into action for a better, more sustainable world. Happy deliberations as we jointly put equations into action for the benefit of the entire world.

Mathematical Modelling: Addressing Environmental Issues with Precision

Olawale O. Oladeji, PhD
(Senior Environmental Soil Scientist, MWRD Chicago)

Abstract

Mathematical models are vital for crafting cost-effective strategies to address diverse environmental challenges, such as pollution control, climate change preparedness and mitigation, and resource management. These models equip researchers and policymakers with the tools to develop evidence-based strategies that enhance environmental conservation and sustainability efforts. By simulating complex environmental systems, mathematical models facilitate understanding of the interactions between various factors, enabling targeted interventions that minimize impacts and risks. Pollution control models predict the dispersion of pollutants in air, water, and soil, guiding strategies that protect public health and promote sustainable communities. In climate change preparedness and mitigation, models simulate different climate scenarios, offering insights into the long-term impacts of climate change and informing policies to mitigate adverse effects and adapt to new conditions. Resource management also benefits from mathematical modeling by optimizing the allocation and use of natural resources, ensuring sustainability and minimizing waste. This session will explore case studies that demonstrate the critical role of mathematical models in addressing environmental problems, saving lives, and fostering sustainable development. The objectives are to underscore the indispensable role of mathematical modeling in tackling environmental issues and to call for interdisciplinary collaboration among scientific communities, policymakers, and other stakeholders. By working together, we can develop innovative solutions, create a more sustainable future, and safeguard the health of our environment and communities.

Background

The increasing demand for essential resources—such as food, water, and energy—driven by rising human populations and technological advancements, has resulted in a variety of environmental challenges (World Bank Report, 2015; United Nations, 2016). Population growth contributes to habitat destruction, deforestation, and a decline in biodiversity (Prakash, 2017; Kumar and Verma, 2017). Urban expansion exacerbates habitat changes and environmental pollution (Prakash and Verma, 2022). Additionally, industrial activities, household waste, agricultural chemicals, and other human activities further degrade ecosystems and impact public health.

Addressing these escalating environmental challenges requires precise tools provided by mathematical modeling to predict and mitigate their effects (Fanous et al, 2023). Models enable the simulation of scenarios, prediction of potential outcomes, and guidance for informed decision-making processes. For example, climate models help forecast climatic conditions and associated disasters, while pollution models assist in designing effective control measures.

The use of mathematical models in environmental science dates back to the 1900s (Streeter and Phelps, 1925; Nirmalakahandan, 2002) and has evolved from simple models of the past to highly sophisticated tools (Lewis et al., 2024). Early models focused on basic ecological processes, whereas contemporary models integrate vast amounts of data and complex algorithms to simulate environmental systems.

Today, mathematical modeling is indispensable for understanding complex environmental systems and developing strategies to address these issues. This session provides an overview of the advances and applications of mathematical models in addressing environmental challenges.

Mathematical models and environmental issues

Environmental issues encompass a wide range of challenges that affect our planet and its inhabitants. Mathematical modeling has become an indispensable tool at addressing the issues by providing a systematic and scientific approach to understanding, predicting, and mitigating the complex environmental phenomena. Below are some pressing environmental issues requiring mathematical modellings.

1. Climate Change: Models integrate atmospheric, oceanic, and terrestrial processes to provide a comprehensive understanding of climate dynamics (Fig. 1). The models integrate vast amounts of data and complex algorithms to simulate global environmental systems (Lewis et al., 2024). Improved algorithms and higher resolution models have led to more accurate predictions of climate trends and extreme weather events (de Burgh-Day and Leeuwenburg, 2023).

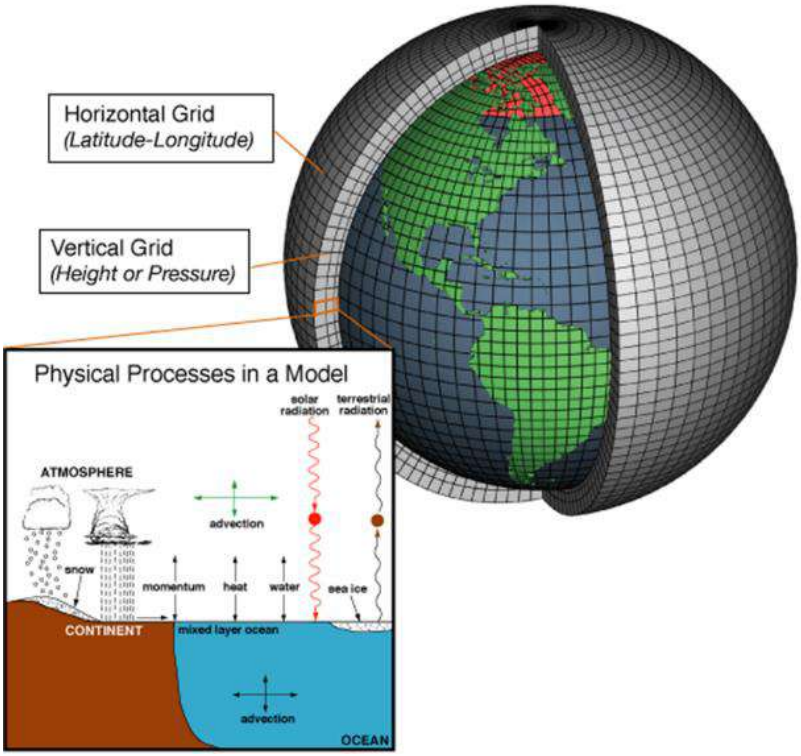

Fig. 1: Mathematical modelling of the climate system based on physical laws and processes
(Source: NOAA, https://celebrating200years.noaa.gov/breakthroughs/climate_model/welcome.html)

Recent inclusion of machine learning (ML) and artificial intelligence (AI) into climate change modellings (Rasp et al. 2024; Ben Bouallègue et al. 2024) are expected to improve the accuracy of climate predictions, fill data gaps, estimate emissions inventories, and refine climate scenario projections (Lewis and Shi, 2024; Rasp et al. 2024). Incorporating ML and AI into modelling is expected to enhance the efficiency of problem-solving in climate research, leading to better

understanding and mitigation strategies (Huntingford et al., 2019; World Economic Forum. 2018). By leveraging advanced technologies and interdisciplinary collaboration, researchers will be better equipped to develop effective strategies for climate change mitigation and adaptation, contributing to sustainable environmental management and protection (Lewis et al., 2024).

It is strongly recommended that mathematical modellings be given the needed supports to adequately forecast the local impacts of climate change such as which streets will flood, when, and by how much, magnitude of drought and impacts on the economy, etc.

2. Pollution Control and Monitoring:

Mathematical models are employed to identify sources of pollution and assess effectiveness of mitigation measures (Wang et al, 2024). Real-time air and water quality monitoring systems use mathematical models to provide accurate forecasts and inform pollution control strategies (Table 1).

Table 1: Uses of mathematical models in pollution monitoring and control.

Environment	**Pollution (examples)**	**Need for Model**
Atmosphere	• air pollution • toxic gas leak • industrial emission • vehicles emissions • dust, etc.	• quantify pollutants • determine exposure • design remediation plan • impact assessment • regulatory compliance • pollutant transport
Surface water	• industrial effluent discharge • oil spills • storm water • agricultural runoffs, etc.	
Subsurface water	• waste disposals in landfills • drainage water • leachates • chemical spills, etc.	
Groundwater	• leaking from waste disposals • leachates from: ✓ agricultural fields ✓ chemical spills, etc.	
Ocean	• sewage disposals • chemical spills, etc.	

Models play a crucial role in predicting, managing, and mitigating pollution, contributing to environmental sustainability and public health. For example, mathematical and computational techniques:

- Simulate the dispersion of pollutants in the atmosphere.
- Predict the spread and impact of contaminants in water bodies
- Simulate water flow, quality, and availability
- Aiding in the planning of sustainable water management practices
- Balance the needs of agricultural, industrial, and domestic water users.
- Monitoring to ensure the long-term health of aquatic ecosystems.

Future research on pollution control and monitoring is expected to integrate advanced technologies such as AI and ML and fostering collaboration among experts from various fields to develop innovative solutions for pollution control and monitoring.

3. Natural Disaster Prediction and Management:

Predictive models use historical data and real-time information to forecast the likelihood and severity of natural disasters such as hurricanes, floods, and wildfires (Venkadesh et al. 2024). Early warning systems of these models help communities prepare and respond effectively.

The use of mathematical models in natural disaster prediction dates back several decades, but recent advancements in computational power and data availability have revolutionized the field. Early models focused on basic statistical methods, while contemporary models integrate data from satellite imagery, sensor networks, and social media (Sun et al., 2019) and complex algorithms to simulate disaster scenarios and predict their impacts.

Applications of mathematical modelling in natural disaster are summarized in Table 2.

Table 2. Use of models in natural disaster prediction and management

Natural disaster Prediction	**Use of models**
Earthquake	Analyze seismic data to predict the likelihood and magnitude of earthquakes. Helps early warning systems.
Flood	Simulate hydrological processes to predict flood events. Provide accurate flood forecasts
Hurricane	Predict path and intensity of hurricanes. Help in planning evacuation and response strategies.
Wildfire	Predict wildfire outbreaks. Allows for rapid response and reduce the spread and impact of wildfires.
Disaster Response and Relief Management	AI-driven systems optimize resource allocation, damage assessment, and relief distribution. Enhance efficiency of disaster response efforts.

4. Integrated Soil Fertility Management (ISFM):

Integrated Soil Fertility Management (ISFM) is a holistic approach to improving crop yields while preserving long-term soil fertility (Mugwe and Otieno, 2021). It combines judicious use of fertilizers, recycled organic resources, responsive crop varieties, and improved agronomic practices to optimize crop yields, minimize nutrient losses, and enhance plant's nutrient-use efficiency.

Success of ISFM was made possible by mathematical models employed to optimize nutrient management practices for different cropping systems and ensure efficient resource use while enhancing soil health and fertility (Otieno et al., 2021). Early models focused on basic ecological processes, but contemporary models integrate vast amounts of data and complex algorithms to simulate nutrient uses. Impacts of model use in ISFM includes:

- Crop yield improvement

- Increase soil organic carbon (SOC
- Identified best management practices to minimize GHG emissions.
- Design effective strategies to promote the adoption of ISFM practices.

5. Water Resource Management:

Models simulate water flow, quality, and availability to support sustainable water management practices. They help in planning and implementing strategies for efficient water use and conservation. Water resource management is a critical field that encompasses the development, control, protection, regulation, and beneficial use of water resources to meet the demands of various users. Modelling plays a crucial role in this process, by providing a scientific basis for decision-making and policy formulation. Below are some cases where mathematical models is being used in water resource management:

- Hydrological models to simulate the movement and distribution of water within a watershed.
- Water allocation and allocation of water resources to various user groups, such as agriculture, industry, and domestic use.
- Assessment models that track impact of climate change on water resources, predicting changes in precipitation patterns, temperature, and water availability.
- Pollution control models predict the dispersion of pollutants in water bodies, aiding in the design of effective control measures.

6. Wildlife Conservation:

Models predict how environmental changes affects wildlife populations and habitats. They assist in developing conservation strategies to protect endangered species and maintain biodiversity. Wildlife conservation is a critical field that aims to protect and manage wildlife populations and their habitats. Modelling plays a crucial role in this effort, providing a scientific basis for decision-making and policy formulation. Some applications of modelling in wildlife conservation includes:

- Habitat Modelling: to simulate the distribution and quality of habitats for various wildlife species.
- Population Dynamics: to predict the growth, decline, and distribution of wildlife populations.
- Species Distribution Modelling: to predict the geographic distribution of species based on environmental variables.
- Agent-Based Models: simulate the behavior and interactions of individual animals within a population.
- Acoustic Monitoring: uses sound recordings to detect and monitor wildlife species.

7. Renewable Energy Optimization:

Mathematical models are also used to optimize the deployment of renewable energy sources, such as solar and wind power. These models help maximize energy production while minimizing environmental impact.

Climate Change as Case Studies

Mathematical models have been very helpful to predict climate change and consequences we are observing today. The scenarios model help understand greenhouse gas emission pathways, enabling policymakers and scientists to understand the potential impacts of climate change and plan mitigation and adaptation strategies. Mathematical models elucidate the complex interactions between different components of the climate system, such as how increased CO_2 levels affect temperature, precipitation, and ocean currents. Models are also used to assess the risks of extreme weather events (e.g. hurricanes, droughts, and heatwaves) which is crucial for disaster preparedness and management. Models can also simulate outcomes of mitigation strategies (e.g. impacts of reducing carbon emissions or increasing renewable energy use), allowing policymakers to evaluate the effectiveness of different approaches to combat climate change.

Consensus among the climate change models are the severe impacts of the extreme weather events that includes droughts, excessive rains and flooding, crop losses, wildfires, etc. (Zscheischler et al. 2020; Seneviratne et al. 2023), all of which requires accurate predictions to minimize the impacts.

Climate change model predicted increasing frequency and intensity of extreme events, leading to disasters that are more disruptive to communities and more costly to infrastructure. The data of disasters in the US between 1980 and 2024 suggest increase in climate change related disaster events and costs (Fig. 2). All the 2024 climate disaster in the US (Fig. 3) are accurately predicted ahead of time (made possible by robust models) and will be more costly in the absence of the warnings.

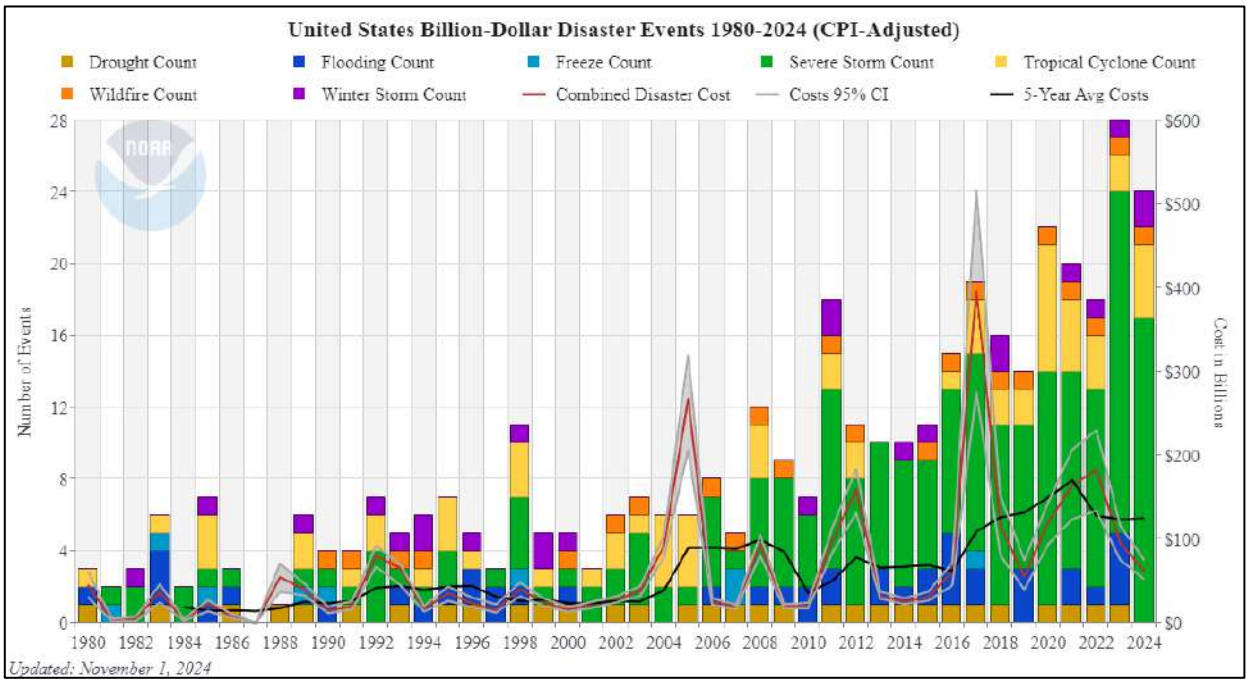

Figure 2: United State billion-dollar disaster events 1990-2024. (Source: NOAA National Centers for Environmental Information (NCEI) U.S. Billion-Dollar Weather and Climate Disasters (2025). https://www.ncei.noaa.gov/access/billions/)

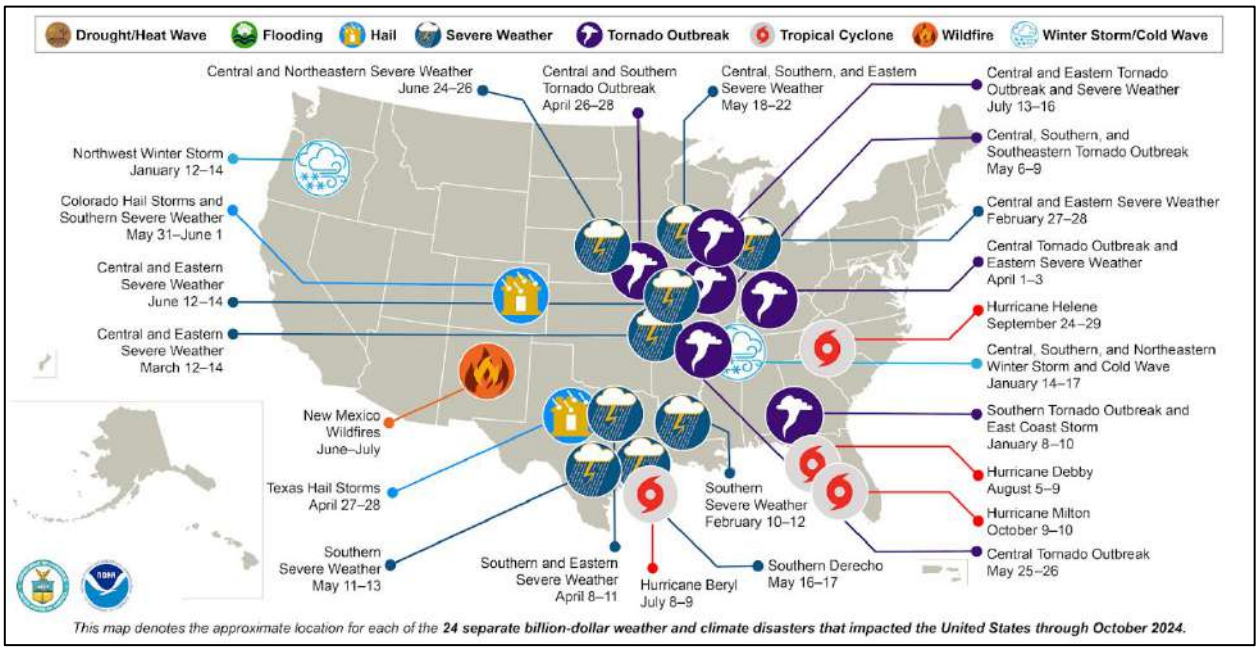

Figure 3: United State 2024-billion-dollar weather and climate disaster. (Source: NOAA National Centers for Environmental Information (NCEI) U.S. Billion-Dollar Weather and Climate Disasters (2025). https://www.ncei.noaa.gov/access/billions/)

A recent notable disaster in Nigeria blamed on climate change was the flooding as a result of collapse of Alau Dam in Borno State, Nigeria in 2024. The dam's embankment gave way, releasing 112 billion liters of water into low-lying areas in Maiduguri, flooded nearby towns and villages (Fig. 4), displacing over one million people. The catastrophe left hundreds homeless and attracted over N13 billion aid donations to the flood victims. Such a costly disaster is preventable and served as a wake-up calls for government to evaluate status of infrastructures and prioritize building climate resiliency into public infrastructures.

Figure 4: The concrete spillway and crest of the Alau dam and the flooding after the dam collapsed in northeastern Nigeria. (Source: New York Times of Oct. 27, 2024; Photographs by Fati Abubakar Ruth Maclean, Ismail Alfa and Fati Abubakar reported in New York Times of Oct. 27, 2024)

Advances in regional climate modeling and infrastructure analysis over the last several years mean that engineers and decision makers are now better prepared and able to take actions today that will enhance the resilience of infrastructure systems. However, African countries are less prepared and most of what is known about climate impacts and risks in Africa are based on findings from global studies that use data largely from outside Africa (e.g., Zhao et al., 2021).

It should be noted that though Africa's contribution to greenhouse gas emissions causing climate change is minimal, the continent is experiencing significant impact of the climate change including biodiversity loss, water shortages, reduced food production, loss of lives and reduced economic growth (IPCC, Climate Change 2014; Adzawla et al., 2019). The growing shifts in temperature, rainfall, storms, and sea levels is shrinking arable lands and contributing to violent conflict experience in some part of Africa because of shortages of resources such as land and water. It is projected that the changing climate will increase sickness, hunger, joblessness, conflict, and social chaos in the continent of Africa. Thus, there is urgent need for modeling to guide policy to address potential impacts of the climate change.

Collaboration and Environmental Challenges

Addressing the environmental challenges requires interdisciplinary collaborations that bring together experts from various fields, including mathematics, environmental science, computer science, and policy. The collaborations can foster the development of innovative solutions and ensure that mathematical models are effectively applied to real-world problems. The integration of machine learning and artificial intelligence (AI) with mathematical modelling holds great promise for addressing environmental challenges. These technologies can analyze vast amounts of data, identify patterns, and improve the accuracy of predictions, leading to more effective environmental management.

Conclusion

Mathematical modelling has made significant advancements in addressing environmental issues, providing valuable insights and guiding effective strategies. From climate change and pollution control to ecosystem management and disaster prediction, models are essential tools for understanding and mitigating the impact of human activities on the environment. As technology and methodologies continue to evolve, mathematical modelling will play an increasingly important role in shaping a sustainable future by resource poor African countries to step up with strategy to address associated environmental challenges.

References

Adzawla, W., Sawaneh, M. and Yusuf, A.M. (2019), "Greenhouse gasses emission and economic growth nexus of Sub-Saharan Africa", Scientific African, Vol. 3, p. e00065.

Ben Bouallègue, Z., Clare M. C. A., Magnusson L., Gascon E., Maier-Gerber M., Janousek M., et al. 2024. The rise of data-driven weather forecasting: A first statistical assessment of machine learning-based weather forecasts in an operational-like context. Bull. Amer. Meteor. Soc., 105: E864–E883, https://doi.org/10.1175/BAMS-D-23-0162.1 .

Cook, B. I., Ault T. R. and Smerdon J. E. 2015. Unprecedented 21st century drought risk in the American Southwest and Central Plains. Sci. Adv. 1, e1400082.

Dai, A. 2011. Drought under global warming: A review. WIREs Clim. Change 2:45–65.

de Burgh-Day, C. O. and Leeuwenburg T. 2023. Machine learning for numerical weather and climate modelling: A review. EGUsphere, 2023, 1- 48.

Dufy, P. B., Brando P., Asner G. P. and Field C. B. 2015. Projections of future meteorological drought and wet periods in the Amazon. Proc. Natl. Acad. Sci. U.S.A. 112:13172 - 13177.

Fanous, M., Eden J. M., Remesan R., and Daneshkhah, A. 2023. Challenges and prospects of climate change impact assessment on mangrove environments through mathematical models. Environmental Modelling and Software 105658.

Field, C. B., Barros, V., Stocker, T. F., Dahe, Q., Dokken, D. J., Ebi, K. L., et al. (2012). Managing the risks of extreme events and disasters to advance climate change adaptation: Special report of the intergovernmental panel on climate change (18, pp. 568 - 599). Cambridge University Press

Fu, Q. and Feng, S. 2014. Responses of terrestrial aridity to global warming. J. Geophys. Res. Atmos. 119:7863 - 7875.

Held, I. M., Delworth T. L., Lu J., Findell K. L. and Knutson T. R. 2005. Simulation of Sahel drought in the 20th and 21st centuries. Proc. Natl. Acad. Sci. U.S.A. 103:17891-17896.

Huntingford C, Jeffers E.S., Bonsall M.B., Christensen H.M., Lees T., Yang H. 2019. Machine learning and artificial intelligence to aid climate change research and preparedness. Environ Res Lett. 14(12): 124007. https://doi.org/10.1088/1748-9326/ab4e55.

IPCC, Climate Change 2014: Impacts, Adaptation, and Vulnerability. Part A: Global and Sectoral Aspects. Contribution of Working Group II to the Fifth Assessment Report of the Intergovernmental Panel on Climate Change, in: P.R.M. Field, C.B., V.R. Barros, D.J. Dokken, K.J. Mach, M.D Mastrandrea, T.E. Bilir, M. Chatterjee, K.L. Ebi, Y.O. Estrada, R.C. Genova, B. Girma, E.S. Kissel, A.N. Levy, S. MacCracken, L.L. White (Eds.), Climate Change 2014: Impacts, Adaptation, and Vulnerability. Part A: Global and Sectoral Aspects. Contribution of Working Group II to the Fifth Assessment Report of the Intergovernmental Panel On Climate Change, Cambridge University Press, Cambridge, United Kingdom and New York, NY, USA, 2014.

Kumar Ajay and Verma A.K. 2017. Biodiversity loss and its Ecological impact in India. International J. Bio Sci. 8: 156-160.

Lewis, J.I., Toney A. and Shi X. 2024. Climate change and artificial intelligence: assessing the global research landscape. Discov Artif Intell 4: 64. https://doi.org/10.1007/s44163-024-00170-z

Maclean, R. and Alf I. 2024. How Years of Government Failures Caused a Flood 'Worse Than Boko Haram'. The New York Times of Oct. 27, 2024. https://www.nytimes.com/2024/10/27/world/africa/nigeria-dam-disaster-flood.html?smid=url-share

Mugwe, J. and E. O. Otieno. 2021. "Integrated soil fertility management approaches for climate change adaptation, mitigation, and enhanced crop productivity," Handbook of Climate Change Management, pp. 1 - 22.

Nirmalakahandan N. 2002. Modeling Tools for Environmental Engineers and Scientists, CRC Press LLC.

NOAA National Centers for Environmental Information (NCEI). 2025. U.S. Billion-Dollar Weather and Climate Disasters. https://www.ncei.noaa.gov/access/billions/

Otieno, E. O., Kiboi M. N., Gian N., Muriuki A., Musafiri C. M., and Ngetich F. K. 2021. Uptake of integrated soil fertility management technologies in heterogeneous smallholder farms in sub-humid tropics. Environmental Challenges, 5: 100394. https://doi.org/10.1016/j.envc.2021.100394.

Prakash S. 2017. Climate change and need of Biodiversity conservation: A review. International Journal of Applied Research. 3:554-557.

Prakash S. and Verma A. K. 2022. Anthropogenic activities and Biodiversity threats. Int. J. Biol. Innov. 4: 94-103.

Prudhomme, C. et al. 2014. Hydrological droughts in the 21st century, hotspots and uncertainties from a global multimodel ensemble experiment. Proc. Natl. Acad. Sci. U.S.A. 111: 3262 - 3267.

Rasp, S., Dueben, P.D., Scher, S., Weyn, J.A., Mouatadid, S., Thuerey, N. 2024: WeatherBench 2: A benchmark for the next generation of data-driven global weather models. J. Adv. Model. Earth Syst., 16, e2023MS004019.

Seneviratne, S. I., and Coauthors, 2023: Weather and climate extreme events in a changing climate. Climate Change 2021: The Physical Science Basis, V. Masson-Delmotte et al., Eds., Cambridge University Press, 1513–1766, https://doi.org/10.1017/9781009157896.013.

Seneviratne, S. I., Nicholls, N., Easterling, D., Goodess, C. M., Kanae, S., Kossin, J., Luo, Y., Marengo, J., McInnes, K., Rahimi, M., Reichstein, M., Sorteberg, A et al., 2012. Changes in climate extremes and their impacts on the natural physical environment. In: Managing the Risks of Extreme Events and Disasters to Advance Climate Change Adaptation [Field, C.B., V. Barros, T.F. Stocker, D. Qin, D.J. Dokken, K.L. Ebi, M.D. Mastrandrea, K.J. Mach, G.-K. Plattner, S.K. Allen, M. Tignor, and P.M. Midgley (eds.)]. A Special Report of Working Groups I and II of the Intergovernmental Panel on Climate Change (IPCC). Cambridge University Press, Cambridge, 109–230.

Streeter, H. W., and E. B. Phelps (1925), A Study of the Pollution and Natural Purification of the Ohio River. III. Factors Concerned in the Phenomena of Oxidation and Reaeration, Public Health Bull. 146. [Reprinted by U.S. Dep. of Health, Educ. and Welfare, Public Health Serv., Washington.].

Sun, A.Y. and Scanlon B.R. 2019. How can big data and machine learning beneft environment and water management: a survey of methods, applications, and future directions. Environ Res Lett 14(7):07300.

United Nations, 2016. Human population and the global environment. United Nations Journal on Human Environment, 97: 123-133.

Venkadesh, P., Divya S.V., Marymariyal P., Keerthana S. 2024. Predicting natural disasters with AI and machine learning, in: Utilizing AI and Machine Learning for Natural Disaster Management, IGI Global, 2024, pp. 39 - 64, https://doi.org/10.4018/979-8-3693-3362-4.ch003

Wang, X.; Wang, Y.; Pang, Y.; Wang, K.; Yu, J. 2024. Pollution Load Coordination and Eco-Compensation for Trans-Boundary Water Pollution Control: The Case of the Tri-Border Region of the Yangtze Delta. Sustainability, 16: 1151.

World Economic Forum. 2018. Harnessing artificial intelligence for the earth. fourth industrial revolution for the earth series. http://www3.weforum.org/docs/Harnessing_Artificial_Intelligence_for_the_Earth_report_2018.pdf.

Zhao Q, Guo Y, Ye T, Gasparrini A, Tong S, Overcenco A, Urban A, Schneider A, Entezari A, Vicedo-Cabrera AM, et al. Global, regional, and national burden of mortality associated

with non-optimal ambient temperatures from 2000 to 2019: a three-stage modelling study. Lancet Planet Health. 5:e415–e425. doi: 10.1016/S2542-5196(21)00081-4

Zscheischler, J., and Coauthors, 2020: A typology of compound weather and climate events. Nat. Rev. Earth Environ., 1 : 333 - 347, https://doi.org/10.1038/s43017-020-0060-z.

ARTICLES

A Mathematical Model of Lassa Fever Dynamics in Nigeria via Caputo–Fabrizio Fractional Order Derivatives

Abdullahi M. Auwal[1,2] and Salisu Usaini[2]

[1]Mathematics and Statistics Department, Federal Polytechnics Bauchi

[2]Department of Mathematics, Faculty of Computing and Mathematical Sciences, Aliko Dangote University of Science and Technology, Wudil Kano State

[1*]Corresponding author: [1]maabdullahi@fptb.edu.ng

Abstract

In this work, we developed and examined a fractional order mathematical model for the dynamics of the Lassa fever epidemic that includes infected, corpse-related infectious, and treated human populations via Caputo fractional order derivatives. In this model, the fixed-point theory is used to prove the existence and uniqueness of the solution. The model is shown to be mathematically well-posed and we computed the basic reproduction number $\mathcal{R}_0$ via the next generation matrix method. The dynamic model is approximated using the Adams-Bashforth-Moulton approach, which is based on the Predator-Corrector algorithm to solve the Caputo-Fabrizio fractional derivatives. Our simulation results suggest a threshold for β_2 and φ below which the outbreak is manageable and does not result in a significant peak, as maintenance of β_2 and φ below this critical value (e.g., $\beta_2 < 0.5$ and $\varphi < 1.0$) is essential for preventing large-scale of rodent-to-human and corpse-related outbreaks respectively. We observed that fractional differential equations (FDEs) simulation results account for memory effects and capture more complex interaction, such as the lingering infectiousness of some individuals. A slower rise in infections and prolonged epidemic duration in FDEs align more realistically with observed outbreaks of the Lassa fever disease.

Keywords: Caputo fractional order derivative, fixed-point theory, Lassa virus; data fitting; numerical scheme

1. Introduction

Lassa hemorrhagic fever, often known as Lassa fever, is an infectious zoonotic virus disease instigated by the Lassa virus (Peterson *et al*., 2014; Ibrahim & Dénes, 2021). The multimammate rat (mastomys) is one of the most prevalent rodent species in Sub-Saharan Africa and serves as the virus's primary host (Zhao et al., 2020). The yearly occurrence and reoccurrences of Lassa virus cases are caused by a number of things, including inadequate medical facilities, Poor personal hygiene and a filthy environment combined with natural climate elements like rainfall and the flow of farmed food into our communities. Mastomys rodents, the host reservoir, are more likely to migrate from their natural habitat to the human environment as a result of these activities. However, Human efforts to lower the disease's transmission proportion are necessary to combat the

prevalence of Lassa fever (Zhao et al., 2020; Onah & Collins, 2020). It is anticipated that infected persons will begin exhibiting signs of Lassa fever after the exposure period, which ranges from 6 to 21 days. In severe cases, an infected person may develop additional complications like facial swelling, nose bleeding, respiratory distress, and low blood pressure, even though about 80% of infected humans only have mild symptoms like headaches, coughing, muscle pain, sore throat, weakness, and fever (Ibrahim & Dénes, 2021; Peter et al., 2020). In more severe cases, neurological issues caused by this illness might result in mortality fourteen days after the onset of symptoms (Ibrahim & Dénes, 2021).

Although secondary infection from human-to-human and laboratory transmissions are also possible, the Lassa virus is mainly transmitted to humans through human contact with food or materials contaminated by the urine or feces of an infected rodent (Musa et al., 2020). Since there is currently no vaccine to prevent Lassa fever, infection prevention is crucial to limiting the disease's spread within a community. As it is currently impractical to eradicate the mastomys rodent population, current strategies to prevent the spread of this infection include encouraging good personal hygiene to avoid coming into contact with the secretions or excretions of infected rodents and establishing standard medical facilities for efficient patient testing, diagnosis, and treatment (Davies et al., 2019). Since there is currently no known cure or vaccine for Lassa fever, ribavirin, an antiviral drug, has been found to be an effective treatment for patients with Lassa fever if used as directed (Mariën et al., 2019; Musa et al., 2020). Thus, it is imperative that researchers investigate novel approaches and strategies to enhance comprehension of the epidemic process and prevent the virus from spreading.

However, over the past ten years, mathematical models have emerged as essential resources for researching the dynamics of diseases in a given population. Recent advances in the application of mathematical models, like the one in (Ibrahim & Dénes, 2021; Musa et al., 2020), have been constructed for various diseases to address particular concerns in an effort to further knowledge of the epidemiology of the disease in question.

Numerous physical problems have been modeled using fractional calculus. Many systems exhibit memory, history, or nonlocal effects, which can be challenging to simulate using integer order derivatives. These are the primary justifications offered for the use of fractional derivatives. Many works now cover the fundamental theory and applications of fractional differential equations and fractional calculus (Mainardi, 1997; Area et al., 2015; Diethelm, 2010 and Kumar et al., 2016). A singularity that arises at the termination point of an interval of definition was identified as the issue with the majority of the early studies' kernels. In the literature, numerous new definitions of fractional derivatives have been put forth as a result.

The primary distinctions between fractional derivatives are their various kernels, which can be chosen to satisfy the needs of various applications. For instance, the Caputo fractional derivative (Diethelm, 2010), the Caputo–Fabrizio derivative (Caputo &Fabrizio, 2015), and the Atangana–Baleanu fractional derivative (Atangana & Gómez-Aguilar, 2018) differ primarily in that the Caputo derivative is defined by a power law, Caputo–Fabrizio derivative described latter by an exponential decay law, and the Atangana–Baleanu derivative latter by a Mittag–Leffler law. Several recent publications have provided examples of how the new fractional operators can be used to solve real-world issues.

For instance, in an investigation of anomalous diffusion, Tateishi et al. (2017) contrasted the classical and new fractional time derivatives. Additionally, in modeling fractional delay differential equations in modeling chaotic systems, Atangana has contrasted the Caputo–Fabrizio fractional derivative and the Atangana–Baleanu fractional derivative (Atangana, 2018). They discovered that because of its unique memory characteristics, the power law derivative of the Riemann–Liouville fractional derivative or the Caputo–Fabrizio fractional derivative gives noisy information. But compared to the power law, the Caputo-Fabrizio fractional derivative produces less noise. Recently, (Caputo & Fabrizio, 2015) created a novel fractional order derivative that accurately depicts the memory effect in a real-world issue and has no singularities in its kernel.

The new fractional derivative's kernel resembles an exponential function. The fractional integral connected to the novel fractional Caputo–Fabrizio fractional derivative was more recently determined by (Losada & Nieto, 2015).

Therefore, this study develops and formulates fractional differential equations (non-integer-order derivatives) for the mathematical model of Lassa fever transmission dynamics by integrating corpse-related infection and treatment of infected humans in order to have percipience on the consequences of various disease transmission pathways based on Nigerian demographic data

2. Description, Formulation, and Analysis of The Mathematical Model

2.1 Model Description

The Lassa fever mathematical model in cooperating infected humans, corpse-related infectious humans, and treated human compartments can be described as follows. The population of total human $N_h(t)$ is considered into susceptible individuals $S(t)$, exposed individuals $E(t)$, infected population $I_1(t)$, corpse-related infections humans $I_2(t)$, the individuals being treated $T(t)$; the individuals who have recovered $R(t)$. Such that $N_h(t) = S(t) + E(t) + I_1(t) + I_2(t) + T(t) + R(t)$. Similarly, the rodent population $N_r(t)$ is considered into Susceptible rodents $S_r(t)$, Infected rodents $I_r(t)$. Such that $N_r(t) = S_r(t) + I_r(t)$.

Hence, we assume that the population is homogeneous in terms of member mixing and that Lassa fever outbreaks in Africa (Nigeria) occur annually for a comparatively long time, allowing a demographic process to occur as a result of new migration and births as well as deaths (natural or disease-related). The following factors served as the foundation for the development of the proposed model.

(a) Before and during burial, deceased humans can still spread the virus to vulnerable groups.
(b) Because environmental contribution is one of the key elements accelerating the transmission process, poor resource countries are primarily at risk of Lassa fever virus environmental transmission.
(c) When rats excrete the virus in their urine or feces, it contaminates the environment. Similarly, when rodents are captured and groomed, infections may arise because they are occasionally eaten.
(d) The human-to-human transmission rate escalates as a result of negligence in healthcare domains prissily due to improper or non-use of personal protective equipment (PPE).

Thus, the human population has the force of infection as $\lambda_h = \frac{\beta_1(I_1+\varphi I_2)+\beta_2 I_r}{N_h}$ and that of the rodent population is $\lambda_r = \frac{\beta_3 I_r}{N_r}$, with β_1 being the effective rate of contact for human-to-human transmission, β_2 is a rodents-to-human effective contact rate, and β_3 is the rodents-to-rodents contact rate. Subsequently, the parameters φ is a modification parameter that measures the transmissibility reduction of corpse-related infectious humans (I_2). Figure 1 displays the model's visual representation, while Tables 1 and 2 provide a detailed description of the flow chart model's parameters and state variables, respectively.

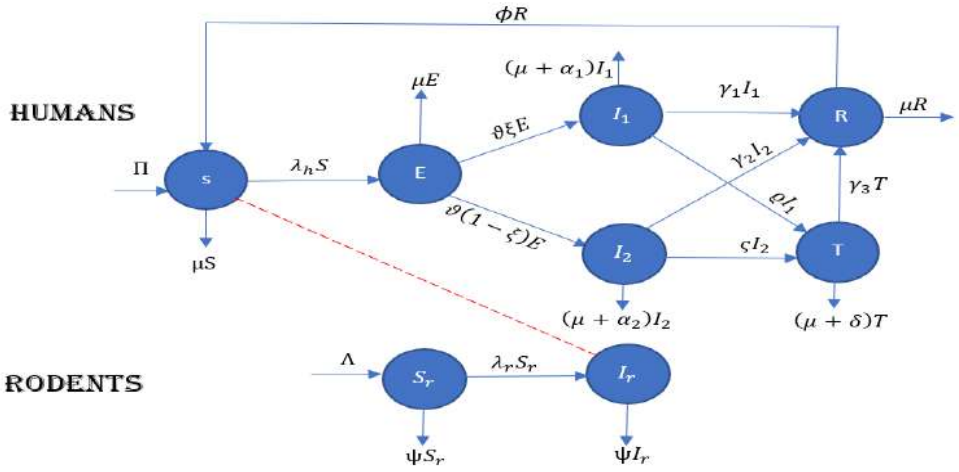

Figure 1. Shows the Model 1 flow diagram.

Table 1.: An Explanation of the Mode's State Variables

Symbol of the Variable	Description
$S(t)$	Susceptible human individuals
$E(t)$	Exposed human individuals
$I_1(t)$	Infected human individuals
$I_2(t)$	Corpse-related infectious humans
$R(t)$	Recovery human individuals
$T(t)$	Treatment human individuals
$S_r(t)$	Susceptible rodents
$I_r(t)$	Infected rodents

Table 2. : An Explanation of the parameters value of the model

Symbol of the Parameters	Descriptions
Π	Recruitment rate of susceptible human population
Λ	Recruitment rate of susceptible rodents' population
μ , ψ	The natural mortality rate for rodents and humans, respectively
ϕ	Immunity decline rate following recovery
$\gamma_1, \gamma_2\ and \gamma_3$	The rate of recovery for infected, treated, and corpse-related infectious individuals
α_1 and α_2	Disease-induced death rate from infected people and infectious humans associated with corpses, respectively
δ	Disease-induced death rate from among infected people in the treated compartment
$\varrho, \varsigma,$	Infected person and corpse-related infectious person rates of transition to treatment class, respectively
$\xi \in (0,1)$	Percentage of newly exposed people who develop symptoms of infection
ϑ	The rate of infectiousness of an exposed person
φ	Transmission rates from coming into contact with the population of infectious humans related to corpses (the transmission rate from contagious human corpses that have not yet been buried)
$\beta_1, \beta_2, \beta_3$	The rate of contact between human-to-human, Rodent-to-human and Rodents-to-Rodent, respectively

2.2 Formulation of Caputo–Fabrizio Fractional Model

Considering the above-mentioned discussions, we now formulate or create the following system of fractional order differential equations to describe the dynamics of Lassa disease transmission:

$$
\begin{aligned}
{}^{CF}D_t^{\rho} S &= \Pi + \phi R - (\lambda_h + \mu)S \\
{}^{CF}D_t^{\rho} E &= \lambda_h S - (\vartheta + \mu)E \\
{}^{CF}D_t^{\rho} I_1 &= \vartheta\xi E - (\gamma_1 + \varrho + \mu + \alpha_1)I_1 \\
{}^{CF}D_t^{\rho} I_2 &= \vartheta(1-\xi)E - (\gamma_2 + \varsigma + \mu + \alpha_2)I_2 \\
{}^{CF}D_t^{\rho} T &= \varrho I_1 + \varsigma I_2 - (\gamma_3 + \mu + \delta)T
\end{aligned} \tag{1}
$$

$$_{CF}D_t^{\rho}R = \gamma_1 I_1 + \gamma_2 I_2 + \gamma_3 T - (\phi + \mu)R$$

$$_{CF}D_t^{\rho}S_r = \Lambda - (\lambda_r + \psi)S_r$$

$$_{CF}D_t^{\rho}I_r = \lambda_r S_r - \psi I_r$$

where $_{CF}D_t^{\rho}$represents the Caputo-Fabrizio fractional derivative of order $0 < \rho \leq 1$, with the non-negative initial conditions

the Caputo-Fabrizio fractional derivative with non-negative initial conditions of order $0 < \rho \leq 1$.

$$S(0) = S_0, E(0) = E_0, I_1(0) = I_{1_0}, I_2(0) = I_{2_0}, T(0) = T_0, R(0) = R_0\ , T(0) = S_{r_0},$$
$$I_r(0) = I_{r_0} \quad (2)$$

3. Fundamental Model Properties

3.1 Existence and Uniqueness of Solutions of The Model

To evaluate and prove the existence and uniqueness of the solutions of the Caputo–Fabrizio fractional model for the Lassa fever virus epidemic in (1) with initial conditions (2), we use fixed point theory as in (Kreyszig, 1978; Hunter & Nachtergaele, 2021).

Applying the Caputo–Fabrizio fractional integral operator on either side of (1), there are

$$S(t) - S(0) = {}_{CF}I_t^{\rho}[\Pi + \phi R - (\lambda_h + \mu)S],$$

$$E(t) - E(0) = {}_{CF}I_t^{\rho}[\lambda_h S - (\vartheta + \mu)E],$$

$$I_1(t) - I_1(0) = {}_{CF}I_t^{\rho}[\,\vartheta\xi E - (\gamma_1 + \varrho + \mu + \alpha_1)I_1],$$

$$I_2(t) - I_2(0) = {}_{CF}I_t^{\rho}[\vartheta(1-\xi)E - (\gamma_2 + \varsigma + \mu + \alpha_2)I_2],$$

$$T(t) - T(0) = {}_{CF}I_t^{\rho}[\varrho I_1 + \varsigma I_2 - (\gamma_3 + \mu + \delta)T\ ], \quad (3)$$

$$R(t) - R(0) = {}_{CF}I_t^{\rho}[\gamma_1 I_1 + \gamma_2 I_2 + \gamma_3 T - (\phi + \mu)R]$$

$$S_r(t) - S_r(0) = {}_{CF}I_t^{\rho}[\,\Lambda - (\lambda_r + \psi)S_r],$$

$$I_r(t) - I_r(0) = {}_{CF}I_t^{\rho}[\lambda_r S_r - \psi I_r],$$

The system (1) kernels can thus be expressed as follows:

$$K_1(t, S) = \Pi + \phi R - (\lambda_h + \mu)S\ ,$$

$$K_2(t, E) = \lambda_h S(t) - (\vartheta + \mu)E(t),$$

$$K_3(t, I_1) = \vartheta\xi E(t) - (\gamma_1 + \varrho + \mu + \alpha_1)I_1(t),$$

$$K_4(t, I_2) = \vartheta(1-\xi)E(t) - (\gamma_2 + \varsigma + \mu + \alpha_2)I_2(t),$$

$$K_5(t,T) = \varrho I_1(t) + \varsigma I_2(t) - (\gamma_3 + \mu + \delta)T(t), \tag{4}$$

$$K_6(t,R) = \gamma_1 I_1(t) + \gamma_2 I_2(t) + \gamma_3 T(t) - (\phi + \mu)R(t),$$

$$K_7(t,S_r) = \Lambda - (\lambda_r + \psi)S_r(t),$$

$$K_8(t,I_r) = \lambda_r S_r(t) - \psi I_r(t),$$

And the functions $\Xi(\rho) = \frac{2(1-\rho)}{(2-\rho)M(\rho)}$ and $\Theta(\rho) = \frac{2\rho}{(2-\rho)M(\rho)}$ (5)

Thus, we assume that S, E, I_1, I_2, T, R, and S_r, I_r are nonnegative bounded functions, when proving the following theorems, i.e.,

$$\|S(t)\| \le \theta_1, \|E(t)\| \le \theta_2, \| I_1(t)\| \le \theta_3, \| I_2(t)\| \le \theta_4,$$

$$\|T(t)\| \le \theta_5, \|R(t)\| \le \theta_6, \| S_r(t)\| \le \theta_7 \text{ and } \|I_r(t)\| \le \theta_8$$

where $\theta_1, \theta_2, \theta_3, \theta_4, \theta_5, \theta_6, \theta_7$ and θ_8 are some positive constants.

Now let

$$\Delta_1 = \lambda_h + \mu, \Delta_2 = \vartheta + \mu, \Delta_3 = \mu + \gamma, \Delta_4 = \gamma_1 + \varrho + \mu + \alpha_1, \Delta_5 = \gamma_2 + \varsigma + \mu + \alpha_2, \Delta_6 = \mu + \gamma, \Delta_7 = \psi \text{ and } \Delta_8 = \lambda_r + \psi \tag{6}$$

We obtain the following equations using the Caputo-Fabrizio fractional integral operator described in (3).

$$\begin{aligned}
S(t) - S(0) &= \Xi(\rho)K_1(t,S) + \Theta(\rho)\int_0^t K_1(y,S)dy,\\
E(t) - E(0) &= \Xi(\rho)K_2(t,E) + \Theta(\rho)\int_0^t K_2(y,E)dy,\\
I_1(t) - I_1(0) &= \Xi(\rho)K_3(t,I_1) + \Theta(\rho)\int_0^t K_3(y,I_1)dy,\\
I_2(t) - I_2(0) &= \Xi(\rho)K_4(t,I_2) + \Theta(\rho)\int_0^t K_4(y,I_2)dy,\\
T(t) - T(0) &= \Xi(\rho)K_5(t,T) + \Theta(\rho)\int_0^t K_5(y,T)dy,\\
R(t) - R(0) &= \Xi(\rho)K_6(t,R) + \Theta(\rho)\int_0^t K_6(y,R)dy\\
S_r(t) - S_r(0) &= \Xi(\rho)K_7(t,S_r) + \Theta(\rho)\int_0^t K_7(y,S_r)dy,\\
I_r(t) - I_r(0) &= \Xi(\rho)K_8(t,I_r) + \Theta(\rho)\int_0^t K_8(y,I_r)dy,
\end{aligned} \tag{7}$$

Theorem 1: If the following inequality holds

$$0 \le M = \max\{\Delta_1, \Delta_2, \Delta_3, \Delta_4, \Delta_5, \Delta_6, \Delta_7, \Delta_8\} < 1, \tag{8}$$

then the kernels $K_1, K_2, K_3, K_4, K_5, K_6, K_7$ and K_8 satisfy Lipschitz conditions and are contraction mappings.

Proof. We consider the kernel K_1. Let S and S_1 be any two functions, then we have

$$\|K_1(t,S) - K_1(t,S_I)\| = \|-\lambda_h(S(t) - S_1(t)) - \mu(S(t) - S_1(t))\| \tag{9}$$

Applying the triangle inequality to the norms on (9), we have

$$\|K_1(t,S) - K_1(t,S_I)\| \le \left\|-\lambda_h\big(S(t) - S_1(t)\big)\right\| + \left\|\mu\big(S(t) - S_1(t)\big)\right\|$$

$$\leq (\lambda_h + \mu)\|S(t) - S_1(t)\|$$
$$\leq (\lambda_h + \mu)\|S(t) - S_1(t)\|$$
$$= \Delta_1\|S(t) - S_1(t)\|.$$

Where Δ_1 is as defined in (6). Comparable outcomes for the kernels $K_2, K_3, K_4, K_5, K_6, K_7$ and K_8 can be obtained using $\{E, E_1\}$,$\{I_1, I_{1_1}\}$, $\{I_2, I_{2_1}\}$,$\{T, T_1\}$, $\{R, R_1\}$,$\{S_r, S_{r_1}\}$ and $\{I_r, I_{r_1}\}$, respectively, as follows:

$$\|K_2(t, E) - K_2(t, E_I)\| \leq \Delta_2\|E(t) - E_1(t)\|$$
$$\left\|K_3(t, I_1) - K_3\left(t, I_{1_I}\right)\right\| \leq \Delta_3\left\|I_1(t) - I_{1_1}(t)\right\|$$
$$\left\|K_4(t, I_2) - K_4\left(t, I_{2_I}\right)\right\| \leq \Delta_4\|I_2(t) - I_{21}(t)\|$$
$$\|K_5(t, T) - K_5(t, T_I)\| \leq \Delta_5\|T(t) - T_1(t)\|$$
$$\|K_6(t, R) - K_6(t, R_I)\| \leq \Delta_6\|R(t) - R_1(t)\| \quad (10)$$
$$\left\|K_7(t, S_r) - K_7\left(t, S_{r_I}\right)\right\| \leq \Delta_7\left\|S_r(t) - S_{r_1}(t)\right\|$$
$$\left\|K_8(t, V) - K_8\left(t, I_{r_I}\right)\right\| \leq \Delta_8\left\|S_r(t) - S_{r_1}(t)\right\|$$

where $\Delta_1, \Delta_2, \Delta_3, \Delta_4, \Delta_5, \Delta_6, \Delta_7$ and Δ_8 are defined in (6).

Therefore, the Lipschitz conditions are satisfied for $K_2, K_3, K_4, K_5, K_6, K_7$ and K_8, Furthermore, since $0 \leq M = \max\{\Delta_1, \Delta_2, \Delta_3, \Delta_4, \Delta_5, \Delta_6, \Delta_7, \Delta_8\} < 1$, The kernels make up contractions.

The state variables can be shown in terms of the kernels as follows, based on (7):

$$S(t) = S(0) + \Xi(\rho)K_1(t, S) + \Theta(\rho)\int_0^t K_1(y, S)dy,$$
$$E(t) = E(0) + \Xi(\rho)K_2(t, E) + \Theta(\rho)\int_0^t K_2(y, E)dy,$$
$$I_1(t) = I_1(0) + \Xi(\rho)K_3(t, I_1) + \Theta(\rho)\int_0^t K_3(y, I_1)dy,$$
$$I_2(t) = I_2(0) + \Xi(\rho)K_4(t, I_2) + \Theta(\rho)\int_0^t K_4(y, I_2)dy,$$
$$T(t) = T(0) + \Xi(\rho)K_5(t, T) + \Theta(\rho)\int_0^t K_5(y, T)dy, \quad (11)$$
$$R(t) = R(0) + \Xi(\rho)K_6(t, R) + \Theta(\rho)\int_0^t K_6(y, R)dy,$$
$$S_r(t) = S_r(0) + \Xi(\rho)K_7(t, S_r) + \Theta(\rho)\int_0^t K_7(y, S_r)dy,$$
$$I_r(t) = I_r(0) + \Xi(\rho)K_8(t, I_r) + \Theta(\rho)\int_0^t K_8(y, I_r)dy,$$

We now present the following recursive formulas using (11);

$$S_n(t) = \Xi(\rho)K_1(t, S_{n-1}) + \Theta(\rho)\int_0^t K_1(y, S_{n-1})dy,$$

$$E_n(t) = \Xi(\rho)K_2(t, E_{n-1}) + \Theta(\rho)\int_0^t K_2(y, E_{n-1})dy,$$

$$I_{n1}(t) = \Xi(\rho)K_3\left(t, I_{(n-1)1}\right) + \Theta(\rho)\int_0^t K_3\left(y, I_{(n-1)1}\right)dy,$$

$$I_{n2}(t) = \Xi(\rho)K_4\left(t, I_{(n-1)2}\right) + \Theta(\rho)\int_0^t K_4\left(y, I_{(n-1)2}\right)dy, \quad (12)$$

$$T_n(t) = \Xi(\rho)K_5(t, T_{n-1}) + \Theta(\rho)\int_0^t K_5(y, T_{n-1})dy,$$
$$R_n(t) = \Xi(\rho)K_6(t, R_{n-1}) + \Theta(\rho)\int_0^t K_6(y, R_{n-1})dy$$
$$S_{nr}(t) = \Xi(\rho)K_7\left(t, S_{(n-1)r}\right) + \Theta(\rho)\int_0^t K_7\left(y, S_{(n-1)r}\right)dy,$$
$$I_{nr}(t) = \Xi(\rho)K_8\left(t, I_{(n-1)r}\right) + \Theta(\rho)\int_0^t K_8\left(y, I_{(n-1)r}\right)dy$$

The following initial conditions determine the initial components of the recursive formulas mentioned above:

$$S_0(t) = S(0), E_0(t) = E(0), I_{1_0}(t) = I_1(0), I_{2_0}(t) = I_2(0), T_0(t) = T(0), R_0(t) = R(0),$$
$$S_{r_0}(t) = S_r(0), I_{r_0}(t) = I_r(0) \quad (13)$$

Hence, for the recursive formulas, the difference between the consecutive terms can be expressed as

$$\Upsilon_{1n}(t) = S_n(t) - S_{n-1}(t) = \Xi(\rho)(K_1(t, S_{n-1}) - K_1(t, S_{n-2})) + \Theta(\rho)\int_0^t (K_1\left(y, S_{n-1} - K_1(t, S_{n-2})\right)dy,$$

$$\Upsilon_{2n}(t) = E_n(t) - E_{n-1}(t) = \Xi(\rho)(K_2(t, E_{n-1}) - K_2(t, E_{n-2})) + \Theta(\rho)\int_0^t (K_2\left(y, E_{n-1} - K_2(t, E_{n-2})\right)dy$$

$$\Upsilon_{3n}(t) = I_{1_n}(t) - I_{1_{n-1}} = \Xi(\rho)(K_3\left(t, I_{1_{n-1}}\right) - K_3\left(t, I_{1_{n-2}}\right)) + \Theta(\rho)\int_0^t (K_3\left(y, I_{1_{n-1}} - K_3\left(t, I_{1_{n-2}}\right)\right)dy,$$

$$\Upsilon_{4n}(t) = I_{2_n}(t) - I_{2_{n-1}}(t) = \Xi(\rho)(K_4\left(t, I_{2_{n-1}}\right) - K_4\left(t, I_{2_{n-2}}\right)) + \Theta(\rho)\int_0^t (K_4\left(y, I_{2_{n-1}} - K_4\left(t, I_{2_{n-2}}\right)\right)dy,$$

$$\Upsilon_{5n}(t) = T_n(t) - T_{n-1}(t) = \Xi(\rho)(K_5(t, T_{n-1}) - K_5(t, T_{n-2})) + \Theta(\rho)\int_0^t (K_5\left(y, T_{n-1} - K_5(t, T_{n-2})\right)dy, \quad (14)$$

$$\Upsilon_{6n}(t) = R(t) - R_{n-1}(t) = \Xi(\rho)(K_6(t, R_{n-1}) - K_6(t, R_{n-2})) + \Theta(\rho)\int_0^t (K_6\left(y, R_{n-1} - K_6(t, R_{n-2})\right)dy,$$

$$\Upsilon_{7n}(t) = S_{r_n}(t) - S_{r_{n-1}}(t) = \Xi(\rho)(K_7\left(t, S_{r_{n-1}}\right) - K_7\left(t, S_{r_{n-2}}\right)) + \Theta(\rho)\int_0^t (K_7\left(y, S_{r_{n-1}} - K_7\left(t, S_{r_{n-2}}\right)\right)dy,$$

$$\Upsilon_{8n}(t) = I_{r_n}(t) - I_{r_{n-1}}(t) = \Xi(\rho)(K_8(t, I_{r_{n-1}}) - K_8(t, I_{r_{n-2}})) + \Theta(\rho)\int_0^t (K_8\left(y, I_{r_{n-1}} - K_8(t, I_{r_{n-2}})\right) dy,$$

For $S_n(t) = \sum_{i=1}^n \Upsilon_{1i}(t), E_n(t) = \sum_{i=1}^n \Upsilon_{2i}(t), I_{1_n}(t) = \sum_{i=1}^n \Upsilon_{3i}(t), I_{2_n}(t) = \sum_{i=1}^n \Upsilon_{4i}(t)$

$, T_n(t) = \sum_{i=1}^n \Upsilon_{5n_i}(t), R_n(t) = \sum_{i=1}^n \Upsilon_{6i}(t), S_{r_n}(t) = \sum_{i=1}^n \Upsilon_{7i}(t), I_{r_n}(t) = \sum_{i=1}^n \Upsilon_{8i}(t)$ (15)

Let's now produce the recursive inequalities for the differences $\Upsilon_{1n}, \Upsilon_{2n}, \Upsilon_{3n}, \Upsilon_{4n}, \Upsilon_{5n}, \Upsilon_{6n}, \Upsilon_{7n}$ and Υ_{8n} as follows

$$\|\Upsilon_{1n}(t)\| = \|S_n(t) - S_{n-1}(t)\| = \left\|\Xi(\rho)(K_1(t, S_{n-1}) - K_1(t, S_{n-2})) + \Theta(\rho)\int_0^t (K_1(y, S_{n-1} - K_1(t, S_{n-2}))dy\right\| \quad (16)$$

Triangle inequality for norms to (16) is used, and we get

$$\|S_n(t) - S_{n-1}(t)\| = \|\Xi(\rho) \| K_1(t, S_{n-1}) - K_1(t, S_{n-2})\| + \Theta(\rho)\int_0^t \|K_1(y, S_{n-1}) - K_1(t, S_{n-2})\|dy$$

Consequently, since the kernel K_1has a Lipschitz constantΔ_1, and satisfies the Lipschitz condition, we obtain

$$\|S_n(t) - S_{n-1}(t)\| \leq \|\Xi(\rho)\Delta_1 \| S_{n-1} - S_{n-2}\| + \Theta(\rho)\Delta_1 \int_0^t \|S_{n-1} - S_{n-2}\|dy$$

therefore, $\|\Upsilon_{1n}(t)\| \leq \Xi(\rho)\Delta_1\left\|\Upsilon_{1(n-1)}(t)\right\| + \Theta(\rho)\Delta_1 \int_0^t \left\|\Upsilon_{1(n-1)}(y)\right\|dy$ (17)

Using the same methods, we obtain

$$\|\Upsilon_{2n}(t)\| \leq \Xi(\rho)\Delta_2\left\|\Upsilon_{2(n-1)}(t)\right\| + \Theta(\rho)\Delta_2 \int_0^t \left\|\Upsilon_{2(n-1)}(y)\right\|dy$$

$$\|\Upsilon_{3n}(t)\| \leq \Xi(\rho)\Delta_3\left\|\Upsilon_{3(n-1)}(t)\right\| + \Theta(\rho)\Delta_3 \int_0^t \left\|\Upsilon_{3(n-1)}(y)\right\|dy$$

$$\|\Upsilon_{4n}(t)\| \leq \Xi(\rho)\Delta_4\left\|\Upsilon_{4(n-1)}(t)\right\| + \Theta(\rho)\Delta_4 \int_0^t \left\|\Upsilon_{4(n-1)}(y)\right\|dy$$

$$\|\Upsilon_{5n}(t)\| \leq \Xi(\rho)\Delta_5\left\|\Upsilon_{5(n-1)}(t)\right\| + \Theta(\rho)\Delta_5 \int_0^t \left\|\Upsilon_{5(n-1)}(y)\right\|dy \quad (18)$$

$$\|\Upsilon_{6n}(t)\| \leq \Xi(\rho)\aleph_6\left\|\Upsilon_{6(n-1)}(t)\right\| + \Theta(\rho)\Delta_6 \int_0^t \left\|\Upsilon_{6(n-1)}(y)\right\|dy$$

$$\|\Upsilon_{7n}(t)\| \leq \Xi(\rho)\Delta_7\left\|\Upsilon_{7(n-1)}(t)\right\| + \Theta(\rho)\Delta_7 \int_0^t \left\|\Upsilon_{7(n-1)}(y)\right\|dy$$

$$\|\Upsilon_{8n}(t)\| \leq \Xi(\rho)\Delta_8\left\|\Upsilon_{8(n-1)}(t)\right\| + \Theta(\rho)\Delta_8 \int_0^t \left\|\Upsilon_{8(n-1)}(y)\right\|dy$$

Theorem 2. If there exists a time $t_0 > 0$ such that the following inequalities hold:

$$\Xi(\rho)\Delta_i + \Theta(\rho)\,\Delta_i t_0 > 1, \text{ for } i = 1,2,\dots,8, \quad (19)$$

then the solution exists for the fractional Lassa fever virus model (1) with (2).

Proof. Assuming the functions $S(t), E(t), I_1(t), I_2(t), T(t), R(t), S_r(t)$ and $I_r(t)$ are bounded and each of the kernels satisfies a Lipschitz condition, then the following relations can be obtained.

Utilizing the idea of (18)– (19) recursively:

$$\begin{aligned}
\|\Upsilon_{1n}(t)\| &\leq \|S(0)\|[\Xi(\rho)\Delta_1 + \Theta(\rho)\Delta_1]^n \\
\|\Upsilon_{2n}(t)\| &\leq \|E(0)\|\,[\Xi(\rho)\Delta_2 + \Theta(\rho)\Delta_2]^n \\
\|\Upsilon_{3n}(t)\| &\leq \|\,I_1(0)\|[\Xi(\rho)\Delta_3 + \Theta(\rho)\Delta_3]^n \\
\|\Upsilon_{4n}(t)\| &\leq \|\,I_2(0)\|[\Xi(\rho)\Delta_4 + \Theta(\rho)\Delta_4]^n \\
\|\Upsilon_{5n}(t)\| &\leq \|T(0)\|[\Xi(\rho)\Delta_5 + \Theta(\rho)\Delta_5]^n \\
\|\Upsilon_{6n}(t)\| &\leq \|R(0)\|[\Xi(\rho)\Delta_6 + \Theta(\rho)\Delta_6]^n \\
\|\Upsilon_{7n}(t)\| &\leq \|\,S_r(0)\|[\Xi(\rho)\Delta_7 + \Theta(\rho)\Delta_7]^n \\
\|\Upsilon_{8n}(t)\| &\leq \|\,I_r(0)\|[\Xi(\rho)\Delta_8 + \Theta(\rho)\Delta_8]^n
\end{aligned} \tag{20}$$

Equation (20) shows the existence and smoothness of the functions defined in (16). To complete the proof, we prove that the functions $S_n(t), E_n(t), I_{1_n}(t), I_{2_n}(t), T_n(t), R_n(t), S_r(t)$ and $I_r(t)$ converge to a solution of (1) $with$ (2).

We introduce $B_n(t), C_n(t), E_n(t), F_n(t), G_n(t), H(t), U_n(t)$ and $W_n(t)$, as the remainder terms after n iteration, so that

$$\begin{aligned}
S(t) - S(0) &= S_n(t) - B_n(t), \\
E(t) - E(0) &= E_n(t) - C_n(t), \\
I_1(t) - I_1(0) &= I_{1_n}(t) - E_n(t), \\
I_2(t) - I_2(0) &= I_{2_n}(t) - F_n(t), \\
T(t) - T(0) &= T_n(t) - G_n(t),, \\
R(t) - R(0) &= R_n(t) - H_n(t), \\
S_r(t) - S_r(0) &= S_{r_n}(t) - U_n(t), \\
I_r(t) - I_r(0) &= I_{r_n}(t) - W_n(t),
\end{aligned} \tag{21}$$

Next, applying the Lipschitz and triangle inequality condition for K_1, we have

$$\begin{aligned}
\|B_n(t)\| &= \left\|\Xi(\rho)(K_1(t,S) - K_1\big(t,S_{n-1)}\big)) + \Theta(\rho)\int_0^t (K_1(y,S) - K_1(y,S_{n-1}))dy\right\| \\
&\leq \Xi(\rho)\|(K_1(t,S) - K_1(t,S_{n-1})\| + \Theta(\rho)\int_0^t \|K_1(y,S) - K_1(y,S_{n-1})\|dy \\
&\leq \Xi(\rho)\Delta_1\|S - S_{n-1}\| + \Theta(\rho)\Delta_1 B_n(t)\|S - S_{n-1}\|t.
\end{aligned}$$

Repeating the same procedure again, we have

$$\|B_n(t)\| \leq [(\Xi(\rho) + \Theta(\rho)t)\Delta_1]^{n+1}\theta_1 \quad (22)$$

At t_0 we have

$$\|B_n(t)\| \leq [(\Xi(\rho) + \Theta(\rho)t_0)\Delta_1]^{n+1}\theta_1 \quad (23)$$

Using condition (19) and taking the limit on(23) as $n \to \infty$, we get $\|Bn(t)\| \to 0$. We have the following relations using the same procedure as previously mentioned:

$$\|C_n(t)\| \leq [(\Xi(\rho) + \Theta(\rho)t_0)\Delta_2]^{n+1}\theta_2 \quad (24)$$

$$\|E_n(t)\| \leq [(\Xi(\rho) + \Theta(\rho)t_0)\Delta_3]^{n+1}\theta_3 \quad (25)$$

$$\|F_n(t)\| \leq [(\Xi(\rho) + \Theta(\rho)t_0)\Delta_4]^{n+1}\theta_4 \quad (26)$$

$$\|G_n(t)\| \leq [(\Xi(\rho) + \Theta(\rho)t_0)\Delta_5]^{n+1}\theta_5 \quad (27)$$

$$\|H_n(t)\| \leq [(\Xi(\rho) + \Theta(\rho)t_0)\Delta_6]^{n+1}\theta_6 \quad (28)$$

$$\|U_n(t)\| \leq [(\Xi(\rho) + \Theta(\rho)t_0)\Delta_7]^{n+1}\theta_7 \quad (29)$$

$$\|W_n(t)\| \leq [(\Xi(\rho) + \Theta(\rho)t_0)\Delta_8]^{n+1}\theta_8 \quad (30)$$

Similarly, using condition (19) and taking the limit on $(24) - (30)$ as $n \to$, we obtain $\|C_n(t)\| \to 0, \|E_n(t)\| \to 0$, $\|F_n(t)\| \to 0, \|G_n(t)\| \to 0, \|H_n(t)\| \to 0, \|U_n(t)\| \to 0$ and $\|W_n(t)\| \to 0$. Hence, the existence of solutions of the model system (1) with (2) is proved.

The following requirements are now taken into consideration for the system of solutions to be unique.

Theorem 3. System (1) along with the initial conditions (2) has a unique solution if the following conditions hold: $(1 - \Xi(\rho)\Delta_i + \Theta(\rho)\Delta_i t > 0)$, for $i = 1,2, \ldots ,8$. (31)

Proof. Assume that $\{S(t), E(t),\ I_1(t),\ I_2(t), T(t), R(t),\ S_r(t)\ ,\ I_r(t)\ \}$ is another set of solutions for the model (1) with (2) in addition to the solution set $\{S(t), E(t),\ I_1(t),\ I_2(t), T(t), R(t),\ S_r(t)\ ,\ I_r(t)\ \}$ proved to exist in Theorem 1 and 2 then

$$S(t) - S_1(t) = \Xi(\rho)(K_1(t,S) - K_1(t,S_1) + \Theta(\rho)\int_0^t (K_1(y,S) - K_1(y,S_1))dy, \quad (32)$$

Using the triangle inequality and the norm on either side of (32), we get

$$\|S(t) - S_1(t)\| \leq \Xi(\rho)\|K_1(t,S) - K_1(t,S_1)\| + \Theta(\rho)\int_0^t \|(K_1(y,S) - K_1(y,S_1)\| \quad (33)$$

With the kernel K_1 and the Lipschitz condition, we determine

$$\|S(t) - S_1(t)\| \leq \Xi(\rho)\Delta_1\|S(t) - S_1(t)\| + \Theta(\rho)\Delta_1 t\|S(t) - S_1(t)\| \quad (34)$$

Rearranging (33), we have

$$\|S(t) - S_1(t)\|1 - \Xi(\rho)\Delta_i + \Theta(\rho)\Delta_i t \leq 0 \quad (35)$$

Lastly, putting in condition (33) for $i\ =\ 1$ to (35), we have

$$\|S(t) - S_1(t)\| = 0 \quad (36)$$

Hence $S(t) = S_1(t)$. Now, putting in a comparable process to each of the subsequent pairs $(E(t), E_1(t)), (I_1(t), I_{1_1}(t))$, $(I_2(t), I_{2_1}(t)), (T(t), T_1(t))$ $(R(t), R_1(t)), (S_r(t), S_{r_1}(t))$

and $(I_r(t), I_{r_1}(t))$ together with inequality (33) for $i = 1,2, \ldots, 8$, respectively, we get

$$E(t) = E_1(t),\ I_1(t) = I_{1_1}(t),\ I_2(t) = I_{2_1}(t), T(t) = T_1(t), R(t) = R_1(t),\ S_r(t) = S_{r_1}(t)$$

$$\text{and}\ \ I_r(t) = I_{r_1}(t). \tag{37}$$

Consequently, it is demonstrated that the fractional order system's solutions are unique. Hence, the proof.

3.2 Positivity and Boundedness of Solutions

Since the system keeps an eye on both rodent and human populations, all related parameters are nonnegative. Therefore, in order to maintain model (1) biological validity, we need to demonstrate that the fractional-order system (1) solutions with the force of infection are bounded and positive for $t > 0$.

Theorem 4. Let the conditions $S(0) > 0, E(0) \geq 0, I_1(0) \geq 0, I_2(0) \geq 0, T(0) \geq 0, R(0) \geq 0, S_r(0) > 0,$ and $I_r(0) \geq 0,$ then $S(t), E(t), I_1(t), I_2(t), T(t), R(t), S_r(t)\ and\ I_r(t)$ of the model (1) are positive for all $t \geq 0$.

Proof. Suppose $S(t)$ is not positive, then there exists a first time, say $t^* > 0$, such that $S(t) > 0$ for all $t \in [0, t^*)$ and $S(t^*) = 0$. By inspection of the equation of $E(t)$, we have that

${}_{CF}D_t^{\rho} E \geq -(\vartheta + \mu)\, E(t), for\ \ t \in [0, t^*)$. Hence, it follows that, $E > 0\ for\ t \in [0, t^*)$.

Therefore, it is evident from model (1) first equation that

$$ {}_{CF}D_t^{\rho} S \geq -(\lambda_h + \mu) S(t), for\ t \in [0, t^*).$$

It follows that $S(t^*) > 0$ which contradicts $S(t^*) = 0$. Therefore, $S(t)$ is positive.

Using a similar approach as that for $S(t)$, it is easy to show that $(t) > 0,\ I_1(t) > 0,\ I_2(t) > 0, T(t) > 0,\ R(t) > 0,\ S_r(t) > 0$ and $I_r(t) > 0$. Hence the proof.

3.3 Invariant Region

We now perform the following analysis of a fractional-order system (1) in a biologically feasible region

$$\Omega = \Omega_h \times \Omega_r \in \mathbb{R}_+^6 \times \mathbb{R}_+^2$$

with

$$\Omega_h = \{(S, E,\ I_1,\ I_2, T, R) \in \mathbb{R}_+^6 : N_h \leq \frac{\Pi}{\mu}\ \} \text{ and } \Omega_r = \left\{ (S_r,\ I_r) \in \mathbb{R}_+^2 : N_r \leq \frac{\Lambda}{\psi} \right\}:$$

It is demonstrated that the set Ω is a globally attractive set and a positively invariant set of this system. The implication is that any phase trajectory that starts in the nonnegative area or region $\mathbb{R}_+^8$ moves into the feasible region Ω and stays there.

Lemma 1. The biologically feasible region $\Omega = \Omega_h \cup \Omega_r \subset \mathbb{R}_+^6 \times \mathbb{R}_+^2$ of the Lassa fever model (1) is positively invariant with nonnegative initial conditions in $\mathbb{R}_+^8$.

Proof To prove that Ω is positively invariant (i.e., for every $t > 0$, solutions in Ω stay in Ω.). The rate at which the total human population is changing $N_h$and that of rodent N_r in Caputo's sense are

$$ {}_{CF}D_t^{\rho} N_h(t) = \Pi - \mu N_h(t) - \{(\alpha_1) I_1(t) + (\alpha_2) I_2(t) + (\delta) T(t)\} $$

and

$$ {}_{CF}D_t^{\rho} N_r(t) = \Lambda - \psi N_r(t) $$

so that,

$$ {}_{CF}D_t^{\rho} N_h(t) \leq \Pi - \mu N_h(t) \; and \; {}_{CF}D_t^{\rho} N_r(t) \leq \Lambda - \psi N_r(t) \tag{38} $$

Hence, $N_h(t) \leq \mu N_h(0) e^{\mu t} + \frac{\Pi}{\mu}(1 - e^{-\mu t})$ and $N_r(t) \leq \psi N_r(0) e^{\psi t} + \frac{\Lambda}{\psi}\left(1 - e^{-\psi t}\right)$.

In particular, $N_h(t) \leq \frac{\Pi}{\mu}$ and $N_r(t) \leq \frac{\Lambda}{\psi}$ if the total human and rodent population at the initial instant of time, $N_h(0) \leq \frac{\Pi}{\mu}$ and $N_r(0) \leq \frac{\Lambda}{\psi}$, respectively. So, the region Ω is positively invariant. Therefore, the dynamics of Lassa fever controlled by a fractional-order system (1) can be appropriately studied in the biologically feasible area Ω, where the model is thought to be mathematically and epidemiologically well posed.

3.4 Lassa Fever Disease-Free Equilibrium

To determine the steady-state solution without Lassa fever infection, one can find the Lassa fever disease-free equilibrium of the fractional-order system (1). This entails solving the ensuing algebraic equations concurrently with setting the right-hand side of equation (1) to zero. Hence, the disease-free equilibrium state is represented by $\mathcal{E}_0$.

$$ \mathcal{E}_0 = (S^*, E^*, {I_1}^*, {I_2}^*, T^*, R^*, S_r^*, I_r^*) = \left(\frac{\Pi}{\mu}, 0,0,0,0,0, \frac{\Lambda}{\psi}, 0\right) \tag{39} $$

3.5 Basic Reproduction Number

The typical number of Lassa fever cases that an infected person can produce in a fully susceptible human population is measured by the epidemiological quantity $\mathcal{R}_0$, often known as the reproduction number. We calculate the reproduction number $\mathcal{R}_0$ of the fractional model (1) using the next-generation matrix approach.

For the new infection terms and the remaining transfer or transition terms, the matrices F and V are as follows, using the notation in (Van den Driessche & Warmouth, 2002).

$$ F = \begin{pmatrix} 0 & \beta_1 & \beta_1 \varphi & \beta_2 \\ 0 & 0 & 0 & 0 \\ 0 & 0 & 0 & 0 \\ 0 & 0 & 0 & \beta_3 \end{pmatrix} \text{ and } V = \begin{pmatrix} \vartheta + \mu & 0 & 0 & 0 \\ -\vartheta\xi & \mu + \alpha_1 + \gamma_1 + \varrho & 0 & 0 \\ -\vartheta(1-\xi) & 0 & \mu + \alpha_2 + \gamma_2 + \varsigma & 0 \\ 0 & 0 & 0 & \psi \end{pmatrix} $$

Therefore, the spectral radius of the next-generation matrix $FV^{-1}$is the basic reproduction $\mathcal{R}_0$ of model (1). Consequently, the corresponding reproduction number, represented by $\mathcal{R}_0$, is provided by

$$\mathcal{R}_0 = \frac{Q_1Q_2Q_4\beta_3+Q_2Q_3\varphi\psi\beta_1+Q_4\vartheta\xi\psi\beta_1}{Q_1Q_2Q_4\psi} = \mathcal{R}_{0h} + \mathcal{R}_{0r} \quad (40)$$

Where $\mathcal{R}_{0h} = \frac{\beta_1(Q_2Q_3\varphi+Q_4\vartheta\xi)}{Q_1Q_2Q_4}$ (41)

$$\mathcal{R}_{0r} = \frac{\beta_3}{\psi} \quad (42)$$

With $Q_1 = (\vartheta + \mu),\ Q_2 = (\mu + \alpha_1 + \gamma_1 + \varrho), Q_3 = \vartheta - \vartheta\xi,\ Q_4 = (\mu + \alpha_2 + \gamma_2 + \varsigma),$

$Q_5 = (\mu + \delta + \gamma_3)$ (43)

The basic reproduction number of the human population, $\mathcal{R}_{0h}$, and the basic reproduction number of the rodent population, $\mathcal{R}_{0r}$, were defined by the threshold quantity $\mathcal{R}_0$ in equation (40). These quantities indicate the respective contributions of the human and rodent populations to the risk of Lassa disease. However, the next-generation method's calculation of $\mathcal{R}_0$ assumes that the disease-free equilibrium is locally stable. This leads to the following Theorem.

Theorem 5. The disease-free equilibrium of model (1) is locally asymptotically stable whenever $\mathcal{R}_0 < 1$ and unstable if $\mathcal{R}_0 > 1$.

Thus, Theorem 5 epidemiologically implies that the transmission of Lassa disease might be mitigated when the value of $\mathcal{R}_0$ is systematically reduced below unity.

4. Data Fitting and Parameter Estimation

The model system's governing equations and the total number of confirmed Lassa fever cases recorded between 2019 and 2021 (Nigeria Centre for Disease Control [NCDC], 2023) were used to fit the model data and estimate some of the unknown parameter values. Using model data fitting procedures via traditional nonlinear least squares methods, we created a program code that was generated and executed on MATLAB ODE45 solvers, as indicated in Table 3. Figure 2 shows the visual depiction of the data fitting of the model using the cumulative confirmed cases.

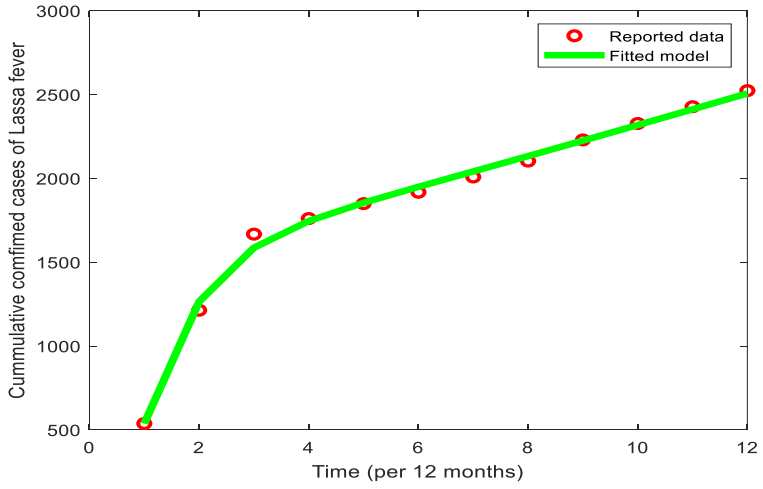

Figure 2. Fitting a Model to Nigerian of cumulative confirmed cases of Lassa fever cases

Table 3. Baseline Parameter values for the model

Parameter	Descriptions	Value	Source
Π	Rate of recruitment of susceptible human	68088	Ojo *et al., (2022)*
Λ	Rate of recruitment of susceptible rodents	557	Ojo *et al., (2022)*
μ	The natural mortality rate for human	0.000053	Ojo *et al., (2022)*
Ψ	The natural mortality rate for rodents	0.003	Collins *et al., (2023)*
ϕ	Immunity decline rate following recovery	0.7246	Fitted
γ_1	The rate of recovery for infected human	0.7194	Fitted
γ_2	The rate of recovery for treated human	0.7285	Fitted
γ_3	The rate of recovery for Corpse-related infectious humans	1.5472	Fitted
α_1	Disease-induced death rate from infected people	0.484	Collins *et al., (2023)*
α_2	Disease-induced death rates from infectious humans associated with corpses	0.484	Collins *et al., (2023)*
δ	Disease-induced death rate from disease among infected people in the treated compartment	0.8	Collins *et al., (2023)*
ς	corpse-related infectious person rates of transition to treatment class	0.4325	Fitted
ϱ	Infected person rates of transition to treatment class	0.7774	Fitted
ξ	Percentage of newly exposed people who develop symptoms of infection	0.4182	Fitted
ϑ	The rate of infectiousness of an exposed person	1.7169	Fitted
φ	Transmission rates from coming into contact with the population of infectious humans related to corpses	0.4955	Fitted
β_1	The rate of contact between human-to-human	0.1682	Fitted
β_2	The rate of contact between rodents -to-human	0.0071	Fitted

β_3	The rate of contact between rodents -to- rodent	0.0209	Fitted

5. Adams-Bashforth-Moulton Scheme of the Model System

Here, we approximate the solution to model (1) based on the Predator-Corrector algorithm using the Adams-Bashforth-Moulton approach. Nonetheless, several numerical methods have been put out to address a broad range of real-world, nonlinear Fractional order derivative models. The analytical techniques developed to handle these problems include Adomian Decomposition, finite difference, and the Homotopy Decomposition Method.

Thus, setting $h = \frac{T}{N}, t_n = nh \; and \; n = 0,1,2,\ldots \mathrm{N}\epsilon\mathbb{Z}^+$ as in (Diethelm *et al.*, 2002; Diethelm *et al.*, 2004), then system (1) can be discretized following the approach (Njagarah & Tabi, 2018; Njagarah &Tabi, 2021). Now the corrector values are

$$S_{n+1} = S_0 + \frac{h^\alpha}{\Gamma(\alpha+2)}\left[\Pi - \left(\frac{\beta_1(I^p_{1(n+1)} + \varphi I^p_{2(n+1)}) + \beta_2 I^p_{r(n+1)}}{N^p_{h(n+1)}} - \mu\right)S^p_{n+1} + \phi R^p_{n+1}\right] + \frac{h^\alpha}{\Gamma(\alpha+2)}\sum_{i=0}^{n} x_{i,n+1}\left[\Pi - \left(\frac{\beta_1(I_{1(i)} + \varphi I_{2(i)}) + \beta_2 I_{ri}}{N_{hi}} - \mu\right)S_i + \phi R_i\right],$$

$$E_{n+1} = E_0 + \frac{h^\alpha}{\Gamma(\alpha+2)}\left[\left(\frac{\beta_1(I^p_{1(n+1)} + \varphi I^p_{2(n+1)}) + \beta_2 I^p_{r(n+1)}}{N^p_{h(n+1)}}\right)E^p_{n+1} - (\vartheta+\mu)E^p_{n+1}\right] + \frac{h^\alpha}{\Gamma(\alpha+2)}\sum_{i=0}^{n} x_{i,n+1}\left[\left(\frac{\beta_1(I_{1(i)} + \varphi I_{2i}) + \beta_2 I_{r(i)}}{N_{hi}}\right)S_i - (\vartheta+\mu)E_i\right],$$

$$I_{1(n+1)} = I_{1(0)} + \frac{h^\alpha}{\Gamma(\alpha+2)}\left[\vartheta\xi E^p_{n+1} - (\gamma_1 + \varrho + \mu + \alpha_1)I^p_{1(n+1)}\right] + \frac{h^\alpha}{\Gamma(\alpha+2)}\sum_{i=0}^{n} x_{i,n+1}\left[\vartheta\xi E_i - (\gamma_1 + \varrho + \mu + \alpha_1)I_{1(i)}\right],$$

$$I_{2(n+1)} = I_{2(0)} + \frac{h^\alpha}{\Gamma(\alpha+2)}\left[\vartheta(1-\xi)E^p_{n+1} - (\gamma_2 + \varsigma + \mu + \alpha_2)I^p_{2(n+1)}\right] + \frac{h^\alpha}{\Gamma(\alpha+2)}\sum_{i=0}^{n} x_{i,n+1}\left[\vartheta(1-\xi)E_i - (\gamma_2 + \varsigma + \mu + \alpha_2)I_{2(i)}\right],$$

$$T_{n+1} = T_0 + \frac{h^\alpha}{\Gamma(\alpha+2)}\left[\varrho I^p_{1(n+1)} + \varsigma I^p_{2(n+1)} - (\gamma_3 + \mu + \delta)T^p_{n+1}\right] + \frac{h^\alpha}{\Gamma(\alpha+2)}\sum_{i=0}^{n} x_{i,n+1}\left[\varrho I_{1(i)} + \varsigma I_{2(i)} - (\gamma_3 + \mu + \delta)T_i\right],$$

$$R_{n+1} = R_0 + \frac{h^\alpha}{\Gamma(\alpha+2)}\left[\gamma_1 I^p_{1(n+1)} + \gamma_2 I^p_{2(n+1)} + \gamma_3 T^p_{n+1} - (\phi+\mu)R^p_{n+1}\right] + \frac{h^\alpha}{\Gamma(\alpha+2)}\sum_{i=0}^{n} x_{i,n+1}\left[\gamma_1 I_{1(i)} + \gamma_2 I_{2(i)} + \gamma_3 T_i - (\phi+\mu)R_i\right],$$

$$S_{r(n+1)} = S_{r(0)} + \frac{h^\alpha}{\Gamma(\alpha+2)}\left[\Lambda - \left(\frac{\beta_3 I^p_{r(n+1)}}{N^p_{r(n+1)}} + \psi\right)S^p_{r(n+1)}\right] + \frac{h^\alpha}{\Gamma(\alpha+2)}\sum_{i=0}^{n} x_{i,n+1}\left[\Lambda - \left(\frac{\beta_3 I_{r(i)}}{N_{r(i)}} + \psi\right)S_{r(i)}\right],$$

$$I_{r(n+1)} = I_{r(0)} + \frac{h^\alpha}{\Gamma(\alpha+2)}\left[\left(\frac{\beta_3 I^p_{r(n+1)}}{N^p_{r(n+1)}}\right)S^p_{r(n+1)} - \psi I^p_{r(n+1)}\right] + \frac{h^\alpha}{\Gamma(\alpha+2)}\sum_{i=0}^{n} x_{i,n+1}\left[\left(\frac{\beta_3 I_{r(i)}}{N_{r(i)}}\right)S_{r(i)} - \psi I_{r(i)}\right],$$

Where

$S^p_{n+1} = S_0 + \frac{1}{\Gamma(\alpha)}\sum_{i=0}^{n} y_{i,n+1}\left[\Pi - \left(\frac{\beta_1(I_{1i}+\varphi I_{2i})+\beta_2 I_{ri}}{N_{hi}} - \mu\right)S_i + \phi R_i\right],$

$E^p_{n+1} = E_0 + \frac{1}{\Gamma(\alpha)}\sum_{i=0}^{n} y_{i,n+1}\left[\left(\frac{\beta_1(I_{1i}+\varphi I_{2i})+\beta_2 I_{ri}}{N_{hi}}\right)S_i - (\vartheta+\mu)E_i\right],$

$I^p_{1(n+1)} = I_{1(0)} + \frac{1}{\Gamma(\alpha)}\sum_{i=0}^{n} y_{i,n+1}\left[\vartheta\xi E_i - (\gamma_1+\varrho+\mu+\alpha_1)I_{1(i)}\right],$

$I^p_{2(n+1)} = I_{2(0)} + \frac{1}{\Gamma(\alpha)}\sum_{i=0}^{n} y_{i,n+1}\left[\vartheta(1-\xi)E_i - (\gamma_2+\varsigma+\mu+\alpha_2)I_{2(i)}\right],$

$T^p_{n+1} = T_0 + \frac{1}{\Gamma(\alpha)}\sum_{i=0}^{n} y_{i,n+1}\left[\varrho I_{1(i)} + \varsigma I_{2(i)} - (\gamma_3+\mu+\delta)T_i\right],$

$R^p_{n+1} = R_0 + \frac{1}{\Gamma(\alpha)}\sum_{i=0}^{n} y_{i,n+1}\left[\gamma_1 I_{1(i)} + \gamma_2 I_{2(i)} + \gamma_3 T_i - (\phi+\mu)R_i\right],$

$S^p_{r(n+1)} = S_{r(0)} + \frac{1}{\Gamma(\alpha)}\sum_{i=0}^{n} y_{i,n+1}\left[\Lambda - \left(\frac{\beta_3 I_{r(i)}}{N_{r(i)}} + \psi\right)S_{r(i)}\right],$

$I^p_{r(n+1)} = I_{r(0)} + \frac{1}{\Gamma(\alpha)}\sum_{i=0}^{n} y_{i,n+1}\left[\left(\frac{\beta_3 I_{r(i)}}{N_{r(i)}}\right)S_{r(i)} - \psi I_{r(i)}\right]$,are the predictor values,

with

$$x_{i,n+1} = \begin{cases} n^{\alpha+1} - (n-\alpha)(n+1), & if\ i = 0, \\ (n-i+2)^{n^{\alpha+1}} + (n-i)^{n^{\alpha+1}} - 2(n-i+1)^{n^{\alpha+1}}, & if\ 1 \le i \le n, \\ 1, & if \quad i = n+1, \end{cases}$$

and

$$y_{i,n+1} = \frac{h^{\alpha}}{\alpha}((n-i+1)^{\alpha}(n-i)^{\alpha}), \qquad 0 \le i \le n,$$

where p is the order of accuracy given by $p = \min(2, 1+\alpha)$ see (Diethelm etal., 2004).

5.1 Numerical Computation, Simulation Results, and Discussion

We fitted the model data and estimated some unknown parameter values using the model system's governing equations and the total number of confirmed Lassa fever cases recorded between 2019 and 2021 (Nigeria Centre for Disease Control [NCDC], 2023). For this objective, we created a program code that produced and executed on MATLAB ODE45 solvers utilizing model data fitting approaches via standard nonlinear least squares methods, as indicated in Table 3. Figure 2 shows the visual depiction of the model's data fitting using the total number of confirmed cases.

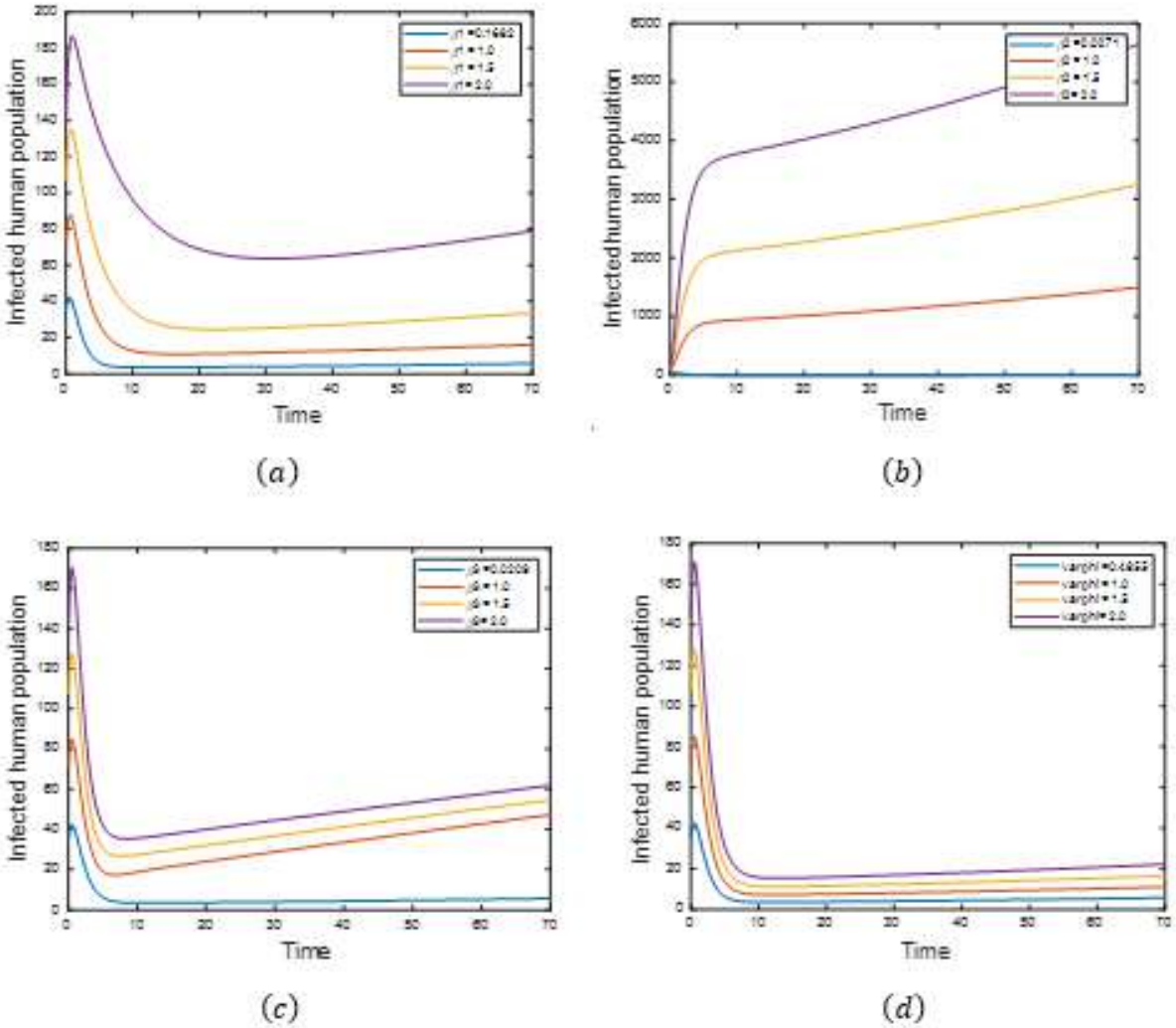

Figure 3. Visual presentation of the infected human population using different initial conditions of $(a)\ \beta_1$, $(b)\ \beta_2$, $(c)\ \beta_3$, (d) φ, with $\rho = 0.7$ at the time in a month

The visual representation of infected human population dynamics under a fractional order $\alpha = 0.7$ with varying $\beta_1$values in Figure 3(a), shows that higher human-to-human contact rates increased disease persistence or sustained the epidemic, although the decay of infections is slower due to persistent memory, representing real-world scenario where past infections influence current dynamics. Moreover, focusing on public health campaigns to promote social distancing and reduce direct contact together with early isolation of symptomatic individuals and contact tracing can significantly lower β_1.

The visual representation of infected human population dynamics under a fractional order $\alpha = 0.7$ with varying β_2 values (rodent-to-human contact rate) indicate that, as β_2 increases, the peak and overall trajectory of the infected human population rise significantly, meaning a higher β_2 indicates an increased rate of transmission from rodent to humans, driving a larger outbreak and sustained infection levels and for smaller values of β_2 the infection remains relatively low, indicating that limiting rat-to-human contact effectively controls the spread. Reducing β_2 should be a primary focus of interventions, as it directly reflects human exposure to infected rodent. Practical measures should include Improved sanitation, rodent control programs and public awareness campaigns. The fractional order effectively slows the disease progression, which can provide a longer window for implementing control measures but might not eliminate the disease without reducing β_2 as depicted in Figure 3(b).

The visual representation of infected human population dynamics under a fractional order $\alpha = 0.7$ with varying β_3 values (rodent-to-rodent contact rate) highlighted that for each β_3, There is an initial sharp peak in the infected human population. The magnitude of the peak is directly proportional to β_3, meaning that higher β_3 values lead to a larger initial outbreak. After the peak, the population exhibits a slower decline or even a steady increase in infections over time. While for lower β_3, the infected population drops quickly and stabilizes near zero, suggesting that controlling rodent interactions effectively limits disease persistence. However, the slower recovery for higher β_3 implies that fractional dynamics capture the prolonged impact of rodent interactions on human infections as depicted in Figure 3(c).

The visual representation of infected human population dynamics under a fractional order $\alpha = 0.7$ with varying φ value (transmission rates due to contact with corpse-related infectious humans) in Figure 3(d) suggesting that limiting corpse-related transmission effectively reduces the outbreak severity and long-term prevalence. The fractional order effectively slows the outbreak's progression, providing more time to implement control measures, these may further delay the peak but require additional strategies (e.g., reducing other transmission parameters like β_2) to achieve eradication.

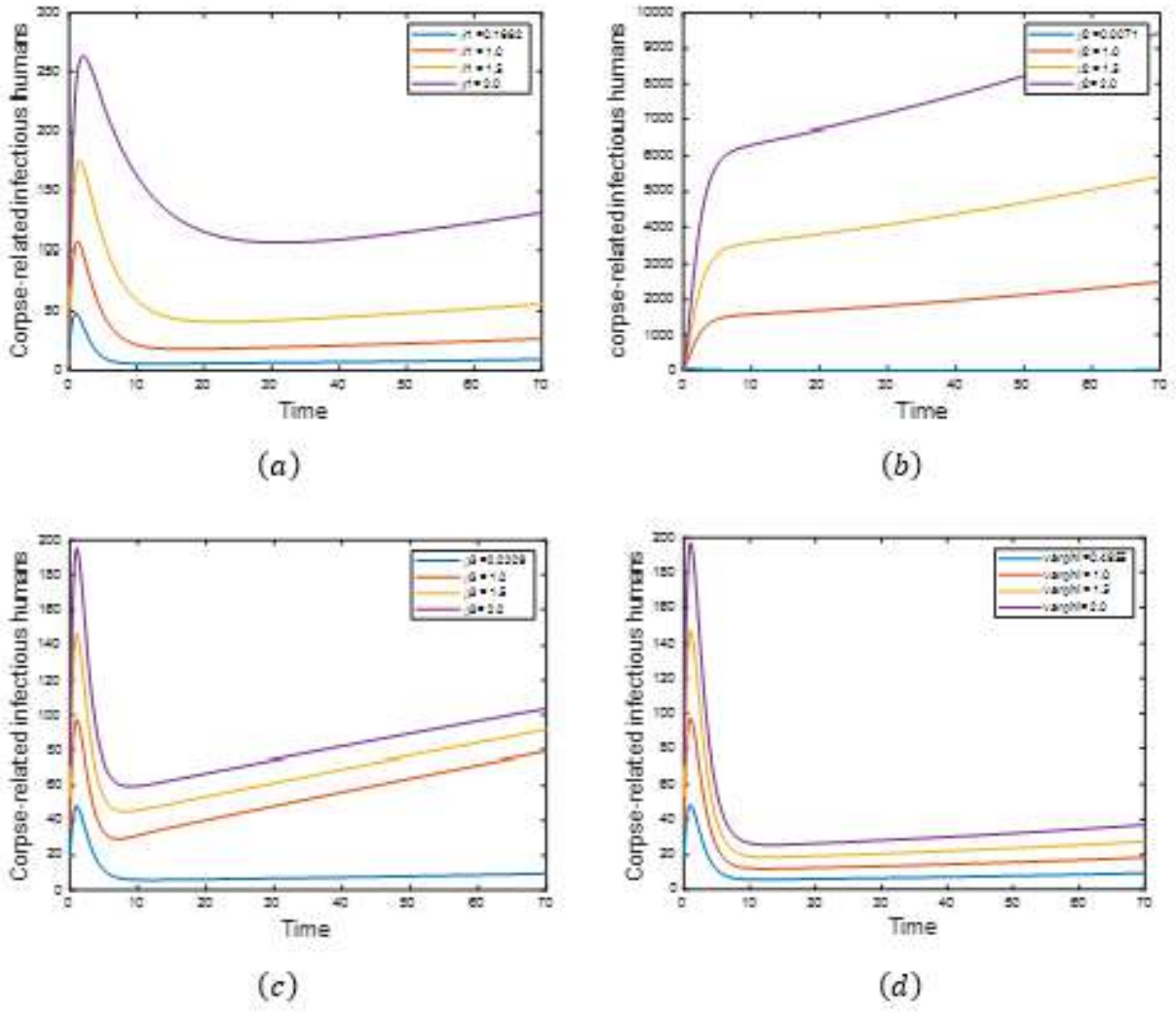

Figure 4. Visual presentation of the corpse-related infectious humans using different initial conditions of $(a)\ \beta_1$, $(b)\ \beta_2$, $(c)\ \beta_3$, (d) φ, with $\rho = 0.7$ at the time in a month

The dynamics of corpse-related infectious humans over time for different values of the human-to-human contact rate β_1 with a fractional derivative of order 0.7, highlighted as β_1 increase, the overall burden of corpse-related infectious humans is significantly higher, both in terms of peak magnitude and steady-state level. This showcases the role of human-to-human transmission in driving the epidemic dynamics, and the choice of 0.7 as the fractional order balances realism and computational feasibility. To target corpse-related infections there is a need to ensure safe burial practices, especially in rural areas where traditional methods may involve direct contact with corpses see Figure 4(a).

The graph in 4(b) illustrates the dynamics of corpse-related infectious humans over time for different values of β_2, the Mastomys rat-to-human contact rate. A fractional order of 0.7 is used to model the system, incorporating memory effects. As β_2 increases, there is a substantial rise in infections, indicating that higher rodent-to-human contact rates greatly amplify the epidemic. The

fractional derivative slows the decay of the epidemic, reflecting the persistence of infection and the long-term memory effects of rat-to-human interactions. This highlights the need of sustained interventions to control the epidemic effectively. The steady-state level of corpse-related infections humans is directly proportional to β_2. This suggests that interventions targeting β_2 have the potential to significantly reduce the long-term burden of the epidemic.

The graph depicted in Figure 4(c) demonstrates the dynamics of corpse-related infectious humans over time for varying values of β_3, which represents the rodent-to-rodent contact rate. A fractional order of 0.7 is applied, capturing memory effects and the long-term impact of rat interactions on the Lassa fever epidemic. The steady-state level of corpse-related infectious humans is directly proportional to β_3. The increasing steady-state population with a higher β_3 values highlight the exponential risk posed by unchecked rat populations in the epidemic spread.

The graph represents the effect of varying φ (the transmission rate due to contact with corpse-related infectious humans on the dynamics of the corpse-related infectious human population over time with a fractional order $\alpha = 0.7$. Based on the graph as φ increases, the peak and overall trajectory of corpse-related infectious humans also increase, with a lower φ corresponds to a reduced and shorter-lived outbreak, while a higher φ results in a larger and more prolonged presence of corpse-related infectious with a decline over time in all cases. The fractional order slows the epidemic progression, offering more time for implementing control measures. Comprehensive control showcases for reducing φ is crucial. A holistic approach targeting other parameters (e.g., human-to-human and rodent-to-human transmission rates) is essential to control the overall epidemic see Figure 4(d).

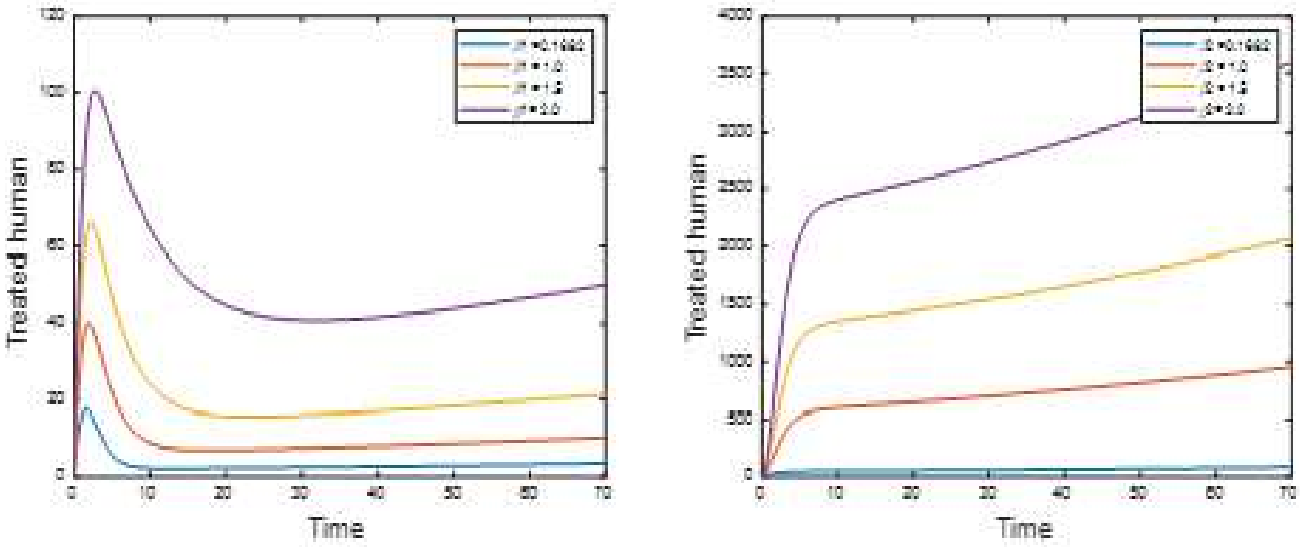

(a) (b)

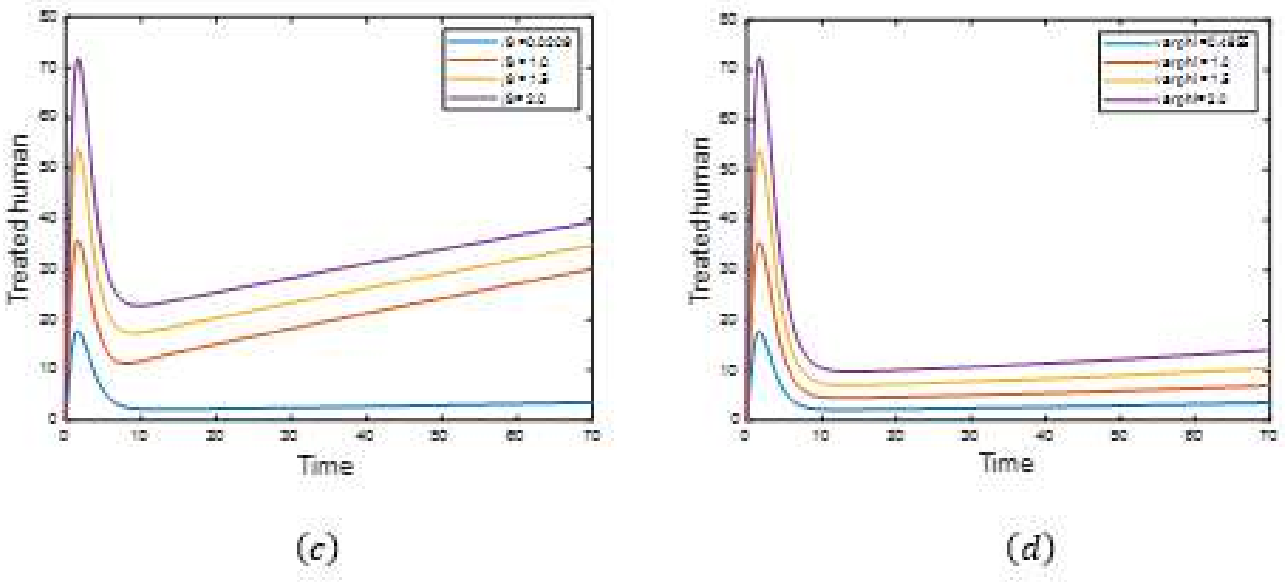

(c) (d)

Figure 5. visual presentation of the treated human using different initial conditions of (a) β_1, (b) β_2, (c) β_3, (d) φ, with $\rho = 0.7$ at the time in a month

This visual representation of the treated human population over time under varying values (β_1) the human-to-human contact rate in Figure 5(a), showcases characteristics of fractional differential equation models, with the initial dynamics of treated human population increase rapidly in early stages of the outbreak, indicating an initial surge in infections requiring treatment. Higher values of β_1 result in higher peaks, suggesting more intense outbreaks driven by increased human-to-human contact. However, the treated human population declines over time for all values of β_1 eventually stabilizing at steady-state levels. The fractional order dynamics highlight the importance of considering the history of transmission events. Short-term interventions are insufficient and so, sustained measures targeting β_1 are necessary to minimize the treated population.

Figure 5(b) depicts the simulation dynamics of the treated population over time under varying values of β_2 (the rodent-to-human contact rate). Higher rodent-to-human interaction rates amplify the spread of Lassa fever, leading to more humans requiring treatment, and controlling β_2 and directly reduce the number of treated individuals, lessening the strain on healthcare systems. The memory effect inherent in the fractional-order model emphasizes the prolonged influence of earlier disease transmission events on the treated population, and it reflects the long-term persistence of cases, highlighting the need for sustained intervention efforts.

The simulation graph of the population of treated humans over time for varying values of β_3The rodent-to-rodent contact rate illustrates that rodents are the key amplifiers of Lassa fever transmission. Increasing β_3 exacerbates the epidemic, leading to greater infection rates and more individuals requiring treatment. Reducing β_3 directly impacts the number of treated humans by lowering the transmission rate within the rat population, thus minimizing spillover to humans. The

trends in treated humans closely mirror those of corpse-related infections in humans, indicating that both metrics are strongly influenced by β_3. Reducing rat-to-rat interactions not only lowers infections but also alleviates treatment needs. Thus, improve diagnostic and treatment facilities to handle the peak demands indicated by the graph in Figure 5(c).

The simulation graph depicted in Figure 5(d) indicates that the height of the peak increases significantly as φ increase. This shows that corpse-related transmission is the major driver of epidemic severity, lower φ lead to more gradual and less severe outbreaks, with significantly smaller peaks. After reaching the peak, the treated population decreases over time, reducing φInterventions like treatment, safe burial practices, and protective measures (e.g., Gloves and face marks) can significantly reduce the treated population and shorten the epidemic duration.

6. Conclusion

In this study, we looked at how humans and rodents interact by formulating and analyzing a mathematical model that describes Lassa fever transmission dynamics via Caputo–Fabrizio fractional order derivatives using demographic data from Nigeria. By presenting the equilibrium points of the model and determining the conditions for local asymptotic stability of the disease-free equilibrium point, we proved the existence and uniqueness of solutions for the system. To explore the application of the Caputo–Fabrizio fractional derivative in modeling real-life issues incorporating memory effects, numerical solutions of the proposed model were generated and compared for various values of the fractional order.

Our study explored that early diagnosis and treatment to boost the recovery rate to reduce infection duration and prevent secondary transmission could be the best strategy for mitigating Lassa fever effectively. We also note that a higher rodent-to-human contact rate (β_2) implies that controlling interactions between rats and humans could be the key to reducing Corpse-related infections. The sensitivity of infection peaks and persistence of β_3 highlights the importance of controlling rodent populations via sanitation measures, rodent-proof housing, public awareness campaigns together with public health interventions to shorten the infection duration and reduce the infected population's size.

References

Atangana, A. (2018). Blind in a commutative world: simple illustrations with functions and chaotic attractors. Chaos Solitons Fractals 114, 347–363.

Atangana, A., & Gómez-Aguilar, J.F. (2018). Decolonisation of fractional calculus rules: breaking commutativity and associativity to capture more natural phenomena. Eur. Phys. J. Plus 133(4), 166.

Atangana, A., & Goufo, E. F. D. (2015). On the mathematical analysis of the Lassa hemorrhagic fever: Fractional order mathematical modeling. *Chaos, Solitons & Fractals*, 81, 278-285.

Area, I., Batarfi, H., Losada, J., Nieto, J.J., Shammakh, W., & Torres, Á. (2015). On a fractional order Ebola epidemic model. Adv. Differ. Equ. 2015(1), 278.

Caputo, M., & Fabrizio, M. (2015). A new definition of fractional derivative without singular kernel. Prog. Fract. Differ. Appl. 1(2), 1–13.

Davies, J., Lokuge, K., & Glass, K. (2019). Routine and pulse vaccination for Lassa virus could reduce high levels of endemic disease: a mathematical modelling study. Vaccine 37(26), 3451–3456.Nigeria Centre for Disease Control: Weekly epidemiological report.

Available from https://ncdc.gov.ng/reports/ weekly.

Diethelm K., Ford, N. J. & Freed, A. D. (2002). A predictor-corrector approach for the numerical solution of fractional differential equations, Nonlinear Dynam., 29 (2002), 3–22. https://doi.org/10.1023/A:1016592219341.

Diethelm K., Ford, N. J. & Freed, A. D. (2004). Detailed error analysis for a fractional Adams method, Numer. Algorithms, 36, 31–52. https://doi.org/10.1023/B:NUMA.0000027736.85078.

Diethelm, K. (2010). The Analysis of Fractional Differential Equations: An Application-Oriented Exposition Using Differential Operators of Caputo Type. Springer.

Hunter, J.K., & Nachtergaele, B. (2001). Applied Analysis. World Scientific, Singapore.

Ibrahim, M.A., & Dénes, A. (2021). A mathematical model for Lassa fever transmission dynamics in a seasonal environment with a view to the 2017–20 epidemics in Nigeria. Nonlinear Anal. Real World Appl. 60, 103310.

Kreyszig, E. (1978). Introductory Functional Analysis with Applications. Wiley, New York.

Kumar, D., Singh, J., & Baleanu, D. (2016). Numerical computation of a fractional model of differential-difference equation. J. Comput. Nonlinear Dyn. 11(6), 061004.

Losada, J., & Nieto, J.J. (2015). Properties of a new fractional derivative without singular kernel. Prog. Fract. Differ. Appl. 1(2), 87–92.

Mariën, J., Borremans, B., Kourouma, F., Baforday, J., Rieger, T., Günther, S., Magassouba, N., Leirs, H., & Fichet-Calvet, E. (2019). Evaluation of rodent control to fght Lassa fever Base on Feld data and mathematical modelling. Emerg. Microbes Infect. 8(1), 640–649.

Musa, S.S., Zhao, S., Gao, D., Lin, Q., Chowell, G., & He, D. (2020). Mechanistic modelling of the large-scale Lassa fever epidemics in Nigeria from 2016 to 2019. J. Theor. Biol. 493, 110209.

Mainardi, F. (1997). Fractional calculus: some basic problems in continuum and statistical mechanics. In: Carpinteri, A., Mainardi, F. (eds.) Fractals and Fractional Calculus in Continuum Mechanics. Springer.

Njagarah, J. B. H. & Tabi, C. B. (2021). Fractional-Order model for myxomatosis transmission dynamics: Significance of contact, vector control and culling, SIAM J. Appl. Math., 81, 641–665. https://doi.org/10.1137/20M1359122.

Njagarah, J. B. H. & Tabi, C. B. (2018). Spatial synchrony in fractional order metapopulation cholera transmission, Chaos Soliton. Fract., 117, 37–49. https://doi.org/10.1016/j.chaos.2018.10.004.

Ortigueira, M. D. (2011). Fractional calculus for scientists and engineers. *Springer Science & Business Media*.

Onah, I.S., & Collins, O.C. (2020). Dynamical system analysis of a Lassa fever model with varying socioeconomic classes. J. Appl. Math. 2020.

Peterson, A.T., Moses, L.M., & Bausch, D.G. (2014). Mapping transmission risk of Lassa fever in West Africa: the importance of quality control, sampling bias, and error weighting. PLoS ONE 9(8), 100711

Peter, O.J., Abioye, A.I., Oguntolu, F.A., Owolabi, T.A., Ajisope, M.O., Zakari, A.G., & Shaba, T.G. (2020). Modelling and optimal control analysis of Lassa fever disease. Inform.

Med. Unlocked 20, 100419.

Tateishi, A.A., Ribeiro, H.V., & Lenzi, E.K. (2017). The role of fractional time-derivative operators on anomalous diffusion. Front. Phys. 5, 52.

Van den Driessche P. & Warmouth, J. (2002). Reproduction numbers and sub-threshold endemic equilibria for compartmental models of disease transmission. *Math Biosci* 2002;180 (1–2):29–48.

Zhao, S., Musa, S.S., Fu, H., He, D., & Qin, J. (2020). Large-scale Lassa fever outbreaks in Nigeria: quantifying the association between disease reproduction number and local rainfall. Epidemiol. Infect. 148, 10.

Optimal Control Analysis of Lymphatic Filariasis Transmission Dynamics

[1*]Abokwara, A. and [2]Madubueze, C. E.

[1,2]Department of Mathematics, Joseph Sarwuan Tarka University, Makurdi, Nigeria
[1*]Corresponding author: agathamicheal@gmail.com

Abstract

Lymphatic filariasis is considered one of the deadliest vector-borne diseases globally, both in mortality rates and economic impact. Thus, modeling the disease is essential for comprehending its spread dynamics. In this paper, we formulate an optimal control model to explore the transmission dynamics of lymphatic filariasis, incorporating the mosquito's aquatic stage. We identify the threshold quantity, the control reproduction number R_c, demonstrating that the disease-free equilibrium is locally asymptotically stable when R_c less than unity and that the system exhibits uniform persistence if R_c greater than unity. A forward bifurcation can occur when the system has two equilibrium states, disease-free and endemic equilibrium states, that are stable for basic reproduction numbers less than and greater than one, respectively. This suggests that introducing control parameters can slow the disease's propagation. Utilizing optimal control theory, we demonstrate the existence of optimal control and outline the necessary conditions to achieve it. Numerical simulations showcase the effectiveness of various control strategies, indicating that public awareness campaigns and the utilization of insecticide-treated bed nets significantly contribute to reducing disease transmission. In particular, control strategies involving public enlightenment campaigns should be a priority.

Keywords: Aquatic mosquitoes, Bifurcation analysis, Lymphatic filariasis, Optimal control, Pontryagin's maximum principle,

1. Introduction

Lymphatic filariasis is a chronic disease caused by tiny parasites that are transmitted by mosquitoes. It is the most commonly neglected tropical disease, impacting many individuals, especially in tropical regions, yet it does not receive the attention it deserves (Stephano *et al*., 2023; Abokwara & Madubueze, 2024). This disease affects everyone, and the parasites responsible are of three types: Wuchereria bancrofti, Brugia malayi, and Brugia timori. These parasites reside in human tissues and can lead to severe swelling and other health complications over time. Different types of filarial parasites tend to affect various areas of the body, including the arms, legs, breasts, vulva, scrotum, and genitals (Oguntolu *et al*., 2021; Febiriana *et al*., 2023; Mendam *et al*., 2015). Lymphatic filariasis can cause significant pain and discomfort, making it challenging for sufferers to lead a normal life (Nwadibia *et al*., 2018).

Numerous researchers, including Simelane *et al*. (2019), Irvine *et al*. (2015), Salonga *et al*. (2021), and Mwamtobe *et al*. (2017), have developed and analyzed mathematical models to understand the dynamics of lymphatic filariasis, yielding valuable insights. However, the disease continues to persist in some populations. The introduction of intervention strategies could potentially reduce the prevalence of lymphatic filariasis in various communities (Irvine *et al*., 2015). This study aims to build upon the research of Abokwara & Madubueze (2024), which examined the impact of aquatic mosquito stages on the transmission dynamics of lymphatic filariasis while incorporating control strategies. To devise an effective optimal strategy for mosquito control, it is crucial to have a comprehensive understanding of mosquito population dynamics and to develop appropriate mathematical models to represent them (Lu & Li, 2011).

The extended study will formulate a model that evolves into an optimal control problem, utilizing four time-dependent controls to decrease the disease transmission dynamics. To minimize human-mosquito contact, we will follow the recommendations of Abokwara & Madubueze (2024) for preventive measures, which include the use of larvicides to manage mosquito maturity. Additionally, we will adopt Mwamtobe *et al.* (2017) guidelines on employing insecticide-treated bed nets to reduce adult mosquito populations and heed Rychtar & Taylor's (2022) call for public awareness campaigns, which are vital for the effective implementation of control measures (Kristina *et al.,* 2024). Furthermore, we will incorporate additional preventive tactics such as indoor residual spraying and screening and testing of asymptomatic individuals, who play a significant role in the transmission of lymphatic filariasis (Stephano *et al.,* 2023).

2. Formulation of the Optimal Control Model

Abokwara & Madubueze's (2024) work explains the model formulation, detailing the differential equations describing the system's work. It shows how different components interact over time, highlighting the main assumptions needed to understand the system's behavior. The model examines the influence of aquatic mosquitoes on the dynamics of lymphatic filariasis. The compartments include, susceptible human population, $S_h(t)$, exposed human population, $E_h(t)$, asymptomatic infected humans, $I_{1h}(t)$, symptomatic infected human, $I_{2h}(t)$, aquatic (stage of) mosquitoes, $L(t)$, susceptible mosquito population, $S_m(t)$, and infected mosquito population, $I_m(t)$, at any time, t. Thus,

$N_h(t) = S_h(t) + E_h(t) + I_{1h}(t) + I_{2h}(t)$ and $N_m = S_m(t) + I_m(t)$,

where, $N_h(t)$ and $N_m(t)$ are the total human and mosquito populations. The aquatic mosquito population, (t), comprises the egg, larva, and pupa stages of mosquito metamorphosis. We extended the model by introducing control parameters to reduce lymphatic filariasis in the human population. Different ways exist to lower mosquito numbers and curb the interaction between humans and mosquitoes. Existing research suggests various methods to fight the spread of mosquitoes and lymphatic filariasis.

However, none of this research considered environmental modifications using insecticide-treated

bed nets, indoor residual spraying and larvicides, screening and testing of asymptomatically infected individuals, attitudinal change, and awareness campaigns. These control functions, $u_1(t), u_2(t), u_3(t), u_4(t)$, are introduced to ascertain the best intervention strategy to curtail the spread of the disease and reduce the cost of executing these strategies. We outline the model system as follows:

$$\left.\begin{aligned}
\frac{dS_h}{dt} &= \Lambda_h - \frac{(1-u_1(t))\beta\theta_1 I_m S_h}{N_h} - \mu_h S_h + \alpha\big(1+u_4(t)\big)I_{1h},\\
\frac{dE_h}{dt} &= \frac{(1-u_1(t))\beta\theta_1 I_m S_h}{N_h} - (\tau+\mu_h)E_h,\\
\frac{dI_{1h}}{dt} &= \tau E_h - \big[\alpha\big(1+u_4(t)\big) + \eta\big(1-u_4(t)\big) + u_h\big]I_{1h},\\
\frac{dI_{2h}}{dt} &= \eta\big(1-u_4(t)\big)I_{1h} - (\delta+\mu_h)I_{2h},\\
\frac{dL}{dt} &= \Lambda\big(1-u_2(t)\big) - \big[\phi+\mu_l\big(1+u_2(t)\big)\big]L,\\
\frac{dS_m}{dt} &= \phi \mathrm{L} - \frac{(1-u_1(t))\beta\theta_2(kI_{1h}+I_{2h})S_m}{N_h} - \mu_m\big(1+u_3(t)\big)S_m,\\
\frac{dI_m}{dt} &= \frac{(1-u_1(t))\beta\theta_2(kI_{1h}+I_{2h})S_m}{N_h} - \mu_m\big(1+u_3(t)\big)I_m,
\end{aligned}\right\} \qquad (1)$$

subject to initial conditions

$$S_h(t), L(0), S_m(0) > 0, E_h(0), I_{1h}(t), I_{2h}(t), u_1(t), u_2(t), u_3(t), u_4(t) \geq 0.$$

Here, $u_1(t)$ is public enlightenment campaigns and usage of insecticide-treated bed nets (PTN) control, $u_2(t)$ preventive measure using larvicides (ILS) control, $u_3(t)$ preventive measure using indoor residual spraying (IRS) while $u_4(t)$ is screening and testing of asymptomatic infected individuals (STA). The system of equations (1) is assumed to have positive parameters. The parameters of the model, as well as their epidemiological interpretation, are displayed in Table 1.

Table 1: Parameters of the Lymphatic Filariasis Model

Parameter	Epidemiological Interpretation	Unit	Value	Source
Λ_h	Human recruitment rate	$\frac{human}{time}$	2500	Mwamtobe *et al.*, (2017)
μ_h	Human mortality rate	$\frac{1}{time}$	0.039	Mwamtobe *et al.*, (2017)
δ	Human disease-induced death rate	$\frac{1}{time}$	0.1	Assumed
α	Treatment rate for I_{1h} class	$\frac{1}{time}$	0.619	Salonga *et al.*, (2021)
τ	Movement rate from E_h to the	$\frac{1}{time}$	0.25	Simelane *et al.*, (2019)

	I_{1h} class			
η	Movement rate from I_{1h} to the I_{2h} class	$\frac{1}{time}$	0.35	Simelane *et al.,* (2019)
ϕ	Aquatic mosquito maturity rate	$\frac{1}{time}$	0.6	Assumed
μ_m	Non-aquatic mosquito mortality rate	$\frac{1}{time}$	0.166	Irvine *et al.,* (2015)
Λ	Aquatic mosquito recruitment rate	$\frac{mosquito}{time}$	40000	Assumed
μ_l	Aquatic mosquito mortality rate	$\frac{1}{time}$	0.019	Garba & Danbaba (2020)
k	Reduction parameter for I_{1h} due to treatment	nil	0.055	Mwamtobe *et al.,* (2017)
β	Mosquito biting rate	$\frac{1}{time}$	0.3	Irvine *et al.,* (2015)
θ_1	Transmission rate for interaction between S_h and I_m class	$\frac{human}{mosquito}$	0.64	Garba & Danbaba (2020)
θ_2	Transmission rate for interaction between S_m and I_{1h} , I_{2h} class	nil	0.64	Garba & Danbaba (2020)

3. Mathematical Analysis

We investigate the fundamental properties of the model (1) when the controls are constants to determine the model's biological significance and mathematical robustness within the domain interior, M, to evaluate the dynamics of the flow produced by the model.

3.1 Boundedness of Solutions

To assess the relevance of the system of equations (1) in epidemiology, we will examine the boundedness of the solutions. We note that there are two distinct populations: humans and mosquitoes. Furthermore, the mosquito population is divided into two stages: aquatic and non-aquatic. Thus,

$M_h = \{S_h(t), E_h(t), I_{1h}(t), I_{2h}(t) \in \mathbb{R}_+^4\}, M_l = L \in \mathbb{R}_+$ and $M_m = \{S_m(t), I_m(t) \in \mathbb{R}_+^2\}$.

Defining

$$\left.\begin{aligned}\frac{dN_h}{dt} &= \Lambda_h - \mu_h N_h - \delta I_{2h} \leq \Lambda_h - \mu_h N_h,\\ \frac{dL}{dt} &= \Lambda - (\phi + \mu_l)L,\\ \frac{dN_m}{dt} &= \phi L - \mu_m N_{m,}\end{aligned}\right\} \quad (2)$$

where disease-induced death of the human population, δ, is negligible and the initial conditions, $N_h(0) = N_{h0}$, $L(0) = L_0$ and $N_m(0) = N_{m0}$, we state the following theorem.

Theorem 1 All feasible solutions of the system of equations (1) are uniformly bounded in a proper subset, $M = M_h \times M_l \times M_m$, where M_h, M_l, M_m are subset regions for the human, aquatic mosquito and non-aquatic mosquito populations.

Proof 1 Using the integrating factor method to solve the first equation in system (2) results in

$$\mathrm{N}_h \leq \frac{\Lambda_h}{\mu_h} - \left(\frac{\Lambda_h - \mu_h N_{h0}}{\mu_h}\right) e^{-\mu_h t}. \quad (3)$$

As $t \longrightarrow \infty$ in equation (3), $\mathrm{N}_h \longrightarrow \frac{\Lambda_h}{\mu_h}$ implying that the realistic solutions of the human populations are in the region, $M_h = \left\{(S_h, E_h, I_{1h}, I_{2h}) \in \mathbb{R}_+^4 : \mathrm{N}_h(t) \leq \frac{\Lambda_h}{\mu_h}\right\}$.

Applying the method of integrating factor to solve the second equation of system (2) results in

$$L \leq \frac{\Lambda}{\phi + \mu_l} - \left(\frac{\Lambda - (\phi + \mu_l)L_0}{\phi + \mu_l}\right) e^{-(\phi + \mu_l)t}. \quad (4)$$

As $t \longrightarrow \infty$ in equation (4), $L \longrightarrow \frac{\Lambda}{\phi + \mu_l}$ indicating that the aquatic mosquito population enter the region $M_l \in \mathbb{R}_+ : L \leq \frac{\Lambda}{\phi + \mu_l}$.

In the same way, using the method of integrating factor technique to solve the third equation of system (2) gives

$$N_m = \leq \frac{\phi L}{\mu_m(\phi + \mu_l)} - \left[\frac{\phi\Lambda - \mu_m(\phi + \mu_l)N_{m0}}{\mu_m(\phi + \mu_l)}\right] e^{-\left(\frac{\phi L}{\mu_m(\phi + \mu_l)}\right)t}. \quad (5)$$

As $t \longrightarrow \infty$ in equation (5), $N_m \longrightarrow \frac{\phi L}{\mu_m(\mu_l + \phi)}$ indicating that the non-aquatic mosquito population enter the region, $M_m = \left\{(S_m, I_m) \in \mathbb{R}_+^2 : N_m \leq \frac{\phi L}{\mu_m(\mu_l + \phi)}\right\}$.

3.2 Control Reproduction Number

The control reproduction number represents the new cases of lymphatic filariasis arising from an infected person entering a susceptible population under implemented intervention strategies (Van den Driessche, 2017). By applying the next generation matrix method from Van den Driessche &

Watmough (2002), we find that the disease-free equilibrium state of the optimal control model (1) and the control reproduction number, R_c, is expressed as

$$E_0=(S_h^0, E_h^0, I_{1h}^0, I_{2h}^0, L^0, S_m^0, 0) = \left(\frac{\Lambda_h}{\mu_h}, 0, 0, 0, \frac{\Lambda}{\phi+\mu_l+u_2(t)}, \frac{\phi\Lambda}{\mu_m(\phi+\mu_l+u_2(t)}, 0\right) \quad (6)$$

and

$$R_c= \sqrt{\frac{\beta^2\theta_1\theta_2\tau\Lambda\phi\mu_h(k(\delta+\mu_h)+\eta)(1-u_1(t))(1-u_3(t))}{(\tau+\mu_h)(\alpha+\eta+\mu_h)(\delta+\mu_h)\mu_m^2\Lambda_h(\phi+\mu_l+u_2(t))}}. \quad (7)$$

Note that if $u_1 = u_2 = u_3 = u_4 = 0$, the control reproduction number, $R_c = R_0$, the basic reproduction number implying that $R_c \leq R_0$. By the second theorem of Van den Driessche & Watmough (2002), we state the following lemma.

Lemma 1 The local stability of equation (6) is locally asymptotically stable for $R_c < 1$ and for $R_c > 1$, it is unstable.

3.3 Bifurcation Analysis

The occurrence of a backward or forward bifurcation is crucial for determining the model's local stability at endemic equilibrium. A backward bifurcation indicates that the system dynamics can lead to multiple stable equilibrium states. This suggests that there exists a critical threshold of basic reproduction number, $R_0 < 1$, where the disease demonstrates complex behaviours. Below this critical value, intervention strategies may have moderate effectiveness, but above it, controlling the disease proves to be significantly challenging (Isa *et al.,* 2023). We conduct a bifurcation analysis of the model (1) excluding the control parameters, specifically, $u_1 = u_2 = u_3 = u_4 = 0$, to examine the possibility of a backward bifurcation stemming from multiple equilibria and reinfection, utilizing the Centre Manifold theory discussed by Castillo-Chavez & Song (2004) as follows.

Let $\theta_1 = \hat{\theta}_1$ and $\theta_2 = \hat{\theta}_2$ be the bifurcation parameters since we are dealing with two separate populations such that, for $R_0 = 1 = R_0^2$, we have

$$\theta_1 = \hat{\theta}_1 = \frac{(\tau+\mu_h)(\alpha+\eta+\mu_h)(\delta+\mu_h)\mu_m^2\Lambda_h(\phi+\mu_l)}{\beta^2\theta_2\tau\Lambda\phi\mu_h(k(\delta+\mu_h)+\eta)} \quad \text{and}$$

$$\theta_2 = \hat{\theta}_2 = \frac{(\tau+\mu_h)(\alpha+\eta+\mu_h)(\delta+\mu_h)\mu_m^2\Lambda_h(\phi+\mu_l)}{\beta^2\theta_1\tau\Lambda\phi\mu_h(k(\delta+\mu_h)+\eta)}.$$

Let $x_1 = S_h$, $x_2 = E_h$, $x_3 = I_{1h}$, $x_4 = I_{2h}$, $x_5 = L$, $x_6 = S_m$, $x_7 = I_m$ and let the right-hand sides of the system of equations (1) be q_1, q_2, q_3, q_4, q_5, q_6, q_7. Therefore, the non-zero second order partial derivatives of q_1, q_2, q_3, q_4, q_5, q_6, q_7 at DFE, E_0 results in

$$\left.\begin{array}{l} \frac{\partial q_1(E_0)}{\partial x_1 \partial x_7} = \frac{\partial q_1(E_0)}{\partial x_7 \partial x_1} = -\frac{\widehat{\theta}_1 \mu_h \beta}{\Lambda_h}, \frac{\partial q_2(E_0)}{\partial x_1 \partial x_7} = \frac{\partial q_2(E_0)}{\partial x_7 \partial x_1} = \frac{\widehat{\theta}_1 \mu_h \beta}{\Lambda_h}, \\ \frac{\partial q_6(E_0)}{\partial x_3 \partial x_6} = \frac{\partial q_6(E_0)}{\partial x_6 \partial x_3} = -\frac{\widehat{\theta}_2 \mu_h \beta k}{\Lambda_h}, \frac{\partial q_6(E_0)}{\partial x_4 \partial x_6} = \frac{\partial q_6(E_0)}{\partial x_6 \partial x_4} = -\frac{\widehat{\theta}_2 \mu_h \beta}{\Lambda_h}, \\ \frac{\partial q_7(E_0)}{\partial x_3 \partial x_6} = \frac{\partial q_7(E_0)}{\partial x_6 \partial x_3} = \frac{\widehat{\theta}_2 \mu_h \beta k}{\Lambda_h}, \frac{\partial q_7(E_0)}{\partial x_4 \partial x_6} = \frac{\partial q_7(E_0)}{\partial x_6 \partial x_4} = \frac{\widehat{\theta}_2 \mu_h \beta}{\Lambda_h}. \end{array}\right\} \quad (8)$$

The left and right eigenvectors, v and w are given as $v = (v_1, v_2, v_3, v_4, v_5, v_6, v_7)$ and $w = (w_1, w_2, w_3, w_4, w_5, w_6, w_7)$, where

$$\left.\begin{array}{l} v_1 = v_5 = v_6 = 0, v_2 = \frac{\tau\beta\widehat{\theta}_2 a_4(\eta+ka_3)v_7}{a_1 a_2 a_3}, v_3 = \frac{\beta\widehat{\theta}_2 a_4(\eta+ka_3)v_7}{a_2 a_3}, v_4 = \frac{\beta\widehat{\theta}_2 a_4 v_7}{a_3}, v_7 > 0, \\ w_1 = \frac{w_7(a_1 a_2+\alpha\tau)\beta\widehat{\theta}_1}{a_1 a_2 \mu_h}, w_2 = \frac{w_7\beta\widehat{\theta}_1}{a_1}, w_3 = \frac{w_7\tau\beta\widehat{\theta}_1}{a_1 a_2}, w_4 = \frac{w_7\eta\tau\beta\widehat{\theta}_1}{a_1 a_2 a_3}, \\ w_5 = 0, w_6 = -\frac{(\eta+k)\beta^2\widehat{\theta}_1\widehat{\theta}_2 a_4\tau w_7}{a_2 a_3 a_1 \mu_m}, w_7 > 0, \end{array}\right\} \quad (9)$$

with

$$a_1 = \tau + \mu_h, a_2 = \alpha + \eta + \mu_h, a_3 = \delta + \mu_h, a_4 = \frac{S_m^0}{N_h^0} = \frac{\Lambda\phi\mu_h}{\Lambda_h\mu_m(\phi+\mu_l)}. \quad (10)$$

The bifurcation coefficients, m and n depend on the left and right eigenvectors as well as the non-zero second partial derivatives at E_0. Using equations (8) and (9) results in

$$m = -w_7 \frac{\tau a_4 \beta^3 \widehat{\theta}_2 \widehat{\theta_1^2}}{a_1^2 a_2^2 a_3 \Lambda_h} \left[\frac{\beta k(k+\eta)\widehat{\theta}_2}{\mu_m} + \frac{\beta\eta\tau(k+\eta)\widehat{\theta}_2}{\mu_m a_3} - (\eta + ka_3)(a_1 a_2 + \alpha\tau)\right]$$

and

$$n = \frac{\beta^2\tau a_4}{a_1 a_2 a_3}\left[(ka_3 + \eta)\hat{\theta}_2 + ka_3\hat{\theta}_1 + \eta\hat{\theta}_1\right] > 0.$$

The transition from a negative unstable equilibrium to a positive one depends on the direction of m. When $m < 0$, it indicates a shift from a negative unstable equilibrium to a positive state that is locally asymptotically stable. This suggests that intervention strategies could reduce the basic reproduction number, R_0, as well as the disease spread within the population. Thus, we state the following theorem.

Theorem 2 For $u_1 = u_2 = u_3 = u_4 = 0$ at $R_0 = 1$, the model (1) demonstrates a forward bifurcation if $m < 0$, otherwise it exhibits a backward bifurcation when $m > 0$.

4. Optimal Control Analysis

In this section, we examine the optimal control model (1), which features time-dependent control parameters, $u_1(t), u_2(t), u_3(t)$ and $u_4(t)$. We applied the Pontryagin Maximum Principle (PMP), Pontryagin *et al.* (1962), to analyze the conditions necessary for disease eradication over time. Additionally, we explore the model's behavior under specific initial conditions using Lebesgue

measurable control. The objective function is defined by

$$\Gamma(u_1, u_2, u_3, u_4) = \int_0^{t_f} \left(C_1 E_h + C_2 I_{1h} + C_3 I_{2h} + C_4 L + C_5 N_v + \frac{1}{2} \sum_{i=1}^{4} A_i u_i^2 \right) dt \quad (11)$$

for $i = 1, 2, 3, 4$, subject to the model (1), where t_f is the final time, C_1, C_2, C_3, C_4, C_5 are positive weights to balance the factors E_h, I_{1h}, I_{2h}, N_v and A_1, A_2, A_3, A_4 are the positive weight constants for PTN, ILS, IRS and STA, respectively. We implemented a quadratic form for the control cost, $A_i u_i^2$ so that $\frac{1}{2}A_1 u_1^2, \frac{1}{2}A_2 u_2^2, \frac{1}{2}A_3 u_3^2,$ and $\frac{1}{2}A_4 u_4^2$ explains the cost PTN, ILS, IRS and STA. The objective of the optimal control problem is to find out the optimal control functions $u_1^*, u_2^*, u_3^*, u_4^*$ such that

$$\Gamma(u_1^*, u_2^*, u_3^*, u_4^*) = min\{\Gamma(u_1, u_2, u_3, u_4), (u_1, u_2, u_3, u_4) \in U\}, \quad (12)$$

subject to system (1), where the control set is defined as

$$U = \{(u_1, u_2, u_3, u_4) | u_i(t) is\ Lebesgue\ measurable\ on\ [0,1], i = 1, 2, 3, 4\}. \quad (13)$$

PMP is used to convert the process of either minimizing or maximizing the objective functional and state variables into pointwise minimization or maximization of the Hamiltonian, H, with respect to the control variable, $u = (u_1, u_2, u_3, u_4)$. To find an optimal solution, we begin by establishing the Lagrangian and Hamiltonian associated with the optimal control problem defined in the equations (1), (11), and (12). The Lagrangian of the optimal problem is given by

$$P = C_1 E_h + C_2 I_{1h} + C_3 I_{2h} + C_4 L + C_5 N_v + \frac{1}{2} \sum_{i=1}^{4} A_i u_i^2. \quad (14)$$

To find the minimum value of the Lagrangian, we define the Hamiltonian, H, for the control problem as follows

$$H = \mathrm{P}(E_h, I_{1h}, I_{2h}, L, N_m, u_1, u_2, u_3, u_4) + \lambda_1 \frac{dS_h}{dt} + \lambda_2 \frac{dE_h}{dt} + \lambda_3 \frac{dI_{1h}}{dt} + \lambda_4 \frac{dI_{2h}}{dt} + \lambda_5 \frac{dL}{dt} + \lambda_6 \frac{dS_m}{dt} + \lambda_7 \frac{dI_m}{dt} \quad (15)$$

where $\lambda_i, i = 1, 2, 3, 4, 5, 6, 7$ are co-state variables. The set of control variables $(u_1, u_2, u_3, u_4) \in U$ is defined as convex and closed. The boundedness of the optimal system ensures the necessary compactness for the existence of an optimal control. Furthermore, the integrand in equation (11) is convex on the control set, U. Also, we can easily see that there exists a constant $\gamma = 2 > 1$ and positive numbers d_1, d_2 such that

$$\Gamma(u_1, u_2, u_3, u_4) \geq d_1(|u_1^2| + |u_2^2| + |u_3^2| + |u_4^2|)^{\frac{\gamma}{2}} - d_2.$$

Since the state variables are limited, an optimal control exists; therefore, we can present the following theorem.

Theorem 3 There exists an optimal control $u^* = (u_1^*, u_2^*, u_3^*, u_4^*) \in U$ such that

$\Gamma(u_1^*, u_2^*, u_3^*, u_4^*) = min_{(u_1^*,u_2^*,u_3^*,u_4^*)\in U} \Gamma(u_1, u_2, u_3, u_4)$, subject to the control system (1) with initial conditions.

We apply the PMP to the Hamiltonian (15) to determine the optimal solution. Consequently, if (x, u) represents an optimal solution for an optimal control problem, there exists a non-trivial vector function $\lambda = (\lambda_1, \lambda_2, \lambda_3, \lambda_4, \lambda_5, \lambda_6, \lambda_7)$ that satisfies the following condition:

$$\left.\begin{aligned} x' &= \frac{\partial H(t,x,u,\lambda)}{\partial \lambda}, \\ 0 &= \frac{\partial H(t,x,u,\lambda)}{\partial u}, \\ \lambda' &= -\frac{\partial H(t,x,u,\lambda)}{\partial u}. \end{aligned}\right\} \tag{16}$$

We apply the necessary conditions to the Hamiltonian, H in equation (15).

Theorem 4 Let $S_h^*, E_h^*, I_{1h}^*, I_{2h}^*, L^*, S_m^*, I_m^*$ be optimal state solutions with associated optimal control variables $u_1^*, u_2^*, u_3^*, u_4^*$ for the optimal control problems (1) and (11). Then, there exist co-state variables $\lambda_1, \lambda_2, \lambda_3, \lambda_4, \lambda_5, \lambda_6, \lambda_7$ satisfying

$$\left.\begin{aligned} \lambda_1' &= (\lambda_1 - \lambda_2)(M_2 - M_1) + \mu_h\lambda_1 + (\lambda_7 - \lambda_6)M_3, \\ \lambda_2' &= -C_1 + (\lambda_2 - \lambda_1)M_1 + (\lambda_2 - \lambda_3)\tau + (\lambda_7 - \lambda_6)M_3 + \mu_h\lambda_2, \\ \lambda_3' &= -C_2 + (\lambda_2 - \lambda_1)M_1 + (\lambda_3 - \lambda_1)\alpha\big(1 + u_4(t)\big) \\ &\quad + \mu_h\lambda_3 + (\lambda_3 - \lambda_4)\eta\big(1 - u_4(t)\big) + (\lambda_6 - \lambda_7)(M_4 k - M_3), \\ \lambda_4' &= -C_3 + (\lambda_2 - \lambda_1)M_1 + \lambda_4(\delta + \mu_h) + (\lambda_7 - \lambda_6)(M_3 - M_4), \\ \lambda_5' &= -C_4 + \lambda_5\mu_l\big(1 + u_2(t)\big) + (\lambda_5 - \lambda_6)\phi, \\ \lambda_6' &= -C_5 + (\lambda_6 - \lambda_7)M_6 + \lambda_6\mu_m\big(1 + u_3(t)\big), \\ \lambda_7' &= -C_5 + (\lambda_1 - \lambda_2)M_5 + \mu_m\big(1 + u_3(t)\big)\lambda_7, \end{aligned}\right\} \tag{17}$$

where

$$\left.\begin{aligned} M_1 &= \frac{(1-u_1(t))\beta\theta_1 I_m S_h}{N_h^2}, \; M_2 = \frac{(1-u_1(t))\beta\theta_1 I_m}{N_h}, \; M_3 = \frac{(1-u_1(t))\beta\theta_2(kI_{1h}+I_{2h})S_m}{N_h^2}, \\ M_4 &= \frac{(1-u_1(t))\beta\theta_2 S_m}{N_h}, M_5 = \frac{(1-u_1(t))\beta\theta_1 S_h}{N_h}, \; M_6 = \frac{(1-u_1(t))\beta\theta_2(kI_{1h}+I_{2h})}{N_h}, \end{aligned}\right\}$$

with boundary conditions $\lambda_i(t) = 0, i = 1, 2, 3, 4, 5, 6, 7$. Furthermore, the control functions are given by

$$\left.\begin{aligned} u_1^* &= \max\{min\left(\frac{1}{A_1}\left[\frac{(\lambda_2-\lambda_1)\beta\theta_1 I_m S_h}{N_h} + \frac{(\lambda_7-\lambda_6)(kI_{1h}+I_{2h})\beta\theta_2 S_m}{N_h}\right], 1\right), 0\}, \\ u_2^* &= \max\left\{\min\left(\frac{\lambda_5(\Lambda+\mu_l L)}{A_2}, 1\right), 0\right\}, \\ u_3^* &= \max\left\{\min\left(\frac{\lambda_6\mu_m S_m + \lambda_7\mu_m I_m}{A_3}, 1\right), 0\right\}, \\ u_4^* &= \max\left\{\min\left(\frac{1}{A_4}[(\lambda_3 - \lambda_1)\alpha I_{1h} + (\lambda_4 - \lambda_3)\eta I_{1h}], 1\right), 0\right\}. \end{aligned}\right\} \tag{18}$$

Proof 2 We utilize the Hamiltonian, H, as described in equation (15) to derive the co-state equations and boundary conditions. The co-state system (17) is obtained from PMP as

$$\frac{d\lambda_1}{dt} = -\frac{dH}{\partial S_h}, \frac{\partial\lambda_2}{dt} = -\frac{dH}{\partial E_h}, \frac{\partial\lambda_3}{dt} = -\frac{dH}{\partial I_{1h}}, \frac{\partial\lambda_4}{dt} = -\frac{dH}{\partial I_{2h}}, \frac{\partial\lambda_5}{dt} = -\frac{dH}{\partial L}, \frac{\partial\lambda_6}{dt} = -\frac{dH}{\partial S_m}, \frac{\partial\lambda_7}{dt} = -\frac{dH}{\partial I_m},$$

with zero final time conditions $\lambda_i(t) = 0$ for $i = 1,2,3,4,5,6,7$. To get the characterization of the optimal control given by equation (17), we solve the equations

$\frac{\partial H}{du_1} = 0, \frac{\partial H}{du_2} = 0, \frac{\partial H}{du_3} = 0$ and $\frac{\partial H}{du_4} = 0$ on the interior of the control set and use the property of the control space U, so we can derive the desired result (18).

5. Numerical Simulations

This section numerically demonstrates the effect of optimal controls on lymphatic filariasis infections. By solving the state and co-state systems along with the transversality conditions, we determined the optimal strategy that significantly decreases the infected population. Our simulations employed parameter values from Table 1, balancing the population and control functions in the objective functional by selecting suitable weight constants ($C_1 = C_2 = 0.001, C_3 = 0.05,\ C_4 = 0.01, C_5 = 0.001, A_1 = 2000, A_2 = 10000, A_3 = 500, A_4 = 4000$). We then generated time series for the infected compartments under scenarios of no control, partial control, and full control, utilizing the initial conditions $(S_h(0),\ E_h(0),\ I_{1h}(0),\ I_{2h}(0), L(0), S_m(0), I_m(0)) = (5000, 0, 0, 0, 8, 800, 1)$. We excluded the single control strategy since it shows minimal impact on the disease burden. The results illustrated in Figure 1 highlight the impact of optimal control measures on the infected compartments over a period of 1000 days with a double control combination. Our analysis indicates that the pairings of u_1 with u_3 and u_1 with u_4 have the greatest effect on eradicating or eliminating the disease. Meanwhile, Figure 2 employs optimal control through a mix of three strategies, showcasing how these measures influence disease dynamics within the infected groups. The results show that the combination of u_1, u_2, and u_3 significantly affects disease eradication within the population. In Figure 3, it is observed that all four control strategies play a crucial role in the disease dynamics, especially when compared to implementations of double or triple control combinations.

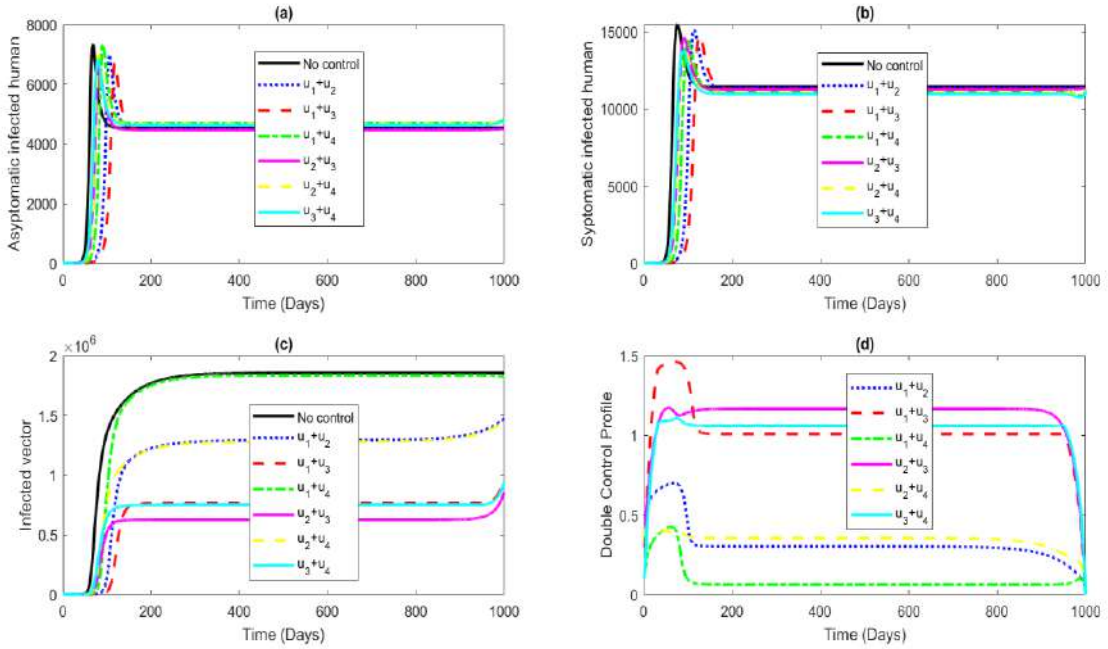

Figure 1: The optimal solutions for the populations of infected humans (I_{1h}, I_{2h}) and infected mosquitoes (I_m) in the context of double control combination and in the absence of intervention strategies.

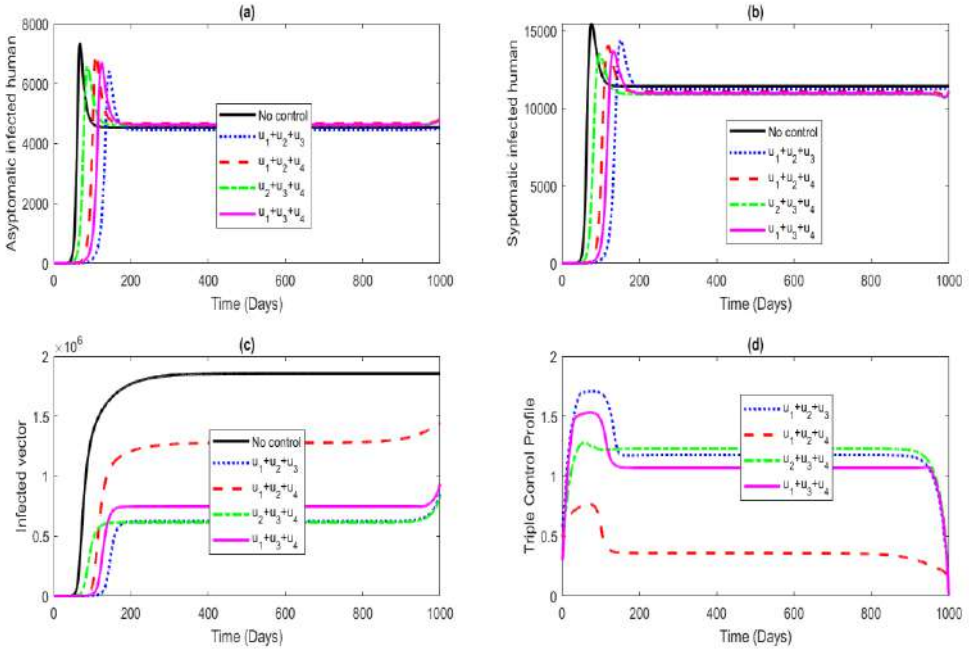

Figure 2: The optimal solutions for the populations of infected humans (I_{1h}, I_{2h}) and infected mosquitoes (I_m) in the context of triple control combination and in the absence of intervention strategies.

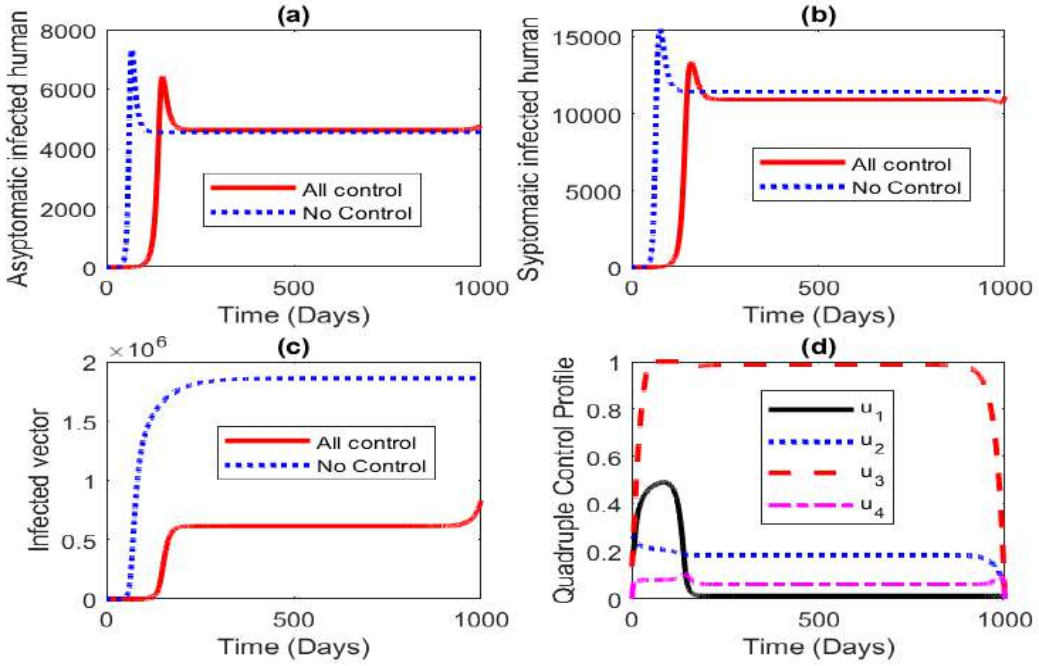

Figure 3: The optimal solutions for the populations of infected humans (I_{1h}, I_{2h}) and infected mosquitoes (I_m) in the context of all control combination and in the absence of intervention strategies.

5. Conclusion

This paper presents an optimal control model for the transmission dynamics of lymphatic filariasis, integrating the aquatic stage of mosquitoes. Our model encompasses intervention strategies such as public awareness campaigns, the implementation of insecticide-treated bed nets, and preventive tactics like larvicides and indoor residual spraying, and the screening and testing of asymptomatic infected individuals. These strategies aim to provide a comprehensive and accurate understanding of their influence on the dynamic behavior of lymphatic filariasis. We established the conditions for backward and forward bifurcations in the model without controls. Additionally, we conducted numerical simulations to evaluate how different combinations of controls impact the endemic levels of infected classes, characterized using PMP. The numerical representation of optimal control effects on the system compares lymphatic filariasis infections under various control strategies. The analysis indicates that optimal control significantly decreases the number of infected individuals. Notably, the control function $u_1(t)$ is crucial in lowering infections compared to other strategies, echoing findings from Rychtar & Taylor (2022) and Mwamtobe *et al.* (2017), and merits special attention in light of remarks by Kristina *et al.* (2024). Any control combination involving

$u_1(t)$ has the potential to alleviate the burden of Lymphatic Filariasis within the community, as well as enhance indoor residual spraying, and the screening and testing of asymptomatic infected individuals.

References

Abokwara, A. & Madubueze, C.E. (2024). The influence of aquatic mosquitoes on lymphatic filariasis transmission dynamics: Mathematical model approach. *International Journal of Mathematical Analysis and Modelling,* 7(2):16-32.

Castillo-Chavez, C. & Song, B. (2004). Dynamical models of tuberculosis and their applications. *Mathematical Biosciences and Engineering,* 1(2):361-404.

Febiriana, I. H., Adisaputri, V., Kamalia, P. Z. & Aldila, D. (2023). Impact of screening, treatment and misdiagnose on lymphatic filariasis transmission: A mathematical model. *Communications and Mathematical Biology,* 67:1-28.

Fleming, W. H. & Rishel, R.W. (1975). *Deterministic and stochastic optimal control.* Springer Verlang, New York.

Garba, S. M. & Danbaba, U. A. (2020). Modelling the effect of temperature variability on malaria control strategies. *Mathematical Modelling of Natural Phenomena,* 65:1-43.

Irvine, M. A., Reimer, L. J., Njenga, S. M., Gunawarden, S., Kelly-Hope, L., Bockarie, M & Hollingsworth, D. (2015). Modelling strategies to break transmission of lymphatic filariasis- Aggregation, adherence and vector competence greatly alter elimination. *Parasites and Vectors,* 8(1):1-19.

Isa, R. S., Hwere, T. S., Garba, U., Abubakar, S. S. & Sebastine, E. (2023). Mathematical modelling of terrorists recycle Induced with backward bifurcation. *Nigerian Society of Physical Sciences,* 2(133):1-22.

Lu, J. & Li, J. (2011). Dynamics of stage-structured discrete mosquito population models. *Journal of Applied Analysis and Computation,* 1(1):53-67.

Kristina, Y., Efanti, E., Botutihe, F., Nurlaily, A. P., Erlyn, P. & Fatmawati, S. T. I. K. (2024). Case study of the role of health education in raising public awareness of the importance of preventing infectious diseases, *Miracle Get Journal,* 1(4):1-6.

Mendam, K., Kavitha, B. & Naik, J. K. (2015). Natural sources used for treatment and prevention of filariasis. *World Journal of Pharmacy and Pharmaceutical Sciences,* 4(10):1621-1628.

Mwamtobe, P. M., Simelane, S. M., Abelonam, S. & Tchuenche, J. M. (2017). Mathematical analysis of a lymphatic filariasis model with quarantine and treatment. *BMC Public Health* 17:265 doi 10.1186/s12889-017-4160-8.

Nwadibia, A.I., Eze, F., Inyama, S.C. Nse, C.A. Omaine, A. & Mbachu, H.I. (2018). Mathematical model of the transmission dynamics of genital elephantiasis (lymphatic filariasis). *Mathematical Theory and Modelling* 8(4):71-113

Oguntolu, F. A., Bolarin, G., Peter, J.O., Enagi, I. A. & Oshinubi, K. (2021). Mathematical model for the control of lymphatic filariasis transmission dynamics. *Communications in Mathematical Biology and Neuroscience,* 17: 1-28.

Rychtar, J. & Taylor, D. (2022). A game-theoretic model of lymphatic filariasis *PLOS Neglected Tropical Diseases,* 16(9):1-28.

Salonga, P. K. N., Mendoza, V. M. P., Mendoza, R. G. & Belizario Jr. V.Y. (2021). A mathematical model of the dynamics of lymphatic filariasis in Caraga region, the Philippians. *Royal Society Open Science,* 8:1-24.

Simelane, S. M., Mwamtobe, P. M., Abelonam, S. & Tchuenche, J. M. (2019). A mathematical model for the transmission dynamics of lymphatic filariasis and intervention strategies. *Acta Biotheorica,* https://doi.org/10.1007/s10441-019-09370-y.

Stephano, M. A., Mayengo, M. M. & Irunde, J. I. (2023). Sensitivity analysis and parameters estimation for the transmission of lymphatic filariasis. *Heliyon,* 9:1-14.

Pontryagin, L. S., Boltyanskii, V. G., Gamkrelize, R. V. & Mishchenko, E. (1962). *The mathematical theory of optimal processes,* Wiley, New York.

Van den Driessche P. & Watmough, J. (2002). Reproduction numbers and sub-threshold endemic equilibria for computational models of disease transmission. *Mathematical Biosciences,* 180:29-48.

Van den Driessche, P. (2017). Reproduction number of infectious disease models. *Infectious Disease Models,* 2(3):288-303.

Modelling HIV Superinfection with Two Unique Viral Strains

[1]Ogunniran, M. A. and [2]Ibrahim, M. O.

[1]Faculty of Basic Applied and Medical Sciences, Trinity University, Lagos, Nigeria
[2]Department of Mathematics, University of Ilorin, Ilorin, Nigeria
Corresponding author: matthewogunniran@gmail.com

Abstract

HIV superinfection, the acquisition of a second distinct viral strain in an individual already infected, presents challenges to HIV management and vaccine development. Understanding the dynamics and implications of superinfection is crucial for advancing HIV research and developing more effective prevention and treatment strategies. While HIV superinfection is recognized, the mechanisms, factors influencing its occurrence, and its impact on disease progression remain inadequately understood. This study addresses the gaps in knowledge regarding HIV superinfection by employing mathematical modelling to analyze the dynamics of coexistence and competition between two unique viral strains within the same host. A HIV superinfection model with two unique viral strains was developed. Numerical simulations showed that in order to prevent HIV superinfection, treatment at 95% level of efficacy should begin at any time, $t < 50$ *days*, before the second strain is fully integrated in the population of primarily infected cells. We conclude that the HIV superinfection model developed in this study minimizes the rate of infection and the rate at which new viruses are produced by the second strain. The models also show that the second strain of HIV contributes to the persistence of HIV in the system, increases viral load, orchestrates the multiplication of infected cells and results in the decline of the population of healthy cells.

Keywords: efficacy, HIV, superinfection, treatment, viral strain

1. Introduction

Acquired Immune Deficiency Syndrome (AIDS) is a well-known and well-documented infectious disease globally. AIDS is caused by a virus called Human Immunodeficiency Virus (HIV) (World Health Organization [WHO], 2024a). The target cells are the body's white blood cells called the Cluster of Differentiation 4 T cells (CD4+T cells) (Hiv.gov, 2024; Ogunniran, et al., 2018). On infesting the body, the virus bind itself to the cell and hijacks its system, so that with the progression of the infection, more viruses are replicated inside its host. HIV weakens and destroys the immune system of human, so that the body becomes susceptible to opportunistic infections such as Tuberculosis, Hepatitis B Virus and some cancers (Hiv.gov, 2024; Ahmad, et al., 2023; Ogunniran, et al., 2018).

HIV has remained a major health concern globally up to date, claiming about 42.3 million. HIV transmission is currently ongoing in all countries. The 2023 statistics on HIV obtained from WHO estimated that about 39.9 million people are currently living with the virus, 65% of this figure lives in Africa (WHO, 2024a; Joint United Nations Programme on HIV/AIDS [UNIAIDS], 2024). About 1.3 million persons were said to be newly infected, 42.3 million people have died from AIDS-related sicknesses since the beginning of the epidemic, while 630 000 died due to AIDS-related sicknesses in 2023 (WHO, 2024a; UNIAIDS, 2024), which is 14.89% of the total infection since the start of

the epidemic. The rate of infection is still high; HIV/AIDS is yet a threatening disease globally.

HIV spreads from the body fluids of a HIV-positive person, including blood, breast milk, semen and vaginal fluids. It is untrue that HIV spread by kisses, hugs or sharing food. There can be mother-to-child transmission (Stanford Health Care, 2024; Centers for Disease Control and Prevention [CDC], 2024). Symptoms can vary depending on the stage of infection. The spread of HIV is more at the onset of infection though a high number of people living with HIV (PLWH) are usually unaware until the later stages. Infected persons may not experience symptoms immediately after infection. Some may have an influenza-like sickness, which may include headache, rash, sore throat and fever (WHO, 2024a; CDC, 2024; Ahmad, et al., 2023; National Health Service [NHS], 2024; WebMed, 2024a). As infection attacks the immune system further without the use of antiretroviral therapy (ART), other signs and symptoms such as cough, diarrhea, weight loss and swollen lymph nodes may surface (WHO, 2024a; CDC, 2024; Ahmad, et al., 2023; Mayo Clinic, 2024).

The use of antiretroviral therapy to control the infection in humans has been one of sciences' breakthroughs of the decade. Though, antiretroviral drugs in themselves do not completely eliminate the virus, they help to block new infections and suppress the activities of HIV so that viral load is kept at a minimum and undetectable level (HIVinfo.nih.gov, 2024). With this, patients living with HIV can live longer and new transmission will be reduced (Kemnie & Gulick, 2022). The successes recorded in the use of HIV drugs has become well-known among partners with one of them testing positive to the virus and the other negative (Kemnie & Gulick, 2022). Progression beyond HIV chronic stage in several parts of the worlds has thereby reduced significantly so that progression to AIDS has become rare (Hiv.gov, 2024). The figure of those accessing antiretroviral drugs globally as at 2023 stands at 30.7 million people (UNIAIDS, 2024).

Without treatment with HIV antiretroviral drugs, HIV infection would progress to advance stage, getting worse over time. HIV infection has three stages; Acute HIV infection, Chronic HIV infection and Acquired Immunodeficiency Syndrome stages (HIVinfo.nih.gov, 2024). At AIDS stage, the body immune system has become weak and vulnerable to attacks by other infections. PLWH are diagnosed with AIDS when their CD4+T cells count is below $200\ cell/mm^3$. At this stage, the viral load of PLWH is very high and can easily be transmitted to others. The survival span for PLWH who are not on ART is about 3 years (HIVinfo.nih.gov, 2024).

Assefa and Gills (2020) in a work posed a question: "Will there be an endgame to HIV?" While the search for a total curative measure for HIV is ongoing, Ogunniran and Ibrahim, 2023; Ogunniran and Ibrahim, 2024, noted that HIV has kept presenting new dimensions for study. One of such areas is that HIV has types, sub-types and sub-subtypes, depending on their genetic composition. About 49 circulating recombinant forms (CRFs) are reported to be in existence (Ogunniran & Ibrahim, 2023; Ogunniran & Ibrahim, 2024; WebMed, 2024b; Public Health Department, 2024). Basically, HIV type is divided in to two, namely HIV-1 and HIV-2. Infection by any of these types can lead to AIDS though they differ. HIV-1 is the commonest (WebMed, 2024b; Healthline, 2024). HIV-2 is found mostly in West Africa, but in a smaller number of people. About 0.01% of all HIV cases are infected with HIV-2, and these are mostly West Africans living in the U.S (WebMed.

2024b). HIV regularly replicates copies of itself within its host. Some strains multiply faster and can be passed from person to person more easily than others. HIV-1 and HIV-2 have multiple groups which branch out even further into subtypes, or strains. Medical practitioners will record much and quicker success in treating HIV persons if they know what strain they have. A blood test can detect this. The same test also can tell if certain HIV drugs will work well or not (WebMed, 2024b; Public Health Department, 2024; Medical News Today, 2024).

This paper uses mathematical modeling as a tool to analyze the dynamics of coexistence and competition between two distinct viral strains within the same host. It provides insights into the mechanisms of HIV superinfection. Furthermore, specific quantitative results on treatment efficacy and timing to prevent HIV superinfection, which can inform treatment strategies were discussed. The study sheds light on the consequences of HIV superinfection. This includes increased viral load, multiplication of infected cells, and decline of healthy cells, which can help advance research in HIV, improve prevention and treatment strategies.

2. Model Formulation

2.1 HIV Superinfection Model without Control Measure

We here provide a brief description to the development of a HIV superinfection model without control strategies. We refer to a previous study conducted by Ogunniran and Ibrahim (2024), where a HIV superinfection model was presented. The model described the dynamics of two unique HIV strains infecting the population of CD4+T cells at different times. It consist five ordinary differential equations representing the population of uninfected CD4+T cells, $U(t)$, population of CD4+T cells infected with strain 1, $I_p(t)$, population of CD4+T cells infected with strain 2, $I_s(t)$, amount of viral strain 1, $V_p(t)$, and amount of viral strain 2, $V_s(t)$. The two viral strains co-exist and co-circulate in their host but do not recombine in their life time. The model constructed by Ogunniran and Ibrahim (2024) is represented by equation (1) – (5).

$$\frac{dU(t)}{dt} = s - \beta V_p(t)U(t) - \mu U(t) \tag{1}$$

$$\frac{dI_p(t)}{dt} = \beta V_p(t)U(t) - \alpha V_s(t)I_p(t) - \mu I_p(t) \tag{2}$$

$$\frac{dI_s(t)}{dt} = \alpha V_s(t)I_p(t) - \mu I_s(t) \tag{3}$$

$$\frac{dV_p(t)}{dt} = \rho N_p I_p(t) + (1-\gamma)N_s I_s(t) - \beta V_p(t)U(t) - \delta V_p(t) \tag{4}$$

$$\frac{dV_s(t)}{dt} = \gamma N_s I_s(t) - \alpha V_s(t)I_p(t) - \delta V_s(t) \tag{5}$$

subject to $U(0) > 0$, $I_p(0) \geq 0$, $I_s(0) \geq 0$, $V_p(0) \geq 0$ and $V_s(0) \geq 0$.

2.2 Incorporating of Control Measures in the HIV Superinfection Model

In the study of infectious diseases, modelers are keen on how to either eliminate the causative agent(s) of disease(s) where possible or the disease(s) itself or minimize their activities. In this wise, control measures are usually introduced. The idea is to target sensitive parameters of the model that enhances or hinders the the growth of the infection in the system. The model discussed in Ogunniran and Ibrahim (2024) do not incorporate any control measure. We now incorporate control measures in the model.

2.3 Model Description

In this work, two control measures, u_1 and u_2, were introduced. u_1 is the potency of drug therapy in blocking new infection (targeted on rate of infections), where u_2 is the potency of drug in preventing viral production (targeted on the number of virions produced). Hence, the rate of infection in the presence of drug becomes $(1-u_1)$, while $(1-u_2)$ is the rate of virion production under drug therapy. The role of CTL immune response was also considered in the extended model, so that a new compartment, C, representing the population of CTL immune response cells, was added to the model. The effects of CTL immune response cells are to slow down the activities of free viruses and kill infected cells (Allali & Torress, 2018).

The new model comprises six classes dealing with cellular and viral populations. The susceptible population is the uninfected CD4+T cells (U), with source terms and natural death rate of s_1 and μ respectively. The two forms of viral strains are denoted by V_p and V_s. Their corresponding infected classes are the primarily-infected class and superinfected class, represented by $I_p$and I_s respectively. The clearance rate of viral strain is δ. Upon infection of the system by the primary viral strain, uninfected cells population are primarily-infected at the rate β. Primarily-infected cells are super-infected at the rate α. Upon the death of the infected cells, new virions are produced at the rate ρ and γ, and progressed into V_p and V_s classes respectively. s_2 is the source term for CTL immune cells, κ is the clearance rate of infected CD4+T cells due to CTL immune cells response. Due to the invasion of V_p and V_s, CTL immune response cells are produced at the rate ρ_1 and ρ_2 respectively. μ_c is the natural death rate of CTL immune cells.

The control model is represented by six ordinary differential equations presented as equations (1) – (6).

$$\frac{dU}{dt} = s_1 - \beta(1-u_1)V_pU - \mu U \tag{6}$$

$$\frac{dI_p}{dt} = \beta(1-u_1)V_pU - \alpha(1-u_1)V_sI_p - (\mu+\kappa C)I_p \tag{7}$$

$$\frac{dI_s}{dt} = \alpha(1-u_1)V_sI_p - (\mu+\kappa C)I_s \tag{8}$$

$$\frac{dV_p}{dt} = \rho N_p(1-u_2)I_p + \gamma N_s(1-u_2)I_s - \beta(1-u_1)V_pU - \delta V_p \tag{9}$$

$$\frac{dV_s}{dt} = \gamma N_s(1-u_2)I_s - \alpha(1-u_1)V_sI_p - \delta V_s \tag{10}$$

$$\frac{dC}{dt} = s_2 + \rho_1 CI_p - \rho_2 CI_s - \mu_c C\delta \tag{11}$$

Equations (6) – (11) are subject to the following inequalities initial conditions: $U(0) > 0$, $I_p(0) \geq 0$, $I_s(0) \geq 0$, $V_p(0) \geq 0$, $V_s(0) \geq 0$ and $C(0) > 0$.

3. Materials and Methods

3.1 Dynamics of the Model

As in Ogunniran and Ibrahim (2024), the populations of uninfected and infected CD4+T cells constitute the total population of the CD4+T cells in system. We denote this total population by N, so that

$$N = U + I_p + I_s \tag{12}$$

To obtain the population dynamics of the model equations (6) – (11), we took the total derivative of equation (12). Taking the derivative of (12) with respect to time, t, the expression in (13) was obtained.

$$\frac{dN}{dt} = s - \mu U - \mu I_p - \mu I_s \quad (13)$$

Equation (13) represents the state at which changes occur in the system.

3.2 Existence and Uniqueness of the Solution of the Model

Theorem 1: Suppose ϑ denote the region $0 \leq N \leq \frac{s}{\mu}$, then the equations (6) – (11) have unique solution.

Proof: It is required to show that the partial derivatives of equations (6) – (11) are continuous and bounded. Let

$$z_1 = s - \beta V_p U(t) - \mu U(t) \quad (14)$$
$$z_2 = \beta(1-u_1)V_p U - \alpha(1-u_1)V_s I_p - (\mu + \kappa C)I_p \quad (15)$$
$$z_3 = \alpha(1-u_1)V_s I_p - (\mu + \kappa C)I_s \quad (16)$$
$$z_4 = \rho N_p(1-u_2)I_p + \gamma N_s(1-u_2)I_s - \beta(1-u_1)V_p U - \delta V_p \quad (17)$$
$$z_5 = \gamma N_s(1-u_2)I_s - \alpha(1-u_1)V_s I_p - \delta V_s \quad (18)$$
$$z_6 = s_2 + \rho_1 C I_p - \rho_2 C I_s - \mu_c C\delta \quad (19)$$

Differentiating each of the equations of equations (14) – (19) partially with respect to U, I_p, I_s, V_p, V_s and C, gives the following:

$$\left|\frac{\partial z_1}{\partial U}\right| = \left|-\beta V_p - \mu\right| = \left(\beta V_p + \mu\right) < \infty \quad (20)$$
$$\left|\frac{\partial z_1}{\partial I_p}\right| = |0| = 0 < \infty \quad (21)$$
$$\left|\frac{\partial z_1}{\partial I_s}\right| = |0| = 0 < \infty \quad (22)$$
$$\left|\frac{\partial z_1}{\partial V_p}\right| = |-\beta U| = \beta U < \infty \quad (23)$$
$$\left|\frac{\partial z_1}{\partial V_s}\right| = |0| = 0 < \infty \quad (24)$$
$$\left|\frac{\partial z_1}{\partial C}\right| = |0| = 0 < \infty \quad (25)$$

For $i = 2, 3, 4, 5, 6$, where $x_i = \{I_p, I_s, V_p, V_s, C\}$, it can be shown that $\left|\frac{\partial z_i}{\partial x_i}\right| < \infty$. Hence, the partial derivatives exist, and are finite bounded, so we conclude that the model has a unique solution.

3.36 Positivity of Solution

Theorem 2: Suppose that the initial inequality conditions satisfy $U(0) > 0$, $I_p(0) \geq 0$, $I_s(0) \geq 0$, $V_p(0) \geq 0$, $V_s(0) \geq 0$ and $C(0) > 0$ then the solution $\{U, I_p, I_s, I_p, V_p, V_s, C\}$ of the system is non-negative for all $t > 0$.

Proof: In the first instance, we use the first equation of the model, that is,

$$\frac{dU}{dt} = s - \beta V_p U - \mu,$$

which can be expressed as

$$\frac{dU}{dt} = \left(\beta V_p + \mu\right)U \geq 0, (\because s > 0) \quad (26)$$

Applying integrating factor method to solve for $U(t)$ in equation (26), the relation becomes

$$\frac{d}{dx}\left\{U(t)\ exp\left(\int_0^t \beta V_p(x)dx + \mu t\right)\right\} \geq 0. \quad (27)$$

Integrating over the time interval $[0, t]$ yields

$$U(t)\ exp\left\{\left(\int_0^t \beta V_p(x)dx + \mu t\right)\right\} - U(0) \geq 0. \quad (28)$$

This leads to

$$U(t) \geq U(0)\ exp\left\{-\left(\int_0^t \beta V_p(x)dx + \mu t\right)\right\} > 0 \text{ for all } t > 0. \quad (29)$$

Using similar procedures, it can be also be shown that $I_p > 0$, $I_s > 0$, $V_p > 0$, $V_s > 0$ and $C > 0$ for all $t > 0$. Since the solution of the system continuously depends on the respective initial conditions in the neighbourhood of zero, then the system is non-negative for all $t > 0$.

4. Numerical Simulation and Discussion of Results

In the implementation of the scheme, the following parameters were used: $s_1 = 1$, = 1, $s_1 = 0.2$, $s_1 = 0.00025$, $\alpha = 0.00024$, $\mu = 0.02$, $\mu_c = 0.2$, $\delta = 0.001$, $\rho = 0.03$, subject to the following initial conditions: $U(0) = 5\ cells/mm^3$, $V_p(0) = 1\ copies/ml$, $V_s(0) = 1\ copies/ml$, $I_p(0) = 1\ cells/mm^3$, $I_p(0) = 1\ cells/mm^3$, $C(0) = 2\ cells/mm^3$.

In carrying out the simulation, two scenarios were considered under different cases. The behaviours of the system were investigated when there was no control measure and when there was control measure. The cases examined the behaviours of uninfected cells, viral strains, infected cells and the CTL cells when the numbers of viruses produced were small on one hand and large on the other hand. From literatures, the number of viruses produced ranges between hundreds and thousands per day (Allali & Torress, 2018). In this paper, $N_p = 500\ copies/ml$ and $N_s = 500\ copies/ml$ were considered to be small, while $N_p = 10{,}000\ copies/ml$ and $N_s = 10{,}000\ copies/m$ were considered to be large. According to WHO, the success rate of HIV drug is considered to be 90% (WHO, 2024b). Hence, we set $u_1 = u_2 = 0.90$ when drug therapy was introduced as control measure and $u_1 = u_2 = 0$ in the absence of drug therapy. Finally, the burden of HIV superinfection on the population of healthy CD4+T cells was investigated.

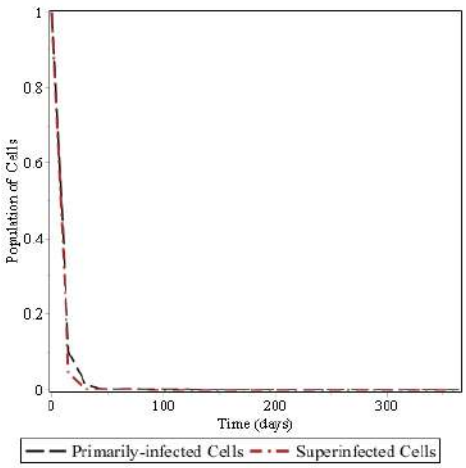

(a)

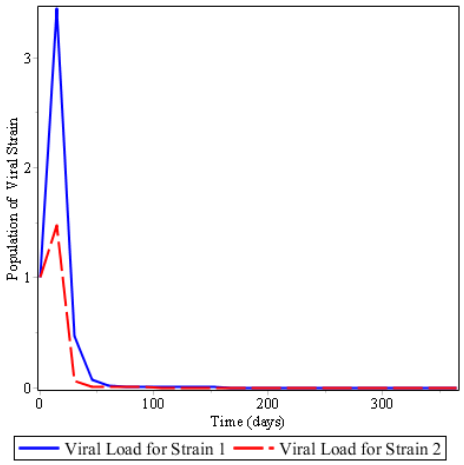

(b)

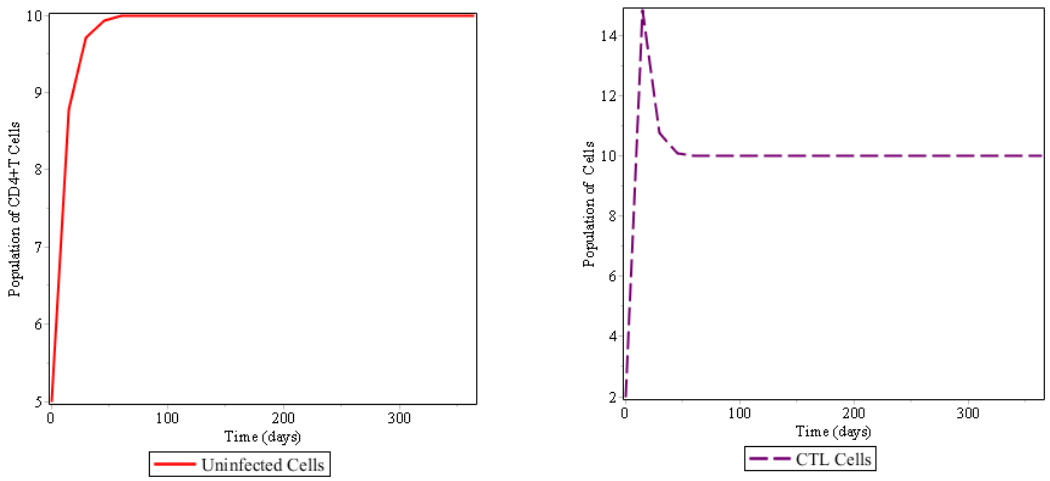

(c) **(d)**

Figure 4.1: *Plots of CD4+T cells , viral strains and CTL immune cells using* $N_p = 500\ copies/ml$ *and* $N_s = 500\ copies/ml$, *and* $u_1 = u_2 = 0$

Figure 4.1(a) illustrates the behaviour of uninfected CD4+T cells at the onset of infection. At this stage, the volume of virions in the system is small. The activities of viral strains were not seen to have obvious negative effects on the population of healthy CD4+T cells. This is usually the case as virions are still loading themselves in the system, HIV is usually undetectable at the early stage of infection. A reverse case is presented in Figure 4.2(a) where the volume of virions in the system is large, and the effects of viral strains become evident.

Figure 4.1(b) shows viral loads for both strains at the onset of the infection. At the initial stage of infection, viral load rose from 1 $copies/ml$ to about 3.5 $copies/ml$ in about 20 $days$. However, since HIV has not been fully integrated into the system, and the numbers of virions in the system are also minimal, a decrease in viral load is observed so that clinical test may not even detect infection at this point. The decline observed may also be due to the natural death rate of viruses.

The scenario in Figure 4.1(c) is a consequence of the behaviour of the viruses observed in Figure 4.1(a). Since this is the beginning of infection and viral loads are yet undetected, the effects of viral strains on healthy cells are minimal as shown in Figure 4.1(a). The decline in the populations of primarily-infected cells and super-infected cells are therefore largely due to the natural death of infected cells.

In Figure 4.1(d), the initial population of CTL cells was 2 $cells/mm^3$. The introduction of viral strains in the system triggered the production of more CTL cells to about 14 $cells/mm^3$. This account for the increase in the population of the CTL cells. Whereas the CTL cells cannot clear all the viruses in the system, they kill some of the infected cells. Hence, in the absence of drug therapy, they act as soldiers to fight infection. Hence, not all CD4+T cells are immediately infected (see Figure 4.2(a)).

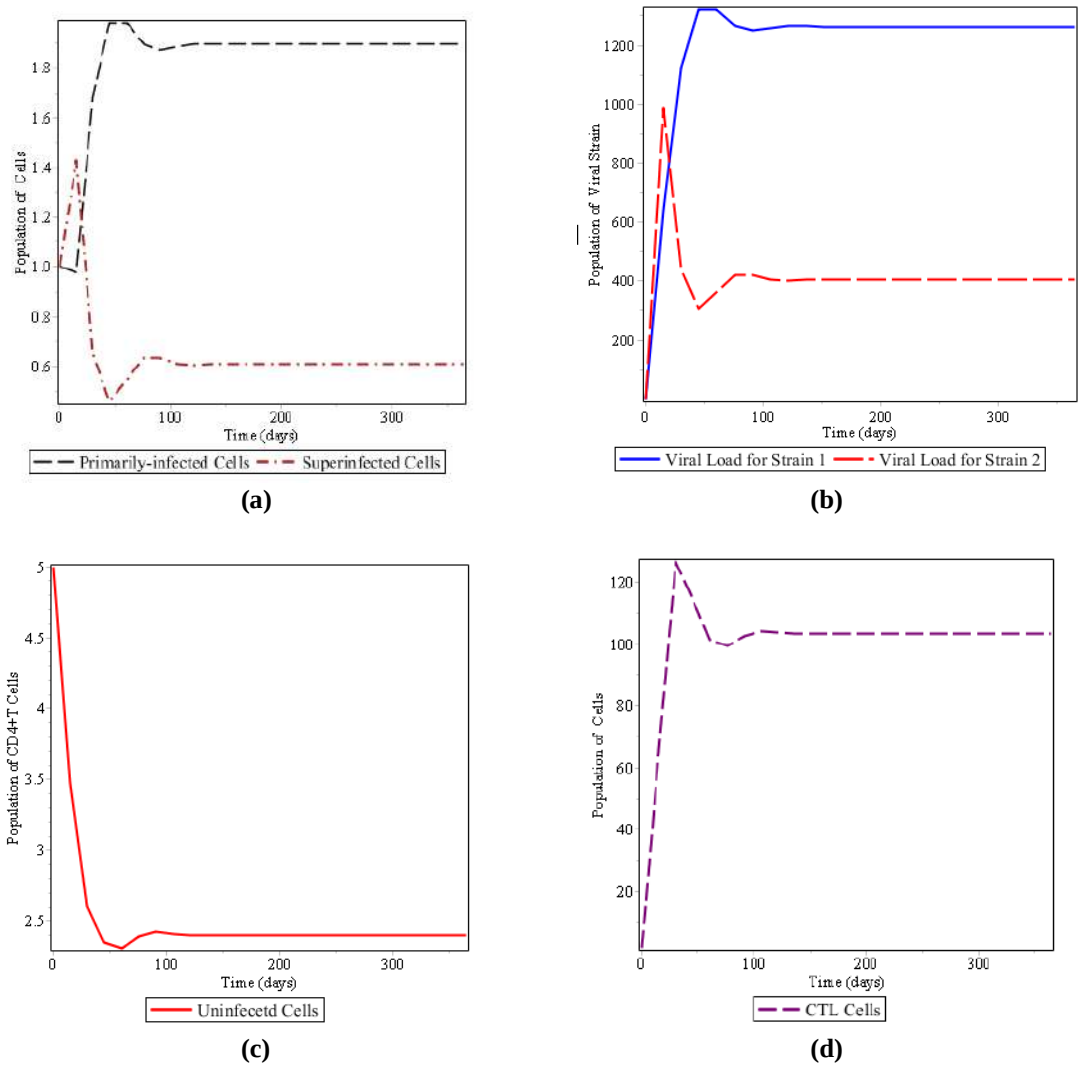

Figure 4.2: *Plots of CD4+T cells , viral strains and CTL immune cells using* $N_p = 10{,}000\ copies/ml$ *and* $N_s = 10000\ copies/ml$, *and* $u_1 = u_2 = 0$

As infection progresses, with no drug therapy, the copies of virions in the system becomes large (see Figure 2(b)). In Figure 4.2(a), it is observed that there is a decline in the population of healthy CD4+T cells as the number of virions produced in the system increases with time. As the population of healthy cells decreases as a result of the effects of the activities of the viral strains, the population of infected cells will increase. The population of virions in the system is now large. The infective speed of the first viral strain is higher than that of the second strain. However, in both cases, the activities of HIV virus rose to their peak and became steady at some points when $t = 50\ days$ (see Figure 4.2(b)). Since there is no control measure, HIV strains persist in the system.

A comparison between Figure 4.2(a) and Figure 4.2(c) shows that there is a direct relationship between the population of healthy CD4+T cells and the population of infected CD4+T cells. Decrease in healthy CD4+T cells lead to increase in infected cells. With large number of viruses in the system, it is observed that primarily-infected cells grow sporadically, though super-infected cells declined but later rose to maintain a steady state about 90 $days$ after the beginning of infection.

More CTL cells are generated as there are more viruses in the system. This accounts for the increase in the population of CTL cells in Figure 4.2(d) as compared to the scenario in Figure 4.1(d). The small amount of decline observed was due to natural death of CTL cells.

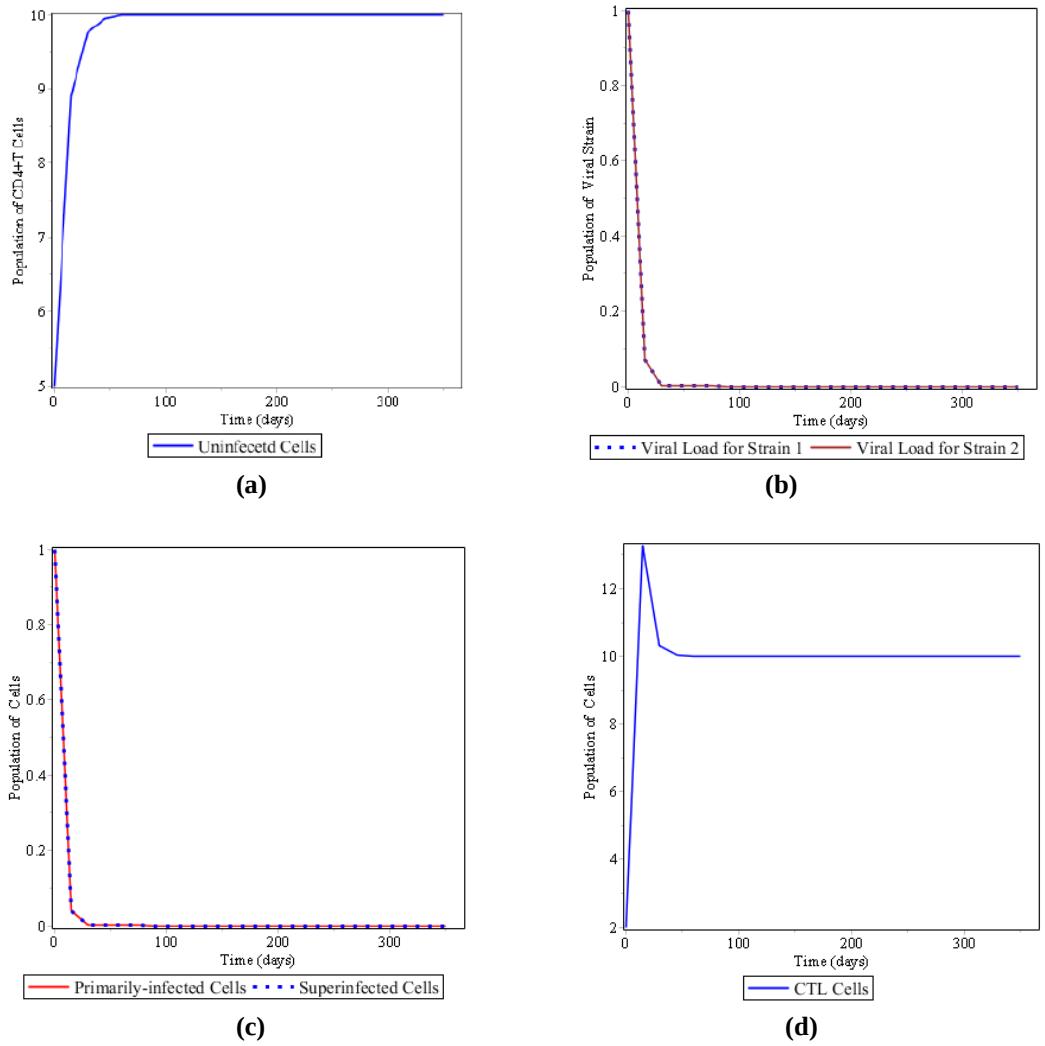

Figure 4.3: *Plots of CD4+T cells , viral strains and CTL immune cells using* $N_p = 500\ copies/ml$ *and* $N_s = 500\ copies/ml$, *and* $u_1 = u_2 = 0.90$

Figure 4.3(a) is similar to Figure 4.1(a), however the progression of HIV infection is not the same in the two scenarios. In Figure 4.3(a), the introduction of drug therapy was the reason why there was a steady increase in the population of healthy CD4+T cells. The former behaves likewise not for this reason but research and clinical results have shown that at the onset of HIV infection, population of healthy CD4+T cells are not immediately depleted as the activities of viruses in the system are yet to be established.

The scenario in Figure 4.3(b) depicts a situation where there is a continuous decline in the viral loads for both viral strains. This is expected because drug therapy has been introduced into the system at an early stage of infection to block both the replication of viruses and new infection. Hence, in less than $50\ days$, viral load for both viral strains became undetected in the system.

Figure 4.3(c) shows the behaviours of primarily-infected CD4+T cells and super-infected CD4+T cells in the presence of drug therapy when the number of viruses in the system is small. Drug therapy and CTL immune response kill and eliminate infected cells so that a quick and progressive decline in the population of infected CD4+T cells was observed. There was corresponding increase in the population of healthy CD4+T cells.

In Figure 4.3(d), the population of CTL cells increased from 2 $cells/mm^3$ to about 13 $cells/mm^3$. The sudden increase was as a result of the signal sent to the memory of the CTL cells as HIV infects the system so that it immediately releases more combatants to fight the invading viruses. Infection of cells releases new CTL cells to fight infection. The decline noticed in the population of CTL cells are due to the natural death rate of CTL cells.

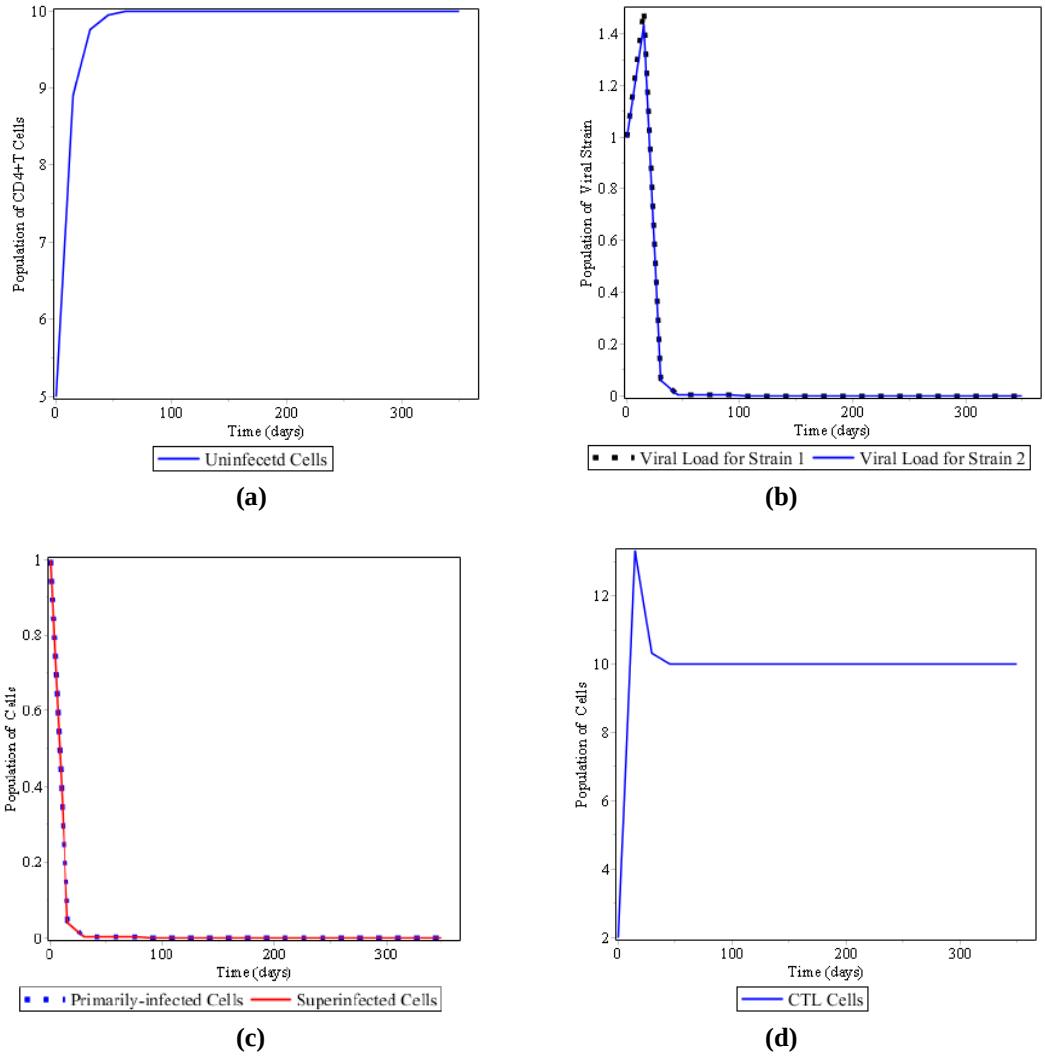

Figure 4.4: *Plots of CD4+T cells , viral strains and CTL immune cells using* $N_p = 10{,}000\ copies/ml$ *and* $N_s = 10000\ copies/ml$, *and* $u_1 = u_2 = 0.90$

Though the number of viruses in the system was large, the population of healthy cells did not deplete (see Figure 4.4(a)). This is true because with effective use of drug therapy, viral replication was prevented and new infection was blocked. Even when new viruses are produced due to the lysing of cells that are already infected, much of them are cleared

due to drug therapy and the effects of CTL immune response cells that fights and kills infected cells.

At the initial stage of infection, viral load rises sharply. The introduction of drug therapy does not preclude this initial rise of viral load. This was evident in Figure 4.4(b). However, with respect to time, the effect of drug therapy on viruses and infected cells slows down and hinders the activities of viruses in the system. This resulted in the decline of viral loads of both strains to almost zero, so that viruses become undetected in the system.

In Figure 4.4(c), the population of infected CD4+T cells was observed to decline in the presence of drug therapy. By implication, the population of healthy cells will increase. This is the expected scenario for the system to be in a state of viral strain-free equilibrium.

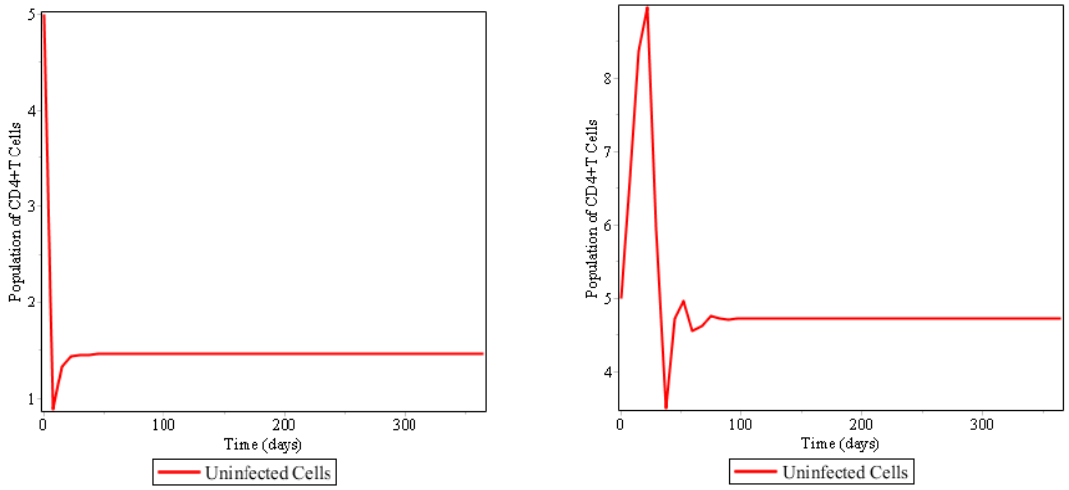

Figure 4.5: *Plots of CD4+T cells with:* ***(a)*** $N_p = 500\ copies/ml$ *and* $N_s = 10000\ copies/ml$, ***(b)*** $N_p = 10{,}000\ copies/ml$ *and* $N_s = 500\ copies/ml$, $u_1 = u_2 = 0.90$

The population of uninfected CD4+T cells was 5 $cells/mm^3$ at the onset of infection in Figure 4.5(a), however, in about 10 $days$ after infection, the population dropped sharply to about 1 $cells/mm^3$, peaked at about 1.4 $cells/mm^3$ in the next 10 $days$, and finally maintained a steady state from time, $t = 20\ days$. The initial effect of the second strain was significant because the rate of decline of healthy CD4+T cells was rapid. The burden of the large number of viruses produced by the second viral strain was significant. Though a steady state was reached for healthy CD4+T cells, the population of healthy cells did not rise above 1.5 $cells/mm^3$ throughout the lifetime of infection.

In Figure 4.5(b), the initial population of healthy CD4+T cells was 5 $cells/mm^3$. It rose to 9 $cells/mm^3$ and declined below 4 $cells/mm^3$ within the first 50 $days$ of infection. However, in another 10 $days$, the population jumped to 5 $cells/mm^3$ and maintained a steady state at $t = 80\ days$ with a population of about 4.8 $cells/mm^3$. The effect of the second strain was significant because in this scenario, it took more time for drug therapy and CTL cells to clear a smaller amount of virus before the state of equilibrium was reached by the healthy CD4+T cells.

The scenarios in Figure 4.5(a) and Figure 4.5(b) show the effect of the second viral strain in the dynamics of HIV superinfection model for all number of viruses produced by the second strain. When $N_p = 500\ copies/ml$ and $N_s = 10000\ copies/ml$, the population of uninfected cells declined from $5\ cells/mm^3$ to about $1\ cells/mm^3 3$. Similarly when $N_p = 10{,}000\ copies/ml$ and $N_s = 500\ copies/ml$, though the population of uninfected cells increased from $5\ cells/mm^3$ to $9\ cells/mm^3$ initially, it decreased within the next $5\ days$ to about $1\ cells/mm^3$. We observed that when $N_s < N_p$, about $5\ cell/mm^3$ of healthy CD4+T cells were depleted. However, more uninfected CD4+T cells were depleted when $N_s > N_p$. In both scenarios, the presence of the second viral strain led to the decrease of healthy CD4+T cells. Thus, the second viral strain plays a significant role in the dynamics of HIV superinfection model.

Conclusion

In this paper, we modified a previously proposed model of HIV superinfection in Ogunniran and Ibrahim (2024), without control measure. Results of data simulation showed that the population of healthy CD4+ T cells declined with respect to time in the presence of HIV strains. The viral loads for both viral strains are observed to be on a steady increase. These situations are not favourable to the system. Thus, this necessitated the introduction of control measures. Sensitivity analysis of parameters of the models were performed in Ogunniran and Ibrahim (2024), and it shows that the rate of infection and the rate at which virions are produced are the most sensitive parameters in that order. Hence, we extended the model in Ogunniran and Ibrahim (2024), and incorporated drug therapy as control measure. The effect of CTL immune response cells was also included in the model. This work reveals that HIV viral strains can co-exist and co-circulate in their host, CD4+T cells. The burden of the second viral strain on the population of healthy CD4+T cells was observed to have great significant in the dynamics of HIV superinfection. Small amount of viruses, that is when $N_p = 500\ copies/ml$, produced by the second viral strain do not only increase the viral load of the first strain, but also increased the production of infected CD4+T cells and caused a significant decline in the population of healthy CD4+T cells. When a larger number of virions, $N_s = 10{,}000\ copies/ml$, are produced by the second viral strains, the effects on healthy cells is more. However, on the introduction of control measures, in this case, HIV drug therapy, at 90% level of efficacy, a significant decline in the population of infected cells and free viruses was observed. Moreso, the population of healthy cells increased significantly. With control measures, infection dies very fast within a period of time, $t < 50\ days$ (see Figure 4.3(b), Figure 4.3(c) and Figure 4.4(c). On the other hand, infection continues to grow in the population of CD4+T cells in all cases with no control measures so that an endemic equilibrium is reached at some point in time when $t \geq 100\ days$, that is in about $3\ months$ (see Figure 4.2(a), Figure 4.2(b) and Figure 4.2(c)).

References

WHO (2024a). HIV and AIDS. Accessed 21st August (2024), https://www.who.int/news-room/fact-sheets/detail/hiv-aids

UNAIDS (2024). Global HIV & AIDS statistics – Fact sheet, Accessed 21st August (2024), https://www.unaids.org/en/resources/fact-sheet

Kemnic, T. R. and Gulick, P. G. (2024). HIV Antiretroviral Therapy. In: StatPearls [Internet]. Treasure Island (FL): StatPearls Publishing; 2024 Jan-. Available from: https://www.ncbi.nlm.nih.gov/books/NBK513308/

HIV.gov. (2024). Global Statistics, Accessed 22nd August (2024), https://www.hiv.gov/hiv-basics/overview/data-and-trends/global-statistics

HIVinfo.nih.gov (2024). The Stages of HIV Infection, Accessed 22nd August (2024), https://hivinfo.nih.gov/understanding-hiv/fact-sheets/stages-hiv-infection

Stanford Health Care (2024). Transmission of HIV/AIDS, Accessed 22nd August (2024), https://stanfordhealthcare.org/medical-conditions/sexual-and-reproductive-health/hiv-aids/causes.html

CDC (2024). Human Immunodeficiency Virus/HIV, Accessed 22nd August (2024), https://wwwnc.cdc.gov/travel/yellowbook/2024/infections-diseases/hiv

Ahmad, N., Khan, Z. A., Akbar, M., & Al-Moneef, A. A. (2023). Analysis of HIV-1 mathematical model using Taylor's series method. *Thermal Science*, No. 27(1), S423 - S431

NHS (2024). Symptoms – HIV/AIDS, Accessed on 22nd August (2024), https://www.nhs.uk/conditions/hiv-and-aids/symptoms/

WebMD (2024). HIV/AIDS, Symptoms, Stages and Early Warning Signs, Accessed 22nd August (2024), https://www.webmd.com/hiv-aids/understanding-aids-hiv-symptoms

Mayo Clinic (2024). HIV/AIDS, Symptoms and Causes, Accessed 22nd August (2024), https://www.mayoclinic.org/diseases-conditions/hiv-aids/symptoms-causes/syc-20373524

Assefa, Y. and Gills, C. F. (2020). Ending the epidemic of HIV/AIDS by 2030: Will there be an endgame to HIV, or an endemic HIV requiring an integrated health systems response in many countries?, *Int. J. Infect. Dis.*, vol. 100, pp. 273 – 277

Ogunniran, M. A. and Ibrahim, M. O. (2023). Application of Elzaki Transform Method for Solving and Interpreting HIV Superinfection Model, *Int. J. Appl. Math. Informatics,* vol. 17, pp. 1 -5, 2023

Ogunniran, M. A. and Ibrahim, M. O. (2024). Sensitivity Analysis of a HIV Superinfection Model. *European Modern Studies Journal,* vol. 8, No. 3, pp. 431 – 437

WebMD, Types and Strains of HIV, Accessed 22nd August (2024), https://www.webmd.com/hiv-aids/types-strains-hiv

Public Health Department, Types of HIV, Accessed 22nd August (2024), https://acphd.org/hiv/hiv-aids-basics/types-of-hiv/

Healthline, How Many HIV Strains, Types, and Subtypes Are There? Accessed 22nd August (2024), https://www.healthline.com/health/hiv/hiv-strains

Ogunniran, M. A., Abdulrahman, S., Oshatuyi, B. O. and Blessing, T. E. (2018). HIV/AIDS In-vivo Model Incorporating Latency Period and the Role of CTL Immune Cells, *Journal of the Nigerian Association of Mathematical Physics,* vol. 46, pp. 347 – 352

Allali, K. H. and Torres, F. M. (2018). Analysis and Optimal Control of an Intracellular Delayed HIV Model with CTL Immune Response. *Math. Comput. Sci.*, pp. 1 – 15

WHO (2024b). HIV Drug Resistance, Accessed 23rd August, 2024, https://www.who.int/news-room/fact-sheets/detail/hiv-drug-resistance

Medical News Today, Differences between HIV-1 and HIV-2, Accessed 23rd August (2024), https://www.medicalnewstoday.com/articles/323893

Mathematical Modelling of Taeniasis and Cysticercosis Transmission Dynamics: Sensitivity Analysis Approach

[1*]Onwubuya, I. O., [2]Madubueze, C. E., [3]Gweryina, R. I., [4]Aboiyar, T.

[1,2,3,4]Department of Mathematics, Joseph Sarwuan Tarka University, Makurdi, Nigeria

[1*]Corresponding author: isaacobiajulu@gmail.com

Abstract

In developing countries, particularly in West Africa, taeniasis and cysticercosis infections pose major public health issues, with a growing incidence in developed nations attributed to migration. This study presents a deterministic model to investigate the transmission dynamics of these infections among humans and pigs via sensitivity analysis. The basic reproduction number, R_0, is calculated using the next-generation matrix method to assess the stability of the disease-free equilibrium. A sensitivity analysis of R_0 and the model's state variables concerning model parameters utilize Latin Hypercube Sampling (LHS) along with Partial Rank Correlation Coefficients (PRCCs) to identify the parameters that most significantly influence taeniasis and cysticercosis transmission. The results show that transmission rate (through the consumption of infected pork by humans), shedding rate for human with taeniasis, rate of consumption of undercooked infected pork, proportion of unconsumed contaminated pork, transmission coefficient of T. solium eggs to pigs, pig slaughter rate, decay rate of Taenia eggs in the environment and the rate at which humans infected with taeniasis recover significantly influence the dynamics of taeniasis and cysticercosis transmission, and the model is simulated numerically to show the endemicity of both infections in the population.

Keywords: taeniasis, cysticercosis, taenia solium, basic reproduction number, mathematical analysis, sensitivity analysis.

1. Introduction

Taeniasis and cysticercosis refer to neglected food-borne zoonotic diseases triggered by larval and adult stages of tapeworms (Symeonidou, 2018). These diseases are associated with the genus Taenia and the family Taeniidae. The species of Taenia that cause taeniasis in humans include Taenia saginata (beef tapeworm), Taenia asiatica (Asian tapeworm), and Taenia solium (pork tapeworm) (Centers for Disease Control and Prevention [CDC], 2023; World Health Organization [WHO], 2019). Notably, T. solium, commonly known as the pork tapeworm, ranks the highest among food-borne parasitic infections globally (Food and Agricultural Organization [FAO] of the United Nations and World Health Organization [WHO], 2014). It is estimated that millions of people worldwide are infected with T. solium, recognized as the most harmful tapeworm species affecting humans (WHO, 2005). Each year, T. solium is responsible for approximately 2.8 million disability-adjusted life-years (DALYs) in high-risk areas due to human cysticercosis (WHO, 2015). These diseases pose considerable risks to public health and food safety. T. solium is unique among

helminth zoonoses because its life cycle relies on humans as the only definitive host and pigs as the secondary or intermediate host.

Human taeniasis is a parasitic intestinal disease caused by adult T. solium. It occurs when individuals consume undercooked or raw pork or beef that contains larval cysts of the tapeworm (cysticerci) (Symeonidou, 2018; WHO, 2019). Those infected with taeniasis start excreting taenia eggs in their feces approximately 8 to 12 weeks after infection (California Department of Public Health. Taeniasis and Cysticercosis [CDPH], 2024; WHO, 2005). Infected humans are the main source of taenia eggs in the environment, as they shed these eggs when they defecate in areas accessible to pigs and other people, increasing the risk of transmission.

Human cysticercosis is a tissue infection caused by the larval form of T. solium (CDC, 2023). People acquire cysticercosis by directly ingesting taenia eggs in contaminated environments, such as through food, vegetables, or water, or due to poor hygiene practices (Brutto, 2013; WHO, 2019). Pigs become infected by consuming infected human feces or indirectly ingesting taenia eggs from contaminated water or feed, where these eggs develop into cysticerci in their bodies (Dermauw et al., 2018; Symeonidou, 2018). This form of pig cysticercosis leads to considerable economic losses for farmers in endemic regions as it reduces the market value of pigs (FAO & WHO, 2014; Winskill et al., 2017). Additionally, this disease represents a serious health risk to humans, making pork unsafe for consumption (Winskill et al., 2017; WHO, 2005).

Taeniasis and cysticercosis are prevalent in low-income and developing regions, such as Africa, Latin America, and Asia, where pork consumption is typical, and pigs roam freely due to traditional husbandry practices combined with inadequate sanitation services (Alemneh & Adem, 2017; Mwasunda et al., 2022; WHO, 2005). In contrast, developed nations have adequate sanitation and animal husbandry that impede the life cycles of these diseases. However, they still face risks from infected individuals immigrating from areas with high infection rates (WHO, 2005). The introduction of these infections to developed countries leads to a resurgence and broader global distribution in non-endemic regions, as human carriers can contaminate the environment, causing secondary infections (WHO, 2005).

Abdominal discomfort, nausea, constipation, diarrhea, weight loss, and loss of appetite are typical symptoms of human taeniasis. Some common manifestations of infected humans with cysticercosis include severe headaches, dizziness, and hypertension. Meanwhile, infected pigs rarely show symptoms, since its being slaughtered before the symptoms show up. Human taeniasis is seldom diagnosed through the laboratory examination of stool samples for the presence of taenia eggs, whereas, the diagnosis of human cysticercosis is through immunodiagnostic tests, imaging technology such as computer tomography (CT) and magnetic resonance imaging (MRI) scans (CDC, 2023; Mwasunda et al., 2021a; WHO, 2005). Some diagnostic technique employed in the diagnoses of infected pigs with cysticercosis includes tongue palpation and meat inspection (FAO & WHO, 2014). Human and pig infections and subsequent environmental contamination with taenia eggs can be prevented through enhanced sanitation and hygiene practices, improved animal (pig) husbandry, proper toiletry (sewage management), health education, avoiding undercooked or raw pork or foods or waters contaminated with faeces, proper meat (pork) inspection, vaccination

of pigs and prompt detection and treatment of infected humans (CDC, 2023; WHO, 2005; WHO, 2019).

The treatment of human taeniasis and cysticercosis infections involves the administration of prescribed medications of praziquantel, albendazole, tribendimidine, niclosamide or nitazoxanide (CDC, 2023; Symeonidou, 2018; WHO, 2019). Whereas, for infected pigs, anthelmintic medicines such as praziquantel, flubendazole, nitazoxanide and oxfendazole are used for effective treatment. These infections should be treated promptly and effectively to avoid their progression to a more severe case known as neurocysticercosis, which is a leading cause of epilepsy worldwide (CDC, 2023; WHO, 2019).

Mathematical models have increasingly been employed in the study and analysis of infectious diseases and their transmission dynamics. However, only a few mathematical models have been developed to study the transmission dynamics of taeniasis, cysticercosis and its co-infection (see Braae et al., 2016; Jose et al., 2018; Sanchez-Torres et al., 2019; Mwasunda et al., 2021(a), 2021(b), 2022; Rwabona et al., 2024; Winskill et al., 2017). Despite the numerous studies that have focused on modeling the transmission dynamics of neglected food-borne zoonotic diseases, little attention is given to the dynamics of taeniasis, cysticercosis and its co-infection. Furthermore, the co-infection resulting from the complex life cycle of T. solium has not received adequate attention. In light of the aforementioned mathematical models, this study aims to enhance the understanding of the transmission dynamics of taeniasis, cysticercosis and its co-infection by proposing a mathematical model that incorporates the recovered compartment and the uninfected pork compartment, since not all slaughtered pig is infected and not all pork is infected. Furthermore, the inclusion of the recovered compartment to account for humans who recover from these infections due to prompt and effective treatment, before returning back to the susceptible compartment is very essential and should be considered in the disease dynamics. This aspect has not been considered or addressed in previous studies within the existing literature. This work will entail conducting qualitative analysis and sensitivity analysis of the model parameters to determine the most significant parameter(s) that should be prioritized for intervention and control strategies for these infections.

The remaining part of this paper is organized as follows: Section 2 presents the model formulation for taeniasis, cysticercosis and its co-infection. In Section 3, the basic model analysis was discussed, followed by the sensitivity analysis of the formulated model in Section 4. Section 5 focuses on the numerical simulation to support the analytical analysis, while Section 6 presents discussion and conclusion regarding the obtained results.

2. Model Formulation

In this section, a deterministic model for the transmission dynamics of taeniasis, cysticercosis and its coinfection in human and pig populations is formulated and analyzed. This study draws inspiration from the work in (Winskill et al., 2017) that considered intervention strategies against T. solium cysticercosis by incorporating the uninfected pork compartment to represent the pork-

free from cyst (tenia eggs) concentration, as well as, the recovered human compartment to account for humans who recover from taeniasis, cysticercosis and its co-infection. At any given time, t, the human population is subdivided into five distinct compartments: Susceptible humans, $S_h(t)$, Infected humans with taeniasis, $I_t(t)$, Infected humans with cysticercosis, $I_c(t)$, Infected humans with cysticercosis and taeniasis, $I_{ct}(t)$, and Recovered humans due to prompt and effective treatment, $R_h(t)$. Individuals within the human population move from one compartment to another as their status changes and the disease progresses. Similarly, the pig population at any time, t, consists of two compartments: Susceptible pigs, $S_p(t)$, and Infected pigs, $I_p(t)$. Also, the pork compartment at any time, t is divided into two, namely the uninfected and infected denoted as $P_u(t)$ and $P_i(t)$, respectively, whereas, the presence of taenia eggs in the environment (contaminated environment) at any time, t is represented by $E_t(t)$.

In formulating the mathematical model, we make the assumptions that the pig farming system that allows pigs to roam freely is practiced, humans cannot recover from the infections without treatment, pigs become carriers for life (they do not suffer disease-induced death), the quantity of raw or undercooked pork (uninfected or infected) consumed by susceptible humans depends on the amount of pork available.

The susceptible human population is increased by the recruitment of humans via birth or immigration into the population at a rate Λ_h. The susceptible human population acquires taeniasis after the consumption of infected pork at a force of infection $\beta_1\alpha_p P_i$, where β_1 is the transmission rate via consumption of infected pork by humans and α_p is the rate of eating raw or undercooked infected pork. Also, the susceptible human acquires cysticercosis infection through effective contact with taenia eggs in the contaminated environment and becomes infected at a force of infection $\theta_1\alpha_1 E_t$, where θ_1 is the transmission rate of T. solium eggs to humans and α_1 is the number of T. solium eggs to the environment. The natural mortality rate for all human population is assumed to be at rate μ_h.

The $I_t(t)$ compartment decreases due to several factors, which include becoming infected at a rate $\beta_{tc}E_tI_t$, and then moves to $I_{ct}(t)$ compartment, with, β_{tc} representing the transmission rate of T. solium eggs to humans infected with taeniasis.

The $I_c(t)$ compartment is influenced by several factors, which include becoming infected at a rate $\beta_{ct}P_iI_c$, and then moves to $I_{ct}(t)$ compartment, with β_{ct} representing the transmission rate via consumption of infected pork by the infected humans with cysticercosis. Also, it further decreased by the cysticercosis-induced death rate denoted as d_1. Meanwhile, the infected human with cysticercosis and taeniasis (co-infection), $I_{ct}(t)$ compartment decreases due to co-infection induced death rate, d_2. After prompt and effective treatment, infected human compartments $I_c(t)$, $I_t(t)$, and $I_{ct}(t)$ progress to the recovered compartment (those who recover from cysticercosis, taeniasis and their co-infection) at the rate σ_1, σ_3, σ_2, respectively. Since the treatment does not confer permanent immunity on recovered humans, they return back to the susceptible compartment at a rate ρ.

For the taenia eggs in the environment (contaminated environment), $\mathrm{E}_t(t)$, it is influenced by the shedding rates of infected humans with taeniasis, τ_2, and its co-infection, τ_1. The $\mathrm{I}_t(t)$ and $\mathrm{I}_{ct}(t)$ compartments via open defecation sheds taenia eggs in the environment, thereby contaminating the environment. The decay rate of the taenia eggs in the environment is assumed to be μ_e.

For the susceptible pig population, we have a recruitment rate, denoted as Λ_p, that occurs through birth and immigration. This process results in the formation of the susceptible pig population, $S_p(t)$ which decreases as a result of the contact with the taenia eggs in the contaminated environment at a rate ψ_p, and thereafter, progresses to the infected pig (pig with cysticercosis) population, $\mathrm{I}_p(t)$. The natural mortality rate for the two pig populations is assumed to be at rate μ_p. The $\mathrm{I}_p(t)$ compartment is decreased by slaughtering at a rate, θ. The number of infected pork, $\mathrm{P}_i(t)$, and uninfected pork, $\mathrm{P}_u(t)$, available for human consumption increases as a result of slaughtering of infected pigs and susceptible pigs at a rate, θ.

The schematic flow diagram depicting the system's dynamics is shown in Fig 1 and the description of the parameters of the model is presented in Table 1. With Fig 1 and the model description in Table 1, we derive the under-listed system of ordinary differential equations that govern the dynamics of taeniasis and cysticercosis in human and pig populations.

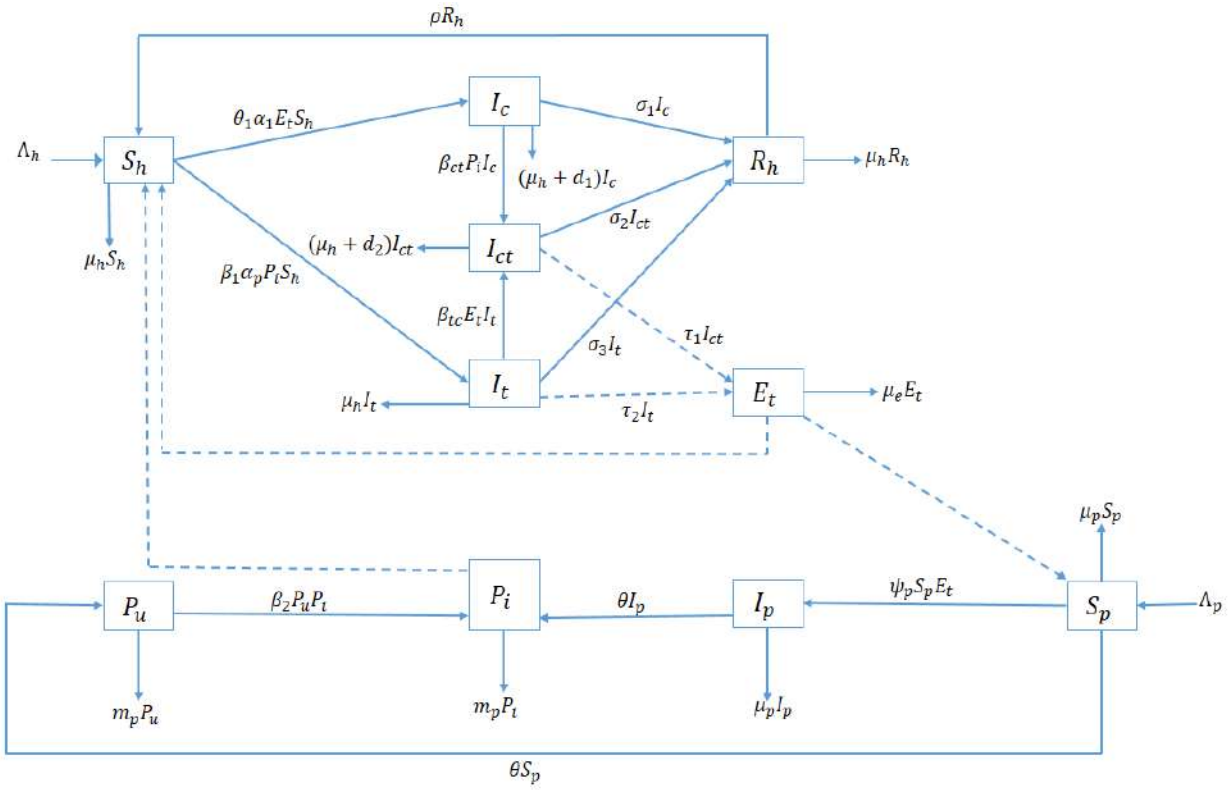

Figure 1. The flow diagram of the taeniasis and cysticercosis model.

Table 1: Model Parameters and their Descriptions

Parameters	Epidemiological Interpretation	Parameter Value	Source
Λ_h	Recruitment rate for the human population	2247	(Winskill et al., 2017)
μ_h	Natural death rate of the human population	0.0141	(Wang et al., 2013)
d_1	Death rate caused by human cysticercosis disease	0.0925	(Wang et al., 2013)
d_2	Death rate induced by taeniasis and cysticercosis in humans	0.1	(Winskill et al., 2017)
Λ_p	Recruitment rate of the pig population	1450	(Mwasunda et al., 2021b)
σ_1	Rate at which infected humans with cysticercosis recover	0.2085	Assumed
σ_2	Rate of recovery for humans infected with taeniasis and cysticercosis	0.1085	Assumed
σ_3	Rate at which humans infected with taeniasis recover	0.0085	Assumed
μ_p	Natural mortality rate for pig population	0.596	Assumed
α_p	Rate of consumption of undercooked infected pork	0.0128	(Mwasunda et al., 2021a)
ψ_p	Transmission coefficient of T. solium eggs to pigs	0.035	Assumed
θ	Pig slaughter rate	0.132	Assumed
m_p	Proportion of unconsumed contaminated pork	0.358	(Mwasunda et al., 2021a)
β_1	Transmission rate through the consumption of infected pork by humans	0.0093	Assumed
β_2	Contamination rate from contact between infected and uninfected pork	0.0005	Assumed
τ_1	Shedding rate for humans with taeniasis and cysticercosis	0.25	Assumed
τ_2	Shedding rate for human with taeniasis	0.025	(Winskill et al., 2017)
θ_1	The transmission coefficient of T. solium eggs to humans for cysticercosis	0.052	(Mwasunda et al., 2021b)
μ_e	Decay rate of Taenia eggs in the environment	0.42	Assumed
α_1	Transmission coefficient of T. solium eggs to the environment	0.05	Assumed
β_{tc}	The transmission rate of T. solium eggs to humans infected with taeniasis	0.0005	Assumed
β_{ct}	The transmission rate in humans with cysticercosis who consume infected pork	0.0003	Assumed
ρ	Rate of how quickly recovered humans return to the susceptible class	0.5	Assumed

$$\left.\begin{aligned}
\frac{dS_h}{dt} &= \Lambda_h - \theta_1\alpha_1 E_t S_h - \beta_1\alpha_p P_i S_h - \mu_h S_h + \rho R_h,\\
\frac{dI_t}{dt} &= \beta_1\alpha_p P_i S_h - \beta_{tc} E_t I_t - (\sigma_3 + \mu_h) I_t,\\
\frac{dI_c}{dt} &= \theta_1\alpha_1 E_t S_h - \beta_{ct} P_i I_c - (\sigma_1 + \mu_h + d_1) I_c,\\
\frac{dI_{ct}}{dt} &= \beta_{ct} P_i I_c + \beta_{tc} E_t I_t - (\sigma_2 + \mu_h + d_2) I_{ct},\\
\frac{dR_h}{dt} &= \sigma_1 I_c + \sigma_2 I_{ct} + \sigma_3 I_t - (\rho + \mu_h) R_h,\\
\frac{dE_t}{dt} &= \tau_1 I_{ct} + \tau_2 I_t - \mu_e E_t,\\
\frac{dS_p}{dt} &= \Lambda_p - \psi_p E_t S_p - (\theta + \mu_p) S_p,\\
\frac{dI_p}{dt} &= \psi_p E_t S_p - (\mu_p + \theta) I_p,\\
\frac{dP_u}{dt} &= \theta S_p - \beta_2 P_u P_i - m_p P_u,\\
\frac{dP_i}{dt} &= \theta I_p + \beta_2 P_u P_i - m_p P_i,
\end{aligned}\right\} \quad (1)$$

with initial conditions $S_h(0) > 0$, $I_t(0) \geq 0$, $I_c(0) \geq 0$, $I_{ct}(0) \geq 0$, $R_h(0) > 0$, $E_t(0) \geq 0$, $S_p(0) > 0$, $I_p(0) \geq 0$, $P_u(0) \geq 0$, $P_i(0) \geq 0$, and all the parameters of the model are non-negative except Λ_h and Λ_p which are positive.

3. Model Analysis

This section demonstrates that the solutions to the model system (1), given non-negative initial conditions, are wholly non-negative and remain bounded.

3.1 Positivity of Solutions of the Model

The model system (1) outlines the dynamics of human and pig populations, the contaminated environment, uninfected pork, and infected pork. Hence, it is crucial to ensure that these populations remain positive at all times.

Theorem 1 The solutions (S_h, I_t, I_c, I_{ct}, R_h, E_t, S_p, I_p, P_u, P_i) of the model system 1 with non-negative initial conditions ($S_h(0) > 0$, $I_t(0) \geq 0$, $I_c(0) \geq 0$, $I_{ct}(0) \geq 0$, $R_h(0) > 0$, $E_t(0) \geq 0$, $S_p(0) > 0$, $I_p(0) \geq 0$, $P_u(0) \geq 0$, $P_i(0) \geq 0$) are positive for all time $t > 0$.

Proof 1 From the first equation of system (1), we have that

$$\frac{dS_h}{dt} = \Lambda_h - \theta_1\alpha_1 E_t S_h - \beta_1\alpha_p P_i S_h - \mu_h S_h + \rho R_h \geq -\theta_1\alpha_1 E_t S_h - \beta_1\alpha_p P_i S_h - \mu_h S_h,$$

such that

$$S_h(t) \geq S_h(0) exp\left\{-\left[\int_0^t (\theta_1\alpha_1 E_t + \beta_1\alpha_p P_i) d\tau + \mu_h t\right]\right\} \geq 0$$

is positive, given that $S_h(0)$ is positive. This concept also demonstrates that other state variables are positive for all $t > 0$. Therefore, the solutions to the model equation (1) stay positive for all $t \geq 0$, given that they are defined by exponential functions.

3.2 Invariant Region

The mathematical well-posedness of the model system (1) is proved in this subsection to establish that the model system 1 holds epidemiological significance. Hence, we state the following theorem.

Theorem 2 All feasible solutions of model system 1 are uniformly bounded in a proper subset $\Omega = \Omega_h \times \Omega_p \times \Omega_E \times \Omega_{pk}$ with non-negative initial conditions where $\Omega_h = (S_h, I_t, I_c, I_{ct}, R_h) \in \mathbb{R}_+^5 : N_h(t) \leq \frac{\Lambda_h}{\mu_h}$, $\Omega_p = (S_p, I_p) \in \mathbb{R}_+^2 : N_p(t) \leq \frac{\Lambda_p}{\theta + \mu_p}$, $\Omega_E = \left\{E_t \leq \frac{(\tau_1 + \tau_2)\Lambda_h}{\mu_h \mu_e}\right\}$ and $\Omega_{pk} = \left\{(P_u, P_i) \in \mathbb{R}_+^2 : N_{pk}(t) \leq \frac{\theta \Lambda_p}{\mu_p m_p}\right\}$ are the subsets for human population, pig population, environment and pork (uninfected and infected), respectively.

Proof 2 Let $N_h(t) = S_h(t) + I_t(t) + I_c(t) + I_{ct}(t) + R_h(t)$ and $N_p(t) = S_p(t) + I_p(t)$ be the total population for the human and pig populations. Adding the human compartments, pig compartments, and the pork compartments gives

$$\left.\begin{aligned}
&\frac{dN_h}{dt} = \Lambda_h - \mu_h S_h - \mu_h I_t - \mu_h I_c - \mu_h I_{ct} - \mu_h R_h - d_1 I_c - d_2 I_{ct} = \Lambda_h - \mu_h N_h - d_1 I_c - d_2 I_{ct},\\
&\frac{dN_h}{dt} \leq \Lambda_h - \mu_h N_h,\\
&\frac{dN_p}{dt} = \Lambda_p - \mu_p S_p - \mu_p I_p - \theta S_p - \theta I_p \leq \Lambda_p - (\theta + \mu_p) N_p\\
&\frac{dN_{pk}}{dt} = \theta S_p + \theta I_p - m_p P_u - m_p P_i \leq \theta N_p - m_p.
\end{aligned}\right\} \quad (2)$$

Applying inequality theorem by (Birkhoff & Rota, 1978), with the initial conditions, $N_h(0) = N_{h0}, N_p(0) = N_{p0}, E_t = E_t(0)$ and $N_{pk}(0) = N_{pk0}$ in Equations (2) gives

$$\left.\begin{aligned}
&N_h(t) \leq \frac{\Lambda_h}{\mu_h} + \left[N_{h0} - \frac{\Lambda_h}{\mu_h}\right] \exp\{-\mu_h t\},\\
&N_p(t) \leq \frac{\Lambda_p}{\theta + \mu_p} + \left[N_{p0} - \frac{\Lambda_p}{\theta + \mu_p}\right] \exp\{-\mu_p t\},\\
&E_t \leq \frac{(\tau_1 + \tau_2)\Lambda_h}{\mu_h \mu_e} + \left[E_t(0) - \frac{(\tau_1 + \tau_2)\Lambda_h}{\mu_h \mu_e}\right] \exp\{-\mu_e t\},\\
&N_{pk}(t) \leq \frac{\theta \Lambda_p}{\mu_p m_p} + \left[N_{pk0} - \frac{\theta \Lambda_p}{\mu_p m_p}\right] \exp\{-m_p t\}.
\end{aligned}\right\} \quad (3)$$

Applying differential inequality to Equation (3) as $t \to \infty$, the total populations for humans and pigs, the contaminated environment and available pork meat approach $N_h(t) \leq \frac{\Lambda_h}{\mu_h}, N_p(t) \leq \frac{\Lambda_p}{\theta + \mu_p}, \frac{(\tau_1 + \tau_2)\Lambda_h}{\mu_h \mu_e}$ and $\frac{\theta \Lambda_p}{\mu_p m_p}$ respectively.

Therefore, for all $t > 0$, the feasible solution set of model system 1 are bounded and will enter and remain in the positive invariant region $\Omega = \Omega_h \times \Omega_p \times \Omega_E \times \Omega_{pk}$. This completes the proof.

3.3 Existence of Disease-free Equilibrium State (DFE)

The disease-free equilibrium (DFE) of model system (1) represents the steady-state solution when taeniasis and cysticercosis are absent in both human and pig populations. To demonstrate the existence of this equilibrium, we set the right-hand side of Equation (1) to zero and solve the equations simultaneously. It is denoted by E_0 and given as follows:

$$E_0 = \left(S_h^0, I_t^0, I_c^0, I_{ct}^0, R_h^0, E_t^0, S_p^0, I_p^0, P_u^0, P_i^0\right) = \left\{\frac{\Lambda_h}{\mu_h}, 0, 0, 0, 0, 0, \frac{\Lambda_p}{\theta + \mu_p}, 0, \frac{\theta \Lambda_p}{\mu_p m_p}, 0\right\}. \quad (4)$$

3.4 Basic Reproduction Number, R_0

In epidemiological models, the basic reproduction number, R_0, is a key quantity defined as the average number of infections produced from introducing one infected individual into a completely susceptible population (Diekmann & Roberts, 2010). Here, R_0 reflects the expected number of secondary infections—specifically taeniasis and cysticercosis—resulting from either an infected human with taeniasis or an infected pig with cysticercosis throughout their entire infectious period in a fully susceptible population. The stability of the disease-free equilibrium, E_0, is determined by R_0, which is a crucial mathematical parameter in the public health analysis of infectious disease epidemiology.

By utilizing the next-generation matrix method described by (Diekmann & Roberts, 2010; Van den Driessche & Watmough, 2002), we calculate the transition matrices that reflect the emergence of new infections, F and the overall rate of transitional terms, V, for the model system (1) at the Disease-Free Equilibrium, E_0, as follows:

$$F = \begin{bmatrix} \mathbf{0} & 0 & 0 & 0 & 0 & g_1 \\ 0 & 0 & 0 & g_2 & 0 & 0 \\ 0 & 0 & 0 & 0 & 0 & 0 \\ 0 & 0 & 0 & 0 & 0 & 0 \\ 0 & 0 & 0 & g_3 & 0 & 0 \\ 0 & 0 & 0 & 0 & 0 & g_4 \end{bmatrix} \quad \text{and} \quad V = \begin{bmatrix} f_1 & 0 & 0 & 0 & 0 & 0 \\ 0 & f_2 & 0 & 0 & 0 & 0 \\ 0 & 0 & f_3 & 0 & 0 & 0 \\ -\tau_2 & 0 & -\tau_1 & \mu_e & 0 & 0 \\ 0 & 0 & 0 & 0 & f_4 & 0 \\ 0 & 0 & 0 & 0 & -\theta & m_p \end{bmatrix} \quad (5)$$

where

$$\left.\begin{aligned} &f_1 = \sigma_3 + \mu_h,\ f_2 = \sigma_1 + \mu_h + d_1,\ f_3 = \sigma_2 + \mu_h + d_2,\ f_4 = \mu_p + \theta, \\ &g_1 = \frac{\beta_1 \alpha_p \Lambda_h}{\mu_h},\ g_2 = \frac{\theta_1 \alpha_1 \Lambda_h}{\mu_h},\ g_3 = \frac{\psi_p \Lambda_p}{\mu_p},\ g_4 = \frac{\beta_2 \theta \Lambda_p}{\mu_p m_p}. \end{aligned}\right\} \quad (6)$$

The basic reproduction number, R_0, of the model system in (1) is defined as the spectral radius of the operator FV^{-1}, where V^{-1} denotes the inverse of the matrix V and is given as

$$R_0 = \frac{1}{2}\frac{g_4}{m_p} + \frac{1}{2}\sqrt{\frac{g_4^2}{m_p^2} + 4\, g_1 g_3 \theta \tau_2}, \quad (7)$$

with g_1, g_2, g_3, g_4 as defined in (6).

Following the biological insight provided by (Diekmann & Roberts, 2010), taeniasis and cysticercosis infection can be eliminated in both human and pig populations if $R_0 < 1$, while the infections may persist in both populations when $R_0 > 1$.

By employing the Next-generation method, we present the following theorem regarding the local stability of the disease-free equilibrium state.

3.5 Local Stability of the Disease-Free Equilibrium

In this subsection, based on the value of R_0, we prove the local stability of the DFE, E_0, for model system (1) using the Jacobian matrix method.

Theorem 3 The disease-free equilibrium, E_0 of model system (1), is locally asymptotically stable if $R_0 < 1$ and unstable when $R_0 > 1$.

Proof 3 We prove the local stability of the DFE, E_0, for model system (1) by showing that all eigenvalues of the Jacobian matrix, $J(E_0)$ at E_0 have negative real parts. Thus, the Jacobian matrix, $J(E_0)$ is given as

$$J(E_0) = \begin{pmatrix} -\mu_h & 0 & 0 & 0 & \rho & -g_2 & 0 & 0 & 0 & -g_1 \\ 0 & -f_1 & 0 & 0 & 0 & 0 & 0 & 0 & 0 & g_1 \\ 0 & 0 & -f_2 & 0 & 0 & g_2 & 0 & 0 & 0 & 0 \\ 0 & 0 & 0 & -f_3 & 0 & 0 & 0 & 0 & 0 & 0 \\ 0 & \sigma_3 & \sigma_1 & \sigma_2 & -(\rho + \mu_h) & 0 & 0 & 0 & 0 & 0 \\ 0 & \tau_2 & 0 & \tau_1 & 0 & -\mu_e & 0 & 0 & 0 & 0 \\ 0 & 0 & 0 & 0 & 0 & -g_3 & -f_4 & 0 & 0 & 0 \\ 0 & 0 & 0 & 0 & 0 & g_3 & 0 & -f_4 & 0 & 0 \\ 0 & 0 & 0 & 0 & 0 & 0 & \theta & 0 & -m_p & -g_4 \\ 0 & 0 & 0 & 0 & 0 & 0 & 0 & \theta & 0 & g_4 - m_p \end{pmatrix}, \quad (8)$$

where $f_1,\ f_2,\ f_3,\ f_4,\ g_1,\ g_2,\ g_3,\ g_4$ are as defined in Equation (6).

The first, third, fifth, seventh, eight, and ninth columns of the Jacobian matrix, $J(E_0)$ in Equation (8) have diagonal entries either in their rows or columns, yielding the six eigenvalues: $-\mu_h,\ -f_2,$

$-(\rho + \mu_h)$, $-f_4$, $-f_4$ and $-m_p$. Thus, Equation (8) reduces to a reduced Jacobian matrix, $J_r(E_0)$ given as

$$J_r(E_0) = \begin{pmatrix} -f_1 & 0 & 0 & g_1 \\ 0 & -f_3 & 0 & 0 \\ \tau_2 & \tau_1 & -\mu_e & 0 \\ 0 & 0 & 0 & g_4 - m_p \end{pmatrix}. \quad (9)$$

We observed that the second and fourth rows of the reduced Jacobian matrix, $J_r(E_0)$ in Equation (9) have diagonal entries, giving the two eigenvalues: $-f_3$, and $g_4 - m_p = m_p\left(\frac{g_4}{m_p} - 1\right)$. The reduce matrix is then given by

$$J_{rr}(E_0) = \begin{pmatrix} -f_1 & 0 \\ \tau_2 & -\mu_e \end{pmatrix},$$

which has the eigenvalues $-f_1$ and $-\mu_e$.

By the expression of R_0 in Equation (7) and definitions in Equation (6), it implies that $\frac{g_4}{m_p} < 1$ if $R_0 < 1$, since the term $\frac{g_4}{m_p}$ is the first term of R_0 in Equation (7). Hence, we have that the eigenvalues of the Jacobian matrix, $J(E_0)$ of Equation (8) have negative real parts whenever $R_0 < 1$. Therefore, by the linearization method of stability, it implies that the disease-free equilibrium, E_0, is locally asymptotically stable if $R_0 < 1$, otherwise it is unstable.

Given the model's complexity, the numerical representation of the endemic equilibrium state will be simplified further.

4. Sensitivity Analysis

Understanding various model parameters that impact disease transmission and prevalence is crucial for targeting interventions to reduce mortality and morbidity. Therefore, a sensitivity analysis is needed. We conducted a sensitivity analysis to identify key parameters affecting the spread and control of taeniasis and cysticercosis in humans and pigs. The Latin Hypercube Sampling (LHS) method and the Partial Rank Correlation Coefficient (PRCC) coded in Matlab, following (Blower and Dowlatabadi, 1994), is used to discover factors affecting the basic reproduction number, R_0, relative to other model parameters. The PRCC index, ranging from −1 to +1, offers insights into the strength of relationships between output variables and parameters, accounting for other effects (Blower and Dowlatabadi, 1994). Positive PRCCs increase the outputs when increased, while negative PRCCs decrease them. The outputs could be R_0 or the subpopulation variables. We performed 1000 simulations per run to generate 1000 parameter sets to enhance accuracy. LHS ranges for the parameter set ranged from 80% (lower) to 120% (upper) of the respective parameter value in Table 1. Identifying essential model parameters effectively examines their qualitative behavior influencing the model. The PRCC plots for the R_0 and the infected state variables are displayed in Figures 2 and 3.

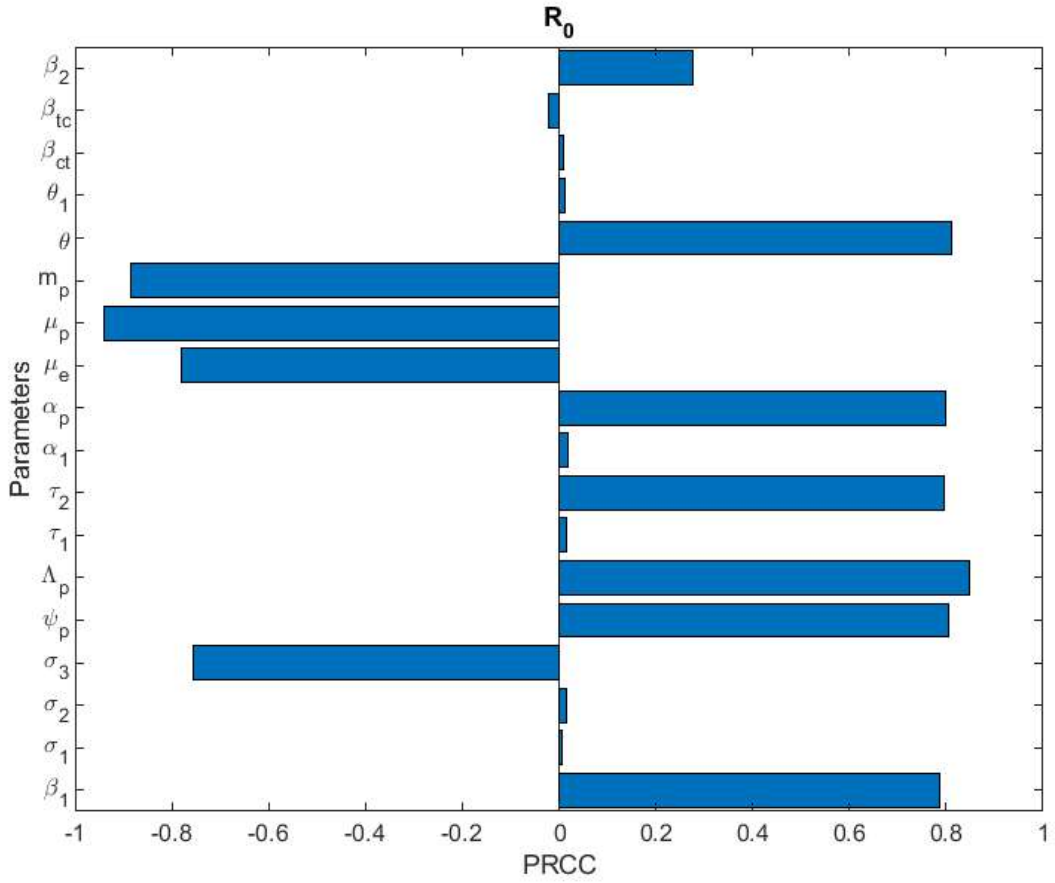

Figure 2. PRCC graph illustrating the values of R_0. The parameter values utilized are listed in Table 1.

Figure 2 presents the PRCC results, illustrating how each disease transmission parameter influences the basic reproduction number, R_0. The parameters that most significantly affect R_0 include β_1, θ, α_p, ψ_p, τ_2, μ_e, μ_p, m_p. In Figure 3(a), the model parameters β_1, σ_2, α_p, μ_e positively influence the number of humans infected with taeniasis, while the parameters β_{tc}, β_{ct}, θ_1, α_1, τ_1 negatively impact infection rates. This suggests that to reduce the number of individuals infected with taeniasis, the values of β_1, σ_2, α_p, μ_e should be decreased, and the values of β_{tc}, β_{ct}, θ_1, α_1, τ_1 should be increased. Figure 3(b) shows that increasing the values of β_{ct}, θ, Λ_p while decreasing σ_2, μ_p, m_p leads to reduced disease transmission in the I_c population. Similarly, Figure 3(c) illustrates that the model parameters β_1, β_2, β_{ct}, θ, Λ_p, σ_2, m_p, μ_p, α_p, ψ_p, τ_2 significantly influence the transmission dynamics of co-infections in humans. Figure 3(d) illustrates that decreasing the shedding rate of infected humans with cysticercosis and taeniasis, alongside increasing the decay rate of taenia eggs in the environment, denoted as μ_e, will significantly and dramatically lower the number of taenia eggs in the environment. This, in turn, contributes to the potential control of taeniasis and cysticercosis infections. Figure 3(e) illustrates

that increasing the model parameters θ and μ_p while decreasing Λ_p reduces the number of infected pigs. Figure 3(f) shows that the model parameters Λ_p and θ exhibit positive PRCCs, indicating a strong correlation between the recruitment rate of pigs Λ_p, the slaughter rate θ and the amount of infected pork P_i. This correlation suggests that as the recruitment and slaughter rates of pigs rise, the likelihood of infected pigs being recruited and slaughtered increases, consequently raising the amount of infected pork available for human consumption. From an epidemiological standpoint, this indicates that these parameters play a crucial role in the transmission dynamics of taeniasis, cysticercosis, and their co-infection among human and pig populations.

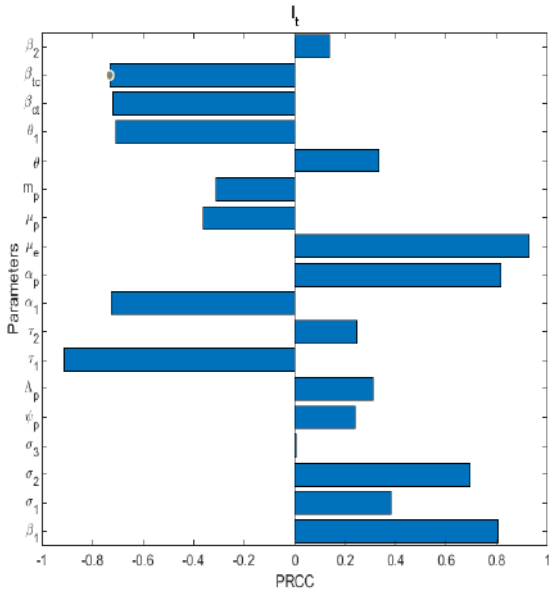

(a) PRCCs plot for the infected human with taeniasis

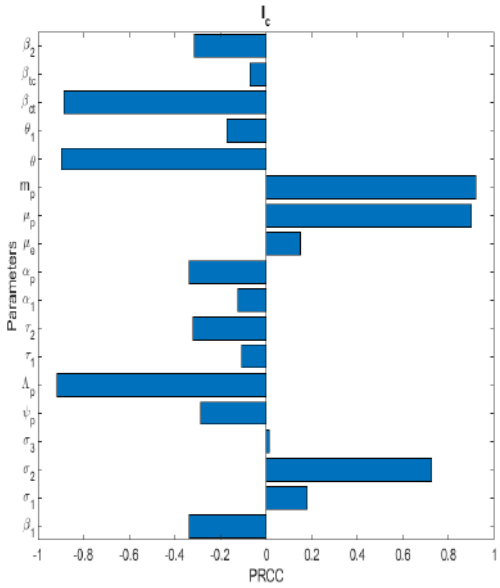

(b) PRCCs plot for the infected human with cysticercosis

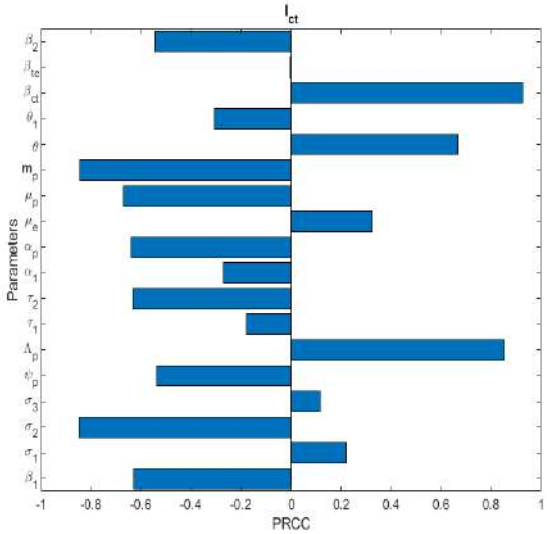

(c) PRCCs plot for the infected human with cysticercosis and taeniasis

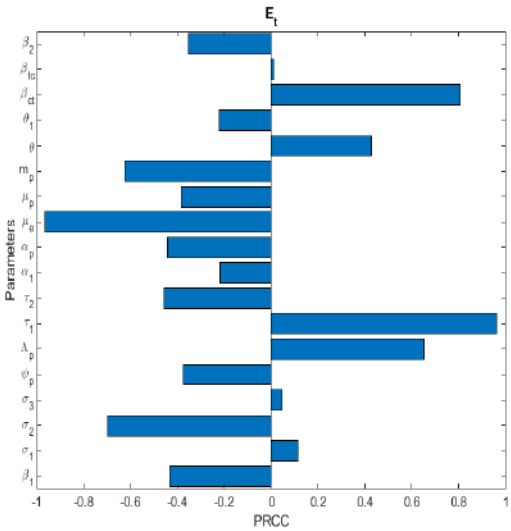

(d) PRCCs plot for the contaminated environment

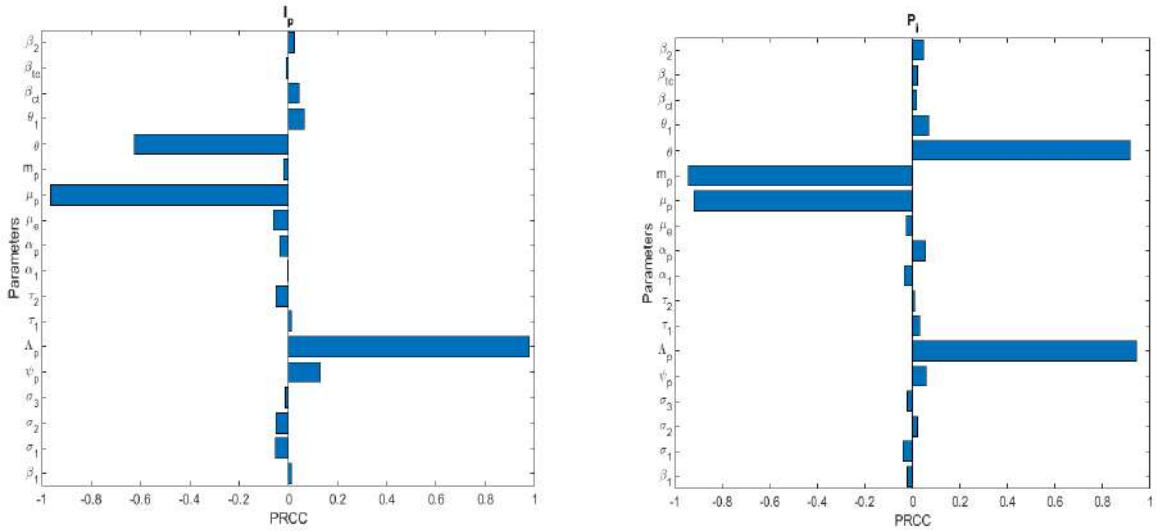

(e) PRCCs plot for the infected pig population **(f) PRCCs plot for the infected pork**

Figure 3: Partial Rank Correlation Coefficient (PRCCs) for important parameters of the infected state variables of model system (1).

5. Numerical Simulations

To validate our model, we performed numerical simulations of the model system (1) using the Fourth order Runge-Kutta method coded in MatLab software. The parameters utilized in these simulations are listed in Table 1, which also specifies the sources from which they were obtained. The initial conditions (population size) used in the simulations are $S_h = 159361$, $I_t = 0$, $I_c = 0$, $I_{ct} = 0$, $R_h = 0$, $E_t = 0$, $S_p = 2432$, $I_p = 1$, $P_u = 897$ and $P_i = 0$ to show the endemic situation of both infections in the population when $R_0 > 1$ is displayed in Figure 4.

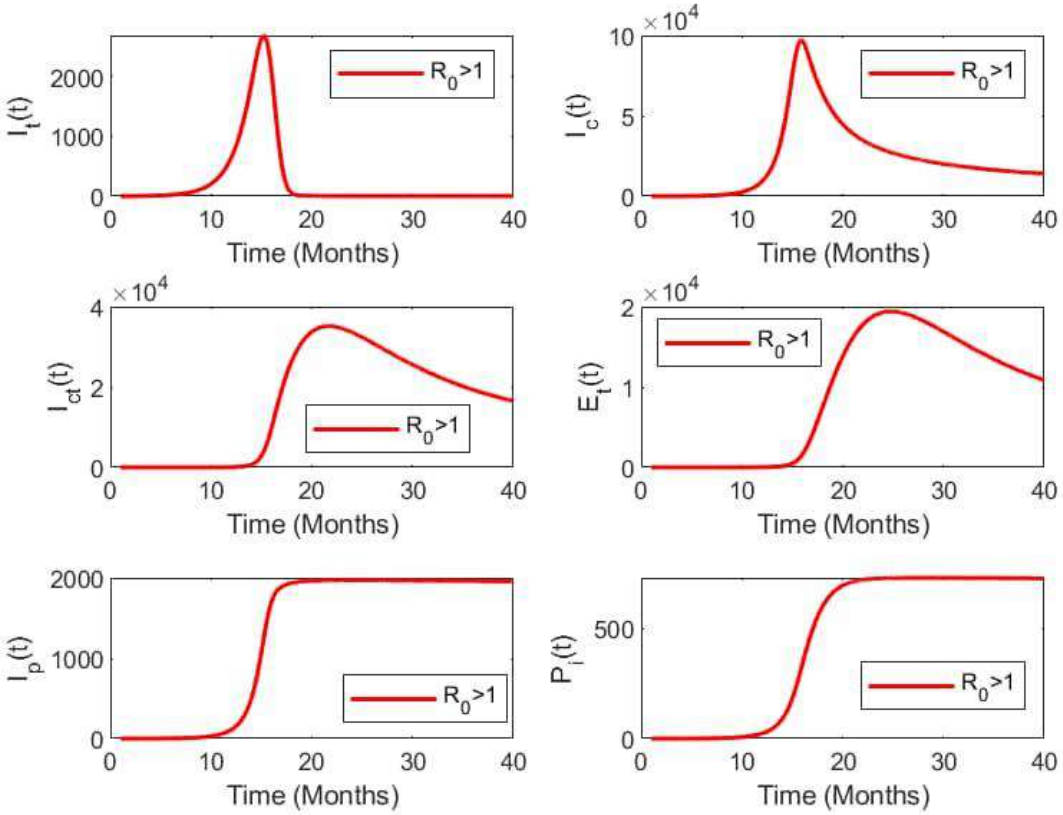

Figure 4. The time series plot illustrates the infected compartments of the model system (1) for the scenario where $R_0 > 1$. The parameter values listed in Table 1 are used. This reflects the ongoing persistence of taeniasis and cysticercosis infections in the population, especially for the presence of cysticercosis infection.

6. Discussion

The time series in Figure 4 illustrates the endemicity of taeniasis and cysticercosis over time when $R_0 > 1$. In Figure 4, it can be seen that the peak of taeniasis infections in humans ($I_t(t)$) decreases to nearly zero after 20 months, while the populations of $I_c(t)$ and $I_{ct}(t)$ reach their peaks and gradually decline, but still remain present. This suggests that the disease will continue to persist and spread within the population. The same trend is observed with the number of eggs in the environment; as the number of infected humans and pigs with cysticercosis rises, the shedding rate of taenia eggs from infected humans with taeniasis and co-infection increases. Conversely, this number approaches zero when the shedding rate of taenia eggs hits its lowest threshold. Therefore, one potential strategy for reducing human and pig cysticercosis is to manage the shedding rate of taenia eggs from the feces of infected humans, which contributes to environmental contamination. It is important to note that infected individuals with taeniasis may not exhibit illness or die from

the infection, allowing them to continue shedding it into the environment and perpetuating the cycle.

The infected pig population ($I_p(t)$) and the infected pork ($P_i(t)$) illustrated in Figure 4 demonstrate a significant correlation within the transmission dynamics of these diseases. This relationship arises from the fact that as more infected pigs are slaughtered, a greater amount of infected pork enters the human food supply. Epidemically, this contributes to the ongoing persistence and spread of taeniasis and cysticercosis infections among host populations.

7. Conclusion

This study presents and analyzes a mathematical model that addresses the transmission dynamics of taeniasis and cysticercosis infections in both human and pig populations, factoring in recovered humans and uninfected pork. We utilized mathematical analysis to evaluate the model systems' boundedness and calculate the basic reproduction number. After determining this number, we conducted a sensitivity analysis on the model parameters employing the Latin Hypercube Sampling (LHS) method alongside the Partial Rank Correlation Coefficient (PRCC) technique. The findings from our sensitivity analysis suggest that timely and effective treatment of infected individuals, thorough cooking of pork, consumption of uninfected pork, screening, and testing of pigs, humane slaughtering of uninfected pigs, reducing the transmission coefficient of T. solium eggs to pigs, proper sewage disposal, and increasing the decay rate of taenia eggs in the environment with disinfectants are essential for controlling and potentially eliminating these diseases. Increasing the consumption of uninfected pork reduces the likelihood of human infections and diminishes environmental contamination, effectively interrupting the transmission cycle and spread of these illnesses.

Furthermore, the contaminated environment significantly influences the progression of taeniasis and cysticercosis infections, highlighted by the strong link between key parameters and environmental conditions. Based on the sensitivity results, it is advisable to implement strategies that target environmental factors, including effective sewage disposal and enhancing the decomposition of taenia eggs through disinfectants. These measures will be critical for controlling, reducing, or possibly eliminating these diseases. This aligns with WHO guidelines for controlling and eradicating taeniasis and cysticercosis in both humans and pigs.

This work has limitations, such as the failure to integrate vaccination for susceptible pigs. However, vaccination is advised as a preventive strategy against pig cysticercosis. Furthermore, the proposed model has not been calibrated with data to assess the validity of the findings; instead, we used parameter estimates from the literature to define the model. The societal impact of taeniasis and cysticercosis infections remains unclear due to a lack of adequate epidemiological data. Thus, developing a mathematical framework incorporating pig vaccinations could benefit the model.

References

[1] Alemneh, T. and Adem, T. (2017). Mini review on bovine cysticercosis. *Archives on Veterinary Science and Technology, 2,* 1 - 9.

[2] Birkhoff, G. and Rota, G.C. (1978). *Ordinary Differential Equations.* (3rd ed.) 342 pages. New York: Wiley; 1978.

[3] Blower, S.M. and Dowlatabadi, H. (1994). Sensitivity and uncertainty analysis of complex models of disease transmission: an HIV model, as an example. *International Statistical Review. 62,* 229 - 243.

[4] Braae, U.C., Devleesschauwer, B., Gabriel, S., Dorny, P., Speybroeck, N., Magnussen, P., Torgerson, P. and Johansen, M.V. (2016). Cystisim - an agent-based model for Taenia solium transmission and control. *PLOS Neglected Tropical Diseases, e0005184. 10(12),* 1 - 17.

[5] Brutto, O. H. D. (2013). Human cysticercosis (Taenia solium). *Tropical Parasitology, 3(2),* 100 - 103. doi: 10.4103/2229-5070.122103

[6] CDC - Taeniasis. www.cdc.gov. 12 June 2023. Retrieved 26 April 24.

[7] California Department of Public Health. Taeniasis and Cysticercosis (Pork Tapeworm). https://www.cdph.ca.gov/Programs/CID/DCDC/Pages/Cysticercosis-PorkTapeworm-Taeniasis.aspx. Retrieved 14 August 2024.

[8] Dermauw, V., Dorny, P., Braae, U. C., Devleesschauwer, B., Robertson, L. J., Saratsis, A., Thomas, L. F. (2018). Epidemiology of taenia saginata taeniasis/cysticercosis: a systematic review of the distribution in southern and eastern Africa. *Parasites Vectors, 11(1),* 1 - 12.

[9] Diekmann, O., Heesterbeek, J. and Roberts, M. G. (2010). The construction of next generation matrices for compartmental epidemic models. *Journal of The Royal Society Interface, 7,* 873 - 885.

[10] Food and Agricultural Organization (FAO) of the United Nations and World Health Organization (WHO) (2014). Multicriteria-Based Ranking for Risk Management of Food-borne Parasite. Microbiological Risk Assessment Series 23, FAO/WHO.

https://www.who.int/foodsafety/publications/mra23/en/.GoogleScholar

[11] Jose, M. V., Bobadilla, J. R., Sanchez-Torres, N. Y. and Laclette, J. P. (2018). Mathematical model of the life cycle of taenia-cysticercosis: transmission dynamics and chemotherapy (Part 1). *Theoretical Biology and Medical Modelling, 15(1),* 1 - 19.

[12] Mwasunda, J. A., Irunde, J. I., Kajunguri, D. and Kuznetsov, D. (2021a). Modeling and analysis of taeniasis and cysticercosis transmission dynamics in humans, pigs and cattle. *Advances in Difference Equations, 2021(1),* 23 pages.

[13] Mwasunda, J. A., Irunde, J. I., Kajunguri, D. and Kuznetsov, D. (2021b). Optimal control and cost-effectiveness analysis of Taeniasis and Cysticercosis in humans, pigs and cattle. *Communications in Mathematical Biology and Neuroscience, 2021,* 83.

[14] Mwasunda, J. A., Irunde, J. I., Kajunguri, D. and Kuznetsov, D. (2022). Optimal Control Analysis of Taenia saginata bovine cysticercosis and human taeniasis. *Parasite Epidemiology and Control, 16(2022),* e00236.

[15] Rwabona, G. E., Masanja, V. G., Mfinanga, S., Degoot, A. and Mirau, S. (2024). A mathematical model for transmission of Taeniasis and Neurocysticercosis. *Computational and Mathematical Methods, Volume 2024, Article ID 2550598,* 14 pages. https://doi.org/10.1155/2024/2550598.

[16] Sanchez-Torres, N. Y., Bobadilla, J. R., Laclette, J. P. and Jose, M. V. (2019). How to eliminate taeniasis/cysticercosis: porcine vaccination and human chemotherapy (part 2). *Theoretical Biology and Medical Modelling, 16(1),* 4.

[17] Symeonidou, I. (2018). Human taeniasis/cysticercosis: a potentially emerging parasitic disease in Europe. *Annals of Gastroenterology, 31,* 406 - 412.

[18] Van den Driessche, P. and Watmough, J. (2002). Reproduction numbers and sub-threshold endemic equilibrium for compartmental models of disease transmission. *Mathematical Biosciences, 2(3),* 77 - 89.

[19] Wang, K., Zhang, X., Jin, Z., Ma, H., Teng, Z. and Wang, L. (2013). Modelling and analysis of the transmission of echinococcosis with application to Xinjiang Uygur autonomous region of China. *Journal of Theoretical Biology, 333,* 78 - 90.

[20] Winskill, P., Harrison, W. E., French, M. D., Dixon, M.A., Abela-Ridder, B. and Basanez, M. G. (2017). Assessing the impact of intervention strategies against taenia solium cysticercosis using the epicyst transmission model. *Parasites Vectors, 10(1),* 1 - 14.

[21] World Health Organization (2005): WHO/FAO/OIE Guidelines for the Surveillance, Prevention and control of Taeniasis/Cysticercosis. *World Organization for Animal Health, Paris (2005).*

[22] World Health Organization (2015). WHO Estimates of the Global Burden of Foodborne Diseases: Foodborne Disease Burden Epidemiology Reference Group 2007 − 2015. *World Health Organization* http://www.who.int/iris/handle/10665/199350

[23] World Health Organization: *Taeniasis/Cysticercosis Fact sheet 2019.* https://www.who.int/news-room/factsheets/detail/taeniasis-cysticercosis. Retrieved 26 April 24.

Mathematical Analysis of a Chlamydia model with Nonlinear Incidence and Recovery Rates

Ashezua, T. T.[1,*], Abu, E. A.[2] and Somma, S. A.[3]
[1,2]Department of Mathematics, Joseph Sarwuan Tarka University, Makurdi, Nigeria.
[3]Department of Mathematics, Federal University of Technology, Minna, Nigeria.

Corresponding author's email/phone number: timothy.ashezua@uam.edu.ng, 07032230542

Abstract.

Chlamydia, one of the commonest sexually transmitted infections (STIs), remain a public health concern in both underdeveloped and developed countries of the world. Chlamydia has caused worrying public health consequences hence much research work is needed to check the spread of the disease in the population. In this paper, a mathematical model for Chlamydia is developed and analyzed with nonlinear incidence and recovery rates. Qualitative analysis of the model shows that the disease-free equilibrium is locally asymptotically stable using the method of linearization. Further, using the comparison theorem method, the disease-free equilibrium is found to be globally asymptotically stable whenever the associated reproduction number is less than unity. Furthermore, mathematical analysis of the reproduction number shows that the intervention levels and the maximum per capita recovery rate due to effective treatment has a significant impact in reducing the burden of Chlamydia in the population. Numerical results show a relationship between the transmission rate, intervention levels, maximum per capita recovery rate and the reproduction number. Sensitivity analysis was conducted on the parameters connected to the reproduction number, R_c and results reveal that the top parameters that significantly drive the dynamics of Chlamydia in the population are the transmission rate, intervention levels and the maximum per capita recovery rate. These parameters need to be checked by healthcare policy makers if the disease must be controlled in the population.

Keywords: Chlamydia, sensitivity analysis, mathematical analysis, nonlinear incidence and recovery rates.

1. INTRODUCTION

Chlamydia, one of the commonest sexually transmitted infections (STIs) is largely transmitted through vaginal, oral and anal sex. It is a preventable and curable STIs caused by the bacterium *Chlamydia trachomatis* (Centers for Disease Control and Prevention (CDC), 2023, World Health Organization (WHO), 2023, Cleveland Clinic, 2023). In 2020, an estimated 128.5 million new infections associated with Chlamydia was reported worldwide amongst adults between 15 to 49 years of age and their prevalence globally was estimated to be 4.0 percent for women and 2.5 percent for men (WHO, 2023). Further, reports from Statista show that in 2020 about 25.5 million people in Africa had Chlamydia. The prevalence rate was higher amongst females with about 14.7 million people infected while 10.8 million males were infected with the disease (Statista, 2023).

In Chlamydia infection, about 80 percent of infected people have no symptoms (WHO, 2023). If symptoms occur, they may not appear for about three weeks after having sex with someone who is infected with Chlamydia. In women, common symptoms include: a change in vaginal discharge, bleeding between menstrual period or after sex, itching or burning in and around the vagina, pain or discomfort in the lower abdomen, burning sensation when urinating while in men, common symptoms include: burning sensation when urinating, discharge from the penis and pain or discomfort in the testicles. Also, anal infection in women and men can equally cause pain, discharge and bleeding (CDC, 2023, WHO, 2023, Cleveland Clinic, 2023).

This bilinear incidence rate does not consider the influence of intervention levels. Also, most mathematical models often use a parameter to represent the rate of recovery after a successful treatment regime, see for example, Iboi and Okuonghae (2016) and Ashezua *et al*. (2023). This parameter cannot be interpreted to mean minimum and maximum per capita recovery rates.

Several authors have developed and analyzed mathematical models on the transmission dynamics of Chlamydia trachomatis without considering the type of nonlinear Monod type incidence and recovery rates as used in the work of Alshammari and Khan, (2021), see for example, Martin *et al.,* (1996), Mirjam *et al*. (1996), Wilson (2006), Sharomi and Gumel (2011) and Samanta and Sharma (2014). In this study, the use of the nonlinear Monod type incidence and recovery rates as used by Alshammari and Khan (2021) is adopted. The principal aim of using this type of nonlinear incidence and recovery rates is mainly to determine mathematically the impact of the intervention levels (d) and the maximum recovery rate (c_1) which are embedded in them.

The present study complements the aforementioned research works, particularly the one by Ashezua *et al.* (2023) by developing and analyzing an equivalent mathematical model for Chlamydia trachomatis transmission dynamics by including nonlinear incidence and recovery rates as used by Alshammari and Khan (2021).

The rest of the paper is organized as follows. The model is developed in Section 2 and analyzed in Section 3. Sensitivity analysis is presented in Sections 4 while the concluding remarks in Section 5

2. MODEL FORMULATION

The total sexually active population at time t, denoted by $N(t)$ is divided into the mutually exclusive compartments of the susceptible individuals $(S(t))$, exposed individuals $(E(t))$, asymptomatic individuals $(I_a(t))$, symptomatic individuals $(I_s(t))$ and recovered individuals $(R(t))$. Let Λ represent the recruitment rate of newborns and sexually active individuals (assumed susceptible) into the population. Further, it is assumed that β_1 is the rate of transmission of chlamydia infection from infectives in the asymptomatic stage to the susceptible and β_2 is the rate of transmission of chlamydia infection from infectives in the symptomatic stage to the susceptibles. The parameter μ is the natural death rate associated to all the epidemiological

classes. Let $\rho\eta$ be the proportion of exposed individuals who are asymptomatic while $(1-\rho)\eta$ is the proportion of exposed individuals who are symptomatic. Let η be the progression rate of individuals in the exposed class to the asymptomatic and symptomatic stages of infection, respectively.

The term κm accounts for the rate at which individuals in class I_a recover naturally and progress to class R while the term $(1-\kappa)m$ is the proportion of individuals in class I_a who progress to class I_s. Individuals in class I_s recover at a rate $c(\alpha, I_s)$ as represented by equation (3). In equation (3), the parameters c_0 and c_1 $(0 < c_0 < c_1)$ represent the minimum and maximum per capita recovery rates due to sufficiency of the health care resources and the number of infected sub-population. The parameter α represents the impact of the number of hospital beds on the transmission dynamics of Chlamydia trachomatis. Also, recovered individuals become susceptible to Chlamydia infection again at a rate ψ.

Putting together these definitions and assumptions, it follows that the model for the transmission dynamics of chlamydia trachomatis in a sexually active population is given by the following system of non-linear ordinary differential equations (the schematic diagram of model (1) is shown in Figure 1, and the state variables and parameters of the model are presented in Table 1):

$$\begin{aligned}
\frac{dtS(t)}{dt} &= \Lambda - \lambda S - \mu S + \psi R,\\
\frac{dE(t)}{dt} &= \lambda S - [\rho\eta + (1-\rho)\eta + \mu]E,\\
\frac{dI_a}{dt} &= \rho\eta E - [\kappa m + (1-\kappa)m + \mu]I_a,\\
\frac{dI_s(t)}{dt} &= (1-\rho)\eta E + (1-k)mI_a - c(a, I_s)I_s - \mu I_s,\\
\frac{dR(t)}{dt} &= c(a, I_s)I_s + kmI_a - (\mu + \psi)R.
\end{aligned} \tag{1}$$

where,

$$\lambda = \frac{(\beta_1 I_a + \beta_2 I_s)}{d + (I_a + I_a)} \tag{2}$$

and

$$c(a, I_s) = \left[c_0 + \frac{(c_1 - c_0)\alpha}{(a + I_s)}\right] \tag{3}$$

The total population size is given by

$$N = S + E + I_a + I_s + R. \tag{4}$$

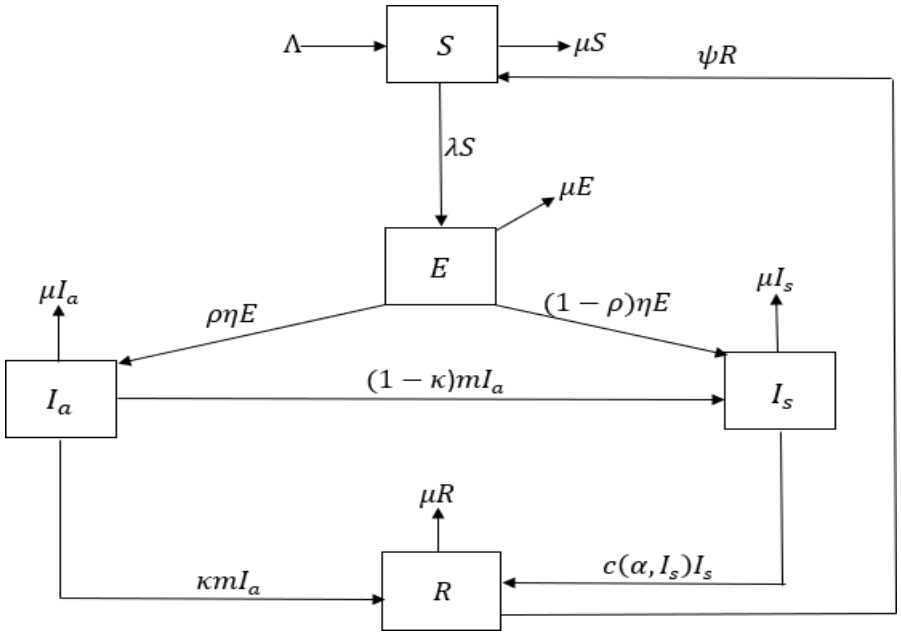

Figure 1: Schematic diagram for model (1)

2.1 Basic properties

For model (1) to be epidemiologically meaningful, it is vital to show that all its state variables are non-negative for all time, *t*. In order words, the solutions of model (1) with positive initial data will remain positive for all $t \geq 0$.

Table 2.1: Interpretation of state variables/parameters in the chlamydia model (1).

Variables/parameters	Interpretation
S	Susceptible individuals
E	Exposed individuals
I_a	Asymptomatic individuals
I_s	Symptomatic individuals
R	Recovered individuals
Λ	Recruitment rate
β_1	The transmission rate from I_a to S
β_2	The transmission rate from I_s to S
μ	Natural death rate
$\rho\eta$	Proportion of exposed individuals who are asymptomatic
$(1-\rho)\eta$	Proportion of exposed individuals who are symptomatic
ψ	The rate at which recovered individuals become susceptible
η, m	Progression rates
km	Accounts for the proportion of the asymptomatic individuals who

	recover and moved to R
$(1 - km)$	Accounts for the proportion of the asymptomatic individuals who progress to the $I_s$stage of infection
λ	Force of infection
d	Intervention levels
α	Impact of the number of hospital beds on the transmission of chlamydia
$c_o(c_1)$	Minimum and maximum per capita recovery rates

2.1.1 Positivity and boundedness of solution.

Since the model (1) monitors the human population, the state variables and parameters of the model are non-negative. Consider the biologically feasible region.

$$\Phi = \{(S, E, I\ , I\ , R)\} \in \mathbb{R}_+^5 : N \leq \frac{\Lambda}{\mu} \tag{5}$$

It can be shown that the set Φ is a positively invariant set and a global attractor of this system. This implies that, any phase trajectory initiated anywhere in the non-negative region $R^5$of the phase space will eventually enter the region Φ and remains in Φ thereafter.

Lemma 2.1. *The region Φ is positively invariant for model (1).*

Proof. The rate of change of the total population with time is given by

$$\frac{dN}{dt} = \Lambda - \mu N. \tag{6}$$

Since the right-hand side of (5) is bounded by $\Lambda - \mu N$, we can show using a standard comparison theorem (Lakshmikantham *et al*. 1989) that

$$N\ (t) \leq\ N\ (0) exp^{-\mu t} + \frac{\Lambda}{\mu}(1 - exp^{-\mu t}) \tag{7}$$

In particular, if $N(0) \leq \frac{\Lambda}{\mu}$ then $N\ (t)\ \leq \frac{\Lambda}{\mu}$. Therefore, Φ is positively invariant.

3 Mathematical analysis

3.1 Asymptotic stability of disease-free equilibrium (DFE)

The DFE of the model (1) is given by $E_1 = (\mathrm{S}^*, \mathrm{E}^*, \mathrm{I}_\mathrm{a}^*, \mathrm{I}_\mathrm{s}^*, \mathrm{R}^*) = \left(\frac{\Lambda}{\mu}, 0,0,0,0\right)$

The reproduction number of model (1) will be obtained using the next generation operator method. The notations as used in (van den Driessche and Watmough, 2002) is adopted, the non-negative

matrix, F, of new infection terms and the M -matrix, V, of transition terms associated with model (1) are

$$F = \begin{pmatrix} 0 & \frac{\beta_1 \Lambda}{\mu d} & \frac{\beta_2 \Lambda}{\mu d} \\ 0 & 0 & 0 \\ 0 & 0 & 0 \end{pmatrix} \text{ and } V = \begin{pmatrix} k_1 & 0 & 0 \\ -\rho\eta & k_2 & 0 \\ -k_3 & -k_4 & (c_1 + \mu) \end{pmatrix}$$

where,

$$k_1 = [\rho\eta + (1-\rho)\eta + \mu], k_2 = [\kappa m + (1-\kappa)m + \mu], k_3 = (1-\rho)m \\ k_4 = (1-\kappa)m\,. \tag{8}$$

It follows that the reproduction number of the model (1), denoted by R_c, is given by

$$R_c = \rho(FV^{-1}) = \frac{\beta_1 \Lambda \rho \eta}{\mu d k_1 k_2} + \frac{\beta_2 \Lambda \rho \eta k_4 + k_2 k_3}{\mu d k_1 k_2 (c_1 + \mu)} \tag{9}$$

With $R_c^1 = \frac{\beta_1 \Lambda \rho \eta}{\mu d k_1 k_2}, R_c^2 = \frac{\beta_2 \Lambda \rho \eta k_4 + k_2 k_3}{\mu d k_1 k_2 (c_1 + \mu)}$ *and* $R_c^3 = \frac{\beta_2 \Lambda k_3}{\mu d k_1 (c_1 + \mu)}$, *where* $\rho(FV^{-1})$, *where* $\rho(FV^{-1})$ is the spectral radius of the matrix(FV^{-1}).

The local stability of E_1 is obtained using the Heffernan *et al.* (2005) method as used in the work of Akinwande *et al.* (2022). It is proved in the following theorem.

Theorem 3.1. *The disease-free equilibrium, E_1 of the system (1) is locally asymptotically stable if $R_c < 1$ and unstable if $R_c > 1$.*

Proof. The stability of E_1 is proved from the roots of the characteristics polynomial which states that the equilibrium is stable if the roots of the characteristics polynomial are all real and negative. Thus, the Jacobian matrix of the system (1) at E_1 is given by

$$J = \begin{pmatrix} \mu & 0 & -\frac{\beta_1 \Lambda}{\mu d} & -\frac{\Lambda \beta_2}{\mu d} & \psi \\ 0 & -k_1 & \frac{\Lambda \beta_1}{\mu d} & \frac{\Lambda \beta_2}{\mu d} & 0 \\ 0 & \rho\eta & -k_2 & 0 & 0 \\ 0 & k_3 & k_4 & -c_1 & 0 \\ 0 & 0 & km & c_1 & -k_5 \end{pmatrix}$$

where,

$$k_1 = [\rho\eta + (1-\rho)\eta + \mu], k_2 = [\kappa m + (1-\kappa)m + \mu], \\ k_3 = (1-\rho)m, k_4 = (1-\kappa)m, k_5 = (\mu + \psi). \tag{10}$$

The characteristics polynomial is given by

$$(-\mu - \lambda)(k_5 + \lambda)[M_3\lambda^3 + M_2\lambda^2 + M_1\lambda + M_0] = 0, \tag{11}$$

with,

$$\begin{aligned} M_3 &= \mu d, \\ M_2 &= \mu d(c_1 + k_1 + k_2), \\ M_1 &= \mu d[k_2(c_1 + k_1) + c_1 k_1[1 - c_1 k_2 R_c^1 - c_1(c_1 + \mu)]R_c^3], \\ M_0 &= \mu d c_1 k_1 k_2[1 - R_c^1 - c_1(c_1 + \mu)(R_c^2 + R_c^3)]. \end{aligned} \tag{12}$$

It is observed from (11) that $\lambda_1 = -\mu \; and \; \lambda_2 = -k_5$. Now, according to Heffernan *et al*. (2005), if M_3, M_2, M_1, M_0 are all positive, then the roots of equation (11) have negative real parts whenever $R_C < 1$. Therefore, the disease-free equilibrium, E_1 is locally asymptotically stable since $M_i > 0, i = 0,1,2,3$ when $R_C < 1$. However, if $R_C > 1, M_0 < 0$. The implication is that positive real parts exist and hence E_1 is unstable if $R_c > 1$.

To establish the global stability of the Chlamydia-free equilibrium, the following results is proved.

Theorem 3.2. *The DFE of model (1) is globally asymptotically stable in* Φ *whenever* $R_C \leq 1$.

Proof. Note here that the equations for the infected classes of the model (1) are written in the matrix-vector form as follows:

$$\frac{dY(t)}{dt} = \left[(F - V) - \left(1 - \frac{S}{N}\right)W\right]Y(t) \tag{13}$$

where $Y(t) = [E(t), I_a(t), I_s(t), R(t)]^T$ and the matrices F and V are given in Section 3. Furthermore,

$$W = \begin{pmatrix} 0 & \frac{\beta_1 \Lambda}{\mu d} & \frac{\beta_2 \Lambda}{\mu d} \\ 0 & 0 & 0 \\ 0 & 0 & 0 \end{pmatrix}$$

Since W is a nonnegative matrix and $S \leq N$ in Φ, it follows that

$$\frac{dY(t)}{dt} \leq [(F - V)]Y(t) \tag{14}$$

Using the fact that the eigenvalues of the matrix $F - V$ all have negative real parts (that is, $\rho(FV^{-1}) < 1$ if $(R_C < 1)$, it follows that the linearized differential inequality system (13) is stable whenever $R_C < 1$. Thus, by the comparison theorem (Lakshmikantham *et al*., (1989)),

$$\lim_{t \to \infty} E(t), \; I_a(t), \; I_s(t), R(t) = (0,0,0,0) \tag{15}$$

It can be shown by substituting the DFE (E_1) into (1) that, $S(t) \longrightarrow \frac{\Lambda}{\mu}$ as $t \longrightarrow \infty$. Hence,

$$\lim_{t \to \infty} S(t), E(t), I(t), I(t), R(t) = \left(\frac{\Lambda}{\mu}, 0,0,0,0\right) = E_1 \tag{16}$$

Thus, every solution to the equation of the model (1) and initial conditions Φ, approaches the DFE (E_1) as $t \to \infty$ whenever $R_C < 1$.

3.2 Analysis of the reproduction number, R_C

In this subsection, the threshold parameter, R_c is used to determine the impact of the maximum recovery rate (c_1), intervention levels (d) for the asymptomatic and symptomatic individuals on the control of Chlamydia infection in the population. It is obvious from (9) that

$$\lim_{t\longrightarrow\infty} R_c = 0,$$
$$\lim_{c_1\longrightarrow\infty} \frac{\beta_1\Lambda\rho\eta}{\mu d k_1 k_2} > 0, \tag{17}$$

Therefore, a Chlamydia control programme that results in high application of intervention levels and maximum per capita recovery rate due to sufficiency of healthcare resources can lead to an effective Chlamydia control in the population if the respective right-hand sides of (17) are less than one. From (17), it is observed that a near total elimination of Chlamydia appears achievable. In this situation, the strategy is to focus on an effective intervention plan(s) such as advising infected individuals (both asymptomatic and symptomatic) to religiously take their drugs, abstaining from unprotected sex while on treatment and susceptible individuals to properly use condoms if they must engage in any form of sexual activity. The aforementioned intervention plan(s) will certainly help in curtailing the spread of Chlamydia in the community.

Further, by computing the partial derivatives of R_C with respect to the intervention levels (d) and maximum per capita recovery rate (c_1) due to effective treatment clearly shows the impact of these parameters on the control of Chlamydia in the population. These yields

$$\frac{\partial R_c}{\partial \psi} = -\frac{\Lambda[\beta_1\rho\eta(c_1+\mu)+\beta_2(\rho\eta k_4 + k_2 k_3)]}{\mu d^2 k_1 k_2 (c_1+\mu)} < 0,$$
$$\frac{\partial R_c}{\partial c_1} = -\frac{\beta_2\Lambda(\rho\eta k_4 + k_2 k_3)}{\mu d k_1 k_2 (c_1+\mu)^2} < 0. \tag{18}$$

It is observed from (18) that the partial derivatives are less than zero. Thus, an effective application of the intervention strategies and maximum per capita recovery rate due to proper adherence to treatment plan will have a positive impact in reducing Chlamydia burden in the community.

4 Sensitivity Analysis

Sensitivity analysis is usually conducted on the parameters of the model connected to the reproduction number R_C using the parameter values in Table 4.1. The essence of this analysis is to determine the relative importance of each parameter in the model that contribute to the Chlamydia transmission. A method similar to the ones outlined in the work Ashezua *et al*. (2023) was utilized to obtain the sensitivity indices of all the parameters contained in the reproduction number using the formula in (19).

$$\Pi_q^{R_c} = \frac{\partial R_c}{\partial \psi} \times \frac{\psi}{R_c}. \tag{19}$$

where Ψ denotes model parameters contained in R_C. It is obtained from (19) the sensitivity indices of the parameters associated with the reproduction number as presented in Table 4.2. The parameters with positive sensitivity indices signify a high impact burden of Chlamydia in the population if their values keep increasing. In a similar manner, parameters in which their sensitivity indices are negative have a great effect in reducing Chlamydia burden in the population as their values increase while the others remain constant. Hence, as their values increase, the reproduction number decreases thus reducing the endemicity of the disease in the population.

Table 4.1: The parameter values of model (1)

Parameter	Nominal value ($year^{-1}$)	Reference
Λ	1000	Sharomi and Gumel, (2011)
β_1	0.1	Sharma and Samanta (2014)
β_2	0.15	Sharma and Samanta (2014)
μ	0.15	Sharma and Samanta (2014)
ψ	0.75	Ashezua *et al*. (2023)
ρ	0.70	Sharma and Samanta (2014)
η	0.50	Sharma and Samanta (2014)
κ	0.70	Sharma and Samanta (2014)
m	0.80	Sharma and Samanta (2014)
c_0	0.20	Alshammari and Khan (2021)
c_1	0.21	Alshammari and Khan (2021)
α	0.20	Alshammari and Khan (2021)

Table 4.2: Sensitivity indices of some parameter values

Parameter	Sensitivity indices
Λ	+1.0000
β_1	+0.2947
β_2	+0.7053
K	−0.6018
P	−0.4912
H	+0.2308
M	−0.1972
c_1	−0.4114
D	−1.0000

From the results of the sensitivity analysis presented in Table 4.2, some of the parameters with high negative indices are the intervention levels (d) and maximum per capita recovery rate due to effective treatment (c_1). These are the top parameters that significantly drive the dynamics of

Chlamydia in the population. Consequently, to control the spread of the disease, these top parameters must be effectively targetted by policy makers in the health sector so that the sensitivity indices of these parameters must be kept negative for an effective control of the disease in the community. This means that the advocacy for the use of condoms by susceptible individuals and proper treatment of infected individuals must be priotized if Chlamydia must be controlled in the population.

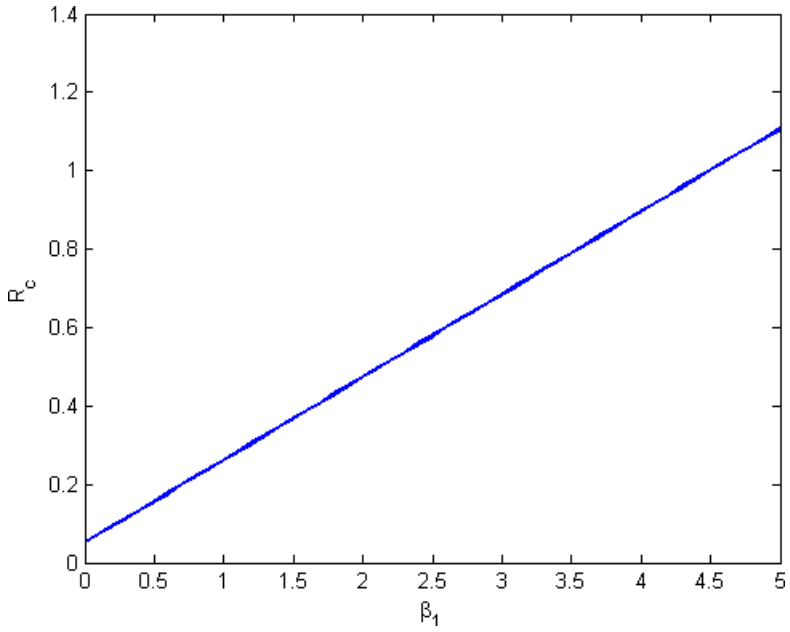

Figure 2: Plot of reproduction number, R_C as a function of progression rate, β_1. Parameter values used are as in Table 4.1.

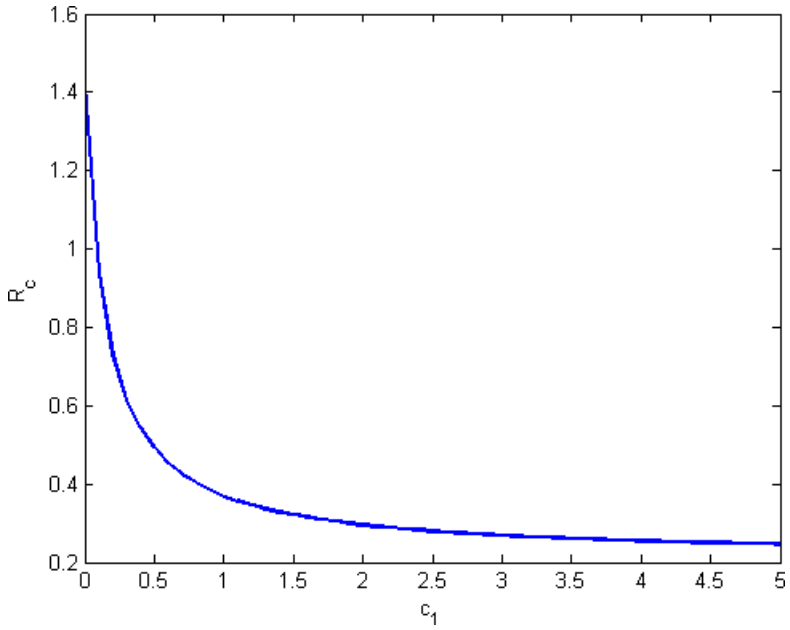

Figure 3: Plot of reproduction number, R_C as a function of progression rate, c_1. Parameter values used are as in Table 4.1.

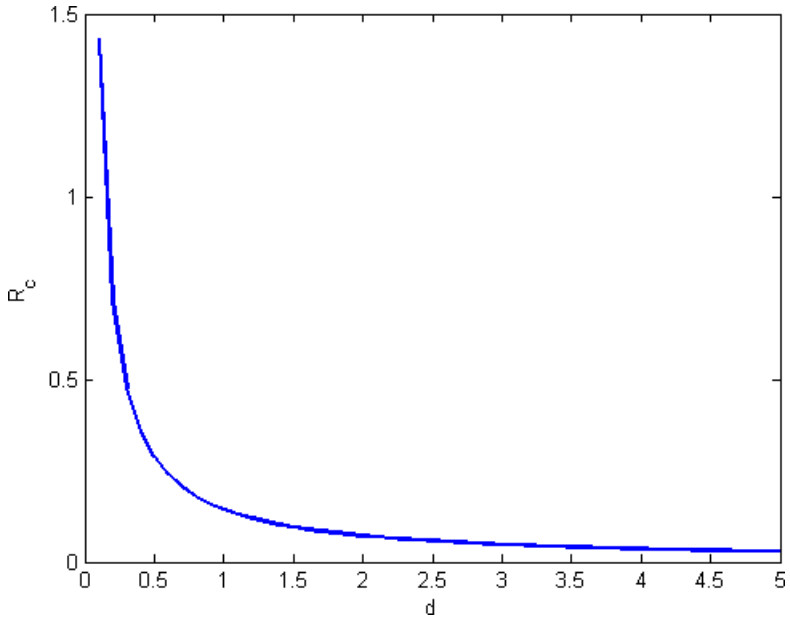

Figure 4: Plot of reproduction number, R_C as a function of progression rate, d. Parameter values used are as in Table 4.1.

5 Conclusion

In this paper, a deterministic mathematical model for gaining insights into the transmission dynamics of Chlamydia trachomatis in a population with nonlinear incidence and recovery rates is developed and analyzed. The aim of this study is to mathematically establish the impact of intervention levels and maximum per capita recovery rate due to effective treatment which are embedded in the nonlinear incidence and recovery rates, respectively. Qualitative analysis of the model shows that the disease-free equilibrium is locally asymptotically stable using the method of linearization. Further, using the comparison theorem method, the disease-free equilibrium was found to be globally asymptotically stable whenever the associated reproduction number is less or equal to unity. Furthermore, mathematical analysis of the reproduction number shows that the intervention levels and the maximum per capita recovery rate due to effective treatment has a significant impact in reducing the burden of Chlamydia in the population. This implies that susceptible individuals should be introduced to the available preventive measures e.g. abstaining from sex and the use of condoms correctly before engaging in any form of sexual activity. Also, effective treatment should be given to the infected individuals in order to control the spread of the disease in the population. Numerical results show a relationship between the transmission rate, intervention levels, maximum per capita recovery rate and the reproduction number. Sensitivity analysis was conducted on the parameters connected to the reproduction number, R_C and results reveal that the top parameters that significantly drive the dynamics of Chlamydia trachomatis in the population are the transmission rates, intervention levels and the maximum per capita recovery rate. These parameters need to be targetted by health policy makers if the disease must be controlled in the population. The present study can be further analyzed to establish the type of bifurcation the model exhibits and carry out cost-effectiveness analysis of the control strategies of Chlamydia trachomatis in the model.

REFERENCES

Alshammari, F. S. & Khan, M. A. (2021). Dynamic behaviors of a modified SIR model with nonlinear incidence and recovery rates. *Alexandria Engineering Journal*, 60: 2997-3005.

Akinwande, N. I., Ashezua, T. T., Gweryina, R. I., Somma, S. A. *et al.* (2022). Mathematical model of COVID-19 transmission dynamics incorporating booster vaccine program and environmental contamination. Heliyon 8 (2022) e11513.

Ashezua, T. T., Ibekwe, J. J. & Somma, S. A. (2023). Modelling and analysis of a model for chlamydia trachomatis transmission dynamics. International Journal of Mathematical Analysis and Modelling, 6(2): 13-30.

Brunham, R. C., Pourbohloul, B., Mak, S. White, R. & M. I. Rekart (2005). The unexpected impact of a Chlamydia trachomatis infection control program on susceptibility to reinfection. *J. Infec. Dis.*, 192:1836–1844.

Burns, J. A., Cliff, I. M. & Doughty, S. E. (2007). Sensitivity analysis and parameter estimation for a model of Chlamydia trachomatis infection. *J. Inverse III-posed Probl.*, 15(3):243–256.

Center for Disease Prevention & Control (2023). Chlamydia statistics. retrieved on August 16, 2023 from https://www.cdc.gov/std/chlamydia/stat.htm.

Cleveland Clinic (2023). Chlamydia. retrieved on August 18, 2023 from https://my.clevelandclinic.org/health/diseases/4023-chlamydia.

Heffernan, J. M., Smith, R. J. & Wahl, L. M. (2005). Perspectives on the basic reproduction ratio, J. R. Soc. Interface 2 (2005) 281–293.

Iboi, E. & Okuonghae, D. (2016). Population dynamics of a mathematical model for syphilis. Applied Mathematical Modelling, 40(2016): 3573-3590.

Lakshmikantham, S., Leela, S. & Martynyuk, A. A. (1989). Stability Analysis of Nonlinear Systems, Marcel Dekker, New York.

Martin, C. F., Allen, I. J. S. & Stamp, M. S. (1996). An analysis of the transmission of Chlamydia in a closed population. *J. Diflerence Equ. Appl.*, 2(1):1–29.

Mirjam, K., Yvonne, T. H., van Duynhoven, P. & Anton. S. J. (1996). Modelling prevention strategies for gonnorrhea and Chlamydia using stochastic network simulations. *Amer. J. Epidemiology*, 144(3):306–317.

Regan, D. G., Wilson, D. P. & Hocking, J. S. (2008). Coverage is the key for effective screening of Chlamydia trachomatis in Australia. *J. Infec. Dis.*, 198:349–358.

Sharma, S. & Samanta, G. P. (2014). Analysis of a Chlamydia epidemic model. *Journal of Biological Systems*, 22(4):714–744, 2014.

Sharomi, O. & Gumel, A. B. (2011). Mathematical study of a risk-structured two group model for Chlamydia transmission dynamics. *Appl. Math. Modell.*, 35(8):3653–3673, 2011.

Statista (2023). Number of people infected with chlamydia in Africa as of 2020, by gender. retrieved on August 18, 2023 from https://www.statista.com/statistics/1128548/prevalence-of-chlamydia-in-africa-by-gender/:: text=as.

van den Driessche, P. & Watmough, J. (2002). Reproduction numbers and sub-threshold endemic equilibria for compartmental models of disease transmission, *J. Math. Biosci.* 180 (2002) 29–48.

World Health Organization (2023). Chlamydia. retrieved on August 16, 2023 from https://www.who.int/news-room/fact-sheets/detail/chlamydia: :text=in.

Zhang, H., Chen, I. & Nieto, J. J. (2008). A delayed epidemic model with stage- structured and pulses for pest management strategy. *Nonlinear Anal. RWA*, 9:1714–1726.

A Model of Two-Body Problem for Planetary and Space Science

T.O. Amuda[1] , A.I Okunnuga[2], Blessing Ashagwu[3] and Y.A. Bello[4]

[1,2,3,4]Department of Mathematics, Faculty of Science, Air Force Institute of technology, Kaduna, Nigeria

[1]teejaymath@gmail.com; to.amuda@afit.edu.ng

Abstract

In this paper, a model of Two-Body Problem for planetary and space science is studied. The trajectories $X_1(t)$ and $X_2(t)$ for the initial positions $X_1(t=0)$ and $X_2(t=0)$, the initial velocities $V_1(t=0)$ and $V_2(t=0)$ are determined. The vector r between the masses with respect to time is computed. It is seen that the position $R(t)$ of the center of mass is determined at all times from the initial positions $X_1(t=0)$, $X_2(t=0)$ and velocities $V_1(t=0)$, $V_2(t=0)$. This study investigates the Two-Body Problem for planetary and space science. The result finding shows detailed mathematical modelling of the motion of two celestial bodies under the influence of gravity.

Keywords: Gravitational Force, Kepler's Laws of Motion, Two-Body Problem, Space Science.

1 Introduction

Unraveling the Physical Behavior of Celestial bodies, in the vast expanse of the cosmos, countless celestial bodies, from planets and moons to asteroids and comets, dance in an intricate ballet governed by the laws of physics. Planetary science, a captivating and multifaceted discipline, delves into understanding the origins, evolution, and physical properties of these celestial bodies, providing insights into the fundamental principles that shape our universe.

The physical behaviour of celestial bodies is governed by the principles and laws of physics, which are fundamental to understanding the universe. The key aspects of physical behaviour in space include gravity, orbits, planetary formulation, planetary atmospheres, space weather, and impact events. Each of these areas contributes to our understanding of the behaviour and interactions of celestial bodies.

Gravity is the primary force that influences the motion and interaction of celestial bodies. It determines the orbits of planets, moons, and other objects around massive bodies such as stars. The study of gravity helps explain the formation of galaxies, star systems, and the dynamics of celestial objects within them. Celestial bodies follow specific paths known as orbits, which can be elliptical in shape. Johannes Kepler formulated three laws of planetary motion, describing the relationship between an object's orbital characteristics and its distance from the central body. These laws provide insights into the regularity and predictability of celestial motion. The formulation of planets is a fascinating area of study within space and planetary science. Space weather is vital for predicting and mitigating potential hazards to spacecraft, satellites and astronauts.

Sergey *et al.* (2024) discussed a solving method for determining the precise coordinates of a mass point in orbit around a significantly more massive primary body, operating within the confines of the restricted two-body problem (R2BP). The system of equations of motion has been successfully explored to identify an analytical means of representing the solution in polar coordinates. An analytical approach for obtaining the function $t = t(r)$, incorporating an elliptic integral, is developed.

Christina *et al.* (2016) review the scientific aspects of planetary space weather at different regions of our Solar System, performing a comparative planetology analysis that includes a direct reference to the circum-terrestrial case. Through an interdisciplinary analysis of existing results based both on observational data and theoretical models. They review the nature of the interactions between the environment of a Solar System body other than the Earth and the impinging plasma/radiation and discussed study of planetary space weather can provide feedback for better understanding the traditional circum-terrestrial space weather.

Xiyun & Xiaosheng (2017) investigated truncating at the second order of the mutual potential between two rigid bodies, time-explicit first order solutions to the rotations and the orbital motion of the two bodies in the planar

Govind *et al.* (2022) study the existence and stability of collinear and noncollinear equilibrium points within the frame of the perturbed restricted problem of 2 + 2 bodies by a planetesimal belt. They compare and investigate the corresponding results of the perturbed and unperturbed models. The impact of the planetesimal belt is observed on collinear and noncollinear equilibrium points. They demonstrate that all equilibrium points are unstable, and we numerically investigate the noncollinear equilibrium points.

Boldrin *et al.* 2016 investigated the evolution of initially non-planar binaries created by fission. Using a two-ellipsoid model, they performed simulations taking only gravitational interactions between components into account. They simulate 91 different initial inclinations of the equator of the secondary body for 19 different mass ratios. After disruption, the binary system dynamics are chaotic, as predicted from theory. Starting the system in a non-planar configuration leads to a larger energy and enhanced coupling between the rotation state of the smaller fissioned body and the evolving orbital system, and enables re-impact to occur. This leads to differences with previous planar studies, with collisions and secondary spin fission occurring for all mass ratios.

Amuda *et al.* 2021 studied the restricted three-body problem (R3BP) describes the motion of a test particle having infinitesimal mass and moving under the gravitational effects of two primaries, which move in circular orbits around their center of mass on account of their mutual attraction and the test particle does not in any way influence the motion of the primaries. The R3BP constitutes one of the most important problems in dynamical astronomy and the study in its many variants has had important implications in several scientific fields, including, among others, galactic dynamics, chaos theory, molecular physics and celestial mechanics.

Scientists use various methods such as telescopic observations, space missions, and computer simulations to explore planets, their atmospheres, geology, and potential habitability. This research helps us gain insights into the broader universe and our place within it.

The paper is organized as follows: Section 3 is the material and methods while the results and discussion is in Section 4. Section 5 conclude the research study

The Two-Body Problem is a model dealing with the orbital motion and rotational motion of two rigid bodies of finite sizes influenced by their mutual gravitational potential. One example of such a system is the binary asteroids in the solar system. Denote the two bodies as *A* and *B*, there are 12 degrees of freedom for this system (3 for the orbital motion and 3 for the rotational motion for each body). By studying their relative orbital motion, the 6 degrees of freedom for the orbital motion can be reduced to 3 degrees of freedom. The mutual dynamics of the system is governed by the mutual potential between the two rigid bodies which depends on their relative orbit and relative attitude. Generally, except for some special cases, there is no closed form for the mutual potential. As a result, except some studies on the qualitative description of the system, works on the motions of the system are usually carried out for potentials truncated at finite orders. A simpler version of the full Two-Body Problem is the planar case where the two bodies are simulated by two ellipsoids. The two ellipsoids are rotating along their primary principal axis and the orbital plane is coincident with the rotational planes of the two bodies. This model is often used to qualitatively describe the fission process of binary asteroids, and is the model that will be analytically treated in this work. A practical application of this model is the orbital motion of spacecraft or ejecta in the binary asteroid system. Most of these studies assume a double synchronous state (both bodies' rotation speed equals that of the orbital motion) of the Two-Body Problem so that the orbital and rotational motions of the two bodies can be treated as constant rotations. However, the double synchronous state is just one special state of the Two-Body Problem. For example, in the solar system, only a minor fraction of the binary asteroid systems is in a double synchronous state. As a result, it's useful to consider more general cases where one or two of the two bodies are not in synchronous rotation with their orbit. In this case, analytical solutions to the orbital and rotational motion of the Two-Body Problem are useful in expressing the equations of motion (EOMs).

The Two-Body Problem is often simplified to consider the motion of a small body orbiting a much larger a much larger, central body. This approximation is valid for many celestial systems, such as the Earth orbit the Sun or a satellite orbiting the Earth. Under this assumption, the gravitational force between the two bodies can be treated as a one-way force, with the larger boding exerting a dominant gravitational pull on the smaller body. A Two-Body Problem is the problem of determining the previous or subsequent motion and the data for computing the places at any time of two bodies when given the Newtonian law of gravitation and the masses of two bodies with their positions and motions at any moment.

The distances between planets in our solar system vary greatly because they all orbit the Sun at different distances. These distances are typically measured in astronomical units (AU), where 1

AU is the average distance from Earth to the Sun, about 93 million miles (150 million kilometers). Here are some approximate average distances of planets from the Sun in AU:

Mercury (0.39 AU), Venus (0.72 AU), Earth (1 AU), Mars (1.52 AU), Jupiter (5.20 AU), Saturn (9.58 AU), Uranus (19.22 AU), Neptune (30.05 AU)

These values are averages and can vary depending on the positions of the planets in their elliptical orbits. The distance between any two planets in our solar system also changes constantly as they move along their orbits. Planets exhibit various physical behaviour and characteristics, which can be studied through observations and scientific research. Here are some key physical behaviors and features of planets;

Orbital Motion; Planets orbit the Sun in elliptical paths, following Kepler's laws of planetary motion. They move at different speeds depending on their distance from the Sun. An ellipse is defined as the set of all points such that the sum of the distance from each point to two foci is a constant. Figure 1.1 shows an ellipse and describes a simple way to create it.

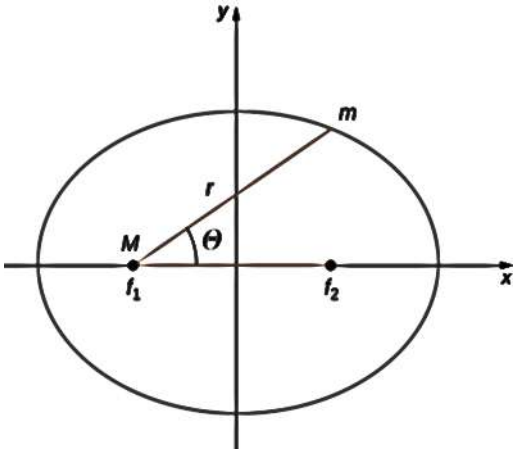

Fig. 1: Orbital Motion

Fig 1, the Orbital Motion and the distance r between the planet (m) and the Sun (M), and the angle measured from the x – axis, which is along the major axis of the ellipse.

Kepler's equation is a fundamental equation in celestial mechanics that helps us to understand the motion of planets and other objects in space. Kepler's equation is expressed as;

$$M = E - e\sin(E)$$

In this equation: M – represents the mean anomaly, E – represents the eccentric anomaly (shape of an elliptic orbit), e – represents eccentricity of the orbit (how much an orbit deviates from being a perfect circle) and Sin(E) – is the sine function.

The study of planetary and Space science and the exploration of the physical behavior hold significant importance to the wellbeing of nature. The Two Body problem is important in finding

stability of the Zodiacal cloud, orbital evolution of cometary meteor streams, asteroidal particles and dust rings around planets. Results considering the shape of the Earth and radiation effect of the Sun, in the Moon-Earth system are good examples.

3 Material and Methods

Model Analysis

This section analysis the model for Two-Body Problem in Planetary and Space Science.

3.1 A Two-Body Problem

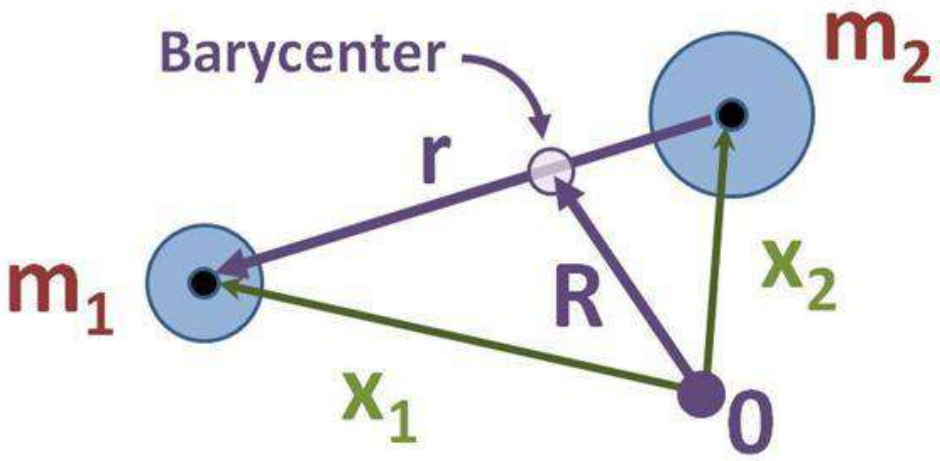

Fig.2: The Barycenter Model

Let X_1 and X_2 be the position vectors, m_1 and m_2 be their masses and vector r is the distance between the two masses.

$$F = \frac{G * m_1 * m_2}{r^2},$$

where G is called the Gravitational constant.

The Jacobi coordinate for the Two-Body Problem

$$R = \frac{m_1}{M} X_1 + \frac{m_2}{M} X_2$$

and

$$r = X_1 - X_2 \text{ with } M = m_1 + m_2$$

From Newton's second law, when applied to the two masses we get;

$$F_{12}\left(X_1, X_2\right) = m_1 \ddot{X}_1 \tag{1}$$

$$F_{21}\left(X_1, X_2\right) = m_2 \ddot{X}_2 \tag{2}$$

Where F_{12} is the force on mass 1 acting on mass 2 as F_{21} is the force on mass 2 acting on mass 1. The position vectors $\ddot{X}(t)$ denote their second derivative with respect to time, or their acceleration vectors.

The Jacobian coordinate for the Two-Body Problem will be used to analysis the Two-Body Problem.

3.2 Position of Center of mass

Let R be the position of the mass (The first part of the Two-Body Problem)

Adding equation (1) and (2) gives;

$$F_{12}\left(X_1, X_2\right) + F_{21}\left(X_1, X_2\right) = m_1 \ddot{X}_1 + m_2 \ddot{X}_2 \tag{3}$$

But $R = \frac{m_1}{M} X_1 + \frac{m_2}{M} X_2$ (4)

Differentiating (4) with respect to R the first time, we have;

$$\dot{R} = \frac{m_1}{M} \dot{X}_1 + \frac{m_2}{M} \dot{X}_2$$

Differentiating (4) with respect to R the second time, we have;

$$\ddot{R} = \frac{m_1}{M} \ddot{X}_1 + \frac{m_2}{M} \ddot{X}_2$$

From $\ddot{R}$ we have

$$\ddot{R} = \frac{m_1 \ddot{X}_1 + m_2 \ddot{X}_2}{M}$$

$$\ddot{R} = \frac{m_1 \ddot{X}_1 + m_2 \ddot{X}_2}{m_1 + m_2}$$

$$\left(m_1 + m_2\right) \ddot{R} = m_1 \ddot{X}_1 + m_2 \ddot{X}_2 = F_{12} + F_{21} \tag{5}$$

$$0 = F_{12} + F_{21} \tag{6}$$

By Newton's second law, $F_{12} = -F_{21}$

Substitute for $F_{12} = -F_{21}$ in equation (6)

$$-F_{21} + F_{12} = 0$$

Therefore $\ddot{R} = 0$ (7)

This implies $\frac{d^2R}{dt^2} = 0$

To get the velocity of the problem, we integrate equation (7)

This gives;

$$\int \frac{d^2R}{dt^2} = \frac{dR}{dt}$$

This implies $V = \frac{dR}{dt}$, a constant (8)

It follows that $m_1v_1 + m_2v_2$ a conservation law of momentum.

Displacement vector motion

For the displacement, we take the difference of equations (1) and (2). The second part of the Two-Body Problem.

Let r be the displacement of the vector motion

Thus, we have;

$$F_{12}\left(X_1, X_2\right) - F_{21}\left(X_1, X_2\right) = m_1\ddot{X}_1 - m_2\ddot{X}_2 \quad (9)$$

But $r = X_1 - X_2$

$$\dot{r} = \dot{X}_1 - \dot{X}_2$$

$$\ddot{r} = \ddot{X}_1 - \ddot{X}_2$$

$$F_{12} - F_{21} = m_1\ddot{X}_1 - m_2\ddot{X}_2 \quad (10)$$

$$F_{12} - m_1\ddot{X}_1 = F_{21} - m_2\ddot{X}_2$$

Divide left-hand side by m_1 and right-hand side by m_2

$$\frac{F_{12}}{m_1} - \frac{m_1 \ddot{X}_1}{m_1} = \frac{F_{21}}{m_2} - \frac{m_2 \ddot{X}_2}{m_2}$$

$$\frac{F_{12}}{m_1} - \ddot{X}_1 = \frac{F_{21}}{m_2} - \ddot{X}_2$$

$$\frac{F_{12}}{m_1} - \frac{F_{21}}{m_2} = \ddot{X}_1 - \ddot{X}_2$$

$$\frac{F_{12}}{m_1} - \frac{F_{21}}{m_2} = \ddot{r} \tag{11}$$

From Newton's second law

$F_{12} = -F_{21}$

Also, $-F_{21} = F_{12}$

Substitute for $F_{12} = -F_{21}$ in equation (11)

$$-\frac{F_{21}}{m_1} - \frac{F_{21}}{m_2} = \ddot{r}$$

OR

$$\frac{F_{12}}{m_1} + \frac{F_{12}}{m_2} = \ddot{r}$$

$$\frac{F_{12}}{m_1} + \frac{F_{12}}{m_2} = \ddot{r}$$

$$F_{12}\left(\frac{1}{m_1} + \frac{1}{m_2}\right) = \ddot{r}$$

$$F_{12}\left(\frac{m_2 + m_1}{m_2 m_1}\right) = \ddot{r} \tag{12}$$

To get F_{12}, we divide both sides by $\left(\frac{m_2 + m_1}{m_1 m_2}\right)$

$$F_{12} = \frac{\ddot{r}}{\left(\frac{m_2 + m_1}{m_1 m_2}\right)}$$

$$F_{12} = \frac{\ddot{r}}{\frac{m_2 + m_1}{m_1 m_2}}$$

$$F_{12} = \ddot{r} \times \frac{m_1 m_2}{m_2 + m_1}$$

But $\mu = \frac{m_1 m_2}{m_2 + m_1}$

Where μ is the mass ratio

Then, $F_{12} = \mu \ddot{r}$ (13)

$$F(r) = F_{12}\left(X_1, X_2\right) = \mu \ddot{r}$$

$$\frac{F(r)}{\mu} = \ddot{r} \quad (14)$$

Recall that

$$X_1 - X_2 = r(t)$$

Let $\frac{m_2 + m_1}{m_1 + m_2} = 1$

$$X_1 - X_2 = \frac{m_2 + m_1}{m_1 + m_2} r\left(t\right)$$

$$X_1 - X_2 = \frac{m_2}{m_1 + m_2} r\left(t\right) + \frac{m_1}{m_1 + m_2} r\left(t\right)$$

Introducing $R\left(t\right)$

$$X_1 - X_2 = R\left(t\right) + \frac{m_2}{m_1 + m_2} r\left(t\right) + \frac{m_1}{m_1 + m_2} r\left(t\right) - R\left(t\right)$$

$$= R\left(t\right) + \frac{m_2}{m_1 + m_2} r\left(t\right) - R\left(t\right) + \frac{m_1}{m_1 + m_2} r\left(t\right)$$

$$X_1 - X_2 = \left[R\left(t\right) + \frac{m_2}{m_1 + m_2} r\left(t\right)\right] - \left[R\left(t\right) - \frac{m_1}{m_1 + m_2} r\left(t\right)\right] \quad (15)$$

Therefore, $X_1 = R(t) + \frac{m_2}{m_1 + m_2} r(t)$ (16)

$$X_2 = R(t) - \frac{m_1}{m_1 + m_2} r(t) \quad (17)$$

Equation (16) and (17) gives the solution of the Two-Body Problem. It can be verified by substituting the value of the center of mass R and the displacement r into the right-hand sides of these equations.

4. Results and Discussion

Solving the equations (1) and (2) for the distance $r(t)$ is the key to the Two-Body Problem. The solution depends on the specific force between the bodies, which is defined by $F(r)$. We use Newton's gravitational law to obtain our formula, where the value of $r(t)$ was determined. Also, with Newton's second law of motion, values of $R(t)$ and $r(t)$ were gotten. Once values of $R(t)$ and $r(t)$ were determined, the original trajectories were obtained for $X_1(t)$ and $X_2(t)$.

In the context of planetary and space science, the "Two-Body Problem" refers to the mathematical modelling of the motion of two celestial bodies under the influence of gravity. It is a fundamental problem in classical mechanics that has been studied for centuries and has played a crucial role in advancing our understanding of the solar system and the universe as whole. The Two-Body Problem is often simplified to consider the motion of a small body orbiting a much larger, central body. This approximation is valid for many celestial systems, such as the Earth orbiting the Sun or satellite orbiting the Earth. Under this assumption, the gravitational force between the bodies can be treated as a one-way force, with the larger body exerting a dominant gravitational pull on the smaller body.

5. Conclusion

The result of the model shows the position $R(t)$ of the center of mass was determined showing that the velocity is a constant and the total momentum is a constant. Hence, the position $R(t)$ of the center of mass can be determined at all times from the initial positions $X_1(t=0)$, $X_2(t=0)$ and velocities $V_1(t=0), V_2(t=0)$. Also, using Newton's gravitational law, values for $r(t)$ was gotten. Once $R(t)$ and $r(t)$ have been determined, the trajectories. $X_1(t)$ and $X_2(t)$ for all times (t) was determined.

References

Amuda, T. O., Oni, L. and Wachin, A. A. (2021). An Investigation on the Circular Restricted Three-Body Problem. *AFIT Journal of Science and Engineering.* Vol. 1 (1), 30-35.

Boldrin, L. A. G., Scheeres, D. J. and Winter, O. C. (2016). Dynamics of rotationally fissioned asteroids: non-planar case. *Monthly Notices of the Royal Astronomical Society*, Vol. 461, 3982-399.

Govind, M., Ashok, K.P., Sawsan, A., Elbaz I. A., and Badam, S. K. (2022). Effect of the Planetesimal Belt on the Dynamics of the Restricted Problem of 2 + 2 Bodies. *Applied Sciences* 12(1):424

Christina, P., Jean, L., Aikaterini, R., Maria, A., Anna, M., Tom A. N., Iannis, D., Athena, C., Davide, G., Valeria, M., Stefano, M., Stefano, O., and Alice, L. (2016). Planetary space weather: scientific aspects and future perspectives. *J. Space Weather Space Clim.* Vol 6: 31-56.

Sergey, E., Ghada, F. M., Idrisi, M. J. and Elbaz I. A. (2024). Revisiting the Dynamics of Two-Body Problem in the Framework of the Continued Fraction Potential. *Mathematics*, *12*(4), 590.

Xiyun, H. and Xiaosheng, X. (2017). A note on the full two-body problem and related restricted full three-body problem. *Astrodynamics* 2(3):1-14.

Stability Analysis of a Mathematical Model of Measles Transmission Dynamics

Adama, Patience Woye[1] and Somma, Samuel Abu[2]

[1]Mathematics Department, The Federal Polytechnic Bida, Nigeria
[2]Department of Mathematics, Federal University of Technology, Minna, Nigeria
[1]Corresponding author: yapacie123@gmail.com

Abstract

Measles is an acute viral infectious disease caused by the Measles morbillivirus, a member of the paramyxovirus family. The virus is primarily transmitted through direct contact and airborne droplets. In this study, a mathematical model was developed to examine the transmission dynamics of measles and explore effective control measures. The stability of measles-free equilibrium was analyzed, and the results indicate that the equilibrium is locally asymptotically stable when the basic reproduction number R_0 is less than or equal to unity. Numerical simulations were conducted to validate the analytical findings, demonstrating that measles can be eradicated if a sufficiently high level of treatment is applied to the infected population.

Keywords: Basic reproduction number, Measles Equilibria State, Measles, Stability, Transmission dynamics

Introduction

Measles is a highly contagious viral disease that exclusively affects humans and is transmitted primarily through direct contact and airborne droplets expelled during coughing, sneezing, or even normal breathing. Historically, measles has been regarded as a more formidable threat than smallpox (Gastanaduy *et al.,* 2021). The virus predominantly infects the respiratory tract, facilitating its rapid spread, especially in settings characterized by high population density and inadequate healthcare infrastructure, such as many African and developing countries. In these regions, the absence of effective birth control measures often leads to overpopulation, exacerbating the risk of widespread outbreaks that can have devastating public health consequences.

The clinical presentation of measles is distinct and severe. It typically begins with a high fever, often reaching or exceeding 40°C, which manifests approximately 10 to 12 days after exposure to the virus. This initial phase is followed by symptoms such as a runny nose, persistent cough, conjunctivitis, and the appearance of small white spots (Koplik spots) on the mucous membranes of the mouth. Subsequently, a characteristic rash emerges, initially appearing on the face and subsequently spreading to the hands, feet, and trunk, usually persisting for 5 to 6 days. The incubation period for measles ranges from 7 to 18 days, underscoring the challenges in early detection and containment of the disease.

Measles, also known by names such as morbilli, rubeola, red measles, and English measles, has been recognized for centuries. The first documented descriptions date back to the 7th century, with a more detailed differentiation from smallpox achieved in the 10th century by the Persian physician Rhazes, who noted its particularly alarming nature (Peter *et al.,* 2022). Despite the introduction of

the measles vaccine, the disease continues to pose a significant public health threat. Historically, prior to widespread immunization, measles epidemics were common, particularly among young children aged 2 to 3 years, leading to millions of cases and an estimated 2.6 million deaths annually.

In recent decades, numerous researchers (Adewale *et al.,* 2014; Bauch & Earn, 2014; Fred *et al.,* 2014; Momoh *et al.,* 2013; Peter *et al.,* 2018; Smith *et al.,* 2016) have developed sophisticated mathematical models to study the transmission dynamics of measles. These models have provided valuable insights into the impact of various parameters on disease spread and have been instrumental in guiding public health interventions.

The present study builds on this body of work by developing a comprehensive mathematical model aimed at elucidating the transmission dynamics of measles within a population. By integrating key epidemiological parameters and simulating different intervention scenarios, this model is intended to generate actionable information for government bodies and public health professionals. Ultimately, the insights gained from this study are expected to inform the development of more effective strategies for controlling and preventing measles outbreaks, thereby mitigating the public health risks associated with this highly contagious disease.

Research has demonstrated that measles can be completely prevented through the administration of two doses of a safe and effective vaccine. The World Health Organization (WHO) recommends that children receive their first dose at their first birthday, aiming for a global vaccination coverage of 95% for this initial dose. In 2021, approximately 81% of children received the first dose, while only 67% had received the second dose, indicating room for improvement in vaccination efforts.

To mitigate the risk of measles outbreaks, particularly in developing and underdeveloped countries where large populations remain vulnerable, the WHO, in collaboration with national governments, the Measles & Rubella Partnership, and other international organizations, has implemented a series of preventive measures. These accelerated immunization activities have been highly effective, preventing an estimated 56 million deaths between 2000 and 2021, and reducing global measles mortality from 761,000 deaths in 2000 to 128,000 deaths in 2021 (WHO, 2023).

Mathematical modeling has emerged as a powerful tool in the fight against infectious diseases, including measles. These models allow researchers to propose, test, and refine theories as well as to plan, implement, compare, and evaluate various intervention strategies for detection, prevention, treatment, and control. Historical studies on measles epidemiology date back to 1846, when Danish physician Peter Panum conducted seminal research during a measles epidemic in the Faroe Islands (Berche, 2022). Since then, numerous models have been developed to understand the transmission dynamics of measles.

For example, (Roberts & Tobias, 2000) employed a compartmental SIR (Susceptible-Infectious-Recovered) model to predict and prevent measles epidemics, considering factors such as population size and age structure. These models collectively underscore the importance of vaccination in conferring group immunity and protecting susceptible individuals.

(Momoh *et al.*, 2013) introduced an SEIR (Susceptible-Exposed-Infectious-Recovered) model to assess the role of individuals in the latent period and to explore control strategies. Similarly, (Sowole *et al.,* 2020) enhanced the SEIR framework by incorporating control measures within the susceptible and exposed classes, specifically targeting measles prevalence and control. Recently (Alemneh & Belay, 2023) explored how measles spreads by developing an improved

compartmental model called SVIRP. This model expands on the traditional SEVIR framework by adding a separate category for the pathogen population, allowing them to account for indirect transmission routes, such as environmental contamination. Also (Ahmed *et al.,* 2024), (Bag *et al.,* 2024) and (Peter *et al.,* 2024) studies the transmission dynamics of measles with different compartment and their control strategies.

Historical investigations, such as Peter Panum's work in 1864, revealed that individuals who recover from measles typically develop lifelong immunity. However, outbreaks continue to occur predominantly in communities with low vaccination coverage. This body of research not only highlights the critical role of vaccination in controlling measles but also emphasizes the need for continued and enhanced immunization efforts to achieve and maintain the levels of coverage necessary to prevent outbreaks.

Model Formulation

In this model a population of human in a community is considered. We divide the population into five compartments; Susceptible class, $S(t)$, Vaccinated class, $V(t)$, Exposed class $E(t)$, Infected class, $I(t)$, and Recovered class, $R(t)$. The susceptible human population increase by recruitment rate α. Individuals in the susceptible class receive a vaccination at a rate τ and loss immunity at a vaccine wane rate ρ, and returns to the susceptible class. The susceptible humans get in contact with the release of the infected person at rate β to get expose to measles virus. If the individual has not received the doses of vaccination, the exposed will be infected by the virus at rate θ which make them move to the infected group. And those that were attended to immediately after being i individuals gain immunity to the disease and do not ever get effected again. Natural mortality occurs in all the classes at a rate μ and death due to the disease at rate δ.

The equations of the model are formulated form of a system of ordinary differential equations of the above diagram.

$$\frac{dS}{dt} = \alpha - \beta IS - (\mu + \tau)S + \rho V \quad (1)$$

$$\frac{dV}{dt} = \tau S - (\rho + \mu + \omega)V \quad (2)$$

$$\frac{dE}{dt} = \beta S\mathrm{I} - (\theta + \mu)E \quad (3)$$

$$\frac{dI}{dt} = \theta E - (\sigma + \mu + \delta)I \quad (4)$$

$$\frac{dR}{dt} = \sigma I + \omega V - \mu R \quad (5)$$

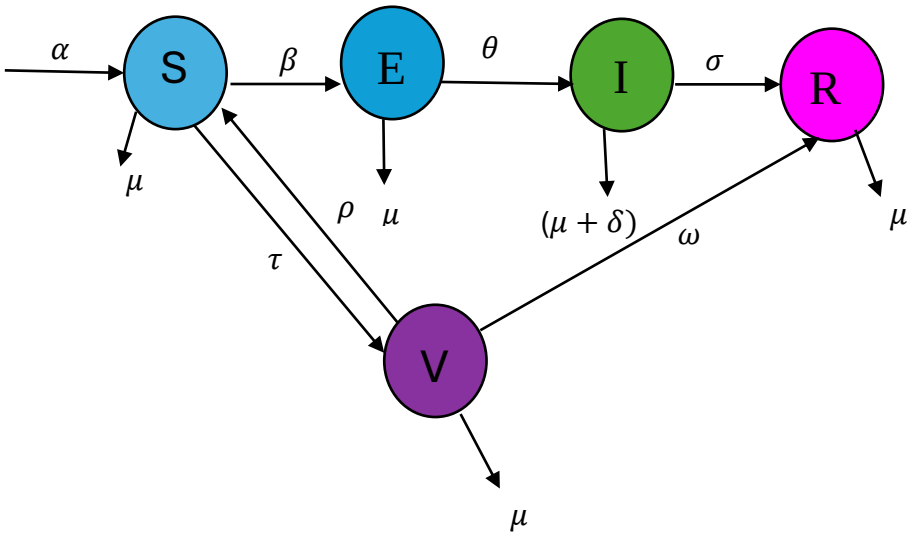

Figure 1: The model flow diagram

Table 1: Table of variables and parameters of the model

Notation	Description of variables and parameters
S(t)	Number of susceptible humans at time t
V(t)	Number of vaccinated humans at time t
E(t)	Number of exposed humans at time t
I(t)	Number of infectious humans at time t
R(t)	Number of recovered humans at time t
α	Recruitment rate of human population
δ	Disease induced death
μ	Natural death rate of human population
θ	The rate at which the exposed get infected by the virus
β	The rate at which susceptible humans get in contact with the release of the infected person
σ	The rate at which the infected get treated and moves to the recovered class
τ	Individuals in the susceptible class receives vaccination
ω	The rate of progression of vaccinated individuals to the recovery class
ρ	The rate at which individuals' losses immunity and returns to the susceptible class

$$N = S + V + E + I + R \tag{6}$$

By adding equations (1) to (5), we have.

$$\frac{dN}{dt} = \frac{dS}{dt} + \frac{dV}{dt} + \frac{dE}{dt} + \frac{dI}{dt} + \frac{dR}{dt} = \alpha - \mu N \tag{7}$$

The basic dynamic features of the model equations (1) to (5) will be explored.

Theorem 1

$D = \{(S,V,E,I,R)\epsilon\Re_+^5 : S+V+E+I+R \leq N\}$ (8)

Is positively invariant and attracting with respect to the basic model equations (1) to (5)

Proof:

From equations (6) and (7)

$\frac{dN}{dt} \leq \alpha - \mu N$ (9)

It follows that $\frac{dN}{dt} \leq 0$ if $N > \frac{\alpha}{\mu}$, (10)

then a standard comparison theorem can be used to show that

$N(t) \leq N(0)e^{\mu(t)} + \frac{\alpha}{\mu}(1 - e^{-\mu(t)})$ therefore $N(t) \leq \frac{\alpha}{\mu}$ if $N(0) \leq \frac{\alpha}{\mu}$. Thus $D$is positively invariant. Hence if if $N(0) > \frac{\alpha}{\mu}$, then either the solution enters Din finite time or $N(t)\ approches\ \frac{\alpha}{\mu}$, and the infected variables $E and\ I$ approaches 0. Hence D is attracting, which means all the solutions in $\Re_+^7$ is enters D. Thus in D, the equations (1) to (5) is well posed epidemiologically and mathematically according to (Hethcote, 1978). Hence it is sufficient to study the dynamics of this model.

The model is based on human population; therefore, it is necessary to show that all stated variables are positive at all time (t), making the model well-posed and biologically meaningful.

Theorem 5.1:

Let the initial data be $\{ S(0) > 0, V(0) \geq 0, E(0) \geq 0, I(0) \geq 0, R(0) \geq 0\} \in \Omega$ (11)

Then, the solution set $S(t), V(t), E(t), I(t), R(t)$ (12)

of the system (1) to (5) is positive if all t > 0.

Proof:

From equation (1)

$\frac{dS}{dt} = \alpha - \beta IS - (\tau+\mu)S + \rho V \geq \alpha - (\tau+\mu)S$ (13)

$\frac{dS}{dt} \geq \alpha - (\tau+\mu)S$ (14)

$\frac{dS}{dt} + (\tau+\mu)S \geq \alpha$ (15)

using integrating factor, we have

$\frac{d}{dt}(Se^{(\tau+\mu)t}) \geq \alpha e^{(\tau+\mu)t}$ (16)

$S(t)e^{(\tau+\mu)t} \geq \frac{\alpha}{(\tau+\mu)}e^{(\tau+\mu)t} + C$ (17)

$S(t) \geq \frac{\alpha}{(\tau+\mu)} + Ce^{(\tau+\mu)t}$ (18)

From (16) substituting $t = 0$ we have

$S(0) \geq \frac{\alpha}{(\tau+\mu)} + C => C \leq S(0) - \frac{\alpha}{(\tau+\mu)}$ (19)

Hence

$S(t) \geq \frac{\alpha}{(\tau+\mu)} + (S(0) - \frac{\alpha}{(\tau+\mu)})e^{(\tau+\mu)t} > 0$ (20)

Therefore

$S(t) > 0$ (21)

From equation (2)

$\frac{dV}{dt} = \tau S - (\rho+\mu+\omega)V \geq -(\rho+\mu+\omega)$ (22)

$\int \frac{dV}{dt} \geq \int (\rho+\mu+\omega)\, V$ (23)

$$\int \frac{d}{dV}(v) \geq \int (\rho + \mu + \omega)\, dt \tag{24}$$

$$V(t) \geq V(0)e^{-(\rho+\mu+\omega)t} \geq 0 \tag{25}$$

From equation (3)

$$\frac{dE}{dt} = \beta S\mathrm{I} - (\theta + \mu)E \geq -(\theta + \mu) \tag{26}$$

$$\int \frac{dE}{dt} \geq \int (\theta + \mu)\, E \tag{27}$$

$$\int \frac{d}{dE}(E) \geq \int (\theta + \mu)\, dt \tag{28}$$

$$E(t) \geq E(0)e^{-(\theta+\mu)t} \geq 0 \tag{29}$$

From equation (4)

$$\frac{dI}{dt} = \theta E - (\sigma + \mu + \delta)I \geq -(\sigma + \mu + \delta)I \tag{30}$$

$$\int \frac{dI}{dt} \geq \int (\sigma + \mu + \delta)\, I \tag{31}$$

$$\int \frac{d}{dI}(I) \geq \int (\sigma + \mu + \delta)\, dt \tag{32}$$

$$I(t) \geq I(0)e^{-(\sigma+\mu+\delta)t} \geq 0 \tag{33}$$

From equation (5)

$$\frac{dR}{dt} = \sigma I + \omega V - \mu R \geq -\mu R \tag{34}$$

$$\int \frac{dR}{dt} \geq \int \mu R \tag{35}$$

$$\int \frac{d(R)}{dR} \geq \int \mu dt \tag{36}$$

$$R(t) \geq R(0)e^{-\mu t} \geq 0 \tag{37}$$

Therefore, all the solutions of the system of equations (1) to (5) are positive for all $t > 0$.

Equilibria State of the model

At equilibrium the time derivatives are equal to zero, i.e.

$$\frac{dN}{dt} = \frac{dS}{dt} = \frac{dV}{dt} = \frac{dE}{dt} = \frac{dI}{dt} = \frac{dR}{dt} = 0 \tag{38}$$

Measles Free Equilibrium (MFE) State

Let $E^0 = (S, V, E, I, R) = (S^0, V^0, E^0, I^0, R^0)$ (39)

Be the DFE point

Substituting equation (8) into (2) to (6) equates to zero and solve gives

$$E^0 = (S^0, V^0, E^0, I^0, R^0) = \left[\frac{\alpha(\rho+\mu+\omega)}{(\mu+\tau)(\rho+\mu+\omega)-\rho\tau}, \frac{\rho S^0}{(\rho+\mu+\omega)}, 0, 0, \frac{\omega\tau S^0}{\mu(\rho+\mu+\omega)}\right] \tag{40}$$

Equation (13) is Measles-Free Equilibrium MFE point of the model.

Measles Endemic Equilibrium (MEE) State

Let $E^* = (S, V, E, I, R) = (S^*, V^*, E^*, I^*, R^*)$

$$\begin{bmatrix} S^* \\ V^* \\ E^* \\ I^* \\ R^* \end{bmatrix} = \begin{bmatrix} \frac{A_1 A_1}{\beta\theta} \\ \frac{\tau A_3 A_4}{\beta\theta A_2} \\ \frac{\rho\tau A_3 A_4 - A_1 A_2 A_3 A_4 + A_2\alpha\beta\theta}{A_2 A_3 \beta\theta} \\ \frac{\rho\tau A_1 A_1 - A_1 A_2 A_3 A_4 + A_2\beta\theta}{A_2 A_3 A_4 \beta} \\ \frac{\omega\tau A_3^2\, A_4^2 + \theta\sigma\rho A_3 A_4 - \theta\sigma A_1 A_2 A_3 A_4 + \theta^2\sigma\alpha A_2\beta}{A_3 A_4 \beta\theta A_2 \mu} \end{bmatrix} \tag{41}$$

The Basic Reproduction Number (R_0)

In this model, the next generation matrix method as described by (Driessche, 2002) is used to get the basic reproduction number of R_0. The basic reproductive number of an infected person is a threshold that indicates the total number of potential diseases that have been developed into a completely susceptible population during its transmission period. Given by $R_0 = \rho(FV^{-1})$. F and V are the matrices created for the new infection and transmission respectively.

The new infection components are $E(t)\ and\ I(t)$ in equation (3) and (4) above is given by

$$F = \begin{pmatrix} \beta SI \\ 0 \end{pmatrix}, \tag{42}$$

$$V = \begin{pmatrix} (\theta + \mu)E \\ (\sigma + \mu + \delta)I - \theta E \end{pmatrix} \tag{43}$$

F and V are the Jacobian matrices which shall be computed at the DFE for (42) and (43)

$$F = \begin{pmatrix} 0 & \beta S \\ 0 & 0 \end{pmatrix} \tag{44}$$

$$V = \begin{pmatrix} (\theta + \mu) & 0 \\ -\theta & (\sigma + \mu + \delta) \end{pmatrix} \tag{45}$$

$$F = \begin{pmatrix} 0 & \beta S \\ 0 & 0 \end{pmatrix}, \tag{46}$$

The inverse of V is computed using guass Jordan method

$$V^{-1} = \begin{pmatrix} \frac{1}{(\theta+\mu)} & 0 \\ \frac{\theta}{(\theta+\mu)(\sigma+\mu+\delta)} & \frac{1}{(\sigma+\mu+\delta)} \end{pmatrix} \tag{47}$$

Using the next generation matrix, we obtain:

$$FV^{-1} = \begin{pmatrix} \frac{\theta\beta S}{(\theta+\mu)(\sigma+\mu+\delta)} & \frac{\beta S}{(\sigma+\mu+\delta)} \\ 0 & 0 \end{pmatrix} \tag{48}$$

The basic reproduction number R_0 is obtained as the $\rho(FV^{-1})$

$$R_0 = \frac{\theta\beta S}{(\theta+\mu)(\sigma+\mu+\delta)} \tag{49}$$

Substituting $S = \frac{\alpha(\rho+\mu+\omega)}{(\mu+\tau)(\rho+\mu+\omega)-\rho\tau}$ gives

$$R_0 = \frac{\theta\beta\alpha(\rho+\omega+\mu)}{(\theta+\mu)(\sigma+\mu+\delta)[(\tau+\mu)(\rho+\omega+\mu)-\rho\tau]} \tag{50}$$

Which can also be written as:

$$R_0 = \frac{\theta\beta\alpha A_2}{A_3 A_4[A_1 A_2 - \rho\tau]} \tag{51}$$

Where $A_1 = (\tau + \mu),\ A_2 = (\rho + \omega + \mu), A_3 = (\theta + \mu), A_4 = (\sigma + \mu + \delta)$

Local Stability of Measles-Free Equilibrium Point

Theorem 1: Measles-free equilibrium point (ε_0) is locally asymptotically stable if $R_0 < 1$ otherwise it is unstable.

Proof:

$$J(S,V,E,I,R) = \begin{bmatrix} -\beta I - \mu - \tau & \rho & 0 & -\beta S & 0 \\ \rho & -\omega & 0 & 0 & 0 \\ \beta I & 0 & -\theta - \mu & \beta S & 0 \\ 0 & 0 & \theta & -\sigma - \mu - \delta & 0 \\ 0 & \omega & 0 & \sigma & -\mu \end{bmatrix} \quad (52)$$

Reducing equation (24) to upper triangular matrix and the characteristic equation gives,

$$\left|J\left((E^0)\right) - \lambda \mathrm{I}\right| = 0$$

$$\begin{vmatrix} -A_1 - \lambda & \rho & 0 & -\beta S_0 & 0 \\ 0 & -\omega - \lambda & 0 & 0 & 0 \\ 0 & 0 & -A_2 - \lambda & \beta S_0 & 0 \\ 0 & 0 & \theta & -A_3 - \lambda & 0 \\ 0 & 0 & 0 & 0 & -\mu - \lambda \end{vmatrix} = 0 \quad (53)$$

$$[(-A_1 - \lambda)(-\omega - \lambda)(-A_2 - \lambda)(-A_3 - \lambda)(-\mu - \lambda)] = 0 \quad (54)$$

Therefore

$$\lambda_1 = -A_1, \text{ or } \lambda_2 = -\omega, \text{ or } \lambda_3 = -A_2 \text{ or } \lambda_4 = -A_3, \text{ or } \lambda_5 = -\mu \quad (55)$$

Where $A_1 = (\beta I + \mu + \tau)$, $A_2 = (\theta + \mu)$ and $A_3 = (\sigma + \mu + \delta)$

From equation (54) we have

$$\lambda_1, \lambda_2, \lambda_3, \lambda_4, \lambda_5 < 0 \quad (56)$$

Hence, we have measles-free equilibrium point to be locally asymptotically stable if (55) holds when $R_0 < 1$ and unstable when $R_0 > 1$.

Results and Discussion

The figure 2 to 5 is the graphical simulation of the basic reproduction number and some selected parameters.

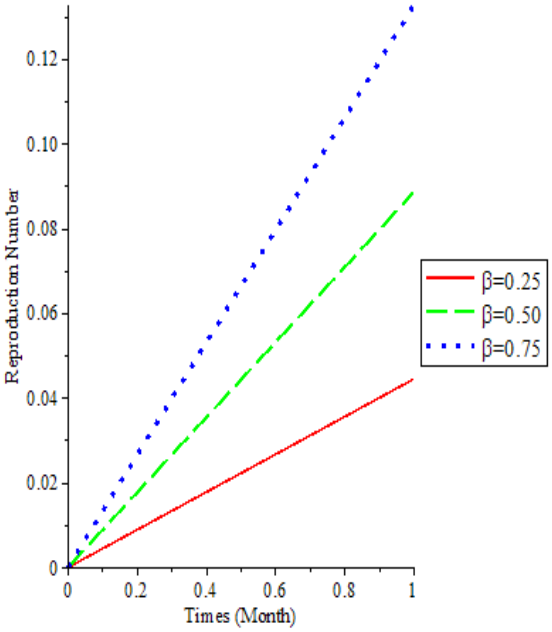

Figure 2: The effect of contact rate on reproduction number

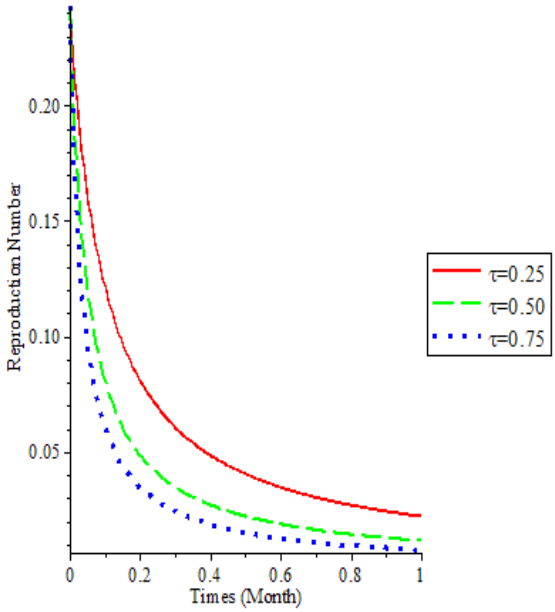

Figure 3: The effect of Vaccination Rate on Reproduction Number

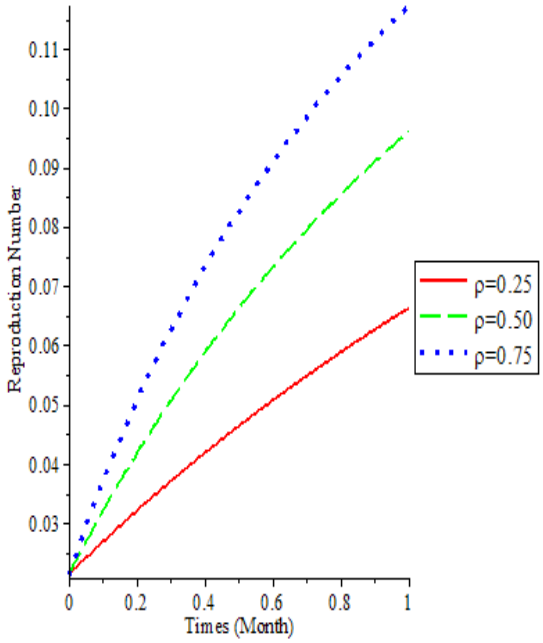

Figure 4: The effect of Immunity loss on Reproduction Number

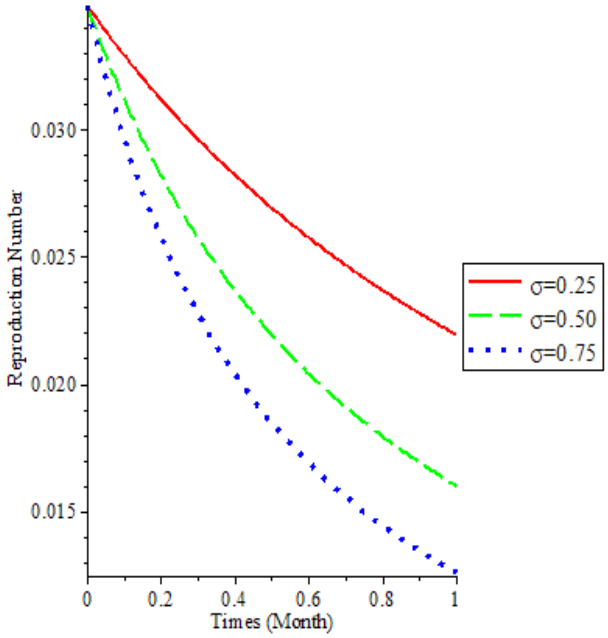

Figure 5: The effect of recovery rate on Reproduction Number

From figure 2 it shows that as the contact rate increases the reproduction number increases. This implies that the more people contact measles the more the reproduction number.

It is observed from figure 3 that as the vaccination rate increases the reproduction number decreases. This implies that the more people are vaccinated the more measles dies down and the less the reproduction number.

we observed from figure 4 that the higher the loss of vaccination, immunity decreases, and the reproduction number also increases. This implies that the more people loss their immunity the more measles persists in the population.

Figure 5 shows that as the recovery rate increases the reproduction number decreases. This implies that the more people recover from measles the less the reproduction number.

Recommendation

Based on our findings, we strongly recommend that governments and health organizations—including international partners like WHO, UNICEF, and those involved in Accelerated Immunization Activities, should collaborate to boost awareness and vaccination efforts. By leveraging local media and social platforms, they can reach a wider audience and ensure that everyone understands the importance of immunization. This unified strategy is essential for eradicating the measles virus soon.

Conclusion

In this study, we developed and analyzed a mathematical model (SVEIR) to understand measles transmission and the role of vaccination. By applying the next-generation matrix method, we derived an expression for the basic reproduction number, R_0. Our findings indicate that if R_0 is less than one, measles will eventually die out, creating a stable, measles-free situation. However, if R_0exceeds one, measles can persist in the population. Numerical simulations were conducted, and it validate the analytical findings. Overall, our analysis strongly supports vaccination as the most effective strategy to control measles outbreaks, paving the way for the measles's eventual eradication.

.

References

Adewale, S. O., Mohammed, I. T., & Olopade, I. A. (2014). Mathematical analysis of effect of area on the dynamical spread of measles. *IOSR J. Eng.*, *4*(3), 43–57.

Ahmed, S., Jahan, S., Shah, K., & Abdeljawad, T. (2024). On mathematical modelling of measles disease via collocation approach. AIMS Public Health, 11 (2), 628–653.

Alemneh, H. T., & Belay, A. M. (2023). Modelling, analysis, and simulation of measles disease transmission dynamics. Discrete Dynamics in Nature and Society, 2023 (1), 9353540.

Bag, A., Mondal, J., & Chatterjee, A. N. (2024). Role of environmental contamination in measles transmission dynamics. Corrosion Management ISSN: 1355-5243, 34 (1), 165–185.

Bauch, C. T., & Earn, D. J. D. (2014). Vaccination and the theory of games. *Proc Natl Acad Sci 101*, 13391–13394.

Berche, P. (2022). History of measles. *Presse Medicale*, *51*(3), 104149.

https://doi.org/10.1016/j.lpm.2022.104149

Fred, M. O., Sigey, J. K., Okello, J. A., Okwoyo, J. M., & Kang'ethe, G. J. (2014). Mathematical modeling on the control of measles by vaccination: case study of KISIICounty, Kenya. *SIJ Trans. Comput. Sci. Eng. Appl. (CSEA)*, *2*, . 61–69.

Gastanaduy, P., Haber, P., Rota, P. A., & Patel, M. (2021). *Measles*. https://www.cdc.gov/vaccines/pubs/pinkbook/meas.html

Momoh, A., Ibrahim, M., Uwanta, I., & Manga, S. (2013). Mathematical model for control of measles epidemiology. *Int. J. Pure Appl. Math*, *87*(6), 707–717.

Peter, O. J., Afolabi, O. A., Victor, A. A., Akpann, C. E., & Oguntolu, F. A. (2018). Mathematical model for the control of measles. *J. Appl. Sci. Environ. Manag.*, *22*(4), 571–576.

Peter, O. J., Ojo, M. M., Viriyapong, R., & Festus Abiodun Oguntolu. (2022). Mathematical model of measles transmission dynamics using real data from Nigeria. *Journal of Difference Equations and Applications*, *May*. https://doi.org/10.1080/10236198.2022.2079411

Peter, O. J., Cattani, C., & Omame, A. (2024). Modelling transmission dynamics of measles: the effect of treatment failure in complicated cases. Modeling Earth Systems and Environment, 10 (5), 5871–5889.

Roberts, M. G., & Tobias, M. I. (2000). Predicting and preventing measles epidemics in New Zealand: Application of a mathematical model. *Epidemiology and Infection*, *124*(2), 279–287. https://doi.org/10.1017/S0950268899003556

Smith, R., Archibald, A., MacCarthy, E., Liu, L., & Luke, N. S. (2016). A mathematical investigation of vaccination strategies to prevent a measles epidemic. *NCJ Math. Stat.*, *2*, 29–44.

Sowole, S. O., Ibrahim, A., Sangare, D., & Lukman, A. O. (2020). Mathematical model for measles disease with control on the susceptible and exposed compartments. *Open Journal of Mathematical Analysis*, *4*(1), 60–75. https://doi.org/10.30538/psrp-oma2020.0053

WHO (2023) *Measles*. Measles. https://www.who.int/news-room/fact-sheets/detail/measles

Dynamics of Diphtheria Epidemic in Nigeria with some Preventive Measures

Sani Musa[1,2], and Salisu Usaini[1,2]
[1]Department of Mathematics, Sule Lamido University Kafin Hausa, Jigawa State
[2]Department of Mathematics, Aliko Dangote University of Science and Technology, Wudil-Kano State

[1*]musasani1010@gmail.com
[2]Salisu.usaini@kustwudil.edu.ng

Abstract

Diphtheria is an infectious disease caused by the Corynebacterium diphtheria bacterium which continues to be a major public health concern despite the availability of vaccines. The aftermath of the COVID-19 pandemic has further worsened diphtheria outbreaks due to delays in routine immunization programs, leading to gaps in the diphtheria vaccine coverage. These gaps in vaccination efforts have led to the resurgence of confirmed diphtheria cases, particularly in some parts of Africa and Asia. The recent diphtheria outbreak in Nigeria is possibly due to poor access to Diptheria-tetanus-pertusis-vaccine (DTap), low coverage of vaccine, limited capabilities for disease surveillance systems, inadequate public enlightenment campaign and poor waste sanitation management. This paper presents a mathematical epidemic diphtheria model that incorporate vaccination's impact as an intervention in reducing the spread of diphtheria. The mathematical analysis of the model reveals two equilibrium points: the diphtheria infection-free equilibrium and the endemic equilibrium. The model is fit using the confirmed diphtheria cases data of Kano State from January to December 2023. Sensitivity analysis indicates that the transmission rate and rate of progression from exposed to either asymptomatic or infected class are influential parameters to be considered in designing effective strategies for diphtheria control and prevention. Finally, Numerical simulations results show that in long term, maintaining a high vaccination rate effectively reduces R_c which significantly reduces the spread of the disease is best control strategy. Moreover, for effective control within a short-term period of time is public enlightenment campaign.

Keyword: diphtheria, mathematical modelling, reproduction number, sensitivity analysis

1. Introduction

Diphtheria is an infectious disease caused by the Corynebacterium diphtheria bacterium which remains a significant public concern despite the availability of vaccines. The bacterium causes acute respiratory infections that can cause severe damage to several organs and, if left untreated, can be fatal (CDC, 2024). Transmission occurs by inhaling air borne droplets during coughing or sneezing, and the disease can also spread through direct contact with contaminated objects (NCDC, 2024). Clinical symptoms appear within 2- 7 days after exposure includes fatigue, sore throat, fever, difficulty swallowing, and blood-stain nasal discharge. In severe cases, diphtheria can destroy respiratory tissues, forming a thick grayish coating known as "Pseudomembrane" which can obstruct airways and cause damage to body organs 28 such as kidneys and the hearts.

In the past, diphtheria was a major cause of childhood mortality until the diphtheria toxoid vaccine was developed in 1923, which has reduced the global incidence of the disease (Islam *et al.*, 2022). Diphtheria is preventable and treatable if interventions such as antimicrobial therapy and diphtheria antitoxin (DTap) or tetnanus toxoids are administered promptly. In developed countries, with high vaccination coverage, the incidence of diphtheria has decreased significantly (Adulrasheed *et al.*, 2023), However, in underdeveloped countries, diphtheria persists, especially among minors under five years of age (Adulrasheed *et al.*, 2023).

The aftermath of the COVID-19 pandemic has further worsened diphtheria outbreaks due to delays in routine immunization programs, leading to gaps in the coverage of the diphtheria vaccine. These gaps in vaccination efforts have led to the resurgence of confirmed diphtheria cases, particularly in parts of Africa and Asia (Oyeyemi *et al.*, 2023). Vaccination remains essential in the fight against diphtheria, preventing vaccinated individuals and strengthening herd immunity among unvaccinated individuals (Oduoye, *et al*., 2020).

It was reported that in Nigeria, diphtheria re-emerged in (2022) due to factors such as poor access to Diptheria tetanus-pertusis-vaccine (DTap), low coverage of vaccine because of hard-to-reach communities, limited capabilities for disease surveillance systems, inadequate public enlightenment campaign and poor waste sanitation management (Adegboye *et al.*, 2023). Kano State which is located in the north-western part of Nigeria, with an estimated population of 15 million with 70% of the population residing in urban and semi-urban areas was identified as the epicenter of the outbreak by the Nigeria Center for Disease Control (NCDC) (NCDC, 2024).

For decades, mathematical models have been employed to study the transmission dynamics of infectious diseases, insights from these models allow researchers and decision-makers to assess the impact of control and preventive measures ((Blythe *et al.*, 1991; Blythe *et al.*, 1995; Burseng *et al.*, 1989; Brauer, 2008; Hethcote, 2000).

2. Literature Review

Adewale *et al.*, (2017) presented a diphtheria disease model with the quarantine of exposed individuals. The model analysis reveals that implementing quarantine measures of exposed individuals will reduce the number of infected individuals in the population. Amalia and Toaha (2022) presented an optimal control mathematical model of diphtheria with vaccination and treatment as control measures. The model analysis shows that the two optimal control measures can reduce the spread of diphtheria in the early stage of bacterial infection. Rahmi and Pratama (2023) presented a diphtheria disease dynamic model with vaccination, quarantine, and hand-washing etiquette. Numerical simulations showed that the basic reproduction can be lowered if the targeted control interventions are adhered to, thereby reducing the number of infected individuals. Egbune *et al.,* (2024) studied a nine compartmental model to assess the effectiveness of Diphtheria antitoxin in reducing the spread of diphtheria. The model analysis and simulation results indicate that Diphtheria antitoxin has a positive impact in containing the diphtheria epidemic. A study by Madubueze *et al.,* (2023), reveals that the best optimal strategy for reducing diphtheria disease spread involves combining three key control measures: administering booster vaccination, identifying and treating asymptomatic carriers, and disinfecting the environment.

In this paper, we extend the work of Adewale *et al.,* (2017) by incorporating the compartment of asymptomatic infection which plays a significant role in the spread of diphtheria, and vaccination strategy as a control measure to reduce diphtheria disease. Furthermore, we include public enlightenment campaign in the model as a preventive measure. The study addresses some setbacks in their model in terms of formulation and analysis as follows:

(i) We changed the quarantine strategy for infected individuals to isolation, as quarantine is more appropriate for exposed individuals
(ii) We obtained the endemic equilibrium point and proved its stability result.
(iii) Model fitting and Parameter estimation were carried out.
(iv) Perform a sensitivity analysis on the model parameters.

The rest of this paper is organized as follows: Section 2 present literature review, Section 3 presents the Methodology, and we carried out model fitting and parameter estimation. In Section 4, sensitivity analysis and numerical simulations are presented. Section 5 presents concluding remarks.

3. Methodology

3.1 Model of Diphtheria transmission

We divide the human population at any given time (t) as Susceptible (humans at risk of contracting diphtheria disease, S), Exposed (humans who have been exposed to the disease but are not yet infectious, E), Asymptomatic (humans infected but without symptoms or showing mild symptoms, A), Infected (human showing symptoms of diphtheria, I), Isolated (infected humans separated from the population due to infection, Q), Recovered (those recovered from diphtheria, R), and Vaccinated (those immunized against diphtheria, V) respectively. The flow between these compartments is represented in figure 1, and their sum equals the population N. We assume that:

(i) Susceptible individuals have an equal chance of getting infected with diphtheria (i.e., homogeneous mixture).

(ii) The transmission rate for isolated individuals is negligible, only asymptomatic and infected individuals can spread the infection.

(iii) The force of infection is given by $\lambda = \beta(1 - c\varepsilon)\frac{\theta A+I}{N}$, Where, $(1 - c\varepsilon)$ account for the role of the public enlightenment campaign as in Akinwande *et al.*, (2022).

(iv) Only infected and isolated individuals die due to the disease.

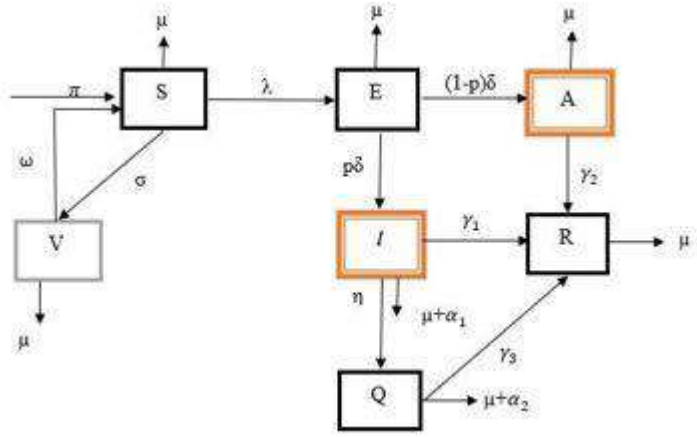

Figure 1. Schematic diagram of model (1)

We can see from Figure 1 that the required system of equation for the diphtheria epidemic model is presented in equation (1)

$$\left.\begin{aligned}
\frac{dS}{dt} &= \pi + \omega V - (\mu+\sigma)\,S - \lambda S,\\
\frac{dV}{dt} &= \sigma\,S - (\omega+\mu)V,\\
\frac{dE}{dt} &= \lambda S - (\mu+\delta)\,E,\\
\frac{dA}{dt} &= (1-p)\delta E - (\mu+\gamma_2)A,\\
\frac{dI}{dt} &= p\,\delta E - (\mu+\alpha_1+\eta+\gamma_1)I\\
\frac{dQ}{dt} &= \eta I - (\mu+\alpha_2+\gamma_3)Q,\\
\frac{dR}{dt} &= \gamma_1 I + \gamma_2 A + \gamma_3 Q - \mu R.
\end{aligned}\right\} \qquad (1)$$

Table 1. Description of parameters of the model.

Parameter	Description
π	Recruitment rate of susceptible individuals
μ	Natural mortality rate
α_1	Mortality rate due to disease in the infected class
α_2	Mortality rate due to disease in the isolated class
$\gamma_1, \gamma_2, \gamma_3$	Rates of progressions from infected, asymptomatic and isolated to recovered classes, respectively
p	Proportion of exposed becoming infectious population
θ	Modification parameter
β	Transmission rate
c	Rate of public enlightenment campaign
ϵ	Efficacy rate of the public enlightenment campaign
δ	Rate of progression from exposed to either asymptomatic or infected class
η	Rate of progression from infected class to isolated class
σ	Vaccine rate
ω	Rate of waning vaccine

3.4 Diphtheria Infection Free Equilibrium (DIFE)

In the absence of diphtheria infection within the population, all infectious compartments in the system (1) are empty, which means ($E = A = I = R = 0$). Thus the DIFE of model (1) is

$$M_0 = (S_0, V_0, E_0, A_0, I_0, Q_0, R_0) = \left(\frac{(\omega+\mu)\pi}{\mu(\omega+\mu+\sigma)}, \frac{\pi\sigma}{\mu(\omega+\mu+\sigma)}, 0,0,0,0,0\right)$$

For the linear stability of the model equilibria to be established, we require a threshold parameter called the basic reproduction number. This parameter is calculated using the next-generation matrix operator method as described in Diekmann *et al.*, (2010). Here, such a threshold parameter is called control reproduction number, as it combines the effects of vaccination, isolation, and public enlightenment campaign aimed at containing the spread of diphtheria. We derive the following

$$F = \begin{bmatrix} 0 & \frac{\theta\psi S}{N} & \frac{\beta\psi S}{N} & 0 \\ 0 & 0 & 0 & 0 \\ 0 & 0 & 0 & 0 \\ 0 & 0 & 0 & 0 \end{bmatrix}, V = \begin{bmatrix} K_3 & 0 & 0 & 0 \\ -(1-p)\delta & K_4 & 0 & 0 \\ -p\delta & 0 & K_5 & 0 \\ 0 & 0 & -\eta & K_6 \end{bmatrix}$$

Where, $\psi = \beta(1 - c\epsilon), K_1 = \mu + \sigma,\ \ K_2 = \omega + \mu,\ \ K_3 = \mu + \delta,\ \ K_4 = \mu + \gamma_2, K_5 = \mu + \alpha_1, K_6 = \mu + \alpha_1 + \eta + \gamma_2$

The control reproduction number is defined as the spectral radius of FV^{-1} given by

$$\mathcal{R}_c = \frac{\beta\delta K_2(1 - c\varepsilon)[K_5\theta(1 - p) + pK_4]}{K_3K_4K_5(K_2 + \sigma)}$$

Theorem 3.1

The diphtheria infection free equilibrium of model (1) is locally asymptotically stable in Ω if $\mathcal{R}_c < 1$ and stable otherwise.

Proof:

In the absence of diphtheria disease, the linearized system (1) gives the following Jacobian matrix.

$$J(M_0) = \begin{bmatrix} -K_1 & \omega & 0 & -j_{14} & -j_{15} & 0 & 0 \\ \sigma & -K_2 & 0 & 0 & 0 & 0 & 0 \\ 0 & 0 & -K_3 & j_{34} & j_{35} & 0 & 0 \\ 0 & 0 & (1-p)\delta & -K_4 & 0 & 0 & 0 \\ 0 & 0 & p\delta & 0 & -K_5 & 0 & 0 \\ 0 & 0 & 0 & 0 & \eta & -K_6 & 0 \\ 0 & 0 & 0 & \gamma_2 & \gamma_1 & \gamma_3 & -\mu \end{bmatrix}$$

with $j_{14} = \frac{\theta\psi}{K_2+\sigma} = j_{34}, j_{15} = \frac{\psi}{K_2+\sigma} = j_{35}$.

By inspection, the first two eigenvalues of the matrix $J(M_0)$ are $\lambda_1 = -\mu$ and $\lambda_2 = -K_6$. The remaining five eigenvalues are associated with sub-matrix $J_1(M_0)$ of the matrix $J(M_0)$, which is obtained by deleting the last row and the last column and sixth row and the sixth of $J(M_0)$ respectively.

$$J_1(M_0) = \begin{bmatrix} -K_1 & \omega & 0 & -j_{14} & -j_{15} \\ \sigma & -K_2 & 0 & 0 & 0 \\ 0 & 0 & -K_3 & j_{34} & j_{35} \\ 0 & 0 & (1-p)\delta & -K_4 & 0 \\ 0 & 0 & p\delta & 0 & -K_5 \end{bmatrix} \qquad (2)$$

Reducing (2) to upper triangle matrix gives

$$J_1(M_0) = \begin{bmatrix} -K_1 & \omega & 0 & -j_{14} & -j_{15} \\ 0 & -\frac{\mu(K_2+\sigma)}{K_1} & 0 & \frac{-\sigma j_{14}}{K_1} & \frac{-\sigma j_{15}}{K_1} \\ 0 & 0 & -K_3 & j_{34} & j_{35} \\ 0 & 0 & 0 & \phi_1 & \phi_2 \\ 0 & 0 & 0 & 0 & \phi_3 \end{bmatrix}$$

where,

$$\phi_1 = -\frac{\delta p j_{34} - \delta j_{34} + K_3K_4}{K_3}, \phi_2 = \frac{\delta j_{35}(1-p)}{K_3}, \phi_3 = \frac{\delta p K_4 j_{35} + \delta K_5 j_{34}(1-p) - K_3K_4K_5}{\delta j_{34}(1-p) + K_3K_4}.$$

The eigenvalues of the matrix $J_1(M_0)$, are as follows:

$$\lambda_3 = -K_1, \lambda_4 = -\frac{\mu(K_2 + \sigma)}{K_1},\ \lambda_5 = -K_3,\ \ \lambda_6 = \phi_1 = -\frac{\delta p j_{34} - \delta j_{34} + K_3K_4}{K_3} = -K_4(1 - \mathcal{R}^*_{c1})$$

$\lambda_7 = \phi_3 = \frac{\delta p K_4 j_{35} + \delta K_5 j_{34}(1-p) - K_3 K_4 K_5}{\delta j_{34}(1-p) + K_3 K_4} = -\frac{K_5(1-\mathcal{R}_c^*)}{1-\mathcal{R}_{c1}^*}$

with $\mathcal{R}_c^* = \frac{\beta\delta(1-c\varepsilon)[K_5\theta(1-p)+pK_4]}{K_3K_4K_5(K_2+\sigma)}$ and $\mathcal{R}_{c1}^* = \frac{\beta\delta\theta(1-p)(1-c\varepsilon)}{K_3K_4(K_2+\sigma)}$.

Clearly, all the five eigenvalues are negative if $\mathcal{R}_c < 1$ which implies that $\mathcal{R}_c^* < 1$ and $\mathcal{R}_{c1}^* < 1$. Therefore, $J(M_0)$ has eigenvalues with negative real parts which implies M_0 is locally asymptotically stable when $\mathcal{R}_c < 1$.

Theorem 3.2

The equilibrium point M_0 of model (1) is stable globally asymptotically in Ω when $\mathcal{R}_c < 1$. It is not stable otherwise.

Proof:

We prove the theorem using the method in Castillo-Chavez *et al.*, (2002). Let $Y = (S, V)$, $Z = (E, A, I, Q, R)$ and $Y^* = \left(\frac{(\omega+\mu)\pi}{\mu(\omega+\mu+\sigma)}, \frac{\pi\sigma}{\mu(\omega+\mu+\sigma)}\right)$, then

$$\frac{dY}{dt} = F(Y,Z) = \begin{pmatrix} \pi + \omega V - (\mu+\sigma)\, S - \lambda S, \\ \sigma\, S - (\omega+\delta)V \end{pmatrix}$$

and

$$\frac{dZ}{dt} = G(Y,Z) = \begin{pmatrix} \lambda S - (\mu+\delta)\, E \\ (1-p)\delta E - (\mu+\gamma_2)A \\ p\,\delta E - (\mu+\alpha_1+\eta+\gamma_1)I \\ \eta I - (\mu+\alpha_2+\gamma_3)Q \\ \gamma_1 I + \gamma_2 A + \gamma_3 Q - \mu R \end{pmatrix}$$

If $Z = 0$ (i.e, $E = A = I = Q = R = 0$) then

$$\frac{dY}{dt} = F(Y,0) = \begin{pmatrix} \pi + \omega V - (\mu+\sigma)\, S - \lambda S, \\ \sigma\, S - (\omega+\delta)V \end{pmatrix}$$

with

$$M = DG(Y^*,0) = \begin{pmatrix} -K_3 & m_{12} & m_{13} & 0 & 0 \\ (1-p)\delta & 0 & 0 & 0 & 0 \\ p\delta & 0 & -K_5 & 0 & 0 \\ 0 & 0 & \eta & -K_6 & 0 \\ 0 & \gamma_1 & \gamma_2 & \gamma_3 & -\mu \end{pmatrix}$$

where $m_{12} = \frac{\theta\psi}{\omega+\mu+\sigma}$ and $m_{13} = \frac{\psi}{\omega+\mu+\sigma}$.

This is a matrix with nonnegative off diagonal entries, known as Metzler matrix.

Now we obtain from $G(Y,Z) = MZ - \hat{G}(Y,Z)$ that

$$\hat{G}(Y,Z) = = \begin{pmatrix} \beta(1-c\varepsilon)\theta A\, \frac{K_2}{(K_2+\sigma)}\left(1-\frac{S}{N}\right) + \beta(1-c\epsilon)I\, \frac{K_2}{(K_2+\sigma)}\left(1-\frac{S}{N}\right) \\ 0 \\ 0 \\ 0 \\ 0 \end{pmatrix}$$

Since $S \leq N$, we have $\hat{G}(Y,Z) \geq 0$. Thus the condition by Castillo-Chavez *et al.*, (2002) are satisfied. Then, $Y^* = \left(\frac{K_2\pi}{\mu(K_2+\sigma)}, \frac{\pi\sigma}{\mu(K_2+\sigma)}\right)$ is globally asymptotically stable for $\frac{dY}{dt} = F(Y,0)$. By the result in Castillo-Chavez *et al.*, (2002), the Diphtheria infection-free equilibrium M_0 is globally asymptotically stable in whenever $\mathcal{R}_c < 1$.

3.5 Endemic Equilibrium

The persistence of diphtheria within a community occurs when at least one of the infectious compartments of model (1) remains non-empty.

$$M^* = (S^*, V^*, E^*, A^*, I^*, Q^*, R^*)$$

Is obtained in terms of λ^* using maple 18 software as presented below

$$S^* = \frac{K_2\Pi}{K_2\lambda^* + \mu(K_2+\sigma)}, V^* = \frac{\Pi\sigma}{K_2\lambda^* + \mu(K_2+\sigma)},$$

$$E^* = \frac{K_2\Pi\lambda^*}{K_3[K_2\lambda^* + \mu(K_2+\sigma)]}, A^* = \frac{\delta K_2\Pi\lambda^*(1-p)}{K_3K_4[K_2\lambda^* + \mu(K_2+\sigma)]}$$

$$I^* = \frac{\delta K_2\Pi\lambda^* p}{K_3K_5[K_2\lambda^* + \mu(K_2+\sigma)]}, Q^* = \frac{\eta\delta K_2\Pi\lambda^* p}{K_3K_5K_6[K_2\lambda^* + \mu(K_2+\sigma)]}$$

$$R^* = \frac{\delta K_2\Pi\lambda^*[pK_4(\eta\gamma_3 + K_6\gamma_1) + K_5K_6\gamma_2(1-p)]}{K_3K_4K_5K_6\mu[K_2\lambda^* + \mu(K_2+\sigma)]}$$

with, $$\lambda^* = \beta(1-c\epsilon)\frac{A^*\theta + I^*}{N^*} \quad (3)$$

To find λ^*, we have from (3) that

$$\lambda^*(S^* + V^* + E^* + Q^* + R^*) + [\lambda^* - \beta(1-c\epsilon)\theta]A^* + [\lambda^* - \beta(1-c\epsilon)]I^* = 0.$$

Then, we obtain after algebraic simplification the following polynomial in terms of λ^*

$$\lambda^*(a_2\lambda^{*2} + a_1\lambda^* + a_0) = 0 \quad (4)$$

with

$$a_2 = K_2\pi\prod_{i=2}^{5}K_i\left\{\delta pK_4[\eta(\mu+\gamma_3) + K_6(\mu+\gamma_1)] + K_5K_6\delta(1-p)(\mu+\gamma_2) + \mu\prod_{i=3}^{6}K_i\right\}$$

$$a_1 = \pi\mu(K_2+\sigma)\prod_{i=2}^{5}K_i\{\prod_{i=3}^{6}K_i[(1-\mathcal{R}_{c1}) + \mu] + \delta(K_5K_6(1-p)(\gamma_2+\mu) + K_4p[K_6(\gamma_1+\mu) + \eta(\gamma_3+\mu)])\}$$

$$a_0 = K_6\pi\mu^2(K_2+\sigma)^2\prod_{i=3}^{5}K_i^2(1-\mathcal{R}_c)$$

where $\mathcal{R}_{c1} = \frac{\beta\delta K_2\theta(1-p)(1-c\varepsilon)}{K_3K_4(K_2+\sigma)}$.

Thus, $\lambda^* = 0$ corresponds to diphtheria infection-free equilibrium and the positive roots of (4) determine the possible number of endemic equilibrium points of model (1) when $\mathcal{R}_c > 1$. Hence, at least one endemic equilibrium points of model (1) exists.

4 Model fitting and Parameter estimation

Fitting models to real-world data known as validation and estimation of parameter values are important in the field of mathematical modeling. The parameter values are often not directly obtainable from the collected data, therefore making parameter estimation essential for a given model. Data obtained from the Kano State Ministry of Health between January and December were utilized to perform a least squares fit for the model parameters. Table 2 enumerates the model's parameters estimated through the model fitting with data. The best fitting curve of the model (1) is shown in Figure 2.

Table 2. Parameter Estimation Table

Parameter	Estimated Value	Sources
μ	0.025	fitted

π	9808999	fitted
θ	0.6667	(CDC,2024)
β	0.000097	Assumed
η	0.11	fitted
c	0.9	(Akinwande *et al.*, 2022)
ϵ	0.6	(Akinwande *et al.*, 2022)
α_1	0.0485	fitted
α_2	0.0315	fitted
γ_1	0.99	fitted
γ_2	0.2	fitted
γ_3	0.5	fitted
δ	0.5	fitted
p	0.8	fitted
ω	0.0406	fitted
σ	0.0083	fitted

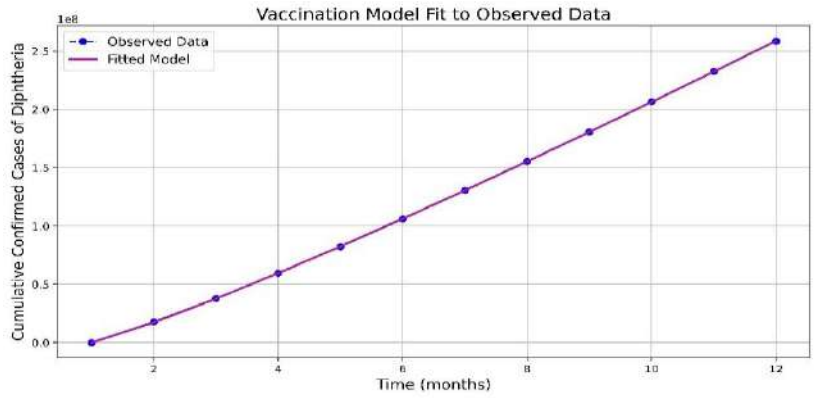

Figure 2**.** Best fit curve of model (1) data fitting of diphtheria for Kano state cumulative confirmed cases from January-December 2023

4.1 Sensitivity Analysis

Here, we assess each model parameter effect on the associated threshold parameter, $\mathcal{R}_c$. This exercise helps to develop effective control strategies to contain the spread of diphtheria in a community. The normalized forward sensitivity index as presented in is (Chitnis *et al.*, 2008) employed to examine the effect each parameter has on R_c For example, the sensitivity index with respect to the parameter c is the following:

$\prod_c^{R_c} = \frac{c}{R_c} \times \frac{\partial R_c}{\partial c} = -\frac{\varepsilon c}{(1-c\epsilon)}$ We obtained the sensitivity indices of the remaining ten model parameters using a similar argument as for c with parameter values in Table 2 and presented in Table 3. The parameters are arranged in the table from the most sensitive to the least sensitive. One can see from Table 3 and Figure 3 that the parameter p

Table 3. Values of Sensitivity Indices for $\mathcal{R}_c$

Parameters	Sensitivity Index
p	-1.3250
c	-1.1740
ϵ	-1.1740
β	1.0000
δ	1.0000
γ_1	-0.8440
ω	0.6190
μ	0.5390
θ	0.4650
σ	-0.1120
α_1	-0.0410

is the most sensitive. model parameter, while α_1 is the least sensitive. Furthermore, parameters with positive sensitivity indices are directly related to $\mathcal{R}_c$, while those with negative indices are inversely related to this threshold parameter. Therefore, a decrease (or increase) in any parameter with a positive sensitivity index results in a decrease (or increase) in $\mathcal{R}_c$. On the other hand, when a parameter with a negative index increases, $\mathcal{R}_c$ decreases and it increases when such a parameter decreases. In conclusion, the persistence of diphtheria infection can be mitigated by either decreasing a parameter with a positive sensitivity index or increasing a parameter with a negative sensitivity index. It is not realistic to increase the proportion p of exposed individuals becoming infectious in order to contain the spread of diphtheria as the sensitivity analysis reveals that. As expected, both the higher the rate of public enlightenment campaign (c) and the

people compliance to the campaign (ϵ) or the vaccination rate (σ), the lower the control reproduction number $\mathcal{R}_c$ thereby reducing the spread of the virus.

4.2 Numerical Simulation

In this section, we compare three different numerical simulations scenarios, that is, simulations with public enlightenment campaign only, simulations with vaccination only, and simulations with both vaccination and public enlightenment campaign so as to get insight into the positive effects of vaccination and public enlightenment campaign in reducing the spread of diphtheria disease within the population. From the three scenarios depicted in Figure 4, one can observe from 4(a) that the susceptible individuals increase rapidly as the asymptomatic individuals decrease and the infectious compartments have insignificant number due to positive impact of the public enlightenment campaign in reducing effective contact between susceptible and infectious individuals.

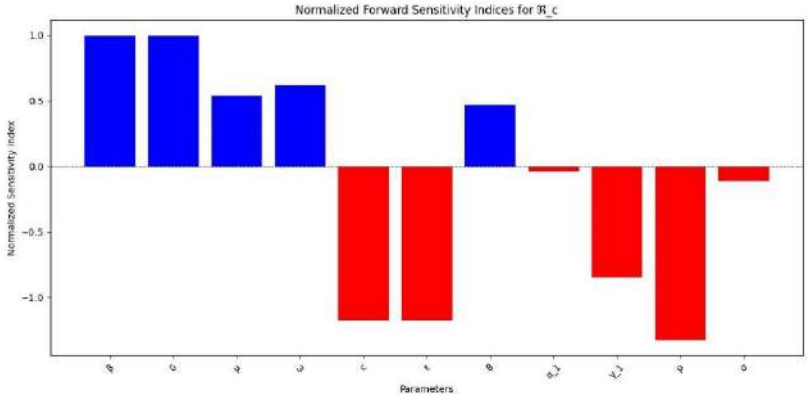

Figure 3. Normalized Forward Sensitivity Indices.

Moreover, the recovered individuals increase at a slower rate as a result of very slow infection rate. In Figure 4(b), recovered individuals increase faster than susceptible individuals and becomes higher than the susceptible as time goes on before they stabilizes after 250 days due to immunity of vaccine. Moreover, vaccinated individuals increase rapidly before 150 days and stabilize thereafter. While exposed, asymptomatic and infected individuals increase rapidly and peak at about 30 days and decrease immediately after that time before they stabilizes as time goes on. Then isolated individuals increase slowly and eventually stabilize after 50 days. This indicates that vaccination contain diphtheria persistence in a community. One can observe that Figure 4(c) is similar to 4(b) indicating that combining vaccination and public enlightenment campaign is not the best control strategy in comparison with 4(a) as well. Now, comparing the simulations results in Figure 4, one can see that while vaccination plays an essential role in containing diphtheria infection, the most effective short term diphtheria control strategy is public enlightenment campaign only. And vaccination only could be the best strategy since Figure 4(c) and 4(b) are almost the same.

5 Conclusion

We presented an extended version of the model of diphtheria transmission dynamics proposed by Adewale *et al.*,(2017). In our extension, we incorporated vaccination compartment, asymptomatic infection compartment and changed the quarantine of infected individuals to isolation. The extended model takes into account the role of public enlightenment campaign and vaccination of susceptible individuals as control

interventions to effectively mitigate the outbreak. We calculated the threshold parameter $\mathcal{R}_c$ that drives the spread of diphtheria infection. Some of our findings from the qualitative and quantitative analyses are as follows:

(i) The diphtheria infection-free equilibrium of model (1) demonstrates both local and global asymptotic stability, indicating disease eradication if $\mathcal{R}_c < 1$.

(ii) The existence of endemic equilibrium amid diphtheria infection has been confirmed. Such an equilibrium point is demonstrated to be stable globally asymptotically stable if R_c is greater than one. It means that endemic persistence of diphtheria infection is possible as long as asymptomatic or infected individuals keep generating new cases within the population.

(iii) We employed nonlinear least squares curve fitting approach leveraging MATLAB's optimization toolbox to fit 23 the model with data for the confirmed cases of Kano state from January to December 2023.

(iv) The sensitivity analysis using PCCR indicated that the rate of effective contact β and rate of progression from exposed to either asymptomatic or infected class δ are the most influential model parameters.

(v) Numerical simulations of model (1) reveal that in a long term, maintaining high vaccination rate (σ) effectively reduces R_C which significantly reduces the spread of the disease is the best control strategy. While for a short term scenario public enlightenment campaign is the best control strategy in containing diphtheria persistence in a community.

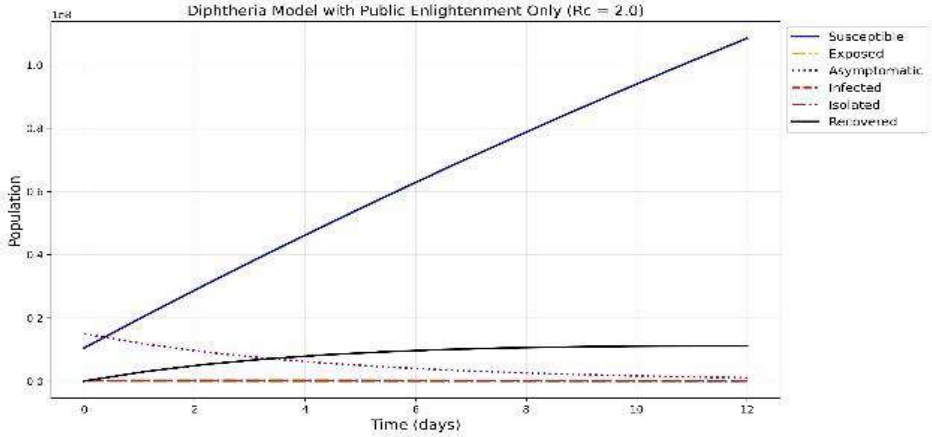

(a)

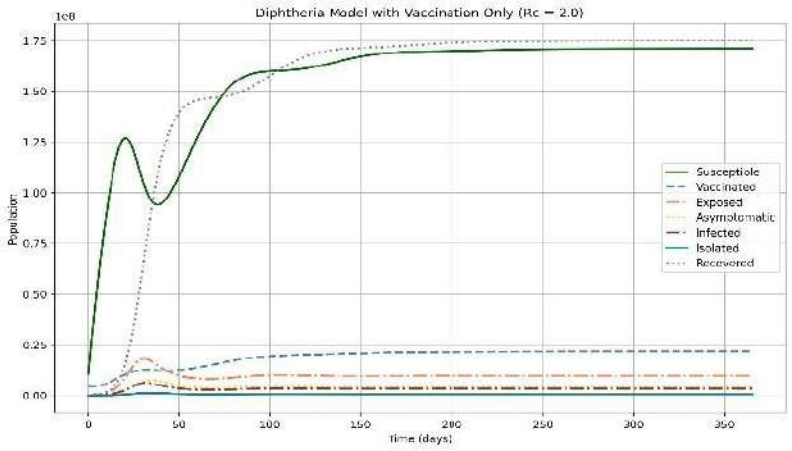

(b)

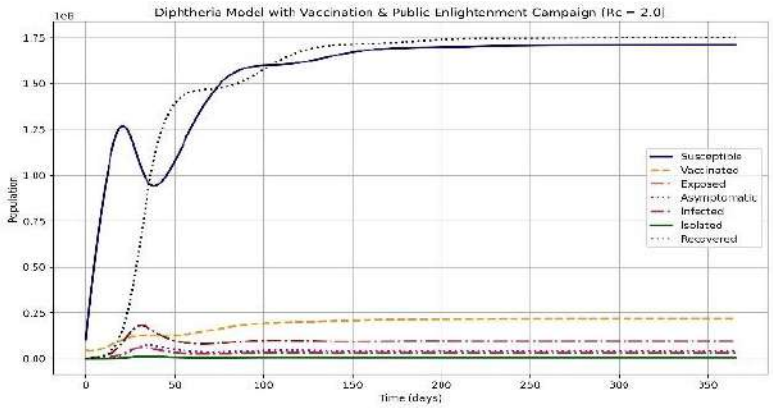

(c)

Figure 4. Simulations of model (1) showing the behaviours of compartments with (a) public enlightenment campaign only, (b) vaccination only and (c) vaccination and enlightenment campaign.

References

Abdulrasheed, N., Lawal, L., Mogaji, A. B., Abdulkareem, A. O., Shuaib, A. K., Adeoti, S. G., and Abdul-Rahman, T. (2023). Recurrent diphtheria outbreaks in Nigeria: A review of the underlying factors and remedies. *Immunity, Inflammation and Disease*, *11*(11), e1096.

Adegboye, O. A., Alele, F. O., Pak, A., Castellanos, M. E., Abdullahi, M. A., Okeke, M. I., and McBryde, E. S. (2023). A resurgence and re-emergence of diphtheria in Nigeria, 2023. *Therapeutic Advances in Infectious Disease*, *10*, 20499361231161936.

Adewale, S. O., Olopade, I. A., Adeniran, G. A., and Ajao, S. O. (2017). Mathematical Analysis of Quarantine on the Dynamical Transmission of Diphtheria Disease. *International Journal of Science and Engineering Investigations*, *6*(5), 8-17.

Amalia, P., and Toaha, S. (2022). Optimal control of mathematical model of diphtheria spreading. *Daya Matematis: Jurnal Inovasi Pendidikan Matematika*, *10*(2), 138-147.

Akinwande, N. I., Ashezua, T. T., Gweryina, R. I., Somma, S. A., Oguntolu, F. A., Usman, A., Abdurrahman, O.N., Kaduna, F.S., Adajime, T.P., Kuta, F.A., Abdurarahman, S., Olayiwola, R.O., Enagi, A.I., Bolarin, G.A., and Shehu, M. D. (2022). Mathematical model of COVID-19 transmission dynamics incorporating booster vaccine program and environmental contamination. *Heliyon*, *8*(11).

Blythe, S. P., Castillo-Chavez, C., Palmer, J. S., and Cheng, M. (1991). Toward a unified theory of sexual mixing and pair formation. *Mathematical biosciences*, *107*(2), 379-405.

Blythe, S., Busenberg, S., and Castillo-Chavez, C. (1995). Affinity in paired event probability. *Mathematical Biosciences*, *128*(1-2), 265-284.

Busenberg, S., and Castillo-Chavez, C. (1989). Interaction, pair formation and force of infection terms in sexually transmitted diseases. In *Mathematical and statistical approaches to AIDS epidemiology* (pp. 289-300). Berlin, Heidelberg: Springer Berlin Heidelberg.

Brauer, F. (2008). Epidemic models with treatment and heterogeneous mixing. *Bulletin of Mathematical Biology*, *70*, 1869-85.

Brauer, F. (2008). Age-of-infection and the final size relation. *Mathematical Biosciences and Engineering*, *5*(4), 681-690.

Castillo-Chavez, C., Feng, Z., Huang, W.: On the computation of Ro and its role on global stability. In: Castillo-Chavez, C., Blower, S., van den Driessche, P., Kirschner, D., Yakubu, A.A. (eds.) *Mathematical Approaches for Emerging and Reemerging Infectious Disease: Models, Methods and Theory*, pp. 229–250. Springer, Berlin (2002)

Chitnis, N., Hyman, J. M., and Cushing, J. M. (2008). Determining important parameters in the spread of malaria through the sensitivity analysis of a mathematical model. *Bulletin of mathematical biology*, *70*, 1272-1296.

Centers for Disease Control and Prevention (CDC). htpp://www.cdc.gov

Cooke, K. L. (1993). *Vertically transmitted diseases: models and dynamics*. Springer-Verlag.

Diekmann, O., Heesterbeek, J. A. P., and Roberts, M. G. (2010). The construction of next-generation matrices for compartmental epidemic models. *Journal of the royal society interface*, *7*(47), 873-885.

Egbune, N. J., Akponana, E. B., Arierhie, E. O., and Okedoye, A. M. (2024). Mathematical Analysis of Spread and Control of Diphtheria with Emphasis on Diphtheria Antitoxin Efficiency. *European Journal of Theoretical and Applied Sciences*, *2*(3), 152-172.

Hethcote, H. W. (2000), The Mathematics of infectious disease. *SIAM Review*, 41:599-635

Islam, Z. (2020). Developing a mathematical model for optimal cost-effective treatment strategies applied to a diphtheria outbreak.

Islam, Z., Ahmed, S., Rahman, M. M., Karim, M. F., and Amin, M. R. (2022). Research Article Global Stability Analysis and Parameter Estimation for a Diphtheria Model: A Case Study of an Epidemic in Rohingya Refugee Camp in Bangladesh.

La Salle, J. P. (1976). *The stability of dynamical systems*. Society for Industrial and Applied Mathematics.

Madubueze, C. E., and Tijani, K. A. (2023). A deterministic mathematical model for optimal control of diphtheria disease with booster vaccination. *Healthcare Analytics*, *4*, 100281.

Nigerian Center for Disease Control and Prevention. www.ncdc.gov.ng

Oduoye, M. O., Musa, Z. M., Tunde, A. M., Nazir, A., Cakwira, H., Abdulkareem, L., and Nyakio, O. (2023). The recent outbreak of diphtheria in Nigeria is a public health concern for all. *IJS Global Health*, *6*(5), e0274.

Oyeyemi, B. O., Suleiman, A. O., Suleiman, B. M., Ajetomobi, B. M., & Ibrahim, A. A report of two clusters of diphtheria outbreak involving three contiguous Local government areas in Katsina State. Abstract.

Rahmi, N., and Pratama, M. I. (2023). Model Analysis of Diphtheria Disease Transmission with Vaccination, Quarantine, and Hand-Washing Behavior. *JTAM (Jurnal Teori dan Aplikasi Matematika)*, *7*(2), 462-474.

A Mathematical Model for Predicting Maize Production in Niger State, Nigeria: The Role of Climatic and Economic Variables

[*1]Yahaya, A. A., [2]Hakimi, D., [2] Shehu, M. D., & [3]Daniya, E.

[1,2]Department of Mathematics, Federal University of Technology, Minna, Niger State Nigeria
[3]Department of Crop Production, Federal University of Technology, Minna, Niger State Nigeria
*Corresponding author's: abuahmad4u@gmail.com

Abstract

Maize production is a complex process influenced by a multitude of factors, including climatic and economic factors. This study developed a mathematical model for predicting maize production in Niger State and analyzes the effects of rainfall, temperature, humidity, farm size, and production cost on maize yield. The model combines various climatic factors like rainfall, temperature, and humidity with essential economic aspects, including farm size and production operating cost. By employing a multivariable technique, the model assesses the connection between these variables and maize production, and it confirmed the accuracy of the developed model by utilizing historical climate data and crop yield statistics. The results of the analysis using the least squares method show that the developed model can accurately predict maize yield based on economic and climatic factors. The independent variable accounts for 94.13% of the variance in maize production, with a low mean squared error of 0.0296 and a high coefficient of determination of 0.9413. Policymakers and maize farmers can improve food security, lower climate-related risks, and increase maize yield by using the insightful information this study offers.

Keywords: Climatic variables, Crop yield, Economic variables, Maize production, Mathematical *model*

Introduction

Maize (*Zea mays*) is one of the most widely cultivated crops globally, playing a vital role in food security, economic growth, and sustainable agriculture (Erenstein *et al.*, 2022). In Nigeria, maize is a crucial cereal crop, contributing significantly to the country's agricultural economy and ensuring food security(Palacios-Rojas *et al.*, 2020). Niger State stands out as one of the leading maize-producing regions due to its vast arable land and favorable agro-climatic conditions.

However, a number of climatic and economic factors have caused significant fluctuations in the state's maize production in recent years, which present significant obstacles for farmers and policymakers seeking to increase productivity and guarantee sustainable maize farming (Ahmed, 2022). In the same way that economic factors like farm size, the cost of inputs (fertilisers, seeds, and labour), market prices, and government policies have a significant impact on maize production (Ghimire & Gyawali, 2023), climatic factors like rainfall patterns, temperature variations, and changes in relative humidity are important determinants of maize growth, yield, and quality (Waris

et al., 2023). It is crucial to comprehend the intricate interactions between these economic and climatic factors in order to maximize output, enhance crop elasticity, and support sustainable agricultural practices (Oriekhoe *et al.,* 2024).

Although earlier research has examined the effects of economic and climatic factors on maize production, many of these studies have oversimplified the complexities by concentrating on particular variables or regional contexts. These models usually ignore how various factors interact, which limits their predictive ability and usefulness in agricultural planning. Therefore, in order to accurately forecast maize yield and guide decision-making, a thorough mathematical model that incorporates numerous variables is required.

Statement of the Problem

Maize production is vulnerable to variations in climatic and economic factors, resulting in reduced crop yields and economic losses (Bedeke *et al.,* 2020). Despite its importance, the complex relationships between rainfall, temperature, humidity, farm size, and production cost on maize yield are not well understood. According to González *et al.,* (2023), a large number of farmers and agricultural decision-makers lack the knowledge and resources necessary to maximize crop yields and reduce losses. Although previous studies have examined the impact of distinct climatic and economic factors on maize production, there aren't many thorough mathematical models that combine the effects of these factors on maize yield.

This study aims to close these gaps by developing a mathematical model to look at the connections between Niger State's maize production, economic factors like land size and production costs, and crucial climate variables like rainfall, temperature, and humidity. In order to forecast future yields and evaluate the possible effects of climate variability, the research uses a data-driven methodology that includes analysis of statistics.

Research Objectives

The objectives of this study are to:

i. Develop a mathematical model that predicts maize yield based on climatic and economic variables.
ii. Investigate the individual and combined effects of rainfall, temperature, humidity, farm size, and production cost on maize yield.
iii. Determine the optimal coefficients that represent the effects of each variable on maize yield.

Materials and Methods

Study Area

The study was conducted in Niger state, a major maize-producing state in Nigeria.

Data Collection

Historical data on maize yield, rainfall, temperature, humidity, farm size, and production cost were obtained from Nigerian Meteorological Agency (NIMET) bulletins and Federal Ministry of Agriculture and Rural Development (FMARD). The Data collected is for the period of twenty one (21) years starting from 2001 to 2021.

Model Development

In this research paper a mathematical model is developed to predict maize yield based on the climatic and economic variables. The model framework consists of the following assumptions:

- Maize production depends on the combined effects of the input variables: rainfall, temperature, humidity, farm size, and production cost.
- Maize yield is affected directly by the variables.
- The relationship between these variables and maize yield is assumed to be Linear and non-linear interaction.

Model Formulation

The mathematical model for predicting maize yield based on climatic and economic variables using multiple linear regressions (MLR) with interaction terms can be formulated as follows:

$$Y_{maize} = \beta_0 + \beta_1 X_1 + \beta_2 X_2 + \beta_3 X_3 + \beta_4 X_4 + \beta_5 X_5 + \beta_{12} X_1 X_2 + \beta_{13} X_1 X_3 + \beta_{14} X_1 X_4 + \beta_{15} X_1 X_5 + \beta_{23} X_2 X_3 + \beta_{24} X_2 X_4 + \beta_{25} X_2 X_5 + \beta_{34} X_3 X_4 + \beta_{35} X_3 X_5 + \beta_{45} X_4 X_5 + \varepsilon \quad (1.0)$$

Where:

Y : *Maize yield* (*dependent* variable)

X_1 : *Rain fall* (*mm*)

X_2 : *Temprature* (^0C)

X_3 : Re*lative Humidity* (%)

X_4 : *Land size* (*Ha*)

X_5 : Pr*oduction Cost* (*Naira*/*Ha*)

β_0 Represents the intercept, the expected yield when all independent variables are zero, which is the base yield without any inputs.

$\beta_1, \beta_2, \beta_3, \beta_4, \beta_5$ *are coefficients for the linear effects of* X_1, X_2, X_3, X_4, X_5.

$\beta_{12}, \beta_{13}, \beta_{14}, \beta_{15}, \beta_{23}, \beta_{24}, \beta_{25}, \beta_{34}, \beta_{35}, \beta_{45}$ *are coefficients for the* interaction *effects between* X_1, X_2, X_3, X_4, X_5.

ε *is the errorr term accounting for the factors not included in the* model

The model above captured both linear and non linear relationships between the variables and is sub-divided into two (2) parts:

(i) **The Linear terms** $(\beta_1 X_1 + \beta_2 X_2 + \beta_3 X_3 + \beta_4 X_4 + \beta_5 X_5)$: To capture the linear relationships between the variables and maize yield and measures the direct impact of each variable on maize yield. The coefficients represent change in maize yield for a unit change in the corresponding independent variable. A positive coefficient will lead to corresponding increase in maize yield, while a negative coefficient will result into decrease in maize yield.

(ii) **The Interaction term** $(\beta_{12} X_1 X_2 + \beta_{13} X_1 X_3 + \beta_{14} X_1 X_4 + \beta_{15} X_1 X_5 + \beta_{23} X_2 X_3 + \beta_{24} X_2 X_{45} + \beta_{25} X_2 X + \beta_{34} X_3 X_4 + \beta_{35} X_3 X_5 + \beta_{45} X_4 X_5)$: The interaction part measures the combine effect of two (2) independent variables on maize yields. This part captures the non linear relationships and interactions between the variables allow one to understand how changes in one variable can influence the impact of another variable on maize yield.

Matrix Representation of the model

The matrix formulation of the developed model can be represented as:

$$Y = X\beta + \varepsilon \tag{2.0}$$

Where:

Y : represents the vector of maize yields

X : represents the matrix of input variables (including both linear and interaction terms).

β : is the vector of coefficients to be determined.

However, the design matrix X can be represented as:

$$X = \begin{bmatrix}
1 & 1249.5 & 33.6 & 49 & 299.4 & 18660 & 41983.2 & 61225.5 & 374100.3 & 23315670 & 1646.4 & 10059.84 & 626976 & 14670.6 & 914340 & 5586804 \\
1 & 1274.5 & 32.7 & 46 & 321.79 & 27560 & 41676.15 & 58627 & 410121.4 & 35125220 & 1504.2 & 10522.53 & 901212 & 14802.34 & 1267760 & 8868532 \\
1 & 1233 & 33.8 & 48 & 450.16 & 36460 & 41675.4 & 59184 & 555047.3 & 44955180 & 1622.4 & 15215.41 & 1232348 & 21607.68 & 1750080 & 16412834 \\
1 & 1294 & 32.6 & 48.8 & 311.77 & 45360 & 42184.4 & 63147.2 & 403430.4 & 58695840 & 1590.88 & 10163.7 & 1478736 & 15214.38 & 2213568 & 14141887 \\
1 & 1108.7 & 34 & 49.6 & 319.69 & 54250 & 37695.8 & 54991.52 & 354440.3 & 60146975 & 1686.4 & 10869.46 & 1844500 & 15856.62 & 2690800 & 17343183 \\
1 & 1423.2 & 34.2 & 46.8 & 320.1 & 63150 & 48673.44 & 66605.76 & 455566.3 & 89875080 & 1600.56 & 10947.42 & 2159730 & 14980.68 & 2955420 & 20214315 \\
1 & 1423.3 & 38.3 & 48.2 & 3175.92 & 72050 & 54512.39 & 68603.06 & 4520287 & 102548765 & 1846.06 & 121637.7 & 2759515 & 153079.3 & 3472810 & 2.29E + 08 \\
1 & 1269.2 & 28.7 & 49.7 & 391860 & 80950 & 36426.04 & 63079.24 & 4.97E + 08 & 102741740 & 1426.39 & 11246382 & 2323265 & 19475442 & 4023215 & 3.17E + 10 \\
1 & 1421.6 & 34.3 & 46.8 & 442190 & 89840 & 48760.88 & 66530.88 & 6.29E + 08 & 127716544 & 1605.24 & 15167117 & 3081512 & 20694492 & 4204512 & 3.97E + 10 \\
1 & 1221.6 & 33.8 & 50.1 & 421120 & 103330 & 41290.08 & 61202.16 & 5.14E + 08 & 126227928 & 1693.38 & 14233856 & 3492554 & 21098112 & 5176833 & 4.35E + 10 \\
1 & 942.8 & 33 & 46.8 & 355 & 78190 & 31112.4 & 44123.04 & 334694 & 73717532 & 1544.4 & 11715 & 2580270 & 16614 & 3659292 & 27757450 \\
1 & 1423 & 34.2 & 46.8 & 294 & 120000 & 48666.6 & 66596.4 & 418362 & 170760000 & 1600.56 & 10054.8 & 4104000 & 13759.2 & 5616000 & 35280000 \\
1 & 1269 & 38.3 & 48.2 & 172 & 133000 & 48602.7 & 61165.8 & 218268 & 168777000 & 1846.06 & 6587.6 & 5093900 & 8290.4 & 6410600 & 22876000 \\
1 & 1185 & 28.7 & 49.7 & 151 & 156200 & 34009.5 & 58894.5 & 178935 & 185097000 & 1426.39 & 4333.7 & 4482940 & 7504.7 & 7763140 & 23586200 \\
1 & 1157 & 34.3 & 46.8 & 150 & 151400 & 39685.1 & 54147.6 & 173550 & 175169800 & 1605.24 & 5145 & 5193020 & 7020 & 7085520 & 22710000 \\
1 & 1422 & 36.1 & 50.1 & 173 & 150000 & 51334.2 & 71242.2 & 246006 & 213300000 & 1808.61 & 6245.3 & 5415000 & 8667.3 & 7515000 & 25950000 \\
1 & 1179 & 34.2 & 46.8 & 376568.5 & 160000 & 40321.8 & 55177.2 & 4.44E + 08 & 188640000 & 1600.56 & 12878641 & 5472000 & 17623404 & 7488000 & 6.03E + 10 \\
1 & 1196 & 38.3 & 48.2 & 387742.4 & 160000 & 45806.8 & 57647.2 & 4.64E + 08 & 191360000 & 1846.06 & 14850535 & 6128000 & 18689186 & 7712000 & 6.2E + 10 \\
1 & 1247 & 38.3 & 48.2 & 282730 & 180000 & 47760.1 & 60105.4 & 3.53E + 08 & 224460000 & 1846.06 & 10828559 & 6894000 & 13627586 & 8676000 & 5.09E + 10 \\
1 & 1157 & 36.7 & 56.7 & 281130 & 180000 & 42461.9 & 65601.9 & 3.25E + 08 & 208260000 & 2080.89 & 10317471 & 6606000 & 15940071 & 10206000 & 5.06E + 10 \\
1 & 872.1 & 34.2 & 46.8 & 258930 & 200000 & 29825.82 & 40814.28 & 2.26E + 08 & 174420000 & 1600.56 & 8855406 & 6840000 & 12117924 & 9360000 & 5.18E + 10
\end{bmatrix} \tag{3.0}$$

And the corresponding maize yield is given by equation (4.0):

$$Y = \begin{bmatrix}
1.15 \\ 1.2 \\ 1.21 \\ 1 \\ 1.13 \\ 1.25 \\ 1.3 \\ 1.4 \\ 1.42 \\ 1.55 \\ 3 \\ 3 \\ 2 \\ 2 \\ 3 \\ 3 \\ 1.89 \\ 1.9 \\ 2.55 \\ 2.48 \\ 2.71
\end{bmatrix} \tag{4.0}$$

The parameter vector β can be can be estimated using the ordinary least square (OLS) method

$$\beta = (X^T X)^{-1} X^T y \tag{5.0}$$

Where:

X is the design matrix (input variables)

X^T is the transpose of X

$\left(X^T X\right)^{-1}$ is the inverse of $X^T X$

y is the vector of observed crop yield

β is the vector coefficient to be determined.

By solving substituting the values into the equation (5.0), we obtained the coefficients of the model as:

$$\beta = \begin{bmatrix} 299.2268731 \\ -0.054741071 \\ -8.984333522 \\ -4.471563413 \\ -4.24982E-05 \\ 0.00010559 \\ 0.001546157 \\ 1.68635E-05 \\ 3.73057E-10 \\ 1.16291E-08 \\ 0.136562239 \\ 3.08761E-07 \\ 2.55901E-06 \\ 7.03943E-07 \\ -3.96092E-06 \\ -3.17634E-11 \end{bmatrix} \tag{6.0}$$

Consequently, the maize model equation is given as:

$$Y_{maize} = \beta_0 + \beta_1 X_1 + \beta_2 X_2 + \beta_3 X_3 + \beta_4 X_4 + \beta_5 X_5 + \beta_{12} X_1 X_2 + \beta_{13} X_1 X_3 + \beta_{14} X_1 X_4 + \beta_{15} X_1 X_5 + \beta_{23} X_2 X_3 + \beta_{24} X_2 X_4 + \beta_{25} X_2 X_5 + \beta_{34} X_3 X_4 + \beta_{35} X_3 X_5 + \beta_{45} X_4 X_5 + \varepsilon \tag{7.0}$$

By substituting the values of the coefficients obtained in (6.0) into the maize model equation (7.0) gives the required predictive maize production model as:

$$Y_{maize} = 299.226873\,1 - 0.05474107\,1X_1 - 8.98433352\,2X_2 - 4.47156341\,3X_3 - 0.00004249\,82X_4 + 0.00010559\,X_5 + 0.00154615\,7X_1X_2 + 0.00001686\,35X_1X_3 + 3.73057 * 10^{-10}X_1X_4 + 1.16291 * 10^{-8}X_1X_5 + 0.13656223\,9X_2X_3 + 3.08761 * 10^{-7}X_2X_4 + 0.00000255\,901X_2X_5 + 7.03943 * 10^{-7}X_3X_4 - 0.00000396\,092X_3X_5 - 3.17634 * 10^{-7}X_4X_5 + \varepsilon \quad (8.0)$$

Results and Discussion

Residual Analysis:

The analysis of differences between the observed and predicted maize yields is shown in Table 1.

Table 1: Residual analysis and maize yield prediction using the developed model

Y Yield	$\bar{Y}$ Y Mean	$\hat{Y}$ Predicted	$(Y-\bar{Y})$	$(Y-\bar{Y})^2$	$(Y-\hat{Y})^2$	$(Y-\hat{Y})$ Error
1.15	1.911429	0.853763	-0.761429	0.579773	0.08776	0.296237
1.2	1.911429	1.42629	-0.711429	0.506131	0.05121	-0.22629
1.21	1.911429	1.01365	-0.701429	0.492002	0.03855	0.19635
1	1.911429	1.321825	-0.911429	0.830702	0.10357	-0.321825
1.13	1.911429	1.278339	-0.781429	0.610631	0.022	-0.148339
1.25	1.911429	1.275621	-0.661429	0.437488	0.00066	-0.025621
1.3	1.911429	1.339394	-0.611429	0.373845	0.00155	-0.039394
1.4	1.911429	1.296107	-0.511429	0.261559	0.01079	0.103893
1.42	1.911429	1.33865	-0.491429	0.241502	0.00662	0.08135
1.55	1.911429	1.754742	-0.361429	0.130631	0.04192	-0.204742
3	1.911429	2.841817	1.0885714	1.184988	0.02502	0.158183
3	1.911429	2.65577	1.0885714	1.184988	0.11849	0.34423
2	1.911429	2.061598	0.0885714	0.007845	0.00379	-0.061598
2	1.911429	2.007668	0.0885714	0.007845	5.9E-05	-0.007668
3	1.911429	3.193965	1.0885714	1.184988	0.03762	-0.193965
3	1.911429	2.994843	1.0885714	1.184988	2.7E-05	0.005157
1.89	1.911429	2.06638	-0.021429	0.000459	0.03111	-0.17638
1.9	1.911429	1.746079	-0.011429	0.000131	0.02369	0.153921
2.55	1.911429	2.624976	0.6385714	0.407773	0.00562	-0.074976
2.48	1.911429	2.439488	0.5685714	0.323273	0.00164	0.040512
2.71	1.911429	2.609035	0.7985714	0.637716	0.01019	0.100965
40.14				**10.58926**	**0.62191**	

Source: Author's computation, 2025

Model Performance:

The performance of the developed model was evaluated using various metrics, including, Mean Squared Error (MSE), Root Mean Squared Error (RMSE) and Coefficient of determination (R^2). The results are presented in Table 2.

Table 2: Performance Evaluation of the Model

Metric	Value
Mean Squared Error (MSE)	0.0296
Root Mean Squared Error (RMSE)	0.1720
Coefficient of determination (R^2)	0.9413

Source: Author's computation, 2025

The results of linear and interaction effects between the input variables are presented in Table 3.

Table 3: ANOVA analysis to show the linear and interaction effects of the model

Coefficients	Estimate	Std. Error	T. value	P. Value
(Intercept)	2.992e+02	8.855e+01	3.379	0.0197 *
X1	-5.474e-02	3.125e-02	-1.752	0.1402
X2	-8.984e+00	3.891e+00	-2.309	0.0690 .
X3	-4.472e+00	1.551e+00	-2.884	0.0344 *
X4	-4.250e-05	4.274e-05	-0.994	0.3657
X5	1.056e-04	1.046e-04	1.010	0.3589
X1:X2	1.546e-03	1.297e-03	1.192	0.2868
X1:X3	1.686e-05	1.184e-03	0.014	0.9892
X1:X4	3.731e-10	1.241e-08	0.030	0.9772
X1:X5	1.163e-08	1.596e-08	0.728	0.4990
X2:X3	1.366e-01	4.931e-02	2.769	0.0394 *
X2:X4	3.088e-07	3.285e-07	0.940	0.3904
X2:X5	2.559e-06	2.463e-06	1.039	0.3465
X3:X4	7.039e-07	6.027e-07	1.168	0.2955
X3:X5	-3.961e-06	2.079e-06	-1.906	0.1150
X4:X5	-3.176e-11	4.239e-11	-0.749	0.4874

Source: (Authors Computation, 2025) using **R** software

Discussion of Result

Analysis from Table1 indicates that the predicted value is closer to the actual yield; this implies that the developed model performs well in predicting maize yield, and the MSE and RMSE values are relatively low as shown in Table 2, indicating that the model is able to accurately predict maize yield. The Coefficient of determination (R^2) indicates that approximately 94.13% of the variation in maize yield can be explained by the input variables.

The estimated coefficients in Table 3; indicates that the individual variables of rainfall (β_1), temperature (β_2) and humidity (β_3) have a negative effect on maize yield, but there interactions

have a positive effect. The relative humidity and the interaction between farm size and production cost are statistically significant, indicating that these variables also have an impact on maize yield.

The study's results have implications for agricultural planning and decision-making. In order to help farmers and policymakers make well-informed decisions about maize production, the model can be used to forecast maize yield under several climatic and economic variables.

Conclusion

A mathematical model was developed in this study to predict maize yield using economic and climatic variables, and the results show that the model provides a good job of predicting maize yield, with a high coefficient of determination (R2) and low root mean squared error (RMSE). The study also discovered that factors such as temperature, humidity, rainfall, farm size, and production cost have a significant impact on maize yield.

References

Ahmed, A. G. (2022). How Covid-19 Pandemic obstructed maize production activities in Niger State of Nigeria. *Journal of Agripreneurship and Sustainable Development*, *5*(2), 95-106.

Bedeke, S. B., Vanhove, W., Wordofa, M. G., Natarajan, K., & Van Damme, P. (2020). Vulnerability to climate change among maize-dependent smallholders in three districts of Ethiopia. *Environment, development and sustainability*, *22*, 693-718.

Erenstein, O., Jaleta, M., Sonder, K., Mottaleb, K., & Prasanna, B. M. (2022). Global maize production, consumption and trade: trends and R&D implications. *Food security*, *14*(5), 1295-1319.

Ghimire, S., & Gyawali, L. (2023). Production Economics of Maize (Zea mays) in Surkhet, Nepal. *Food and Agri Economics Review (FAER)*, *3*(1), 22-27.

González, X. I., Bert, F., & Podestá, G. (2023). Many objective robust decision-making model for agriculture decisions (MORDMAgro). *International Transactions in Operational Research*, *30*(4), 1617-1646.

Oriekhoe, O. I., Adisa, O., & Ilugbusi, B. S. (2024). Climate change and food supply chain economics: a comprehensive analysis of impacts, adaptations, and sustainability. *International Journal of Applied Research in Social Sciences*, *6*(3), 267-278.

Palacios-Rojas, N., McCulley, L., Kaeppler, M., Titcomb, T. J., Gunaratna, N. S., Lopez-Ridaura, S., & Tanumihardjo, S. A. (2020). Mining maize diversity and improving its nutritional aspects within agro-food systems. *Comprehensive Reviews in Food Science and Food Safety*, *19*(4), 1809-1834.

Waris, U., Tariq, S., Mehmood, U., & ul-Haq, Z. (2023). Exploring potential impacts of climatic variability on production of maize in Pakistan using ARDL approach. *Acta Geophysica*, *71*(5), 2545-2561.

Reformulation of Three Step Block Hybrid Linear Multi-Step Method (TSBHLMM) into Runge – Kutta Type Method (RKTM) for the Solution of Second Order Initial Value Problem (IVP)

[*1]Aliyu A., [2]Muhammad R. and [3]Abdulhakeem Y.

[*1, 2 & 3]Department of Mathematics, School of Physical Sciences, Federal University of Technology Minna, Niger State, Nigeria
[1*]Corresponding author: aliyu.abubakar1@st.futminna.edu.ng

Abstract

Problems in the fields of sciences and engineering are often expressed in differential equations. This research paper will focus on the reformulation of three-step block hybrid linear multistep method into a seven-stage Runge-Kutta type method (7SRKTM) for the solution of second-order initial value problems (IVPs) in ordinary differential equations (ODEs). A three-step with three-off-grid-point implicit block hybrid collocation method for first-order IVPs was derived. We determined the order of the method as 7, 7, 7, 7, 7 and 8 and their respective errors constants are $\frac{275}{6193152}, \frac{1}{30240}, \frac{9}{229376}, \frac{1}{30240}, \frac{275}{6193152}, and -\frac{9}{716800}$. The block method derived was reformulated into a seven-stage Runge-Kutta type method (RKTM) for the solution of first-order ODEs. The Runge-Kutta type method formulated for first order ODEs was extended for direct solution of second-order IVPs in ODEs. The Runge-Kutta-type method derived was implemented on numerical examples. The results from the proposed method was closer to the exact solutions than the existing methods in the literature.

Keywords: implicit, block method, collocation, Runge-Kutta type method, linear multistep method.

1. Introduction

The numerical solutions for differential equations are important in scientific and engineering fields since problems in these areas are sometimes in ordinary differential equations (ODEs) (Abuasbeh *et al.*, 2023; Gbenro *et al.*, 2024; Tassaddiq *et al.*, 2022). Problems arising in the fields of applied mathematics, physics, sciences and engineering need efficient and accurate numerical methods because of their analytical solutions are sometimes complex (Abuasbeh *et al.*, 2023). Conventional linear multi-step methods (LMMs) have been universally adopted for this reason (Mulatu *et al.*, 2020); however, their restrictions in stability, convergence and efficiency have called for the development of hybrid method (Ibrahim and Nasarudin, 2020). Among the methods is the three-step block hybrid linear multi-step method (BHLMM), it gives a reliable scheme for solving initial value problems (Kayode *et al.*, 2025).

Despite the strength of block hybrid linear multistep methods it also present several challenges, including stability limitations, high computational complexity, difficulties in step-size adaptation, intricate derivation, limited effectiveness for stiff problems, complex initialization, convergence constraints, and increased memory demands, affecting their efficiency and practical implementation (Tassaddiq *et al.*, 2022). Hence reformulating the block hybrid linear multistep method into a Runge–Kutta-type method (RKTM) will improve the stability properties (Muhammad and Oyedeji, 2024).

The second-order initial value problems can be expressed generally as (Muhammad *et al.*, 2020):

$$y''(x) = f(x, y, y'), y(x_0) = y_0, y'(x_0) = y'_0 \tag{1}$$

The classical fourth-order Runge–Kutta (RK4) method is given by (Walters *et al.*, 2022):

$$\left.\begin{aligned} k_1 &= f(x_n, y_n) \\ k_2 &= f\left(x_n + \frac{h}{2}, y_n + \frac{h}{2}k_1\right) \\ k_3 &= f\left(x_n + \frac{h}{2}, y_n + \frac{h}{2}k_2\right) \\ k_2 &= f\left(x_n + h, y_n + hk_3\right) \\ y_{n+1} &= y_n + \frac{h}{6}\left(k_1 + 2k_2 + 2k_3 + k_4\right) \end{aligned}\right\} \tag{2}$$

The general linear multi-step method (LMM) can be written as (Omole *et al.*, 2024):

$$\sum_{j=0}^{k} \alpha_j y_{n+j} = h\sum_{j=o}^{k} \beta_j f_{n+j,} \tag{3}$$

where the coefficients α_j and β_j determine the characteristic of the method, including stability and accuracy.

Similarly, the general form of a block hybrid linear multi-step method for the solution of second-order IVPs can be expressed as (Duromola *et al.*, 2024):

$$\sum_{j=0}^{k} \alpha_j y_{n+j} = h^2\sum_{j=0}^{k} \beta_j f_{n+j} + h\sum_{j=0}^{k} \gamma_j y'_{n+j,} \tag{4}$$

where $\alpha_j, \beta_j, and \gamma_j$ are method-dependent coefficients, h is the step size, and y_{n+j} and f_{n+j} are function values at discrete points.

This study focuses on the reformulation of the three-step with two off grid points block hybrid linear multistep method into a Runge–Kutta-type method for solving second-order initial value problems. While existing research has explored various hybrid block methods and their advantages, there remains a gap in seamlessly integrating the strengths of both multi-step and Runge–Kutta techniques to improve performance.

2. Materials and Methods

The derivation of seven – stage Runge – Kutta type method reformulated from three step block hybrid linear multistep method with three off-grids points is discussed in this section. First order three step block hybrid linear multistep method with three off-grids point was reformulated to first order Runge - Kutta Type method.

The general form of first order initial value problem (IVP) in ordinary differential equations (ODEs) is given as:

$$y'(t) = f(t, y), y(t_0) = y_0 \tag{5}$$

We use power series as the basis function which is of the form:

$$y(t) = \sum_{i=0}^{n} \varphi_i t^i \tag{6}$$

Differentiating (3) we obtained:

$$y^1(t) = \sum_{i=0}^{n} i\varphi_i t^{i-1} \tag{7}$$

By the use of matrix inversion techniques we find the values of φ_i's to obtain a continuous implicit scheme given in the form:

$$y(t) = \alpha_0(t) y_n + h\left(\sum_{i=0}^{2} \beta_{n+\frac{2i+1}{2}} f_{n+\frac{2i+1}{2}} + \sum_{i=0}^{3} \beta_i f_{n+i}\right) \tag{8}$$

Interpolating (3) at $t = \{t_n\}$ and collocating (4) at $t = \left\{t_n, t_{n+\frac{1}{2}}, t_{n+1}, t_{n+\frac{3}{2}}, t_{n+2}, t_{n+\frac{5}{2}}, t_{n+3}\right\}$.

Which can be expressed in matrix form:

$$\begin{bmatrix} 1 & t_n & t_n^2 & t_n^3 & t_n^4 & t_n^5 & t_n^6 & t_n^7 \\ 0 & 1 & 2t_n & 3t_n^2 & 4t_n^3 & 5t_n^4 & 6t_n^5 & 7t_n^6 \\ 0 & 1 & 2t_{n+\frac{1}{2}} & 3\left(t_{n+\frac{1}{2}}\right)^2 & 4\left(t_{n+\frac{1}{2}}\right)^3 & 5\left(t_{n+\frac{1}{2}}\right)^4 & 6\left(t_{n+\frac{1}{2}}\right)^5 & 7\left(t_{n+\frac{1}{2}}\right)^6 \\ 0 & 1 & 2t_{n+1} & 3(t_{n+1})^2 & 4(t_{n+1})^3 & 5(t_{n+1})^4 & 6(t_{n+1})^5 & 7(t_{n+1})^6 \\ 0 & 1 & 2t_{n+\frac{3}{2}} & 3\left(t_{n+\frac{3}{2}}\right)^2 & 4\left(t_{n+\frac{3}{2}}\right)^3 & 5\left(t_{n+\frac{3}{2}}\right)^4 & 6\left(t_{n+\frac{3}{2}}\right)^5 & 7\left(t_{n+\frac{3}{2}}\right)^6 \\ 0 & 1 & 2t_{n+2} & 3(t_{n+2})^2 & 4(t_{n+2})^3 & 5(t_{n+2})^4 & 6(t_{n+2})^5 & 7(t_{n+2})^6 \\ 0 & 1 & 2t_{n+\frac{5}{2}} & 3\left(t_{n+\frac{5}{2}}\right)^2 & 4\left(t_{n+\frac{5}{2}}\right)^3 & 5\left(t_{n+\frac{5}{2}}\right)^4 & 6\left(t_{n+\frac{5}{2}}\right)^5 & 7\left(t_{n+\frac{5}{2}}\right)^6 \\ 0 & 1 & 2t_{n+3} & 3(t_{n+3})^2 & 4(t_{n+3})^3 & 5(t_{n+3})^4 & 6(t_{n+3})^5 & 7(t_{n+3})^6 \end{bmatrix} \begin{bmatrix} \varphi_0 \\ \varphi_1 \\ \varphi_2 \\ \varphi_3 \\ \varphi_4 \\ \varphi_5 \\ \varphi_6 \\ \varphi_7 \end{bmatrix} = \begin{bmatrix} y_n \\ hg_n \\ hg_{n+\frac{1}{2}} \\ hg_{n+1} \\ hg_{n+\frac{3}{2}} \\ hg_{n+2} \\ hg_{n+\frac{5}{2}} \\ hg_{n+3} \end{bmatrix} \quad (9)$$

Making Use of Maple Mathematical software to obtain the values of φ's in (9) that result in the continuous formula:

$$y(t) = \alpha_0 y_n + h\left[\beta_n g_n + \beta_{n+\frac{1}{2}} g_{n+\frac{1}{2}} + \beta_{n+1} g_{n+1} + \beta_{n+\frac{3}{2}} g_{n+\frac{3}{2}} + \beta_{n+2} g_{n+2} + \beta_{n+\frac{5}{2}} g_{n+\frac{5}{2}} + \beta_{n+3} g_{n+3}\right] \quad (10)$$

Taking $t_1 = \dfrac{t - t_{n+2}}{h} \Rightarrow \dfrac{dt_1}{dt} = \dfrac{1}{h}$ (11)

We evaluate (7) at $t = t_{n+i}, \mathrm{i} = \dfrac{1}{2}, 1, \dfrac{3}{2}, 2, \dfrac{5}{2} and 3$, we obtain a block hybrid linear multistep method as

$$\begin{bmatrix} y_{n+\frac{1}{2}} \\ y_{n+1} \\ y_{n+\frac{3}{2}} \\ y_{n+2} \\ y_{n+\frac{5}{2}} \\ y_{n+3} \end{bmatrix} = \begin{bmatrix} 1 \\ 1 \\ 1 \\ 1 \\ 1 \\ 1 \end{bmatrix} \left[y_n\right] + h \begin{bmatrix} \frac{19087}{120960} & \frac{2713}{5040} & \frac{-15487}{40320} & \frac{293}{945} & \frac{-6737}{40320} & \frac{263}{5040} & \frac{-863}{120960} \\ \frac{1139}{7560} & \frac{47}{63} & \frac{11}{2520} & \frac{166}{945} & \frac{-269}{2520} & \frac{11}{315} & \frac{-37}{7560} \\ \frac{137}{896} & \frac{81}{112} & \frac{1161}{4480} & \frac{17}{35} & \frac{-729}{4480} & \frac{27}{560} & \frac{-29}{4480} \\ \frac{143}{945} & \frac{232}{315} & \frac{64}{315} & \frac{752}{945} & \frac{29}{315} & \frac{8}{315} & \frac{-4}{945} \\ \frac{3715}{24192} & \frac{725}{1008} & \frac{2125}{8064} & \frac{125}{189} & \frac{3875}{8064} & \frac{235}{1008} & \frac{-275}{24192} \\ \frac{41}{280} & \frac{27}{35} & \frac{27}{280} & \frac{34}{35} & \frac{27}{280} & \frac{27}{35} & \frac{41}{280} \end{bmatrix} \begin{bmatrix} g_n \\ g_{n+\frac{1}{2}} \\ g_{n+1} \\ g_{n+\frac{3}{2}} \\ g_{n+2} \\ g_{n+\frac{5}{2}} \\ g_{n+3} \end{bmatrix} \quad (12)$$

2.1 Analysis of the TSBHLMM

2.1.1 Order and error constant of the TSBHLMM

We analyze the approximation of the order and error constant of the derived block using the difference equation:

$$L[y(t),h]=\sum_{i=0}^{k}\left[\alpha_i y(t+ih)-h\beta y'(t+ih)\right] \tag{13}$$

We assume $y(t)$ to have as many higher derivatives we require, expanding the terms in (13) as a Taylor series about the point x we obtain the expansion

$$\left.\begin{aligned} &L[y(t),h]=C_0 y(t)+C_1 h y^{(1)}(t)+\ldots+C_q h^q y^{(q)}(t)+\ldots \\ &\text{where} \\ &C_0=\alpha_0+\alpha_1+\ldots+\alpha_k \\ &C_1=(\alpha_1+\alpha_2+\ldots+k\alpha_k)-(\beta_0+\beta_1+\ldots.+k^{(q-1)}\beta_k \text{ where } q=2,3,\ldots,k \end{aligned}\right\} \tag{14}$$

$$y_{n+3}=y_n+h\left(\frac{41}{280}g_n+\frac{27}{35}g_{n+\frac{1}{2}}+\frac{27}{280}g_{n+1}+\frac{34}{35}g_{n+\frac{3}{2}}+\frac{27}{280}g_{n+2}+\frac{27}{35}g_{n+\frac{5}{2}}+\frac{41}{280}g_{n+3}\right)$$

Where $\alpha_0=-1,\alpha_3=1,\beta_0=\frac{41}{280},\beta_{\frac{1}{2}}=\frac{27}{35},\beta_1=\frac{27}{280},\beta_{\frac{3}{2}}=\frac{34}{35},\beta_2=\frac{27}{280},\beta_{\frac{5}{2}}=\frac{27}{35},\beta_3=\frac{41}{280}$

The order and error constant is obtained by substituting these coefficients into (14)

Table 2.1: Order and Error Constants of the TSBHLMM

Scheme	Order	Error Constant
$y_{n+\frac{1}{2}}$	7	$\frac{275}{158723712}$
y_{n+1}	7	$\frac{8}{6200145}$
$y_{n+\frac{3}{2}}$	7	$\frac{1}{653184}$
y_{n+2}	7	$\frac{8}{6200145}$
$y_{n+\frac{5}{2}}$	7	$\frac{275}{158723712}$
y_{n+3}	8	$-\frac{1}{3061800}$

2.2 Reformulation of $k=3$ Block Hybrid Linear Multistep Method into Runge – Kutta Type Method

2.2.1: Proposed RKTM for first order ODE

Muhammad, (2020) defined an s-stage implicit Runge - Kutta methods for fist order ODEs in the form:

$$\left.\begin{aligned} y_{n+1} &= y_n + h\sum_{i=0}^{s} a_{ij}k_i \\ where i &= 1,2,3,\ldots,n \\ k_i &= f\left(x_i + \alpha_i h, y_n + h\sum_{i=0}^{s} a_{ij}k_i\right) \end{aligned}\right\} \quad (15)$$

The parameters α_j, k_j and a_{ij} defined the method. In Butcher array form, it can be written as

α	β
	W^T

The Butcher array conditions for first order differential equation is stated as:

$$\left.\begin{aligned} &(i).\sum_{j=1}^{s} a_{ij} = c_i \\ &(ii).\sum_{j=1}^{s} b_j = 1 \end{aligned}\right\} \quad (16)$$

Source: (Muhammad, 2020)

C	A						
0	0	0	0	0	0	0	0
$\frac{1}{6}$	$\frac{19087}{362880}$	$\frac{2713}{15120}$	$\frac{-15487}{120960}$	$\frac{293}{2835}$	$\frac{-6737}{120960}$	$\frac{263}{15120}$	$\frac{-863}{362880}$
$\frac{1}{3}$	$\frac{1139}{22680}$	$\frac{47}{189}$	$\frac{11}{7560}$	$\frac{166}{2835}$	$\frac{-269}{7560}$	$\frac{11}{945}$	$\frac{-37}{22680}$
$\frac{1}{2}$	$\frac{137}{2688}$	$\frac{81}{189}$	$\frac{1161}{4480}$	$\frac{17}{7560}$	$\frac{-243}{4480}$	$\frac{9}{560}$	$\frac{-29}{13440}$
$\frac{2}{3}$	$\frac{143}{2835}$	$\frac{232}{945}$	$\frac{64}{945}$	$\frac{752}{2835}$	$\frac{29}{945}$	$\frac{8}{945}$	$\frac{-4}{2835}$
$\frac{5}{6}$	$\frac{3715}{72576}$	$\frac{725}{3024}$	$\frac{2125}{24192}$	$\frac{125}{567}$	$\frac{3875}{24192}$	$\frac{235}{3024}$	$\frac{-275}{72576}$
1	$\frac{41}{840}$	$\frac{9}{35}$	$\frac{9}{280}$	$\frac{34}{105}$	$\frac{9}{280}$	$\frac{9}{35}$	$\frac{41}{840}$
b=1	$\frac{41}{840}$	$\frac{9}{35}$	$\frac{9}{280}$	$\frac{34}{105}$	$\frac{9}{280}$	$\frac{9}{35}$	$\frac{41}{840}$

(17)

Hence (12) is modified to satisfy the conditions where we obtained the Butcher table.

2.2.2: Proposed RKTM for the second order ordinary differential equations

Consider general second order ODEs with initial conditions of the form of (1)

Muhammad, (2020) defined an s-stage implicit Runge - Kutta type methods for second order ODEs in the form:

$$\left.\begin{aligned} y_{n+1} &= y_n + \alpha_j h y'_n + h^2 \sum_{i=1}^{s} a_{ij} k_i \\ y'_{n+1} &= y'_n + h \sum_{i=1}^{s} \overline{a}_{ij} k_i, \; where i = 1, 2, 3, \ldots s \\ k_i &= f\left(x_i + \alpha_j h, y_n + \alpha_j h y'_n + h^2 \sum_{i=1}^{s} a_{ij} k_i, y'_n + h \sum_{i=1}^{s} \overline{a}_{ij} k_i \right) \end{aligned}\right\} \quad (18)$$

The parameters α_j, k_j, a_{ij} and $\bar{a}_{ij}$ defined the method. In Butcher array form, it can be written as:

α	$\bar{A}$	A
	$\bar{b}^T$	b

where

$$A = a_{ij} = \beta^2, \overline{A} = \overline{a_{ij}} = \beta, \beta = \beta\ell, \bar{b} = w, b = w^T \beta$$

Extending (14) to Butcher array for second order ODEs as:

C	β	β^2
	$\overline{b}^T$	b

(19)

where

$$\overline{b}^T = \left[\frac{41}{840} \quad \frac{9}{35} \quad \frac{9}{280} \quad \frac{34}{105} \quad \frac{9}{280} \quad \frac{9}{35} \quad \frac{41}{840} \right], b = \left[\frac{41}{840} \quad \frac{3}{14} \quad \frac{3}{140} \quad \frac{17}{105} \quad \frac{3}{280} \quad \frac{3}{70} \quad 0 \right]$$

$$\beta = \begin{bmatrix} 0 & 0 & 0 & 0 & 0 & 0 & 0 \\ \frac{19087}{362880} & \frac{2713}{15120} & \frac{-15487}{120960} & \frac{293}{2835} & \frac{-6737}{120960} & \frac{263}{15120} & \frac{-863}{362880} \\ \frac{1139}{22680} & \frac{47}{189} & \frac{11}{7560} & \frac{166}{2835} & \frac{-269}{7560} & \frac{11}{945} & \frac{-37}{22680} \\ \frac{137}{2688} & \frac{81}{189} & \frac{1161}{4480} & \frac{17}{7560} & \frac{-243}{4480} & \frac{9}{560} & \frac{-29}{13440} \\ \frac{143}{2835} & \frac{232}{945} & \frac{64}{945} & \frac{752}{2835} & \frac{29}{945} & \frac{8}{945} & \frac{-4}{2835} \\ \frac{3715}{72576} & \frac{725}{3024} & \frac{2125}{24192} & \frac{125}{567} & \frac{3875}{24192} & \frac{235}{3024} & \frac{-275}{72576} \\ \frac{41}{840} & \frac{9}{35} & \frac{9}{280} & \frac{34}{105} & \frac{9}{280} & \frac{9}{35} & \frac{41}{840} \end{bmatrix},$$

$$C = \begin{bmatrix} 0 & \frac{1}{6} & \frac{1}{3} & \frac{1}{2} & \frac{2}{3} & \frac{5}{6} & 1 \end{bmatrix}^T,$$

$$\beta^2 = \begin{bmatrix} 0 & 0 & 0 & 0 & 0 & 0 & 0 \\ \frac{647}{103680} & \frac{275}{18144} & \frac{-12013}{725760} & \frac{9}{560} & \frac{-7289}{725760} & \frac{323}{90720} & \frac{-79}{145152} \\ \frac{337}{22680} & \frac{299}{5670} & -\frac{16}{567} & \frac{79}{2835} & \frac{-53}{3240} & \frac{31}{5670} & \frac{-1}{1260} \\ \frac{125}{5376} & \frac{3}{32} & -\frac{171}{8960} & \frac{5}{112} & \frac{-219}{8960} & \frac{9}{1120} & \frac{-31}{26880} \\ \frac{2}{63} & \frac{76}{567} & -\frac{16}{2835} & \frac{232}{2835} & -\frac{16}{567} & \frac{4}{405} & \frac{-4}{2835} \\ \frac{5825}{145152} & \frac{3175}{18144} & \frac{125}{20736} & \frac{125}{1008} & -\frac{1625}{145152} & \frac{275}{18144} & \frac{-275}{145152} \\ \frac{41}{840} & \frac{9}{35} & \frac{9}{280} & \frac{34}{105} & \frac{9}{280} & \frac{9}{35} & \frac{41}{840} \end{bmatrix}$$

The Butcher table extended from (14) satisfied the conditions for second order differential equations which is:

$$(i). \sum_{j=1}^{s} b_j = \frac{1}{2} \tag{20}$$

Source: (Muhammad, 2020)

We obtain seven stage implicit Ruge-Kutta type method from Butcher table (19) as (21) – (29):

$$y_{n+1} = y_n + hy'_n + h^2\left(\frac{14}{849}k_1 + \frac{3}{14}k_2 + \frac{3}{140}k_3 + \frac{17}{105}k_4 + \frac{3}{280}k_5 + \frac{3}{70}k_6\right) \tag{21}$$

$$y'_{n+1} = y'_n + h\left(\frac{41}{840}k_1 + \frac{9}{35}k_2 + \frac{9}{280}k_3 + \frac{34}{105}k_4 + \frac{9}{280}k_5 + \frac{9}{35}k_6 + \frac{41}{280}k_7\right) \tag{22}$$

$$k_1 = f\left(x_n, y_n, y'_n\right) \tag{23}$$

$$k_2 = f\left(x_n + \frac{1}{6}h, y_n + \frac{1}{6}hy'_n + h^2\left(\frac{647}{103680}k_1 + \frac{275}{18144}k_2 - \frac{12013}{725760}k_3 + \frac{9}{560}k_4 - \frac{7289}{725760}k_5 + \frac{323}{90720}k_6 - \frac{79}{145152}k_7\right),\right.$$
$$\left. y'_n + h\left(\frac{19087}{362880}k_1 + \frac{2713}{15120}k_2 - \frac{15487}{120960}k_3 + \frac{293}{2835}k_4 - \frac{6737}{120960}k_5 + \frac{263}{15120}k_6 - \frac{863}{362880}k_7\right)\right) \tag{24}$$

$$k_3 = f\left(x_n + \frac{1}{3}h, y_n + \frac{1}{3}hy'_n + h^2\left(\frac{125}{5376}k_1 + \frac{3}{32}k_2 - \frac{171}{8960}k_3 + \frac{5}{112}k_4 - \frac{219}{8960}k_5 + \frac{9}{1120}k_6 - \frac{31}{26880}k_7\right),\right. \tag{25}$$
$$\left. y'_n + h\left(\frac{137}{2688}k_1 + \frac{27}{112}k_2 - \frac{171}{8960}k_3 + \frac{5}{112}k_4 - \frac{219}{8960}k_5 + \frac{9}{1120}k_6 - \frac{31}{26880}k_7\right)\right)$$

$$k_5 = f\left(x_n + \frac{1}{2}h, y_n + \frac{1}{2}hy'_n + h^2\left(\frac{125}{5376}k_1 + \frac{3}{32}k_2 - \frac{171}{8960}k_3 + \frac{5}{112}k_4 - \frac{219}{8960}k_5 + \frac{9}{1120}k_6 - \frac{31}{26880}k_7\right),\right. \tag{26}$$
$$\left. y'_n + h\left(\frac{137}{2688}k_1 + \frac{27}{112}k_2 + \frac{387}{4480}k_3 + \frac{17}{105}k_4 - \frac{243}{4480}k_5 + \frac{9}{560}k_6 - \frac{29}{13440}k_7\right)\right)$$

$$k_5 = f\left(x_n + \frac{2}{3}h, y_n + \frac{2}{3}hy'_n + h^2\left(\frac{2}{63}k_1 + \frac{76}{567}k_2 - \frac{16}{2835}k_3 + \frac{232}{2835}k_4 - \frac{16}{567}k_5 + \frac{8}{405}k_6 - \frac{4}{2835}k_7\right),\right. \tag{27}$$
$$\left. y'_n + h\left(\frac{143}{2835}k_1 + \frac{232}{945}k_2 + \frac{64}{945}k_3 + \frac{752}{2835}k_4 + \frac{29}{945}k_5 + \frac{8}{945}k_6 - \frac{4}{2835}k_7\right)\right)$$
$$k_6 = f\left(x_n + \frac{5}{6}h, y_n + \frac{5}{6}hy'_n + h^2\left(\frac{5825}{145152}k_1 + \frac{3175}{18144}k_2 + \frac{125}{20736}k_3 + \frac{125}{1008}k_4 - \frac{1625}{145152}k_5 + \frac{275}{18144}k_6 - \frac{275}{145152}k_7\right),\right. \tag{28}$$
$$\left. y'_n + h\left(\frac{3715}{72576}k_1 + \frac{725}{3024}k_2 + \frac{2125}{24192}k_3 + \frac{125}{567}k_4 + \frac{3875}{24192}k_5 + \frac{235}{3024}k_6 - \frac{275}{72576}k_7\right)\right)$$

$$k_7 = f\left(x_n + h, y_n + hy'_n + h^2\left(\frac{41}{840}k_1 + \frac{3}{14}k_2 + \frac{3}{140}k_3 + \frac{17}{105}k_4 + \frac{3}{280}k_5 + \frac{3}{70}k_6\right),\right. \tag{29}$$
$$\left. y'_n + h\left(\frac{41}{840}k_1 + \frac{9}{35}k_2 + \frac{9}{280}k_3 + \frac{32}{105}k_4 + \frac{9}{280}k_5 + \frac{9}{35}k_6 + \frac{41}{840}k_7\right)\right)$$

3 Results and Discussion

To verify the credibility of our proposed scheme, problems were selected for testing and the results compared with other existing method in the literature.

Test Problem 1: $y''(t) = y(t) + t - 1, t \in [0,1], y(0) = 2, y'(0) = -2, h = 0.1$

Exact solution: $y(t) = 1 - t + e^{-t}$ (Akinnukawe and Okunuga, 2024)

Test Problem 2: $y''(x) = -1001y' - 1000y, \mathrm{y}(0) = 1, \mathrm{y}'(0) = -1, \mathrm{h} = 0.1$

$y(x) = e^{-x}$ Source: (Atsi *et al.*, 2024)

Table 1: Comparison of the Result between Exact Solution, RKTM and Akinnukawe and Okunuga, (2024) for Test Problem 1

x	Exact Solution	Proposed Method	Error in Proposed Method	Error in Akinnukawe and Okunuga, (2024)
0.1	1.98004983374916805357390597718	1.98004983374916805357390598223	5.05 E -27	3.55271E-15
0.2	1.96019867330675530222081410422	1.96019867330675530222081411423	1.001 E -26	1.22125E-14
0.3	1.94044553354850817693252835196	1.94044553354850817693252836682	1.486 E -26	2.59792E-14
0.4	1.92078943915232320943921069132	1.92078943915232320943921071094	1.962 E -26	4.32987E-14
0.5	1.90122942450071400909142531978	1.90122942450071400909142534405	2.427 E -26	6.55032E-14
0.6	1.88176453358424870953715278327	1.88176453358424870953715281211	2.884 E -26	9.19265E-14
0.7	1.86239381990594822885797263248	1.86239381990594822885797266580	3.332 E-26	1.22236E-13
0.8	1.84311634638663578291075984957	1.84311634638663578291075988726	3.769 E -26	1.56430E-13
0.9	1.82393118527122818674735354650	1.82393118527122818674735358848	4.198E -26	1.94844E-13
1.0	1.80483741803595957316424905945	1.80483741803595957316424910563	4.618 E -26	2.37643E-13

Table 3.1 show the exact solution, computed solution, absolute errors $|Y(x_n) - y_n|$ of the Runge-Kutta type method and Akinnukawe and Okunuga, (2024) on test problem 1 for $h = 0.1$. The table shows that the Runge-Kutta type method approach the exact solution faster than Akinnukawe and Okunuga, (2024) within the interval of $0 \le x \le 1$ for $h = 0.1$ on experimental problem 1

Table 2: Comparison of the result between exact solution, Runge Kutta type method and Tumba *et al.*, (2024) for Test Problem 2

x	Exact Solution	Proposed Method	Error in the proposed method	Error in Atsi *et al.*, (2024)
0.1	0.90483741803595957316	0.90483741803595957778	4.620 *e* -18	8.0*e* – 10
0.2	0.81873075307798185867	0.81873075307798186703	8.360 *e* -18	4.1*e* – 09
0.3	0.74081822068171786607	0.74081822068171787742	1.135 *e* -17	9.3*e* – 09
0.4	0.67032004603563930074	0.67032004603563931444	1.370 *e* -17	3.2*e* – 09
0.5	0.60653065971263342360	0.60653065971263343910	1.550 *e* -17	7.0*e* – 10
0.6	0.54881163609402643263	0.54881163609402644945	1.682 *e* -17	2.3*e* – 09
0.7	0.49658530379140951470	0.49658530379140953246	1.776 *e* -17	6.0*e* – 10
0.8	0.44932896411722159143	0.44932896411722160979	1.836 *e* -17	3.5*e* – 09
0.9	0.40656965974059911188	0.40656965974059913057	1.869 *e* -17	6.6*e* – 09
1.0	0.36787944117144232160	0.36787944117144234038	1.878 *e* -17	3.3*e* −09

Table 3.2 show the exact solution, computed solution, absolute errors $|Y(x_n) - y_n|$ of the Runge-Kutta type method and Atsi *et al.*, (2024). on test problem 1 for $h = 0.1$. The table shows that the Runge-Kutta type method appear to be so closer to the exact solution than Atsi *et al.*, (2024). The Runge-Kutta type method approaches the exact solution faster than Atsi *et al.*, (2024) within the interval of $0 \le x \le 0.1$. for $h = 0.1$ on the experimental problem 2

4 Conclusion

Reformulation of the three-step block hybrid linear multi-step method into a Runge–Kutta-type method (RKTM) for the solution of second-order IVPs in ODEs represents a significant improvement in numerical methods for the solution of second order ODEs. The reformulated RKTM maintains the stability properties of the block hybrid method. RKTM reformulated from block hybrid linear multistep also incorporate the adaptability and self-starting properties of Runge–Kutta method. The RKTM derived shows computational accuracy and efficiency since it has better performance in numerical experiments than the existing methods in the literature. The method's strength to handle second-order ODEs without reducing to first order equivalent form provides a crucial tool for its wide applications in scientific and engineering fields. Based on the results obtained, it is recommended that further research be conducted to enable expansion of the method's application. Further research could allow investigation of its performance, its adaptability to variable step-size for improved computational efficiency. Also, finding out its application to higher-order ODEs, it would further validate its flexibility and reliability. In all, the proposed Runge–Kutta-type method gives an important contribution to the field of numerical analysis especially initial value problems.

References

Abuasbeh, K., Qureshi, S., Soomro, A., & Awadalla, M. (2023). An Optimal Family Of Block Techniques To Solve Models Of Infectious Diseases: Fixed And Adaptive Stepsize Strategies. *Mathematics*, *11*(5), 1135.

Akinnukawe, B. I. & Okunuga, S. A. (2024). One-Step Block Scheme With Optimal Hybrid Points For Numerical Integration Of Second-Order Ordinary Differential Equations. *Journal Of Nigerian Society Of Physical Sciences*, *6*(2).

Atsi, K., Tumba, P., & Suleiman, E. (2024). A Treatment Of A Multistep Collocation Method For The Direct Solution Of Second-Order Ordinary Differential Equations. *Fudma Journal Of Sciences*, *8*(6), 234-238.

Duromola, M., Lawal, R., & Akinmoladun, O. (2024). Numerical Integration Of Linear Hybrid Multistep Block Method For Third-Order Ordinary Differential Equations (Ivps). *Scientific African*, E02129.

Gbenro, S., Areo, E., Olabode, B., & Momoh, A. (2024). Seventh Order Second Derivative Method With Optimized Hybrid Points For Solving First-Order Initial Value Problems Of Odes.

Ibrahim, Z. B. & Nasarudin, A. A. (2020). A Class Of Hybrid Multistep Block Methods With A–Stability For The Numerical Solution Of Stiff Ordinary Differential Equations. *Mathematics*, *8*(6), 914.

Kayode, S. J., Obarhua, F. O., & Daodu, F. T. (2025). A Three-Step Hybrid Block Method For Direct Integration Of Third Order Ordinary Differential Equations. *Sch. J. Phys. Math. Stat.* Https://Doi.Org/10.36347/Sjpms.2025.V12i01.003

Muhammad, R. (2020). The Order And Error Constant Of A Runge-Kutta Type Method For The Numerical Solution Of Initial Value Problem.

Muhammad, R. & Oyedeji, A. (2024). A 4-Stage Runge-Kutta Type Method For Solution Of Stiff Ordinary Differential Equations. *Pan-American Journal Of Mathematics*, *3*, 21.

Muhammad, R., Yahaya, Y. A., & Abdulkareem, A. S. (2020). An Implicit Runge-Kutta Type Method For The Solution Of Initial Value Problems.

Mulatu, L., Shiferaw, A., & Gebregiorgis, S. (2020). Block Procedure For Solving Stiff Initial Value Problems Using Probabilists Hermite Polynomials. *Engineering And Applied Science Letters*, *3*(3), 20-29.

Omole, E. O., Adeyefa, E. O., Emadifar, H., Abualigah, L., Onu, P., Ajewole, K. P., Adeniji, T. O., Okoro, J. O., & Amoyedo, F. E. (2024). Development And Implementation Of A Top-Order Multi-Step Block Method For Boundary Value Problems: The Advancement Of Numerical Accuracy. 2024 International Conference On Science, Engineering And Business For Driving Sustainable Development Goals (Seb4sdg),

Tassaddiq, A., Qureshi, S., Soomro, A., Hincal, E., & Shaikh, A. A. (2022). A New Continuous Hybrid Block Method With One Optimal Intrastep Point Through Interpolation And Collocation. *Fixed Point Theory And Algorithms For Sciences And Engineering*, *2022*(1), 22.

Walters, S. J., Turner, R. J., & Forbes, L. K. (2022). A Comparison Of Explicit Runge–Kutta Methods. *The Anziam Journal*, *64*(3), 227-249.

Analytical Approximation of Integro Delay Differential Equation

[1*]Aminu Barde and [2]Nehemiah Yohanna
[1,]Department of Mathematics, Abubakar Tafawa Balewa University, Bauchi, Nigeria
[2]Department of Mathematics, Abubakar Tafawa Balewa University, Bauchi, Nigeria
[1*]Corresponding author: bardealamin@yahoo.com

Abstract

Delay differential equations (DDEs) are a type of the functional differential equation that has an extensive application in many disciplines in science and engineering. In many years, such equations have been applied in control theory and of recent in numerous biological models. However, a lot of methods have been experience series of difficulties in order to obtain the approximation analytically of certain types of those equations. Therefore, the current work applies the Sumudu variational iteration method via modified He's polynomial for the analytically handling of integro delay differential equation. The considered method combined the Sumudu transform with variational iteration method. The introduced approach gives solution of this equation in the form of a speedy convergent series and modified He's polynomial has applied to calculate the nonlinear terms. Hence, the outcomes point that the familiarized method is efficiently handling this kind of DDEs analytically.

Keywords: He's Polynomial, integro delay differential equation, Sumudu transform, variational iteration method.

1. Introduction

Delay differential equation is among the branches of the functional differential equations use in a number of arenas of studies. These include: population in dynamics, applied sciences, engineering, and many others (Liu and Kalmar 2010; Rihan *et a*l., 2014; Rihan *et a*l., 2018) Therefore, numerous problems in different areas of research have delay element (Fatemeh and Mehdi, 2008; Mohammad and Mehdi, 2008; Mehdi and Rezvan 2010). Thus, DDEs is significant in modelling the real-life applications and help to gain insights into complex equation where the delay element significantly impacts the equation behavior and prediction. Hence, such equations provide more accurate modelling and analysis of various real-life scenarios across multiple disciplines than ordinary differential equations (ODEs).

There exist many similarities in ODEs and DDEs theories. At some point a lot of analytical approaches that solve ODEs are prolonged to DDEs. However, the existing differences that is naturally among those equations, these techniques tackle to solve linear and some category of nonlinear DDEs. Therefore, handling DDEs of nonlinear kinds analytically is very tough because of the transcendental nature they possess. Hence, numerical means are applied mostly for their solution especially for a domain that is more complex in computation. Though, in sciences and engineering models, analytical methods are primarily used to determine the critical variables and how they relate to others. This also is of uses in measuring the effect of an input to the output in accordance of mathematical guide. Thus, analytical results are supplementary general and consistent in related problems (Aminu and Jafar 2022).

In this work, the Sumudu variational iteration method via modified He's polynomial (SVIMH) is used to obtain the approximate analytical solution of integro delay differential equation. The method is from the combination of Sumudu transform and variational iteration method (VIM), and modified He's polynomial was successfully applied in computation of nonlinear terms of the equation. This approach provides solution in form of polynomial series which converged to exact solution of the equation using two iterations only. A figure is demonstrably shows the behavior for exact solution with second order approximation of our proposed technique. Hence, the technique gives rise to a straightforward means for the analytic treatment of such equation.

3. Materials and Methods

To establish the procedure of the method, we consider the following form of nonlinear Retarded delay differential equations (RDDEs) $v_i^{(n)}(t) =$

$$f_i\left(t, \boldsymbol{v}(t), \boldsymbol{v}'(t), \dots \boldsymbol{v}^{(n-1)}(t), \boldsymbol{v}\left(\alpha_j(t)\right), \boldsymbol{v}'\left(\alpha_j(t)\right), \dots \boldsymbol{v}^{(n-1)}\left(\alpha_j(t)\right)\right), \; t \in [0,\infty), \quad (1)$$

for $i = 1,2,\dots,m,\;\; j = 0,1,2,\dots r,\;\; f_i: [0,\infty) \times \mathbb{R}^{nm} \times \mathbb{R}^{nmr} \to \mathbb{R}$ are continuous functions $\boldsymbol{v}^{(k)}\left(\alpha_j(t)\right) = \left[v_1^{(k)}\left(\alpha_j(t)\right), v_2^{(k)}\left(\alpha_j(t)\right), \dots, v_m^{(k)}\left(\alpha_j(t)\right)\right]$ for $k = 0,1,2\dots, n-1,\;\; \boldsymbol{v}^{(k)}(t) = \left[v_1^{(k)}(t), v_2^{(k)}(t), \dots, v_m^{(k)}(t)\right]$ and $\alpha_j(t)$ is continuous delay function. This work put two classes of real time delay under consideration; the first is proportional and second is constant type of delay. Therefore, the delay function $\alpha_j(t)$ is defined as follows:

(i) Proportional delay: $\alpha_j(t) = b_j t$, for $b_j \in (0,1)$

(ii) Constant delay: $\alpha_j(t) = t - \tau_j$, where $\tau_j > 0$ are real constants.

The initial condition of Equation (1) with respect to proportional delay is defined as follows:

$$v_i(0) = \mu_{i.0}, v_i'(0) = \mu_{i,1}, v_i''(0) = \mu_{i,2}, \dots, v_i^{(n-1)}(0) = \mu_{i,n-1}, \quad (2)$$

where $\mu_{i,0}, \mu_{i,1}, \dots, \mu_{i,n-1}$ are constants real numbers. While the initial condition with constant delay is given as:

$$v_i(t) = p_i(t), t \in [-D, 0], i = 1,2,\dots,m, \quad (3)$$

where $p_i(t), p_i'(t), \dots, p_i^{(n-1)}(t)$ are continuous functions on $[-D,0]$ and $D = \max_{j=1,2,\dots,r}[\tau_j]$.

The idea here is to obtain the unknown Lagrange multiplier. Therefore, the equation below provided the conversion of equation (1) in algebraic form:

$$\frac{d^n[v_i(t)]}{dt^n} + R_i[\mathbf{v}(t)] + F_i\left[\left(\mathbf{v}(\boldsymbol{t})\right)\right] = g_i(t), \quad (4)$$

with Equations (2) and (3) as initial condition, $\boldsymbol{v}(t) = \left(v_1(t), v_2(t), \dots, v_m(t)\right)$, R_i are linear

operators and $N_i$are nonlinear operators represent the nonlinear terms. Apply Sumudu transform to (4) and simplify using its fundamental properties we obtain the following equation.

$$u^{-m}v_i(u) - u^{-m}v_i(0) - \cdots - u^{-1}v^{m-1}{}_i(0) + S(R_i[\mathrm{V}] + F_i[(\mathrm{V})]) = \mathrm{S}\big(g_i(t)\big). \qquad (5)$$

Then, the concept variational iteration method gives the correction functional as:

$$\tilde{\mathrm{v}}_{i(nt1)}(u) = \tilde{\mathrm{v}}_{i(n)}(\mathrm{u}) + \lambda(\mathrm{u})\big[u^{-m}\tilde{\mathrm{v}}_i(u) - u^{-m}v_i(0) - \cdots - u^{-1}v^{m-1}{}_i(0) + S(R_i[\mathrm{V}] + F_i[(\mathrm{V})]) - \mathrm{S}\big(g_i(t)\big)\big]. \qquad (6)$$

Considering the terms $S(R_i[\tilde{\mathrm{v}}_n] + F_i[(\tilde{\mathrm{v}}_n)]) - \mathrm{S}\big(g_i(t)\big)$ as restricted variations, we let (6) to be stationary with respect to $\tilde{\mathrm{v}}_n$ that is

$$\delta\tilde{\mathrm{v}}_{i(nt1)}(u) = \delta\tilde{\mathrm{v}}_n(u) + \lambda(\mathrm{u})\left(\frac{1}{u^m}\,\delta\tilde{\mathrm{v}}_n(u)\right), \qquad (7)$$

From (5), the Lagrange multiplier can be defined as:

$$\lambda(\mathrm{u}) = -u^m. \qquad (8)$$

Subsequent approximations is attained when taking the inverse of Sumudu transform S^{-1} of (5) and (6) and arrived at given equation

$$v_{i(nt1)}(t) = v_{i(n)}(\mathrm{t}) - S^{-1}\Big[u^m\Big\{u^{-m}v_i(u) - u^{-m}v_i(0) - \cdots - u^{-1}v^{m-1}{}_i(0) + S\Big(R_i[\mathrm{V}] + H_{i,n}\big(\boldsymbol{v}_1(t), \boldsymbol{v}_2(t), \dots, \boldsymbol{v}_m(t)\big)\Big) - \big(g_i(t)\big)\Big\}\Big], \qquad (9)$$

where the nonlinear operator$F_i[(\mathbf{v})]$ are computed using the modified He's polynomial $H_{i,n}\big(\boldsymbol{v}_1(t), \boldsymbol{v}_2(t), \dots, \boldsymbol{v}_m(t)\big)$ defined as

$$H_{i,n}\big(\boldsymbol{v}_1(t), \boldsymbol{v}_2(t), \dots, \boldsymbol{v}_m(t)\big) = \frac{1}{n!}\frac{\partial^n}{q^n}F\big(\textstyle\sum_{P=0}^{n} q^p \boldsymbol{v}_p(t)\big)|_{q=0}, \qquad (10)$$

where,$\boldsymbol{v}_i(t) = \big(v_{i,1}(t), v_{i,2}(t), \dots, v_{i,n}(t)\big)$ for $i = 1,2,\dots,m$ and $\boldsymbol{v}_p(t) = \big(v_{1,p}(t), v_{2,p}(t), \dots, v_{m,p}(t)\big)$.

The initial approximation is given as:

$$v_0(t) = S^{-1}\big(v(0) + \cdots + u^{m-1}v^{m-1}(0)\big) = v(0) + v'(0) + \cdots + \frac{t^{m-1}v^{m-1}(0)}{(m-1)!}. \qquad (11)$$

Now, as $n \to \infty$, $v_{i.n}(t)$ converges to the exact solution $v_i(t)$

4. Results and Discussion

In this section, the method established in Section 2 is applied to have the analytical approximation of the integro delay differential equation. Thus, the equation has the following form.

$$v''(t) + \frac{1}{2}(t-4)v'(t) + \frac{1}{2}v(t) - 2v^2\left(\frac{t}{2}\right) = 0, \quad t \geq 0, \tag{12}$$

with initial condition

$$v(0) = 0, \;\; v'(0) = 1. \tag{13}$$

By following the procedure of the developed method we first take the Sumudu transform of both sides of (12) to obtain

$$\frac{v(u)}{u^2} - \frac{v(0)}{u^2} - \frac{v'(0)}{u} + S\left[\frac{1}{2}(t-4)v'(t) + \frac{1}{2}v(t) - 2v^2\left(\frac{t}{2}\right)\right] = 0. \tag{14}$$

Using equation (9) for $i = 1$the iteration formula of (12) is obtained as:

$$v_{n+1}(t) = v_n(t) + S^{-}\{u^2 S[R(v_n(t)) - H_n(v_0, v_1, \dots, v_n)]\}, \;\; n \geq 0, \tag{15}$$

where $H_n(v_0, v_1, \dots, v_m)$ is He's polynomial of nonlinear operator $F(v) = 2v^2\left(\frac{t}{2}\right)$ defined by

$$H_n(v_0, v_1, \dots, v_n) = \frac{1}{n!}\frac{\partial^n}{\partial q^n}\left[2\left(\sum_{p=0}^{n} q^p v_p\left(\frac{t}{2}\right)\right)^2\right]|_{q=0}, \;\; n \geq 0. \tag{16}$$

By choosing the initial approximation $v_0(t) = t$ and using (15) we obtained the following.

$$v_0(t) = t$$

$$v_1(t) = t - \frac{t^4}{4} + \frac{t^3}{6}$$

$$v_2(t) = t + t^2 + \frac{t^3}{2} + \frac{t^4}{6} + \frac{t^5}{24} + \frac{t^6}{120} + \cdots \tag{17}$$

As $n \to \infty$ (17) converged to closed-form solution of te^t which is the same as the exact result of integro delay differential equation (12). Figure 1 is demonstrably shows the behavior for exact solution with second order approximate solution of our proposed technique.

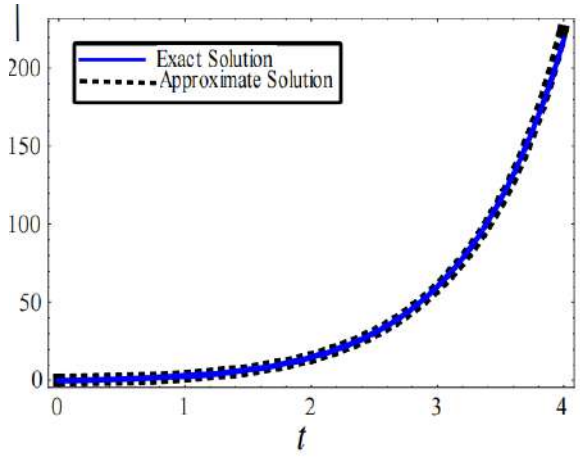

Figure 1. The behaviour of the Exact and the Approximate Solution of the Problem.

Observe that, (17) converges to te^t which gives the exact result of the equation. Therefore, only two iterations of the introduced method converged to the exact solution of integro delay differential equation. Whereas, the same solution is obtained from three numbers of iterations using He-natural Homotopy analysis method for solving nonlinear delay differential equations (HeNHAM) by Normah and Barde (2020).

5. Conclusion

In this work, a combination of Sumudu transform and variational iteration method provides a robust analytical approach suitable for solving integro delay differential equation. By this technique, the modified He's polynomial is adopted for the computation of nonlinear terms of such equation. The developed technique offers in the form of a speedy convergent series, which leads to the exact using only two iterations. To show the accuracy of the developed method Figure 1 is provided the behavior between the exact solution and the approximate solution. The result of this figure indicated that there is a good agreement between the exact solution with second-order approximation of developed method. Therefore, the technique provides an easiest means for the analytical approximation of this equation and can also be used to other nonlinear DDEs.

References

Barde, A. & Jafar, A.B. (2022). Analytical approximation for spread of a SIRS model. *Science Journal of Advanced and Cognitive Research*, 3(1), 11-20.

Fatemeh, S. & Mehdi, D. (2008). Solution of a model describing biological species living together using the variational iteration method. *Mathematical and computer modelling,* 48(5-6) ,685-699.

Liu, L. & Kalmar, T. (2010). High-dimensional harmonic balance analysis for second-order delay differential equations. *Journal of Vibration and Control*,16(7-8),1189– 1208.

Mehdi, D. & Rezvan, S. (2010). Solution of a nonlinear time-delay model in biology via semi-analytical approaches. *Computer Physics Communications*, 181(7), 1255-1265.

Mohammad S. & Mehdi D. (2008). On the numerical solution of nonlinear systems of Volterra integro-differential equations with delay arguments. *Computing*, 82(4), 241-260.

Normah, M. & Barde, A. He-natural homotopy analysis method for solving nonlinear delay differential equations. *International Journal of Advance Science and Technology,* 29(10S), 851-862.

Rihan, F. A., Rahman, D. A., Lakshmanan, S. & Alkhajeh, A. A. (2014). Time delay

model of tumour-immune system interactions: Global dynamics, parameter estimation, sensitivity analysis. *Applied Mathematics and Computation*, 23(2), 606–623.

Rihan, F. A., Azamov, A. A. & Al-Sakaji, H. J. (2018). An Inverse problem for delay differential equations: Parameter estimation, nonlinearity, sensitivity. *Applied Mathematics & Information Sciences*, 12(1), 63–74.

Comparison Rate of the Convergence of Single Step and Triple Steps Iteration Schemes

Kehinde Femi Adedapo[1], Oluwamuyiwa Olupitan[2], Musilimu Taiwo[3], Abdullahi Usman[4] , Rapheal Oladipo Fifelola[5]

[1,2,3,4]Federal University of Health Sciences, Ila-Orangun, Nigeria

[5]Nigerian Defence Academy, Kaduna, Nigeria

[1*]Corresponding author: adeisrael1978@gmail.com

Abstract

A fixed point of a function $f: X \to X$ is defined as an element $k \in X$ such that $f(k) = k$. In this study, we analyze fixed point iterative procedures, which are essential for solving equations in various physical formulations. We rigorously establish and compare the convergence and convergence rates of single-step and triple-step iterative schemes with errors in Banach spaces, employing the Zamfirescu operator. Specifically, we demonstrate that for a contraction mapping $T: X \to X$, the sequences generated by these iterative schemes converge to a unique fixed point $p \in X$. Additionally, we explore the existence and stability of Mann iterations defined by the iterative scheme $x_{n+1} = (1 - \alpha_n)x_n + \alpha_n T(x_n)$ and Noor iterations given by $x_{n+1} = (1 - \beta_n)x_n + \beta_n T(T((x_n))$, where α_n, β_n are appropriate step sizes. Our results not only elucidate the effectiveness of these iterative methods but also contribute to the broader understanding of fixed point theory in Banach spaces.

Keywords: Fixed point; Banach space; Convergence; Normed space; Metric Space; Banach fixed point

1. Introduction

The concept of a fixed point is a fundamental aspect of mathematics, with widespread applications in various fields, including analysis, topology, and applied mathematics. A fixed point of a function f is defined as a point k in the function's domain such that $f(k) = k$. This self-mapping property, often referred to as an invariant point, is crucial in understanding the behavior of dynamical systems and iterative processes. Fixed point theory is not merely a theoretical concept; it serves as a vital tool for solving equations, optimizing functions, and analyzing stability. Berinde (2007) emphasizes the importance of fixed point theory in iterative methods, which are algorithms designed to find such points, underscoring their application in numerical analysis and computational tasks.

In computational mathematics, iterative methods generate sequences of approximate solutions to complex problems. These methods rely on initial guesses to produce successive approximations, with convergence to a fixed point being essential for guaranteeing a reliable solution. In contrast to direct methods that provide solutions through a finite sequence of operations, iterative methods are often the only viable approach for nonlinear equations and large systems where direct solutions

would be computationally prohibitive. The convergence of these methods is closely tied to fixed point theory, particularly illustrated by the Banach fixed point theorem. This theorem asserts that under specific conditions, a contraction mapping will have a unique fixed point, a finding that has broad implications in mathematical analysis and numerical methods.

Recent advancements have broadened the scope of fixed point theory, introducing alternative iterative procedures when traditional methods fail. For example, in situations where contraction mappings are not applicable, techniques such as Mann and Ishikawa iterations have emerged, providing robust alternatives for achieving convergence in Banach spaces (Chidume, 1994; Koti *et al.*, 2013). Furthermore, Agarwal *et al*. (2007) introduced the S-iteration process, a novel approach that operates independently of conventional methods, thereby enriching the field with new strategies for solving fixed point problems.

In addition to these techniques, numerous researchers have explored the applicability of fixed point theory in various contexts, such as nonlinear differential equations, dynamic programming, and game theory. Fixed point methods are also used in economics to analyze equilibrium states and in computer science for algorithm convergence. The ongoing advancements in fixed point theory illustrate the dynamic interplay between mathematical theory and computational practice, highlighting the relevance of fixed points in both theoretical and applied contexts.

This review aims to synthesize recent developments in fixed point theory, particularly focusing on the evolution of iterative methods and their applications in solving complex mathematical problems. By examining both classical and contemporary approaches, this work seeks to emphasize the significance of fixed point theory in today's mathematical landscape and pave the way for future innovations and applications iterations.

2. Preliminaries

The Picard iteration method is a fundamental approach for identifying fixed points in metric spaces. Consider a metric space (X, d) where $D \subset X$ is a closed subset, typically assumed to be $D = X$. Given a self-map $T: D \to D$ that has at least one fixed point $p \in FT$, we define a sequence of iterates $\{x_n\}_{n=0}^{\infty}$ as follows:

$$x_{n+1} = T(x_n) = T_n(x_0), n \in N \tag{1}$$

Our goal is to determine conditions on T, D, and X that ensure the convergence of the sequence $\{x_n\}_{n=0}^{\infty}$ to a fixed point of T in D. The concept of Picard iteration with an error term is given by:

$$x_{n+1} = T(x_n) + U_n, n \in N \tag{2}$$

where the error sequence $\{U_n\}$ satisfies $\sum_{n-1}^{\infty} \|U_n\| < \infty$

Definition: In a metric space (X, d), a map $T: X \to X$ is defined as a contraction mapping if there exists a constant $p \in (0,1)$ such that:

$$d\big(T(x),T(y)\big) \leq p.d(x,y) \tag{3}$$

for all $x, y \in X$ (Banach, 1922).

Banach Fixed Point Theorem: For any non-empty complete metric space (X, d) and a contraction mapping $T: X \to X$, there exists a unique fixed point $x^* \in X$ such that $T(x^*) = x^*$. Starting from any element $x^0 \in X$, the sequence $\{x_n\}$ defined by

$$x_n = T(x_{n-1}) \tag{4}$$

will converge to x ∗ (Banach, 1922).

In cases where the contraction condition is not strictly met, convergence of Picard iterations may not be achieved. Alternative iteration techniques such as Mann, Ishikawa, S-iteration, Thianwan, and Noor iterations can be utilized (Ishikawa, 1974).

The Mann iteration process begins with an initial point $x_0 \in E$ and follows:

$$x_{n-1} = (1 - a_n)x_n + a_nTx_n, n = 0,1,2, \ldots \tag{5}$$

where the parameters $\{a_n\}$ lie within [0, 1] and satisfy certain conditions. The Mann iteration with error is given by:

$$x_{n+1} = (1 - a_n)x_n + a_nTx_n + U_n, n = 0, 1, 2, \ldots \tag{6}$$

with U_n meeting the condition $P\|U_n\| < \infty$ (Mann, 1953).

The Ishikawa iteration, initially formulated to establish strong convergence for specific mappings in a Hilbert space, is structured as:

$$x_{n+1} = (1 - a_n)x_n + a_nT[(1 - b_n)x_n + b_nTx_n],\ n \in N \tag{7}$$

where $\{a_n\}, \{b_n\} \to 0$ within [0, 1] (Ishikawa, 1974). Interpreting Ishikawa as a two-step Mann iteration allows for distinct parameter sequences. Notably, when $b_n = 0$, Ishikawa iteration reduces to Mann iteration, although their convergence results are generally not equivalent.

To address computational limitations, Agarwal et al. (2007) proposed an S-iteration method applicable to contraction and non-expansive mappings, shown to be more efficient than Picard, Mann, and Ishikawa iterations:

$$\begin{cases} x_{n+1} = (1 - a_n)Tx_n + a_nTy_n \\ y_n = (1 - b_n)x_n + b_nTx_n \end{cases}, n \in N \tag{8}$$

The Thianwan iteration process was defined independently, characterized by:

$$\begin{cases} x_{n+1} = (1 - a_n)y_n + a_nTy_n \\ y_n = (1 - b_n)x_n + b_nTx_n \end{cases}, n \in N \tag{9}$$

where $\{a_n\}$ and $\{b_n\}$ are positive sequences within [0, 1], ensuring $\sum a_n = \infty$.

Finally, Chugh et al. (2014) developed a Noor iteration scheme, known for its three-step process:

$$\begin{cases} x_{n+1} = (1 - a_n)x_n + a_n T y_n \\ y_n = (1 - b_n)x_n + b_n T z_n \quad , n \in N \\ z_n = (1 - c_n)x_n + c_n T x_n \end{cases} \tag{10}$$

where sequences $\{a_n\}, \{b_n\}, \{c_n\} \subset [0, 1]$ and their respective error terms $\{U_n\}$, $\{V_n\}$, $\{W_n\}$ fulfill the conditions $\sum_{n=1}^{\infty}\|U_n\| < \infty, \sum_{n=1}^{\infty}\|V_n\| < \infty, \sum_{n=1}^{\infty}\|W_n\|$ (Chugh et al., 2014).

This section provides a foundation of iterative techniques, with each method contributing uniquely to fixed-point approximation across a range of operators within Banach spaces.

3. Results and Discussion

In this section, we study the convergence and the rate of convergence of three iterative schemes. We present our main results using Z-operators in a Banach space for the iterative schemes with errors, and at the end, we tabulate computational results for the rate of convergence of the Mann and Noor iterations.

The results of the schemes are given in the following theorems:

Let F be a non-empty subset of a normed linear space $(E, \|\cdot\|)$. Let $K: F \to F$ be a self-map of F satisfying the Zamfirescu operator for each$x, y \in F$. Let $\{x_n\}$ be the Mann iterative scheme defined by

$$x_{n+1} = (1 - a_n)x_n + a_n K(x_n) + v_n. \tag{11}$$

If $F(T) \neq \emptyset$, $\sum_{n=1}^{\infty} a_n = \infty$, and $\|V_n\| = 0$, then:

(i) The mapping T has a unique fixed point p;

(ii) The Mann iterative scheme converges strongly to a fixed point of T.

Proof. (i) We first establish that the mapping T has a unique fixed point. Suppose there exist $p_1, p_2 \in FT$ such that $p_1 \neq p_2$ and $\|p_1 - p_2\| > 0$. Then,

$$0 < \|p_1 - p_2\| = \|Tp_1 - Tp_2\| \leq a\|p_1 - p_2\| + 2a\|p_1 - Tp_2\|.$$

This implies

$$\|Tp_1 - Tp_2\| \leq a\|p_1 - p_2\|.$$

Thus,

$$(1 - a)\|p_1 - p_2\| \leq 0.$$

Since $a \in [0,1]$, we have $1 - a > 0$, which leads to $\|p_1 - p_2\| = 0\|$.

Therefore,

$$p_1 = p_2 = p.$$

Hence, T has a unique fixed point p.

(ii)Next, we establish that $\lim_{n\to\infty} x_n = p$, showing that the Mann iterative scheme converges strongly to p.

From the iterative scheme, we have:

$$\begin{aligned}\|x_{n+1} - p\| &= \|(1 - a_n)x_n + a_n K(x_n) - p + V_n\| \\ &= (1 - a_n)\|x_n - p\| + a_n\|K(x_n - p)\| + \|V_n\|. \end{aligned} \quad (12)$$

Now, using the properties of the mapping K, we can deduce that:

$$\|x_{n+1} - p\| \leq (1 - a_n)\|x_n - p\| + a_n\delta\|x_n - p\| + \|V_n\|, \quad (13)$$

leading to:

$$\|x_{n+1} - p\| \leq [1 - (1 - \delta)a_n]\|x_n - p\| + \|V_n\|. \quad (14)$$

Given the assumptions of the theorem and the condition$\|V_n\| = 0$, we find that:

$$\lim_{n\to\infty} \|x_{n+1} - p\| = 0. \quad (15)$$

Thus, the Mann iterative scheme converges strongly to p.

Let F be a non-empty subset of a normed linear space $(E, \|\cdot\|)$. Let $K: F \to F$ be a self-map of F satisfying the Zamfirescu operator for each $x, y \in$x, y ∈ F. Let $\{x_n\}_{n=0}^{\infty}$ be the Noor iterative scheme defined by

$$x_{n+1} = (1 - a_n)x_n + a_n K(y_n) + U_n. \quad (16)$$

If $F(T) \neq \emptyset$, $\sum_{n=1}^{\infty} a_n = \infty$, and $\|V_n\| = 0$, then:

(i) The mapping T has a unique fixed point p;
(ii) The Noor iterative scheme converges strongly to a fixed point of T.

Proof. (i) We first establish that the mapping T has a unique fixed point. Suppose there exist $p_1, p_2 \in F_T$ such that $p_1 \neq p_2$ and $\|p_1 - p_2\| > 0$. Then,

$$0 < \|p_1 - p_2\| = \|Tp_1 - Tp_2\| \leq 2a\|p_1 - Tp_2\| + a\|p_1 - p_2\|.$$

This implies

$$\|Tp_1 - Tp_2\| \leq a\|p_1 - p_2\|.$$

Thus,

$$(1 - a) > 0 \text{ and } \|p_1 - p_2\| \leq 0.$$

Since the norm is non-negative, it follows that $\|p_1 - p_2\| = 0$. Therefore, $p_1 = p_2 = p$.

Hence, T has a unique fixed point p.

(ii) Next, we establish that $\lim_{n\to\infty} x_n = p$, demonstrating that the Noor iterative scheme converges strongly to p. From the iterative scheme, we have:

$$\|K(x_n) - p\| \leq \delta\|x_n - p\| + 2\delta\|x_n - K(x_n)\| \forall x, y \in \mathbb{C}. \quad (17)$$

Applying this to the Noor scheme, we get:

$$\begin{aligned} \|x_{n+1} - p\|) &\leq \|(1 - a_n)x_n + a_n K(x_n) - p + V_n\| \\ &\leq (1 - a_n)\|x_n - p\| + a_n\|K(x_n) - p\| + \|V_n\| \\ &\leq (1 - a_n)\|x_n - p\| + a_n\delta\|x_n - p\| + \|V_n\| \\ &\leq [(1 - a_n) + a_n\delta]\|x_n - p\| + \|V_n\|. \quad (18) \end{aligned}$$

Thus, $\lim_{n\to\infty} \|x_{n+1} - p\| = 0$ as $n \to \infty$. Therefore, the Noor iterative scheme converges strongly to p.

4 **Numerical Example**

In this section, we use the following example to compare our iterative schemes with the help of MATLAB.

The function defined by $f(x) = (1 - x)^2$ is a function with multiple zeros. By taking the initial approximation $x_0 = 0.9$ and $\alpha_n = \beta_n = \frac{1}{2}$, the convergence of these iterative schemes to the exact fixed point $p = 0.38196601$is shown in Table 1 below.

The error estimation ϵ_n in Table 1, choosing n at intervals of 5 iterations, is presented in Table 2, where $\epsilon_n = \|q - x_n\|$.

5. Conclusion

In conclusion, our analysis has demonstrated that the Banach fixed point theorem is inherently constructive. Various methods can be employed to achieve results, with the choice of method

dependent on the specific nature of the problem and the desired outcomes that satisfy the conditions of contraction mappings.

The Banach fixed point theorem has extensive applications across various branches of mathematical science. In this study, we have successfully established the convergence and convergence rates of several iterative schemes with error estimations using the Zamfirescu operator in Banach spaces. Our findings indicate that the Mann iterative method converges faster than the Noor iteration concerning the convergence rate. This insight underscores the importance of selecting appropriate iterative techniques based on their performance characteristics, thus enhancing the efficiency of solving fixed-point problems in practical applications.

n	Mann Iteration	Noor Iteration
0	0.90000000	0.90000000
1	0.45500000	0.53059611
2	0.37601250	0.41092632
3	0.38268645	0.38648213
4	0.38188123	0.38263205
5	0.38197602	0.38396925
6	0.38196483	0.38225969
7	0.38196615	0.38200889
8	0.38196599	0.38197227
9	0.38196601	0.38196692
10	0.38196601	0.38196614
11	0.38196601	0.38196603
12	0.38196601	0.38196601
13	0.38196601	0.38196601
14	0.38196601	0.38196601
15	0.38196601	0.38196601

Table 1: The results for various iterations of the example.

n	Mann Iteration	Noor Iteration
0	0.00001001	0.00200323
1	0.00000000	0.00000013
2	0.00000000	0.00000000
3	0.00000000	0.00000000
4	0.00000000	0.00000000
5	0.00000000	0.00000000

Table 2: The result error estimation for various iterations of the example.

References

Agarwal, R. P., O'Regan, D., & Sahu, D. R. (2007). Iterative construction of fixed points of nearly asymptotically nonexpansive mappings. *Journal of Nonlinear and Convex Analysis, 8(1), 67-79.*

Banach, S. (1922) Sur les op´erations dans les ensembles abstraits et leur application aux ´equations int´egrales, *Fund. Math. 3, 133-181. MR3949898. JFM 48.0201.01.*

Berinde, V. (2007). Iterative approximation of fixed points. *Springer Berlin Heidelberg.*

Chidume, C. E. (1994). Approximation of fixed points of strongly pseudo-contractive mappings. *Proceedings of the American Mathematical Society, 192, 545-551.*

Ishikawa, S. (1974). Fixed points by a new iteration method. *Proceedings of the American Mathematical Society, 44(1), 147-150.*

Koti, N. V., Vara Prasad, J., Jagannadha Rao, G. V. V., & Narasimham, K. V. (2013). Convergence of the Ishikawa iteration process for a general class of functions. *Mathematical Theory and Modeling, 3(6), 133. Retrieved from www.iiste.org*

Mann, W. R. (1953). Mean value methods in iterations. *Proceedings of the American Mathematical Society, 4, 506-510.*

Chugh, V. , Dhiman, R., Gautan, P., & Sharma, S. (2014). Fixed point theorems in metric and probabilistic metric spaces. *Journal of Mathematics and computer Science, 19 (2), 243-252.*

Numerical Assessment of Some Almost Runge-Kutta and Runge-Kutta Methods for First-Order Differential Equation

Khadeejah James Audu[1], Muideen Taiwo Kharashi[2], Yusuph Amuda Yahaya[3], James Nkereuwem Essien[4], Abraham Ajeolu Oluwasegun[5]

[1,2,4,5]Department of Mathematics, Federal University of Technology, Minna, Niger State, Nigeria.
[3] Department of Mathematics, North-Eastern University, Gombe, Nigeria
Corresponding email: k.james@futminna.edu.ng

Abstract

Numerical methods play a critical role in solving first-order Ordinary Differential Equations (ODEs), with their efficiency and accuracy being key considerations. This study conducts a detailed comparative analysis of four numerical schemes: the Almost Runge-Kutta fourth-order scheme (ARK4), the Almost Runge-Kutta third-order fourth-stage scheme (ARK34), the classical Runge-Kutta fourth-order scheme (RK4), and the Runge-Kutta fourth-order fifth-stage scheme (RK45). The methods are evaluated based on their computational accuracy, error behavior, and efficiency. Numerical experiments reveal that all methods deliver highly accurate solutions, with ARK4 emerging as the most effective due to its lower computational complexity. ARK4 demonstrates superior performance in achieving minimal absolute error with reduced computational effort, making it a suitable choice for solving first-order ODEs. This study highlights ARK4 as a viable alternative to conventional Runge-Kutta methods for practical applications.

Keywords: Numerical analysis, runge-kutta method, first-order ODEs, almost runge-kutta method, computational efficiency

1. Introduction

First-order differential equations are essential in describing a multitude of dynamic systems across various scientific and engineering disciplines. In physics, they model essential phenomena such as radioactive decay, Newton's law of cooling, and electrical circuits governed by Ohm's and Kirchhoff's laws. Engineering applications often rely on first-order differential equations to design and analyze systems, including control systems, thermal dynamics in buildings and fluid flow in pipelines. In finance, these equations are critical for modeling the time evolution of economic variables, such as interest rates and stock prices, which are pivotal for investment strategies and risk management. (Arora and Joshi, 2020; Audu *et al.* 2023; Benjamin and Okisamen, 2020; Audu *et al*. 2024).

The precise and efficient resolution of these equations is vital for progress in these areas. Traditional analytical approaches frequently prove inadequate because of the complexity and nonlinearity present in many real-world challenges, requiring the application of numerical methods. Among these, the Runge-Kutta methods are notable for their balance of simplicity, effectiveness, and precision. The fourth-order, four-stage Runge-Kutta method (RK4) and fourth-order, five-stage Runge-Kutta method (RK45) are particularly renowned for their ability to provide

high-precision solutions with relatively modest computational effort (Esekhaigbe and Aitusi, 2022; Workineh *et al.*, 2024; Paudel and Bhatta, 2023; Hetmaniok and Pleszczyński, 2022; Sundaram, 2022). Researchers in their works (Shior *et al.*, 2024; Kalogiratou *et al.*, 2020) provided essential insights into their accuracy, stability, and computational efficiency. However, ongoing research aims to enhance these methods further, leading to the development of variants such as the Almost Runge-Kutta (ARK) method. ARK method was developed by Rattenbury (2005) and other researchers (Abraham, 2010; Alimi, 2014; Ishaq, 2017; Adeboye *et al*., 2013; Ndanusa and Audu, 2016a) have improved on the method in establishing the third-order, four- stage (ARK34) method and fourth-order Almost Runge-Kutta method (ARK4) method. These ARK methods seek to improve upon the classical approaches by offering better stability and accuracy under certain conditions, making them a compelling subject for comparative analysis. Research on numerical methods for solving first-order differential equations lacks comprehensive comparative studies between Almost Runge-Kutta methods (ARK34 and ARK4) and Runge-Kutta methods (RK4 and RK45). A detailed investigation into their accuracy, stability and efficiency could offer valuable insights into their respective strengths and applications.

This paper presents a direct comparison of the selected methods by highlighting their errors and proximity of the approximate solution to the exact solution when used to solve equation of the form

$$\frac{dt}{du} = t'(u) = f(t,u) \tag{1}$$

The study fills a key gap in numerical analysis by comparing the selected methods. Its findings offer practical guidance for selecting optimal numerical techniques, improving simulations, and optimizing computational resources for solving complex first-order differential equations.

2. Materials and Methods

In this section, we analyzed the four methods chosen for the numerical assessment on first-order differential equations.

2.1 The Runge-Kutta Fourth-Order Method

Given a first-order differential equation in the form of (1), the RK4 method for solving ODE can be expressed in the following equation

$$t_{b+1} = t_b + \frac{s}{6}\left(\underline{k}_1 + 2\underline{k}_2 + 2\underline{k}_3 + \underline{k}_4\right) \tag{2}$$

where the stages $\left(\underline{k}_1, \underline{k}_2, \underline{k}_3 \; and \; \underline{k}_4\right)$ are represented in (3)

$$\begin{aligned} \underline{k}_1 &= f\left(t_b, u_b\right) \\ \underline{k}_2 &= f\left(t_b + \frac{s}{2}, u_b + \frac{\underline{k}_1}{2}\right) \\ \underline{k}_3 &= f\left(t_b + \frac{s}{2}, u_b + \frac{\underline{k}_2}{2}\right) \qquad b = 0, 1, 2, 3, 4, \cdots, M \\ \underline{k}_4 &= f\left(t_b + s, u_b + \underline{k}_3\right) \end{aligned} \tag{3}$$

with an initial estimates (u_0 and t_0), step interval (s) and a total number of steps (M **),** the popular RK4M can be employed to compute solutions of any linear or non-linear ODEs utilising the following steps:

Step 1: Express the function $f(t,u)$ in a way such that $f(t,u) \in [q, f]$, select the step interval $\left(s = \frac{f-q}{M}\right)$ and initialize $t = t_0, u = u_0$.

Step 2: Iterate through M steps for each step $b = 0, 1, 2, 3, 4, \cdots, M$ and repeatedly perform the tasks:

(i) Compute the intermediate values $\underline{k}_1, \underline{k}_2, \underline{k}_3$ *and* $\underline{k}_4$ as represented in equation (3).

(ii) Update the solution t: $t_{b+1} = t_b + \frac{s}{6}\left(\underline{k}_1 + 2\underline{k}_2 + 2\underline{k}_3 + \underline{k}_4\right)$.

(iii) Update the independent variable $u : u_{b+1} = u_0 + bS$.

Step 3: Return the final solution after M iterations or output approximate solutions t_b for u_b.

Step 4: Terminate the procedure if $t_b \geq f$ provided that $\left\| t_{b+1} - t_b \right\| < \varepsilon$.

2.2 The Runge-Kutta Five Stage Fourth-Order Method

The explicit Runge-Kutta method of fourth-order with five stages, denoted by $k_1, ..., k_5$ for a single step, enables the solution of the equation using the general Runge-Kutta principles stated in works of authors (Fawzi *et al*., 2024). The RK45 method considered by Benjamin and Okisamen (2020) for obtaining solutions regarding first-order ODE can be expressed in the relation

$$t_{b+1} = t_b + \frac{s}{6}\left(\underline{k}_1 + 4\underline{k}_3 + \underline{k}_5\right) \tag{4}$$

where the stages $\left(\underline{k}_1, \underline{k}_3 \text{ and } \underline{k}_5\right)$ are denoted in (5)

$$\begin{aligned}
\underline{k}_1 &= f\left(t_b\right) \\
\underline{k}_2 &= f\left(t_b + \frac{s}{4}\underline{k}_1\right) \\
\underline{k}_3 &= f\left(t_b + s\left[\frac{1}{4}\underline{k}_1 + \frac{1}{4}\underline{k}_2\right]\right) \qquad b = 0, 1, 2, 3, 4, \cdots, M \\
\underline{k}_4 &= f\left(t_b + s\left[\frac{17}{8}\underline{k}_1 + \frac{4}{8}\underline{k}_2 - \frac{15}{8}\underline{k}_3\right]\right) \\
\underline{k}_5 &= f\left(t_b + s\left[-\frac{7}{4}\underline{k}_1 + \frac{9}{4}\underline{k}_2 + \frac{3}{4}\underline{k}_3 - \frac{1}{4}\underline{k}_4\right]\right)
\end{aligned} \tag{5}$$

Focusing on the RK45 formula in equations 4 and 5, if given an initial guess (u_0 and t_0) with step interval (s) for a total number of steps (M **),** then the numerical RK45 method can be applied in solving any linear or non-linear ODEs using the following procedure as follows:

Step 1: Express the function $f(t,u)$ in a way such that $f(t,u) \in \left[q, f\right]$, select the step interval $\left(s = \frac{f-q}{M}\right)$ and initialize $t = t_0, u = u_0$.

Step 2: Iterate through M steps for each step $b = 0, 1, 2, 3, 4, \cdots, M$ and repeat the following:

(i) Compute the intermediate values $\underline{k}_1, \underline{k}_2, \underline{k}_3, \underline{k}_4 \text{ and } \underline{k}_5$ as stated in equation (5).

(ii) Update the solution t: $t_{b+1} = t_b + \frac{s}{6}\left(\underline{k}_1 + 4\underline{k}_3 + \underline{k}_5\right)$.

(iii) Update the independent variable $u : u_{b+1} = u_0 + bS$.

Step 3: Return the final solution after M iterations, that is return t_b

Step 4: Terminate the procedure if $t_b \geq f$ provided that $\left\|t_{b+1} - t_b\right\| < \varepsilon$.

2.3 The Almost Runge-Kutta Method

2.3.1 The Third-Order, Four-Stage ARK Method

The general third-order four stages scheme for ARK method is governed by (6)

$$\left[\begin{array}{c|c} M & \underline{U} \\ \hline N & P \end{array}\right] = \left[\begin{array}{cccc|ccc} 0 & 0 & 0 & 0 & 1 & \underline{c}_1 & \frac{1}{2}\underline{c}_1^2 \\ m_{21} & 0 & 0 & 0 & 1 & \underline{c}_2 - m_{21} & \frac{1}{2}\underline{c}_2^2 - m_{21}\underline{c}_1 \\ m_{31} & m_{32} & 0 & 0 & 1 & \underline{c}_3 - m_{31} - m_{32} & \frac{1}{2}\underline{c}_3^2 - m_{31}\underline{c}_1 - m_{32}\underline{c}_2 \\ n_1 & n_2 & n_3 & 0 & 1 & n_0 & 0 \\ \hline n_1 & n_2 & n_3 & 0 & 1 & n_0 & 0 \\ 0 & 0 & 0 & 1 & 0 & 0 & 0 \\ \lambda_1 & \lambda_2 & \lambda_3 & \lambda_4 & 0 & \lambda_0 & 0 \end{array}\right] \tag{6}$$

The four matrices M, N, $\underline{U}$ and P are utilized to construct the ARK methods where $M = [m_{ij}]$ s,s, $N = [n_{ij}]$ r,s, $\underline{U} = [\underline{u}_{ij}]$ s,r and $P = [p_{ij}]$ r,r . These methods transfer values in between steps for different stages. *r* represents the transferred quantity (valued) and *s* denotes the desired stage. The vector of abscissa is denoted as

$$\underline{c} = \begin{bmatrix} \underline{c}_1 \\ \underline{c}_2 \\ \underline{c}_3 \\ 1 \end{bmatrix}, \quad n = \begin{bmatrix} n_1 \\ n_2 \\ n_3 \\ 0 \end{bmatrix}, \quad \lambda = \begin{bmatrix} \lambda_1 \\ \lambda_2 \\ \lambda_3 \\ \lambda_4 \end{bmatrix}$$

Many authors have developed various ARK34M suitable for solving initial value problems related to first-order (Ndanusa and Audu, 2016; Butcher, 1997; Rattenbury, 2005; Ochoche, 2011). However, this study will consider the variant formulated by Ndanusa and Audu (2016b). A representation of the selected ARK34 method with $\underline{c}^T = [0.25, 0.5, 1.0, 1.0]$ is

$$\left[\begin{array}{c|c} M & \underline{U} \\ \hline N & P \end{array}\right] = \left[\begin{array}{cccc|ccc} 0 & 0 & 0 & 0 & 1 & 0.50 & 0.03125 \\ 0.89 & 0 & 0 & 0 & 1 & -0.39 & -0.0972 \\ -0.67 & 0.50 & 0 & 0 & 1 & 1.167 & 0.4167 \\ 0 & 0.67 & 0.17 & 0 & 1 & 0.17 & 0 \\ \hline 0 & 0.67 & 0.17 & 0 & 1 & 0.17 & 0 \\ 0 & 0 & 0 & 1 & 0 & 0 & 0 \\ -0.89 & 0 & -0.67 & 2 & 0 & -0.444 & 0 \end{array}\right] \tag{7}$$

2.3.2 The Fourth-Order, Four-Stage ARK Method

A general fourth-order, four-stage concerning ARK method is equally governed by the representation in equation (5). This study is interested in employing the ARK4 method constructed by Ndanusa and Audu (2016a) for the solutions of first-order ODE. The selected method with

$\underline{c}^T = [0.4412, 0.5, 1.0, 1.0]$, $\lambda_4 = 4$ is presented as

$$\left[\begin{array}{c|c} M & \underline{U} \\ \hline N & P \end{array}\right] = \left[\begin{array}{cccc|ccc} 0 & 0 & 0 & 0 & 1 & 0.4412 & 0.0097 \\ 0.1510 & 0 & 0 & 0 & 1 & 0.3495 & 0.0586 \\ -0.6021 & 2 & 0 & 0 & 1 & -0.3979 & -0.2344 \\ 0 & 0.6667 & 0.1667 & 0 & 1 & 0.1667 & 0 \\ \hline 0 & 0.6667 & 0.1667 & 0 & 1 & 0.1667 & 0 \\ 0 & 0 & 0 & 1 & 0 & 0 & 0 \\ -12.844 & 10.667 & -2.6667 & 4 & 0 & -0.844 & 0 \end{array}\right] \tag{8}$$

3. Numerical Investigations

This section aims to compare the performance of the four numerical methods discussed in the previous section for solving ordinary differential equations. The computations were conducted using Maple 2021 software and Python 2021 software to obtain the desired results for the problems.

Problem 1: We solve the ODE using the 4 methods.

$u' = t + u \qquad s = 0.1$, within the interval $0 \le t \le 1$

Exact solution can be obtained from the relation $u_E(t) = 2e^t - t - 1$

Problem 2: The ODE is solved using ARK34, ARK4, RK4 and RK45.

$u' = \frac{u}{4}\left(1 - \frac{u}{20}\right), \quad s = 0.1 \qquad 0 \le t \le 1,$

The exact solution is $u_E(t) = \frac{20}{1 + 19e^{\frac{-t}{4}}}$

Problem 3: We resolve the following ODE by methods of ARK34, ARK4, RK4 and RK45.

$u' = \frac{u+t}{u-t}, \quad u_0 = 1, \quad t_0 = 0, \quad s = 0.1, \quad 0 \le t \le 1$

Exact solution = $u_E(t) = t + \sqrt{1 + 2t^2}$

The computational and graphical results of problems 1 to 3 are tabulated in the following Tables and Figures.

Table 3.1: Numerical Output of RK4 and RK45 for Problem 1

t	Exact	RK4	RK4 Error	RK45	RK45 Error
0.0	1.0000000000	1.0000000000	0.0000000000	1.0000000000	0.0000000000
0.1	1.1103418362	1.1103416667	0.0000001695	1.1103417643	0.0000000718
0.2	1.2428055163	1.2428051417	0.0000003746	1.2428053576	0.0000001588
0.3	1.3997176152	1.3997169941	0.0000006210	1.3997173520	0.0000002632
0.4	1.5836493953	1.5836484802	0.0000009151	1.5836490074	0.0000003878
0.5	1.7974425414	1.7974412772	0.0000012642	1.7974420056	0.0000005358
0.6	2.0442376008	2.0442359242	0.0000016766	2.0442368902	0.0000007105
0.7	2.3275054149	2.3275032532	0.0000021617	2.3275044988	0.0000009162
0.8	2.6510818570	2.6510791266	0.0000027304	2.6510806998	0.0000011572
0.9	3.0192062223	3.0192028276	0.0000033948	3.0192047836	0.0000014387
1.0	3.4365636569	3.4365594883	0.0000041686	3.4365618902	0.0000017667

Table 3.2: Numerical Output of ARK4 and ARK34 for Problem 1

t	Exact	ARK4	ARK4 Error	ARK34	ARK34 Error
0.0	1.0000000000	1.0000000000	0.0000000000E+00	1.0000000000	0.0000000000E+00
0.1	1.1103418362	1.1103416667	7.1899999954E-08	1.1103384722	3.3639999999E-06
0.2	1.2428055163	1.2428051417	2.6670000008E-07	1.2427988608	6.6555000000E-06
0.3	1.3997176152	1.3997169941	5.0180000000E-07	1.3997069895	1.0625700000E-05
0.4	1.5836493953	1.5836484801	7.8329999997E-07	1.5836340388	1.5356500000E-05
0.5	1.7974425414	1.7974412771	1.1185000000E-06	1.7974215765	2.0964900000E-05
0.6	2.0442376008	2.0442359241	1.5155999997E-06	2.0442100176	2.7583200000E-05
0.7	2.3275054149	2.3275032531	1.9838000003E-06	2.3274700532	3.5361700000E-05

0.8	2.6510818570	2.6510791265	2.5338000000E-06	2.6510373858	4.4471200000E-05
0.9	3.0192062223	3.0192028275	3.1774000000E-06	3.0191511166	5.5105700000E-05
1.0	3.4365636569	3.4365594882	3.9284000004E-06	3.4364961717	6.7485200000E-05

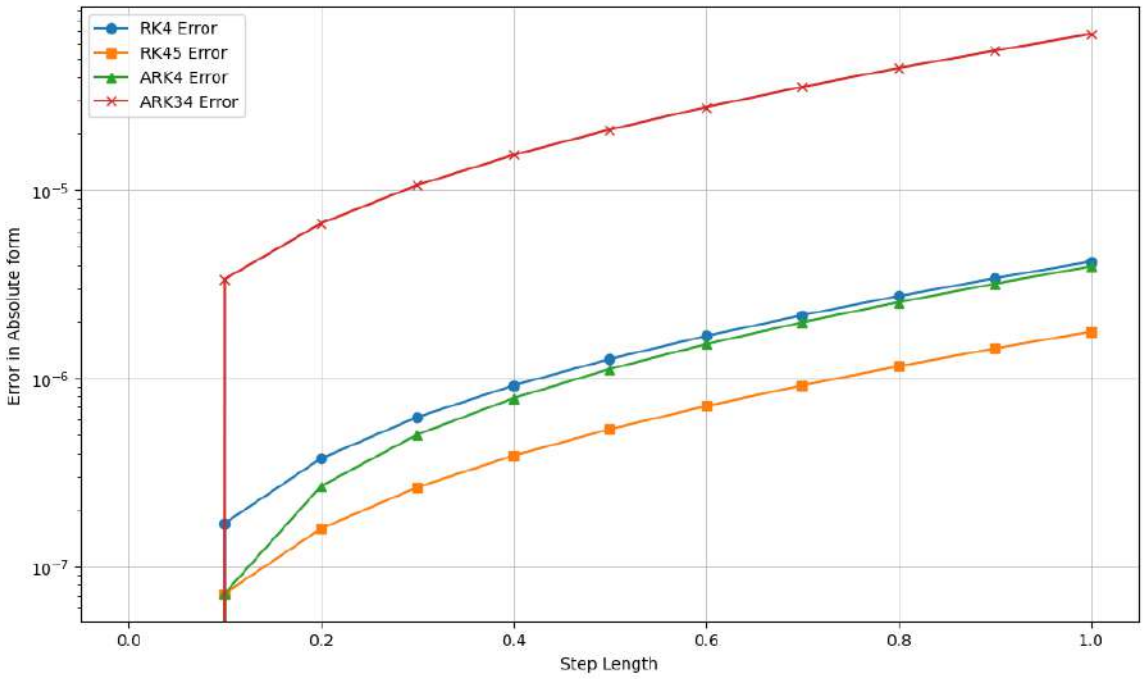

Figure 1. Error graph for problem 1

The provided graph illustrates the calculated errors for ARK 34, ARK 4, RK 4, and RK45 in relation to problem 1.

Table 3.3: Numerical Output of RK4 and RK45 for Problem 2

t	Exact	RK4	RK4 Error	RK45	RK45 Error
0.0	1.0000000000	1.0000000000	0.0000000000	1.0000000000	0.0000000000
0.1	1.0240189624	1.0240189623	0.0000000001	1.0240189623	0.0000000001
0.2	1.0485829964	1.0485829963	0.0000000001	1.0485829963	0.0000000001
0.3	1.0737029288	1.0737029287	0.0000000001	1.0737029287	0.0000000001
0.4	1.0993897267	1.0993897265	0.0000000002	1.0993897265	0.0000000002

0.5	1.1256544953	1.1256544950	0.0000000003	1.1256544950	0.0000000003
0.6	1.1525084759	1.1525084755	0.0000000004	1.1525084755	0.0000000004
0.7	1.1799630432	1.1799630427	0.0000000005	1.1799630428	0.0000000004
0.8	1.2080297028	1.2080297022	0.0000000006	1.2080297023	0.0000000005
0.9	1.2367200876	1.2367200870	0.0000000006	1.2367200871	0.0000000005
1.0	1.2660459552	1.2660459545	0.0000000007	1.2660459546	0.0000000006

Table 3.4: Numerical Output of ARK4 and ARK34 for Problem 2

t	Exact	ARK4	ARK4 Error	ARK34	ARK34 Error
0.00	1.0000000000	1.0000000000	0.0000000000E+00	1.0000000000	0.0000000000E+00
0.1	1.0240189623	1.0240189623	0.0000000000E+00	1.0240189584	3.9000001010E-09
0.2	1.0485829964	1.0485829963	1.0000000830E-10	1.0485829943	2.0999999520E-09
0.3	1.0737029289	1.0737029287	2.0000001650E-10	1.0737029286	3.0000002480E-10
0.4	1.0993897267	1.0993897266	1.0000000830E-10	1.0993897285	1.8000001490E-09
0.5	1.1256544953	1.1256544951	2.0000001650E-10	1.1256544992	3.8999998790E-09
0.6	1.1525084759	1.1525084756	3.0000002480E-10	1.1525084820	6.1000000610E-09
0.7	1.1799630432	1.1799630429	2.9999980280E-10	1.1799630516	8.4000000290E-09
0.8	1.2080297028	1.2080297024	4.0000003310E-10	1.2080297136	1.0800000010E-08
0.9	1.2367200876	1.2367200871	5.0000004140E-10	1.2367201010	1.3400000000E-08
1.0	1.2660459552	1.2660459547	5.0000004140E-10	1.2660459713	1.6100000000E-08

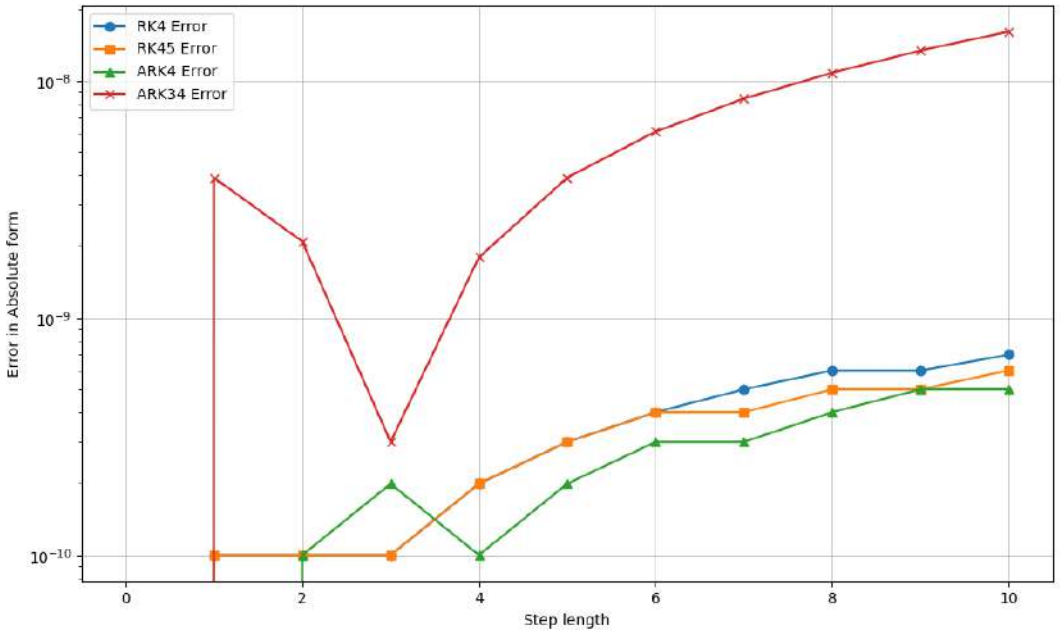

Figure 1. Error graph for problem 2

The provided graph displays the computed errors for ARK 34, ARK 4, RK 4, and RK45 in relation to Problem 2.

Table 3.5: Numerical Output of RK4 and RK45 for Problem 3

t	Exact	RK4	RK4 Error	RK45	RK45 Error
0.0	1.0000000000	1.0000000000	0.0000000000	1.0000000000	0.0000000000
0.1	1.1099504938	1.1099505755	0.0000000817	1.1066539351	0.0032965588
0.2	1.2392304845	1.2392307736	0.0000002891	1.2329046017	0.0063258829
0.3	1.3862780491	1.3862785808	0.0000005317	1.3774301541	0.0088478950
0.4	1.5489125293	1.5489132614	0.0000007321	1.5381571140	0.0107554153
0.5	1.5489125293	1.7247457310	0.0000008596	1.7126819218	0.0120629496
0.6	1.9114877049	1.9114886243	0.0000009194	1.8986292382	0.0128584666
0.7	2.1071247279	2.1071256588	0.0000009309	2.0938695410	0.0132551870
0.8	2.3099668871	2.3099677997	0.0000009126	2.2966059595	0.0133609276
0.9	2.5186414056	2.5186422842	0.0000008786	2.5053765792	0.0132648264
1.0	2.7320508076	2.7320516450	0.0000008374	2.7190159000	0.0130349076

Table 3.6: Numerical Output of ARK4 and ARK34 for Problem 3

t	Exact	ARK4	ARK4 Error	ARK34	ARK34 Error
0.0	1.0000000000	1.0000000000	0.0000000000E+00	1.0000000000	0.0000000000E+00
0.1	1.1099504938	1.1099505178	2.3999999987E-08	1.1099504239	6.9900000010E-08
0.2	1.2392304845	1.2392307341	2.4960000000E-07	1.2392278329	2.6516000000E-06
0.3	1.3862780491	1.3862786072	5.5809999999E-07	1.3862720147	6.0343999999E-06
0.4	1.5489125293	1.5489133617	8.3240000004E-07	1.5489029640	9.5652999998E-06
0.5	1.7247448714	1.7247458896	1.0182000001E-06	1.7247322162	1.2655200000E-05
0.6	1.9114877049	1.9114888194	1.1144999998E-06	1.9114727000	1.5004900000E-05
0.7	2.1071247279	2.1071258718	1.1439000001E-06	2.1071081495	1.6578400000E-05
0.8	2.3099668871	2.3099680179	1.1308000003E-06	2.3099494034	1.7483700000E-05
0.9	2.5186414056	2.5186424999	1.0942999999E-06	2.5186235316	1.7874000000E-05
1.0	2.7320508076	2.7320518540	1.0464000000E-06	2.7320329124	1.7895200000E-05

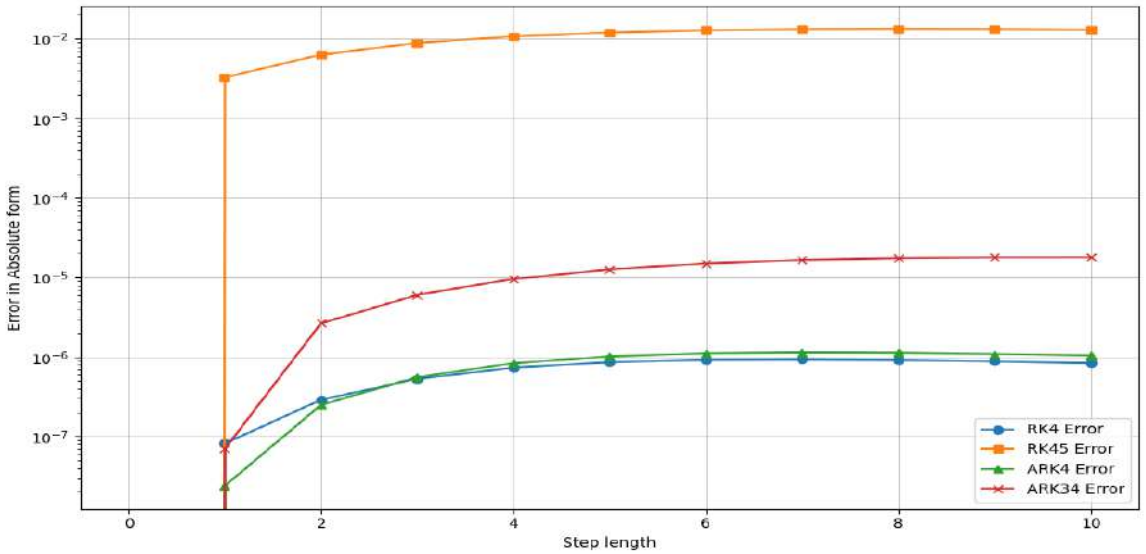

Figure 1. Error graph for problem 3

The provided graph presents the computed errors of ARK34, ARK4, RK4 and RK45 in relation to problem 3.

4. Discussion of Results

The results obtained are presented in Tables 1-6. The approximate numerical solutions were calculated using step size 0.1 and the results were compared with the exact solution. Further analysis on the error was carried out using graphical representation. The results provide insights into the efficiency of these numerical techniques.

Comparison of Numerical Approximations (Tables 1-6)

i. The tables indicate that using a consistent step size of 0.1, the RK4, RK45, ARK4, and ARK34 methods yield numerical solutions for all three problems that closely match the analytical results.
ii. The results from the RK4, RK45, ARK4, and ARK34 methods exhibit some variation, indicating that these approaches offer comparable levels of approximation to the exact solution.
iii. The findings highlight the efficiency of the four numerical methods in addressing the specified problems.

Error Comparison (Figures 1-3)

i. The graphical error representations yield a deeper insight into the effectiveness of each technique.
ii. It is evident that the ARK4 method consistently produces more accurate results and exhibits lower error values compared to the other methods.
iii. The error curves for the ARK4 method shown in Figures 1-3 demonstrate a trend toward zero, indicating convergence to the exact solution as long as the step size is kept constant.

Discoveries

i. The comparative assessment clearly demonstrates that the ARK4 method surpasses the other three approaches in solving Problems 1-3.
ii. The ARK4 technique stands out for its high accuracy and efficiency, consistently converging to the analytical solution with minimal error.

5. Conclusion

This study compared four numerical methods applied to solve first-order ordinary differential equations. Extensive numerical exploration yielded compelling results, demonstrating the exceptional accuracy of all four methodologies. An analysis of the result tables and graphical figures indicated that all methods converged. Error comparisons revealed that the ARK4 method provides more accurate results than the RK4, RK45, and ARK34 methods. The comparative assessment highlights the relative advantages and disadvantages of the RKMs and ARKMs concerning accuracy and computational efficiency. The findings of this research have practical implications for both researchers and practitioners in the field of numerical methods for differential equations. They enhance the understanding of the trade-offs involved in selecting an appropriate numerical method for specific problem types and guide the application of the ARK4 method in real-world scenarios. Future research would focus on conducting a comparative study of ARK4 with various numerical approaches for higher-order differential equations, such as second-order ODEs.

References

Aida, M. (2022). Fourth-Order Runge-Kutta Method for Solving Applications of System of First-Order Ordinary Differential Equations. *Enhanced Knowledge in Sciences and Technology*, *2*(1), 517-526. https://doi.org/10.30880/ekst.2022.02.01.056

Adeboye, K. R., Ochoche, A. & Olumide A. K. (2013). On Error Estimation in Almost Runge-Kutta (ARK) Methods. *Journal of Applied Mathematics & Bioinformatics, 3*(2)*,* 2013, 125-135.

Arora, G. & Joshi, V. (2020). Developments in Runge–Kutta Method to Solve Ordinary Differential Equations, *Recent Advances in Mathematics for Engineering*, 1-11.

Audu, K. J., Taiwo, A. R. & Soliu, A. A. (2023). Assessment of Numerical Performance of Some Runge-Kutta Methods and New Iteration Method on First Order Differential Problems. *Dutse Journal of Pure and Applied Sciences*, *9*(4a), 58-70. https://dx.doi.org/10.4314/dujopas.v9i4a.5

Audu, K. J., Udoh, V. J. & Garba, J. (2025). An Investigation Comparison of Higher Order Runge Kutta techniques for resolving first order differential equations," *Turkish Journal of Science and Technology*, *20*(2), 1-15. https://doi.org/10.55525/tjst.1433935

Abraham, O. & Adeboye, K. R. (2009). *On the derivation of third-order Almost Runge-Kutta (ARK) methods with four stages* $(s = 4, p = 3)$. Paper presented at the *28th Annual Conference of Nigerian Mathematical Society,* University of Ilorin, Ilorin, Nigeria.

Abraham, O. (2010). *Development of some new classes of explicit Almost Runge-Kutta methods for non-stiff differential equations*. Unpublished doctoral dissertation. Federal University of Technology, Minna, Nigeria.

Alimi, O. K. (2014). *On the performance of Richardson extrapolation technique in estimating local truncation errors for explicit Almost Runge-Kutta methods.* Unpublished Master's thesis, Federal University of Technology, Minna, Nigeria.

Butcher, J. C. (1997). An introduction to Almost Runge-Kutta methods. *Applied Numerical Mathematics*, 24, 331-342. https://doi.org/10.1016/S0168-9274(97)00030-5

Benjamin, O. C. & Okisamen, A. B. (2020). On the Derivation and Implementation of a Fifth-Stage Fourth-Order Formula for Solving Initial Value Problems in Ordinary Differential Equations, *Journal of Mathematics*, *16*(4), 29-39. https://doi.org/10.9790/5728-1604042939

Esekhaigbe, A. C., & Aitusi, D. (2022). On the Consistency and Convergence Analysis of a Derived Explicit Fourth-Stage Fourth-Order Runge-Kutta Method. *Journal of Advance Research in Mathematics and Statistics, 9*(1), 29-35. https://doi.org/10.61841/9hxxvy46

Fawzi, F. A., Mechee, M. S. & AbdAllah, S. M. (2024). Development and Analysis of Embedded Explicit Runge-Kutta Methods for Directly Solving Special Fifth-Order Quasi-Linear Ordinary Differential Equations. *Mathematical Modelling of Engineering Problems*, *11*(8), 2136-2142. https://doi.org/10.18280/mmep.110815

Hetmaniok, E. & Pleszczyński, M. (2022). Comparison of the selected methods used for solving the ordinary differential equations and their systems, *Mathematics*, *10*(3), 06 **https://doi.org/10.3390/math10030306**

Ishaq, Z. A. (2017). Some Explicit Almost Runge – Kutta Methods of Orders Four and Five. Unpublished BTech thesis, Federal University of Technology, Minna, Nigeria.

Ndanusa, A., & Audu, K. J. (2016a). Design and Analysis of Some Third-Order Explicit Almost Runge-Kutta Methods. *Journal of Applied Mathematics, 2016,* 6, 13-21. https://doi.org/10.4236/am.2016.71002

Ndanusa, A. & Audu, K. J. (2016b). On Fourth and Fifth Order Explicit Almost Runge-Kutta Methods, *International Journal of Scientific and Innovative Mathematics Research*, *4*(1), 88-96. https://doi.org/10.4236/am.2016.71002

Paudel, D. R. & Bhatta, M. R. (2023). Comparative Study of Euler's Method and Runge-Kutta Method to Solve an Ordinary Differential Equation through a Computational Approach, *Academic Journal of Mathematics Education*, *6*(1), 81-85. https://doi.org/10.3126/ajme.v6i1.63802

Shior, M. M., Agbata, B. C., Gbor, G. D., Ezugorie, I. U., Topman, N. N. (2024) Solution of First Order Ordinary Differential Equations Using Fourth Order Runge-Kutta Method with MATLAB, *International Journal of Mathematics and Statistics Studies*, *12* (1), 54-63. https://doi.org/10.37745/ijmss.13

Sundaram, A. (2022). Application of runge – kutta method to population equations, *International Journal for Research in Applied Science and Engineering Technology*, 10(4), 719–724. https://doi.org/10.22214/ijraset.2022.41358

Workineh,Y., Mekonnen, H. & Belew, B. (2024). Numerical methods for solving second-order initial value problems of ordinary differential equations with Euler and Runge-Kutta fourth-order methods. *Frontier Applications in Mathematics and Statistics*. 10, 1360628. https://doi.org/10.3389/fams.2024.1360628

An Approximate Solution of Some Nonlinear Fractional Partial Phenomena in Mathematical Physics Using Laplace Differential Transform Method

Musilimu Taiwo[1], Gabriel. O. Olupitan[2], Musibau A. Omoloye[3] and Kehinde, F. Adedapo[4]
[1,2,4]Department of Physical and Chemical Sciences, Federal University of Health Sciences, Ila-Orangun, Nigeria
[3]Department of Mathematical Science, Nigerian Defence Academy Kaduna, Nigeria

Corresponding author email: musilimu.taiwo@fuhsi.edu.ng

Abstract

In this work, we demonstrate the Laplace transform coupled with the differential transform method LDTM for solving nonlinear fractional partial differential equations in the Caputo sense. An iterative procedure is defined to investigate the approximate solution to the proposed fractional Kaup-Kupershmidt and generalized fractional Drinfeld-sokolov equations. We compared the numerical result with an exact solution at $\propto = 1$ classical order and different values of $\propto$ are presented which demonstrates the efficiency, validity and applicability of the scheme for many other nonlinear fractional differential equation in mathematical physics.

Keywords: Fractional Kaup-Kupershmidt, Generalized Fractional Drinfeld-sokolov equations, Laplace Differential Transform Method, Nonlinear Partial differential equations.

1. Introduction

In the last three decades, fractional differential equations have gained much attention from researchers due to their broad enhancement in the mathematical modeling of physical issues used in various fields of engineering and applied sciences. The use of fractional calculus in fluid mechanics, Biology, Chemistry, Economics and image processing has greatly impacted research in these fields [3][5][7][11]. Currently, fractional calculus has been very helpful in several research which include fluid flow dynamics, signal processing and optics, application of dynamic processing in self-similar and porous structures, diffusion and diffusive transport systems, applied probability and statistics, Bio-chemical physics, Viscosity, Viscoelasticity and Electrochemistry of corrosion, Optics and Signal processing just to mention but few [14][16][19][20][21]. Severally, fractional order differential equations have been to describe more accurately physical phenomenon than the conventional classical order, giving more stable convergence and stability of the system of differential equations The above therefore gives strong motivation for finding numerical solutions of fractional order differential equations.

However, nonlinear partial differential equations (NLPDEs) which are commonly used to express complex dynamical processes from real life scenarios around us are useful mathematical models for this study. The application of NLPDEs are common in field of science and engineering such as fluid dynamics, plasma physics, hydrodynamics, solid state physics, optical fibers, and acoustics, and in several other disciplines.

In the recent year, lot of attempts has been made at finding appropriate solutions of NLPDEs and their applications, which has led to the involvement of several mathematical techniques in the solution of NLPDEs. In the same vein, dynamical techniques like Adomian decomposition method (ADM) [1], Variational Iteration (VIM) [2], Homotopy Perturbation (HPM) [8], Homotopy Analysis (HAM) [9], *F*-Expansion [10], Exp-function [11], differential transform method (DTM) [12–16], and reduced differential transform [17-18] have all been applied on a wide range of systems of linear and nonlinear problems of diversified physical nature. In this research, we apply Laplace transform coupled with differential transform method (LDTM) in Caputo sense, subject to the appropriate initial conditions to solve the popular fractional Kaup-Kupershmidt equation and the generalized fractional Drinfeld- Sokolov equations.

2. Definitions

Basic definition of the generalized Laplace transform, Riemann-Liouville and Caputo fractional derivatives are given below:

Definition 2.1: Let $f(x)$ be a function defined for $x \geq 0$. The Laplace transform of $f(x)$ denoted by $\boldsymbol{F}(s) = \boldsymbol{\mathcal{L}}\{f(x)\}$ is defined as [25-28]

$$\boldsymbol{F}(x) = \{f(x)\} = \int_0^{\infty} e^{-sx} f(x)dx,$$

$$\boldsymbol{F}(s) = \{f(x)\} = \int_0^{\infty} e^{-sx} dx,$$

$$= \lim_{a\to\infty} \int_0^{a} e^{-sx} f(x)dx.$$

Also, the inverse Laplace transform denoted by $\boldsymbol{\mathcal{L}}^{-1}\{\boldsymbol{F}(s)\}$ is equal $f(x)$ if and only if $\boldsymbol{F}(s) = \{f(x)\}$.

The table below show the Laplace transform of some functions calculated with the help of definition 2.1.

$f(x)$	$\boldsymbol{F}(s)$
1	$\frac{1}{s}$
$x^n, n = 1,2, \ldots$	$\frac{n!}{s^n + 1}$
e^{bx}	$\frac{1}{s-b}, s > a$
$\sin(bx)$	$\frac{b}{s^2 + b^2}$
$\cos(bx)$	$\frac{s}{s^2 + b^2}$
$\sinh(bx)$	$\frac{b}{s^2 - b^2}$
$\cosh(bx)$	$\frac{s}{s^2 - b^2}$
$\mathcal{L}\{f'(x)\}$	$s\mathcal{L}\{f(x)\} - f(0)$
$\mathcal{L}\{f^{(n)}(x)\}$	$s^n\mathcal{L}\{f(x)\} - s^{n-1}f'(0) - s^{n-2}f''(0) - \cdots - sf^{(n-1)}(0) - f^{(n)}(0)$

Definition 2.2: The fractional integral of Riemann-Liouville type of order $\alpha\epsilon(0,1)$ of a function $f \in L'(0,\infty), R)$, is defined as [22][23]

$$J^{\propto} f(t) = \frac{1}{\Gamma(\alpha)} \int_0^{t} (t-s)^{\propto-1} f(s)ds,$$

Provided that the integral on the right-hand side of (1.2) converges point-wise on $(0,\infty)$.

Definition 2.3: The Caputo fractional order derivative of a function f on the interval $(0,\infty) \times (0,\infty)$ is defined as [22][24]

$$D^{\alpha} f(x,t) = \frac{1}{\Gamma(n-\alpha)} \int_0^{t} (t-s)^{n-\alpha-1} f^{(n)}(x,s)ds,$$

Where $n = [\alpha] + 1$ and $[\alpha]$ represents the integer part of α. In particular for $0 < \alpha < 1$, one has

$$D^{\alpha}f(x,t) = \frac{1}{\Gamma(1-\alpha)}\int_0^t \frac{1}{(t-s)^{\alpha}}\frac{\partial}{\partial s}f(x,s)ds.$$

Definition 2.4: The Laplace transform of Caputo derivative defined as [23]

$$\mathcal{L}[D^{\alpha}f(x,t)] = s^{\alpha}f(x,s) - \sum_{k=0}^{n-1} s^{\alpha-k-1}f^{(k)}(0),$$

$$\mathrm{n}-1 < \alpha < n, \qquad n \in N$$

We consider fractional derivate in the Caputo sense, which allows for easy interpretation of initial conditions and boundary values. Such that when bounded, the derivative of the constant is equal to zero

3. The concept of Laplace Differential Transform Method

According to Adomian (1994); a general differential equation can be written as

$$Lu(x,t) + Ru(x,t) + Nu(x,t) = f(x,t) \tag{3.1}$$

Where L is an invertible operator, R is the linear differential operator, N indicates the nonlinear term of differential equation, and $f(x,t)$ is the source term.

Introduction of Laplace transform to equation (3.1) yields;

$$\mathcal{L}[Lu(x,t)] + \mathcal{L}\,[Ru(x,t) + Nu(x,t)] = \mathcal{L}\,[f(x,t)]. \tag{3.2}$$

The Laplace operator is (denoted by $\mathcal{L}$) and the Laplace transform of invertible operator is

$$\mathcal{L}[Lu(x,t)] = s^n u(x,t) - \sum_{r=0}^{n-1} s^{-n}.s^{n-1-r}f^r(0), \tag{3.3}$$

Substituting equation (3.3) into equation (3.2) and simplifying, gives

$$U(x,t) = \frac{1}{s^n}\mathcal{L}[Ru(x,t) + Nu(x,t)] + \frac{1}{s^n}\mathcal{L}[f(x,t)] + \sum_{r=0}^{n-1} s^{-n}.s^{n-1-r}f^r(0), \tag{3.4}$$

Rearranging the terms, gives

$$U(x,t) = \frac{1}{s^n}\mathcal{L}[f(x,t)] + \sum_{r=0}^{n-1} s^{-(r+1)}f^r(0) + \frac{1}{s^n}\mathcal{L}[Ru(x,t) + Nu(x,t)]. \tag{3.5}$$

Introducing the Laplace inverse transform to equation (3.5), yields

$$u(x,t) = \mathcal{L}^{-1}\left[\frac{1}{s^n}\mathcal{L}[f(x,t)] + \sum_{r=0}^{n-1} s^{-(r+1)}.\, f^r(0)\right] + \mathcal{L}^{-1}\left[\frac{1}{s^n}\mathcal{L}\,[Ru(x,t) + Nu(x,t)]\right]. \tag{3.6}$$

And equation (3.6) can be written as;

$$u(x,t) = g(x,t) + \mathcal{L}^{-1}\left[\frac{1}{s^n}\mathcal{L}\,[Ru(x,t) + Nu(x,t)]\right]. \tag{3.7}$$

Where $g(x,t)$ denotes the expression that arises from the given initial condition and the source term which is given as

$$g(x,t) = \mathcal{L}^{-1}\left[\frac{1}{s^n}\mathcal{L}[f(x,t)] + \sum_{r=0}^{n-1} s^{-(r+1)}.\, f^r(0)\right]. \tag{3.8}$$

Then, the solution form an infinite series as

$$u(x,t) = \sum_{n=0}^{\infty} u_n(x,t), \tag{3.9}$$

The nonlinear term in equation (3.7) is resolved in term of Differential Transform Method.
If the function $w(x,t) = u(x,t)v(x,t)$ the transform is

$$W_k = \sum_{r=0}^{k} u_r(x)v_{(k-r)}(x), \tag{3.10}$$

If the function $w(x,t) = u^2(x,t)$ the transform is

$$W_k = \sum_{r=0}^{k} u_r(x)u_{(k-r)}(x), \tag{3.11}$$

Simplifying equation (3.8) gives

$$u_0(x,t) = g(x,t) \tag{3.12}$$

And the recursive relation is given as:

$$u_{n+1} = \mathcal{L}^{-1}\left[\frac{1}{s^n}\mathcal{L}\left[Ru_n(x,t) + A_n\right]\right]. \tag{3.13}$$

Here $n = 0,1,2,3,\ldots$ and analytical solution $u(x,t)$ can be approximated by a truncated series

$$u(x,t) = \lim_{N\to\infty} \sum_{n=0}^{N} u_n(x,t). \tag{3.14}$$

4. Laplace Differential Transform Scheme on Fractional Differential Equations

From Elzaki (2018), Let us study the following fractional differential equation

$$D^{\alpha}u(t) + a_n u^m(t) + a_{n-1}u^{m-1}(t) + \cdots + a_1 u'(t) + a_0 u(t) + N\big(u(t), u'(t)\big) = f(t), \quad t > 0, \quad m-1 < \alpha \le m. \tag{4.1}$$

Subject to the initial conditions,

$$u^{(i)}(0) = b_i, \ \ i = 0,1,2,\ldots \tag{4.2}$$

Where a_i, b_i are known real constants, N is a nonlinear Operator and $f(t)$ is known function. The equation (4.1) is transformed into the following system:

$$D^{\alpha}u(t) + a_n u^m(t) + a_{n-1}u^{m-1}(t) + \cdots + a_1 u'(t) + a_0 u(t) + N\big(u(t), u'(t)\big) = f(t) \ge 0, \tag{4.3}$$

Subject to initial conditions

$$u^{(i)}(0) = b_i, \ \ i = 0,1,2,\ldots,m-1. \tag{4.4}$$

Taking Laplace transform of (4.3), gives

$$\mathcal{L}[D^{\alpha}u(t)] + a_n\mathcal{L}[u^m(t)] + a_{n-1}\mathcal{L}[u^{m-1}(t)] + \cdots + a_1\mathcal{L}[u'(t)] + a_0\mathcal{L}[u(t)] + \mathcal{L}\big[N\big(u(t), u'(t)\big)\big] = \mathcal{L}[f(t)]. \tag{4.5}$$

$$\mathcal{L}[D^{\alpha}u(t)] = s^{\alpha}F(s) - \sum_{k=0}^{m-1} s^{\alpha-k-1}f^{(k)}(0), \tag{4.6}$$

Substituting (4.6) into (4.5), gives

$$s^{\alpha}\mathcal{L}[u(t)] = \sum_{k=0}^{m-1} s^{\alpha-k-1}f^{(k)}(0) - \mathcal{L}[f(t)] - a_n\mathcal{L}[u^m(t)] - a_{n-1}\mathcal{L}[u^{m-1}(t)] - \cdots - a_1\mathcal{L}[u'(t)] - a_0\mathcal{L}[u(t)] - \mathcal{L}[N\big(u(t), u'(t)\big)] \tag{4.7}$$

Equation 4.7 Implies,

$$\mathcal{L}[u(t)] = \sum_{k=0}^{m-1} s^{-(k+1)} f^{(k)}(0) - \frac{1}{s^{\alpha}}\mathcal{L}[f(t)] + \frac{1}{s^{\alpha}}\{a_n\mathcal{L}[u^m(t)] - a_{n-1}\mathcal{L}[u^{m-1}(t)] - \cdots - a_1\mathcal{L}[u'(t)] - a_0\mathcal{L}[u(t)] - \mathcal{L}[N(u(t), u'(t))]\}. \quad (4.8)$$

The Laplace Differential Transform Method represents the solution as an infinite series

$$u(t) = \sum_{r=0}^{k} u_r(t), \quad (4.9)$$

And the nonlinear term $N(u(t), u'(t))$ be analyzed in terms of the Differential Transform Method

$$N(u(t), u'(t)) = \sum_{r=0}^{k} A_r(t), \quad (4.10)$$

Where

$$A_r(t) = \sum_{r=0}^{k} u_r u'_{(k-r)}(t), \quad (4.11)$$

Substituting 4.9, 4.10 and 4.11 into 4.8, yields

$$\mathcal{L}\left[\sum_{r=0}^{k} u_r(t)\right] = \sum_{k=0}^{m-1} u^{(i)} s^{-(k+1)} + \frac{1}{s^{\alpha}}\mathcal{L}[f(t)] + \frac{1}{s^{\alpha}}\left\{a_n\mathcal{L}\left[\sum_{r=0}^{k} u^m{}_r(t)\right] - a_{n-1}\mathcal{L}\left[\sum_{r=o}^{k} u_r{}^{(m-1)}(t)\right] - \cdots - a_1\mathcal{L}\left[\sum_{r=0}^{k} u'{}_r(t)\right] - a_0\mathcal{L}\left[\sum_{r=0}^{k} u_r(t)\right] - \mathcal{L}\left[\sum_{r=0}^{k} A_r(t)\right]\right\} \quad (4.12)$$

The iterations are defined by the recursive relations,

$$\mathcal{L}[u_0(t)] = \sum_{k=0}^{m-1} u^k s^{-(k+1)} + s^{-\alpha}\mathcal{L}[f(t)]. \quad (4.13)$$

And then

$$\mathcal{L}[u_r(t)] = -s^{-\propto}\{a_n\mathcal{L}[u^m{}_{(r-1)}(t)] + \cdots + a_1\mathcal{L}[u'{}_{(r-1)}(t)] - a_0\mathcal{L}[u_{(r-1)}(t)]\} - s^{-\propto}\mathcal{L}[A_{(r-1)}(t)], \quad r = 1,2,3,\ldots \quad (4.14)$$

5. Application

Problem 5.1. Consider the nonlinear Fractional Kaup-Kupershmidt equation (Syed *et al* (2015)).

$$\frac{\partial^{\alpha} u}{\partial t^{\alpha}} - \frac{\partial^5 u}{\partial x^5} - 5u\frac{\partial^3 u}{\partial x^3} - \frac{25}{3}\frac{\partial u}{\partial x}\frac{\partial^2 u}{\partial x^2} - 5u^2\frac{\partial u}{\partial x} = 0, \quad (5.1)$$

With the initial condition

$$u(x,0) = -2k^2 + \frac{24k^2}{1+e^{kx}} - \frac{24k^2}{(1+e^{kx})^2}. \quad (5.2)$$

Where k is an arbitrary constant, By taking the Laplace transform of (5.1), gives

$$\mathcal{L}\left[\frac{\partial^{\alpha} u}{\partial t^{\alpha}}\right] = \mathcal{L}\left[\frac{\partial^5 u}{\partial x^5} + 5u\frac{\partial^3 u}{\partial x^3} + \frac{25}{3}\frac{\partial u}{\partial x}\frac{\partial^2 u}{\partial x^2} + 5u^2\frac{\partial u}{\partial x}\right]. \quad (5.3)$$

From the Caputo definition, (5.3) becomes

$$s^{\alpha}\mathcal{L}[u(x,t)] = s^{(\alpha-1)}u(x,0) + \mathcal{L}\left[\frac{\partial^5 u}{\partial x^5} + 5u\frac{\partial^3 u}{\partial x^3} + \frac{25}{3}\frac{\partial u}{\partial x}\frac{\partial^2 u}{\partial x^2} + 5u^2\frac{\partial u}{\partial x}\right]. \quad (5.4)$$

Substituting the initial condition (5.2) and simplifying (5.4) gives

$$u(x,t) = s^{-1}\left(-2k^2 + \frac{24k^2}{1+e^{kx}} - \frac{24k^2}{(1+e^{kx})^2}\right) + s^{-\alpha}\mathcal{L}\left[\frac{\partial^5 u}{\partial x^5} + 5u\frac{\partial^3 u}{\partial x^3} + \frac{25}{3}\frac{\partial u}{\partial x}\frac{\partial^2 u}{\partial x^2} + 5u^2\frac{\partial u}{\partial x}\right]. \quad (5.5)$$

Taking the Laplace inverse Transform of (5.5), yields

$$u(x,t) = -2k^2 + \frac{24k^2}{1+e^{kx}} - \frac{24k^2}{(1+e^{kx})^2} + \mathcal{L}^{-1}\left\{s^{-\alpha}\mathcal{L}\left[\frac{\partial^5 u}{\partial x^5} + 5u\frac{\partial^3 u}{\partial x^3} + \frac{25}{3}\frac{\partial u}{\partial x}\frac{\partial^2 u}{\partial x^2} + 5u^2\frac{\partial u}{\partial x}\right]\right\}. \quad (5.6)$$

Then (5.6) can easily be written in the form

$$u_n(x,t) = -2k^2 + \frac{24k^2}{1+e^{kx}} - \frac{24k^2}{(1+e^{kx})^2} - \mathcal{L}^{-1}\left\{s^{-\alpha}\mathcal{L}\left[\frac{\partial^5 u_n(x)}{\partial x^5} + 5A_n(x,t) + \frac{25}{3}B_n(x,t) + 5C_n(x,t)\right]\right\}. \quad (5.7)$$

From (5.7), it shows that

$$u_0(x,t) = -2k^2 + \frac{24k^2}{1+e^{kx}} - \frac{24k^2}{(1+e^{kx})^2}. \quad (5.8)$$

The recursive relation is given as follow:

$$u_{n+1}(x,t) = -\mathcal{L}^{-1}\left\{s^{-\alpha}\mathcal{L}\left[\frac{\partial^5 u_n(x)}{\partial x^5} + 5A_n(x,t) + \frac{25}{3}B_n(x,t) + 5C_n(x,t)\right]\right\}. \quad (5.9)$$

Where $A_n(x)$, $B_n(x)$ and $C_n(x)$ are the transformed form of the nonlinear terms.
For the convenience of the reader, the first few nonlinear terms are

$$A_n(x) = u\frac{\partial^3 u}{\partial x^3} = \sum_{r=0}^{k} u_r(x)u_{xxx(n-r)}(x),$$
$$A_0 = u_0u_{0xxx}$$
$$A_1 = u_1u_{0xxx} + u_0u_{1xxx}$$
$$A_2 = u_2u_{0xxx} + u_1u_{1xxx} + u_0u_{2xxx}$$
$$B_n(x) = \frac{\partial u}{\partial x}\frac{\partial^2 u}{\partial x^2} = \sum_{r=0}^{k} u_{x(r)}(x)u_{xx(n-r)}(x),$$
$$B_0 = u_{0x}u_{0xx}$$
$$B_1 = u_{1x}u_{0xx} + u_{0x}u_{1xx}$$
$$B_2 = u_{2x}u_{0xx} + u_{1x}u_{1xx} + u_{0x}u_{2xx}$$
$$C_n(x) = u^2\frac{\partial u}{\partial x} = \sum_{r=0}^{k} u_r u_{(n-r)}(x)u_{(n-r)x}(x),$$
$$C_0 = u^2{}_0u_{0x}$$
$$C_1 = 2u_0u_1u_{0x} + u^2{}_0u_1$$
$$C_2 = 2u_0u_2u_{0x} + u^2{}_1u_{0x} + 2u_0u_1u_{1x} + u^2{}_0u_{2x} \quad (5.10)$$

From (5.9), when $n = 0$, gives

$$u_1(x,t) == -\mathcal{L}^{-1}\left\{s^{-\alpha}\mathcal{L}\left[\frac{\partial^5 u_0(x)}{\partial x^5} + 5A_0(x) + \frac{25}{3}B_0(x) + 5C_0(x)\right]\right\}. \quad (5.11)$$

Putting the values $A_0(x)$, $B_0(x)$ *and* $B_0(x)$ in (5.10) then simplifying

$$u_1(x,t) = -\mathcal{L}^{-1}\left\{s^{-\alpha}\mathcal{L}\left[\frac{\partial^5 u_0(x)}{\partial x^5} + 5u_0u_{0xxx} + \frac{25}{2}u_{0x}u_{0xx} + 5u^2{}_0u_{0x}\right]\right\}. \quad (5.12)$$

$$u_1(x,t) = \frac{-264k^7\left(-e^{kx}+e^{2kx}\right)}{(1+e^{kx})^3}\frac{t^{\propto}}{\Gamma(\alpha+1)}. \quad (5.13)$$

In the same manner,

$$u_2(x,t) = -\frac{1452k^{12}\left(e^{3kx}-4e^{2kx}+e^{kx}\right)}{(1+e^{kx})^4}\frac{t^{2\alpha}}{\Gamma^2(\alpha+1)}. \quad (5.14)$$

$$u_3(x,t) = \frac{3524e^{17}\left(e^{4kx}-11e^{3kx}+11e^{2kx}-e^{kx}\right)}{(1+e^{kx})^5}\frac{t^{3\alpha}}{\Gamma^3(\alpha+1)}. \quad (5.15)$$

The approximate analytic series solution is

$$u(x,t) = u[0]+u[1]+u[2]+u[3]\ldots$$

$$u(x,t) = -2k^2 + \frac{24k^2}{1+e^{kx}} - \frac{24k^2}{(1+e^{kx})^2}\frac{-264k^7\left(-e^{kx}+e^{2kx}\right)}{(1+e^{kx})^3}\frac{t^{\alpha}}{\Gamma(\alpha+1)} - \frac{1452k^{12}\left(e^{3kx}-4e^{2kx}+e^{kx}\right)}{(1+e^{kx})^4}\frac{t^{2\alpha}}{\Gamma^2(\alpha+1)} + \frac{3524e^{17}\left(e^{4kx}-11e^{3kx}+11e^{2kx}-e^{kx}\right)}{(1+e^{kx})^5}\frac{t^{3\alpha}}{\Gamma^3(\alpha+1)}. \quad (5.16)$$

The solution (5.16) is convergent to the exact solution at classical order $\alpha = 1$.

$$u(x,t) = -2k^2 + \frac{24k^2}{1+e^{kx+11k^5t}} - \frac{24k^2}{\left(1+e^{kx+11k^5t}\right)^2}. \quad (5.17)$$

Problem 5.2. Consider the generalized fractional Drinfeld-Sokolov (gDs) equations

$$\frac{\partial^\alpha u}{\partial t^\alpha} + \frac{\partial^3 u}{\partial x^3} - 6u\frac{\partial u}{\partial x} - 5\frac{\partial v^\beta}{\partial x} = 0,$$
$$\frac{\partial^\alpha v}{\partial t^\alpha} - 2\frac{\partial^3 v}{\partial x^3} + 6u\frac{\partial v}{\partial x} = 0, \quad (5.18)$$

Subject to the initial conditions

$$u(x,0) = \frac{-b^2-4k^4}{4k^2} + 2k^2\tanh^2(kx),$$
$$v(x,0) = b\tanh(kx) \quad (5.19)$$

Where β is a constant.

Taking Laplace transform of eqn. (5.18)

$$\mathcal{L}\left[\frac{\partial^\alpha u}{\partial t^\alpha}\right] = -\mathcal{L}\left[\frac{\partial^3 u}{\partial x^3} - 6u\frac{\partial u}{\partial x} - 5\frac{\partial v^\beta}{\partial x}\right]$$
$$\mathcal{L}\left[\frac{\partial^\alpha v}{\partial t^\alpha}\right] = -\mathcal{L}\left[-2\frac{\partial^3 v}{\partial x^3} + 6u\frac{\partial v}{\partial x}\right] \quad (5.20)$$

From the Caputo definition, (5.20) becomes

$$s^\alpha\mathcal{L}[u(x,t)] = s^{(\alpha-1)}u(x,0) - \mathcal{L}\left[\frac{\partial^3 u}{\partial x^3} - 6u\frac{\partial u}{\partial x} - 5\frac{\partial v^\beta}{\partial x}\right]$$
$$s^\alpha\mathcal{L}[v(x,t)] = s^{(\alpha-1)}u(x,0) - \mathcal{L}\left[-2\frac{\partial^3 v}{\partial x^3} + 6u\frac{\partial v}{\partial x}\right] \quad (5.21)$$

Thus, using the procedure (4.12), gives

$$u_n(x,t) = \frac{-b^2-4k^4}{4k^2} + 2k^2\tanh^2(kx) - \mathcal{L}^{-1}\left\{s^{-\alpha}\mathcal{L}\left[\frac{\partial^3 u}{\partial x^3} - 6A_n(x,t) - 5B_n(x,t)\right]\right\}$$

$$v_n(x,t) = btanh(kx) + \mathcal{L}^{-1}\left\{s^{-\alpha}\mathcal{L}\left[2\frac{\partial^3 v}{\partial x^3} - 6uC_n(x,t)\right]\right\} \quad (5.22)$$

Where the nonlinear terms of (5.22) are represented by A_n, B_n, C_n. Comparing both sides of (5.22), gives

$$u_0(x,t) = \frac{-b^2-4k^4}{4k^2} + 2k^2 tanh^2(kx)$$
$$v_0(x,t) = btanh(kx) \quad (5.23)$$
$$u_1(x,t) = \frac{2t^{\alpha}(4k^4+3b^2)sinh(kx)}{\Gamma(\alpha+1)cosh(kx)^3}$$
$$v_1(x,t) = \frac{t^{\propto}b(4k^4+3b^2)}{\Gamma(\alpha+1)2cosh(kx)^2k} \quad (5.24)$$
$$u_2(x,t) = \frac{t^{2\propto}(4k^4+3b^2)^2(2cosh(kx)^2-3)}{\Gamma(\alpha+1)^2cosh(kx)^4} \quad (5.25)$$
$$v_2(x,t) = \frac{6t^{\propto}}{\Gamma(\alpha+1)} - \frac{8t^{2\propto}sinh(kx)bk^2(4k^4cosh(kx)^2)+3b^2cosh(kx)^2-12k^4-9b^2}{cosh(kx)^5\Gamma(\alpha+1)^2}$$

The approximate analytic series solutions is

$$u(x,t) = u[0]+u[1]+u[2]+\cdots$$
$$v(x,t) = v[0]+v[1]+v[2]+\cdots$$
$$u(x,t) = \frac{-b^2-4k^4}{4k^2} + 2k^2tanh^2(kx) + \frac{2t^{\alpha}(4k^4+3b^2)sinh(kx)}{\Gamma(\alpha+1)cosh(kx)^3} + \frac{t^{2\propto}(4k^4+3b^2)^2(2cosh(kx)^2-3)}{\Gamma(\alpha+1)^2cosh(kx)^4}$$
$$v(x,t) = btanh(kx) + \frac{t^{\propto}b(4k^4+3b^2)}{\Gamma(\alpha+1)2cosh(kx)^2k} + \frac{6t^{\propto}}{\Gamma(\alpha+1)} - \frac{8t^{2\propto}sinh(kx)bk^2(4k^4cosh(kx)^2)+3b^2cosh(kx)^2-12k^4-9b^2}{cosh(kx)^5\Gamma(\alpha+1)^2}. \quad (5.26)$$

Table 1: Result of approximate solutions of example 1 equation of fractional k.k equation using LDTM for different values of α.

t	x	$\propto = 0.2$	$\propto = 0.4$	$\propto = 0.6$	$\propto = 0.8$	$\propto = 1.0$
0.1	0.1	0.2499017113	0.2499166471	0.2499264052	0.2499325326	0.2499362699
	0.2	0.2496914786	0.2497184010	0.2497365819	0.2497482874	0.2497555523
	0.3	0.2493644561	0.2494033313	0.2494299124	0.2494471813	0.2494579647
	0.4	0.2489210517	0.2489718312	0.2490067794	0.2490295903	0.2490438787
	0.5	0.2483618172	0.2484244379	0.2484677096	0.2484960339	0.2485138097
0.2	0.1	0.2498949357	0.2499078168	0.2499179978	0.2499255479	0.2499309112
	0.2	0.2496795682	0.2497023654	0.2497208869	0.2497349630	0.2497451662
	0.3	0.2493474258	0.2493801105	0.2494069494	0.2494275338	0.2494425641
	0.4	0.2488989226	0.2489414542	0.2489765770	0.2490036441	0.2490234828
	0.5	0.2483346170	0.2483869425	0.2484303054	0.2484638216	0.2484884439

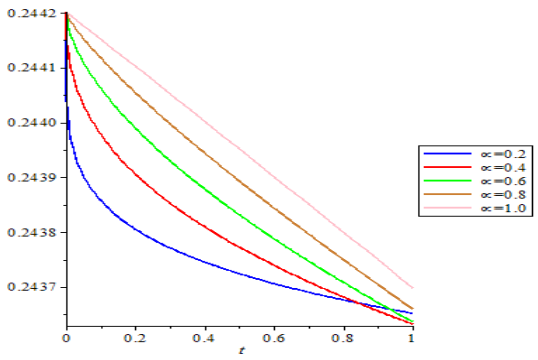

Figure 3: The LDTM solution of $u(x,t)$ of example 1 for different value of $\propto$.

Table 2: Result of approximate solutions of example 2 of $u(x,t)$ generalized fractional Drinfeld- Sokolov equations using LDTM for different values of α.

t	x	$\propto= 0.2$	$\propto= 0.4$	$\propto= 0.6$	$\propto= 0.8$	$\propto= 1.0$
0.1	0.1	0.002599999754	0.002599999771	0.002599999782	0.002599999790	0.002599999794
	0.2	0.002599999112	0.002599999143	0.002599999165	0.002599999179	0.002599999188
	0.3	0.002599998071	0.002599998116	0.002599998148	0.002599998169	0.002599998182
	0.4	0.002599996629	0.002599996689	0.002599996731	0.002599996759	0.002599996776
	0.5	0.002599994787	0.002599994862	0.002599994914	0.002599994948	0.002599994970
0.2	0.1	0.002599999746	0.002599999761	0.002599999772	0.002599999781	0.002599999788
	0.2	0.002599999098	0.002599999125	0.002599999146	0.002599999163	0.002599999176
	0.3	0.002599998050	0.002599998089	0.002599998120	0.002599998145	0.002599998164
	0.4	0.002599996602	0.002599996653	0.002599996694	0.002599996727	0.002599996751
	0.5	0.002599994754	0.002599994817	0.002599994868	0.002599994909	0.002599994939

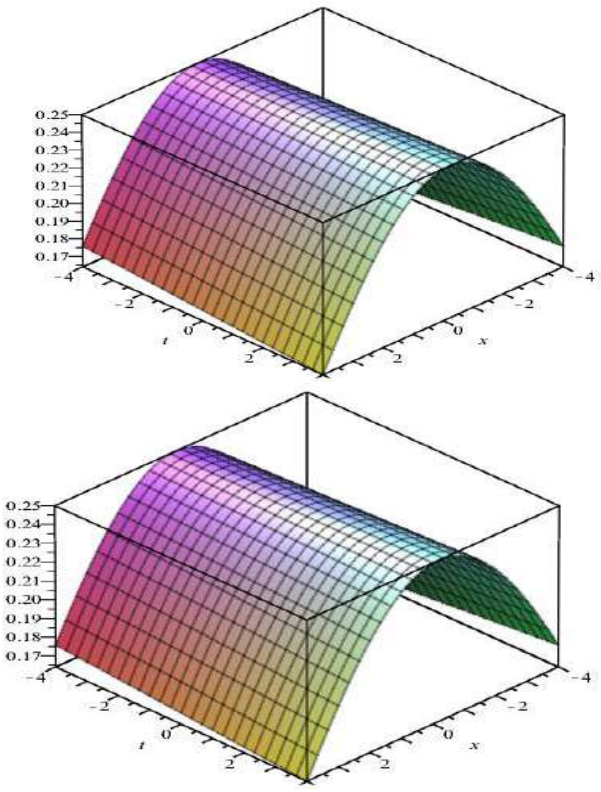

Figure 1: The (a) exact and (b) LDTM solutions of example 1 at $\propto = 1$

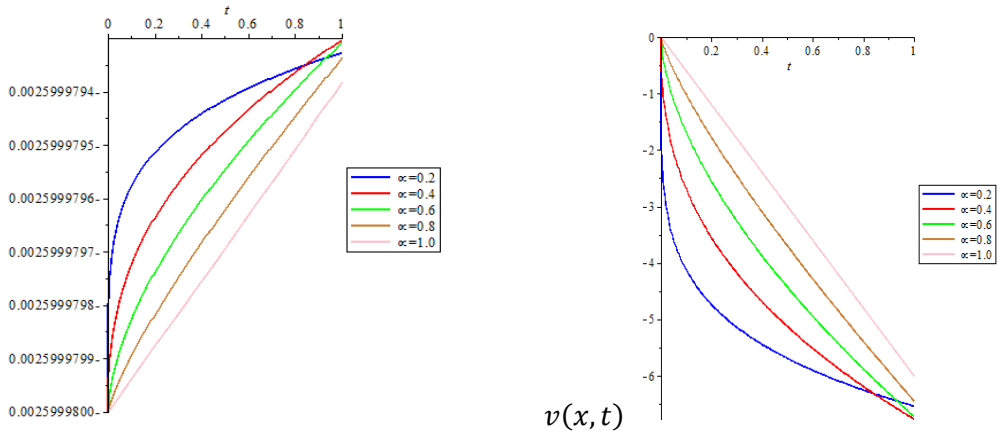

$v(x,t)$

Figure 4: The LDTM solution of $u(x,t)$ of example 2 for different values of $\propto$.
Figure 5: The LDTM solution of $v(x,t)$ of example 2 for different values of $\propto$.

Table 3: Result of approximate solutions of example 2 of $v(x,t)$ generalized fractional Drinfeld-Sokolov equation using LDTM for different values of α.

t	x	$\propto = 0.2$	$\propto = 0.4$	$\propto = 0.6$	$\propto = 0.8$	$\propto = 1.0$
0.1	0.1	-4.123145211	-2.692144128	-1.686743186	-1.020991550	-0.5999989848
	0.2	-4.123144211	-2.692143128	-1.686742186	-1.020990550	-0.5999979848
	0.3	-4.123143211	-2.692142128	-1.686741186	-1.020989550	-0.5999969848
	0.4	-4.123142211	-2.692141128	-1.686740186	-1.020988550	-0.5999959848

	0.5	-4.123141211	-2.692140128	-1.686739186	-1.020987550	-0.5999949848
0.2	0.1	4.736250269	-3.552305792	-2.556625106	-1.777650279	-1.1999989700
	0.2	4.736249269	-3.552304792	-2.556624106	-1.777649279	-1.1999979700
	0.3	-4.736248269	-3.552303792	-2.556623106	-1.777648279	-1.1999969700
	0.4	-4.736247269	-3.552302792	-2.556622106	-1.777647279	-1.1999959700
	0.5	-4.736246269	-3.552301792	-2.556621106	-1.777646279	-1.1999949700

6. Discussion of results

The tables and figures above presenting the results of nonlinear fractional K.K equation and generalized fractional drinfeld-sokolov equations using LDTM are valid for $\boldsymbol{\alpha = 0 \ldots N}$ and comparing with the classical order $\boldsymbol{\alpha = 1}$ above, we observe the proposed method produces more realistic solutions compared to others, which demonstrate the efficacy and efficiency as well as the reliability of the LDTM in the convergence on nonlinear fractional K.K equations and its derivatives.

7. Conclusion

In this research work, we apply the Laplace Differential transform method in solving nonlinear fractional Kaup-Kupershmidt equation and the generalized fractional Drinfeld-sokolov equations respectively. Giving the analytical background of the system of equation, with numerical results to confirm that LDTM is an efficient and more reliable method of obtaining the approximate solution for the type nonlinear fractional partial differential equations examined in our work. Therefore, by comparing the results with analytical solution at classical order shows that our method is efficient and a simpler tool in finding numerical solution of nonlinear fractional partial differential equations.

References

[1] Adomian, G. (1984). A new approach to nonlinear partial differential equations. *Journal of Mathematical Analysis and Applications*, *102*(2), 420-434.

[2] Abbasbandy, S. (2007). Numerical solution of non-linear Klein–Gordon equations by variational iteration method. *International Journal for Numerical Methods in Engineering*, *70*(7), 876-881.

[3] Ahmad, J., Mushtaq, M., & Sajjad, N. (2015). Exact solution of whitham broer-kaup shallow water wave equations. *Journal of Science and Arts*, *15*(1), 5.

[4] Bairwa, R. K., & Singh, K. (2021). Analytical solution of time-fractional Klien-Gordon equation by using Laplace-Adomian decomposition method. *Annals of Pure and Applied Mathematics*, *24*(1), 27-35.

[5] Carpinteri, A., & Mainardi, F. (Eds.). (2014). *Fractals and fractional calculus in continuum mechanics* (Vol. 378). Springer.

[6] Frassu, S., van der Mee, C., & Viglialoro, G. (2021). Boundedness in a nonlinear attraction-repulsion Keller–Segel system with production and consumption. *Journal of Mathematical Analysis and Applications*, *504*(2), 125428.

[7] Gorenflo, R., & Mainardi, F. (1997). *Fractional calculus: integral and differential equations of fractional order* (pp. 223-276). Springer Vienna.

[8] Noor, M. A., & Mohyud-Din, S. T. (2009). Homotopy perturbation method for solving Thomas-Fermi equation using Pade approximants. *International Journal of Nonlinear Science*, *8*(1), 27-31.

[9] Liao, S. (2003). Beyond perturbation: introduction to the homotopy analysis method.

[10] Zhang, J. L., Wang, M. L., Wang, Y. M., & Fang, Z. D. (2006). The improved F-expansion method and its applications. *Physics Letters A*, *350*(1-2), 103-109.

[11] Mainardi, F. (1997). *Fractional calculus: some basic problems in continuum and statistical mechanics* (pp. 291-348). Springer Vienna.

[12] Tauseef Mohyud-Din, S., Aslam Noor, M., Noor, K. I., & Hosseini, M. M. (2010). Variational iteration method for re-formulated partial differential equations. *International Journal of Nonlinear Sciences and Numerical Simulation*, *11*(2), 87-92.

[13] Wazwaz, A. M. (2004). A sine-cosine method for handlingnonlinear wave equations. *Mathematical and Computer modelling*, *40*(5-6), 499-508.
[14] Zhou, J. K. (1986). Differential transformation and its applications for electrical circuits.
[15] Ahmad, J., & Mohyud-Din, S. T. (2014). An efficient algorithm for some highly nonlinear fractional PDEs in mathematical physics. *Plos one*, *9*(12), e109127.
[16] Arikoglu, A., & Ozkol, I. (2007). Solution of fractional differential equations by using differential transform method. *Chaos, Solitons & Fractals*, *34*(5), 1473-1481.
[17] Kurnaz, A., & Oturanç, G. (2005). The differential transform approximation for the system of ordinary differential equations. *International Journal of Computer Mathematics*, *82*(6), 709-719.
[18] Saravanan, A., & Magesh, N. (2013). A comparison between the reduced differential transform method and the Adomian decomposition method for the Newell–Whitehead–Segel equation. *Journal of the Egyptian Mathematical Society*, *21*(3), 259-265.
[19] Kilbas, A. A., Srivastava, H. M., & Trujillo, J. J. (2006). *Theory and applications of fractional differential equations* (Vol. 204). elsevier.
[20] Li, T., Pintus, N., & Viglialoro, G. (2019). Properties of solutions to porous medium problems with different sources and boundary conditions. *Zeitschrift für angewandte Mathematik und Physik*, *70*, 1-18.
[21] Li, T., & Viglialoro, G. (2021). Boundedness for a nonlocal reaction chemotaxis model even in the attraction-dominated regime.
[22] Jafari, H., & Daftardar-Gejji, V. (2006). Solving linear and nonlinear fractional diffusion and wave equations by Adomian decomposition. *Applied Mathematics and Computation*, *180*(2), 488-497.
[23] Ali, A., Shah, K., & Khan, R. A. (2018). Numerical treatment for traveling wave solutions of fractional Whitham-Broer-Kaup equations. *Alexandria Engineering Journal*, *57*(3), 1991-1998.
[24] Ray, S. S. (2008). A new approach for the application of Adomian decomposition method for the solution of fractional space diffusion equation with insulated ends. *Applied Mathematics and Computation*, *202*(2), 544-549.
[25] Ivanescu, M. (2003). Mechanical Engineering's Handbook, Academic press series in Engineering, 611-714
[26] Khatib, A. (2016). Differential Transform Method for Differential Equations.
[27] Ali, G. E., Asaad, A. A., Elagan, S. K., Mawaheb, E., & AlDien, M. S. (2017). Using Laplace transform method for obtaining the exact analytic solutions of some ordinary fractional differential equations. *Global Journal of Pure and Applied Mathematics*, *13*(9), 5021-5035.
[28] Prakash, M. K. P. (2017). Solving Initial Value Problems by using the Method of Laplace Transforms. *International Journal of Mathematics Trends and Technology-IJMTT*, *41*.

Investigating Copper Deposit in Azara, Nasarawa State Transformation of Landsat8 Imagery

Bello YA[1], Idris HU[1], Alao JO[1], Lawal HA[1], Hussaini SM[1], Yakubu MB[2], Mashood LO [3] and Daramola D[4]

[1]Physics Department, Air Force Institutes of Technology, Kaduna

[2]Physics Department, Ahmadu Bello University, Zaria

[3]Department of Statistics, Air Force Institute of Technology, Kaduna

[4]Department of Mathematics, Air Force Institute of Technology, Kaduna

Corresponding Email: belloya@afit.edu.ng

Abstract

A deposit of copper, a top-rated commodity, was reported in Azara, Awe local government of Nasarawa State. Little is known about the deposit as no geophysical study has been reported about it, to the best of our knowledge. Various image transformation techniques; band ratio, colour composite and PCA, were applied on the Landsat8 imagery of the study area to investigate the deposit. Bright pixels were noticed around the deposit on the map of some band ratios. This has been reported as a representation of copper mineralization. Linear structures were also observed in the map of some transformation techniques around the deposit, suggesting hydrothermal alteration. This alteration trends in the NW direction which is in addition to NS and NE trending linear features observed in the DEM map of the study area. The result of the transformation of the imagery was verified with the report on the deposit by the NGSA and maps of digital elevation and Google earth.

Keywords: Copper, band ratio, PCA, hydrothermal alteration.

1. Introduction

Copper is an essential component in the production of solar cells, wind turbines and also electric vehicle. It is a malleable and soft metal that useful in the production of electrical cables and wires, due to its conductivity. Because of its strength, machinability, resistance to corrosion, and capacity for highly accurate casting, it is useful in plumbing, industrial machinery and construction material.

The identification of hydrothermally altered host rocks is the first step in the detection of man y ore deposits, and remote sensing studies can be used to identify hydrothermally altered rock s and explore a variety of ore deposits, including massive sulfide, uranium, porphyry copper, and epithermal gold (Moradi and Boomeri, 2017; Daneshfar et al., 2006; Madani, 2009; Shala by et al., 2010; Pour and Hashim, 2013; Ciampalini et al., 2013; Pour and Hashim, 2014; Ali and Pour, 2014; Pour and Hashim, 2015a, 2015b, 2015c; Zhang et al., 2016; Safari et al., 201 7; Gahlan and Ghrefat, 2017; Zhang et al., 2023; Chen et al., 2025). Significant hydrothermal alteration is frequently linked to porphyry copper ore, changing the rocks initial mineralogical characteristics.

For porphyry carbon exploration, it is therefore essential to extract alteration information from

remote sensing data (Lui et al., 2023).The aforementioned minerals can be identified and the buried reserves explored by applying both spectral and statistical analysis of remotely sensed data (Masoumi *et al.*, 2016).

Remote sensing data is widely used in lithological mapping and hydrothermal alteration. For l ithology mapping and mineral exploitation, free access and the almost appropriate spectral res olution of Landsat data are beneficial (Mwaniki *et al.*, 2015). The desirable distribution of alteration zones around the limited borders of an ore body facilitates narrowing down the exploration activities into smaller targets (Pirajno, 2008). Generally, hydrothermal alteration processes lead to emanation of clay and other silicate minerals, including kaolinite, sericite, illite, quartz, chlorite, epidote, and calcite (Ranjbar et al., 2004). Landsat8 has been very effective in the exploration of several copper deposits (Pour and Hashim, 2015c; Pour *et al*., 2019; Safari *et al.*, 2017; Howari *et al.*, 2020; Ghozali *et al*., 2022).

Pour and Hashim (2015c) reported that Landsat8 bands (bands 2 and 4 in the visible and near infrarer; 6 and 7 in the shortwave infrared; 10 in the thermal infrared spectra) contain useful information for porphyry copper investigation. An overview of the alteration mineral zones in the metallogenic province of the Inglefield Mobile Belt (IMB) is given by Landsat-8 (Pour *et al*., 2019). Ghozali *et al*., (2022) showed that the detected alteration zones in satellite imagery was related to the different lithological types and rock origin, the dense vegetation covers also influenced the optical remote sensing techniques. However, the imagery has not been used to investigate any of the copper deposit in Nigeria. No geophysical investigation has been reported in the study area, to the best of the knowledge of the authors.

This research focused on the use of Landsat 8 imagery to investigate the copper deposit reported by the Nigerian Geological Survey Agency (NGSA). This was achieved through the application of band ratio, colour composite and PCA on the Landsat 8 data covering the study area. The result was compared the DEM and Google Earth maps of the study to discern features related to the terrain and vegetation from that of mineralization. This has provided some insights to the mineralization of the copper deposit in Azara, Nasarawa State.

1.1 The study area

The copper ore deposit in the study area, Azara in Awe Local Government Area of Nasarawa state, was reported by NGSA on its official website. The study area on the latitude 8º 22ˈ00ˈˈ N longitude 9º 15ˈ 00ˈˈE. it is located at about 99.3km away from Lafia, the state capital along Makurdi, Road Benue state.
About 5 kilometers east of Azara Village is the vein that contains the copper ore in Awe. Nasa rawa State is home to the Basement Complex, Younger Granite, and Sedimentary Rocks—the three main geological components that comprise Nigerian geology. Nonetheless, tertiary v olcanic rocks have intruded into the sedimentary rock strata that cover the Awe region (Figure 1) (Ambo et al., 2023).

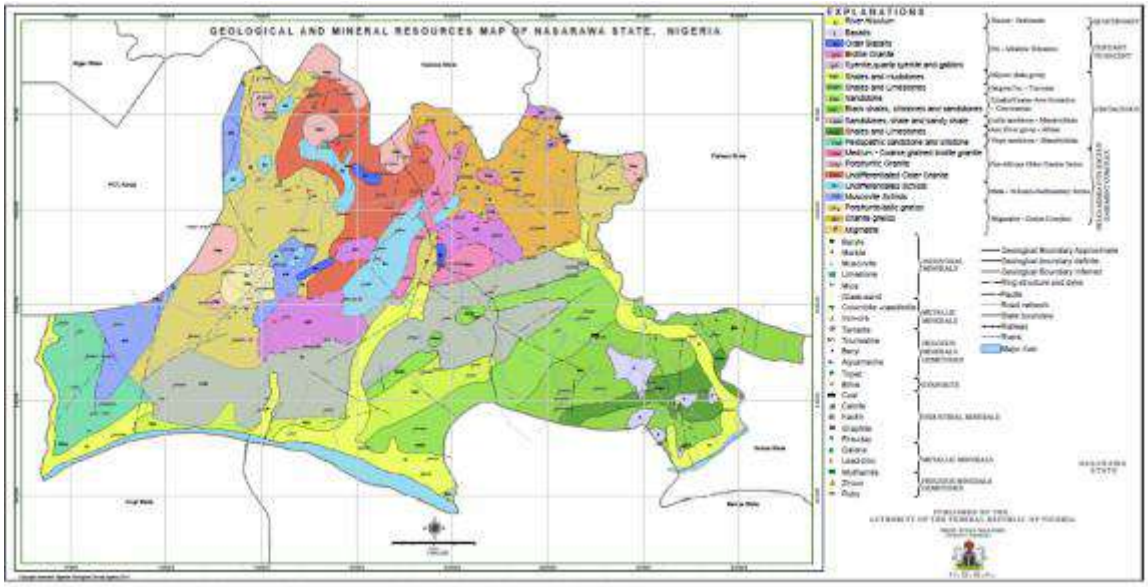

Figure 1. Outline geology map of Nasarawa state, aadapted from Ambo *et al*. (2023)

2. Material and Method

2.1 Material

The primary material used to achieve the objectives of this research includes Landsat8, Google Earth Pro, Global Mapper and ArcGis Pro. A cloud-free L1 T Landsat-8 picture of the research region in 16-
bit format was obtained for free from the Earth Resources Observation and Science Center of the US Geological Survey (USGS) for this investigation (http://earthexplorer.usgs.gov) on 28 February 2024.
The Landsat program's eight satellites are equipped with two instruments: the thermal infrare d sensor (TIRS), which includes two thermal bands (bands 10 and 11) collected with 100 m s patial resolution but resampled to 30 m, and the Operational Land Imager (OLI), which consis ts of nine bands with a spectral resolution of 30 m (bands 1-
7 and 9) and 15 m for a panchromatic band (band 8). Every 16 days, this satellite can reach w orldwide coverage.
ArcGIS Pro is a powerful geographic information system (GIS) software developed by Esri. It allows users to create, edit, analyze, and share geospatial data in a variety of formats. ArcGIS Pro is designed to be more intuitive and user friendly than its predecessor, ArcMap, and offers a range of advanced features and tools for spatial analysis, data visualization, and mapping. In this study ArcGIS Pro is used to perform the following task; importing and processing Landsat-8 data.

2.2 Methods

i. Band ratio: It is based on the division of one spectral band by another in a multispectral environment. As so, the division establishes the ratio between the spectral reflectance and spectral reflectance mea sured in two different spectral bands.

The spectrum differences of the particular materials to be mapped are stressed by the band ratio technique; also, these surface materials must have enough distinct spectral properties for the information to segregate into distinct bands (Corumluoglu *et al*., 2015). The technique is A straightforward and useful method for minimizing the impact of topography and highlighting the minute variations in the spectral reflectance properties of rocks and soils is band ratio (Rowan *et al.*, 2003; van der Meer *et al.*, 2012; Langford, 2015).

To improve lithology and alteration zones, a number of band ratios and fake color composites of ETM+ in RGB have been proposed, such as 5/7 for hydroxyl-bearing minerals and 3/1 for iron oxide (van der Meer et al., 2012). According to Beiranvpour and Hashim (2015), 4/2, 6/7, 5 and 10 in RGB are the most effective combinations of Landsat-8 band ratios for differentiating between vegetation, lithological units, and altered rocks.

ii. PCA: This transformation is a statistical method that uses orthogonal transformation of a group of potentially correlated variables to identify uncorrelated linear variables known as principle components (PC) (Crosta *et al*., 2003; Ranjbar *et al*., 2004; Richards, 2012). Owing to the fact that multispectral data bands are often highly correlated, the PC transformation is used to produce uncorrelated output bands. This procedure is carried out by finding a new set of orthogonal axes that have their origin at the data mean and are rotated so that the data variance can be maximized (Richards, 2012).

Based on input bands and their combination in the new PCs, the PCA minimizes spectral redundancy in multispectral data, separates noise components, and produces a new set of images with better interest targets. Mapping hydrothermal alteration with Landsat data is a common application of this well-known technique (e.g., Tangestani & Moore, 2001; Ranjbar et al., 2004; Mia & Fujimitsu, 2012; Corumluoglu et al., 2015; Mokhtari et al., 2015)..

2.3 Validation of result

When paired with a thorough knowledge of the related landforms, Landsat 8 provides valuable image products for regional exploration and discovery (Langford, 2015. The digital elevation map of the study area was produced using Global Mapper to view the variation of the terrain of the area. It revealed that the location of interest is on a hilly terrain, brighter surface (fig. 2). The hilly region is observed to be of less vegetation as compared to its surrounding (see fig 3). Regions with lower elevation (NE, and central regions of the study area), dark surface, are observed to be river channels. The result of the applied techniques on the Landsat8 image was compared with these identified features.

3. Result and Discussion

The DEM map revealed linear structures trending NS and NE, the NE trend is elongated indicating regional structure, around the location of the copper deposit (see Fig 2). Linear structures play a role in the process of hydrothermal fluid flow and creating an alteration zone

(Ghozali *et al.*, 2022). Hydrothermal alteration is a complex process that involves changing

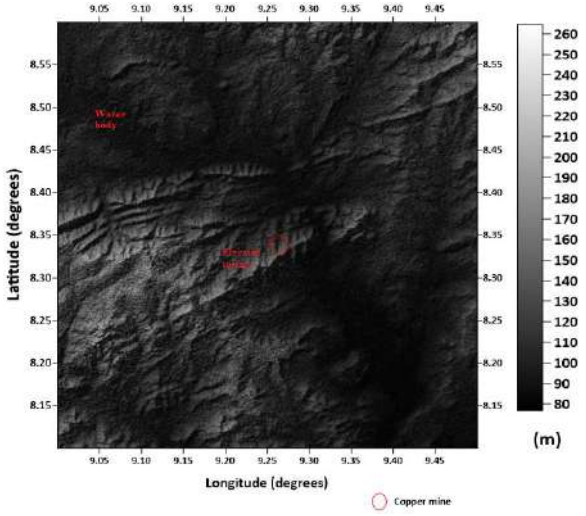

Figure 2. DEM map of the study area. Figure 3. Google earth map of the study area

mineralogy, chemistry, and texture, resulting from the circulation of hydrothermal fluids . The alteration zone is a consequent of hydrothermal alteration and consists of mineral assemblage that are stable alteration minerals in certain interval of temperature and pH. this is important information for reconstructing the temperature and geochemical structure of a hydrothermal system (Pirajno, 2008).

To create a representative reflectance in the imagery to define copper mineralization, various band ratios, colour composite and PCA were tested. The band ratio images enhanced copper minerals as bright (Trinh and Vu, 2015). Band ratio 5 and 7 produced brighter pixels over the water body in the NW of the study area but, slightly bright pixels on the less hilly terrain with less vegetation hosting the copper deposit. The location of the copper deposit has bright pixels. A NW trending linear structure is noticed in the within the location of the deposit (Figure 4a). The nature of the pixel and linear structure is similarly observed with the band ratio of 6 and 7 (Figure 4b). The NW trend also manifest in the map of the band ratio 7 and 6, colour composite maps (4/2:6/7:5 and 4/2:6/7:10) in Fig 4d and e. The linear feature and bright pixel are indication of hydrothermal alteration, a signature of mineralization in the region of interest. However, no evidence of alteration was noticed on the PCA maps despite reflecting the hilly terrain and the water body (Figure 4 g and h).

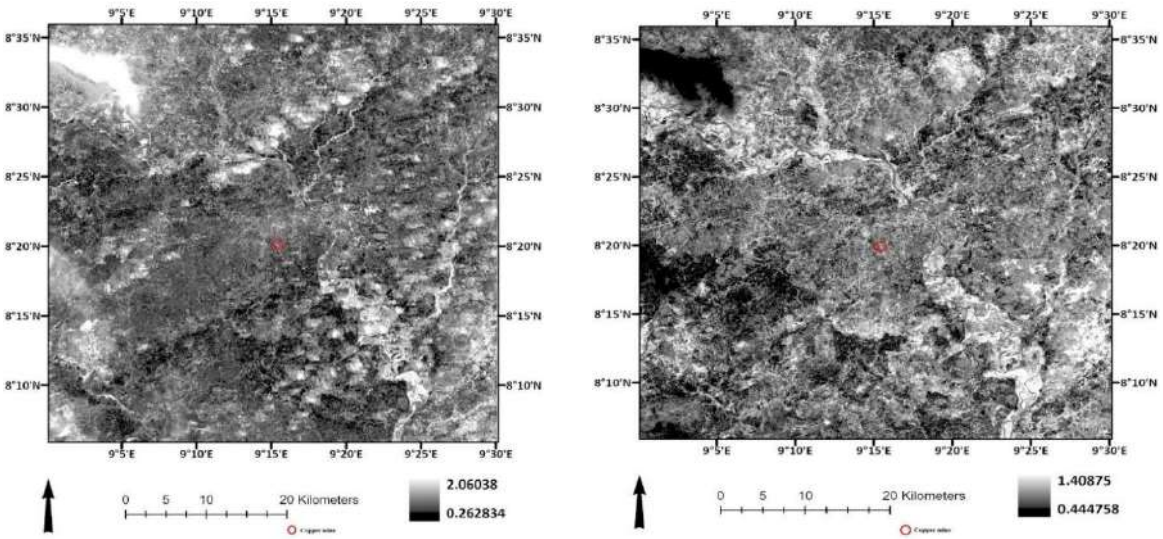

Figure 4 a and b. Map of band ratios 5 and 7, and 6and 7 of the study area

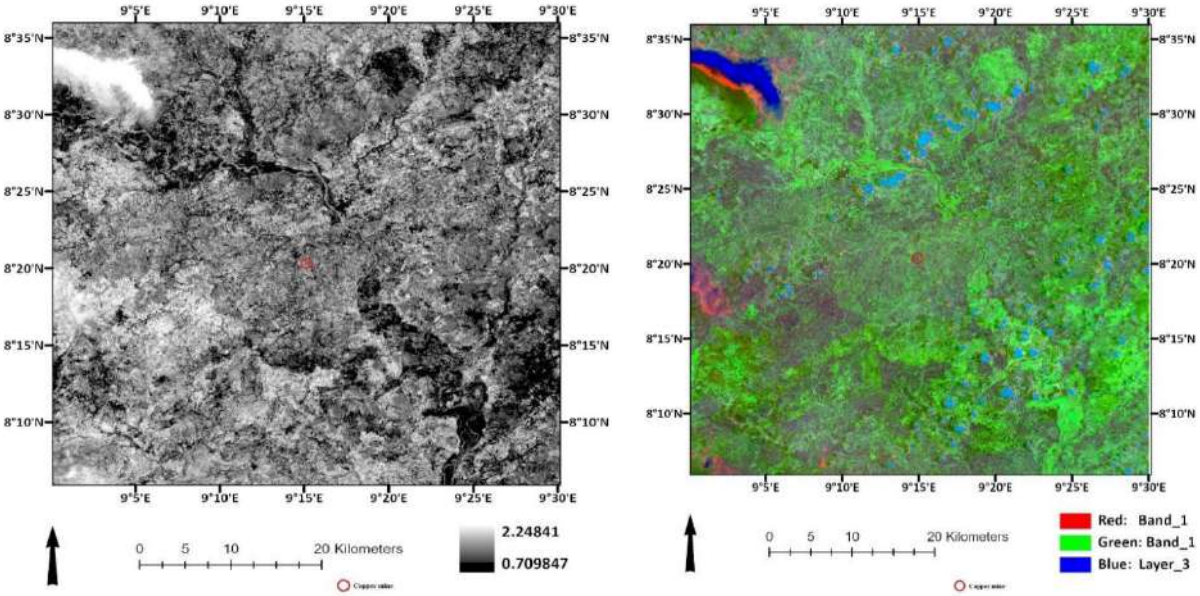

Figures 4c and d. The maps of the ratio of bands 7 and 6, and colour composite of bands 4/2:6/7:5 of the study area

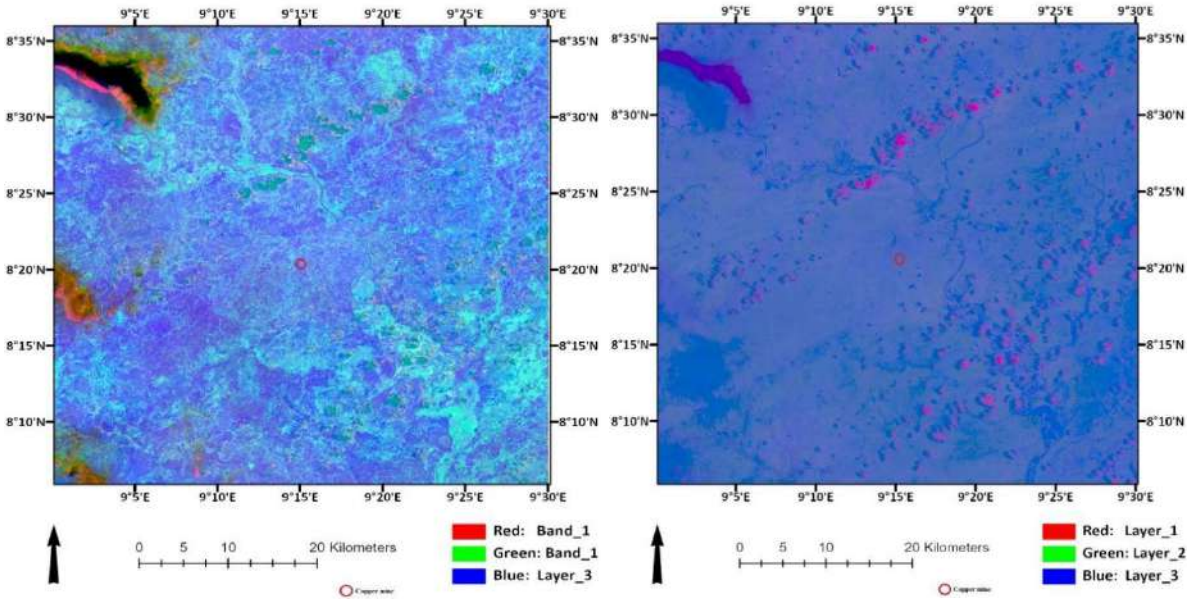

Figures 4e and f. Colour composite map of bands 4/2:6/7:10, and PCA map of bands 3,5,6,7 of the study area.

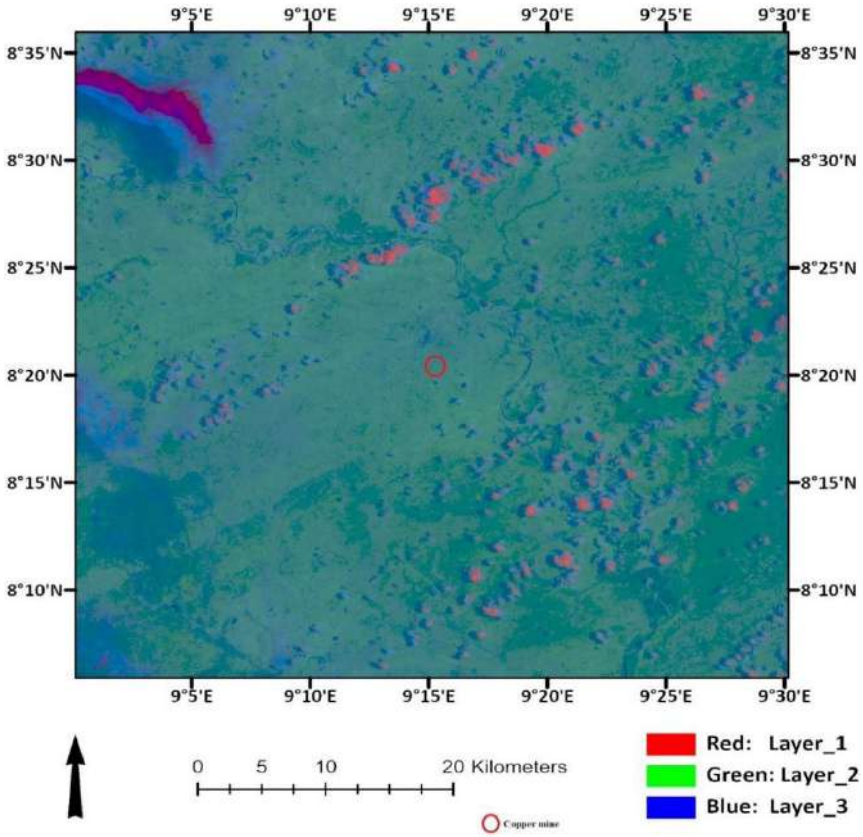

Figure 4g. PCA map for bands 2,3,4,6 for the study area

The results of the band ratio, color composite, and PCA surrounding the copper deposit were confirmed on the ground using the NGSA fieldwork and the study area's DEM and Google Earth maps, A good correspondence was observed among the transform techniques, field data, and DEM and Google Earth maps.

4 Conclusion

The current study demonstrated the value of mapping copper mineralization zones using multispectral Landsat 8 (OLI) data (0.4–2.5 μm).. The techniques, band ratio, colour combination and PCA applied on the Landsat 8 image of the study area to map copper mineralization reported in the study by the NGSA. The results were verified with DEM and Google Earth map of the study area. Evidence of hydrothermal alteration was observed which is a signature of mineralization in the study area. However, the PCA result does not reveal any alteration around the deposit. Geochemical studies is necessary in the study area to strengthen the findings in this study.

References

Ali, A., and Pour, A., (2014). Lithological mapping and hydrothermal alteration using Landsat 8 data: A case study in Ariab mining district, Red Sea Hills, Sudan. *International Journal of Basic and Applied Sciences*. 3, 199–208.

Ambo A. I., Abubakar S. A., Mohammed A. M., Alafara A. B. (2023). Mineralogical and Chemical Analysis of Ore Resources in Nasarawa State for Processing Application. *Science World Journal*, 18(1): 31 – 36.

Beiranvandpour, A. and Hashim, M. (2015) Hydrothermal alteration mapping from Landsat-8 data, Sar Cheshmeh copper mining district, south-eastern Islamic Republic of Iran. *J. Taibah Univ. Sci.*, 9, 155–166.

Chen Q, Cal D, Xia J, Zeng M, Yang H, Zhang R, He Y, Zhang X, Chen Y, Xu X, and Zhao Z (2025). Remote sensing identification of hydrothermal alteration minerals in the Duobuza porphyry copper mining area in Tibet using WorldView-3 and GF-5 data: The impact of spatial and spectral resolution. *Ore Geology Reviews, Elsevier*, 180, 106573. https://doi.org/10.1016/j.oregeorev.2025.106573

Ciampalini, A., Garfagnoli, F., Antonielli, B., Moretti, S., and Righini, G., (2013). Remote sensing techniques using Landsat ETM+ applied to the detection of iron ore deposits in Western Africa. *Arabian Journal of Geosciences*, 6, 4529 – 4546.

Corumluoglu, O., Vural, A. and Asri, I. (2015) Determination of Kula basalts (geosite) in Turkey using remote sensing techniques. *Arab. J. Geosci.*, 8, 10105–10117.

Crosta, A. P., De Souza Filho, C. R., Azevedo, F. and Brodie, C. (2003) Targeting key alteration minerals in epithermal deposits in Patagonia, Argentina, using ASTER imagery and principal component analysis. *Internat. J. Remote Sens.*, 24, 4233 – 4240.

Daneshfar, B., Desrochers, A., and Budkewitsch, P., (2006). Mineral-potential mapping for MVT deposits with limited data sets using Landsat data and geological evidence in the Borden Basin, Northern Baffin Island, Nunavut, Canada. Natural Resources Research. 15, 129 – 149.

Gahlan, H., and Ghrefat, H., (2017). Detection of gossan zones in arid regions using Landsat-8 OLI data: implication for mineral exploration in the eastern Arabian shield, Saudi Arabia. *Natural Resources Research*, 1 - 16.

Ghozali, N. Q., Saepuloh, A., Basuki, N. I., Suhendi, D. D., and Bari, A. (2022). Exploring and evaluating copper-gold mineralization based on ground and Landsat-8 data in Pacitan Regency, East Java, Indonesia. Proceedings, PIT IAGI 51, Makassar, South Sulawesi.

Hedenquist, J. W. (2000). Exploration for epithermal gold deposits. Canada: Society of Economic Geologist Reviews Vol. 13; 245 - 277.

Howari, F. M., Ghrefat, H., Nazzal, Y., Galmed, M. A., Abdelghany, O., Fowler, A. R., Sharma, M., AlAydaroos, F., and Xavier, C. M. (2020). Delineation of Copper Mineralization Zones at Wadi Ham, Northern Oman Mountains, United Arab Emirates Using Multispectral Landsat 8 (OLI) Data. *Front. Earth Sci.*, 8: 578075. doi: 10.3389/feart.2020.578075

Langford, R. L. (2015) Temporal merging of remote sensing data to enhance spectral regolith, lithological and alteration patterns for regional mineral exploration. *Ore Geol. Rev.*, 68, 14–29.

Liu, C., Qui, C., Wang, L., Feng, J., Wu, S., and Wang, Y. (2023). Application of Aster Remote Sensing Data to Porphyry Copper Exploration in the Gondwana Region. *Minerals, MDPI*, 13(4),501. http://doi.org/10.3390/min13040501.

Madani, A. M., (2009). Utilization of Landsat ETM+ data for mapping gossans and iron rich zones exposed at Bahrah area, western Arabian Shield, Saudi Arabia. Journal of King Abdulaziz University. *Earth Sciences*, 20,35 – 49.

Masoumi, F., Eslamkish, T., Honarmand, M. and Abkar, A. A. (2016). A Comparative Study of Landsat-7 and Landsat-8 Data Using Image Processing Methods for Hydrothermal Alteration Mapping. *Resource Geology*, 67(1): 72 – 88. doi: 10.1111/rge.12117.

Mia, M. B. and Fujimitsu, Y. (2012) Mapping hydrothermal altered mineral deposits using Landsat 7 ETM+ image in and around Kuju volcano, Kyushu, Japan. *J. Earth Syst. Sci*., 121, 1049 – 1057.

Mokhtari, Z., Boomeri, M. and Bagheri, S. (2015) Digital Image Processing and Analysis Techniques for Detection of Hydrothermal Alteration Zones: A Case Study in Siah-Jangal Area, North of Taftan Volcano, Southeastern Iran. *J. Indian Soc. Remote Sens.*, 43, 363 – 377.

Moradi, R., and Boomeri, M. (2017). Remote sensing detection of altered zones associated with Cu-Mo mineralization in North of Zahedan, SE Iran using Landsat-8 data. Yerbilimleri, Bulletin of the Earth Sciences Application and Research Centre of Hacettepe University, 38 (3), 275 – 294.

Mwaniki, M. W., Matthias, M. S. and Schellmann, G. (2015). Application of remote sensing technologies to map the structural geology of central Region of Kenya. *IEEE J. Sel. Top. Appl. Earth Obs. Remote Sens.*, 8, 1855 – 1867.

Pirajno, F. (2008). Hydrothermal processes and mineral systems. *Springer, Perth*, 1250p

Pour, A. B., Park, T. S, Park, Y., Hong, J. K., Muslim, A. M., Läufer, A., Crispini, L., Pradhan B., Zoheir, B., Rahmani, O., Hashim, M., and Hossain, M.S. (2019). Landsat-8, Advanced Spaceborne Thermal Emission and Reflection Radiometer, and WorldView-3 Multispectral Satellite Imagery for Prospecting Copper-Gold Mineralization in the Northeastern Inglefield Mobile Belt (IMB), Northwest Greenland. *Remote sensing, MDPI*, 11, 2430 – 2469. doi:10.3390/rs11202430

Pour, B. A., and Hashim, M., (2013). Fusing ASTER, ALI and Hyperion data for enhanced mineral mapping. *International Journal of Image and Data Fusion*, 4, 126 -145.

Pour, B. A., and Hashim, M., (2014). ASTER, ALI and Hyperion sensors data for lithological mapping and ore minerals exploration. *Springerplus*, 3, 130.

Pour, B. A., and Hashim, M., (2015a). Evaluation of Earth Observing-1 (EO1) Data for Lithological and Hydrothermal Alteration Mapping: A Case Study from Urumieh-Dokhtar Volcanic Belt, SE Iran. *Journal of the Indian Society of Remote Sensing*, 43, 583 - 597.

Pour, B. A., and Hashim, M., (2015b). Integrating PALSAR and ASTER data for mineral deposits exploration in tropical environments: a case study from Central Belt, Peninsular Malaysia. *International Journal of Image and Data Fusion*, 6, 170 - 188.

Pour, A. B., and Hashim, M., (2015c). Hydrothermal alteration mapping from Landsat-8 data, Sar Cheshmeh copper mining district, southeastern Islamic Republic of Iran. *Journal of Taibah University for Science*, 9, 155 - 166.

Pour, B. A., Hashim, M., and Marghany, M., (2014). Exploration of gold mineralization in a tropical region using Earth Observing-1 (EO1) and JERS-1 SAR data: a case study from Bau gold field, Sarawak, Malaysia. *Arabian Journal of Geosciences*, 7, 2393 - 2406

Ranjbar, H., Honarmand, M. and Moezifar, Z. (2004). Application of the Crosta technique for porphyry copper alteration mapping, using ETM+ data in the southern part of the Iranian volcanic sedimentary belt. *J. Asian Earth Sci*., 24, 237–243.

Richards, J. A. (2012) Remote Sensing Digital Image Analysis: An Introduction, 5th edn. *Springer, Canberra, ACT*, 494p.

Rowan, L. C., Hook, S. J., Abrams, M. J. and Mars, J. C. (2003) Mapping hydrothermally altered rocks at Cuprite, Nevada, using the Advanced Spaceborne Thermal Emission and Reflection Radiometer (ASTER), a new satellite-imaging system. *Econ. Geol.*, 98, 1019–1027.

Roy, D. P., Wulder, M. A., Loveland, T. R., Woodcock, C. E., Allen, R. G., Anderson, M. C., et al. (2014). Landsat-8: science and product vision for terrestrial global change research. *Remote Sens. Environ.* 145, 154 – 172. doi:10. 1016/j.rse.2014.01.009

Safari, M., Maghsoudi, A., and Pour, A.B., (2017). Application of Landsat-8 and ASTER satellite remote sensing data for porphyry copper exploration: a case study from Shahr-e-Babak, Kerman, south of Iran. *Geocarto International*, 1 - 16.

Shalaby, M.H., Bishta, A.Z., Roz, M.E., and Zalaky, M.A., (2010). Integration of geologic and remote sensing studies for the discovery of uranium mineralization in some granite plutons, Eastern Desert, Egypt. Journal of King Abdulaziz University, *Earth Sciences*, 21, 1–25.

Tangestani, M. H. and Moore, F. (2001) Comparison of three principal component analysis techniques to porphyry copper alteration mapping: a case study, Meiduk area, Kerman, Iran. *Can. J. Remote Sen.*, 27, 176–182.

Trinh, L. H. and Vu, D. T. (2015). Application of Remote Sensing Technique to Detect Copper Mineral based Principal Component Analysis and Band Ratio Methods. A Case Study: Laocai Province, Vietnam. *European Geographical Studies*, 7(3): 137 – 145. DOI: 10.13187/egs.2015.7.137.

van der Meer, F. D., van der Werff, H. M. A., van Ruitenbeek, F. J. A. et al. (2012) Multi-and hyperspectral geologic remote sensing: A review. *Int. J. Appl. Earth Obs. Geoinf*., 14, 112–128.

Zhang, T., Yi, G., Li, H., Wang, Z., Tang, J., Zhong, K., Li, Y., Wang, Q., and Bie, X., (2016). Integrating Data of ASTER and Landsat-8 OLI (AO) for Hydrothermal Alteration Mineral Mapping in Duolong Porphyry Cu-Au Deposit, Tibetan Plateau, China. *Remote Sensing*, 8, 1 - 23.

Zhang X, Zhao Z, Chen Q, Chai W, Li Z, Zhang G, Yang H, Niu L, (2023). Mapping hydrothermal alteration of the Pulang porphyry copper deposit, SW China, using ASTER and ZY1-02D satellite data. *Ore Geology Reviews, Elsevier*, 161, 105605. https://doi.org/10.1016/j.oregeorev.2023.105605

Delineating Younger Granites in Jos Using Aero-radiometric Maps

Bello YA[1], Rabiu M[1], Daramola D[2] Lawal HA[1], Alao JO[1], Mashood LO[3] and Yakubu MB[4]
[1]Physics Department, Air Force Institute of Technology, Kaduna
[2]Department of Mathematics, Air Force Institute of Technology, Kaduna
[3]Department of Statistics, Air Force Institute of Technology, Kaduna
[4]Physics Department, Ahmadu Bello University, Zaria
Corresponding email: belloya@afit.edu.ng

Abstract

This study utilizes aero-radiometric data to delineate Younger Granites in Plateau State, Nigeria, leveraging on the measure of natural gamma radiation emitted from the Earth's surface. The Younger Granites is the primary source of tin and columbite which are essential materials in the manufacturing industry. On that basis, the study area has attracted the attention of several researchers, but with few reports on the use of aero-radiometric data which can provide regional details of the Younger Granites. The data of the aero-radiometric survey across the study area were processed to create detailed maps highlighting gamma-ray anomalies associated with granitic rocks. The results reveal significant concentrations of potassium, often correlating with known Younger Granite outcrops, thus confirming the effectiveness of aero-radiometric mapping in identifying granitic boundaries. Additionally, the study integrates remote sensing and geological mapping techniques to enhance the delineation process, providing a comprehensive understanding of the geological context and potential mineral resources associated with Younger Granites. The radiometric maps also revealed linear structures within the study area trending NE, NW, and NNE which align with previous reports. Furthermore, the result reveals signatures of Younger Granites in locations that were hitherto overlain by older granites, suggesting unexposed Younger Granites in those locations.

Keywords: Younger granites, unexposed younger granites, spectrometric data, lineaments

1. Introduction

Tin is possibly one of the first metals used by man (bronze; alloy of copper and tin), its alloy, bronze, is useful in the production of weapons, tools, jewellery etc (Ogunyele and Akingboye, 2018). The primary source of tin is the Younger Granite Complexes (YGC) of northern Nigeria, attracting the attention of several researchers in the province (Bello *et al*., 2025; Alkali and Gaya, 2011; Hossain and Turaki, 1983 Ugwu *et al.*, 2017; Mustapha *et al*., 2020; Ugodulunwa and Yakubu, 2007; Ejeh and Ugbe, 2010; Abdullahi, 2021; Alkali and Yusuf, 2010; Ibeneme *et al*., 2018; Onyeanuna, 2016; Opara *et al*., 2015; Obaje, 2019; Peter *et al*., 2014; Alkali *et al.,* 2012; Ajakaiye *et al*., 1985; Kankgolo, 1984)

The NE and NNE trending lineaments found in the structural interpretation of the aeromagnetic data covering the western portion of the YGC in northcentral Nigeria are said to be part of

significant fracture lines, which most likely influence the emplacement of the granite and the NE trending joints (Alkali and Gaya,2011; Hossain and Turaki, 1983 Ugwu *et al.*, 2017; Mustapha *et al*., 2020; Ugodulunwa and Yakubu, 2007; Ejeh and Ugbe, 2010; Abdullahi, 2021; Alkali and Yusuf, 2010; Ibeneme *et al*., 2018; Onyeanuna, 2016; Opara *et al*., 2015; Obaje, 2019; Peter *et al*., 2014; Alkali *et al.,* 2012). Therefore, it is believed that the NE set represents faults linked to significant movement caused by previous tectonics activity (Ajakaiye *et al*., 1985). The NNE linear structures are linked to pegmatite zones and quartz veins. (Alkali and Gaya,2011). In an NS trending zone, the Jurassic ring tectonic complexes—younger granites—intruded into late Precambrian basement rocks (Szentes, 2009). Ajakaiye *et al*., (1985;) observed a magnetic boundary that separates the YGC into two groups, petrologically different, and suggesting the boundary may be a fault line with uplift to the south. Some reports (Ajakaiye *et al*., 1985; Kankgolo, 1984) also suggested that the larger complexes, nearly vertical sides, extend to 12 km depth, and the smaller ones to 6 km. The Nigerian Younger Granites have some of the most extensive primary mineralization and joint-controlled greisen vein development (Ike, 1979).

The Jos- Bukuru Younger Granite complex (Figure 1) is characterized by a low Bouguer value, which aligns with the residual anomaly map (Alkali and Yusuf, 2010). Additionally, gravity depth models suggest that the volcanic rocks can reach depths of 13.96 km and the plutonic rocks up to 18.75 km. The enormous depths are due to the presence of a large-scale fault connected with the Romanche fracture zone in the basement around the Jos – Bukuru YGC (Alkali and Yusuf, 2010). Younger granitic rocks in the north central region (primarily alkaline) are peraluminous in composition and categorized as A-type according to the granite classification system because to their alkalinity, anhydrous characteristic, and assumed anorogenic tectonic context (Imeokparia, 1989). Given that the more fractionated granite porphyry had greater values than the biotite granite, they demonstrated evidence of a significant degree of fractionation, indicating that the REE patterns are LREE enriched (Abdullahi, 2021; Aga and Haruna, 2019). The granitic rocks' negative eU anomalies demonstrate that during fractional crystallization, a significant amount of plagioclase was extracted from the felsic magma (Shola, 2020; Adubok, 2008; Bowden, 1970). Despite the characteristics of the YGC extracted from several geophysical and geochemical investigations, few researchers have applied the radiometric method despite its correlation to lithology.

There is a strong link between un-weathered rocks and interpreted radiometric data, and the radiometric method maps surface geology more successfully than other geophysical methods. Consequently, mapping soil characteristics and regolith can benefit by knowing the quantity and proportion of K, Th, and U released from the surface (Fall *et al*., 2020; Elkhateeb and Abdullatif 2018). Additionally, the technique can be applied to the search for non-radioactive deposits linked to elements like zirconium and titanium (Bassey and Unachukwu, 2019; Onyejiuwaka 2021). In their study of the Ropp Younger granite Complex of the Jos Plateau, Ashano and Olasehinde (2010) used an integrated approach (Landsat, total count radioactive, and total magnetic field data) and found that some highly altered Younger granites had higher radioactivity than their unaltered counterparts, which had much lower values. According to the authors, the alteration process may

have produced significant radioactivity in the changed rocks by releasing potassium from feldspar (when kaolinite is created) into the environment as free positive ions in soil and groundwater.

This research aimed to investigate the distribution of the concentration of the three radioelements within the YGC in the Jos-Bukuru axis. This was essential in delineating the spatial extent of the Younger Granites in the area and identifying possible presence of unexposed Younger Granites. This was achieved through the application various techniques on the aero-radiometric data of the study area. Thus providing further understanding about the YGC of the north central Nigeria.

1.1 The Study area

The study area is within Jos, Plateau state covering an area of about 22000km^2 in the North-central region of Nigeria. The complex is located in the center of Nigeria's YG magmatic activity (Opara *et al.,* 2015). It is thought that the younger granites are discordant high-level intrusions that were inserted piecemeal through the primary block that fell (Ajigo and Ayodele, 2021). Many of the structures' sizes result from the stacking and overlap of distinct intrusive cycles (Nyako, 2013). The Younger Granites is 140 – 190 MA.

2. Materials and Methods

2.1 Material

A portion of the airborne survey conducted by Fugro Airborne Survey, between 2005 and 2009, for the Nigerian Geological Survey Agency (NGSA) served as the primary source of data for this investigation. The coordinates od the study area is longitude 8.5ºE - 9ºE and latitude 9.5ºN - 10ºN. The data were collected at a height of 100 meters, with a terrain clearance of 80 meters, a flight line spacing of 500 meters orientated in a NW-SE direction, and a tie line spacing of 2000 meters (Adewumi *et al.,* 2021).

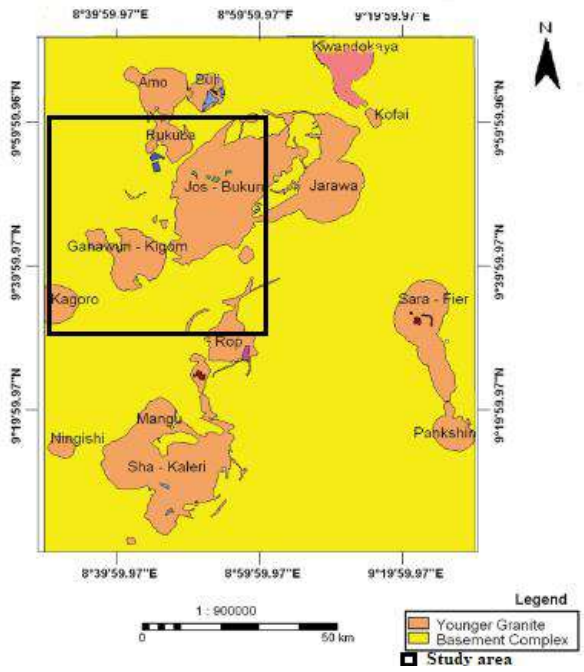

Figure 1. Geology map of the study area showing the Younger Granites around Jos. Modified after Ajigo and Ayodele (2021).

GPS position data is saved in the digital data stream, and on-board sodium iodide scintillation counters monitor gamma energy. Channels for the total gamma count, U, Th, and K are independently accumulated based on the aircraft's speed, frequently at one-second intervals, corresponding to 30 to 60 meters across the ground (Walker *et al.,* 2018).

2.2 Method

The radiation levels from uranium (U), thorium (Th), and potassium (K) in percentage, ppm, and %, respectively, were measured. Geosoft (Oasis Montaj, version 8.4) software was used to process the initial data. The concentration grids for the radio-elements were created using a minimal curvature technique. Potassium (%K), equivalent thorium (eTh ppm), and equivalent uranium (eU ppm) maps, as well as ratio maps and composite images of the three radioactive elements, the ternary map, were produced as a result of the data transformation techniques used. The elements' relative concentrations were displayed on the ternary map (Onyejiuwaka, 2021).

The summary of the data transformation to achieve the set objectives of this research are as follows;

(1) A collection of radioelements (K, eU, and eTh) and their ratios (eU/eTh, eU/K, etc.) are shown on the Total Count (TC) map to illustrate the surface distribution of these elements.

(2) Four composite image maps were established: one for radioelements (K, eU, and eTh); one for uranium (eU, eU/eTh, and eU/K); one for thorium (eTh, eTh/eU, and eTh/K); and one for potassium (K, K/eU, and K/eTh)..

Results and Discussion

The three radioelement distributions and the TC's nature are highlighted in gamma-ray spectrometric maps (Figures 2–5), making them more appropriate for identifying geological features. A general relationship to different rock units and structural trends is depicted in these maps. The four—TC, K, eU, and eTh—as well as the ratio maps—eU/eTh and eU/K—were carefully examined before being qualitatively evaluated. An analysis of the aero-radiospectrometric maps shows that there is a large range of levels, which is indicative of the fact that rocks of different compositions cover the research area.

Regional association between various rock units and measured gamma radiation levels makes it clear that the aeroradioactivity pattern is intimately related to the local surface geology. A succinct explanation of the qualitative interpretation of the aero-radiospectrometric maps pertaining to the various rock units' locations.

The TC map (Figure 2) shows three radiometric levels, high, intermediate and low. The high level is observed over younger granites. Two regions; north (close to the Rukuba YG) and south (near Ganawun-Kigom YG) of the study, also recorded high TC concentrations. Although, they are within the basement complex of the study area, but believed to represent unexposed Younger Granite Complexes (Un-YGCs) due to similar TC concentration with the YGs. Cases of Un-YGC are notable in the YGC of Nigeria (Raimi *et al*., 2014). The intermediate level is prominent in some parts of YGCs in the study area. They were reported to be associated mainly with the older granites (Youssef and Elkhodary, 2013). The low level is prominent within the basement complex of the study area. The linear structures in the study area as revealed by the TC map are NW, N-S, and the majority in the NE direction. These are in tandem with previous reports (Opara *et al.*, 2015).

The total spatial distribution of the relative potassium concentrations In the research area is displayed by the K concentration map (Figure 3) It indicates that the YGCs and possible Un-YGCs are characterized by high concentration, although the larger part of the Jos-Bukuru YGC his characterized of low potential concentrations. The highlighted linear structures are trending in NE, NW, and NS directions

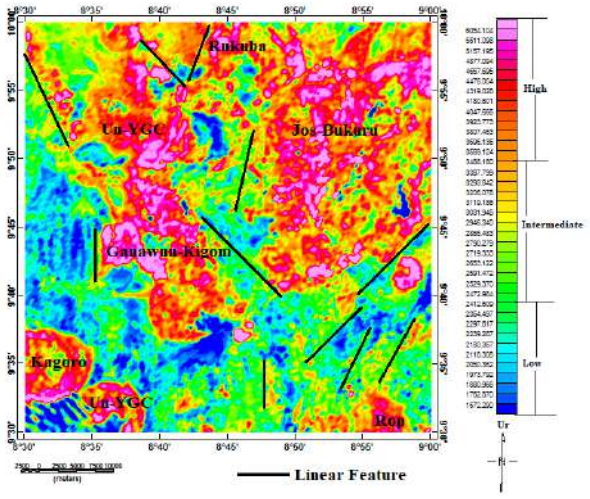

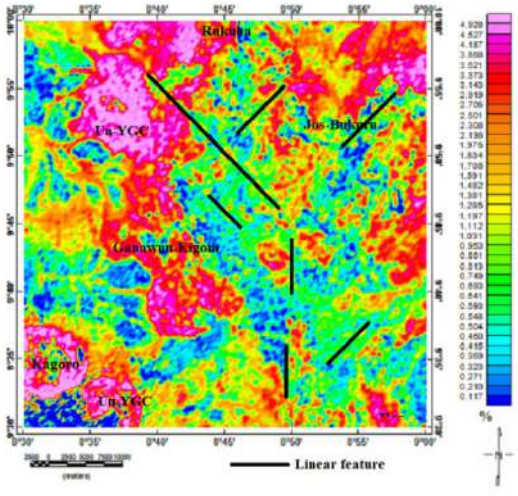

Figure. 2: Map showing the distribution of the total count (TC).

Figure 3: Map showing potassium concentration distribution.

Based on the eTh concentration grid map (Figure 4), the research area's greatest values are found in the younger granites and ring complex, including the potential Un-YGC. The result also reveals lineaments in NW and NE directions, NE is dominant. These are consistent with the result of TC. As observed in other results, the extent of Rop YGC appears to be beyond the current dimension on the Geologic map.

The high eU concentration is associated with younger granites and Un-YGC (Figure 5). The low concentration of Uranium is associated with the older granites in the basement complex. The NW trending lineaments are dominant in the uranium concentration map of the study area.

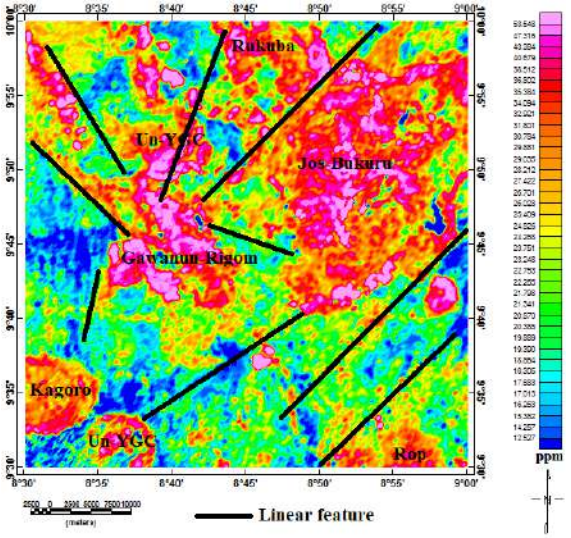

Figure 4. Map showing thorium concentration distribution.

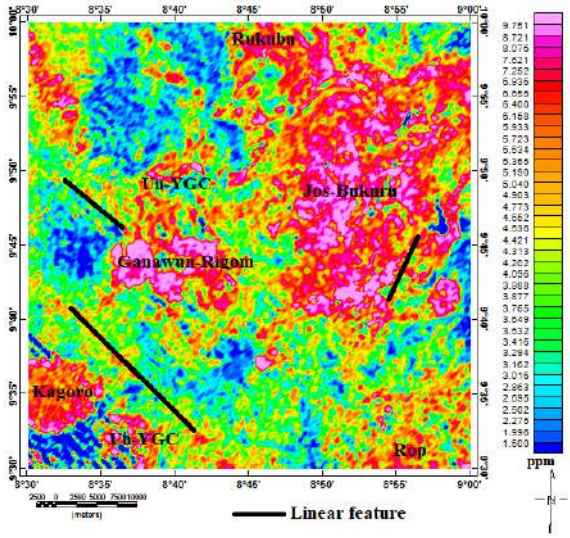

Figure 5. Map showing uranium concentration distribution.

Red, green, and blue are modulated in proportion to the radioelement concentration values of the K, eTh, eU, and their ratio grids to create ternary maps, which are color composite images. The ternary maps of these ratios are a valuable geological and mineral exploration tool for differentiating the zones of consistent lithology and contacts between contrasting lithologies since specific rock types frequently exhibit unique ratios of the three radioactive elements (Duval 1983).

The characteristic concentrations of the three primary radioelements vary depending on the type of rock. The K (in %), eU (in ppm), and eTh (in ppm) concentrations are shown by various ink colors in the ternary map of the three radioelements (Figure 6). The color hue created by combining the three colors in the right amounts at any given place represents the relative concentrations of the three radioelements. (1990 Brooche; 2003 IAEA). The ternary map of the three radioelements (Figure 6) suggests the YGCs and Un-YGCs are of similar petrological configurations, except the Jos-Bukuru YGC which possesses a high concentration of thorium. This is similar to the result of the potassium composite map of the study area (Figure 7). The results around the Jos-Bukuru axis could be due to the mining activities recorded in the area as thorium does not respond alterations.

The thorium (Figure 8) and Uranium (Figure 9) composite map reveal high concentration of thorium and uranium concentration around the YGCs and Un-YGCs.

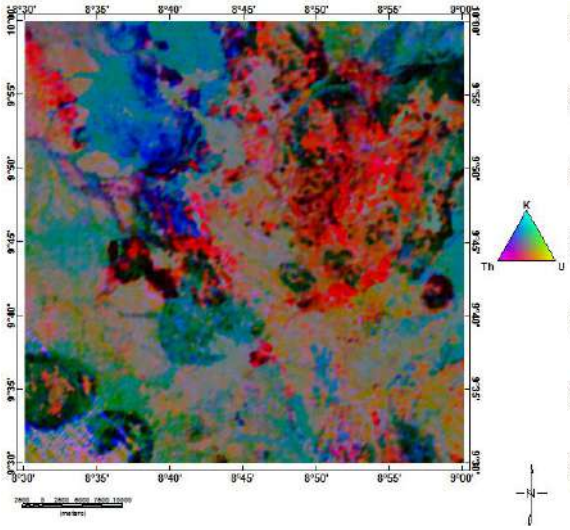

Figure 6. Composite map of the three radioelements

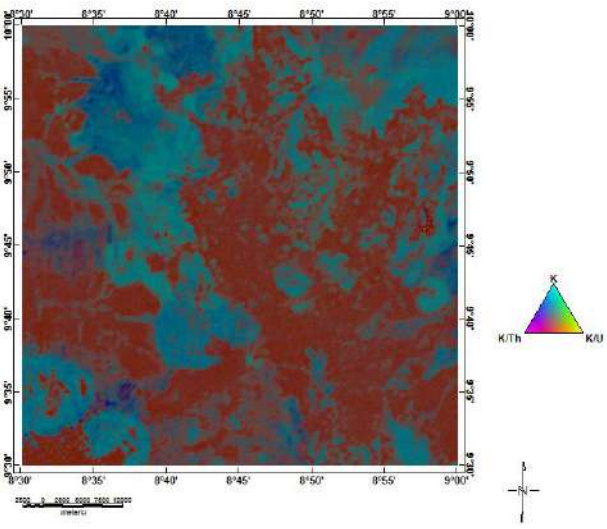

Figure 7. Potassium composite map of the study area

4. Conclusion

The techniques adopted in this research effectively mapped the known younger granite complexes in the study area. Possible unexposed younger granite complexes were also mapped around the known Younger Granites. The younger granites were believed to be of various petrological compositions. The linear structures in the study area are in the NW, N-S, and NE direction. Geochemical studies will be necessary in this study area, especially around some identified features of interest.

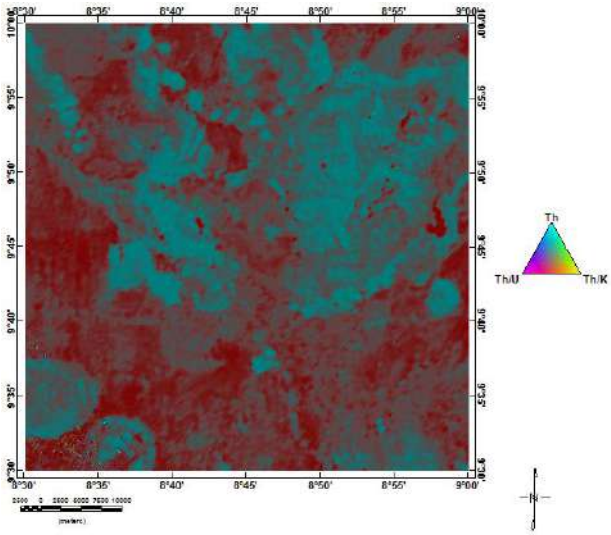

Figure 8. Thorium composite map of the study area

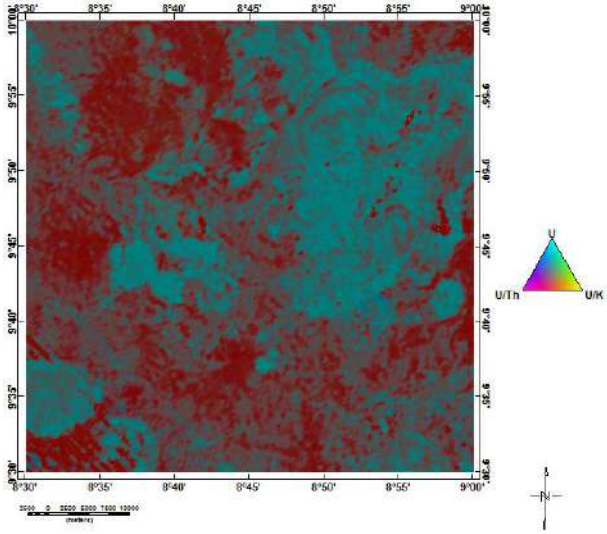

Figure 9. Uranium composite map of the study area

References

Abdullahi, Y.A. (2021). Geology, petrography and geochemical studies of rocks around Zaria road and environs part of Naraguta sheet 168 NW, Jos, northcentral Nigeria. B.Sc. Project, Gombe State University.

Adewumi, T., Salako, K.A., Alhassan, U.D., Adetona, A.A., Abdulwaheed, R.A. and Udensi, E.E. (2021) "Interpretation of Airborne Radiometric data for possible hydrocarbon presence over Bornu basin and its environs, Northeast Nigeria using Thorium normalisation method". Iranian *Journal of Earth Sciences,* 13(3); 161 – 172. DOI: 10.30495/ijes. 2021.682863.

Adubok, A.S. (2008). Evolutionary trend of the Jarawa Younger Granites ring complex, Jos Plateau, Central Nigeria. *Science World Journal*, 3(2); 121 – 126.

Aga, T. and Haruna, A.I. (2019). The Geochemistry and Petrogenesis of the Kofayi Younger Granite Complex, Central Nigeria. *SSRG International Journal of Geoinformatics and Geological Science (SSRG-IJGGS)*, 6(3).

Ajakaiye, D.E., Hall, D.H. and Millar, T.W. (1985). Interpretation of aeromagnetic data across the central crystalline shield area of Nigeria. *Geophys. J. R. astr. Soc*., 83; 503 – 517.

Ajigo, I.O. and Ayodele, O.S. (2021). Litho-Structural Analysis of the Sara-Fier Ring Complex, Northcentral Nigeria. *International Journal of Earth Science and Geophysics*, 7: 055 – 066. DOI: 10.35840/2631-5033/1855

Alkali, S.C. and Gaiya, S. (2011). Delineation of Linear Structures from Digitized Aeromagnetic Data of The Western Part of The Younger Granite Complex of North Central Nigeria. *New York Science Journal*, 4(9): 56 - 62. (ISSN: 1554-0200). http://www.sciencepub.net/newyork.

Alkali, S.C. and Yusuf, S.N. (2010). Gravity Study over Jos–Bukuru Younger Granite Complex, North Central Nigeria. *Archives of Physics Research*, 1(4); 178 – 191.

Alkali, S.C. Gaiya, S. and Musa, B.A. (2012). Depth Estimation of Digitized Aeromagnetic Data of the Western Part of the Younger Granite Rocks of North Central Nigeria, West Africa. *Research Journal of Applied Sciences, Engineering and Technology* 4(15); 2444 - 2450.

Ashano, E.C. and Olasehinde, A (2010). An integrated study of economic mineral potential of Ropp Complex, Northcentral Nigeria. *Global Journal of Geological Sciences*, 8(1): 1 – 15.

Bassey, N.E. and Unachukwu, H.N. (2019). Geological analysis of ground radiometric survey data of Hong hills, Hawal basement complex, NE Nigeria. *Journal of Geology and Mining Research*, 11(3): 22 – 30. Doi: 10.5897/JGMR2018.0301.

Bello Y.A., Lawal K.M., Magaji S.S., Raimi J., Amuda T.O., Daramola D., Yakubu M.B., Lawal H.A. (2025). Investigating the connectivity of Geshere and Rishiwa younger granite using aero-radiometric data. Proceedings of the Nigerian Society of Physical Sciences 2, 151

Bowden, P. (1970). Origin of the Younger Granites of Northern Nigeria. *Contr. Mineral. and Petrol.*, 25; 153 – 162.

Broome, H.J. (1990). Generation and interpretation of Geophysical images with examples from the Rae Provinces, Northwestern Canada Shield. *Geophysics,* 55(8), 977 - 997

Duval, J.S. (1983). Composite colour images of aerial gamma-ray spectrometry data, Geophysics, 48, 722 – 735.

Ejeh, O.I. and Ugbe, C.F. (2010). Fracture systems in the younger granite rocks around Fobur, northern Nigeria: product of residual stress. *Global Journal of Geological Sciences*, 8(1); 57 – 64.

Elkhateeb, S.O. and Abdellatif, M.A.G. (2018). Delineation potential gold mineralization zones in a part of Central Eastern Desert, Egypt using Airborne Magnetic and Radiometric data. *NRIAG Journal of Astronomy and Geophysics, Taylor and Francis*, 7: 361 – 376. https://doi.org/10.1016/j.nrjag.2018.05.010

Fall, M., Baratoux, D, Jessell, M., Ndiaye, P.M., Vanderhaeghe, O., Mayen, J.F., Baratoux, L. and Bonzi, W.M. (2020). The redistribution of thorium, uranium, potassium by magmatic and hydrothermal processes versus surface processes in the Saraya Batholith (Eastern Senegal): Insights from airborne radiometrics data and topographic roughness. *Journal of Geochemical Exploration*, 219(2): 106633. https://doi.org/10.1016/j.gexplo.2020.106633

Hossain, M.T. and Turaki, U.M. (1983). Bibliography on the Younger Granite Ring Complexes and tin mineralization in West Africa with emphasis on Nigeria. *Journal of African Earth Sciences*, 1(1); 73 – 81.

Ibeneme, S.I., Oha, I.A. Abdulsalam, N.N. and Onuoha, M.K. (2018). Improved Mapping of the Structural Disposition of Some Younger Granite Ring Complexes of Nigeria Using High Resolution Aeromagnetic Data. *Journal of Geology & Geophysics*, 7(4); 443. DOI: 10.4172/2381-8719.1000443.

IAEA (2003). Guideline for radioelement mapping using gamma-ray spectrometry data, IAEA-TECDOC-1363, Vienna, Austria, pp 179.

Ike, E.C. (1979). The structure, petrology and geochemistry of the Tibchi Younger Granite ring complex, Nigeria. PhD Thesis, University of St Andrews.

Imeokparia, E.G. (1989). Geochemical trends in the Jos-Bukuru granites of central Nigeria: magmatic and metallogenic implications. *Journal of African Earth Sciences*, 9(3/4); 689 - 700.

Kangkolo, R. (1984). Interpretation of the aeromagnetic anomalies over the Younger Granites of Jos-Pankshin area in Plateau State, Nigeria. M.Sc. Thesis, Ahmadu Bello University, Zaria, Nigeria.

Mustapha S., Suleman S., Iliyasu S. R., Udensi E. E., Sanusi Y.A., Dahuwa D. and Abba L. (2020). Interpretation of Aeromagnetic Data and Landsat Imagery over the Nigerian Younger

Granites in and around Kafanchan Area, North-Central Nigeria. FUDMA Journal of Sciences, 4 (4); 323 – 333. DOI: https://doi.org/10.33003/fjs-2020-0404-489.

Nyako AA (2013). Trace elements as pathfinders for gemstone deposits: Jarawa and Eastern part of shere complex as a case study. M.Sc. Thesis, University of Jos, Nigeria.

Obaje, N.G. (2009) Geology and Mineral Resources of Nigeria, Lecture Notes. Earth Sciences 120, DOI 10.1007/978-3-540-92685-6 3

Onyeanuna, C.C. (2016). Interpretation of Ring Structures in Jos Plateau Using NigeriaSat 1 Imagery. *International Journal of Mathematics and Physical Sciences Research*, 4(2); 95 – 104.

Onyejiuwaka, I.S. (2021). Delineation of Geologic Units, Mineral Potentials and Distribution in Udegi Complex and Environs, North Central Nigeria, Using Airborne Radiometric Data. *IOSR Journal of Applied Geology and Geophysics (IOSR-JAGG)*, 9(3): 01 - 14. DOI: 10.9790/0990-0903020114

Opara A.I., Udoete R.L., Emberga T.T., Ijeoma K.C., Echetama H.N., Ugwuegbu I.E., Nwokocha K.C., Chinaka J.C., Onyema J.C. (2015). Structural Interpretation of the Jos-Bukuru Younger Granite Ring Complexes Inferred from Landsat-TM Data. *Journal of Geosciences and Geomatics, Science and Education Publishing*, 3(3): 56 – 67. DOI:10.12691/jgg-3-3-2.

Peter, J.S. Odubia, E.O. and Longpia, C.B. (2014). Relating Geology and Geological Structures with Regional Episodes: Implication for Groundwater Exploration and Development around Kwal-Kanke Area, Jos Plateau. *International Journal of Engineering Research & Technology (IJERT)*, 3(2).

Raimi, J., Dewu, B. B. M. and Sule P. (2014). An Interpretation of Structures from the Aeromagnetic Field over a Region in the Nigerian Younger Granite Province. *International Journal of Geosciences*, 5; 313 – 323. http://dx.doi.org/10.4236/ijg.2014.53031

Shola, O.C. (2020). Geological Settings and Geochemistry of Younger Granitic Rocks from Kuba Area, Ropp Complex, North-Central Nigeria. *FUPRE Journal of Scientific and Industrial Research,* 4(2); 9 – 21.

Szentes, G. (2009). Granite formations and granite cavities in northern Nigeria. *Cadernos Lab. Xeolóxico de Laxe Coruña*, 34; 13 – 26.

Ugodulunwa, F.X.O. and Yakubu, H.M. (2007). Application of GIS technique to the interpretation of the aeromagnetic map and landsat imagery of Buji Younger Granite Complex, northern Nigeria. *Journal of Engineering and Applied Sciences*, 3; 61 – 6.

Ugwu, S.A., Nwankwoala, H.O. and Agada, E.A. (2017). Structural Analysis and Aeromagnetic Interpretation of Spot Image for Mineral Potentials in the Jos-plateau Area, North Central

Nigeria. *Middle-East Journal of Scientific Research,* 25(8); 1715 – 1723. DOI: 10.5829/idosi.mejsr.2017.1715.1723.

Walker, S., Harmen, K and Donovan, D. (2018). Airborne Gamma-ray surveying in Hydrocarbon Exploration. GeoConvention, Canada, 2018.

Youssef, M. A. S. and Elkhodary, S. T. (2013). Utilization of airborne gamma ray spectrometric data for geological mapping, radioactive mineral exploration and environmental monitoring of southeastern Aswan city, South Eastern Desert, Egypt. *Geophys. J. Int.* (2013) 195, 1689 – 1700

Phishing Attack Detection Techniques: Systematic Literature Review

[1]Aji Livius Igba, [2]Ismaila Idris, [3]Olawale Surajudeen Adebayo [4]Joseph Adebayo Ojeniyi, [5]Sikiru Olanrewaju Subairu
[1,2,4,5] Department of Cyber Security Science, School of Information and Communication Technology, Federal University of Technology, Minna.
[3]Cybersecurity Department, Faculty of Computing, National Open University of Nigeria
aji.pg202319399@st.futminna.edu.ng

Abstract

This paper examines the most popular models or algorithms for phishing detection in this systematic literature overview of phishing detection techniques with summaries of the methods used to identify phishing assaults. Citations of research community publications are highlighted in the study as an indicator of their impact and importance to the corpus of knowledge, using selected related research documents from IEEE Xplore, ScienceDirect, Google Scholar, ResearchGate, and SpringerLink between 2015 and 2024. The study examines phishing detection techniques under four main headings: visual similarity-based, heuristic-based, blacklist/whitelist-based, and machine learning, which includes deep learning as a sub-technique of those above. This study has shown machine learning methods performed better than the other phishing detection methods reviewed. However, it still suggests a need for adaptable models for emerging threats, pointing to the fact that robust models handle polymorphic URL attacks while ensuring data confidentiality.

Keywords: AI security, Cyber Threats, Deep learning, Machine Learning, Phishing Detection

1.0 INTRODUCTION

Phishing, a deceptive practice aimed at stealing personal information, poses a persistent and evolving threat to cybersecurity. (Apurv et al. 2022) Phishing can be classified into two key categories: technical subterfuge, which exploits system vulnerabilities, and social engineering, which manipulates human behavior. (Alkhalil et al. 2021) Discuss sophisticated techniques such as spoofing and man-in-the-middle attacks, where attackers compromise systems and extract sensitive information without detection. (Dinesh et al. 2023) further emphasize psychological deception, where attackers use trust-based methods to trick individuals into revealing personal data.

Despite the development of advanced detection technologies, such as machine learning and artificial intelligence, attackers continually adapt their strategies to evade detection, employing the same innovative tools to bypass security measures. Existing research tends to address specific facets of phishing, such as technical methods or psychological tactics, but often lacks a unified perspective that bridges these domains. Furthermore, reviews of existing solutions frequently overlook emerging trends and the dynamic nature of phishing attacks A systematic literature review (SLR) is essential to address these gaps by consolidating existing knowledge, evaluating current approaches, and identifying research gaps. An SLR allows for a holistic understanding of phishing threats by integrating insights from technical, behavioral, and psychological studies. This comprehensive approach is critical for improving detection methods, enhancing prevention strategies, and guiding future research to combat the ever-evolving nature of phishing attacks effectively.

(Rania et al. 2024) utilize tokenization, vectorization, machine learning, and deep learning to detect phishing, efficiently processing blacklists and heuristics for adaptive threat identification of social engineering phishing.

2.0 LITERATURE REVIEW

Numerous scholars have conducted a comprehensive literature review on identifying phishing websites. (Apurv et al., 2022) developed DARTH, an NLP-based neural network tool, achieving 99.97% precision in phishing email detection. (Dinesh et al., 2023) analyzed phishing attack dynamics and used machine learning to classify websites but faced challenges with email legitimacy. (Swagat et al., 2024) Examined machine learning techniques for detecting malicious URLs, emphasizing adaptive models for evolving threats. Ayesha et al. (2021) found machine learning most effective against phishing. (Ghazala et al. 2024) achieved 99.14% spam detection accuracy with GWO-BERT. (Kousik et al., 2024) achieved up to 99.36% intrusion detection accuracy with WCSAN-PSO. (Brij & Ankit, 2020) use a search engine-based method to identify phishing websites 99.05%, but struggle with non-HTML or compromised sites. (Routhu et al., 2020) use Twin Support Vector Machine Classifier (TWSVM) for detecting malicious sites, (Barraclough et al. 2021) introduce machine learning for detecting cyber-phishing attacks. (Ahmed et al. 2021) achieved 96.91% accuracy using Random Forest, while (Yan et al. 2019) reached 98.9% with SHLR. (Adebowale et al. 2019) propose an ANFIS-based web-phishing detector with 98.3% accuracy, integrating diverse features technology. (Gunikhan & Kuppusamy, 2017) developed a 92.72%-accurate PhiDMA model for visually impaired users. (Brizka et al. 2022) proposed a feature-free phishing detection method with 98.68% AUC, 90% true positive rate, and low false positives.

3.0 RESEARCH METHODOLOGY This systematic literature review aims to evaluate previous research through preparation, performance, and documentation, using criteria from (Bai & Sudha 2023; Asadullah & Satwinder 2023). Figure 2 shows the methodology adopted by this research.

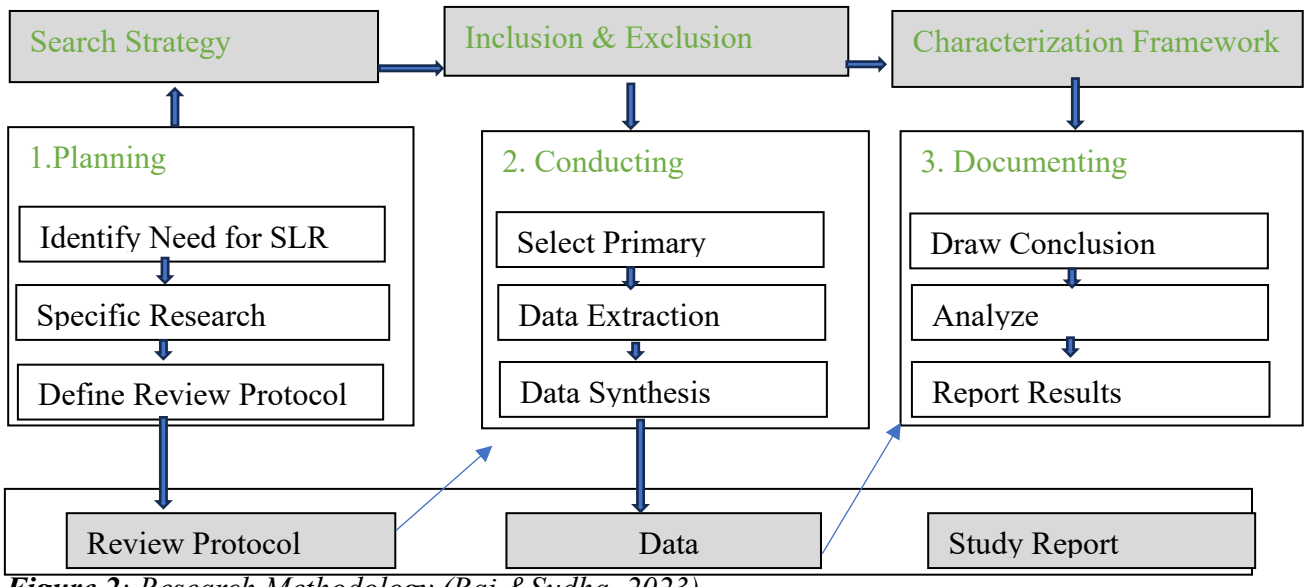

***Figure 2**: Research Methodology (Bai &Sudha, 2023)*

3.1 METHODOLOGY OF THE REVIEW

The study uses research questions and databases for detection of phishing websites. It uses electronic databases and PRISMA 2020 for analysis. The study focuses on 45 publications from 2015 to 2024, with data gathered from 45 main articles verified by a reputable cybersecurity professional.

3.2 RESEARCH QUESTIONS

The research aims to identify relevant studies and data sets by examining phishing detection techniques, prevention strategies, data sets, algorithms, and their maximum accuracy.

RQ1 What is the best-performing model or algorithm for each approach used?

RQ2: What is the most impacted of publications of the approaches reviewed?

RQ3 The systematic literature review conducted and analyzed electronic databases like?
RQ4 The studies have utilized various phishing detection techniques like?

3.3 COLLECTION OF RELEVANT LITERATURE

The study used three tiers of inclusion and exclusion criteria to conduct a systematic review, selecting 45 publications from five databases to ensure timely and pertinent results, excluding unrelated papers, multidisciplinary domains, and articles in languages other than English.

TABLE 1: Inclusion and exclusion criteria

	Criteria
Electronic Database search	Explored: 1. https://ieeexplore.ieee.org/, 2. Elsevier(https://www.sciencedirect.com/) 3. Google Scholar (scholar.google.com, 4. https://www.researchgate.net/ 5. Springer Link (link.springer.com)
Searched item	Conference, journal, and books Chapters
Inclusion	The article includes relevant phishing detection resources.
Exclusion	Irrelevant from the extracted literature
Language	English
Publication	2015-2024

3.3 APPRAISAL OF HIGH-QUALITY RESEARCH

The review analyzed indexed sources with quality criteria rated 1–4, Correlation coefficients assess links between modern detection strategies: list-based, shoulder surfing, heuristics, visual similarity, and machine learning.

3.3.1 CLASSIFICATION PROCESS

The study used VOSviewer to classify and visualize bibliometric networks for phishing attack detection techniques in Figure 3, revealing key author relationships, influential authors, and trends, and highlighting topic evolution through visuals as seen in Figure 4. Table 2 presents the review summary of the selected articles.

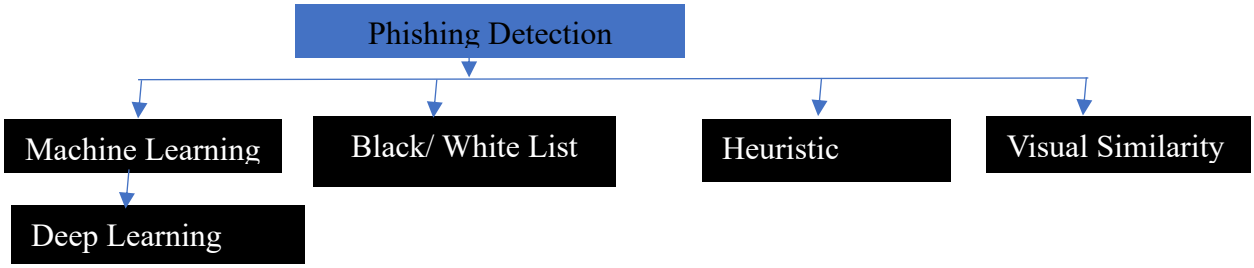

Figure 3: *Phishing detection approaches*

Table 2: Review summary

Author & year	Citation	Articles Analyzed	Approach	Findings	Weakness	DB-Id
Sahingoz et al., 2019	451	43	NLP	RF 97.02% accuracy.	Limited dataset	2
Aniruddh &Tanuja, (2019)	0	16	RF and ReliefF,	97.63% accuracy	Limited dataset	
Kapan & Sora, (2023)	2	46	SVM, K-NN, DT, SGD, MLP	99% accuracy	Used feature classifiers.	5
Naaz, S. (2021).	31	49	RF classifiers and logistic regression	96.85% accuracy	nonnumeric values drop from the dataset	3

Abdulrahaman *et al.*, 2019	14	23	Bagging, Naive.	RF 97.25% accuracy.	Needs more feature selection.	3
Shahrivari, V., *et al* 2020	93	23	XGBoost	98.3235% accuracy	Limited feature in the dataset	3
Patil et al., 2018	73	14	Evaluation of various features of URL websites	RF 96.58% accuracy	Poor detection	1
Yadollahi et al., 2019	49	27	Using a set of outstanding features from a web browser.	98.39% accuracy	…	1
Korkmaz *et al*., 2021	72	29	Classification URLs	94.59% accuracy	Small datasets	1
Catal *et al.*,2022	84	121	SLR	URL data.	Existing models delay detection.	3
Kumar *et al.*,2024	0	28	ANN classification	98.04% accuracy	weakness feature selection required	3
Sahingoz *et al.*,2024	3	35	ANN, CNN, RNN.	CNN 98.74%. accuracy	Limited dataset	1
Jawad, & Alnajjar, 2024	0	22	An ensemble optimization and machine learning.	RF- PSO achieved 97%	Require more datasets.	3
Linh *et al.*,2024	3	36	CNN	98.4% accuracy	Limited coverage	4

Alazaidah et al.,2024	8	46	classifier based on metric and feature selection.	92.409% accuracy	Not good with feature selection.	4
Aldakhel et al.,2023	22	40	Employed CNN-based model	98.77% accuracy	Required larger dataset	5
Adebowale et al.,2020	103	24	CNN + LSTM	93.28% accuracy was achieved	Web plugin required.	3
Korkmaz et al.,2022	12	37	GAN+CNN.	98.37% accuracy	Need evolutionary algorithms.	3
Jain, & Gupta, 2016	230	32	URL/DNS matching with an auto-updated whitelist.	89.36% accuracy in web attack detection.	Few features used	3
Mityukov et al.,2019	14	10	URLs List-based	Achieved 91.59% accuracy.	Improving the accuracy of phishing detection.	3
Mahmood & Ali, 2016	277	31	support vector machine (SVM) algorithm to classify webpages.	Accuracy of 99.14%	Detection of legitimate inconsistent	2
Jhen-Hao & shege-De., 2016	26	35	PhishBox	The Random Forest achieved 98.44%.	….	3
Ritika and Kumar., 2018	1	15	Compares Bayesian algorithm among others.	88% accuracy	Larger dataset required	3
Routh & M, 2015	90	21	Phishshield application.	96.57% accuracy	Benchmarks aid	2

					prevention .	
Luke. *et al.*, 2020	23	29	WebPhish, neural network trained.	98.1% accuracy	The model lacks evaluation for spear phishing.	1
Chidim. *et al.*, 2024	17	51	Comparing Option1 (LSTM) Option2(URL) Option3(HTML)	98.1% accuracy	Adaptive capturing semantic are required.	1
Brij & Ankit, 2023	30	20	Five heuristics and search features boost accuracy for unindexed sites.	99.05%. accuracy	Missed non-HTML	3
Mehdi *et al.*, 2019	140	35	The decision tree and wrapper achieved 96.32% accuracy.	94.13% accuracy.	Improving the Dataset limit requires.	5
Rizka *et al.*, 2022	18	41	NCD for website similarity.	99.82% accuracy		1
Routh and Alwyn, 2019	105	60	PSHCS.	Accuracy of 98.61%,	Phishing page fails on hosted compromised server.	2
Jiann-Liang,2020	20	20	phishing websites Classification	99.95% accuracy	Incorrect threshold setting	5

4.0 TECHNIQUES FOR DETECTING PHISHING ATTACKS

There are several methods for identifying and thwarting phishing attacks. In this study, it is categorized into four different approaches, in order discussed below.

4.1 MACHINE LEARNING APPROACHES

These techniques enable automated, scalable, and dynamic detection of phishing threats. Deep Learning, a sub-technique of machine learning, uses neural networks to automate and dynamically detect phishing threats by classifying malicious URLs and websites based on common elements.

4.2 Black-List-based and White-List-based

This a common technique where browsers use whitelists and blacklists to detect fraudulent sites.

4.3 HEURISTIC-BASED APPROACH

The heuristic-based phishing detection method uses pre-established rules to identify typical email traits but may struggle against novel or complex attempts that don't fit these patterns.

4.4 VISUAL SIMILARITY APPROACH

The technique detects phishing attempts by analyzing subtle component presentation variations, through physical observation.

5.0 RESULTS AND DISCUSSION

The systematic literature review analyzed 45 relevant works related to phishing attack detection and the analysis of authors shows fragmented collaboration: 1 cluster of 3 authors and 9 clusters of 2 authors. These highlight limited connectivity, suggesting the need to foster broader collaboration. This investigation addresses research issues using metadata on authors, affiliations, and geographical locations for dimension analysis and literature classification using the VOS viewer tool with cluster visualization shown in Figure 4.

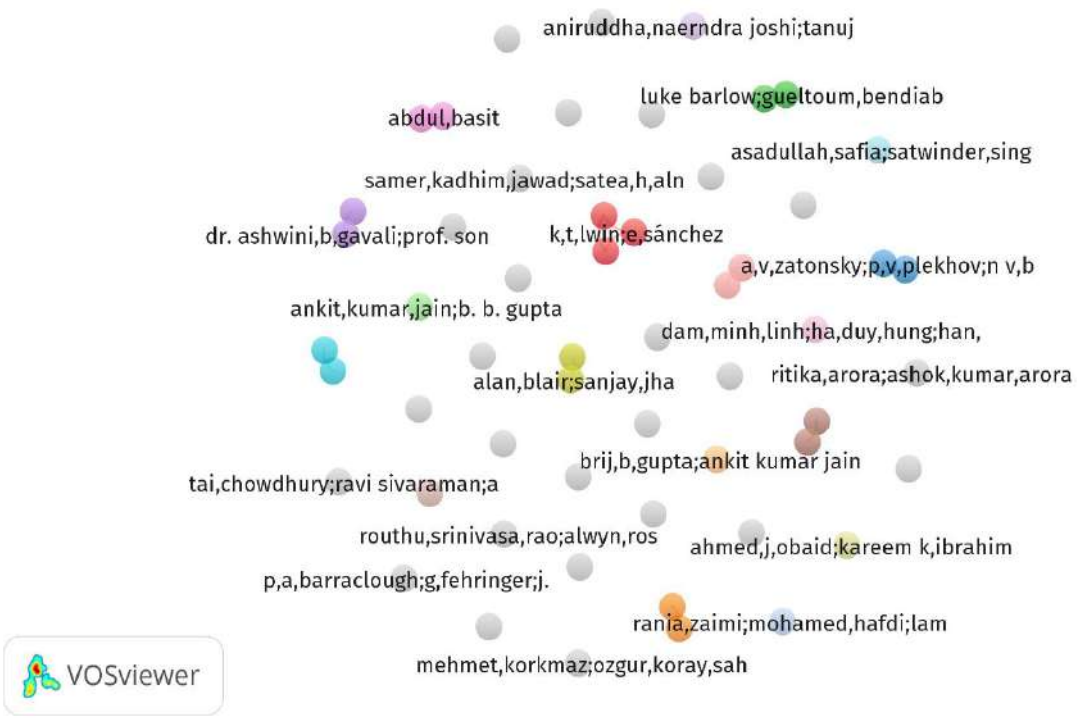

Figure 4: VOSviewer Classification Process

i. **RQ1:** What is the best-performing model or algorithm for each approach use Figure 5 provides an answer to RQ1 stating the most performed model of each technique reviewed.

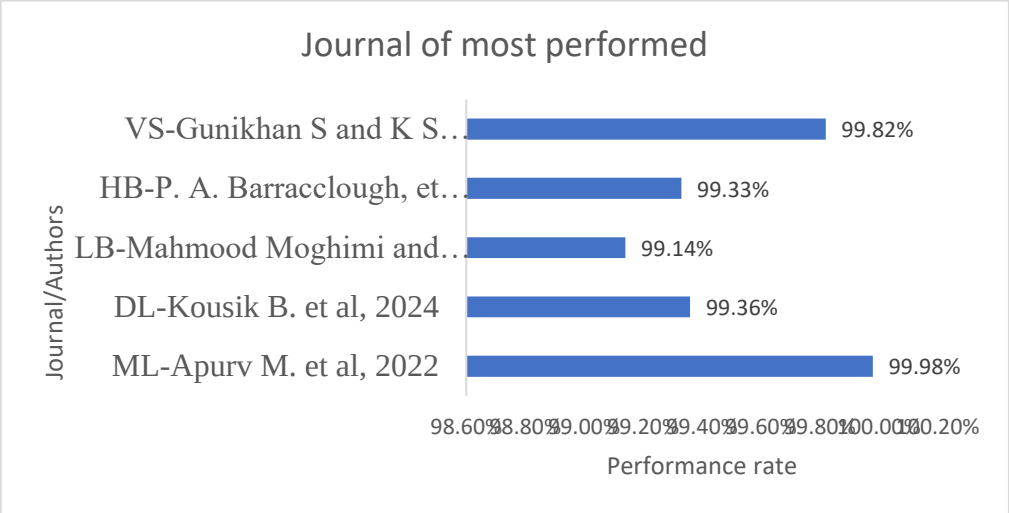

***Figure 5**: Journal of most performed*

ii. **RQ2** What is the most impacted on publications of the approaches reviewed?

Figure 6 provides an answer to RQ2 stating journal impact in terms of citations.

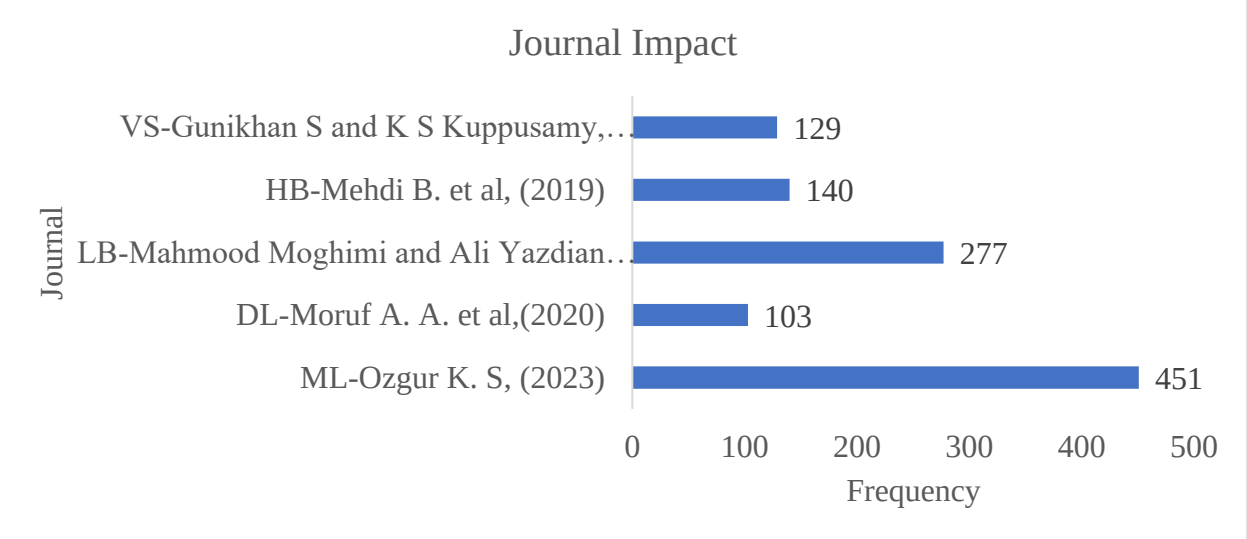

Figure 6: ***Journal Impact***

iii. **RQ3** The systematic literature review conducted and analyzed electronic databases like?

Figure 7 provides an answer to RQ3 stating in % each electronic database explored.

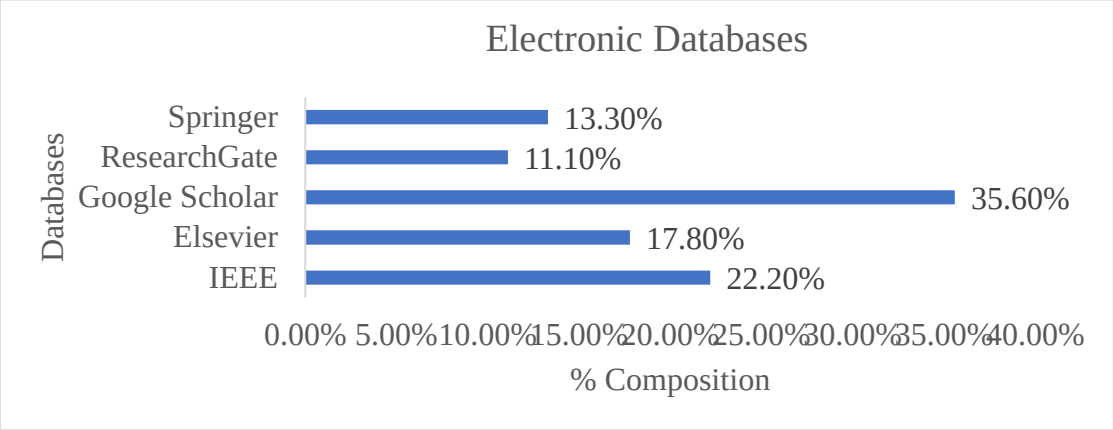

Figure7: *Electronic Databases*

iv. RQ4 The studies have utilized various phishing detection techniques like?

Figure 8 provides an answer to RQ4 stating the number of each concerning article on all the techniques.

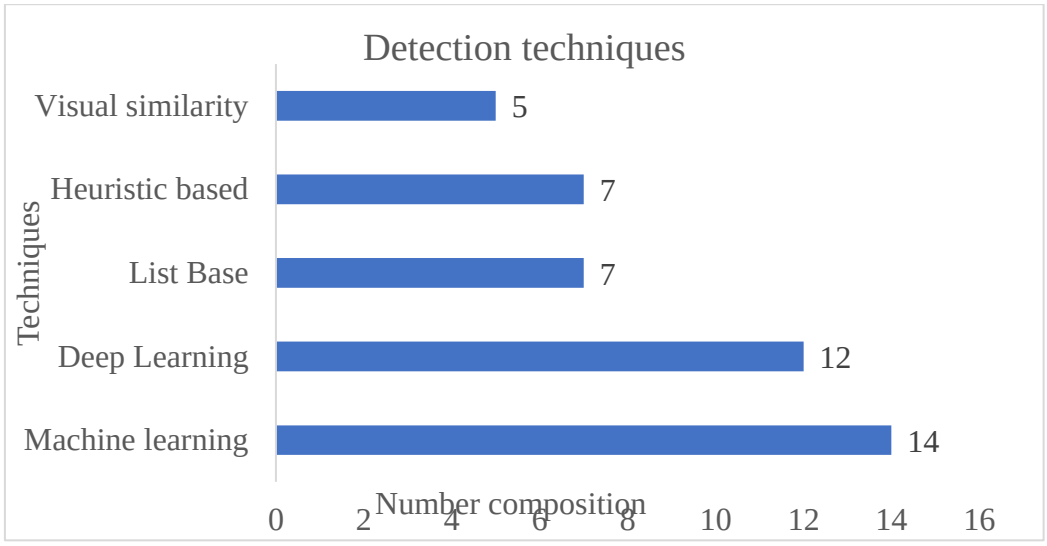

Figure 8: *Detection techniques*

CONCLUSION

Artificial intelligence-driven infrastructure is transforming phishing detection, with machine learning especially deep learning proving the most effective due to its adaptability and scalability. As cyber threats evolve, including polymorphic URL attacks, AI-based security frameworks must advance to ensure resilience. The frontier of AI in cybersecurity lies in developing robust, self-evolving models that enhance real-time threat intelligence. By integrating deep learning with dynamic defense mechanisms, Artificial intelligence fortifies phishing detection, enabling proactive threat mitigation. Continuous innovation in AI-driven security infrastructure is essential to counter increasingly sophisticated cyber threats in a rapidly shifting digital landscape. Defense mechanisms in an ever-changing digital landscape.

Reference

Adebowale, M. A., K. T. Lwin, E. Sánchez, and M. A. Hossain. (2019). "Intelligent Web-Phishing Detection and Protection Scheme Using Integrated Features of Images, Frames and Text." *Expert Systems with Applications* 300–3013.

Adebowale, Moruf Akin, Khin T. Lwin, and M. A. Hossain. (2023). "Intelligent Phishing Detection Scheme Using Deep Learning Algorithms." *Journal of Enterprise Information Management* 36(3):747–66. doi: 10.1108/JEIM-01-2020-0036.

Alazaidah, R., A. Al-Shaikh, M. R. AL-Mousa, H. Khafajah, G. Samara, M. Alzyoud, N. Al-Shanableh, and S. Almatarneh. (2024). "Website Phishing Detection Using Machine Learning Techniques." *Journal of Statistics Applications and Probability* 13(1):119–29. doi: 10.18576/jsap/130108.

Aldakheel, Eman Abdullah, Mohammed Zakariah, Ghada Abdalaziz Gashgari, Fahdah A. Almarshad, and Abdullah I. A. Alzahrani. (2023). "A Deep Learning-Based Innovative Technique for Phishing Detection in Modern Security with Uniform Resource Locators." *Sensors* 23(9). doi: 10.3390/s23094403.

Alkhalil, Zainab, Chaminda Hewage, Liqaa Nawaf, and Imtiaz Khan. (2021). "Phishing Attacks: A Recent Comprehensive Study and a New Anatomy." *Frontiers in Computer Science* 3.

Aniruddha Narendra Joshi, Tanuja R. Pattanshetti. (2019). "Phishing Attack Detection Using Feature Selection Techniques." *International Conference on Communication and Information Processing*. Elsevier-SSRN.

Arora, Ritika, and Ashok Kumar Arora. (2018). "Phishing Web Pages Detection Using Feature Selection and Extraction Method." *International Journal of Scientific Research in Civil Engineering © 2018 IJSRCE* 2(11):1–12.

Arshad, Ayesha, Attique Ur Rehman, Sabeen Javaid, Tahir Muhammad Ali, Javed Anjum Sheikh, and Muhammad Azeem. (2021). "A Systematic Literature Review on Phishing and Anti-Phishing Techniques." *Pakistan Journal of Engineering and Technology, PakJET* 4:163–68.

Babagoli, Mehdi, Mohammad Pourmahmood Aghababa, and Vahid Solouk. (2019). "Heuristic Nonlinear Regression Strategy for Detecting Phishing Websites." *Soft Computing* 23(12):4315–27. doi: 10.1007/s00500-018-3084-2.

Barik, Kousik, Sanjay Misra, and Luis Fernandez-Sanz. (2024). "Adversarial Attack Detection Framework Based on Optimized Weighted Conditional Stepwise Adversarial Network." *International Journal of Information Security* 23(3):2353–76. doi: 10.1007/s10207-024-00844-w.

Barlow, Luke, Gueltoum Bendiab, Stavros Shiaeles, and Nick Savage. (2020). "A Novel Approach to Detect Phishing Attacks Using Binary Visualisation and Machine Learning." in *IEEE World Congress on Services (SERVICES)*. IEEE.

Barraclough, P. A., G. Fehringer, and J. Woodward. (2021). "Intelligent Cyber-Phishing Detection for Online." *Computers and Security* 104. doi: 10.1016/j.cose.2020.102123.

Basit, Abdul, Maham Zafar, Abdul Rehman Javed, and Zunera Jalil. (2020). "A Novel Ensemble Machine Learning Method to Detect Phishing Attack." in *Proceedings - 2020 23rd IEEE International Multi-Topic Conference, INMIC (2020)*. Institute of Electrical and Electronics Engineers Inc.

Catal, Cagatay, Görkem Giray, Bedir Tekinerdogan, Sandeep Kumar, and Suyash Shukla. (2022). "Applications of Deep Learning for Phishing Detection: A Systematic Literature Review." *Knowledge and Information Systems* 64(6):1457–1500. doi: 10.1007/s10115-022-01672-x.

Chen, Jiann Liang, Yi Wei Ma, and Kuan Lung Huang. (2020). "Intelligent Visual Similarity-Based Phishing Websites Detection." *Symmetry* 12(10):1–16. doi: 10.3390/sym12101681.

Dinesh, P. M., M. Mukesh, B. Navaneethan, R. S. Sabeenian, M. E. Paramasivam, and A. Manjunathan. (2023). "Identification of Phishing Attacks Using Machine Learning Algorithm." in *E3S Web of Conferences*. Vol. 399. EDP Sciences.

Ding, Yan, Nurbol Luktarhan, Keqin Li, and Wushour Slamu. (2019). "A Keyword-Based Combination Approach for Detecting Phishing Webpages." *Computers and Security* 84:256–75. doi: 10.1016/j.cose.2019.03.018.

Gupta, Brij B., and Ankit Kumar Jain. (2020). "Phishing Attack Detection Using a Search Engine and Heuristics-Based Technique." *Journal of Information Technology Research* 13(2):94–109. doi: 10.4018/JITR.2020040106.

Jain, Ankit Kumar, and B. B. Gupta. (2016). "A Novel Approach to Protect against Phishing Attacks at Client Side Using Auto-Updated White-List." *Eurasip Journal on Information Security* 2016(1). doi: 10.1186/s13635-016-0034-3.

Jawad, Samer Kadhim, and Satea H. Alnajjar. (2024). "Optimizing Phishing Threat Detection: A Comprehensive Study of Advanced Bagging Techniques and Optimization Algorithms in Machine Learning." *Journal for Scientific Engineering Research* 3(1). doi: 10.58564/IJSER.3.1.2027.146.

Jhen-Hao Li Shenge-De Wange. (2017). "PhishBox; An Approach for Phishing Validation and Detection." *2017 IEEE 15th Intl Conf on Dependable, Autonomic and Secure Computing, 15th Intl Conf on Pervasive Intelligence and Computing, 3rd Intl Conf on Big Data Intelligence and Computing and Cyber Science and Technology Congress*.

Kapan, Sibel, and Efnan Sora Gunal. (2023). "Improved Phishing Attack Detection with Machine Learning: A Comprehensive Evaluation of Classifiers and Features." *Applied Sciences (Switzerland)* 13(24). doi: 10.3390/app132413269.

Karve, Swagat M., Shital Kakad, Swapnaja Amol Ubale, Ashwini B. Gavali, Sonali B. Gavali, and Shrinivas T. Shirkande. (2023). *International Journal of INTELLIGENT SYSTEMS AND APPLICATIONS IN ENGINEERING An Identification and Analysis of Harmful URLs through the Application of Machine Learning Techniques*. Vol. 2024.

Korkmaz, Mehmet, Emre Kocyigit, Ozgur Koray Sahingoz, and Banu Diri. (2022). "A Hybrid Phishing Detection System Using Deep Learning-Based URL and Content Analysis." *Elektronika Ir Elektrotechnika* 28(5):80–89. doi: 10.5755/j02.eie.31197.

Korkmaz, Mehmet, Ozgur Koray Sahingoz, and Banu DIri. (2020). "Detection of Phishing Websites by Using Machine Learning-Based URL Analysis." in *2020 11th International Conference on Computing, Communication and Networking Technologies, ICT 2020*. Institute of Electrical and Electronics Engineers Inc.

Kumar, Pritam, Sujeet Gautam, and Surendra Vishwakarma. (2024). "Artificial Neural Network Approach of Deep Learning for Prediction of Phishing Websites." *International Journal of Scientific Research & Engineering Trend* 10(2):2395–566x.

Linh, Dam Minh, Ha Duy Hung, Han Minh Chau, Quang Sy Vu, and Thanh Nam Tran. (2024). "Real-Time Phishing Detection Using Deep Learning Methods by Extensions." *International Journal of Electrical and Computer Engineering* 14(3):3021–35. doi: 10.11591/ijece. v14i3.pp3021-3035.

Mittal, Apurv, Harsha Kommanapalli, Ravi Sivaraman, Taifur Chowdhury, Tai Chowdhury, and Daniel W. Engels. (2022). "Phishing Detection Using Natural Language Processing and Machine Learning." *SMU Data Science Review* 6(2).

Mityukov, E. A., A. V. Zatonsky, P. V. Plekhov, and N. V. Bilfeld. (2019). "Phishing Detection Model Using the Hybrid Approach to Data Protection in Industrial Control System." in *IOP Conference Series: Materials Science and Engineering*. Vol. 537. Institute of Physics Publishing.

Moghimi, Mahmood, and Ali Yazdian Varjani. (2016). "New Rule-Based Phishing Detection Method." *Expert Systems with Applications* 53:231–42. doi: 10.1016/j.eswa.2016.01.028.

Mohammad Mehdi Yadollahi, Farzaneh Shoeleh, Elham Serkani, Afsaneh Madani, Hossein Gharaee. (2019). "2019 5th International Conference on Web Research (ICWR): Tehran, Iran, April 24-25, 2019." *5th International Conference on Web Research (ICWR)*.

Musbau Dogo Abdulrahaman, John K. Alhassan, Olawale Surajudeen Adebayo,Joseph A, Ojeniyi Morufu Olalere. (2019). "Based on Random Forest with Wrapper Feature Selection Method." *International Journal of Information Proceeding and CCommunication* 7:209–24.

Naaz, Sameena. (2021). "Detection of Phishing in Internet of Things Using Machine Learning Approach." *International Journal of Digital Crime and Forensics* 13(2):1–15. doi: 10.4018/IJDCF.2021030101.

Nasreen, Ghazala, Muhammad Murad Khan, Muhammad Younus, Bushra Zafar, and Muhammad Kashif Hanif. (2024). "Email Spam Detection by Deep Learning Models Using Novel Feature Selection Technique and BERT." *Egyptian Informatics Journal* 26:1–11. doi: 10.1016/j.eij.2024.100473.

Obaid, Ahmed J., Kareem K. Ibrahim, Azmi Shawkat Abdulbaqi, and Salwa Mohammed Nejrs. (2021). "An Adaptive Approach for Internet Phishing Detection Based on Log Data." *Periodicals of Engineering and Natural Sciences* 9(4):622–31.

Opara, Chidimma, Yingke Chen, and Bo Wei. (2024). "Look before You Leap: Detecting Phishing Web Pages by Exploiting Raw URL and HTML Characteristics." *Expert Systems with Applications* 236. doi: 10.1016/j.eswa.2023.121183.

Purwanto, Rizka Widyarini, Arindam Pal, Alan Blair, and Sanjay Jha. (2022). "PhishSim: Aiding Phishing Website Detection With a Feature-Free Tool." *IEEE Transactions on Information Forensics and Security* 17:1497–1512. doi: 10.1109/TIFS.2022.3164212.

Rao, Routhu Srinivasa, and Syed Taqi Ali. (2015). "PhishShield: A Desktop Application to Detect Phishing Webpages through Heuristic Approach." Pp. 147–56 in *Procedia Computer Science*. Vol. 54. Elsevier.

Rao, Routhu Srinivasa, and Alwyn Roshan Pais. (2019). "Jail-Phish: An Improved Search Engine Based Phishing Detection System." *Computers and Security* 83:246–67. doi: 10.1016/j.cose.2019.02.011.

Rao, Routhu Srinivasa, Alwyn Roshan Pais, and Pritam Anand. (2021). "A Heuristic Technique to Detect Phishing Websites Using TWSVM Classifier." *Neural Computing and Applications* 33(11):5733–52. doi: 10.1007/s00521-020-05354-z.

Safi, Asadullah, and Satwinder Singh. (2023). "A Systematic Literature Review on Phishing Website Detection Techniques." *Journal of King Saud University - Computer and Information Sciences* 35(2):590–611. doi: 10.1016/j.jksuci.2023.01.004.

Sahingoz, Ozgur Koray, Ebubekir Buber, Onder Demir, and Banu Diri. (2019). "Machine Learning Based Phishing Detection from URLs." *Expert Systems with Applications* 117:345–57. doi: 10.1016/j.eswa.2018.09.029.

Sahingoz, Ozgur Koray, Ebubekir Buber, and Emin Kugu. (2024). "DEPHIDES: Deep Learning Based Phishing Detection System." *IEEE Access* 12:8052–70. doi: 10.1109/ACCESS.2024.3352629.

Saraswathi Bai, Vadetay, and T. Sudha. (2023). "International Journal of INTELLIGENT SYSTEMS AND APPLICATIONS IN ENGINEERING A Systematic Literature Review on Cloud Forensics in Cloud Environment." *Original Research Paper International Journal of Intelligent Systems and Applications in Engineering IJISAE* 2023(4s):565–78.

Shahrivari, Vahid, Mohammad Mahdi Darabi, and Mohammad Izadi. (2020). "Phishing Detection Using Machine Learning Techniques." *ArXiv:2009.11116v1 [Cs.CR] 20 Sep 2020*.

Sonowal, Gunikhan, and K. S. Kuppusamy. (2020). "PhiDMA – A Phishing Detection Model with Multi-Filter Approach." *Journal of King Saud University - Computer and Information Sciences* 32(1):99–112. doi: 10.1016/j.jksuci.2017.07.005.

Vaibhav Patil, Pritesh Thakkar, Tushar Bhat, Prof. S. P. Godse. (2018). "2018 Fourth International Conference on Computing Communication Control and Automation (ICCUBEA)." *International Conference on Computing Communication Control and Automation (ICCUBEA)*.

Zaimi, Rania, Mohamed Hafidi, and Lamia Mahnane. (2024). "A Permutation Importance Based Feature Selection Method and Deep Learning Model to Detect Phishing Websites." *Research Square* 1–33. doi: 10.21203/rs.3.rs-3943049/v1.

Systematic Review on Stateful Hash-Based Digital Signature Scheme

Bello Zainab Lapai, Ismail Idris, Joseph A Ojeniyi, A.O.Isah, S.O.Subairu
Department of Cyber Security Science Federal University of Technology, Minna. Nigeria
zainabbellolapai@gmal.com

Abstract

This research presents a systematic review and analysis of stateful hash-based digital signature schemes, focusing on their security properties, potential vulnerabilities, and integration with emerging technologies like block chain and IoT, and the current regulatory landscape. Through a rigorous selection process, 15 relevant studies were identified and critically analyzed. The findings highlight the inherent security advantages of stateful hash-based signatures, including resistance to quantum computing attacks and strong nonrepudiation properties. However, challenges such as state management, side-channel vulnerabilities, and performance trade-offs are identified. The integration of these schemes with blockchain, IoT, and cloud computing is explored, presenting opportunities for enhanced security and scalability, along with interoperability and state synchronization issues. Recommendations are provided for strengthening security through side-channel resistant implementations, robust state management mechanisms, and formal verification techniques. Additionally, strategies for seamless technology integration, standards updates, and future research directions are proposed to address emerging threats and challenges in the digital signature domain

Keyword: Blockchain integration, Cloud computing, IoT, Security analysis, Stateful hash-based signature

1.0 Introduction

The rapid advancement of digital technologies has revolutionized the way transactions are conducted, necessitating robust security measures to safeguard the integrity and authenticity of online interactions (Fang *et al*., 2020). In this context, digital signature schemes play a crucial role in ensuring secure authentication and non-repudiation of digital transactions. However, the looming threat of quantum computing has raised concerns about the vulnerability of traditional cryptographic algorithms, such as RSA and ECC, to quantum attacks. This has prompted the need for quantum-resistant cryptographic solutions, with stateful hash-based digital signature schemes emerging as promising candidates (Karale, 2021).

Stateful hash-based digital signature schemes leverage the well-studied cryptographic properties of hash functions and rely on minimal mathematical assumptions, making them resistant to both classical and quantum attacks (Suhail *et al.,* 2020). These schemes offer a high level of security and efficiency, with their security proofs based on the properties of hash functions rather than computationally complex number-theoretic assumptions (Tan *et al.,* 2022). However, despite their security advantages, stateful hash-based digital signature schemes face challenges in terms of

adaptability, integration with emerging technologies such as blockchain, Internet of Things (IoT), and cloud computing, and compliance with regulatory standards due to the ever-evolving landscape of cyber threats (Alagheband & Mashatan, 2022). This research aims to conduct a comprehensive analysis of stateful hash-based digital signature schemes, exploring their security strengths and weaknesses, potential applications in emerging technologies, and the current regulatory landscape.

2.0 Prior Studies

Stateful hash-based digital signature schemes, rooted in one-way cryptographic hash functions, have gained renewed interest for their resilience against quantum computing threats. Unlike traditional public-key cryptosystems like RSA and ECC, their security relies on well-established computational hardness assumptions rather than the intractability of specific mathematical problems.ECC) (Fernandez-Carames and Fraga-Lamas, 2020). Stateful hash-based digital signature schemes rely on the one-way nature of cryptographic hash functions, ensuring it is computationally impractical to reverse a hash. This makes them highly secure against classical and quantum threats, positioning them as a reliable option for safeguarding digital transactions in the post-quantum era. However, the adoption of stateful hash-based digital signature schemes is challenging due to the need for state management, which adds complexity and potential vulnerabilities, especially in distributed or multi-party environments with synchronization and cloning issues (Lou *et al.,* 2021). Researchers have proposed solutions like state reservation, hierarchical signatures, and hybrid schemes to address state management challenges, enhancing security and performance while leveraging the strong security of these schemes for protecting critical data and transactions (Yaacoub *et al.*, 2022). Stateful schemes require careful adaptation due to state management and performance trade-offs. Acknowledging their significance, NIST has included them in post-quantum cryptography standardization efforts (Chawla and Mehra, 2023). Ongoing evaluation, standardization, and regulation updates are essential for stateful hash-based schemes. Recent studies have explored optimizing schemes like LMS and XMSS on platforms, including resource-constrained devices (Syed *et al.,* 2022). Additionally, researchers have explored the potential applications and benefits of integrating stateful hash-based digital signature schemes with emerging technologies, such as blockchain and cryptocurrencies (Noel *et al.,* 2019; Darzi *et al.,* 2023).

3.0 Methodology

3.1 Information Sources and Search Strategy

A comprehensive search strategy was used across multiple databases, including IEEE Xplore, ScienceDirect, Scopus, Web of Science, ACM Digital Library, and Google Scholar, to identify relevant studies for the review. The search used keywords related to stateful hash-based digital signature schemes, emerging technologies, security, performance, scalability, and regulatory standards, including terms like "stateful hash-based signatures," "blockchain integration," "IoT,"

"cloud computing," and "security analysis. The search used Boolean operators and truncation to capture relevant studies published between 2014 and 2024. Backward and forward reference searching was conducted, and results were exported to reference management software for deduplication and screening, ensuring transparency and reproducibility.

3.2 Research Question

This research addresses three key questions focused on the security, efficiency, and regulatory landscape of stateful hash-based digital signature schemes.

Q1: What are the security strengths and weaknesses of stateful hash-based digital signature schemes, and how can they be improved?

Q2: How can stateful hash-based digital signatures enhance security and efficiency in blockchain, IoT, and cloud computing?

Q3: What are the current standards for stateful hash-based signatures, and how can they be updated for modern security threats?

3.2 Study Selection Process

The study selection followed a systematic approach to include relevant, high-quality studies, consisting of the following stages:

i Initial Screening: The search results were initially screened based on the title and abstract by the research supervisor. Studies that clearly did not meet the eligibility criteria were excluded at this stage.

ii Full-Text Screening: The remaining studies were then subjected to full-text screening by the researcher. Each study was carefully evaluated against the eligibility criteria.

iii Final Selection: The studies that met all the eligibility criteria after the full-text screening were included in the final selection for data extraction and synthesis

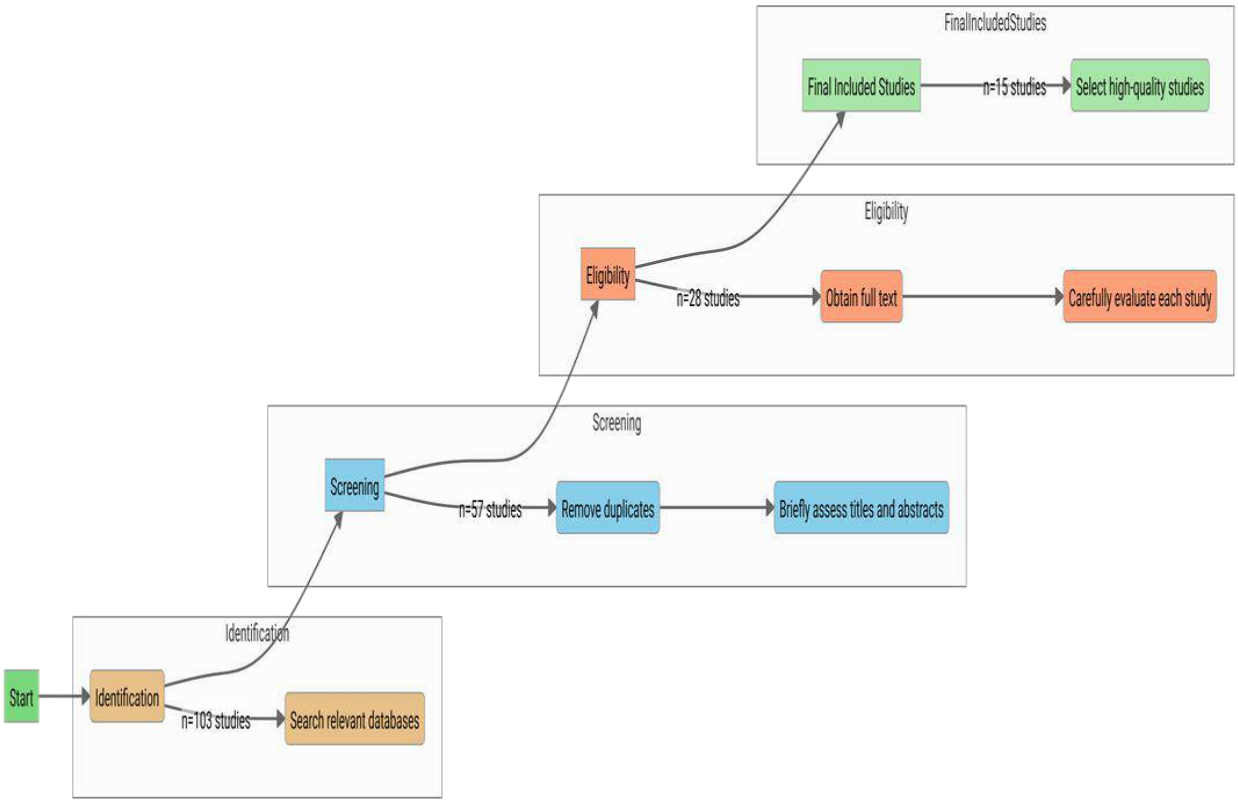

Figure 1: Scoping Review Process

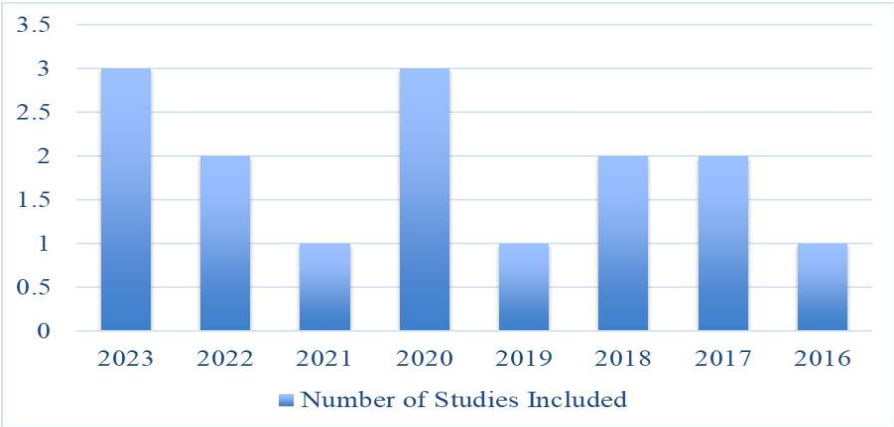

Figure 2: The Number of Publications per Year of Studies Included

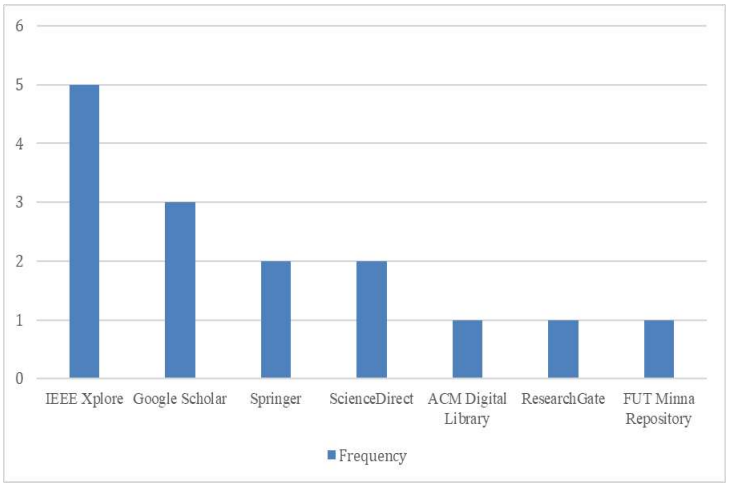

Figure 3: Journal Articles Frequency Plotted against Database

3.3 Data Extraction and Quality Assessment

A standardized data extraction form was created for this systematic review to ensure accurate and consistent extraction of relevant information. The form was designed based on the research questions and objectives, capturing key data from each included study. A pilot data extraction was conducted on a subset of studies, refining the form based on feedback. The extracted data were stored in a secure spreadsheet for efficient management and analysis, with the process thoroughly documented to ensure transparency and reproducibility. Table 1 shows the extraction of subsets of the Study and the inclusion and exclusion criteria are presented in Table 2.

Table 1: Extraction on Subsets of the Study

S/N	Study Characteristics	Study Objectives and Methodology	Key Findings	Recommendations and Future Research Directions
i.	Author(s)	Research questions or objectives	Security strengths and weaknesses	Improving security and performance
ii.	Year of publication	Methodological approach (security analysis, performance evaluation, blockchain	Performance and scalability results	Proposed updates to standards and regulations

		integration)		
iii.	Publication type (journal article, conference proceeding)	Type of stateful hash-based digital signature scheme investigated	Challenges and potential solutions for technology integration	Suggested areas for future research
iv.	Country of origin	Emerging technologies integrated (if applicable)	Regulatory landscape and standards	
v.	Study design (experimental, simulation, analytical)			

Table 3: Inclusion and Exclusion Criteria

S/N	Criteria	Inclusion	Exclusion
i	Studies on stateful hash-based digital signatures, covering security, performance, and vulnerabilities.	✓	x
ii	Studies on integrating stateful hash-based digital signatures with blockchain, IoT, and cloud computing.	✓	x
iii	Studies on regulations and standards for stateful hash-based digital signatures.	✓	x
iv	Publications between 2015 and 2024	✓	x
v	Studies using experimental, simulation, or analytical methods to assess stateful hash-based digital signature schemes.	✓	x

Quality and bias were assessed using criteria adapted from the Cochrane Tool and Newcastle-Ottawa Scale (Luchini *et al*., 2017: Luchini *et al*., 2021). The quality assessment criteria focused on stateful hash-based digital signature schemes and their integration with emerging technologies, evaluating key domains:

Table 4: Quality Assessment Criteria

Study Design and Methodology	Security Analysis	Performance and Scalability Evaluation	Integration with Emerging Technologies	Regulatory Landscape and Standards	Reporting and Presentation
Appropriateness of the study design for objectives	Comprehensiveness of security analysis	Appropriateness of performance metrics	Relevance of integrated technologies	Comprehensiveness of regulatory analysis	Clarity and completeness of reporting
Clarity and robustness of the methodology	Consideration of security threats	Validity and reliability of performance evaluation	Robustness of integration approach	Consideration of standards and guidelines	Transparency and reproducibility
Validity and reliability of data analysis	Rigorous evaluation of security	Scalability and real-world applicability	Interoperability and compatibility	Validity of proposed updates	Appropriate interpretation of findings

Studies were rated for bias and quality, with results transparently reported to ensure reliable findings on stateful hash-based digital signature schemes.

4.0 Result

4.1. Summary and Result of Included Studies

Notable contributions are highlighted by Wagner *et al.* (2022), flexible co-design for post-quantum secure boot, supporting both stateful (LMS, XMSS) and stateless (SPHINCS+) hash-based

signatures were presented ensuring quantum resistance and hardware adaptability. Gagnidze et al. (2018) critically analyze the Lamport and Winternitz one-time signature schemes, providing insights into their security, limitations, and practical implications. McGrew et al. (2016) examine state management in N-time hash-based signature schemes, proposing methods to address synchronization and cloning issues. De Oliveira et al. (2017) optimize LMS and XMSS schemes, improving performance with modern processors. Rohde et al. (2018) assess the efficiency of hash-based signatures on embedded devices, demonstrating the Merkle scheme's strengths. Despite these contributions, further research is needed on integrating these schemes with emerging technologies like IoT and cloud computing and updating regulations to address modern security challenges.

Authors and Study Title	**Methodology**	**Key Findings**
Thanalakshmi et al. (2023): A Quantum-Resistant Blockchain System: A Comparative Analysis	Performance evaluation of NIST in blockchain	Dilithium3 is efficient but has large public keys; IPFS improves efficiency for all schemes.
Farhad and Pyun (2023): LoRaWAN Meets ML: A Survey on Enhancing Performance with Machine Learning	Systematic literature review	Reviews ML solutions for LoRaWAN resource management and future recommendations.
Bhat et al. (2020): Edge Computing and Its Convergence With Blockchain in 5G and Beyond	Literature review	Explores security challenges in merging edge computing with blockchain for 5G.
Khatri et al. (2021): A Systematic Analysis on Blockchain Integration With Healthcare Domain	Systematic literature review	Analyzes blockchain challenges in healthcare for protecting patient records.
Joseph et al. (2022): Transitioning organizations to post-quantum cryptography	Perspective paper	Discusses strategies and risks in transitioning to post-quantum cryptography. SNDL attacks focus.
Gomes et al. (2023): Fortifying the Blockchain: A Systematic Review of Post-Quantum Consensus Solutions	Systematic literature review	Analyzes post-quantum blockchain consensus solutions to enhance security and scalability.
Noel et al. (2019): Stateful hash-based digital signature schemes for Bitcoin	Analysis of the schemes	Explores stateful hash-based signatures for Bitcoin.
A. C. Onuora et al. (2020): Post-Quantum Cryptographic Algorithm:	Systematic review	Overview of post-quantum cryptographic algorithms, including

A systematic review of round-2 candidates		hash-based schemes.
Endignoux (2017): Design and implementation of a post-quantum hash-based cryptographic signature scheme	Implementation and cryptanalysis	Focuses on making stateless hash-based signatures stateful and addresses cryptanalysis of subset-resilience.
Alenizi and Alreshidi (2023): Secure framework for mitigating ransomware attacks in smart healthcare using blockchain.	Systematic review	ML detects ransomware attacks but has high false positives and lacks generalizability.
Gagnidze et al. (2018): Critical Analysis of Hash-Based Signature Schemes	Analytical study	Winternitz scheme reduces signature size but increases computational load.
Wagner et al. (2022): To Be, or Not to Be Stateful: Post-Quantum Secure Boot using Hash-Based Signatures	Flexible co-design for secure boot	Demonstrates feasibility of post-quantum secure boot using stateful or stateless schemes.
De Oliveira et al. (2017): High Performance of Hash-based Signature Schemes	AVX2 optimization on Intel processors	Achieves high performance for LMS and XMSS with vector instructions.

4.2 Quality Assessment

Each study was rated as "High Quality," "Moderate Quality," or "Low Quality" based on factors like research design, methodology, security analysis, scalability, and reporting clarity. The table below presents the quality assessment results for the 15 studies.

S/N	Quality Domain	High Quality	Moderate Quality	Low Quality
i.	Study Design and Methodology	7 (47%)	6 (40%)	2 (13%)
ii.	Security Analysis	8 (53%)	5 (33%)	2 (13%)
iii.	Performance and Scalability Evaluation	5 (33%)	7 (47%)	3 (20%)

iv.	Integration with Emerging Technologies	3 (20%)	5 (33%)	7 (47%)
v.	Regulatory Landscape and Standards Analysis	2 (13%)	5 (33%)	8 (53%)
vi.	Reporting and Presentation	9 (60%)	5 (33%)	1 (7%)

4.3 RQ1, Security Analysis of Stateful Hash-based Digital Signature Schemes

Stateful hash-based digital signature schemes like Lamport, Winternitz One-Time Signature, and XMSS offer quantum resistance, long-term security, and efficient signature verification, making them ideal for code signing, data archiving, and IoT environments (Rohde et al., 2018).

Stateful hash-based schemes face challenges in state management, synchronization issues, and vulnerability to state cloning attacks (McGrew et al., 2016). Larger signature and public key sizes can be problematic in resource-limited settings and depend on hash function robustness (Wagner et al., 2022).

Recommendations for Improvement include using techniques like state reservation and hybrid schemes to mitigate synchronization and cloning risks (McGrew et al., 2016; Wagner et al., 2022), optimization methods to improve performance (Rohde et al., 2018), optimal parameter selection and balancing security and efficiency (Gagnidze et al., 2018; Wagner et al., 2022), and hybrid schemes.

4.4 RQ2, Integration with Emerging Technologies

Stateful hash-based digital signature schemes show potential for enhancing security in emerging technologies including quantum resistance for blockchain, small code size and efficient verification for IoT (Rohde et al., 2018), and long-term security and quantum resistance for cloud computing. However, key challenges include state management, performance optimization, key distribution, interoperability, and regulatory compliance. Solutions like state reservation and optimization techniques are being researched (McGrew et al., 2016; de Oliveira et al., 2017).

4.5 RQ3, Regulatory Landscape and Standards Review

Current standards for stateful hash-based digital signature schemes are evolving to ensure security and interoperability including LMS and XMSS by NIST, IETF, and ISO/IEC, focusing on their post-quantum security. However, the regulatory landscape is still evolving to address new threats.

4.5 Recommendations for Updates

To address gaps in stateful hash-based signature schemes, the following recommendations are made: Promote adoption through industry collaboration for long-term security, Develop unified guidelines for consistent industry implementation, Address state management with guidance for environments like cloud computing (McGrew et al., 2016), and Integrate with emerging technologies by updating standards for blockchain and IoT (Gomes et al., 2023). These measures aim to enhance the regulatory landscape, promote adoption, and improve security and efficiency in digital transactions.

4.6 Key Findings, Strengths and Limitations, and Future Research Direction

Stateful digital signatures offer quantum attack resistance but are vulnerable to side-channel attacks and flaws. Blockchain integration enhances security and scalability, while IoT and cloud computing provide efficient storage. Challenges remain in state management, side-channel risks, and interoperability. Current standards lack comprehensive, unified standards, requiring updated protocols for security threats and technology integration.

The study adheres to PRISMA guidelines, selects diverse studies, and conducts robust quality assessments. However, it faces limitations like potential publication bias, focusing on 2014-2024 studies, and potential omission of relevant ones.

Future research should focus on developing efficient side-channel resistant techniques, scalable and secure state management mechanisms for distributed systems (e.g., blockchain, IoT), and formal verification methods to reduce implementation vulnerabilities.

5.0 Conclusion

Stateful hash-based digital signature schemes show promise as quantum-resistant solutions, offering strong security. However, challenges remain in state management, performance, and integration with emerging technologies. Improvements in side-channel resistance, state management, and formal verification, along with updated regulatory standards, are essential for widespread adoption.

REFERENCE

Alagheband, M. R., & Mashatan, A. (2022). Advanced digital signatures for preserving privacy and trust management in hierarchical heterogeneous IoT: Taxonomy, capabilities, and objectives. *Internet of Things*, *18*, 100492.

Alenizi, J., & Alrashdi, I. (2023). SFMR-SH: Secure framework for mitigating ransomware attacks in smart healthcare using blockchain technology.

Bhat, S. A., Sofi, I. B., & Chi, C. Y. (2020). Edge computing and its convergence with blockchain in 5G and beyond: Security, challenges, and opportunities. *IEEE Access*, *8*, 205340-205373.

Chawla, D., & Mehra, P. S. (2023). A roadmap from classical cryptography to post-quantum resistant cryptography for 5G-enabled IoT: Challenges, opportunities and solutions. *Internet of Things*, 100950.

Darzi, S., Ahmadi, K., Aghapour, S., Yavuz, A. A., & Kermani, M. M. (2023). Envisioning the future of cyber security in post-quantum era: A survey on pq standardization, applications, challenges and opportunities. *arXiv preprint arXiv:2310.12037*.

De Oliveira, A. K. D., & Cabral, R. (2017). High performance of hash-based signature schemes. International Journal of Advanced Computer Science and Applications, 8(3).

Endignoux, G. (2017). Design and implementation of a post-quantum hash-based cryptographic signature scheme. *Master's thesis, École polytechnique fédérale de Lausanne*.

Fang, W., Chen, W., Zhang, W., Pei, J., Gao, W., & Wang, G. (2020). Digital signature scheme for information non-repudiation in blockchain: a state of the art review. *EURASIP Journal on Wireless Communications and Networking*, *2020*, 1-15.

Farhad, A., & Pyun, J. Y. (2023). LoRaWAN Meets ML: A Survey on Enhancing Performance with Machine Learning. *Sensors*, *23*(15), 6851.

Fernandez-Carames, T. M., & Fraga-Lamas, P. (2020). Towards post-quantum blockchain: A review on blockchain cryptography resistant to quantum computing attacks. *IEEE access*, *8*, 21091-21116.

Gagnidze, A., Iavich, M., Inassaridze, N., Iashvili, G., & Vyalkova, V. (2017). Critical analysis of Hash based signature schemes. *International Journal of Cyber-Security and Digital Forensics*, *7*, 47-55.

Gomes, J., Khan, S., & Svetinovic, D. (2023). Fortifying the blockchain: A systematic review and classification of post-quantum consensus solutions for enhanced security and resilience. IEEE Access.

Joseph, D., Misoczki, R., Manzano, M., Tricot, J., Pinuaga, F. D., Lacombe, O., ... & Hansen, R. (2022). Karale, A. (2021). The challenges of IoT addressing security, ethics, privacy, and laws. *Internet of Things*, *15*, 100420.

Karale, A. (2021). The challenges of IoT addressing security, ethics, privacy, and laws. Internet of Things, 15, 100420

Khatri, S., Alzahrani, F. A., Ansari, M. T. J., Agrawal, A., Kumar, R., & Khan, R. A. (2021). A systematic analysis on blockchain integration with healthcare domain: scope and challenges. *IEEE Access*, *9*, 84666-84687.

Lou, X., Zhang, T., Jiang, J., & Zhang, Y. (2021). A survey of microarchitectural side-channel vulnerabilities, attacks, and defenses in cryptography. ACM Computing Surveys (CSUR), 54(6), 1-37.

McGrew, D., Kampanakis, P., Fluhrer, S., Gazdag, S. L., Butin, D., & Buchmann, J. (2016). State management for hash-based signatures. In *Security Standardisation Research: Third International Conference, SSR 2016, Gaithersburg, MD, USA, December 5–6, 2016, Proceedings 3* (pp. 244-260). Springer International Publishing.

Noel, M. D., Waziri, O. V., Abdulhamid, M. S., & Ojeniyi, A. J. (2019, December). Stateful hash-based digital signature schemes for bitcoin cryptocurrency. In *2019 15th International Conference on Electronics, Computer and Computation (ICECCO)* (pp. 1-6). IEEE.

Rohde, S., Eisenbarth, T., Dahmen, E., Buchmann, J., & Paar, C. (2018). Efficient hash-based signatures on embedded devices. *SECSI-Secure Component and System Identification, Berlin, Germany*.

Suhail, S., Hu7ssain, R., Khan, A., & Hong, C. S. (2020). On the role of hash-based signatures in quantum-safe internet of things: Current solutions and future directions. *IEEE Internet of Things Journal*, *8*(1), 1-17.

Syed, N. F., Shah, S. W., Shaghaghi, A., Anwar, A., Baig, Z., & Doss, R. (2022). Zero trust architecture (zta): A comprehensive survey. *IEEE Access*, *10*, 57143-57179.

Tan, T. G., Szalachowski, P., & Zhou, J. (2022). Challenges of post-quantum digital signing in real-world applications: A survey. *International Journal of Information Security*, *21*(4), 937-952.

Thanalakshmi, P., Rishikhesh, A., Marion Marceline, J., Joshi, G. P., & Cho, W. (2023). A Quantum-Resistant Blockchain System: A Comparative Analysis. *Mathematics*, *11*(18), 3947.

Wagner, A., Oberhansl, F., & Schink, M. (2022, November). To be, or not to be stateful: Post-quantum secure boot using hash-based signatures. In *Proceedings of the 2022 Workshop on Attacks and Solutions in Hardware Security* (pp. 85-94).

Yaacoub, J. P. A., Noura, H. N., Salman, O., & Chehab, A. (2022). Robotics cyber security: Vulnerabilities, attacks, countermeasures, and recommendations. *International Journal of Information Security*, *21*(1), 115-158.

Ensemble Learning Models with Feature Selection to Predict the Onset of Alzheimer's Disease

F. T. Olayiwola[1 *] and O. A. Abisoye[1]

[1]Department of Computer Science, Federal university of Technology, Minna, Nigeria
[1*]Corresponding author: [1*]olayiwolafadhilat@gmail.com

Abstract

This paper presents an ensemble method using machine learning classification algorithms and the popular and widely used Open Access Series of Imaging Studies (OASIS) dataset for Alzheimer's disease detection. The proposed work performs an in-depth feature examination and a training-test split in a 70:30 ratio on the datasets and applies nine different ML algorithms, comprised of six ensemble algorithms and three individual algorithms. The AD detection outcome is obtained using six ensemble algorithms and three individual algorithms. The use of full important features revealed that one individual model, namely the support vector machine (SVM) achieves an overall test accuracy of 88.89% whereas four ensemble techniques, namely AdaBoost, Bagging, Blending and Gradient Boosting achieve an overall test accuracy of 88.89% just like SVM. The use of top two important features revealed that two individual models, namely random Forest (RF) and support vector machine (SVM) achieve an overall test accuracy of 88.89%, whereas two ensemble techniques, namely AdaBoost and Blending achieve an overall test accuracy of 88.89% just like RF and SVM. This study showed that the evaluation results on the OASIS dataset in individual and ensemble models were not promising due to the size of the data available. However, the accuracy, precision and sensitivity scores demonstrated no superior detection performance of the ensemble method over the individual method on ML algorithms. These results suggest that ensemble-learning algorithms can be used to make relatively accurate predictions of AD even when the disease is in its early stage.

Keywords: Alzheimer's disease detection, ensemble learning, feature selection, machine learning

1. Introduction

Alzheimer's disease (AD) is a type of dementia that affects a person's memory, thought, and behaviour. It is a disease that begins with mildly affecting parts of the brain, which makes an individual have difficulty in remembering any newly learned information, constant changes in mood, and confusion with events, times, and places. AD usually starts in an individual after the age of 60 years and its risk increases as the person ages. Therefore, the early detection of the disease can help the doctors start the treatment which can significantly help alleviate some symptoms, reduce their intensity, and thus contribute to a better quality of life for patients and their families (Bandyopadhyay *et al*., 2023).

We live in the age of data, where everything around us is connected to a data source, and everything in our lives is digitally recorded (Sarker *et al*., 2020a; Sarker, 2021b). For instance, the current electronic world has a wealth of various kinds of data, such as the Internet of Things (IoT) data, cybersecurity data, smart city data, business data, smartphone data, social media data, health data, COVID-19 data, and many more. The data can be structured, semi-structured, or unstructured.

Machine learning usually provides systems with the ability to learn and enhance from experience

automatically without being specifically programmed and is generally referred to as the most popular latest technologies in the fourth industrial revolution (Sarker *et al*., 2020a; Sarker *et al*., 2020b).

In general, the effectiveness and efficiency of a *machine learning* solution depend on the nature and characteristics of *data* and the performance of the *learning algorithms*. In the area of machine learning algorithms, classification analysis, regression, data clustering, feature engineering and dimensionality reduction, association rule learning, or reinforcement-learning techniques exist to effectively build data-driven systems (Sarker, 2021b; Sarker, 2021c). Thus, selecting a proper learning algorithm that is suitable for the target application in a particular domain is challenging.

In the last decade, several studies were conducted on machine learning to support reasoning and finding solutions for certain problems like in the area of health and medicine. This section briefly summarizes some of these studies as shown in Table 1.1.

Table 1.1: Summary of Related Works

S/N	Author(s)	Methodology	Result	Limitation
1.	Antor *et al*. (2021)	The performance of four machine learning algorithms namely, Support Vector Machine (SVM), Logistic Regression, Decision Tree and Random Forest was compared in their ability to detect dementia, both before and after fine-tuning.	Accuracy gotten includes 92%, 80%, 80% and 74.7%	Only one dataset obtained from the OASIS database was used to experiment.
2.	Fathi *et al*. (2024)	Proposed an ensemble method based on deep learning for the early diagnosis of AD using MRI images.	The evaluation showed an accuracy rate of 98.57, 96.37, 94.22, 99.83, 93.88, and 93.92.	The models were evaluated based on ADNI data, and the trained model was validated based on the local dataset.
3.	Mukka (2023)	Three algorithms were selected for the study, Random Forest, AdaBoost and Logistic Regression, which were then evaluated on the accuracy of their predictions.	An accuracy level of 79.78%, 76.40% and 74.16% was achieved.	Only one dataset obtained from the OASIS database was used to experiment.
4.	Zhang *et al*. (2021)	Proposed based on MRI data, a method combining a 3D convolutional neural network and ensemble learning to improve the	The model proposed achieves 95.2% accuracy in AD vs. NC tasks.	Only one dataset obtained from (ADNI) database was used to experiment.

		diagnosis accuracy.		
5.	Nguyen *et al*. (2022)	Proposed an ensemble learning framework that combines deep learning and machine learning.	Cross-validation implementation achieved an average AUC of 100% during training and 96% during testing.	Only one dataset obtained from (ADNI) database was used to experiment.

While many reviewed studies reported promising results, most did not address all clinically valuable classification groups. Based on the literature review, a simple observation has been noted that very few researchers have used more than four or five machine learning algorithms in their research. For this research, reserchers aim to implement nine of the supervised machine learning techniques namely: AdaBoost, Bagging, Decision Tree, Extreme Gradient Boosting (XGB), Gradient Boost, Random Forest, Stacked generalisation (Blending), Support Vector Machine (SVM) and Voting.

Thus, this research focuses on building a classification model that accurately predicts Alzheimer's disease (AD) using a machine learning technique called ensemble learning.

2. Materials and Methods

Here, the methodology used in this study is presented.

2.1 Machine Learning Theory

Machine learning is the process of using computational methods that learn from experience in order to make accurate predictions. There are several standard machine-learning tasks such as Classification: the categorising of a set of data into classes, Regression: the prediction of real values, and Ranking: the ordering of items according to a specified criterion (Mukka, 2023). The problem at hand in the experiments of this paper is the categorisation of subjects into belonging to one of the two classes: No AD or early-stage AD, which makes this a binary classification problem.

2.2 Machine Learning Tools and Scikit-Learn

There are many different software tools available to build machine-learning models and to apply these models to new, unseen data. There are also a large number of well-defined machine-learning algorithms available. These tools typically contain libraries implementing some of the most popular machine learning algorithms and can be categorised as pre-built application-based solutions or, programming language-based with specialised machine learning libraries.

The programming options we looked at included Python with the popular SciKit-Learn library. Python was our preferred choice, primarily because of the SciKit-learn library extensions and the documentation available with it.

It also provides utilities for extracting features, processing data and evaluating models. It provides

in-built code for many of the algorithms contained in ML.

2.3 Overview of the Proposed Model

The dataset is chosen from the OASIS project data. A framework devised is shown in Figure 2.1. The model involves the following steps:

1. Firstly, the data was collected. The preparation and pre-processing of data were done.

2. Exploratory analysis of data was done to determine the hidden relationships and patterns in the dataset. Data pre-processing also involves the imputation of null, label encoding, data transformation, feature selection, and feature scaling.

3. Different variations of feature selection techniques have been implemented for learning and building models.

4. After feature selection, the splitting of data into train and test sets was done on the ratio of 7:3. We assigned 70% of the dataset for training purposes and 30% for testing purposes.

5. Data splitting was followed by the process of selecting inputs to predict outcomes. These were fed into the classifiers to learn.

6. A qualified model was formed, which was loaded with the testing dataset to categorise it into AD and non-demented contro (NDC). Supervised classifiers have been used in our model.

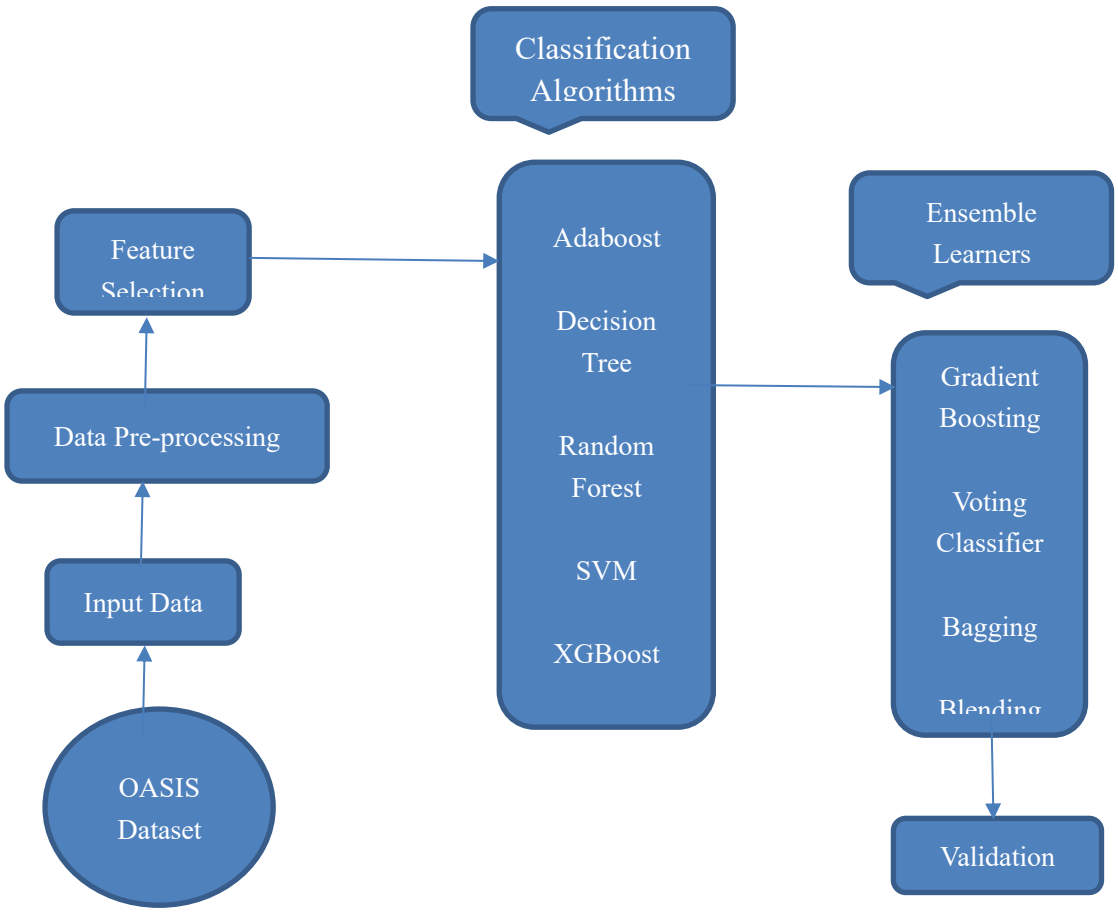

Figure 2.1: Graphical Representation of Our Proposed Model.

2.4 Methods and Experiments

This research is interested in two outcomes: probable and possible AD (AD) and non-demented control (NDC). Probable and possible AD is the terminology used in all clinical settings (An *et al*., 2020).

This section presents the methodology used for the experiments in this study. This roughly consists of three stages: the pre-processing of the data, the reduction of features and the fine-tuning of the algorithms. The experiments were conducted by utilizing the *sklearn* library for Python which contains implementations of various machine learning classifiers.

2.4.1 Datasets

For our experiments, the dataset that has been used in this work was provided by the Open Access Series of Imaging Studies (OASIS) project which aims at making MRI data sets of the brain freely available for future discoveries (Bandyopadhyay *et al*., 2023; Dhakal *et al*., 2023). It contains two sets of data Cross-sectional MRI data in young, middle-aged, nondemented and demented older adults and Longitudinal MRI data in nondemented and demented older adults. The first set has a cross-sectional assortment of 416 subjects aged 18 to 96 years. The second set comprises a

longitudinal assortment of 373 subjects aged 18 to 96 years. When we removed the duplicate visit or assessment entries we were left with 150 unique subjects aged 60 to 96 years.

Researchers have chosen the latter one for the prediction. Longitudinal MRI data has the following attributes:

(i) This dataset consists of a longitudinal collection of 150 subjects aged 60 to 96.
(ii) Each subject was scanned on two or more visits.
(iii) There are both men and women and everyone is right-handed.
(iv) 72 subjects were characterised as 'nondemented'.
(v) 64 subjects were characterised as 'demented'.
(vi) 14 subjects were grouped as 'Nondemented' at the time of their visit, who later were characterised as 'Demented' on their following visits. These fall under the 'Converted' category.

Classes in the independent categories were ID (patient ID), M/F (male or female), Hand (which hand is more dominant, L/R), Age, Educ (level of education), SES (socio-economic status), MMSE (mini-mental state examination), CDR (clinical dementia rate), eTIV (estimated total intracranial volume) and nWBV (Normalize whole brain volume) along with target column (Non-demented / Demented).

2.4.2 *Data collection*

For this study, we used data from the OASIS project (https://www.oasis-brains.org/) described earlier in subsection 2.4.1. As a basis for training a supervised classifier, we apply the scikit-learn environment described in section 2.2. This generated an IPython notebook that contains the Python code developed to make predictions with the data.

The target column (Group), with the entries (Non-demented / Demented / Converted), was chosen as the classifier feature for the experiments. The intention is to classify the participants as having either no AD, an entry (Non-demented), or early-stage AD, an entry (Demented).

To do this, a subset of the OASIS dataset was created in which only those participants with an entry 'Non-demented' (72 participants), or an entry 'Demented' (78 participants) were included.

2.4.3 *Feature selection*

Feature selection is the method of choosing the features to be used and removing input features that are not important for classification (Karim *et al*., 2019; Antony *et al*., 2021). 2.4.4 *Data segregation*

The next step is data segregation. The clean data obtained from the data pre-processing was further segregated. Data segregation helps to avoid overfitting, and underfitting issues. The dataset was split into two portions: training and testing. The train and test set were divided in the ratio of 70:30.

2.4.5 *Model building*

The data prepared in the model segregation step was used for model building. Building a model is training an ML algorithm that can predict the label (target variable) from the features (independent variables). The training data was supplied into the ML algorithm, where it was learnt, and a model was generated. The output of the model training process was an ML model which was used to make predictions using the sample output (test data).

2.5 Model Evaluation

The goal of model evaluation, which is what we are doing throughout this research, is to help estimate how well a particular model of the data will be generalised to new data so that we can choose between different models. For this, not only do we need an evaluation procedure such as train/test split or cross-validation, but we also need an evaluation metric in order to quantify the performance of different models.

A very simple metric is classification accuracy, which measures how often a model correctly predicts the class of an instance in the validation set. As such, classification accuracy alone does not give a clear picture of how a classifier is actually performing. Another metric in use for model evaluation in the literature for machine learning is the confusion matrix. Performance metrics such as Precision, Recall and F1-score can be calculated from the confusion matrix and we do use these as they are applicable to this work since they depend on a ranking.

2.5.1 *Confusion matrix*

In our diagnosis tasks, the predicted results are divided into the following four situations:

1. **True Positive (TP)**: Correctly predicted positive cases.
2. **False Positive (FP)**: Incorrectly predicted as positive (also known as a Type I error).
3. **True Negative (TN)**: Correctly predicted negative cases.
4. **False Negative (FN)**: Incorrectly predicted as negative (also known as a Type II error).

A confusion matrix is a table used to evaluate the performance of a classification model. It summarizes the model's predictions compared to the actual values, allowing you to see where errors occur in a structured way. Here is a typical confusion matrix layout for a binary classifier:

Table 3.1: Confusion Matrix for AD Prediction

		Predicted Outcome	
		AD	NDC
Actual Outcome	AD	**TP**	**FN**
	NDC	**FP**	**TN**

Table 3.1 presents an example of a confusion matrix for AD classification with two outcomes. TP is the number of AD patients that are correctly classified as AD. FP is the number of NDC participants who are diagnosed with AD. FN is the number of AD patients that are incorrectly classified as NDC. TN is the number of NDC participants that are classified correctly as NDC.

2.5.2 *Performance measures*

We employ the following four indicators to evaluate our diagnosis model: Accuracy, Precision, Specificity, Sensitivity, and F-measure. From Table 3.1, we can calculate various evaluation metrics:

Accuracy is the proportion of correctly diagnosed samples among the whole testing samples. That is, accuracy is the probability of correct diagnosis of the outcome for each participant. It is formulated as follows.

$$Accuracy = \frac{(TP + TN)}{(TP + FP + TN + FN)} \tag{3.1}$$

Precision denotes the proportion of predicted AD cases that are correctly real AD.

$$\text{Pr}ecision = \frac{TP}{(TP + FP)} \tag{3.2}$$

Recall, also known as sensitivity, measures the ensemble model's capability to identify positive samples. Recall is the proportion of AD participants that are correctly classified. Its desirable feature is that it reflects how many of the relevant participants predicted the positive rule of the classifier picks up. In a medical context, recall is regarded as a primary measure, as the aim is to identify all real positive cases.

$$Sensitivity = \frac{TP}{(TP + FN)} \tag{3.3}$$

Specificity measures how well the model identifies negative samples. The equation is defined as:

$$Specificity = \frac{TN}{(FP + TN)} \tag{3.4}$$

F-measure provides a way to integrate precision and recall into a single measure. It takes a value from 0 to 1. If the F-measure of a classifier equals 1, the classifiers can correctly classify all participants. The equation is defined as:

$$F - Measure = \frac{2 \times \text{Pr}ecision \times \text{Re}call}{(\text{Pr}ecision + \text{Re}call)} \tag{3.5}$$

We use the following four measures to evaluate the AD classifiers. The higher the accuracy, precision, recall rate and F-measure, the better the constructed classifier.

3. Results and Discussion

This section presents the results and discussion as follows:

3.1 Results Analysis

A confusion matrix is a visualization tool typically used to present the results attained by the learner. Each column of the matrix represents the instances in a predicted class, while each row represents the instances in an actual class. One benefit of a confusion matrix is that it is easy to see if the model is confusing two classes.

In this study, all nine machine learning algorithms were applied to: (i) all important features of the OASIS dataset, and (ii) the top two important features of the OASIS dataset. Some of the results obtained are presented in sections 3.2 and 3.3..

3.2 Model Evaluation Using OASIS Data

This section presents the confusion matrix and the classification report of one of the classification

models, namely AdaBoost, used in this study.

Table 3.1: Confusion Matrix for Adaboost with All the Important Features

		Predicted Outcome	
		AD	NDC
Actual Outcome	AD	**14**	**5**
	NDC	**0**	**26**

In Table 3.1 above, of the 19 actual Alzheimer's disease (AD) patients, the model predicted that 5 were Non-Dementia Control (NDC) patients.

Table 3.2: Classification Report for Adaboost with All the Important Features

	Precision	**Recall**	**F1-score**	**Support**
AD	1.0000	0.7368	0.8485	19
NDC	0.8387	1.0000	0.9123	26
Accuracy			0.8889	45
macro avg	0.9194	0.8684	0.8804	45
weigted avg	0.9194	0.8684	0.8804	45

As shown in Table 3.2, the precision for Alzheimer's disease scores the highest rate (100%) followed by Non-Dementia control (83.87%). The recall for Non-Dementia control is 100%, which is the highest score. The weighted average precision is 91.94%, which shows that Adaboost has an accuracy of 91.94% in diagnosing patient cases, that is, of the 45 patient cases, 91.94% of the cases are diagnosed correctly. Similarly, the weighted average recall is 86.84%, which shows the ability of the Adaboost to select instances from a set of cases.

3.3 Model Comparison

This section compares the outcomes of the different classification models with different input features. Different performance metrics as explained in the previous section are also evaluated to evaluate the predicted outcomes.

Table 3.3: Evaluation Scores for all Important Features selected from the OASIS Dataset

Classifier	**Accuracy**	**Precision**	**Recall**	**F1-score**
AdaBoost	**88.89**	**91.94**	**86.84**	**88.04**
Bagging	**88.89**	**91.94**	**86.84**	**88.04**
Decision Tree	82.22	82.25	81.07	81.48
Gradient Boosting	**88.89**	**91.94**	**86.84**	**88.04**
Random Forest	86.67	88.00	84.92	85.82
Stacked Generalisation	**88.89**	**91.94**	**86.84**	**88.04**

Support vector machine	**88.89**	**91.94**	**86.84**	**88.04**
Voting	86.67	88.00	84.92	85.82
Xgboost	86.67	88.00	84.92	85.82

Table 3.4: Evaluation Scores for Top Two Important Features Selected from OASIS Dataset

Classifier	**Accuracy**	**Precision**	**Recall**	**F1-score**
AdaBoost	**88.89**	**91.94**	**86. 84**	**88.04**
Bagging	84.44	85.13	83.00	83.64
Decision Tree	84.44	85.13	83.00	83.64
Gradient Boosting	86.67	88.00	84.92	85.82
Random Forest	**88.89**	**91.94**	**86.84**	**88.04**
Stacked Generalisation	**88.89**	**91.94**	**86.84**	**88.04**
Support vector machine	**88.89**	**91.94**	**86.84**	**88.04**
Voting	86.67	88.00	84.92	85.82
Xgboost	86.67	88.00	84.92	85.82

Table 3.3 gives the Scores for the case of all Important Features selected from the OASIS dataset. Considering all important features, the highest level of accuracy of 88.89% was achieved by AdaBoost, Bagging, Gradient Boosting, Stacked Generalisation (Blending) and Support Vector Machine (SVM). The least accurate prediction of 82.22% was obtained from the Decision Tree (DT) classifier. Considering all important features, DT had the lowest precision score of 82.25% in precision. The highest precision of 91.94% was shared between five classifiers, AdaBoost, Bagging, Gradient Boosting, Blending and SVM. Five classifiers, AdaBoost, Bagging, Gradient Boosting, Blending and SVM achieved the highest recall score (86.84%) and Random Forest (RF), Voting and Xgboost received the second-highest score (84.92%) when applied to all important features. For all important features, the highest F1-score is achieved with the five classifiers, AdaBoost, Bagging, Gradient Boosting, Blending and SVM which outperformed other algorithms. Table 3.4 gives the Scores for the case of the Top Two Important Features selected from the OASIS dataset. When evaluating the top two important features, AdaBoost, RF, Blending and SVM generate the highest accuracy (88.89%). We got the lowest accuracy for Bagging and DT of 84.44%. The best precision result was recorded from AdaBoost, RF, Blending and SVM with an accuracy of 91.94%. The lowest precision of 85.13% was for Bagging and DT. AdaBoost, RF, Blending and SVM showed the highest recall score of 86.84%. A very poor recall score (83%) has been generated by Bagging and DT algorithms. The highest F1-score is 88.04% for AdaBoost, RF, Blending and SVM.

3.4 Discussion of Results

The OASIS datasets consisted of many disease classes, so we first trained and evaluated a binary classification model based on OASIS data. The performance of the ensemble model and its constituent models was evaluated and compared on binary classification group, NDC/AD. Two sets of features such as all important features and the top two important features were considered in the evaluation process. Tables 3.1 – 3.4 above report the performance results for evaluating the

proposed models based on OASIS datasets.

We can see from the matrix that the model can make the distinction between Non-Dementia Control (NDC) and Alzheimer's disease (AD) pretty well.

Tables 3.3 and 3.4 show the results of using all important features and the top two important features respectively.

Although evaluation results on the OASIS dataset in individual and ensemble models were not promising due to the size of the data available. The results indicate that using the ensemble of multiple classifiers and data is promising for improving diagnostic accuracy.

4. Conclusion

The spread and increasing Alzheimer's disease affect world health badly every day. The absence or delay in the care of patients can also cause death. Therefore, prediction of Alzheimer's disease is a crucial medical function. This research based on the literature review of previous works and aims to answer the research gap as observed. With the primary motive of designing and developing a model for AD prediction, OASIS dataset has been utilized. The motive was to predict the results of the classification of AD from the available data by employing machine-learning methods in a way to increase and come up with higher accuracy and improved performance. Nine supervised machine-learning algorithms have been applied to different feature sets to identify the best combination for the detection of Alzheimer's disease. The best result was achieved with the ensemble techniques with both the full set of important features and the top two important features. Our approach allowed us to develop ML classifiers with high performance in the distinction between NDC and patients with AD. Implementation of other feature selection techniques and feature reduction techniques are recommended, to make the model more accurate.

References

An, N., Ding, H., Yang, J., Au, R. & Ang, T. F. A. (2020). Deep ensemble learning for Alzheimer's disease classification. *Journal of Biomedical Informatics*, 105(2020): 103411.

Antony, L., Azam, S., Ignatious, E., Quadir, R., Beeravolu, A. R., Jonkman, M. & Boer, F. D. A Comprehensive Unsupervised Framework for Chronic Kidney Disease Prediction. IEEE Access, 9 (2021), 126481-126501.

Antor, M. B., Jamil, A., Mamtaz, M., Khan, M. M., Aljahdali, S., Kaur, M., Singh, P. & Masud, M. (2021). A comparative analysis of machine learning algorithms to predict Alzheimer's disease. *Journal of Healthcare Engineering*, 2021, 1–12.

Bandyopadhyay, A., Ghosh, S., Bose, M., Singh, A., Othmani, A. & Santosh, K. C. (2023). Alzheimer's Disease Detection using Ensemble Learning and Artificial Neural Networks. *Recent Trends in Image Processing and Pattern Recognition*, 12 – 21.

Dhakal, S., Azam, S., Hasib, K. M., Karim, A., Jonkman, M., & Farhan Al Haque, A. S. M. (2023). Dementia Prediction Using Machine Learning. *Procedia Computer Science*, 219, 1297-1308. https://doi.org/10.1016/j.procs.2023.01.414

Fathi, S., Ahmadi, A., Dehnad, A., Almasi-Dooghaee, M. & Sadegh, M. (2024). A Deep Learning-Based Ensemble Method for Early Diagnosis of Alzheimer's Disease using MRI Images. *Neuroinformatics*, 22: 89–105. https://doi.org/10.1007/s12021-023-09646-2

Karim, A., Azam, S., Shanmugam, B., Kannoorpatti, K., Alazab, M. A comprehensive survey for intelligent spam email detection, IEEE Access. 7 (2019) 168261–168295. doi:10.1109/access.2019.2954791.

Mukka, J. (2023). *Detecting Early-stage Alzheimer's Disease with Machine Learning Algorithms*. Bachelor's Thesis, UMEA University.

Nguyen, D., Nguyen, H., Ong, H., Le, H., Ha, H., Duc, N. T. & Ngo, H. T. (2022). Ensemble learning using traditional machine learning and deep neural networks for diagnosis of Alzheimer's disease. *IBRO Neuroscience Reports*, 13 (2022): 255–263.

Sarker, I. H. (2021a). Ai-driven cybersecurity: an overview, security intelligence modelling and research directions. SN Comput Sci. 2021.

Sarker, I. H. (2021b). Deep cybersecurity: a comprehensive overview from neural network and deep learning perspective. SN Computer Science, 2021.

Sarker, I. H., Hoque, M. M., MdK Uddin, & Tawfeeq, A. (2020a). Mobile data science and intelligent apps: concepts, ai-based modeling, and research directions. *Mobile Network Application*, 1–19.

Sarker, I. H., Kayes, A. S. M., Badsha, S., Alqahtani, H., Watters, P. & Ng, A. (2020b). Cybersecurity data science: an overview from machine learning perspective. *Journal of Big Data*, 7(1): 1–29.

Sarker, I. H. (2021c). Machine Learning: Algorithms, Real-World Applications and Research Directions. *SN Computer Science*, 2:160. https://doi.org/10.1007/s42979-021-00592-x

Zhang, P., Lin, S., Qiao, J. & Tu, Y. (2021). Diagnosis of Alzheimer's Disease with Ensemble Learning Classifier and 3D Convolutional Neural Network. *Sensors*, 21, 7634. https://doi.org/10.3390/s21227634

Optimizing Renewable Energy Systems through Computational Models

[1]Umar Barau Sani & [2]Abdulhamid Usman Nuruddeen

[1]Department of Computer Hardware Engineering Technology, Katsina State Institute of Technology and Management, Katsina, Nigeria

[2]Department of Computer Science and Information Technology, Al-Qalam University, Katsina, Nigeria

[1*]Corresponding author: umar.barau@ksitm.edu.ng

Abstract

The global transition to renewable energy demands innovative approaches to overcome challenges such as resource intermittency, grid integration, and energy demand variability. This research focuses on optimizing renewable energy systems using computational models that incorporate advanced tools, including artificial intelligence, machine learning, and simulation software. The proposed framework integrates predictive models for energy demand forecasting, optimization algorithms for resource allocation, and hybrid systems combining multiple renewable sources. It also addresses energy storage optimization to mitigate supply inconsistencies. The study highlights the effectiveness of computational models in enhancing energy efficiency, reducing costs, and lowering carbon emissions. The findings offer a roadmap for policymakers and energy planners to adopt data-driven solutions, facilitating sustainable energy transitions and contributing to climate change mitigation efforts.

Keywords: computational models, renewable energy, optimization, artificial intelligence, energy forecasting

1. Introduction

The global energy landscape is undergoing a transformative shift as nations strive to transition from conventional fossil fuels to cleaner, renewable energy sources (Zhang & Umair, 2023). This transition is driven by the urgent need to combat climate change, reduce greenhouse gas emissions, and achieve sustainable energy security (Gao & Serrenho, 2023). Renewable energy sources such as solar, wind, and hydropower offer promising solutions, but their inherent challenges, including resource intermittency, grid integration, and demand variability, necessitate innovative approaches to ensure efficiency and reliability in the energy sector (Niaz & Nwagwu, 2023).

Recent surveys and studies highlight the growing interest in computational models as vital tools for optimizing renewable energy systems. These models leverage advanced computational techniques, including artificial intelligence (AI), machine learning, and simulation software, to tackle the complexities of renewable energy systems (Huang *et al*., 2022). By integrating predictive algorithms, optimization frameworks, and hybrid systems, computational models can address the challenges posed by fluctuating energy supply and demand.

This research focuses on the application of computational models to enhance the performance and reliability of renewable energy systems. The scope includes energy demand forecasting, resource allocation optimization, hybrid system integration, and energy storage analysis. By encompassing multiple renewable energy sources such as solar, wind, and energy storage systems this study aims to create a holistic framework that can be adapted to diverse energy scenarios worldwide.

Additionally, the research examines the role of computational models in grid integration and scalability, emphasizing their potential to meet future energy demands sustainably.

2. Literature Review

The optimization of renewable energy systems is a critical area of research, as these systems play a pivotal role in achieving global sustainability goals. Computational models have emerged as indispensable tools for addressing the challenges of renewable energy integration, such as intermittency, energy demand variability, and grid stability. This section reviews the existing literature on mathematical and computational models, integration of IT tools, and the challenges faced in renewable energy optimization (Chakraborty *et al*., 2022).

Mathematical and computational models are essential for analyzing, simulating, and optimizing renewable energy systems. These models use mathematical formulations to represent physical systems and computational algorithms to solve complex optimization problems (Huang *et al.*, 2022). Linear programming (LP), dynamic programming (DP), and mixed-integer linear programming (MILP) are widely used techniques for optimizing resource allocation and energy dispatch. For example, a study by Patel *et al*. (2020) demonstrated the use of MILP to optimize the operation of hybrid renewable energy systems, achieving improved cost efficiency and system reliability. Additionally, computational tools such as agent-based modeling (ABM) and finite element analysis (FEA) have been employed to simulate energy flow and predict system performance under varying conditions (Kaestner, 2016).

The integration of IT tools with renewable energy systems has significantly enhanced their efficiency and scalability. Advanced software like MATLAB, HOMER, and PVSyst has been instrumental in modeling and simulating renewable energy systems (Hoarca *et al*., 2023). Moreover, the adoption of Internet of Things (IoT) devices and cloud computing enables real-time data collection and analysis, facilitating predictive maintenance and demand-side management (Hafeez *et al*., 2023). Studies, such as those by Chen *et al*. (2021), highlight the role of IT tools in enabling smart grids, where renewable energy sources can be dynamically integrated with conventional energy systems. These tools provide critical insights for decision-making, ensuring optimal system performance.

Despite the advancements in mathematical models and IT tools, several challenges remain in optimizing renewable energy systems. Scalability is a significant issue, as models often fail to perform efficiently when applied to large-scale systems (Stathakopoulou *et al*., 2022). Another challenge is the uncertainty associated with renewable energy sources, such as variations in solar irradiance and wind speed, which complicates accurate forecasting and resource planning (Malik *et al*., 2022). Furthermore, the lack of interoperability among IT tools and legacy systems hinders seamless integration. A review by Singh *et al*. (2022) emphasizes the need for standardized

frameworks and protocols to overcome these barriers. Addressing these challenges is crucial for maximizing the potential of renewable energy systems.

The reviewed studies highlight the critical role of mathematical and computational models, alongside IT tools, in optimizing renewable energy systems. While significant progress has been made, addressing challenges such as scalability, uncertainty, and interoperability remains essential for the widespread adoption and success of these technologies in the renewable energy sector (Ahmadi *et al*., 2023).

3. Computational Modelling Techniques in Renewable Energy

Renewable energy systems rely heavily on computational models to address challenges such as resource intermittency, energy demand variability, and efficient grid integration (Liu *et al*., 2023). These techniques enable the optimization, prediction, and integration of renewable energy systems to improve efficiency and reliability. Below is a detailed breakdown of computational modelling techniques in renewable energy:

3.1 Optimization Models

Optimization models are used to maximize efficiency, minimize costs, and ensure the reliability of renewable energy systems (Alonso-Travesset *et al*., 2022). These models apply mathematical and heuristic techniques to allocate resources and optimize system performance. Here are some examples of the developed algorithms: Linear Programming (LP); Mixed-Integer Linear Programming (MILP); Dynamic Programming (DP); Genetic Algorithms (GA); Particle Swarm Optimization (PSO); and Artificial Bee Colony (ABC) Optimization.

3.2 Predictive Models

Predictive models leverage artificial intelligence (AI) and machine learning (ML) techniques to forecast energy demand and supply (Butcher & Smith, 2020). These models are critical for managing the intermittency of renewable energy sources. Here are some examples of the developed algorithms: Neural Networks (NN); Support Vector Machines (SVM); Decision Trees and Random Forests; and Reinforcement Learning (RL).

3.3 Storage and Hybrid Systems

Computational models play a crucial role in managing energy storage systems and optimizing hybrid setups that combine multiple renewable sources (Bonaccorso *et al*., 2015). This includes Energy Storage Optimization and Hybrid System Integration.

3.4 Simulation Tools for Modelling

Several software tools and platforms are used for computational modelling in renewable energy: MATLAB/Simulink; HOMER (Hybrid Optimization Model for Electric Renewables); PVSyst; and RETScreen (Lucchino *et al*., 2019).

4. Trends and Emerging Technologies in Renewable Energy Systems

The rapid advancements in computational models and renewable energy technologies are revolutionizing the energy sector (Nazari-Heris *et al*., 2023). These trends and emerging technologies focus on enhancing the efficiency, scalability, and integration of renewable energy systems. Below is a detailed discussion of the key trends and innovations driving the sector:

4.1 Hybrid Energy Systems

Hybrid energy systems, which combine multiple renewable sources, are gaining traction as they address the limitations of single-source systems. Computational models play a crucial role in their design and operation by: Complementary Resource Integration; Multi-Objective Optimization; and Increased Adoption.

4.2 Artificial Intelligence (AI) and Real-Time Optimization

AI technologies are transforming renewable energy systems by enabling real-time monitoring and optimization. Key advancements include: Predictive Analytics; Dynamic System Optimization; and Fault Detection and Predictive Maintenance (Arrieta *et al*., 2019).

4.3 Smart Grid Technologies

Smart grids are reshaping the way energy systems operate by integrating renewable sources with intelligent management systems. Computational models are critical for: Demand-Supply Balancing; Self-Healing Capabilities; and Decentralized Energy Management (Gungor *et al*., 2011).

4.4 Internet of Things (IoT) in Energy Systems

The IoT is revolutionizing energy systems by providing real-time monitoring and data-driven insights. Key applications include: Energy Resource Monitoring; Data Integration; and Energy Efficiency Optimization (Wilkinson, 2019).

4.5 Advanced Energy Storage Solutions

Energy storage technologies are becoming increasingly sophisticated, addressing the challenges of intermittency and demand variability in renewable energy systems: Battery Advancements; Hydrogen Storage Systems; and Thermal Energy Storage (Muqeet *et al*., 2022).

4.6 Cloud Computing and Big Data Analytics

Cloud computing and big data analytics are empowering renewable energy systems by providing scalable and efficient solutions for data processing and decision-making: Scalable Computing Power; Big Data Insights; and Collaborative Platforms (Mell & Grance, 2011).

4.7 Emerging Simulation Tools

Innovative simulation tools are enhancing the design, analysis, and optimization of renewable energy systems: MATLAB/Simulink and HOMER; Agent-Based Modeling (ABM); and Digital Twins (Kurylyk *et al*., 2014).

4.8 Blockchain in Energy Systems

Blockchain technology is being explored as a means of decentralizing energy systems and ensuring transparency in transactions: Peer-to-Peer Energy Trading; and Energy Certificates (Zheng *et al*., 2017).

The adoption of these trends and emerging technologies is transforming the renewable energy sector, making it more efficient, reliable, and scalable. Continued advancements in AI, IoT, and energy storage will play a pivotal role in overcoming challenges like intermittency, scalability, and integration. These innovations offer a promising path toward achieving global sustainability and energy security goals.

5. Challenges and Limitations in Optimizing Renewable Energy Systems

Despite significant advancements in computational models and renewable energy technologies, several challenges and limitations hinder the seamless optimization and integration of these systems (Alzahrani *et al*., 2023). These issues span technical, economic, environmental, and data-related aspects. Below is a detailed exploration of these challenges:

5.1 Technical Challenges

Renewable energy systems are inherently complex, and computational models often face technical limitations in accurately simulating and optimizing these systems. Such as: Model Accuracy; Scalability Issues; Real-Time Implementation; and Interoperability of Systems.

5.2 Economic Barriers

Financial constraints remain a significant challenge in deploying and maintaining optimized renewable energy systems. Such as: High Initial Investment; Cost of Maintenance; and Market Uncertainty.

5.3 Environmental and Resource Limitations

Renewable energy systems are heavily dependent on natural resources, which introduces variability and environmental constraints. Such as: Resource Intermittency; Land and Resource Availability; and Environmental Impact of Energy Storage.

5.4 Data-Related Challenges

The effectiveness of computational models in renewable energy optimization depends on the quality, availability, and management of data. And also: Data Availability and Accessibility; Data Quality and Consistency; and Cybersecurity Risks.

5.5 Social and Policy Challenges

Social acceptance and policy frameworks play a crucial role in the adoption of renewable energy systems. Here are some examples of the challenges: Public Perception; Policy Gaps; and Skilled Workforce.

6. Addressing the Challenges

To overcome these challenges and limitations, the following measures are essential:

6.1 Improving Model Robustness and Scalability

Develop advanced computational algorithms that can handle large-scale systems while maintaining accuracy and efficiency.

6.2 Reducing Costs

Encourage public-private partnerships and subsidies to lower the initial investment and operational costs of renewable energy systems.

6.3 Enhancing Data Collection and Management

Invest in IoT devices, weather monitoring systems, and standardized data protocols to improve the availability and quality of data.

6.4 Strengthening Policies

Implement clear and consistent policies to incentivize renewable energy adoption, including tax credits, grants, and renewable energy mandates.

6.5 Raising Public Awareness

Conduct educational campaigns to improve public understanding and acceptance of renewable energy systems.

Addressing these challenges will be critical for achieving the full potential of computational models and renewable energy systems, enabling a sustainable, scalable, and resilient energy future

7. Conclusion

Computational models play a crucial role in optimizing renewable energy systems by addressing challenges like resource intermittency, grid integration, and demand variability. This study highlights their effectiveness in energy demand forecasting, resource allocation, hybrid system modeling, and storage optimization, resulting in improved efficiency, cost reduction, and carbon emission mitigation. Emerging trends, such as AI-driven optimization, hybrid systems, and smart grids, demonstrate significant progress, though challenges like technical limitations, economic constraints, and data issues persist. Overall, the research provides a roadmap for adopting data-driven solutions to advance sustainable, scalable, and reliable renewable energy systems.

References

Ahmadi, A., Nabipour, M., Taheri, S., Mohammadi-Ivatloo, B., & Vahidinasab, V. (2022). A new false data injection attack detection model for cyberattack resilient energy forecasting. IEEE Transactions on Industrial Informatics, 19(1), 371-381.

Alonso-Travesset, À., Martín, H., Coronas, S., & de la Hoz, J. (2022). Optimization models under uncertainty in distributed generation systems: a review. Energies, 15(5), 1932.

Alzahrani, A., Rahman, M. U., Hafeez, G., Rukh, G., Ali, S., Murawwat, S., ... & Abed, A. M. (2023). A strategy for multi-objective energy optimization in smart grid considering renewable energy and batteries energy storage system. IEEE Access, 11, 33872-33886.

Arrieta, A. B., Díaz-Rodríguez, N., Del Ser, J., Bennetot, A., Tabik, S., Barbado, A., ... & Herrera, F. (2020). Explainable Artificial Intelligence (XAI): Concepts, taxonomies, opportunities and challenges toward responsible AI. Information fusion, 58, 82-115.

Bonaccorso, F., Colombo, L., Yu, G., Stoller, M., Tozzini, V., Ferrari, A. C., ... & Pellegrini, V. (2015). Graphene, related two-dimensional crystals, and hybrid systems for energy conversion and storage. Science, 347(6217), 1246501.

Butcher, B. D., & Smith, B. J. (2020). Feature Engineering and Selection: A Practical Approach for Predictive Models. The American Statistician.

Catto Lucchino, E., Goia, F., Lobaccaro, G., & Chaudhary, G. (2019, February). Modelling of double skin facades in whole-building energy simulation tools: A review of current practices and possibilities for future developments. In Building Simulation (Vol. 12, pp. 3-27). Tsinghua University Press.

Chakraborty, I., Chubynsky, M. V., & Sprittles, J. E. (2022). Computational modelling of Leidenfrost drops. Journal of Fluid Mechanics, 936, A12.

Gao, Y., & Cabrera Serrenho, A. (2023). Greenhouse gas emissions from nitrogen fertilizers could be reduced by up to one-fifth of current levels by 2050 with combined interventions. Nature Food, 4(2), 170-178.

Gungor, V. C., Sahin, D., Kocak, T., Ergut, S., Buccella, C., Cecati, C., & Hancke, G. P. (2011). Smart grid technologies: Communication technologies and standards. IEEE transactions on Industrial informatics, 7(4), 529-539.

Huang, L., Zhang, L., & Chen, X. (2022). Updated review of advances in microRNAs and complex diseases: towards systematic evaluation of computational models. Briefings in bioinformatics, 23(6), bbac407.

Kaestner, E. (2016). Finite Element Method Linear Static And Dynamic Finite Element Analysis.

Kurylyk, B. L., MacQuarrie, K. T., & McKenzie, J. M. (2014). Climate change impacts on groundwater and soil temperatures in cold and temperate regions: Implications, mathematical theory, and emerging simulation tools. Earth-Science Reviews, 138, 313-334.

Liu, W., Shen, Y., & Razzaq, A. (2023). How renewable energy investment, environmental regulations, and financial development derive renewable energy transition: Evidence from G7 countries. Renewable Energy, 206, 1188-1197.

Malik, P., Gehlot, A., Singh, R., Gupta, L. R., & Thakur, A. K. (2022). A review on ANN based model for solar radiation and wind speed prediction with real-time data. Archives of Computational Methods in Engineering, 29(5), 3183-3201.

Mell, P. (2011). The NIST Definition of Cloud Computing. Recommendations of the National Institute of Standards and Technology.

Muqeet, H. A., Javed, H., Akhter, M. N., Shahzad, M., Munir, H. M., Nadeem, M. U., ... & Huba, M. (2022). Sustainable solutions for advanced energy management system of campus microgrids: Model opportunities and future challenges. Sensors, 22(6), 2345.

Nazari-Heris, M., Tamaskani Esfehankalateh, A., & Ifaei, P. (2023). Hybrid energy systems for buildings: a techno-economic-enviro systematic review. Energies, 16(12), 4725.

Niaz, M., & Nwagwu, U. (2023). Managing Healthcare Product Demand Effectively in The Post-Covid-19 Environment: Navigating Demand Variability and Forecasting Complexities. American Journal of Economic and Management Business (AJEMB), 2(8), 316-330.

Stathakopoulou, C., Pavlovic, M., & Vukolić, M. (2022, March). State machine replication scalability made simple. In Proceedings of the Seventeenth European Conference on Computer Systems (pp. 17-33).

Wilkinson, J. S. (2019). The Internet of Things. Geographies of the Internet.

Zhang, Y., & Umair, M. (2023). Examining the interconnectedness of green finance: an analysis of dynamic spillover effects among green bonds, renewable energy, and carbon markets. Environmental Science and Pollution Research, 30(31), 77605-77621.

Zheng, Z., Xie, S., Dai, H., Chen, X., & Wang, H. (2017, June). An overview of blockchain technology: Architecture, consensus, and future trends. In 2017 IEEE international congress on big data (BigData congress) (pp. 557-564). Ieee.

Digital Preservation of Nigerian Cultural Heritage: A Computer Science Perspective

[1]Usman Nuruddeen Abdulhamid & [2]Musbahu Salisu

[1,2]Department of Computer Science and Information Technology, Al-Qalam University, Katsina, Nigeria

[2*]Corresponding author: musbahusalisu300@gmail.com

Abstract

The digital age has transformed cultural interaction and preservation, offering both opportunities and challenges. In Nigeria, country rich in cultural diversity, digital technologies profoundly impact cultural expression and heritage. This study examines how computer science tools, such as artificial intelligence, machine learning, and data science, can document, preserve, and promote Nigerian cultural artifacts. While digital platforms and technologies present vast potential for safeguarding cultural diversity, they also threaten traditional practices and heritage sustainability. Through analyzing these dynamics, the research highlights strategies to address challenges like data authenticity and accessibility while maximizing the benefits of digital preservation. This exploration contributes to the broader discourse on digital heritage, showcasing how technology can be harnessed to protect and promote Nigerian cultural heritage in a rapidly evolving digital world.

Keywords: digital preservation, Nigerian cultural heritage, Artificial Intelligence (AI), cultural sustainability, digitization

1. Introduction

The digital age has revolutionized how cultures interact, evolve, and preserve their unique identities. With the rapid proliferation of digital technologies, cultural heritage an invaluable asset for nations faces both unprecedented opportunities and pressing challenges (Dinçer & Akgül, 2022). Nigeria, renowned for its rich cultural diversity spanning music, art, language, folklore, and architecture, stands at a critical juncture. While globalization and technology offer tools for the preservation and dissemination of Nigerian culture, they also pose risks of cultural erosion and loss of authenticity (Tabassum *et al.*, 2021).

Digital technologies have emerged as powerful tools for documenting and preserving cultural heritage. Techniques such as artificial intelligence, machine learning, and data science are increasingly being employed globally to digitize artifacts, archive oral traditions, and recreate cultural experiences through virtual and augmented reality (Desu *et al.*, 2018). For Nigeria, these advancements represent an opportunity to safeguard its cultural heritage, ensuring its transmission to future generations in a rapidly digitizing world (UNESCO, 2005). However, this endeavor is not without challenges, including issues of accessibility, sustainability, and the risk of technological dependency.

The purpose of this study is to explore how computer science can be applied to preserve Nigerian cultural heritage, addressing key questions: How can digital technologies be leveraged to document and disseminate cultural artifacts effectively? What strategies can mitigate the threats to traditional practices and ensure sustainability? Through an Anais of case studies, technological tools, and theoretical frameworks, this research aims to highlight actionable strategies for protecting Nigeria's

cultural identity in the digital era.

In summary, this study bridges the disciplines of computer science and cultural heritage, demonstrating how technological advancements can be harnessed to preserve Nigeria's rich cultural legacy. By addressing the complexities of digital preservation, it seeks to contribute to the broader global discourse on safeguarding cultural diversity in the 21st century

2. Overview of Cultural Heritage Preservation Efforts

Cultural heritage preservation has long been a cornerstone of global efforts to safeguard the identity and history of communities (Edwards *et al*., 2023). Traditional preservation methods, such as archiving physical artifacts and oral storytelling, have evolved significantly with the advent of technology. Globally, institutions like UNESCO and various cultural organizations have spearheaded initiatives to digitize historical artifacts, texts, and traditions, ensuring their longevity in a rapidly globalizing world (Omolewa, 2007; Hong, 2022). These efforts emphasize the role of digital technologies in making cultural heritage accessible to broader audiences while protecting it from environmental and social.

In Nigeria, cultural preservation remains a pressing issue, given the nation's vast repository of cultural expressions ranging from ancient Nok sculptures to Yoruba folklore and Hausa music (Sun *et al*., 2017; Guha & Saikat, 2016; Ames & King, 1971). However, many of these treasures are at risk due to inadequate documentation, neglect, and modern influences. Efforts such as the digitization of oral histories by organizations like the National Archives of Nigeria and initiatives to preserve indigenous languages have marked significant progress. Despite this, challenges such as insufficient funding, technological gaps, and a lack of awareness persist.

2.1 The Role of Technology in Cultural Preservation

Advancements in technology have transformed the landscape of cultural preservation, offering innovative tools for documentation, storage, and dissemination (Hiswara *et al*., 2023). Artificial intelligence (AI) has been used to analyze and recreate historical artifacts, while machine learning (ML) aids in identifying patterns and classifying vast datasets related to cultural heritage. For instance, projects such as Google Arts & Culture have employed AI to digitize and virtually display artworks and cultural artifacts from around the world, enabling global audiences to engage with heritage in new ways (Verde & Valero, 2021).

In the Nigerian context, digital tools hold promise for preserving indigenous knowledge systems, oral traditions, and cultural artifacts. Virtual reality (VR) and augmented reality (AR) technologies provide immersive ways to experience cultural sites and traditions (Al-Ansi *et al.*, 2023), while data science techniques can be applied to analyze and organize cultural archives. Despite these advancements, the adoption of these technologies in Nigeria is still in its infancy, hindered by issues such as limited infrastructure and technical expertise.

2.2 Theoretical Frameworks for Digital Preservation

The digital preservation of cultural heritage can be analyzed through various theoretical frameworks, such as the Open Archival Information System (OAIS) model, which outlines best

practices for managing and maintaining digital archives (Ccsds Secretariat & Navigation Office, 2012). This model emphasizes the importance of preserving data authenticity, accessibility, and usability over time. Additionally, the concept of "cultural sustainability" highlights the need to balance innovation with the preservation of traditional practices and knowledge systems.

In Nigeria, the application of these frameworks can guide efforts to create sustainable and inclusive digital preservation strategies. By adopting international standards and tailoring them to local contexts, Nigerian cultural heritage initiatives can align with global practices while addressing unique challenges.

Although there is a growing body of literature on the use of technology for cultural preservation, research specific to Nigeria remains limited. Most studies focus on global or Western contexts, with few addressing the socio-cultural, infrastructural, and policy challenges unique to Nigeria (Abdulazeez *et al*., 2022). Additionally, while some initiatives have explored the digitization of Nigerian artifacts and traditions, there is limited research on the integration of advanced technologies like AI and ML in this process. These gaps highlight the need for more localized and interdisciplinary approaches to digital preservation in Nigeria.

3. Analysis and Discussion

This section examines the impact of digital technologies on Nigerian culture, the opportunities they present for digital preservation, and the challenges that must be addressed to ensure sustainability and authenticity.

3.1 Benefits of AI, Machine Learning, and Data Science

AI and machine learning offer transformative possibilities for documenting and preserving cultural heritage: Natural Language Processing (NLP): NLP tools can be applied to transcribe, translate, and analyse indigenous Nigerian languages, many of which are at risk of extinction. Computer Vision: This technology enables the digitization and classification of artifacts and artworks, creating detailed digital records for future generations. Data Science: Through analysing cultural data, patterns and trends can be identified, informing strategies for targeted preservation efforts.

3.2 Examples of Cultural Heritage Digitization Initiatives

In addition to local projects, global examples like Google Arts & Culture provide a model for digital preservation. These platforms use advanced imaging and metadata techniques to create detailed digital archives. Nigeria can adapt such models to document artifacts from places like the Benin Kingdom and Sukur Cultural Landscape, ensuring their preservation and accessibility.

4. Challenges and Risks

While digital preservation offers immense opportunities for safeguarding Nigerian cultural heritage, it also presents significant challenges and risks that must be addressed to ensure sustainable and authentic preservation.

4.1 Threats to Traditional Practices and Data Authenticity

The digitization of culture introduces risks such as the erosion of traditional practices. As younger generations gravitate toward digital representations of culture, traditional modes of storytelling, art

creation, and language use may decline (Han & Cai, 2023). Furthermore, ensuring the authenticity of digital records is a challenge, as digitized data can be altered or misrepresented

4.2 Issues of Accessibility, Funding, and Technological Adoption

Accessibility remains a significant barrier to digital preservation in Nigeria. Rural areas often lack the infrastructure required for digitization and access to preserved content (Jiang, 2022). Additionally, inadequate funding for cultural preservation projects hampers progress. Many initiatives are dependent on foreign funding, raising concerns about sustainability and potential cultural exploitation.

Technological adoption is another critical issue. While tools like AI and machine learning are promising, their implementation in Nigeria is hindered by a shortage of skilled professionals and resources. This technological gap limits the scalability and impact of digital preservation efforts.

5. Strategies for Mitigation and Sustainability

To ensure the effective and sustainable digital preservation of Nigerian cultural heritage, it is essential to address challenges such as accessibility, authenticity, and funding while leveraging opportunities presented by digital technologies (Shuaib, 2020). This section outlines actionable strategies to mitigate risks and promote long-term preservation efforts.

5.1 Effective Use of Technology

The effective use of technology is central to preserving Nigeria's cultural heritage in the digital age. By leveraging advanced tools and techniques, cultural assets can be documented, protected, and made accessible to a global audience. Below are key aspects of how technology can be effectively applied in this context.

Capacity Building and Technical Expertise: Building local capacity is critical for the successful implementation of digital preservation initiatives. This includes:

Training Programs: Developing training programs for cultural workers, archivists, and technologists in using AI, machine learning, and data science tools for cultural documentation.

Partnerships with Universities: Encouraging collaborations between universities and cultural organizations to foster research and innovation in digital preservation technologies (Mohiuddin *et al*., 2022).

Adoption of Open-Source Tools: Using open-source technologies can make digital preservation more cost-effective and accessible. Platforms like Omeka and Mukurtu, designed for cultural heritage projects, offer scalable and customizable solutions. These tools enable local organizations to digitize and manage cultural artifacts without heavy reliance on expensive proprietary software (Benefiel, 2023).

Integration of Blockchain Technology: Blockchain technology has the potential to enhance data authenticity and prevent tampering by creating secure, immutable records of cultural artifacts and histories (Jangid & Sharma, 2023). This ensures that digitized data remains credible and can be trusted for generations.

5.2 Addressing Accessibility Challenges

Accessibility challenges are a significant barrier to the effective digital preservation of cultural heritage, especially in a diverse and developing country like Nigeria. Addressing these challenges requires targeted strategies to bridge technological, infrastructural, and socio-economic gaps.

Expanding Digital Infrastructure: Improving digital infrastructure in underserved areas is key to ensuring equitable access to digitized cultural heritage. This involves expanding broadband internet access, especially in rural areas. Promoting the use of mobile-friendly platforms is also crucial, given the widespread use of smartphones in Nigeria.

Localization of Content: Ensuring that digitized content is accessible in indigenous languages will make it more relevant and engaging to local communities. AI-driven translation tools can play a pivotal role in achieving this goal.

Funding and Resource Mobilization: Sufficient funding and resource mobilization are critical for the sustainability of digital preservation initiatives in Nigeria. Given the resource-intensive nature of digitization, creative and collaborative strategies are necessary to secure financial and material support.

Government and Private Sector Involvement: Government policies and funding are essential to sustain digital preservation projects. This can be achieved by: Establishing a dedicated cultural preservation fund and offering tax incentives for private companies that invest in cultural heritage projects.

Crowdsourcing and Community Participation: Encouraging community participation through crowdsourcing initiatives can generate both financial and intellectual resources. Platforms can invite contributions such as oral histories, photographs, and artifacts from local communities, fostering a sense of ownership and involvement.

5.3 Policy Development

Policy development plays a critical role in creating a framework for the effective, inclusive, and sustainable preservation of cultural heritage in Nigeria. Well-designed policies can guide the use of digital technologies, ensure accountability, and foster collaboration among stakeholders.

Development of National Frameworks: Nigeria needs a comprehensive digital preservation policy that addresses standards for digitization, data storage, and content dissemination. This framework should align with international standards, such as those established by UNESCO and the International Federation of Library Associations and Institutions (IFLA) (Raju *at al*., 2023). Additionally, the policy should consider emerging approaches to data storage.

Intellectual Property Rights: Clear policies on intellectual property rights are necessary to protect the ownership of digitized cultural content and prevent exploitation. These policies should ensure that communities retain control over their heritage while allowing for educational and research use.

5.4 Role of Stakeholders

The successful digital preservation of Nigeria's cultural heritage requires the active involvement of multiple stakeholders, each playing a distinct but interconnected role. Collaboration between these groups ensures that digital preservation efforts are comprehensive, sustainable, and culturally sensitive.

Government: The Nigerian government should play a leading role in coordinating preservation efforts by providing funding and infrastructure for digitization projects. Enacting policies that prioritize cultural preservation and technological development.

Technology Companies: Tech companies can contribute by offering technical expertise and resources for digitization projects. Partnering with cultural organizations to develop innovative preservation tools and platforms (Herawati *et al*., 2023).

Cultural Organizations and Communities: Cultural organizations and local communities are the custodians of cultural heritage. Their roles include: Identifying and prioritizing cultural elements for digitization (Yang *et al*., 2023). Ensuring that preservation efforts respect cultural traditions and values.

6. Conclusion

This study investigates the role of digital technologies, including AI, machine learning, and data science, in preserving Nigeria's rich cultural heritage. While these technologies offer significant opportunities for documenting, disseminating, and enhancing access to cultural expressions, challenges such as threats to traditional practices, data authenticity, and limited resources remain. The study emphasizes the need for proactive strategies, including capacity building, policy development, and collaborative efforts between stakeholders, to effectively leverage digital tools for cultural preservation. By addressing these challenges and embracing technological advancements, Nigeria can safeguard its cultural heritage for future generations, foster national identity, and share its unique cultural tapestry with the world.

References

Abdulazeez, H., Magaji, S., & Musa, I. (2022). Analysis of Infrastructural Challenges, Cybercrime, and the Cashless Policy in Nigeria: Infrastructural Challenges, Cybercrime, and the Cashless Policy. ARIS2-Advanced Research on Information Systems Security, 2(1), 13-27.

Adair Radney, E. R. (2024). African American Redemption in the Pan-African Metropolis: Africanized Identities, Pan-African Lives and the African World Festival in Detroit. Journal of Black Studies, 55(2), 158-182.

Al-Ansi, A. M., Jaboob, M., Garad, A., & Al-Ansi, A. (2023). Analyzing augmented reality (AR) and virtual reality (VR) recent development in education. Social Sciences & Humanities Open, 8(1), 100532.

Ames, D. W., & King, A. V. (1971). Glossary of Hausa music and its social contexts. (No Title).

Benefiel, A. (2023). Onward to Omeka: A Migration Tale. TCB: Technical Services in Religion & Theology, 31(4), 7-11.

Butar, E. L. B., & Katemba, C. V. (2023). EFL Students' Perceptions Toward Vocabulary Learning by Listening to English Songs on Spotify. Journey: Journal of English Language and Pedagogy, 6(1), 194-205.

Desu, H., Gothandaraman, R., & Muthuswamy, S. (2018, December). 3d digital reconstruction of heritage artifacts: Parametric evaluation. In 2018 Tenth International Conference on Advanced Computing (ICoAC) (pp. 333-338). IEEE.

Dinçer, F. F. İ., & Akgül, S. Ö. (2022). Digital cultural heritage. In Handbook of research on digital communications, Internet of Things, and the future of cultural tourism (pp. 183-202). IGI Global.

Edwards, H. G., Vandenabeele, P., & Colomban, P. (2023). Raman spectroscopy in cultural heritage preservation. Cham, Switzerland: Springer.

Guha, S. (2016). Wole Soyinka's redeployment of Yoruba folklore in the Strong Breed. Glocal Colloquies, An International Journal of the World of Literature and Culture, 2.

Han, A., & Cai, Z. (2023, June). Design implications of generative AI systems for visual storytelling for young learners. In Proceedings of the 22nd Annual ACM Interaction Design and Children Conference (pp. 470-474).

Herawati, H., Khairinal, K., & Idrus, A. (2023). Harmonizing Nature and Knowledge: Crafting Engaging Thematic Teaching Tools for Expedition on Environmental Preservation. Tekno-Pedagogi: Jurnal Teknologi Pendidikan, 13(1), 21-31.

Hiswara, A., Aziz, A. M., & Pujowati, Y. (2023). Cultural Preservation in a Globalized World: Strategies for Sustaining Heritage. West Science Social and Humanities Studies, 1(03), 98-106.

Hong, S. (2022). A Legal Study on the UNESCO's 'the Recommendation on the Ethics of Artificial Intelligence'. The Journal of Legal Studies.

Jangid, H., & Sharma, M. R. (2023). An Overview of Blockchain Technology: Architecture, Consensus, and Future Trends. PRATIBODH, (NCDSNS).

Jiang, C. (2022). The making of popstar fembots: Participation, co-creation, or online cultural exploitation?. Hybrid. Revue des arts et médiations humaines, (8).

Mohiuddin, M., Hosseini, E., Faradonbeh, S. B., & Sabokro, M. (2022). Achieving human resource management sustainability in universities. International Journal of Environmental Research and Public Health, 19(2), 928.

Nwanaji-Enwerem, O., Bain, P., Marks, Z., Nwanaji-Enwerem, P., Staton, C. A., Olufadeji, A., & Nwanaji-Enwerem, J. C. (2022). Patient satisfaction with the Nigerian National Health Insurance Scheme two decades since establishment: A systematic review and recommendations for improvement. African Journal of Primary Health Care & Family Medicine, 14(1), 3003.

Omolewa, M. (2007). UNESCO as a Network. Paedagogica Historica, 43(2), 211-221.

Radney, E. A. (2023). African American Redemption in the Pan-African Metropolis: Africanized Identities, Pan-African Lives and the African World Festival in Detroit. Journal of Black Studies, 55, 158-182.

Raju, J., Chu, C. M., & Cunningham, C. (2023). The IFLA Guidelines for Professional LIS Education Programmes: Competencies Toward Excellence in Professional Practice. In Proceedings of the ALISE Annual Conference, 2023.

Secretariat, C. C. S. D. S. (2012). Reference model for an open archival information system (OAIS). Recommendation for Space Data System Practices.

Shuaib, S. O. (2020). Advancing Theatre Costume and Makeup As Agents Of Cultural Transmission And Rejuvenation In Duroladipo's Ọbakò So. International Online Journal of Language, Communication, and Humanities, 3(1), 101-122.

Sun, Z. J., Martin, F., Cai, Q. S., & Lassell, S. (2017). Instrumental neutron activation analysis (INAA) of Nok sculptures in IP Stanback Museum. Journal of Radioanalytical and Nuclear Chemistry, 313, 85-92.

Tabassum, F., Akram, N., & Meo, H. K. (2016). CULTURAL EROSION AND CULTURAL MEMORY IN TAUFIQ RAFAT'S ARRIVAL OF THE MONSOON. Hayat, 1638.

UNESCO. (2005). Convention on the Protection and Promotion of the Diversity of Cultural Expressions. Paris: UNESCO.

Verde, A., & Valero, J. M. (2021). Virtual museums and Google arts & culture: Alternatives to the face-to-face visit to experience art. International Journal of Education and Research, 9(2), 43-54.

Yang, S., Hou, M., & Li, S. (2023). Three-dimensional point cloud semantic segmentation for cultural heritage: a comprehensive review. Remote Sensing, 15(3), 548.

Systematic Literature Review on Protection against Fileless Malware: Understanding and Mitigating Emerging Cyber Threats

*Oladotun O.P.[1], Alhassan J.K [2], Isah, A.O.[3], Ojeniyi, J.O.[4], Ismaila, I.[5] and Sherif, B.A.[6]
[1,6]Department of Computer Science, Newgate University Minna, Nigeria
[2,3,4,5]Department of Cyber Security Science, Federal university of Technology, Minna, Nigeria
[1*]Corresponding author: peter.o@newgateuniversityminna.edu.ng

Abstract

Fileless malware is an advanced cyber threat that exploits memory and system tools like PowerShell and WMI, leaving no disk-based traces, making detection and forensic analysis difficult. Despite advances in cybersecurity, minimizing false positives and improving real-time detection remain major challenges. Existing detection methods, such as behavioral analysis and machine learning, face issues with adversarial evasion and resource-intensive processes. This study has conducted a systematic literature review of 80 peer-reviewed articles, published between 2018 and 2024, from various databases such as IEEE Xplore, ScienceDirect, Scopus, Web of Science, ACM Digital Library, and Google Scholar, following the PRISMA protocol. The results of this study revealed that memory forensics reached 95%, while behavioral and machine learning methods ranged from 85% to 94%, with hybrid techniques reaching 96%. This review emphasizes various mitigation strategies, including endpoint detection, application whitelisting, Zero Trust security, network segmentation, and AI-driven monitoring. The study emphasizes the need for adaptive, real-time detection and mitigation frameworks to strengthen cybersecurity defenses against fileless malware.

Keywords: Advanced Persistent Threats, Endpoint Detection and Response, Living Off the Land Attacks, PowerShell, Windows Management Instrumentation, Registry Persistence Detection.

1.0 Introduction

Malware or malicious software are programs that are specifically designed to harm or exploit computer systems without the user's consent. Examples include viruses, worms, Trojans, ransomware, spyware, cryptocurrency miners, adware, and other malicious programs. Such programs can pilfer personal data, hijack system processes and inflict all sorts of other damage. Malware has different objectives according to its design, but tends to have similar goals — to steal personal information from infected devices, compromise device systems to gain access to sensitive data, or execute broad cybersecurity attacks. Antivirus provides detection, prevention, and take action to block or remove malicious software and its files from your computer. It will also scan your computer for behaviors that may signal the presence of new, unknown malware. (Khushali, 2020)

Traditional malware detection and prevention methods are facing increasingly serious challenges from sophisticated attack vectors in the ever-evolving landscape of cybersecurity. Among them, fileless malware is a rather insidious threat. Fileless malware is a kind of malicious software that infects a computer system through its vulnerabilities and the programs installed on it (Khalid *et al*., 2023). As the name suggests, it does not depend on the files on the hard disk. Instead, it works by exploiting the memory of the system, and for this reason, it is quite difficult to detect by conventional file-based security means. Instead of replicating to files like traditional malware, a fileless malware executes its payload directly in a computer's RAM with few remnants. As a result, it can evade traditional detection methods that rely on identifying malicious files stored on a system's hard disk.

Fileless malware is nothing new; it has been around since 2001. This type of malware uses legitimate system processes to run its malicious payload, and it is very hard to detect and remove. Popular malware detection systems, such as signature-based and static analysis techniques, are largely ineffective at detecting fileless malware because it does not leave residual traces in the file system once an attack has concluded. Consequently, fileless malware has an advantage in evading traditional detection solutions, posing a significant risk to modern computer systems and networks (Barnes, 2021).

Recent studies show that cyber thugs are increasingly using fileless malware to attack high-profile organisations, government agencies, and financial institutions. Most of the time, such attacks involve the exploitation of vulnerabilities in installed software applications, web browsers, and network configurations. Some of the common methods used for fileless attacks include PowerShell scripting, memory injection techniques, registry manipulation, and others. The attackers use living-off-the-land binaries, also known as LOLBins, which are genuine system tools abused to run malicious code without detection.

This research paper is intended to study the ever-evolving threat landscape of fileless malware, identify its key characteristics and attack vectors, and analyze the most effective detection and mitigation strategies. A systematic literature review will be conducted to understand how protection against fileless malware can be enhanced and emerging cyber threats mitigated effectively.

1.2 Study Research Questions

With fileless malware on the rise, it is important to address the following research questions:

1. What are the characteristics and mode of operations of fileless malware?
2. What effective detection techniques and mitigation strategies can be employed to prevent fileless malware from taking root?

By investigating these questions, this research aims to contribute to the ongoing efforts in strengthening cybersecurity defenses against fileless malware, ensuring more resilient systems and networks in the face of evolving cyber threats.

2.0 Review of Related Literature

Fileless malware, a stealthy and sophisticated attack vector, continues to evolve as a significant challenge to traditional cybersecurity defenses. This class of malware operates directly in memory or leverages legitimate system tools, making it hard to detect using conventional signature-based detection methods (Baldin, 2019). Unlike traditional malware that leaves traces on disk, fileless threats hide within existing system processes, making post-infection forensics and threat mitigation more difficult. Therefore, a proactive, layered defense strategy is critical to detecting and preventing such attacks.

Recently, malware has gained significant growth and developers adopted the high-level language for creating malicious codes that affect the whole malware industry. The fileless malware has the ability to compromise the system without downloading malicious files or inject any content into the disk. The Fileless malware is attacked by the attack vectors and makes an entry for its persistence. In the emerging growth of fileless malware various researchers' community has significantly contributed towards various detection mechanism.(Sudhakar & Kumar, 2020) presented a study on fileless malware and proposed a novel investigative model of incident handling and response.

Recent research in fileless malware detection and analysis has indicated the potency of memory-based forensic techniques in countering their evasion strategies. (Alzubaidi *et al*., 2023) developed a method using the use of memory dumps to detect transient malware activity, which was shown to be effective in combating malware like Kovter, which is memory-resident and employs registry-based evasion techniques. (Lee *et al*., 2022) classified fileless attacks as memory- and script-based and suggested the use of YARA for detection. (Wu *et al*., 2023) analyzed the technical methods of well-known fileless threats like Poweliks, focusing on registry manipulation and persistence. Further, (Zhang & Li, 2023) proposed a set of countermeasures to identify fileless malware using memory and registry. Meanwhile, (Kim *et al*., 2022) showed the use of PowerShell with Windows Management Instrumentation (WMI) for real-time detection of fileless activity. Together, these contributions point out the growing importance of dynamic and memory-based methods, including network traffic inspection, anomaly detection, and behavioral analysis, in response to the evolving sophistication of fileless malware attacks.

The article "Best practices for fighting the fileless threat" (Baldin, 2019) provides insights into a multi-layered defense strategy. The authors recommend leveraging security frameworks such as Microsoft's Enhanced Mitigation Experience Toolkit (EMET) and enabling exploit protection features that can detect and block exploit attempts before malware can execute. Additionally, the use of application whitelisting and PowerShell Constrained Language Mode has been highlighted as key techniques to mitigate fileless malware, as these methods prevent unauthorized scripts from executing on a system.

Current research has focused on enhancing fileless cyberattack detection using behavioral analysis, along with AI- and ML-based algorithms. (Chen *et al*., 2023) performed a survey of fileless attacks in Internet of Things (IoT) devices and found that 12% of the malware samples they had gathered were fileless, thus highlighting the utmost need for prevention mechanisms in IoT systems. (Lee *et al*., 2022) divided fileless attacks into two broad categories: memory-based and script-based and suggested the use of YARA rules along with enhanced operating system capabilities for detection. (Kim *et al*., 2023) presented the application of machine learning algorithms by Endpoint Detection and Response (EDR) solutions, highlighting challenges in reducing false positives while effectively separating malicious from legitimate endpoint activity. (Wu *et al*., 2023) analyzed notable fileless threats such as Poweliks and Emotet and suggested mitigation that included a multitude of layers for defense. Additionally, (Zhang & Li, 2023) offered a categorization of fileless malware's persistence methods alongside detection models that could curtail their impacts. Collectively, the research demonstrates how fileless attack mechanisms continue to evolve and lack sufficient detection protocols, necessitating new and versatile detection paradigms within cybersecurity.

Fileless malware is a sophisticated type of cyber-attack that runs without the usual signs or executable files on the hard drive of a computer. Instead, the attacks use legitimate system utilities such as Windows Management Instrumentation (WMI) and PowerShell to execute malicious activity in the actual memory space of the system, which makes them challenging to identify and fix (Microsoft, 2023; Kara, 2023). Memory-based attacks bypass signature-based detection mechanisms and pose a major challenge to conventional cybersecurity (Wu *et al*., 2024). The systematic review outlines the existing knowledge on preventive controls for preventing fileless malware attacks and establishing the effectiveness of the controls in real-world implementation.

3.0 Research Methodology

To answer the research questions on understanding fileless malware and determining effective measures to mitigate its impact, a systematic literature review (SLR) was conducted. This methodology ensures a comprehensive, transparent, and evidence-based analysis of existing literature on fileless malware. By focusing on technical aspects, detection techniques, and countermeasures, the study aims to provide actionable insights into combating this emerging cybersecurity threat.

3.1 Approach

The study follows the PRISMA (Preferred Reporting Items for Systematic Reviews and Meta-Analyses) framework to maintain rigor and transparency. This approach involves systematically identifying, screening, and reviewing relevant studies to ensure the comprehensiveness of the findings.

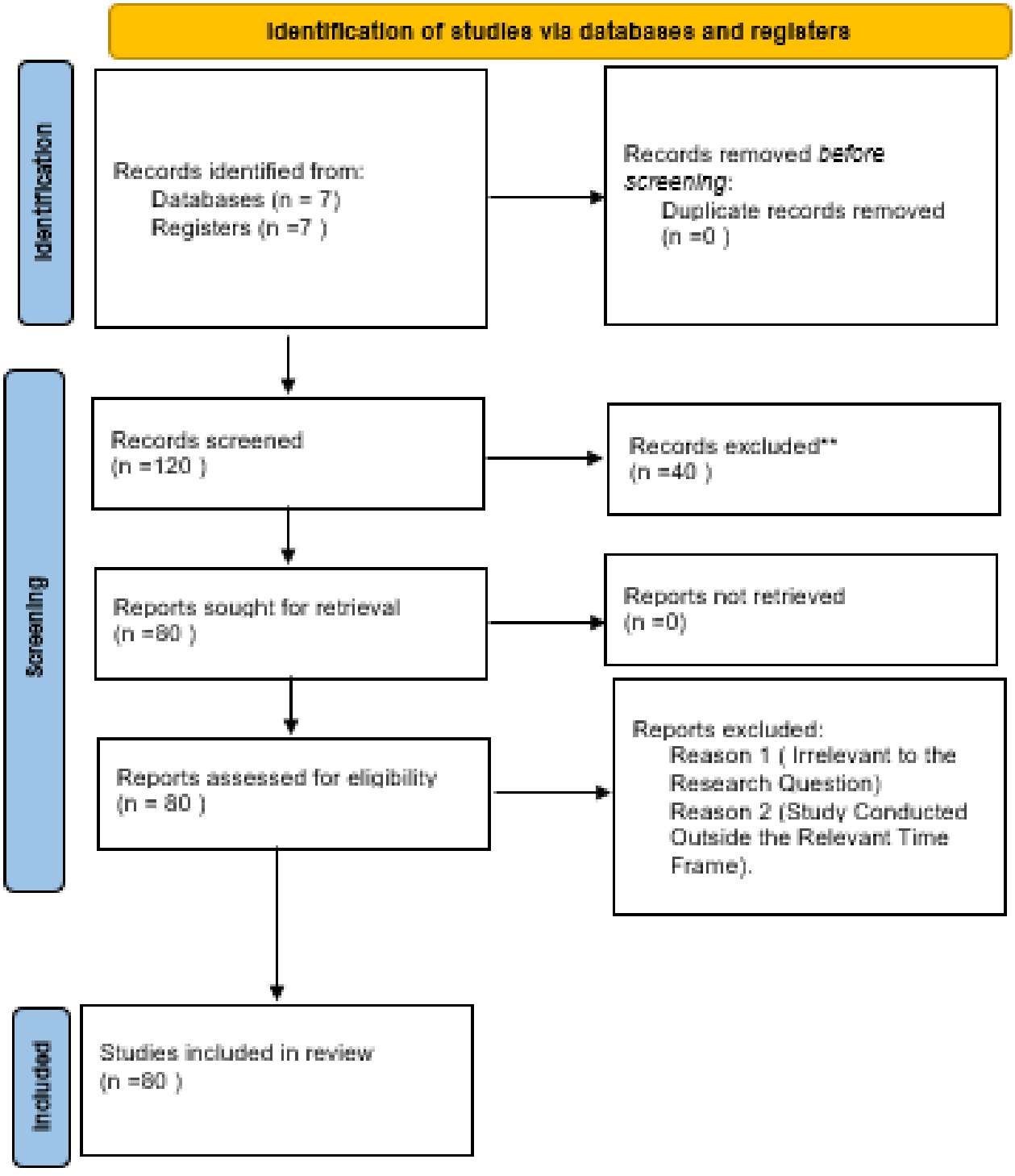

Figure 1. PRISMA Framework

3.2 Identification Stage and Search Process

The study utilized six academic databases, namely IEEE Xplore, Science Dedicator, Scopus, Web of Science (Social Science Citation Index), ACM Digital Library, Google Scholar, and ResearchGate. The databases were selected because they have excellent coverage of the subjects of cybersecurity and fileless malware detection. Relevant research was queried using keywords such as fileless malware analysis, detection methods, machine learning algorithms, memory forensics, malware behavioral analysis, APTs, registry-based detection, LOLBins, LOLScripts, and PowerShell exploitation. Boolean operators (AND/OR/NOT) were used to refine the search and ensure exhaustive coverage. The study took place over the period of October 15, 2024, through peer-reviewed journal articles, white papers, dissertations, and conference proceedings.

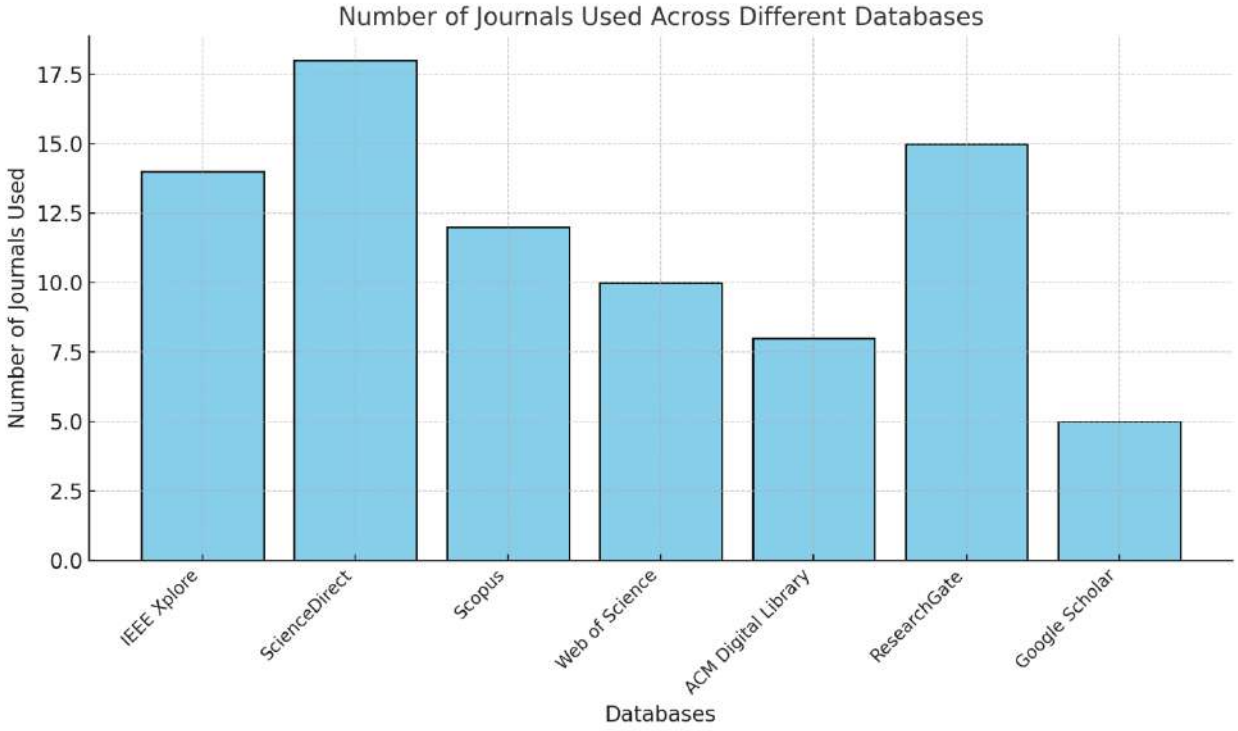

Figure 2. Total Journal articles distribution per database

3.3 Screening Stage

A preliminary search revealed 120 studies. Titles, abstracts, metadata, and conclusions were read to exclude irrelevant works. A total of 80 studies were found relevant at the eligibility stage.

3.4 Eligibility Stage:

Peer screening of the 80 studies assessed their validity and relevance. The studies need to cover fileless malware detection using machine learning or behavioral analysis and quality. Citation records, metadata, and full texts confirmed that all 80 studies met the inclusion criteria and proceeded to synthesis.

3.5 Data Extraction and Synthesis

Data extraction included detection techniques (Machine Learning, Memory Forensics, PowerShell Monitoring), datasets (Drebin, VirusTotal), and evaluation metrics

4. Result and Discussion

This chapter provides the knowledge obtained from the literature reviewed, highlighting the research questions on protection against fileless malware. The analysis and discussion assess the effective protection model in preventing and defending against fileless malware.

RQ1: Fileless Malware Features and Mode of Operations

Fileless malware is an advanced cyber threat that exists nowhere at all but in memory without touching the hard disk, thus rendering it extremely evasive to conventional signature-based antivirus tools. It employs legitimate system utilities like PowerShell and Windows Management Instrumentation (WMI) to run malicious operations without downloading files to disk. This "Living Off the Land" approach causes it to masquerade as normal system processes, and detection and remediation are difficult.

Table 1: Comparison Between Traditional File-Based Malware and Fileless Malware

Attribute	Traditional File-Based Malware	Fileless Malware
Source Code	Yes	No
Malicious File	Yes	No
Malicious Process	Yes, initiated by the execution of a malicious file (e.g., .exe, .dll)	No, runs in-memory via legitimate processes like PowerShell, making detection harder
Complexity	Moderate, depending on the obfuscation techniques used	Very High, as it leverages sophisticated techniques and trusted system tools
Detection Complexity	Moderate to High, depending on the anti-virus heuristics and signature databases	Very High, as it leaves little to no file artifacts for detection
Stealth Techniques	Alters system files and hides within file structures Manipulates file metadata	Operates exclusively in-memory. Avoids writing any malicious files to disk

	Modifies Windows registry for persistence	Disguises malicious code as part of legitimate processes
Execution Environment	Typically requires interaction from the victim (e.g., opening a file, downloading an attachment)	Completely fileless, leveraging legitimate, pre-installed system tools to execute the malicious payload without user interaction

4.2 Key Techniques and Modes of Operation:

Fileless malware is supported by its ability to exist alongside legitimate system activity with ease, essentially "Living off the Land." The following are the significant techniques employed:

4.2.1 Memory Injection: The Foundation of Fileless Attacks

Memory injection continues to be a fundamental aspect of fileless attacks. Malicious code is injected directly into the memory space of a legitimate process, typically taking advantage of vulnerabilities in applications or system processes. This approach enables the malware to execute within the context of the compromised process, making it very hard to differentiate from normal activity. A number of injection techniques are commonly referenced:

• *Process Hollowing (Process Replacement):* A legitimate process is created but suspended before its main code executes. The process's memory is filled with malicious code, and the process is resumed. This effectively executes the attacker's payload within an apparently innocuous process, hiding its true purpose.

• *Code Injection:* Injecting malicious code directly into the memory of a running process. This method requires more privilege and technical skill but can be very effective, with fine-grained control over the compromised process.

• *Reflective DLL Injection:* A more advanced method where the DLL is loaded from memory without being written to disk, enhancing stealth and avoiding some memory scanning techniques.

4.2.2 Script-Based Attacks: Utilizing Authorized Scripting Platforms

Scripting languages like PowerShell, JavaScript, and VBScript are hazardous tools that can quite easily be used for malicious purposes. Fileless malware usually utilizes these scripts, executing them directly from memory without writing them to the disk. They can download other payloads, carry out malicious action, or even gain persistence via registry modifications or scheduled tasks. They can be embedded within what seem like harmless documents, emails, or web pages and thus constitute an extremely viable vector for infection.

4.2.3 Registry Exploitation: Persistence and Stealth

The Windows Registry is a basic database for system configuration that can be manipulated to store and run malicious code. Attackers can insert malicious scripts or shellcode into registry keys, then use legitimate system utilities, like regsvr32, to invoke their execution. This creates a persistence mechanism, allowing the malware to survive system restarts and maintain control over the infected system. Attackers can also utilize the registry to hold encrypted payloads that are decrypted and run in memory.

4.2.4 WMI (Windows Management Instrumentation) Abuse: System Administration Turned Malicious:

Windows Management Instrumentation (WMI) is a robust management system that provides system administrators with the ability to manage and monitor computer systems. WMI may be utilized by attackers to execute malicious code, control processes, and potentially propagate malware throughout a network. Due to the fact that WMI is a legitimate system utility, its exploitation can remain unnoticed because it typically appears as part of normal administrative activity.

4.2.5 Living-off-the-Land Binaries (LOLBins) and Scripts (LOLBAS): Blending into the Environment:

LOLBins are legitimate system utilities (e.g., PowerShell, wmic, certutil, regsvr32, bitsadmin) that have malicious applications. LOLBAS (Living Off the Land Binaries and Scripts) extends this to scripts and other files that are already present on the system. By leveraging existing utilities, an attacker can engage in malicious behavior without introducing new executables, making detection more challenging. The utilization of LOLBins and LOLBAS gets mixed up with legitimate system activity, and it becomes more challenging to detect malicious activity.

4.2.6 Exploiting Application Vulnerabilities: Gaining Entry Through Weaknesses:

Fileless malware will often exploit vulnerabilities in commonly used applications such as web browsers, PDF readers, or Microsoft Office. Using malicious documents or exploiting vulnerabilities in web applications, the attackers are able to inject malicious code into the memory of such applications without depending on file-based protections. Zero-day exploits for unknown vulnerabilities are particularly hazardous in this instance.

RQ2: What effective detection techniques and mitigation strategies can be employed to prevent fileless malware from taking root?

In order to effectively block fileless malware from taking hold, sophisticated detection techniques, real-time scanning, and proactive protection technologies need to be employed together in conjunction with each other. Fileless malware works because it leverages legitimate system tools like PowerShell and Windows Management Instrumentation (WMI) and only resides in memory with no footprint on the disk. These distinguishing characteristics necessitate solutions beyond traditional antivirus software

Table 2: Detection Techniques and Effectiveness

Technique	Detection Accuracy (%)	False Positive Rate (FPR)	Strengths	Limitations
Memory Forensics	95	3%	Highly effective for memory-resident malware; uncovers runtime artifacts.	Requires expertise and cannot detect dormant threats.

Behavioral Analysis	85-90	7-10%	Effective against unknown and obfuscated threats; captures runtime behaviors.	Resource-intensive; may generate false positives.
PowerShell Monitoring	85-90	8-10%	Crucial for detecting PowerShell-based fileless malware; provides real-time monitoring.	Prone to false positives; limited to PowerShell exploitation.
Machine Learning	88-94	5-7%	Adaptable to evolving threats; highly effective against obfuscated and polymorphic malware.	Requires high-quality data and is vulnerable to adversarial evasion.

Memory forensics has been highly effective in identifying memory-resident malware and exposing runtime artifacts with a detection rate of 95% and a 3% false positive rate. However, it is expert-dependent and cannot detect dormant threats. Behavioral analysis is 85-90% accurate and has 7-10% FPR, and is great in detecting unknown and obfuscated threats since it watches behaviors at runtime, but is expensive and can result in false positives. PowerShell monitoring is 85-90% accurate and has 8-10% FPR, is very important in detecting fileless malware relying on PowerShell, provides real-time monitoring, but is PowerShell exploitation only and can lead to false positives. Machine learning is a versatile approach with 88-94% detection rate and 5-7% FPR and works very well for obfuscated and polymorphic malware, but relies on good quality data and is vulnerable to adversarial evasion.

4.3 Fileless Malware Mitigation Strategies

Mitigating fileless malware requires a multi-layered security approach, as traditional antivirus solutions are often ineffective. One of the most effective strategies is deploying Endpoint Detection and Response (EDR) solutions, which continuously monitor system behavior for anomalies such as unusual PowerShell activity, unauthorized registry modifications, or suspicious use of Windows Management Instrumentation (WMI). These solutions rely on behavioral analytics and machine learning to detect and respond to potential threats.

Application whitelisting is yet another crucial method to avoid fileless malware attacks. By restricting only allowed applications and scripts from running, organisations can minimize the threat of unauthorised code execution. As fileless malware usually exploits native scripting tools, like PowerShell and macros, disabling or limiting their usage can limit attack pathways. Adding strict Group Policy configurations for script execution adds to the security.

Artificial intelligence (AI) and behavior analysis are important components of today's threat detection. As opposed to the conventional signature-based antivirus software, AI-powered security products examine patterns of behavior in the system to identify malicious activity. This is especially helpful in the detection of fileless malware, which usually resides in legitimate processes.

Memory forensics and proactive threat hunting are essential components of a robust defense strategy. Since fileless malware operates in system memory rather than on disk, security teams must use forensic tools such as Volatility and Rekall to analyze memory dumps and uncover hidden threats. Regular threat hunting helps identify indicators of compromise (IOCs) that may not be detected by automated security tools.

Keeping systems and software up to date is another crucial defense mechanism. Many fileless attacks exploit vulnerabilities in outdated software and operating systems. Regular patching ensures that attackers cannot leverage known security weaknesses to gain unauthorized access.

Network monitoring and segmentation also help prevent fileless malware from spreading across an organization’s infrastructure. By analyzing network traffic for unusual activity, security teams can identify potential threats before they cause damage. Implementing network segmentation limits the ability of malware to move laterally, reducing the overall risk of widespread infection.

Human factors play a significant role in cybersecurity, and user awareness training is a critical part of any mitigation strategy. Many fileless malware infections begin with phishing attacks or malicious email attachments. Educating employees about recognizing suspicious emails, links, and social engineering tactics helps reduce the likelihood of successful attacks.

A Zero Trust security model further strengthens defenses by ensuring that no user or device is automatically trusted. Continuous authentication, least-privilege access policies, and strict identity verification prevent attackers from easily infiltrating systems.

Logging and continuous monitoring provide valuable insights into potential security threats. Enabling logging for PowerShell and script execution, combined with Security Information and Event Management (SIEM) systems, helps organizations detect and respond to suspicious activities in real time.

By combining these strategies, organizations can significantly enhance their ability to detect, prevent, and respond to fileless malware threats. A proactive approach to cybersecurity, incorporating both technological solutions and human awareness, is essential in defending against modern cyber threats.

5.0 Conclusion

This analysis emphasizes the covert behavior of fileless malware, which resides in system memory and employs tools such as PowerShell and WMI, rendering conventional antivirus measures inadequate. Effective mitigation demands a comprehensive strategy encompassing endpoint monitoring, access control, and behavioral analysis in real time.

Detection techniques are not created equal: memory forensics (95% efficacy) is effective at exposing runtime artifacts but is skill-intensive, and PowerShell monitoring and behavior analysis (85-90% efficacy) help uncover obfuscated threats but generate false positives. Machine learning (88-94% efficacy) adapts to evolving threats but is susceptible to adversarial evasion.

A hybrid detection solution that combines memory forensics, behavioral analysis, and ML-based models offers the best defense. Real-time detection, adaptive security frameworks, and AI-powered threat intelligence need to be enhanced by future research to provide improved cybersecurity resilience to future attacks.

REFERENCES

Andy Baldin (2019). Best practices for fighting the fileless threat. *Cyber Defense Magazine, 9*(6), 12-19.

Ahmadi, M., Ulyanov, D., & Kharraz, A. (2020). Fileless malware: Threats, techniques, and defense mechanisms. *IEEE Transactions on Dependable and Secure Computing, 17*(2), 345-362.

Alzubaidi, M., Al-Dujaili, A., & Hammad, M. (2023). Memory dump analysis for transient malware detection. *Journal of Digital Forensics, 19*(2), 145-160.

Barnes, L. (2021). The evolution of fileless malware: Challenges for traditional antivirus systems. *Cybersecurity Today, 14*(3), 78-92.

Carr, M., & Lee, R. (2019). Behavioral detection of fileless malware: A case study. *ACM Computing Surveys, 52*(1), 1-35.

Chen, W., Liu, X., & Wang, Z. (2023). Fileless attacks in IoT systems: A survey and mitigation framework. *Internet of Things Journal, 9*(4), 5678-5692.

Kara, I. (2023). Memory-based cyberattacks and detection challenges. *Journal of Information Warfare, 22*(1), 33-48.

Khalid, A., Rahman, S., & Ahmed, T. (2023). Fileless malware: Exploitation techniques and defense paradigms. *IEEE Transactions on Information Forensics and Security, 18*(4), 1123-1137.

Khushali, V. (2020). Antivirus mechanisms for modern malware detection. *Journal of Cybersecurity Innovations, 5*(2), 45-60.

Kim, S., Park, H., & Lee, J. (2019). Machine learning approaches for detecting fileless malware: A behavioral-based perspective. *Journal of Artificial Intelligence & Cybersecurity, 7*(2), 210-225.

Kolosnjaji, B., Zarras, A., & Eckert, C. (2020). A hybrid detection framework for fileless malware: Combining rule-based and machine learning techniques. *Security and Communication Networks, 15*(4), 1456-1472.

Kumar, S. (2020). An emerging threat: Fileless malware—a survey and research challenges. *Cybersecurity, 3*(1), 1–12. https://doi.org/10.1186/s42400-019-0043-x

Lee, S., Kim, J., & Park, M. (2022). Classification and detection of fileless attacks using YARA rules. *Computers & Security, 117*, 102691.

Li, Z., & Clark, D. (2020). EDR tools for malware detection: A comparative study. *Journal of Computer Science, 28*(3), 295-305.

Microsoft. (2023). Fileless threats: Understanding memory-based cyberattacks. *Microsoft Defender Security Research*. https://learn.microsoft.com/en-us/defender endpoint/malware/fileless-threats

Sudhakar, R., & Kumar, S. (2020). A novel investigative model for fileless malware incident response. *International Journal of Cyber Forensics, 11*(1), 22-35.

Wu, X., Zhang, W., & Li, T. (2022). Leveraging threat intelligence to combat fileless malware: Case studies and future directions. *Journal of Cybersecurity Innovation, 19*(3), 317-332.

Zhang, Y., & Li, Q. (2023). Registry-based persistence detection for fileless malware. *IEEE Access, 11*, 23456-23467.

A Study of Diabetes Risk Factors Using Artificial Neural Network

Saidu, A. A. and *James, T. O.

[1]Department of Mathematics, Kebbi State University of Technology, Aliero, Kebbi State, Nigeria
[2] Department of Mathematics, Kebbi State University of Technology, Aliero, Kebbi State, Nigeria
[1*]Corresponding author: tolujam@gmail.com

Abstract

This study used Artificial Neural Network (ANN) model in predicting the risk factors of diabetic Patients from a certain Hospital in Birnin Kebbi, Kebbi State, Nigeria from the samples of 465 patients. Two (2) models were generated from Artificial Neural Network (ANN) from the data. The training data for the model was 30% (1 to 140) of the data and 70% (141-465) was used to test the model. The first model comprising of all the suspected risk factors ANN (6-2-1) defected that Gender was not a statistically significant risk factor of Diabetes, while the second Model consisting of only the significant variables showed that ANN (5-2-1) shows that, Blood Sugar Concentration, Body Mass Index (BMI), Family History (FH), Age and Blood Pressure (BP) were Diabetes risk factors having 92.7% predictive accuracy. Comparing the two Models showed that Model 2 was the best Model having the minimum information criterion of Akaike Information criterion (AIC) and Schwarz Information Criterion (SIC) and with least Mean Square Error (MSE) and Root Mean Square Error (RMSE). This study demonstrates the potential of ANN in identifying significant diabetes risk factors and recommended targeted interventions on improving patient outcomes.

.

Keywords: artificial neural network, diabetes, risk factors, study

1. Introduction

Diabetes still remain a global health challenge. It is a chronic, metabolic disease characterized by elevated levels of blood glucose (or blood sugar), which leads over time to serious damage to the heart, blood vessels, eyes, kidneys and nerves. (World Health Organization, [WHO], 2024b). If not well controlled, could cause blindness, kidney failure, lower limb amputation and several other long-term consequences that impact significantly on quality of life. There are no global estimates of diabetes-related end-stage renal disease, cardiovascular events, lower-extremity amputations or pregnancy complications, though these conditions affect many people living with diabetes. (WHO, 2024b). There are different types of diabetes including Type 1 diabetes (known as insulin-dependent), Type 2 diabetes (formerly called non-insulin-dependent or adult- onset diabetes), Gestational diabetes (GDM) (Is a temporary condition that occurs in pregnancy and carries long- term risk of type 2 diabetes). Pre-diabetes otherwise known as “impaired glucose tolerance”, is a pre-cursor to Type 2 diabetes (WHO, 2024a).

In 2017, approximately 5 million deaths worldwide were attributable to diabetes in the 20-99

years age range (Cho et.al, 2018). Approximately 535 million adults (20-79 years) are living with diabetes and there is a projection of an increase rise to 643 million by 2030(International Diabetes Federation [IDF], Diabetes Atlas, 2021). Although, many studies on the prediction of diabetes using Artificial Neural Network have been done by Yinghui, et al., (2018), Srivastava, et al. (2019), Pradhan, et al., (2020), Muhammad, et al.,(2021), Abdulaziz et al., (2022) Evwiekpaefe & Abdulkadir (2023), (Sahu and Mantri, 2023), Kabiru et al., (2025) and many more researchers, yet there is still need for more study on the risk factors of Diabetes.

2. Materials and Methods

2.1 ARTIFICIAL NEURAL NETWORK

An artificial Neural network (ANN) is an information processing paradigm that is inspired by the way biological nervous systems, such as the brain, process information. It is a network consisting of neurons and paths connecting the neurons (Rumelhart et al., 1986, Bishop, 1995). There are two main categories of network architectures depending on the type of the connections between the neurons, "feed-forward neural networks" and "recurrent neural networks". If there is no "feedback" from the outputs of the neurons towards the inputs throughout the network as in figure 1, then it is a "feed-forward neural network" (Murat, 2006).

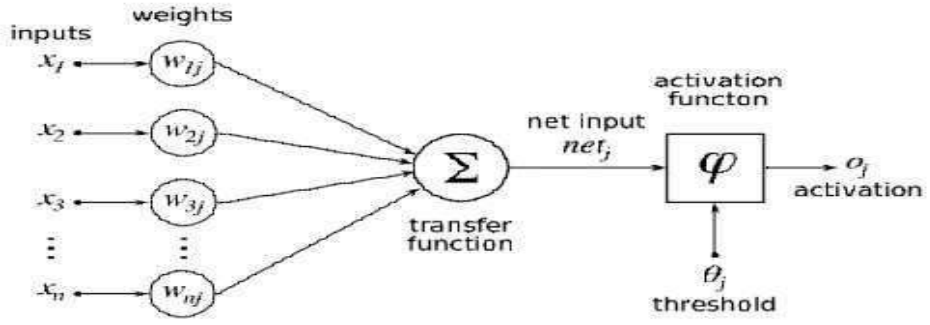

Figure 1: Artificial Neural Networks Data Processing in a Neuron. (Srivastava et al., 2019).

A Feed-Forward Neural Network is a basic neural network comprising of an input layer, output layer, and at least one layer of a neuron. It is commonly seen in its simplest form as a single layer perceptron. In this model, a series of inputs enter the layer and are multiplied by the weights. Each value is then added together to get a sum of the weighted input values.

Figure 2 represents this type of neural network. It as a one-layer feed forward network among two outputs on account of the output layer is the alone layer with an activation computation.

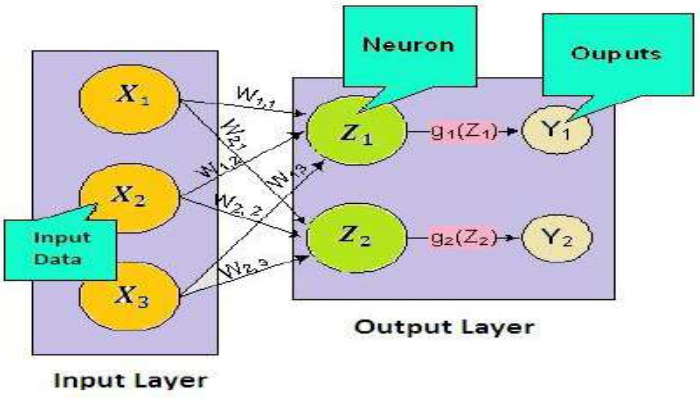

Figure 2. A Single Hidden Layer Feed Forward Neural Network

In this single hidden layer feed forward neural network, the network's inputs are directly connected to the output layer nodes, Z_1 and Z_2. The output nodes use activation functions g and g_2 to yield the outputs Y_1 and Y_2.

$$Z_1 = \sum_{i=1}^{3} W_{1,i}x_i + \mu_1$$

$$Z_1 = \sum_{i=1}^{3} W_{2,i}x_i + \mu_2$$

$$Y_1 = g_1(Z_1) = g_1 \sum_{i=1}^{3} W_{1,i}x_i + \mu_1 \quad (1)$$

and

$$Y_2 = g_2(Z_2) = g_1 \sum_{i=1}^{3} W_{2,i}x_i + \mu_2 \quad (2)$$

When the activation functions g_1 and g_2 are similar activation functions, the single hidden layer feed forward neural network is similar to a linear regression model. In this study, the sigmoid function equation (3) was the activation used.

$$\frac{1}{1+e^{-x}} \quad (3)$$

2.2 Data Processing

The data in this study was collected from the Laboratory Record Section of a hospital in Birnin Kebbi, Kebbi State, Nigeria. The study took a sample data of 465 tested patients with six variables as expected risk factors with 1 dependent variable which is the test outcome. The variables used as

the study input were set of risk factor to a diabetic patient, which include Body Mass Index (BMI), Age, Blood Pressure (BP), Blood Sugar Concentration, Family History (FH), Gender of the tested patient and Test outcome which was considered as dependent variable as seen in Table 1.

2.3 Data Scaling/ Normalization

Data scaling or normalization is a process of making model data in a standard format so that the training segment of data will be improved, accurate, and faster. The method of scaling data in neural networks is similar to data normalization in any machine learning problem (Taiyu et al., 2020). The data in this study was scaled as seen in Table 2

2.3 Data Scaling Maximization

Activation maximization method was used to find representation for features that neurons/filters in neural networks have learned as seen in table 3.

2.4 Data Training

The network was trained to respond correctly to each input pattern from the training set. In this study we trained 30% of the data and it was used for training while the remaining 70% was used to test the modelling ability or performance. Hence, the data have 140 series of training segment in table 4.

2.5 Data Testing

The Test dataset provides the gold standard used to evaluate the model. The 70% of the data was used for testing the process capability as seen in table 5. Once the model was completely trained (using the train and validation sets).

3. Results and Discussion

These are the characteristic information of the data set on the patients

Table 1: Statistic on Demographic Information of the Patient

	Blood Sugar	**Blood Pressure**	**BMI**	**Age**	**Test Outcome**	**Family History**	**Gender**
N	465	465	465	465	465	465	465

Missing	0	0	0	0	0	0	0
Mean	122.2	69.87	33.0	50.1	0.42	0.46	0.4602
Median	119.0	72.00	32.8	51.0	0.00	0.00	0.0000
Std. Deviation	31.98	19.869	7.49	9.65	0.494	0.499	0.49895

Table 1 depicted that Family History, Gender and Test Outcome were distributed closely in terms of mean, median and standard deviation. In the dependent variable (Test Outcome), 0 is coded as [diabetic] which means the diagnose person is diabetic while (1) is coded as [not diabetic] which means the diagnose person is not diabetic

Table 2: Scaling of Diabetic Data

BloodSugar	BloodPressure	BMI	Age	TestOutcome	FamilyHistory	Gender
[1,]-0.475045996	-0.396040948	0.47697102	-0.02003881	1.1754309	-0.9183792	1.0818386
[2,] 0.681643271	-0.597362665	-0.18999092	-2.50485113	1.1754309	-0.9183792	-0.9223644

Data scaling Continue.

[463,]-0.349998508	1.013211072	-0.61684656	-0.02003881	-0.8489223	-0.9183792	1.0818386
[464,] 0.369024550	0.006602486	0.31690015	-0.12357266	1.1754309	-0.9183792	-0.9223644

[465,] 1.119309480 0.711228496 0.85046971 -0.02003881 1.1754309 -0.9183792 -0.9223644

Table 2. shows that the scaling in this process, was step forwards during the process 465 times with respect to the study of the risks factor all at a time.

Table 3: Data Maximization

	Blood Sugar	Blood Pressure	BMI	Age	Test Outcome	FH	Gender
1	0.5404040	0.5081967	0.5454545	0.48076923	1	0	1
2	0.7272727	0.4754098	0.4709389	0.01923077	1	0	0
3	0.6464646	0.5573770	0.4545455	0.48076923	1	1	0
4	0.5707071	0.4098361	0.4396423	0.48076923	0	1	1
5	0.5656566	0.6065574	0.4709389	0.15384615	1	1	0
6	0.4393939	0.4754098	0.4873323	0.38461538	0	1	0

Maximization continues.

140	0.5606061	0.7377049	0.4232489	0.48076923	0	0	1
141	0.6767677	0.5737705	0.5275708	0.46153846	1	0	0
142	0.7979798	0.6885246	0.5871833	0.48076923	1	0	0

Since maximizing aims to find the input that activates the strongest activation within a certain neuron or set of neurons. In table 3 the training process, it was observed that the most efficient hidden layers to use are two (2). Specifically, the first hidden layer at 2 levels while second hidden

activation layers at five levels. Five variables were significantly fitted in the best generated model.

Table 4: Model Training

	BloodSugar	BloodPressure	BMI	Age	TestOutcome	FH	Gender
1	0.5404040	0.5081967	0.5454545	0.48076923	1	0	1
2	0.7272727	0.4754098	0.4709389	0.01923077	1	0	0
3	0.6464646	0.5573770	0.4545455	0.48076923	1	1	0
4	0.5707071	0.4098361	0.4396423	0.48076923	0	1	1
5	0.5656566	0.6065574	0.4709389	0.15384615	1	1	0
6	0.4393939	0.4754098	0.4873323	0.38461538	0	1	0
Model Training continue.							
138	0.6515152	0.6557377	0.4649776	0.15384615	0	1	0
139	0.5555556	0.5409836	0.4754098	0.48076923	0	0	0
140	0.5606061	0.7377049	0.4232489	0.48076923	0	0	1

Training a neural network involves using an optimization of algorithm to find a set of weights to best map inputs to outputs. Thus, training set is a set of pairs of input patterns with corresponding desired output patterns.

Table 5: Data Testing Set

	BloodSugar_	BloodPressure	BMI	Age	TestOutcome	FH	Gender
141	0.6767677	0.5737705	0.5275708	0.46153846	1	0	0
142	0.7979798	0.6885246	0.5871833	0.48076923	1	0	0
143	0.7474747	0.4918033	0.4605067	0.48076923	1	1	0
144	0.6161616	0.5573770	0.5216095	0.48076923	0	0	1
145	0.7373737	0.6229508	0.5692996	0.48076923	0	0	1
146	0.5353535	0.4918033	0.3949329	0.57692308	1	1	0
147	0.6010101	0.7049180	0.6795827	0.28846154	1	0	1
148	0.7373737	0.5737705	0.4172876	0.28846154	1	0	1
149	0.6060606	0.6229508	0.5916542	0.19230769	0	0	0
150	0.9191919	0.6065574	0.4545455	0.30769231	1	0	0
151	0.4646465	0.6557377	0.6289121	0.34615385	0	0	0
152	0.9898990	0.6229508	0.5439642	0.09615385	1	0	0

Testing of Dataset or sample of data used to provide an unbiased evaluation of a final model fit on the training dataset as seen in Table 5.

Model 1: Model with all Parameters (Diabetic Risk Factors)

Table 6: ANN Architecture: Model 1 of FFNN (6-2-1)

Coefficients:

	Estimate	Std. Error	z value	Pr(>|z|)
(Intercept)	-9.505616	1.400578	-6.787	1.15e-11 ***
Blood Sugar	0.029156	0.005288	5.514	3.51e-08 ***
Blood Pressure	-0.022305	0.008290	-2.691	0.00713 **
BMI	0.124447	0.023720	5.246	1.55e-07 ***
Age	0.031789	0.015346	2.071	0.03832 *
Family History	3.049907	0.332940	9.161	< 2e-16 ***
Gender	-0.457182	0.310149	-1.474	0.14046
Signif. codes :	'***' 0.001	'**' 0.01	'*' 0.05	

Gender was the only parameter found to be statistically insignificant in table 6

Table 7: ANN Model 1: Classification

Sample	**Observed**	**Predicted**		**Percent**
		Diabetics	**No Diabetics**	**Correct**
Training	Diabetics	172	16	91.5%
	No Diabetics	25	105	80.8%
	Overall Percent	**61.9%**	**38.1%**	**87.1%**

Testing	Diabetics	46	7	86.8%
	No Diabetics	4	36	90.0%
	Overall	**53.8%**	**46.2%**	**88.2%**
	Percent			

Dependent variable: Test Outcome

Table 7 depicted that in training model 1, an overall of 87.1% accurate prediction and make 88.2% while testing the model.

Table 8: Model 2 of FFNN (5-2-1)

Coefficients:

	Estimate	**Std. Error**	**z value**	**Pr(>|z|)**
(Intercept)	-9.632003	1.388665	-6.936	4.03e-12 ***
BloodSugar	0.028947	0.005236	5.529	3.23e-08 ***
BloodPressure	-0.020739	0.008233	-2.519	0.0118 *
BMI	0.121456	0.023454	5.179	2.24e-07 ***
Age	0.030641	0.015198	2.016	0.0438 *
FamilyHistory	3.044978	0.330341	9.218	< 2e-16 ***
Signif. codes : '*' 0.001**		**'**' 0.01**		**'*' 0.05**

Blood Sugar Concentration, Body Mass Index (BMI) and Family History were highly significant even at 0.001, while Age and Blood Pressure were not significant at 0.05 which was the standard choosing level of significant. With this we can conclude that all factor in model 2,

in table 8 can be classify as risk factor to a diabetic patient.

Models Evaluations

Table 9: Models Evaluation

Model 1	**Akaike criterion**	**Schwarz criterion**
ANN (6-2-1)	**291.56**	**329.55**
Model 2		
ANN (5-2-1)	**285.21**	**324.25**
Model Performances	Model 1 FFNN	**Model 2 FFNN**
Mean Squared Error	0.0825	**0.00468**
Root Mean Squared Error	0.2872	**0.06841**

Model Accuracy	Model 1 FFNN	**Model 2 FFNN**
Number of cases 'correctly predicted'	88.2%	**92.7%**

4.1 Discussions

In modelling the diabetic data, the performance of all models was evaluated. The result in Table 10, shows that Model 2 of the Feed Forward Neural Network (FFNN) achieved the highest predictive accuracy of 92.7%. Consistently, Model 2 of FFNN also demonstrated best performance, with the lowest error

rates: as Mean Squared Error (MSE) of 0.00468 and a Root Mean Squared Error (RMSE) of 0.06841.

5. Conclusion

This study investigates the risk factors for diabetes among patients of a certain hospital in Birnin Kebbi, Nigeria using an Artificial Neural Network (ANN) approach. Six potential risk factors were analyzed: age, body mass index (BMI), blood pressure (BP), blood sugar concentration, family history (FH), and gender. The analysis shows that gender was not a significant predictor of diabetes in this patient population. Two Feed Forward Neural Network (FFNN) models was developed and Model 2 demonstrated superior performance compared to Model 1. Model 2 exhibited the highest prediction accuracy and the lowest Mean Squared Error (MSE) and Root Mean Squared Error (RMSE)

References

Abdulaziz alsalem, A. F., Alqahtani, Z. M., Alshammari, A. A., Alzamanan, H. R., Alsarhan, S. M., Alwallah, S. A., Alismail, R. S., & Atiah, H. M. (2022). Evaluating the risk of type 2 diabetes mellitus using artificial neural network. *International Journal of Pharmaceutical and Bio Medical Science*, *2(11)*, 546–551. https://doi.org/10.47191/ijpbms/v2-i11-13

Bishop C. M. (1995). *Neural Networks for Pattern Recognition.* Oxford: Oxford University Press, UK.

Cho, N. H., Shaw, J. E., Karuranga, S., Huang, Y., da Rocha Fernandes, J. D., Ohlrogge, A. W., & Malanda, B. (2018). IDF Diabetes Atlas: Global estimates of diabetes prevalence for 2017 and projections for 2045. *Diabetes research and clinical practice, 138,* 271–281. https://doi.org/10.1016/j.diabres

Evwiekpaefe, A.E., & Abdulkadir, N. (2023). A predictive model for diabetes mellitus using machine learning techniques (a study in Nigeria). *African Journal of Informative Systems, 15(1).* https://digitalcommons.kennesaw.edu/ajis/vol15/iss1/1

Gulumbe, S.U., Suleiman, S., Badamasi, S., Tambuwal, A H., & Usman, U. (2019). Predicting diabetes mellitus sing artificial neural network through a Simulation Study. *Machine Learning Research*. *4(2),* 33-38. https://doi.org/10.11648/j.mlr

International Diabetes Federation (IDF) (2021). https://idf.org/about-diabetes/diabetes-facts- figures/

Kabiru, H., Buhari S. A, & Idris Aliyu Kankara. (2025). "Application of artificial neural networks for early detection of diabetes mellitus: Insights from a case study in Kaura Namoda Nigeria". *Archives of Current Research International* 25(1), 302-13. https://doi.org/10.9734/acri/2025/v25i11060.

Murat H. S (2006). A brief review of feed-forward neural networks. *Communications Faculty of Sciences University of Ankara Series A2-A3 Physical Sciences and Engineering · A2-A3.* 50(1), 11-17.

Muhammad, M. B., Bader F. A., Saddam, H., Abdu, G., Adel, A., and Syed, S. U., (2021). An improved artificial neural network model for effective diabetes prediction. *Complexity* (10) https://doi.org/10.1155/2021/5525271

Pradhan, N., Rani, G., Dhaka, V.S., & Poonia, R.C. (2020). Diabetes prediction using artificial neural network. *Journal of Science Direct, 18(5)*. https://doi.org/10.1016/jsd.8978-0-12-819061-6.00014-8

Rumelhart, D.E., Hinton G.E., and Williams R.J. (1986). Learning representations by back propagating errors. *Nature*, 323, 533-536.

Sahu, P., & Mantri, J.K. (2023). Artificial neural network based diabetes prediction model and reducing impact of class imbalance on its performance. Journal of SSRN, 15. https://doi.org/10.2139/ssrn.4538967

Srivastava, S., Sharma, L., Sharma, V., Kumar, A., & Darbari, H. (2019). Prediction of Diabetes Using Artificial Neural Network Approach: *ICoEVCI*, India. 10.1007/978-981-13-1642-5_59

Taiyu, Z., Kezhi, L., Jianwei, C., Pau, H. and Pantelis, G., (2020). "Dilated Recurrent Neural Networks for Glucose Forecasting in Type 1 Diabetes". *Journal of Healthcare Informatics Research* 4:308–324. https://doi.org/10.1007/s41666-020-00068-2

Yinghui, Z., Zihan, L., Yubeen, K., Ruoci, N. & Yuqi, M., (2018). Feed-Forward Neural Network model for the accurate prediction of diabetes mellitus. *International Journal of Scientific & Technology Research 7(8)*, 2277-8616.

World Health Organization, (2024a). Definition, Diagnosis and Classification of Diabetes Mellitus and its Complications. Part 1: Diagnosis and Classification of Diabetes Mellitus (WHO/NCD/NCS/99.2). Geneva.
https://www.who.int/health-topics/diabetes#tab=tab_1

World Health Organization (2024b) https://www.who.int/healthtopics/diabetes#tab=tab_1

Literature Survey on the Usability Evaluation of Mobile Banking Applications.

[1*]Abdullahi T., [2]Samson I., [3]Mansur S., [4]Habibu Y. M., [5]Amina B. J.
[1, 2, 4, 5] Department of Informatics, Faculty of Computing Kaduna state University
[3] Department of Computer Science, Nuhu Bamalli Polytechnic, Zaria, Nigeria

[1*]Corresponding author: abdullahi.tanimu@kasu.edu.ng

Abstract

Mobile banking application is one of the tools that were used to maintain social distancing in the banking sector during the covid-19 pandemic and it is proved to be one of the necessary requirements for achieving the objectives of green banking which enhances healthy banking within our environment. However, the drawback of Mobile Banking Applications is usability and trust as users will need a reliable MBAP whose user interface is easy to navigate in performing any banking transaction. Most of the existing reviews on mobile banking applications' usability evaluation are on the basis of the method used. This work, reviews and compares various literatures that attempted to evaluate the usability of mobile banking applications based on the usability evaluation model (the set of usability attributes) used for evaluation and the supposed objective of usability in order to provide insight for mobile banking application developers, usability researchers and financial Institutions. The study focuses on researches conducted from 2020 to 2024. We adopted a systematic literature review that compare the MBAPs usability evaluation models used by various papers reviewed and whether the supposed objective of usability is evaluated by the authors. Result shows that, most of the literatures do not evaluate all the usability attributes required for a mobile banking applications and as contribution, we recommended that a model that integrate all the usability attributes should be developed.

Keywords: MBAPs, Usability, Usability evaluation, usability evaluation model

1. Introduction

Today, there is increase in the use of mobile banking applications for banking transactions, this boost can be largely due to increase in the number of smartphones, improvement in internet infrastructure, restrictions to human movement occasioned by the Covid-19 pandemic (Omotosho, 2021) as well as its benefits in reducing issues that has to do with the complexity of travelling to banks for such transaction as it involves the use of software application in mobile device (smartphone, apple iPad, etc.) to perform banking transactions such as transfer, checking account balance, bill payment, introduction of cashless policy in some countries, etcetera. Mobile banking application is also a very important component required to achieve "green banking" which is a proactive technique for energy conservation and environmental protection. This use of mobile

banking app present the need for a study into how usable are the applications used for mobile banking so as to find how the usability of such applications can be improved.

To understand how usable particular app is, we have to determine the usability of the application. In determining usability, we study how a particular application possessed some attributes that makes the application easy to use. The process of assessing whether a system possessed such ease of use attributes is known as usability evaluation.

In usability evaluation, the degree to which a system provide such qualities is assessed using different techniques which are generally classified as analytical or empirical. In Analytical (or inspection) techniques which is the cheaper method compared to the other method, usability experts are used to study the system's usability and give their assessment on how usable is the studied user interface, while in the experimental technique, we used actual users to test the usability of user interface (Habeeb, 2023). Usability is a necessary attribute for mobile banking applications as customers need not to take time on learning how to use the application. Such importance of usability made it one of the considerable challenge to mobile banking application developers.

Research in the area of mobile banking applications' usability evaluation has become one of the areas of research which has limited methodologies to address (Adamu, 2017). Several literatures available on mobile banking applications usability evaluation attempted to use attributes defined by some proposed usability evaluation models, but none of these models captures all the attributes required to evaluate the usability of mobile banking applications.

Several literatures addresses the usability of mobile banking application using different techniques of usability evaluation. This work will review some of these literatures based on the usability attributes used in evaluating the usability of a mobile banking application.

1.1 Brief Overview On Mobile Banking Application

Mobile Banking Applications (MBAPs) is one of the recent fads in mobile trading applications (Apps). MBAPs permit users to execute exchanges of money and many banking services conveniently (Hamid *et al,* 2022). Bank, customer, mobile Network operator and Mobile Banking Technology are the major components required for a successful mobile banking transaction.

Mobile banking technologies can be classified into two environments

1. Server-side technologies which are applications built on a server, away from the consumer's Subscriber's Identity Module or mobile hand set. Examples of server-side technologies would be Short Message Service, Interactive Voice Response, Unstructured Supplementary Service Data and Wireless Application Protocol.
2. Client-side Technologies which are those applications, built or embedded on consumer SIMs or Mobile handsets. Example of client-side application are s@T and J2ME (JAVA).

Each of these technologies require registration with the Bank, vendo, or Mobile Network Operator that provides such services.
The service provider is responsible for defining the registration process which must include initial identification of consumer as an enforcement of necessary security mechanism to ensure trust.

1.2 Usability

Usability is a quality attribute that concerns with how easy to use the user interface of a particular product. Nielsen (2012) defines usability as a method for improving ease of use during the design process that is defined by the quality components; learnability, efficiency, memorability, errors, satisfactions, etc.

Usability is referring to the ease of use and is one of the major requirements to achieve the usefulness of a product. A system will be most useful if a user can easily understand and navigate through the user interface. A system can only be useful if it has the attributes; usability and utility which are mostly measured through user testing.

1.2.1 Usability Evaluation

This is the assessment of how easy to use a particular product or system. It composed of qualitative and quantitative research process of assessing the user friendliness of a system or product and whether it satisfied users' need. Usability evaluation therefore composed of methodologies for measuring the usability aspects of the user interface of a system. Usability evaluation is an important component of user interface design process. Usability evaluation can be performed at any point in a product's life cycle. The objectives of usability evaluation are to understand how users interact with the product or service, and identify ways to improve it.

1.2.2 Some Usability Evaluation Methods

Methods for usability evaluation are categorized into analytical or inspection and empirical testing (Habeeb, 2023). The analytical technique proposed by Boehm *et al.* (1976), testing and evaluation of design layout of a software system is done by expert. The technique therefore, provide expert views and opinions essential for the development of a system. Some of the main methods for usability evaluation are:

Cognitive Walkthrough (CW): It employs process simulation of an individual's behaviour for a specific purpose, concentrating on cognitive issues by analyzing the user's thought process, which assist assessors in evaluating the user interface (Holzinger, 2005**).** The drawback of this method is that the evaluation becomes ineffective if the scenarios are not clearly outlined and proper guidance is not given (Desak and Gintoro, 2020).

Heuristic evaluation (HE): it is a quick, inexpensive and informal method where a small group of usability assessors reviews and evaluates the user interface. It helps identify significant and minor usability issues during the development phase. It can be applied using a set of usability principles, but this method has limitations, such as the need for evaluators to be experts for accurate results and un-reliability in detecting domain specific problems. (Holzinger, 2005).

Questionnaire: it is used to assess user satisfaction with the interface. Instead of evaluating the user interface itself, it focuses on gathering user feedback and analyzing the result statistically. However, a large number of responses must be collected to ensure significance (Holzinger, 2005).

Thinking-aloud (TA): This method involves the real users, allowing them to express their thought while interacting with the user interface, enabling assessors to understand exactly how users

perceived the system. The downside of this method is that it is time consuming and may feel somewhat unnatural if implemented. However, this issue is addresses through cross-education, where two users use the interface together and provide feedback collectively (Habeeb *et al.,* 2020; Holzinger, 2005).

1.2.3 Usability Evaluation Models

Shackel in 1991 suggested a set of four attributes (Effectiveness, Learnability, and Flexibility & Attitude) to evaluate usability. Shackel's idea places a strong emphasis on considering the environment in which the system is utilized. This model was described as applicable to any evaluation process (i.e. Expert Review, Simulation trials & Task-Based Evaluation) (Ali *et al*, 2022). Chen *et al*. (2015) conducted a study for library practitioners, adopting a technology-focused approach to define usability, which strongly supported Shackel's approach.

In addition of Shackel's model, Nielsen in 1993 provided his definition of usability which originally comprises of 4 attributes (Learnability, Effectiveness, Efficiency, and Satisfaction), He later replaced ''Effectiveness'' with ''Memorability and Errors'' hence 5 attributes. This definition was widely accepted and gained greater attention from the HCI community because it incorporated attributes related to users' perception and Recall (Satisfaction and Memorability). Muqtadiroh *et al.* (2018) conducted a web usability study based on Nielsen's usability attributes and found the approach to be satisfactory. Farahani and Khajouei (2020) also conducted a usability study of HIS (Hospital Information System) by combining ISO recommended usability attributes and the attributes proposed by Nielsen model. In 1994, Nielsen introduced a process for conducting heuristic (checklist) evaluation which was also well received by the Software Engineering community and was documented in (Holland et al, 2017) and (Wong, 2020).

With the adoption of Nielsen's model, the ISO (International Standard organization) in 1998 introduced their definition for usability evaluation ''ISO 92411-11'' (Orlovska *et al.,* 2018) in the hope of establishing a global standard. This definition consists of 3 attributes (Effectiveness, Efficiency, and Satisfaction). This attribute selection was the already familiarity with usability attributes in the research community. As ISO presented the model, it was well accepted by the community. Farahani *et al.* (2020) and Moumane et al. (2016) performed usability evaluation on mobile applications using this model, while Mkpojiogu *et al*. (2015) and Pradnyana *et al*. (2019) performed usability evaluation on web-based applications using this model.

In 2001, ISO updated the previous model (9241-11) into ''ISO 9126-1'' and also updated their attribute set from ''Effectiveness, Efficiency, and Satisfaction'' to ''Functionality, Maintainability, Portability, Reliability, Efficiency and Usability'' for usability evaluation to keep up with the continuously changing field of software development. To date, this model is widely used in the HCI community for both general and web-based applications in terms of attribute based evaluation. The authors in (Moumane, et al, 2016), (Chua and Dyson, 2004) and (Fahmy *et al*, 2012) conducted usability evaluation of mobile applications using this set of attributes proposed by ISO 2001 model, while Suwawi *et al*. (2013) performed usability evaluation of academic website using the attributes proposed by this model.

Harrison *et al*. (2013) introduced their usability evaluation model called People At The Center Of Mobile Application Development (PACMAD), which comprises seven attributes ''Effectiveness,

Efficiency, Satisfaction, Learnability, Memorability, Errors and Cognitive load,'' the primary goal of this model was to extend the existing models (ISO 9241-11, Nielsen 1993 and ISO 9126-1) in evaluation of mobile applications usability. The key contribution of this model was the incorporation of ''Cognitive load (context in which application is being used)'' as a metric factor. The authors established new definition and measurement criteria for each attribute especially ''Cognitive load'' as for the first time, it's utilised as a dependent variable in conjunction with other attributes. Dalal *et al.* (2015) presented some guidelines while testing mobile applications in extension with the PACMAD model. A review was conducted by Saleh *et al.* (2015) on current usability practices, revealing the suitability of PACMAD for mobile applications. Additionally, the author introduced GQM (Goal Question Metrics) approach for PACMAD (an extension) proposing PACMAD be considered as Heuristics-based evaluation model rather than an attribute. Kasali *et al.* (2019) conducted a usability study utilising the feature (Attribute) selections from the PACMAD model & Integrated Measurement Model (IMM) on a mobile health application. Zahra *et al.* (2019) performed usability study of a mobile E-Marketplace application utilizing these set of attributes proposed by PACMAD model.

Table 1: Usability Evaluation Models and their set of Attributes

Usability Evaluation Model	**Attributes**
Shackel (1991)	Effectiveness Flexibility Learnability Attitude
Nielsen (1993)	Efficiency Learnability Satisfaction Memorability Errors
ISO 9241 – 11 (1998)	Effectiveness Efficiency Satisfaction
ISO 9126 (2001)	Portability Functionality Reliability Usability Maintainability Efficiency
PACMAD (2013)	Effectiveness Efficiency Learnability Satisfaction Memorability Error Cognitive Load

2. Literature Survey

In this section, we review some works proposed for mobile banking usability evaluation.

Adilla *et al* (2022) evaluate the usability of BSI mobile banking facility using usability testing and SUS to determine the degree of the usability attributes; learnability, efficiency and error

Hamid *et al.* (2022) proposed a work that determine the degree of usability issues and experience of mobile banking users. They adopted quantitative method and experiment some usability attributes with mobile banking users. The usability attributes that were measured are effectiveness, trustfulness, learnability, and satisfaction after which a post experiment survey were conducted using interview and questionnaire to obtain the opinion of expert group. After that comparison of opinions of experts and mobile banking users was conducted. The results indicated that, the measure issues are; privacy and trust with mobile banking apps, and gap between users and experts which they recommend adding concept of user mode as solution.

Adediran (2024) assesses the usability of mobile banking applications using SUS scales and ISO 9241 11 standard for usability

Oyekunle *et al.* (2024) assessed the usability of MBAPs in Nigeria by examination of some usability metrics using a survey research that employs a quantitative approach on usual users of mobile banking apps. The usability metrics considered in this research are error, customization capabilities, design features, security and privacy, ease of navigation, information clarity, accuracy, reliability, accessibility and inclusivity. Finding reveals different variability in usability across different applications in the usability attributes considered.

Yohanness (2021) evaluates the usability of mobile banking in Ethiopia using Nielsen model and ISO usability evaluation standard. The finding of the study reveals that mobile banking usage has more issues on trustfulness than effectiveness, efficiency and learnability. The study also indicate a significant relationship between IT knowledge, age of mobile banking users and usability.

Naufal *et al.* (2024) studies the usability of mobile banking application using retrospective think aloud (RTA) and a post study system usability questionnaire (PSSUQ). The study reveals that users encounter little difficulty when navigating the transfer and purchase menus. Also, the study reveals that the usability of the system and the quality of the mobile banking app are still lacking but the application can be accepted by it users.

Malik *et al.* (2021) examine the usability issues of mobile banking app after checking usability satisfaction level through system usability scale (SUS). User Testing and Heuristic evaluation to compare the degree of usability issues. The finding indicate that the novice users faces difficulties in performing certain tasks but were able to cope with that with time. The usability attributes used in the evaluation are efficiency, learnability, memorability, satisfaction and error.

Alhejji *et al.* (2022) analysis the usability of mobile banking applications using ISO 9241 standard. They also recognised and examined the most significant weaknesses of mobile banking applications with regard to offering an adequate solution to developers. The result revealed that the

most critical issues were found in the user interface and functionality of the apps that regularly receive updates.

Setiyawati and Bangkalang (2022) evaluate the user experience and usability of four Indonesian mobile banking applications using user experience questionnaire and system usability scale (SUS). The attributes evaluated are the attributes proposed by PACMAD model of 2013 with the exception of cognitive load. They compared the outcome of the measurement of each application in their analysis of both user experience and usability of mobile banking applications. The minimum rating was neutral and the usability was considered as satisfactory. Their results showed that users have embraced the mobile banking applications they are using.

Huseynov *et al.* (2024) employ a machine learning technique to predict a perceived system usability scores of mobile banking apps. They used the system usability scale to evaluate perceived system usability with the inclusion of demographic data, system usage data, and device technical specification as factors in the prediction. The work demonstrated that a machine learning technique can be used to effectively predict the perceived usability of MBAPPs influenced by gender, age, education, occupation, screen size, usage frequency, and previous app experience.

3. Methodology

To perform this study, we used a systematic literature review which is a method of assessing the existing research related to a specific topic. The aim of systematic review is to provide an impartial assessment of a research topic using reliable, thorough, and verifiable methodology. A systematic review composed of several stages as follows:

Planning stage: here, the necessity for the review is recognised, specification of the research questions and the protocol to adopt for the review.

Conducting the review stage where the primary studies for the review are selected, quality assessments used to include studies are defined, the data extraction and the monitoring is performed, and the collected data is integrated.

Reporting the review stage: here, the methods of dissemination are outlined, and the review report is provided. The activities related to planning and carrying out the review stages are detailed in the following subections.

3.1 Research Questions

To achieve the aim of this study, the following research questions were identified:
What usability evaluation models are available in the literature?
Does a study evaluate the usability of MBAP?
Was the study carried out from 2020 to 2024?
Which of the usability evaluation models used for the study
What usability attributes considered in the study?

3.2 Identifying and Selecting Primary Studies

To carry out this study, various sources were used to gather information such as IEEExplore, ACM library, research gate, etc. we have also visited various conference proceedings.

The search query employed to retrieve studies is: *usability evaluation of mobile banking applications.* We used various search strings but this one yielded the highest number of relevant papers. It was used in IEEExplore, the ACM digital library and other sources that were examined.

The period reviewed was from 2020 to 2024. Regarding the digital libraries, we made sure that our search strategy was applied to magazines, journals and conference proceedings.

3.3 Inclusion Criteria and Procedure

Each selected study was assessed, the researchers performing the review determined whether or not the study should be included. The studies that met the following conditions were included:

- Studies showcasing usability evaluation methods applied to MBAPs from 2020 to 2024.
- Full research papers.
- The paper must also be written in English

3.4 Data Extraction Strategy

The extracted data were compared based on the research questions outlined, which are broken down into the following criteria:

- What usability evaluation models have been used by researchers to assess MBAPs usability?
- Is it a new evaluation model or an existing model from the HCI field? (New, Existing)
- To what extent does the particular model evaluate usability of MBAP
- What type of usability evaluation method is used? (Inspection method, User testing, Others)

TABLE 2: Comparison of Usability Evaluation Models Used By Different Authors Found In The Literature

S/N	AUTHOR	EVALUATION MODEL USED	ADVANTAGES	DRAWBACK
1.	Hamid *et al*. (2022)	Nielsen model of 1993 with addition of trustfulness	It added trustfulness to the Nielsen model of 1993, it therefore, measure efficiency with addition of attributes that test the honesty and reliability of the app.	The model were developed with desktop application in mind. Therefore, it is not sufficient to cover all the usability expectations of the current mobile banking users.

2	Adilla *et al.* (2022)	Nielsen model of 1993 with the exception of memorability and satisfaction	It evaluated MBAPs' usability using three important attributes.	These paper didn't evaluate MBAPs with all the attributes that considered all manners of users.
3	Oyekunle *et al.* -(2024)	Didn't adopted any traditional usability evaluation model but evaluated using some usability attributes proposed by the authors as framework for evaluating Nigeria's MBAPs	They addressed some usability problems which are not directly addressed by other usability evaluation models.	Didn't address some important usability issues.
4	Adediran (2024)	ISO 9241 – 11 (1998)	It measures the usability with effectiveness, efficiency and satisfaction	Does not evaluate all the usability attributes required for mobile banking applications.
5	Yohanness (2021)	Nielsen model and ISO standard	Using the two evaluation models make it possible to evaluate some attributes missing in each of the models.	Some of the attributes required for mobile banking applications are missing in this model
6	Alhejji *et al* (2022)	ISO 9241 model	The model used evaluate effectiveness as accuracy and completeness.	Evaluate only three usability attributes which are not sufficient to evaluate the usability of MBAPs.
7	Setiyawati and Bangkalang (2022)	Nielsen model + effectiveness	It added an attribute to Nielsen model to evaluate effectiveness	Some usability attributes were also not evaluated by these researchers.
8	Husseynov and Balcioglu (2024)	Machine Learning model to predict using ISO 9241	It makes user specific usability evaluation very easy.	It do not evaluate all the attributes necessary for MBAP usability

TABLE 3: Comparison of Various Work Proposed for MBAPs Usability Based on the Usability attributes evaluated.

Author/ Usability attributes	**Adilla *et al.* (2022)**	**Hamid *et al.* (2022)**	**Oyekunle *et al.* (2024)**	**Adediran (2024)**	**Yohanness (2021)**	**Husseynov *et al.* (2024)**	**Alhejji *et al.* (2022)**	**Setiyawati and Bangkalang *(2022)***
Effectiveness	No	Yes	No	Yes	Yes	Yes	Yes	Yes
Efficiency	Yes	Yes	No	Yes	Yes	Yes	Yes	Yes
Satisfaction	No	Yes	No	Yes	Yes	Yes	Yes	Yes

Learnability	Yes	Yes	No	No	Yes	No	No	Yes
Memorability	No	Yes	No	No	Yes	No	No	Yes
Reliability	No	No	Yes	No	No	No	No	No
Trustfulness	No	Yes	No	No	No	No	No	No
Error	Yes	Yes	Yes	No	Yes	No	No	Yes
Cognitive load	No	No	No	No	No	No	No	No
Any other attribute	No	No	Yes	No	No	No	No	No

4. Discussion

Here, we perform a comparison of the current techniques on the basis of evaluation models used by the various authors and discuss the present status.

Table 1 shows the various Usability evaluation models and a set of attributes that constitute that particular model. It is obvious from the table that different evaluation models proposed different attributes to evaluate the usability of software system.

Table 2 shows a Comparison of the current techniques based on the usability evaluation models used by the authors. The table also show the advantages and drawback of the models used by these authors. Based on the table 2, the conclusion is that all the models used have some drawback.

In table 3, we compare these methods based on whether a particular evaluation model evaluate usability with inclusion of all the attributes that should be included in mobile banking application's usability evaluation. The result shows that all these models are missing in evaluating some usability attributes.

5. Future Work

The future work will focus on evaluating MBAPs usability using an improved method of usability evaluation. The solution should be able to evaluate mobile banking applications with inclusion of all the attributes required for mobile banking applications' usability. The evaluation model to proposed will involve the use of Machine learning model to evaluate the usability of MBAPs using the attributes proposed by PACMAD model (2013) with addition of trustfulness and also the model must be able to distinguish between users (i.e. experienced and new users). The model should also be able to identify any attribute that may be required to make an MBAP more usable in a particular context of use.

6. Conclusion

Mobile banking applications present the benefit of conveniences in banking transaction within its capabilities. This paper reviewed some proposed techniques for evaluating MBAPs usability. We compare these evaluation methods based on the usability attribute used, advantages and drawback of the model proposed. From our comparison of the various usability evaluation models it is obvious that all the evaluation models used to evaluate mobile banking applications' usability found in the literature have some drawback as none of these models evaluate all the attributes that should be evaluated to determine MBAPs usability. However, we recommended that a model that integrate all the attributes required for usability evaluation should be developed.

References

Adamu, R. (2017). 'A Usability Evaluation of Mobile Banking Applications in Nigeria'. *International Journal of Technology and Engineering Studies 3(1).* Available at: http://kkgpublications.com/technology/

Adederan, O. E. (2024) 'An Evaluation of Usability and Security in Mobile Banking, *Research Square.* Available at: https://doi.org/10.21203/rs.3.rs-4881972/v1

Alhejji, S., Albesher, A., Wahsheh, H. & Albarrak, A. (2022). 'Evaluating and Comparing the Usability Mobile Banking Applications in Saudi Arabia'. Information 2022MDPI , Besel, Switzerland. Available at: https:// doi.org/10.3390/info/13120559

Ali, W., Riaz, O., Mumtaz, S., Khan, A. R., Saba, T. & Bahaj, S. A. (2022). 'Mobile Application Usability Evaluation: a study based on Demography' IEEE Access vol. 10 2022. Available at: https://doi.org/10.1109/ACCESS.2022.3166893

Az-zahra, H. M. Fauzi, N. & Kharisma, A. P. (2019). ``Evaluating E-marketplace mobile application based on people at the center of mobile application development (PACMAD) usability model," in *Proc. Int. Conf. Sustain. Inf. Eng. Technol. (SIET)*, Lombok, Indonesia, Sep. 2019, pp. 72_77.

Branagan, R. &+ Foster, L. B. (2021) 'Usability Evaluation' Research Collective' available at: https://doi.org/10.1007/978-3-030-64433-8_4

Chen, Y. H., Rorissa, A. & C. Germain, A. (2015). ``Usability definitions in a dynamically changing information environment," *Portal: Libraries Acad.*, 15(4), pp. 601_621.

Chua, B. & Dyson, L. (2004) ``Applying the ISO 9126 model to the evaluation of an e-learning system," in *Proc. 21st ASCILITE Conf.*, Perth,WA, Australia, 2004, pp. 1_7.

Dalal N. N. & Patel, P. (2013). ``Usability evaluation of mobile applications,". *International Journal of Engineering Resources and Technology (IJERT)*, 2(11) pp. 299_302.

Gonzalez-Holland, E. Daphne, W., Moralez, L. & Mouloua, M. (2017). ``Examination of the use of Nielsen's 10 usability heuristics & outlooks for the future," in *Proc. Hum. Factors Ergonom. Soc. Annu. Meeting*, 2017, 61(1) pp. 1472_1475.

Habeeb, I. Q. & Ramadan, M. J. (2023). 'A Systematic Review of Recent trends of e-learning usability evaluation techniques. Al-khadum 2nd International Conference on Modern Applications of Information and Communication Technology. Available at: https://. doi.org/10.1053/5.0121800

Hamid, K., Muhammad, H. A., Iqbal M. W. & Fuzail M. Z. (2022). 'Usability Evaluation of Mobile Banking Applications in Digital Business as Emerging Economy'. *IJCSNS International Journal of Computer Science and Network Security.* 22(2) available at: https://doi.org/10.22937/IJCSNS.2022.22.32

Harrison, R., Flood, D., & Duce, D (20130. 'Usability of Mobile Applications: Literature review and rationale for a new usability model'. Journal of Interaction Science. Available at: https://doi.org/10.1186/2194-0827-1-1

Holzinger A. (2005), "Usability engineering methods for software developers," *Communications of the ACM,* vol. 48, no. 1, pp. 71-74, 2005.

Hussain, A. Mkpojiogu, E. & Zakaria, H. (2015). ``Usability evaluation of a webbased health awareness portal on Smartphone devices using ISO 9241-11 model," *Jurnal Teknologi*, vol. 77, no. 4, pp. 1_5, 2015.

Huseynov, F. & Balcioglu, Y. F. (2024). 'Application of Machine Learning Technique to Predict Perceived Usability of Mobile Banking Applications in Tuyrkey'. Journal of Business Research Turkey 2024, 16(2), 1001-1011 available at: https://doi.org/10.20491/isarder.2024.1838

ISO (1998). Ergonomic Requirements for Of_ce Work With Visual Display Terminals (VDTs)_Part 11: Guidance on Usability, Standard ISO 9241-11:1998,

ISO (2001) Software Product Evaluation-Quality Characteristics and Guidelines for Their Use, Standard ISO 9126.

Khajouei R. & Farahani, F. (2020). ``A combination of two methods for evaluating the usability of a hospital information system," *BMC Med. Informat. Decis. Making*, 20(1) pp. 1_10.

Koohang, A. (2004) ``Expanding the concept of usability," *Int. J. Emerg. Trans-discipline*, vol. 7, pp. 129_141.

Malik, H. A. M. & Sajid, U. (2021) 'Analysing Usabil4 ity of Mobile banking Applications in Pakistan' *Sukkur IBA Journal of Computing and Mathematical Sciences* 5(2). Available at: https://doi.org/10.30537/sjcms.v5i2.883

Moumane, K. Idri, A. & Abran, A. (2016) ``Usability evaluation of mobile applications using ISO 9241 and ISO 25062 standards," *SpringerPlus*, 5(1) p. 548.

Muqtadiroh, F. A., Astuti, H. Darmaningrat, E. W. T. & Aprilian, F. (2017). ``Usability evaluation to enhance software quality of cultural conservation system based on nielsen model (wikibudaya)," *Proc. Comput. Sci.*, vol. 124, pp. 513_521, Jan. 2017.

Naufal, M., Ahsyar, T.K., Jazman, M. & Inggih, P. (2024). *Indonesian Journal of Computer* Science. Available at: ijcs.net

Nielsen, J. (1994). 10 Usability Heuristics. Accessed: January. 24, 2025. [Online]. Available at: https://www.nngroup.com/articles/ten-usability-heuristics/

Omotosho, B. S. (2021). 'Analysing User Experience of Mobile Banking Applications in Nigeria: A Text Mining Approach'. Central Bank of Nigeria Journal of Applied Statistics. 12(2) 2021. Available at: https://doi.org/10.33429/Cjas.12121.4/6

Oyekuynle, R., A., Ibrahim, L. A. & Ibrahim, A. (2024). 'Usability Evaluation of Nigerian Banks' Mobile Application'. *Journal of Applied Sciences, Information and Computing*. 5(2). Available at:https://doi.org/10.59568/JASIC-2024-5-2-01

Setiyawati, N., & Bangkalang, D. H. (2022). 'The Comparison of Evaluation on User Experience and Usability of Mobile Banking Applications Using User Experience Questionnaire and System Usability Scale'. *Proceeding of the International Academic Symposium of Social Sciences, 2022.* Available at: https//doi.org/10.3390/proceedings2022082087

Shackel, B. (2009) ``Usability_context, framework, definition, design and evaluation," *Interacting Comput.*, vol. 21, nos. 5_6, pp. 21_37, 2009.

Suwawi, D. D. J. Darwiyanto, E. & Rochmani, M. (2015). ``Evaluation of academic website using ISO/IEC 9126," in *Proc. 3rd Int. Conf. Inf. Commun. Technol. (ICoICT)*, Nusa Dua, Bali, Indonesia pp. 222_227.

Wong, E. (2020). *Heuristic Evaluation: How to Conduct a Heuristic Evaluation*. Available at: https://www.interactiondesign.org/literature/article/heuristic-evaluation-how-to-conduct-aheuristic-evaluation+++++

Yohannesse, E. (2021) . 'Usability Evaluation of Mobile Banking Applications in Ethiopia'. College of Natural and Computational Sciences, Addis ababa University.

Orlovska, J., Wickman C. & Soderberg R. (2018). 'Big Data Can Be a Solution for User Behaviour Evaluation: An Automative Industry Example. 51st CIRP Conference on Manufacturing Systems. Available at: www.sciencedirect.com

Biometric Authentication Based on Facial Features in IoT System Using Optimised CNN

Aminu Dau , *PhD*
Department of Computer Science, Hassan Usman Katsina Polytechnic, Katsina State Nigeria.
dauaminu@gmail.com

Abstract

Biometric authentication using facial features has emerged as a secure and user-friendly method for identity verification, particularly in Internet of Things (IoT) systems. However, deploying high-accuracy facial recognition models in resource-constrained IoT environments remains challenging due to computational and memory limitations. This paper proposes an optimized Convolutional Neural Network (CNN) model designed specifically for facial biometric authentication in IoT systems. The optimization techniques include model pruning, quantization, and the use of lightweight CNN architectures to ensure computational efficiency while maintaining high accuracy. The proposed model is evaluated on widely-used datasets, including Labeled Faces in the Wild (LFW) and CelebA. Results demonstrate that the optimized CNN achieves state-of-the-art performance with an accuracy of 96.7% on LFW and 95.2% on CelebA, outperforming several existing models in terms of precision, recall, F1-score, and overall computational efficiency. Furthermore, comparative studies with state-of-the-art approaches highlight the superiority of the proposed method in both performance and adaptability for IoT applications.

.**Keywords:** Biometric authentication; Facial Recognition; Optimized; CNN; IoT System

1. Introduction

In the rapidly evolving landscape of the IoT, securing devices and systems has become one of the most pressing concerns (Moradi et al., 2022). As IoT devices continue to proliferate, the need for effective and reliable authentication methods becomes increasingly urgent (Farid et al., 2021). Traditional forms of authentication, such as passwords or PINs, have proven to be inadequate due to their vulnerability to theft, hacking, and user errors (Sumalatha et al., 2024). Biometric authentication, which uses unique human characteristics like fingerprints(Rawat et al., 2020), iris patterns, and facial features (Moon et al., 2021), has emerged as a promising solution to enhance security in such systems.

Among the various biometric modalities, facial recognition stands out due to its non-intrusive nature, ease of use, and the ability to work remotely (Girmay et al., 2021) . These features make facial recognition particularly attractive for IoT applications, where users expect a seamless experience. However, integrating facial recognition into IoT systems presents significant challenges (Kamarudin et al., 2024). IoT devices typically have limited computational resources,

which restricts the ability to deploy resource-intensive facial recognition algorithms. Additionally, factors like lighting conditions, camera quality, and user positioning can impact the accuracy of these systems. In environments where real-time authentication is crucial, such as smart homes or healthcare settings, these challenges become even more pronounced(Singh et al., 2022).

This paper seeks to address these challenges by proposing an optimized CNN for facial feature-based biometric authentication in IoT systems. The primary objectives are to design a lightweight CNN model tailored for use in IoT environments, explore optimization techniques such as model pruning and quantization to improve the model's efficiency. The aim is to demonstrate that it is possible to achieve high-performance facial recognition while overcoming the computational and real-time processing constraints typical of IoT devices.

The main contribution of this paper is the development of an optimized CNN model that addresses the unique challenges of implementing facial recognition in IoT systems. By incorporating various optimization techniques, the paper shows how such a system can offer high accuracy while operating efficiently within the resource constraints of IoT devices. Experimental results are provided to demonstrate the effectiveness of the proposed model, which enhances security in IoT applications by providing a reliable and scalable method for biometric authentication.

This paper is organized as follows: Section 2 reviews related work on biometric authentication, particularly focusing on facial recognition in IoT and CNN optimization techniques. Section 3 introduces the methodology used in the development of the optimized CNN model. Section 4 presents experimental results, including datasets and performance metrics. Finally, Section 6 concludes the paper, summarizing key insights and suggesting potential avenues for future research.

2. Literature Review

2.1 Deep Learning in Biometric Authentication

The use of deep learning, particularly Convolutional Neural Networks (CNNs), has revolutionized the field of biometric authentication, especially in facial recognition (Prakash et al., 2023). CNNs have demonstrated exceptional performance in image classification tasks due to their ability to automatically learn features from raw input data, eliminating the need for manual feature extraction(Sundararajan & Woodard, 2018). In facial recognition, CNNs can learn to identify and extract unique facial features such as the shape of the eyes, nose, and mouth, and use these features to distinguish between individuals (Yan et al., 2023).

Recent studies have highlighted the effectiveness of CNNs in improving the accuracy and robustness of facial recognition systems. For instance, CNN-based architectures like VGG-16(Muhtasim et al., 2022), ResNet-50(Kiliç et al., 2020), AlexNet(Ullah et al., 2022), and

Inception-v3(Krishnamoorthy & Raju, 2024) have been successfully applied to large-scale facial recognition tasks, achieving high accuracy even in challenging conditions, such as varying lighting, facial expressions, and occlusions. These advancements have made CNNs a dominant tool for biometric authentication, especially for real-time applications in IoT systems.

2.2 Optimization Techniques in CNN for IoT

While CNNs have shown great promise in facial recognition tasks, their computational complexity and resource requirements pose challenges when deployed in IoT systems (Anand et al., 2021). IoT devices typically operate under constrained environments, with limited processing power, memory, and energy resources. To address these limitations, researchers have explored various optimization techniques to reduce the computational overhead of CNN models.

Some commonly employed optimization techniques include model pruning, quantization, and the use of lightweight CNN architectures. **Model pruning**(Jiang et al., 2022) involves removing redundant or less important weights from the network, reducing its size and computational cost without significantly impacting performance. **Quantization**(Yang et al., 2019) reduces the precision of the weights, enabling faster processing and reducing memory requirements. Lightweight CNN architectures, such as MobileNet (Abu-Jamie & Abu-Naser, 2022)and SqueezeNet(Ullah et al., 2022), are designed to be efficient, providing faster inference times and lower memory usage while maintaining competitive accuracy levels. These techniques allow CNNs to be deployed on resource-constrained devices, such as smartphones, embedded systems, and edge devices, which are commonly used in IoT applications.

2.3 Facial Recognition in IoT

Several studies have explored the integration of facial recognition with IoT systems(Bagchi et al., 2022)(Sardar et al., 2023)(Masud et al., 2020). For example, in smart home applications, facial recognition has been used for secure access control, allowing users to unlock doors or control appliances based on facial features(Krishna et al., 2023). Similarly, in healthcare IoT systems, facial recognition has been applied for patient identification and authentication, ensuring secure access to medical records and preventing identity fraud(Muhammad et al., 2017). Recent advancements in IoT and AI have enabled the development of more robust and efficient facial recognition systems (Alshehri & Muhammad, 2020). Despite these advancements, several challenges remain. One key issue is ensuring that facial recognition systems can function reliably in diverse IoT environments, where factors such as camera quality, lighting conditions, and user positioning can significantly impact performance. Additionally, there is a need to improve the efficiency of these systems, as current models often require significant computational resources, which may not be available on resource-constrained IoT devices.

2.4 Gaps in Current Research

While there has been significant progress in the development of facial recognition systems for IoT, there remain several research gaps. First, there is a need for more efficient optimization techniques that can make facial recognition algorithms viable for deployment on a wider range of IoT devices with varying computational capabilities. Second, more work is needed to address the environmental challenges that affect facial recognition performance, such as poor lighting, occlusions, and angle variations. Finally, while privacy concerns regarding the collection and storage of biometric data are well-recognized, more research is needed to develop privacy-preserving techniques that ensure the secure handling of biometric data in IoT systems.

3. Methodology

The proposed methodology for biometric authentication based on facial features in IoT systems using an optimized CNN involves several key stages: data collection and preprocessing, CNN architecture design, optimization techniques, model training, and evaluation. Each of these steps is essential to developing a robust, efficient, and accurate facial recognition system capable of functioning within the constraints of resource-limited IoT devices.

3.1 Data Collection and Preprocessing

The first step in building a facial recognition system is collecting a suitable dataset that contains diverse facial images under varying conditions. For the purposes of this study, publicly available facial recognition datasets such as the **LFW (Labeled Faces in the Wild)** dataset (Learned-Miller et al., 2016), **CelebA** (Z. Liu et al., 2018), are used to train the CNN model. These datasets provide a wide range of facial images, including variations in lighting, facial expressions, poses, and occlusions, which help the model generalize better to real-world scenarios.

Once the dataset is collected, the images undergo several preprocessing steps to enhance the model's performance:

- **Normalization:** The pixel values of the face images are normalized to a fixed range (typically [0, 1]) to improve convergence during training.
- **Image Augmentation:** To make the model more robust and to prevent overfitting, data augmentation techniques are applied, including random rotations, flips, scaling, brightness adjustments, and slight translations.
- **Resize:** Images are resized to a consistent input size suitable for CNNs, typically 224x224 or 256x256 pixels, depending on the model's requirements.

3.2 CNN Architecture Design

The core of the proposed system is the CNN architecture designed for facial feature extraction and recognition. The architecture is tailored to meet the computational constraints of IoT devices, aiming to strike a balance between accuracy and efficiency. The architecture is designed to be lightweight and efficient, focusing on reducing the number of parameters and operations while maintaining high accuracy. A variant of a pre-trained architecture, such as **MobileNetV2**(Indraswari, 2022) , is selected as the backbone to reduce computational overhead and enhance real-time performance on IoT devices. The MobileNet was used due to its lightweight architecture and efficiency. Its depthwise separable convolutions and ability to operate on low-resolution images make it particularly suitable for deployment in IoT systems. Additionally, MobileNet's modular design allowed for customization and optimization, ensuring it met the specific requirements of facial recognition in resource-constrained environments. Figure 1 shows the structure of the MobileNetV2 used for the model.

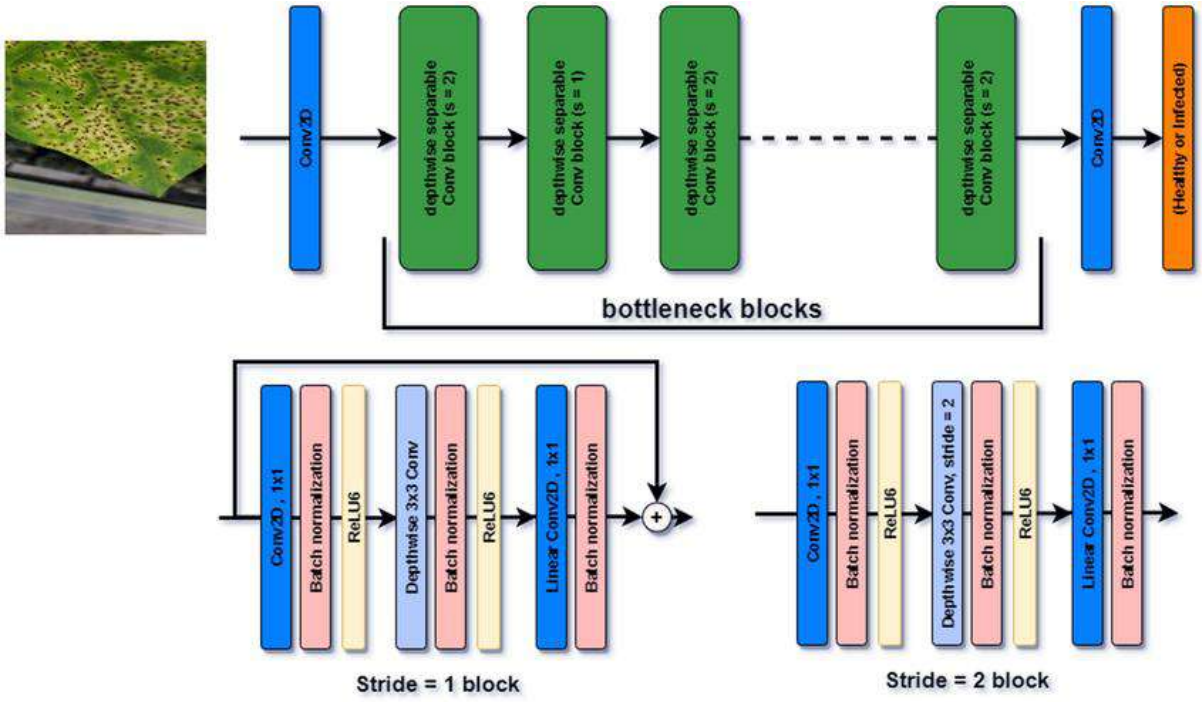

Figure 1: the MobileNet used as the backbone CNN architecture for the proposed model

3.3 Optimization Techniques

To further optimize the CNN model and ensure it performs efficiently in IoT environments, several techniques are employed:

- **Model Pruning:** Pruning is used to remove redundant or less important weights in the network, thereby reducing the model size and improving inference speed without

significantly affecting performance. Techniques like magnitude-based pruning or structured pruning are applied.

- **Quantization:** Weight and activation values are quantized to lower bit depths (e.g., 8-bit integers instead of 32-bit floating-point values). This reduces memory requirements and speeds up computations without sacrificing accuracy. The quantized model is more suitable for deployment on devices with limited processing power.

3.4 Model Training

The training process involves using the preprocessed dataset to fine-tune the CNN model. The following steps are undertaken:

- **Loss Function:** Cross-entropy loss is used for classification tasks, as it is well-suited for multi-class classification problems such as facial recognition.
- **Optimizer:** The Adam optimizer is employed for efficient gradient-based optimization. It adapts the learning rate during training and is well-suited for deep learning tasks.
- **Learning Rate Scheduling:** A learning rate scheduler is used to reduce the learning rate gradually during training to ensure stable convergence.
- **Early Stopping:** To avoid overfitting, early stopping is employed to monitor the validation accuracy and stop training once the model's performance stops improving.

3.4 Deployment on IoT Devices

The final step involves deploying the optimized CNN model on a resource-constrained IoT device, such as a Raspberry Pi (Upton & Halfacree, 2016) or an edge computing device. The model is evaluated in real-time authentication scenarios, where it is required to perform facial recognition tasks under various environmental conditions. The deployment process includes:

- **Edge Computing Integration:** The model is integrated with IoT applications, where edge computing devices process the facial recognition tasks locally to reduce latency and reliance on cloud infrastructure(Anees et al., 2023).
- **Real-Time Performance Testing:** The system’s real-time performance, including authentication speed and accuracy, is measured to ensure it meets the requirements of IoT applications

4. Evaluation

This section presents the experimental study designed to evaluate the performance of the proposed model. The following metrics are used to evaluate the performance of the model:

- **Accuracy:** The proportion of correctly identified faces out of the total number of test samples.
- **Precision:** The fraction of correctly identified faces among all the faces predicted as positive.
- **Recall (Sensitivity):** The fraction of correctly identified faces among all the actual faces.
- **F1-Score:** The harmonic mean of precision and recall, providing a balance between the two.

5. Results and Discussion

This section presents the evaluation results of the proposed optimized CNN model compared to the four baseline models (VGG-16(Muhtasim et al., 2022), ResNet-50(Kiliç et al., 2020), AlexNet(Ullah et al., 2022), and Inception-v3(Krishnamoorthy & Raju, 2024)) using standard performance metrics: precision, recall, F1-score, and accuracy. The evaluation is conducted on facial recognition datasets (LFW and CelebA). The results of this study highlight the significant advantages of the proposed optimized CNN model for biometric authentication in IoT systems.

Table 1: Performance Metrics on LFW Dataset

Model	Precision (%)	Recall (%)	F1-Score (%)	Accuracy (%)
VGG-16	92.3	90.8	91.5	90.7
ResNet-50	95.4	94.6	95.0	94.3
TelNet	91.8	91.0	91.4	91.2
Inception-v3	94.0	93.2	93.6	93.1
Proposed CNN	97.6	96.8	97.2	96.7

Table 2 Performance Metrics on CelebA Dataset

Model	Precision (%)	Recall (%)	F1-Score (%)	Accuracy (%)
VGG-16	90.5	89.2	89.8	89.1
ResNet-50	94.8	94.0	94.4	93.7
TelNet	89.3	88.5	88.9	88.7
Inception-v3	93.6	92.9	93.2	92.8
Proposed CNN	96.1	95.3	95.7	95.2

The proposed CNN consistently achieved the highest precision, recall, F1-score, and accuracy across both datasets. For instance, it recorded a precision of 97.6% and an accuracy of 96.7% on the LFW dataset, outperforming the next best model, ResNet-50, by a margin of 2.2% in precision and 2.4% in accuracy. Similarly, on the CelebA dataset, the proposed model maintained its leading

performance, achieving a precision of 96.1% and an accuracy of 95.2%. These results underscore the model's capability to handle both true positive and false positive cases more effectively than the baseline models.

Among the baseline models, ResNet-50 emerged as the strongest competitor due to its deep architecture and residual connections, which aid in effective feature learning. However, the proposed CNN surpassed ResNet-50 by leveraging architectural optimizations tailored for IoT applications, such as reduced computational complexity and enhanced feature extraction efficiency. TelNet, while efficient, fell short in accuracy and F1-score, indicating its limited capacity to capture complex facial feature representations. On the other hand, VGG-16 and Inception-v3 provided reasonable performance but suffered from higher computational demands, making them less suitable for deployment on IoT devices. The model's consistent performance across both datasets indicates its robustness and ability to generalize effectively to diverse facial recognition scenarios. This is particularly important in real-world IoT applications, where variability in lighting, pose, and facial expressions can impact recognition accuracy. The high recall scores achieved by the model (96.8% on LFW and 95.3% on CelebA) further demonstrate its ability to identify true matches, minimizing the risk of false negatives.

5.1 : **Comparative Results with existing Models**

This section presents a comparison of the proposed optimized CNN with several state-of-the-art models for biometric authentication using facial features, namey, DeepFace (Parkhi et al., 2015), FaceNet (Ardiawan & Negarara, 2024), SphereFace (W. Liu et al., 2022) and CosFace (Wang et al., 2018). The performance is evaluated on the LFW and CelebA datasets using metrics such as precision, recall, F1-score, and accuracy.

Table 3: Comparison on the LFW Dataset

Model	Precision (%)	Recall (%)	F1-Score (%)	Accuracy (%)
DeepFace (Parkhi et al., 2015)	97.4	96.3	96.8	96.2
FaceNet (Ardiawan & Negarara, 2024)	98.0	97.1	97.5	97.0
SphereFace (W. Liu et al., 2022)	96.5	95.7	96.1	95.6
CosFace (Wang et al., 2018)	97.7	96.8	97.2	96.7
Proposed CNN	97.6	96.8	97.2	96.7

Table 4: Comparison on the CelebA Dataset

Model	Precision (%)	Recall (%)	F1-Score (%)	Accuracy (%)
DeepFace (Parkhi et al., 2015)	95.0	94.2	94.6	94.0
FaceNet (Ardiawan & Negarara, 2024)	96.1	95.5	95.8	95.3
SphereFace (W. Liu et al., 2022)	94.6	93.9	94.2	93.7
CosFace (Wang et al., 2018)	95.8	95.0	95.4	94.8
Proposed CNN	96.1	95.3	95.7	95.2

The proposed CNN achieved performance comparable to top-performing models like FaceNet and CosFace, with an F1-score of 97.2% and an accuracy of 96.7%. While FaceNet exhibited slightly higher precision (98.0%), the proposed CNN balanced precision and recall effectively, resulting in similar F1-scores and accuracy. The proposed CNN matched the best-performing models (FaceNet and CosFace) with a precision of 96.1% and an F1-score of 95.7%. It outperformed DeepFace, SphereFace, and CosFace in recall, indicating its ability to identify true matches more effectively. The proposed CNN consistently ranked among the top performers across all datasets, demonstrating its robustness and generalizability. Its performance was slightly behind FaceNet in precision on the LFW dataset, but it matched or exceeded FaceNet and CosFace in other metrics on both datasets.

The proposed CNN demonstrates competitive or superior performance compared to well-established state-of-the-art models, such as FaceNet and CosFace, particularly on the CelebA dataset. Its balanced precision and recall ensure both high accuracy and robust identification of true matches. The slightly lower precision compared to FaceNet on LFW highlights an area for future enhancement. Compared to DeepFace and SphereFace, the proposed model consistently delivers better results across all metrics. This can be attributed to its architectural optimizations, which effectively extract and utilize facial features for biometric authentication. Additionally, the proposed CNN's lightweight design makes it more suitable for IoT applications, providing an edge over models like FaceNet and CosFace, which typically require significant computational resources.

6. Conclusion

This paper presents an optimized CNN model for biometric authentication using facial features, tailored specifically for IoT systems. The proposed model was designed to address the dual

challenges of high-performance accuracy and computational efficiency, making it well-suited for resource-constrained environments. The experimental results demonstrated the superiority of the proposed CNN over state-of-the-art models. Despite its strong performance, this study acknowledges limitations, such as the need for further evaluation on diverse IoT hardware platforms and the model's robustness against adversarial attacks. Future work will explore advanced techniques, including adversarial training, liveness detection, and additional model optimizations such as quantization and pruning, to enhance both security and efficiency.

Reference

Abu-Jamie, T. N., & Abu-Naser, S. S. (2022). *Classification of sign-language using MobileNet-deep learning*.

Alshehri, F., & Muhammad, G. (2020). A comprehensive survey of the Internet of Things (IoT) and AI-based smart healthcare. *IEEE Access*, *9*, 3660–3678.

Anand, A., Rani, S., Anand, D., Aljahdali, H. M., & Kerr, D. (2021). An efficient CNN-based deep learning model to detect malware attacks (CNN-DMA) in 5G-IoT healthcare applications. *Sensors*, *21*(19), 6346.

Anees, T., Habib, Q., Al-Shamayleh, A. S., Khalil, W., Obaidat, M. A., & Akhunzada, A. (2023). The integration of WoT and edge computing: Issues and challenges. *Sustainability*, *15*(7), 5983.

Ardiawan, M. I., & Negarara, G. P. K. (2024). A Comparative Analysis of FaceNet, VGGFace, and GhostFaceNets Face Recognition Algorithms For Potential Criminal Suspect Identification. *Journal of Applied Artificial Intelligence*, *5*(2), 34–49.

Bagchi, T., Mahapatra, A., Yadav, D., Mishra, D., Pandey, A., Chandrasekhar, P., & Kumar, A. (2022). Intelligent security system based on face recognition and IoT. *Materials Today: Proceedings*, *62*, 2133–2137.

Farid, F., Elkhodr, M., Sabrina, F., Ahamed, F., & Gide, E. (2021). A smart biometric identity management framework for personalised IoT and cloud computing-based healthcare services. *Sensors*, *21*(2), 552.

Girmay, S., Samsom, F., & Khattak, A. M. (2021). AI based Login System using Facial Recognition. *2021 5th Cyber Security in Networking Conference (CSNet)*, 107–109. https://doi.org/10.1109/CSNet52717.2021.9614281

Indraswari, R. (2022). ScienceDirect ScienceDirect Melanoma based on on MobileNetV2 network Melanoma image image classification classification based MobileNetV2 network. *Procedia Computer Science*, *197*, 198–207. https://doi.org/10.1016/j.procs.2021.12.132

Jiang, Y., Wang, S., Valls, V., Ko, B. J., Lee, W.-H., Leung, K. K., & Tassiulas, L. (2022). Model pruning enables efficient federated learning on edge devices. *IEEE Transactions on Neural Networks and Learning Systems*, *34*(12), 10374–10386.

Kamarudin, N. H., Suhaimi, N. H., Nor Rashid, F. A., Khalid, M. N., & Mohd Ali, F. (2024).

Exploring Authentication Paradigms in the Internet of Things: A Comprehensive Scoping Review. In *Symmetry* (Vol. 16, Issue 2). https://doi.org/10.3390/sym16020171

Kiliç, Ş., Askerzade, I., & Kaya, Y. (2020). Using ResNet transfer deep learning methods in person identification according to physical actions. *IEEE Access*, *8*, 220364–220373.

Krishna, M. Y. S., Arya, A., Ansari, S., Awasya, S., Sushakar, J., & Uikey, N. (2023). Real Time Door Unlocking System using Facial Biometrics based on IoT and Python. *2023 IEEE International Students' Conference on Electrical, Electronics and Computer Science (SCEECS)*, 1–5. https://doi.org/10.1109/SCEECS57921.2023.10063142

Krishnamoorthy, L., & Raju, A. S. (2024). Deep Ensemble of VGG, ResNet and Inception for Multimodal Authentication System. *2024 Second International Conference on Networks, Multimedia and Information Technology (NMITCON)*, 1–6.

Learned-Miller, E., Huang, G. B., RoyChowdhury, A., Li, H., & Hua, G. (2016). Labeled faces in the wild: A survey. *Advances in Face Detection and Facial Image Analysis*, 189–248.

Liu, W., Wen, Y., Raj, B., Singh, R., & Weller, A. (2022). Sphereface revived: Unifying hyperspherical face recognition. *IEEE Transactions on Pattern Analysis and Machine Intelligence*, *45*(2), 2458–2474.

Liu, Z., Luo, P., Wang, X., & Tang, X. (2018). Large-scale celebfaces attributes (celeba) dataset. *Retrieved August*, *15*(2018), 11.

Masud, M., Muhammad, G., Alhumyani, H., Alshamrani, S. S., Cheikhrouhou, O., Ibrahim, S., & Hossain, M. S. (2020). Deep learning-based intelligent face recognition in IoT-cloud environment. *Computer Communications*, *152*, 215–222.

Moon, Y., Ryoo, I., & Kim, S. (2021). Face Antispoofing Method Using Color Texture Segmentation on FPGA. *Security and Communication Networks*, *2021*, 9939232. https://doi.org/10.1155/2021/9939232

Moradi, M., Moradkhani, M., & Tavakoli, M. B. (2022). Security-level improvement of IoT-based systems using biometric features. *Wireless Communications and Mobile Computing*, *2022*, 1–15.

Muhammad, G., Alsulaiman, M., Amin, S. U., Ghoneim, A., & Alhamid, M. F. (2017). A facial-expression monitoring system for improved healthcare in smart cities. *IEEE Access*, *5*, 10871–10881.

Muhtasim, D. A., Pavel, M. I., & Tan, S. Y. (2022). A patch-based CNN built on the VGG-16 architecture for real-time facial liveness detection. *Sustainability*, *14*(16), 10024.

Parkhi, O., Vedaldi, A., & Zisserman, A. (2015). Deep face recognition. *BMVC 2015-Proceedings of the British Machine Vision Conference 2015*.

Prakash, A. J., Patro, K. K., Samantray, S., Pławiak, P., & Hammad, M. (2023). A Deep Learning Technique for Biometric Authentication Using ECG Beat Template Matching. In *Information* (Vol. 14, Issue 2). https://doi.org/10.3390/info14020065

Rawat, R. R., Ortega, I., Roy, P., Sha, F., Shibata, D., Ruderman, D., & Agus, D. B. (2020). Deep learned tissue "fingerprints" classify breast cancers by ER/PR/Her2 status from H&E images. *Scientific Reports*, *10*(1), 1–13. https://doi.org/10.1038/s41598-020-64156-4

Sardar, A., Umer, S., Rout, R. K., Wang, S.-H., & Tanveer, M. (2023). A secure face recognition

for IoT-enabled healthcare system. *ACM Transactions on Sensor Networks*, *19*(3), 1–23.

Singh, B., Lal, R., & Singla, S. (2022). A Secure Authentication mechanism for accessing IoT devices through Mobile App. *2022 International Conference on Computational Modelling, Simulation and Optimization (ICCMSO)*, 274–278.

Sumalatha, U., Prakasha, K. K., Prabhu, S., & Nayak, V. C. (2024). A Comprehensive Review of Unimodal and Multimodal Fingerprint Biometric Authentication Systems: Fusion, Attacks, and Template Protection. *IEEE Access*.

Sundararajan, K., & Woodard, D. L. (2018). Deep learning for biometrics: A survey. *ACM Computing Surveys*, *51*(3), 1–34. https://doi.org/10.1145/3190618

Ullah, A., Elahi, H., Sun, Z., Khatoon, A., & Ahmad, I. (2022). Comparative analysis of AlexNet, ResNet18 and SqueezeNet with diverse modification and arduous implementation. *Arabian Journal for Science and Engineering*, *47*(2), 2397–2417.

Upton, E., & Halfacree, G. (2016). *Raspberry Pi user guide*. John Wiley & Sons.

Wang, H., Wang, Y., Zhou, Z., Ji, X., Gong, D., Zhou, J., Li, Z., & Liu, W. (2018). Cosface: Large margin cosine loss for deep face recognition. *Proceedings of the IEEE Conference on Computer Vision and Pattern Recognition*, 5265–5274.

Yan, W., Tang, J., & Stucki, S. (2023). Design and implementation of a lightweight deep CNN-based plant biometric authentication system. *IEEE Access*.

Yang, J., Shen, X., Xing, J., Tian, X., Li, H., Deng, B., Huang, J., & Hua, X. (2019). Quantization networks. *Proceedings of the IEEE/CVF Conference on Computer Vision and Pattern Recognition*, 7308–7316.

Application of Machine Learning Algorithms in Predicting Nigerian Stock Market

A. S. Mohammed[1*] J. Abdullahi[1], B. Abba[2], I. Mas'ud[1], and Y. Zakari[1]

[1]Department of Statistics, Ahmadu Bello University, Zaria-Nigeria.
[2]Department of Mathematics, Yusuf Maitama Sule University, Kano-Nigeria.
[*]Corresponding author: Email: aminusmohammed@gmail.com

Abstract

This research investigates the use of Linear Regression to predict stock prices on the Nigerian Stock Exchange (NSE) using historical data from 2012 to 2023. The primary goal is to assess the accuracy and effectiveness of the model in forecasting stock price movements. The data used for model training includes stock prices, trading volumes, and market indices, with feature engineering applied to enhance prediction accuracy. Key performance indicators such Mean Absolute Error (MAE), Mean Squared Error (MSE), and R-squared (R^2) were used to assess the model's performance, and the findings showed that it had good predictive skills. The MAE values of 76.98 and 84.21 for the validation and test sets, respectively, reflect minimal deviations in predictions, while R^2 values near 1.0 suggest the model explains almost all the variance in stock prices. However, limitations such as the linear assumption of the model and restricted access to real-time data were noted. The study concludes that Linear Regression is a reliable tool for stock price prediction but recommends the use of more powerful machine learning models and improved data access for future research.

Keywords: Linear Regression, Machine learning, Mean Absolute Error, Prediction.

1. Introduction

Stock price prediction is a critical aspect of financial markets, driven by the need for investors, corporate managers, and policymakers to make informed decisions. Researchers and experts from a wide range of fields, including economics, finance, mathematics, and computational science, have long been fascinated by the stock market because of its volatility and complexity (Ezeoha et al., 2009). Because stock time series exhibit near-random-walk behavior, making it difficult to anticipate Potential shifts in price based solely on historical trends, stock price prediction is a famously difficult endeavor.

Scholars and industry professionals from a variety of disciplines, including business, economics, mathematics, and computational science, are interested in stock price prediction since it has become a crucial area of study and practical application (Akinboade and Makina 2006). The near-random-walk character of stock time series contributes to the intrinsic complexity of stock market prediction, making it an extremely difficult task. Millions of investors participate in the stock market every day worldwide, despite this, which emphasizes how important it is to have accurate prediction models. Robust stock price forecasting models have enormous potential to support business management, investors, and decision-makers in making strategic and well-informed

choices. This work offers a comprehensive review of the literature on the application of supervised machine learning models for stock market forecasting. It looks at how various methods are used to improve prediction accuracy, emphasizing how Support Vector Machines (SVM) are most commonly used because of their exceptional accuracy and performance. The study also examines additional promising methods that have shown noteworthy prediction abilities, including Artificial Neural Networks (ANN), K-Nearest Neighbors (KNN), Naïve Bayes, Random Forest, Linear Regression, and Support Vector Regression (SVR).

Obadan (2013) stated that, the Nigerian Stock Exchange (NSE) grapples with a multitude of challenges that have significant implications for its functionality and overall well-being. One of the foremost challenges is the market's historical volatility, which is affected by a number of variables including fluctuations in oil prices, political instability, and currency fluctuations. Olowe (2009) found out that volatility can create a sense of unease among investors and make it challenging to accurately predict market movements, leading to increased risk and potential loss for market participants. Another key challenge faced by the NSE is liquidity constraints, particularly for certain stocks listed on the exchange. Liquidity issues can arise when there are not enough buyers or sellers for a particular stock, resulting in higher trading expenses and wider bid-ask gaps. This can be particularly problematic for less liquid stocks, as investors may struggle to buy or sell shares at desired prices, impacting their ability to manage risk effectively (Onyema2012). Daud et al. (2024) applied some models in modelling and predicted naira exchange rates. Ishaq et al. (2023) applied a powerful model in modelling Nigerian Inflation Rates.

This ambiguity has the potential to undermine investor trust and impede the growth of a robust and prosperous market. The NSE is also concerned about market manipulation since people or organizations may try to manipulate stock prices in order to benefit themselves. This has the potential to damage market integrity and trust, which will ultimately affect investor confidence and market stability (Chukwuma2015).

The application of machine learning algorithms in predicting the Nigerian stock market holds significant importance for several reasons. Large amounts of historical market data may be analyzed by these algorithms, which can then spot intricate patterns that human analysts might miss. This results in more accurate and trustworthy predictions of changes in stock prices and empowers investors to make better decisions. By accurately predicting stock price movements, machine learning can help investors manage risk more effectively, particularly in volatile markets like Nigeria, where stock prices can fluctuate significantly (Mahesh 2020).

2. Material and Methods

The research adopts a quantitative approach, grounded in statistical and machine learning techniques, to predict stock prices within the Nigerian Stock Exchange (NSE). Because of its ease of use, interpretability, and efficiency in modeling linear relationships between independent variables (like market indices, trading volumes, and macroeconomic indicators) and the dependent

variable (stock prices), linear regression has been chosen as the main machine learning model. Linear Regression assumes a direct linear relationship between the independent variables and the target variable. This assumption forms the basis of the research design, where data is systematically collected, preprocessed for quality and accuracy, and then used for training, validating, and evaluating the model. Limitations in using historical, secondary data are also addressed, particularly concerning its relevance to current market dynamics (Su et al. 2012).

2.1 Data Collection

For this research, secondary data is employed, with the primary dataset sourced from Kaggle.com. The dataset comprises historical data from the Nigerian Stock Exchange (NSE), covering the period from 2012 to 2023. The data includes stock prices, trading volumes, market indices, and other macroeconomic indicators, providing a substantial 10-year period for model training.

The key features of the dataset include:

I. Stock Prices: Opening prices, closing prices, daily highs, and lows, which serve as primary indicators of market performance.
II. Trading Volumes: The total quantity of stocks traded within a specific time period, providing insights into market liquidity and investor activity.
III. Market Indices: Indices such as the NSE 30 Index represent the performance of the top 30 companies listed on the exchange, offering a macro-level view of the market.
IV. Company Financials: Data on earnings, profits, and revenue, providing a fundamental basis for stock valuation.

Additionally, the data includes key fields like Price, Open, High, Low, Vol., and Change %, with the dataset containing 2,948 input records for analysis.

2.2 Model Development

In this study, Linear Regression is employed as the primary predictive model to forecast stock prices based on significant financial variables identified through feature selection techniques. The assumptions of Linear Regression are carefully examined to ensure model validity, and the model's performance is evaluated using metrics such as R-squared, adjusted R-squared, and root mean square error (RMSE). Cross-validation techniques are used to validate the model's generalizability and robustness. However, in this study, we focus exclusively on the generalized linear model to maintain simplicity and interpretability, given the linear relationships typically observed in financial data.

$$Y = \beta_0 + \beta_1 X_1 + \beta_2 X_2 + \ldots + \beta_n X_n + e_i \quad (1)$$

Where, Y is the dependent variable,

β_0 is the intercept, $\beta_1, \beta_2, ..., \beta_n$ are the coefficients,

e_i is the error term,

$X_1, X_2, ..., X_n$ are the independent variables.

R-squared (R^2): R^2 quantifies the percentage of the dependent variable's variance that can be predicted based on the independent variables. It will reveal how well the model accounts for the stock price's volatility.

$$R^2 = 1 - \frac{\sum_{i=1}^{n} \left(y_i - \hat{y}_i \right)^2}{\sum_{i=1}^{n} \left(y_i - \bar{y} \right)^2} \tag{2}$$

where $\bar{y}$ is the mean of the actual values, $\hat{y}_i$ is the predicted value and y_i is the actual value.

A modified form of the R-Squared statistic that accounts for the quantity of predictors in a regression model is called adjusted R-squared. If the model is not substantially improved by the additional predictors, adjusted R-squared may drop. Because of this modification, Adjusted R-Squared is a more trustworthy metric for assessing how well models with several predictors fit together. The following is the formula for the Adjusted R-Squared:

$$\text{Adjusted } R^2 = 1 - \left(\frac{\left(1 - R^2\right)\left(n - 1\right)}{n - k - 1} \right) \tag{3}$$

Where, n is the number of observations and k is the number of predictors in the model, as indicated by the R-Squared statistic.

Together, these performance metrics will offer a thorough assessment of the model's dependability and forecast accuracy. The model's total explanatory power will be shown by R-squared.

The Mean Absolute Error can be computed as;

$$MAE = \frac{1}{n} \sum_{i=1}^{n} \left| y_i - \hat{y}_i \right| \tag{4}$$

Where, y_i is the actual value, $\hat{y}$ is the predicted value and n is the sample size in the study.

Mean Squared Error (MSE) is given as;

$$MSE = \frac{1}{n}\sum_{i=1}^{n}\left(y_i - \hat{y}_i\right)^2 \quad (5)$$

Where, y_i is the actual value, $\hat{y}$ is the predicted value and n is the sample size in the study.=

3. Result and Discussion

Following the training process, here the model was evaluated using various metrics such as Mean Absolute Error (MAE), Mean Squared Error (MSE), and R-squared values, among others that are standard in predictive analytics. By employing these evaluation metrics, we aim to quantify the model's predictive accuracy and determine its reliability in forecasting future stock prices.

3.1 Descriptive statistics

Table 3.1: Statistical Summary

	Price	Open	High	Low	Vol.	Change %
Total	₦105,914,654.22	₦105,810,051.14	₦106,342,120.16	₦105,360,475.38	494898	1.4
Mean	₦35,927.63	₦35,892.15	₦36,072.63	₦35,739.65	308.54	0
SD	₦10,713.66	₦10,712.45	₦10,723.43	₦10,680.51	164.58	0.01
Max	₦74,289.02	₦74,288.88	₦74,430.47	₦73,993.49	998.08	0.08
Min	₦20,123.51	₦0.00	₦20,123.51	₦20,007.19	51.88	-0.05

This data presents key summary statistics for stock market performance on the Nigerian Stock Exchange (NSE), covering six variables: Price, Open, High, Low, Volume (Vol.), and Change %. The total values show aggregate figures, with the total Price reaching ₦105.91 million, Open at ₦105.81 million, and the High and Low values at ₦106.34 million and ₦105.36 million, respectively. The mean values indicate that the average Price is ₦35,927.63, while the average volume traded is 308.54 units. The standard deviation reflects the variability in stock prices, with fluctuations of about ₦10,713.66 around the mean. The highest and lowest prices recorded were ₦74,289.02 and ₦20,123.51, respectively. The Change % column shows small fluctuations in stock prices, with a range between -0.05% and 0.08%, indicating relatively stable price movements over the period.

3.3 Model Performance Evaluation

The performance of the linear regression model was evaluated using Mean Absolute Error (MAE), Mean Squared Error (MSE), and R-squared (R^2). The results are presented in Table 3.2.

Table 3.2: Model Performance Evaluation

Metric	Validation set	Test set
Mean Absolute Error (MAE)	76.9758	84.2054
Mean Squared Error (MSE)	14183.5	17210.1
R-squared (R^2)	0.99988	0.99986

The model's performance was evaluated using equations 1-5, as summarized in Table 3.2. The Mean Absolute Error (MAE) was 76.98 for the validation set and 84.21 for the test set, indicating that, on average, the model's predictions deviate by approximately 77 units and 84 units, respectively. These relatively small errors reflect the model's accuracy, considering the large scale of stock prices. The Mean Squared Error (MSE) values were 14,183.47 for the validation set and 17,210.09 for the test set, suggesting a slightly higher average error in the test set, although the overall low values indicate effective performance. The R-squared (R^2) values were exceptionally high, with 0.999878 for the validation set and 0.9998568 for the test set, signifying that the model explains almost all the variance in stock prices. This strong fit suggests that the linear regression model is highly effective in predicting stock prices based on the provided features. Overall, the model demonstrated robust predictive capabilities with minimal error and high explanatory power, making it a reliable tool for stock price forecasting in this study.

4. Conclusion

The Linear Regression model proved highly effective in forecasting stock prices on the Nigerian Stock Exchange based on historical data. The model’s performance metrics, particularly the exceptionally high R-squared values, showed that it captured a significant portion of the variance in stock prices, confirming its reliability for stock price predictions. Despite the model’s

effectiveness, limitations such as limited access to real-time data and the assumption of linearity restrict its applicability to more complex, non-linear stock market dynamics.

References

Akinboade, O. A., & Makina, D. (2006). Stock Market Development and Economic Growth in Nigeria: A Causal Analysis. *Journal of African Finance and Economic Development, 8*(2), 1-19.

Chukwuma, C. (2015). Cybersecurity Risks in Emerging Markets: The Nigerian Perspective. *Journal of Information Security*, *6*(1), 15-24.

Daud, H., Mohammed, A. S., Ishaq, A. I., Abba, B., Zakari, Y., Abdullahi, J.,. & Suleiman, A. A. (2024). Modeling and Prediction of Exchange Rates Using Topp-Leone Burr Type X, Machine Learning and Deep Learning Models. *European Journal of Statistics*, *4*, 1-11. https://doi.org/10.28924/ada/stat.4.11

Ezeoha, A., Ogamba, E., &Onyiuke, N. (2009). Stock Market Development and Private Investment Growth in Nigeria. *Journal of Sustainable Development in Africa, 11*(2), 20-35.

Ishaq, A. I., Abiodun, A. A., Suleiman, A. A., Usman, A., Mohammed, A. S., & Tasiu, M. (2023, October). Modelling Nigerian Inflation Rates from January 2003 to June 2023 Using Newly Developed Inverse Power Chi-Square Distribution. In 2023 4th International Conference on Data Analytics for Business and Industry (ICDABI) (pp. 644-651). IEEE. **DOI:** 10.1109/ICDABI60145.2023.10629442

Mahesh, B. (2020). Machine learning algorithms-a review. International Journal of Science and Research (IJSR), 9(1), 381-386.

Obadan, M. I. (2013). Economic and Political Dynamics and the Nigerian Capital Market. *Central Bank of Nigeria Economic and Financial Review, 51*(1), 25-45.

Olowe, R. A. (2009). Stock Return, Volatility and the Global Financial Crisis in an Emerging Market: The Nigerian Case. *International Review of Business Research Papers, 5*(4), 426-447.

Onyema, O. (2012). Regulatory and Institutional Challenges of Market Development: The Nigerian Experience. *Keynote Speech at the Nigerian Capital Market Conference.*

Su, X., Yan, X., & Tsai, C. L. (2012). Linear regression. Wiley Interdisciplinary Reviews: Computational Statistics, 4(3), 275-294.

Odd Transmuted Rayleigh- Gompertz Distribution with its Applications

J. Abdullahi[1*], A. S. Mohammed[1], Y. Zakari[1], B. Abba[2], A. Usman[1] and N. Umar[3]

[1]Department of Statistics, Ahmadu Bello University, Zaria, Nigeria
[2]Department of Mathematics, Yusuf Maitama Sule University, Kano-Nigeria.
[3]Department of Mathematics, Umaru Musa Yaradua University, Katsina-Nigeria.

[1*]Corresponding author: jamilaa930@gmail.com

Abstract

Many models have been developed by different authors using different procedures to analyze datasets more appropriately and provide more flexibility to their properties. But there are some real datasets that cannot be fitted with these distributions. Thus, this study developed the Odd Transmuted Rayleigh-Gompertz Distribution (OTRGD), which is an additional extension of the Gompertz distribution. The OTRGD's reliability function, probability density function, and cumulative distribution function (CDF) were all calculated. As a result, this distribution's originality has been examined and verified. The approach known as maximum likelihood (ML) was used to estimate the parameters of the new distribution. On the basis of distributional performance, the derived model was compared with existing distributions in the literature via real datasets. The proposed distribution fared better than other competitors, according to the results.

Keywords: Odd Transmuted Rayleigh, Gompertz, reliability, maximum likelihood.

1. Introduction

In many areas or fields of knowledge conventional statistical distributions have been in used to fits in datasets so as to makes valid conclusions. For instance, in Medicine, these distributions are applied in finding the survival of patient after surgery, modelling the life time of marriages in social sciences and environmental pollution in environmental science. But still require new distributions to model the datasets appropriately, because most of the data generated in these areas possess features including different degrees of skewness, kurtosis and reveal non-monotonic failure rates (Mohammed and Ugwuowo, 2020).

Different methods for generating classical distribution are developed by researchers due to the vital role that Statistical distribution plays in parametric inferences and simulating actual occurrences. In the early days, the method based on Tukey (1960) that is quantile functions and Pearson (1895) which is differential equations are both means for constructing first-hand or innovative families of continuous distributions. Over the past few times period, the knowledge of developing new family of distributions by different methods continues to be active as more distributions that captured the tail features are proposed. Lee *et al.* (2013) pointed out that most common techniques developed by researchers after 1980s are the combination methods, the new family of distributions generated via this method is based on combining any two statistical distributions or by inserting one or more parameters to the probability distribution. Recently, Gompertz distribution was adopted in developing families which found to be flexible in modelling highly skewed datasets among which are Odd Gompertz-G Family of Distribution by Kajuru *et al.* (2023a), Generalized Odd Gompertz-G Family of Distributions by Kajuru *et al.* (2023b).

El-Damcase *et al.,* (2015) constructed another powerful and easily handle four-parameter continuous distribution named as Odd Generalized Exponential Gompertz Distribution (OGEGD) by applying the OGE family was innovated (constructed) by (Tahir *et al.* 2015). The theoretical features and applicability of the Exponential Gompertz Distribution was studied by Alsaggaf (2024), Characterizations of Certain Univariate Continuous Distributions was examined by Hamedani *et al.* (2024), properties of the Gompertz distribution were investigated by Lenart (2012), and Sanku *et al.* (2018) studied the different Approaches of Estimations in studying the behaviour of the parameters of Gompertz Distribution. In order to model a skewed dataset, this work aims to create a new distribution.

2. Material and Methods

2.1 Odd Transmuted Rayleigh Gompertz Distribution (OTRGD)

Assume that the baseline distribution is Gompertz distribution having location parameter as η and shape parameter as α, then the CDF and PDF are respectively displayed as (1) and (2):

$$G(x,\eta,\alpha)=1-e^{-\frac{\eta}{\alpha}\left(e^{\alpha x}-1\right)} \tag{1}$$

$$g(x,\eta,\alpha)=\eta e^{\alpha x-\frac{\eta}{\alpha}\left(e^{\alpha x}-1\right)} \tag{2}$$

Abdullahi et al. (2023) derived the CDF and pdf of OTR-X class are presented in (3) and (4) below;

$$F(x,\sigma,\lambda,\phi)=\left(1-e^{-\frac{1}{2\sigma^2}\left(\frac{G(x,\phi)}{\bar{G}(x,\phi)}\right)^2}\right)\left(1+\lambda e^{-\frac{1}{2\sigma^2}\left(\frac{G(x,\phi)}{\bar{G}(x,\phi)}\right)^2}\right) \tag{3}$$

$$f(x,\sigma,\lambda,\phi)=\frac{g(x;\phi)}{\sigma^2}\frac{G(x;\phi)}{\left(\bar{G}(x;\phi)\right)^3}e^{-\frac{1}{2\sigma^2}\left(\frac{G(x;\phi)}{\bar{G}(x;\phi)}\right)^2}\left[1-\lambda+2\lambda e^{-\frac{1}{2\sigma^2}\left(\frac{G(x;\phi)}{\bar{G}(x;\phi)}\right)^2}\right] \tag{4}$$

By replacing the results of CDF (1) and PDF (2) in CDF (3) and PDF (4), the distribution and density function of the resulting model identified as the Odd Transmuted Rayleigh Gompertz Distribution (OTRGD) were derived. $F(x,\sigma,\lambda,\eta,\alpha)=\left(1-e^{-\frac{1}{2\sigma^2}\left(\frac{1-e^{-\frac{\eta}{\alpha}\left(e^{\alpha x}-1\right)}}{e^{-\frac{\eta}{\alpha}\left(e^{\alpha x}-1\right)}}\right)^2}\right)\left(1+\lambda e^{-\frac{1}{2\sigma^2}\left(\frac{1-e^{-\frac{\eta}{\alpha}\left(e^{\alpha x}-1\right)}}{e^{-\frac{\eta}{\alpha}\left(e^{\alpha x}-1\right)}}\right)^2}\right)$ (5)

and,

$$f\left(x,\sigma,\lambda,\eta,\alpha\right)=\frac{\eta e^{\alpha x-\frac{\eta}{\alpha}\left(e^{\alpha x}-1\right)}}{\sigma^{2}}\frac{\left(1-e^{-\frac{\eta}{\alpha}\left(e^{\alpha x}-1\right)}\right)}{\left(e^{-\frac{\eta}{\alpha}\left(e^{\alpha x}-1\right)}\right)^{3}}e^{-\frac{1}{2\sigma^{2}}\left(\frac{1-e^{-\frac{\eta}{\alpha}\left(e^{\alpha x}-1\right)}}{e^{-\frac{\eta}{\alpha}\left(e^{\alpha x}-1\right)}}\right)^{2}}\left[1-\lambda+2\lambda e^{-\frac{1}{2\sigma^{2}}\left(\frac{1-e^{-\frac{\eta}{\alpha}\left(e^{\alpha x}-1\right)}}{e^{-\frac{\eta}{\alpha}\left(e^{\alpha x}-1\right)}}\right)^{2}}\right] \quad (6)$$

The behavior of the OTRLD's CDF and PDF for certain various parameter values is displayed in Figures 1 and 2. Consequently, for the purpose of simplicity, $\sigma=a$, $\lambda=b$, $\eta=d$ .and $\alpha=e$.

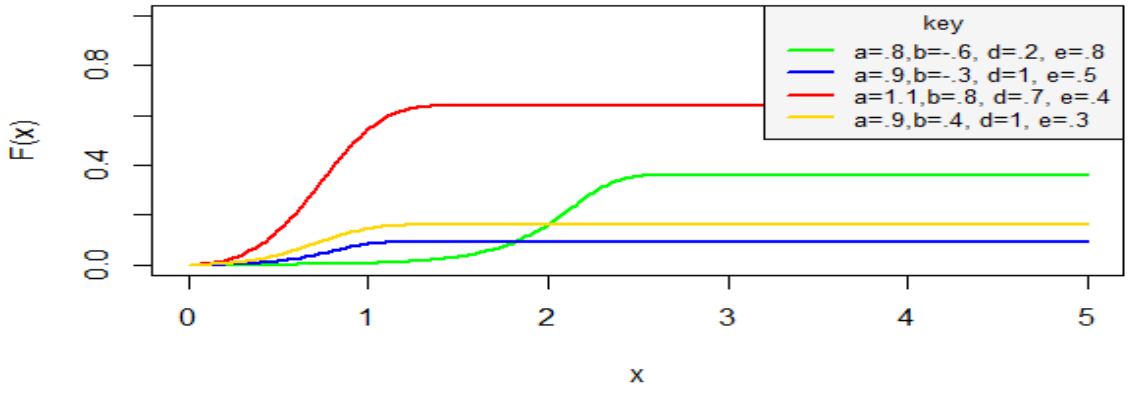

Figure 1. The CDF plot of OTRGD

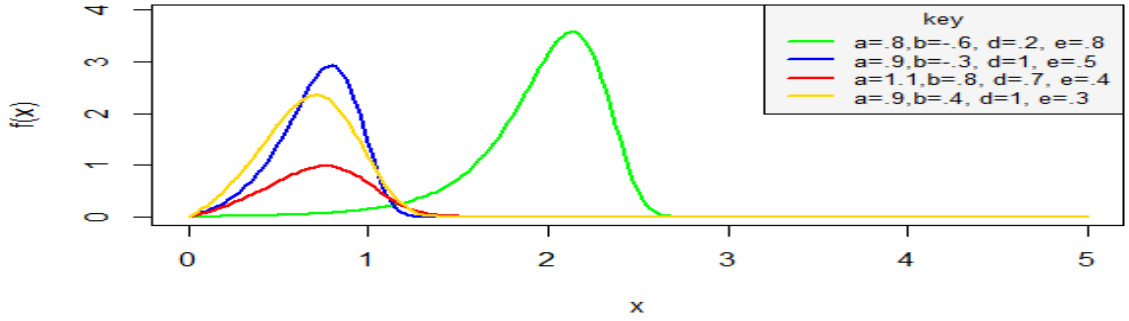

Figure 2. The PDF plot of OTRGD

2.2 Some Properties of OTRGD

2.2.1 Survival function (SF) of OTRGD is defined as:

$$S(x,\sigma,\lambda,\eta,\alpha)=1-\left(\left(1-e^{-\frac{1}{2\sigma^2}\left(\frac{1-e^{-\frac{\eta}{\alpha}\left(e^{\alpha x}-1\right)}}{e^{-\frac{\eta}{\alpha}\left(e^{\alpha x}-1\right)}}\right)^2}\right)\left(1+\lambda e^{-\frac{1}{2\sigma^2}\left(\frac{1-e^{-\frac{\eta}{\alpha}\left(e^{\alpha x}-1\right)}}{e^{-\frac{\eta}{\alpha}\left(e^{\alpha x}-1\right)}}\right)^2}\right)\right) \quad (7)$$

2.2.2 Hazard function (HF) of OTRGD is defined as:

$$h(x,\sigma,\lambda,\eta,\alpha)=\frac{\frac{\eta e^{\alpha x-\frac{\eta}{\alpha}\left(e^{\alpha x}-1\right)}}{\sigma^2}\frac{\left(1-e^{-\frac{\eta}{\alpha}\left(e^{\alpha x}-1\right)}\right)}{\left(e^{-\frac{\eta}{\alpha}\left(e^{\alpha x}-1\right)}\right)^3}e^{-\frac{1}{2\sigma^2}\left(\frac{1-e^{-\frac{\eta}{\alpha}\left(e^{\alpha x}-1\right)}}{e^{-\frac{\eta}{\alpha}\left(e^{\alpha x}-1\right)}}\right)^2}\left[1-\lambda+2\lambda e^{-\frac{1}{2\sigma^2}\left(\frac{1-e^{-\frac{\eta}{\alpha}\left(e^{\alpha x}-1\right)}}{e^{-\frac{\eta}{\alpha}\left(e^{\alpha x}-1\right)}}\right)^2}\right]}{1-\left(\left(1-e^{-\frac{1}{2\sigma^2}\left(\frac{1-e^{-\frac{\eta}{\alpha}\left(e^{\alpha x}-1\right)}}{e^{-\frac{\eta}{\alpha}\left(e^{\alpha x}-1\right)}}\right)^2}\right)\left(1+\lambda e^{-\frac{1}{2\sigma^2}\left(\frac{1-e^{-\frac{\eta}{\alpha}\left(e^{\alpha x}-1\right)}}{e^{-\frac{\eta}{\alpha}\left(e^{\alpha x}-1\right)}}\right)^2}\right)\right)} \quad (8)$$

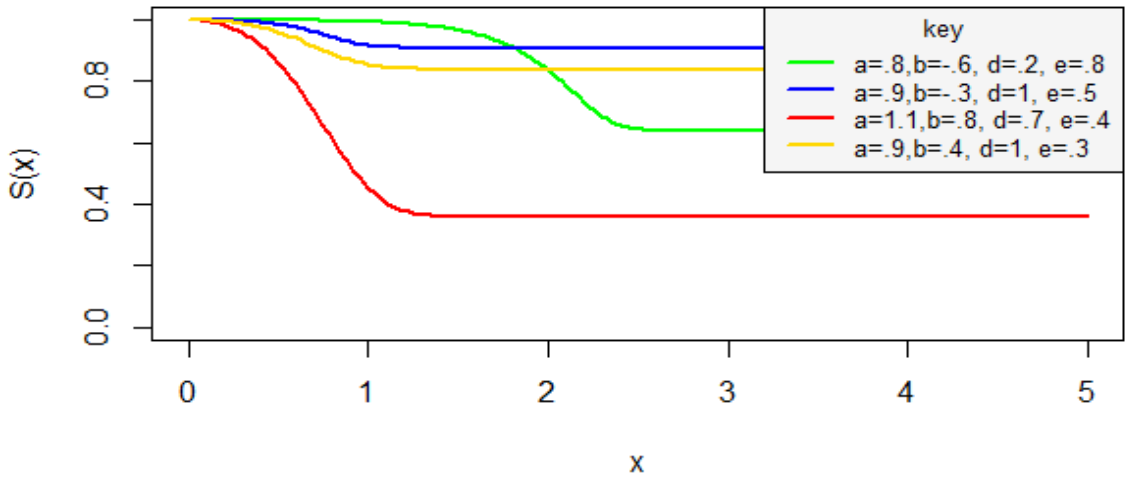

Figure 3: OTRGD's Survival Function diagram

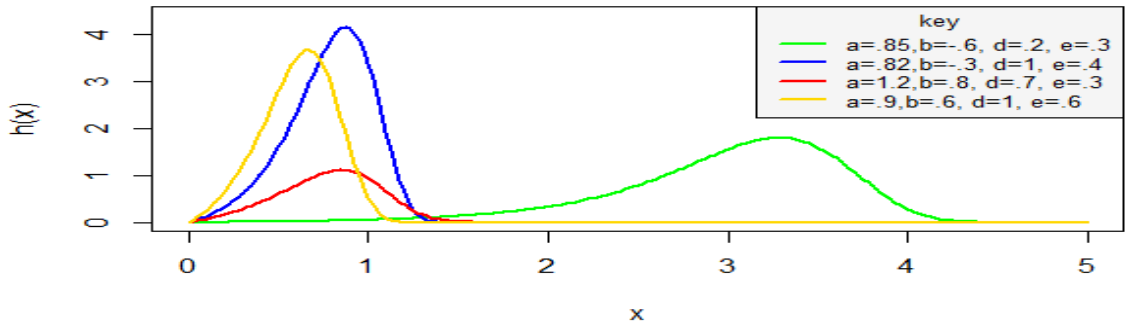

Figure 4: OTRGD's Hazard Function graph

3. Estimation of Parameters of the OTRGD

Here, the estimation via ML technique is used for determining the parameters of the newly formed distribution. With sample values $x_1, x_2, ..., x_n$ with joint PDF as $f(x_1, x_2, ..., x_n; \Theta)$, where $\Theta = (\sigma, \lambda, \eta, \alpha)^T$ is a vector of an unknown parameter, let $X_1, X_2, ..., X_n \sim$ OTRGD. The ℓ is thus explained as follows:

$$\ell = -2n\log\sigma + \sum_{i=1}^{n}\log\left(\eta e^{\alpha x - \frac{\eta}{\alpha}\left(e^{\alpha x}-1\right)}\right) + \sum_{i=1}^{n}\log\left(1-e^{-\frac{\eta}{\alpha}\left(e^{\alpha x}-1\right)}\right) - 3\sum_{i=1}^{n}\log\left(e^{-\frac{\eta}{\alpha}\left(e^{\alpha x}-1\right)}\right)$$
$$-\frac{1}{2\sigma^2}\sum_{i=1}^{n}\left(\frac{\left(1-e^{-\frac{\eta}{\alpha}\left(e^{\alpha x}-1\right)}\right)}{\left(e^{-\frac{\eta}{\alpha}\left(e^{\alpha x}-1\right)}\right)}\right)^2 + \sum_{i=1}^{n}\log\left(1-\lambda+2\lambda e^{-\frac{1}{2\sigma^2}\left(\frac{\left(1-e^{-\frac{\eta}{\alpha}\left(e^{\alpha x}-1\right)}\right)}{\left(e^{-\frac{\eta}{\alpha}\left(e^{\alpha x}-1\right)}\right)}\right)^2}\right) \quad (9)$$

By carrying out partial differentiation for ℓ with regard to λ, σ, η and α and setting the outcome to zero, one can determine the score vector's component, $U(\Theta)$.

4. Results and Discussion

4.1 The OTRGD and Competing Models

To evaluate the versatility of the OTRGD, it was applied to two distinct real-world datasets. The Transmuted Gompertz Distribution (TGD), Generalized Gompertz Distribution (GGD), and Gompertz Distribution (GD) were evaluated against the performance of the created OTRGD, which is a component of the OTR-X. We compared the proposed distributions using a number of metrics which are mathematical expression for these statistics is as follows:

$$AIC = -2\ell + 2m\ , \qquad BIC = -2\ell + m\log(n)\ , \qquad CAIC = -2\ell + \frac{2mn}{(n-m-1)}$$

and $HQIC = -2\ell + 2m\log\left(\log\left(n\right)\right)$

where, n, ℓ, m stand for size, log-likelihood function, parameters of the distribution respectively. **Note**: The model that exhibits the lowest value of these statistics is considered to be the most favourable or best -fitting model among the models we evaluated.

4.2 Datasets

The researchers described the first dataset, which shows the number of years that a group of patients who received only chemotherapy lived (Abdullahi et al., 2023).

The second dataset contains the times of survival expressed in years for 46 patients. The details are as follows: 0.197, 0.203, 0.260, 0.282, 0.296, 0.334, 0.395, 0.458, 0.466, 0.501, 0.507, 0.529, 0.534, 0.540, 0.641, 0.644, 0.696, 0.841, 0.863, 1.447, 1.485, 1.553, 0.115, 0.121, 0.132, 0.164, 0.047, 1.581, 1.589, 2.178, 2.343, 2.416, 2.444, 2.825, 2.830, 3.578, 3.658, 3.743, 3.978, 1.099, 1.219, 1.271, 1.326, 4.003, 4.033.

Table 4.1: Estimates of the models' parameters Data I

Model	σ	λ	$\hat{\eta}$	α	θ
OTRGD	0.02914	0.1118	0.1422	0.85994	-
TGD	-	0.2175	0.2655	4.8688	-
GGD	-	-	0.5533	0.2849	0.8
GD	-	-	0.602	0.1229	-

Table 4.2: Results of the Goodness-of-Fit Statistics for Data I

Model	$-\ell$	*AIC*	*CAIC*	*HQIC*	*BIC*	RANK
OTRGD	-439.41	-870.819	-869.819	-868.125	-863.593	1
TGD	-176.218	-346.436	-345.851	-344.415	-341.016	2
GGD	59.6533	125.3065	125.8919	127.327	130.7265	4
GD	58.0707	120.1414	120.4271	121.4884	123.7548	3

Table 4.3: Estimates of the models' parameters for Data II

Model	σ	λ	$\hat{\eta}$	α	θ
OTRGD	0.0024	0.2359	0.1678	0.7037	-
TGD	-	0.3744	0.2899	4.9013	-
GGD	-	-	0.1775	1.9741	3.0488
GD			0.0286	2.7848	-

Table 4.4: Results of the Goodness-of-Fit Statistics for Data II

Model	$-\ell$	***AIC***	***CAIC***	***HQIC***	***BIC***	***RANK***
OTRGD	867.3345	1726.669	1725.979	1723.297	1718.097	1
TGD	297.9529	589.9058	589.4991	587.3771	583.4764	2
GGD	15.8547	37.7093	38.1161	40.2381	44.1387	3
GD	18.2678	40.5356	40.7356	42.2214	44.8218	4

In tables 4.2 and 4.4, we observed that the stated distribution (OTRGD) had the lowest values of the goodness of fit statistics and is, thus, regarded as the best model for both data I and II in this study. Tables 4.1 and 4.3 show the MLEs of the parameters of the OTRGD and other distributions derived from the body of existing literature.

5. Conclusion

The performance in terms of best-fit of the new proposed distribution were illustrated with application to real life datasets. Similarly, the model generated was compared with its competitors in the existing literature using different real datasets and assess its flexibility and robustness. The criteria used for model selection are; ℓ, AIC, CAIC, BIC, and HQIC. Based on these criteria, the OTRGD was found to have the minimum value of these statistics as such considered the best fitted model when compared with its competitors.

References

Abdullahi, J., Gulumbe, S. U., Usman, U., & Garba, A. I. (2023). The Transform-Transformer Approach: Unveiling the Odd Transmuted Rayleigh-X Family of Distributions. *International Journal of Science for Global Sustainability*, *9*(2), 85-98.

Alsaggaf, I. A. (2024). A New Exponential Gompertz Distribution: Theory and Applications. *Journal of Reliability and Statistical Studies*, 289-320.

Alzaatreh, A., Lee, C., and Famoye, F. (2013). A new method for generating families of continuous distributions. *Metron*, 71(1): 63-79.

El-Damcese, M, A., Abdullfattah, M., El-Desouky, B, S. & Mustafa, M, E. (2015). The odd generalized exponential Gompertz distribution. *Mathematical Statistics,* 3(4): 1-14.

Hamedani, G. G., Roshani, A., & Butt, N. S. (2024). Characterizations of Certain (2023-2024) Introduced Univariate Continuous Distributions. *Pakistan Journal of Statistics and Operation Research*, 661-692.

Kajuru, J. Y., Dikko, H. G., Mohammed, A. S., & Fulatan, A. I. (2023a). Odd Gompertz-G Family of Distribution, Its Properties and Applications. *Fudma Journal of Sciences*, *7*(3), 351-358.

Kajuru, J. Y., Dikko, H. G., Mohammed, A. S., & Fulatan, A. I. (2023b). Generalized Odd Gompertz-G Family of Distributions: Statistical Properties and Applications. *Communication in Physical Sciences*, *10*(2).

Lenart, A. (2012). The moments of the Gompertz distribution and maximum likelihood estimation of its parameters. *Scandinavian Actuarial Journal. 3*, 255-277.

Mohammed, A. S. and Ugwuowo, F. I. (2020). A new family of distributions for generating skewed models: properties and applications. *Pakistan Journal of Statistics,*36 (2), 149-168.

Pearson, K. (1895). Contributions to the mathematical theory of evolution. II. Skew variation in homogeneous material. Philos Trans R Soc Lond, 186: 343–414.

Sanku, D., Fernando, A. M., & Devendra, K. (2018). Statistical Properties and Different Methods of Estimation of Gompertz Distribution with Application. *Journal of Statistics and Management Systems,* 21, 5, pp. 839-876.

Tukey, J. W. (1960). The Practical Relationship between the Common Transformations of Percentages of Counts and Amounts. Technical Report 36. Princeton University, Princeton, NJ, Statistical Techniques Research Group.

Renewable Energy Modeling: An Hypothetical Case Study of Nigeria

[1*]Jegede, Emmanuel Oladele, [2]Ajibola, Johnson Jimoh, [3]Samuel B. Aromino [4]Akinlotan, Oluyinka Omoyeni and [5]Enesi I. Dongo

[1]Department of Mathematics, Kogi State College Education (Technical), Kabba.
[2] Department of Computer Science, Kogi State College of Education (Technical), Kabba.
[3,4]Department of Chemistry, Kogi State College of Education (Technical), Kabba.
[5]School of Engineering, Kogi State Polytechnic, Lokoja
.emmjegs2017@gmail.com

Abstract

This study explores the formulation of mathematical models for renewable energy forecasting in Nigeria, focusing on solar and wind energy as primary sources. Given Nigeria's abundant solar irradiance and favorable wind conditions, renewable energy holds significant potential for enhancing energy stability and reducing dependence on fossil fuels. The research employs both deterministic and stochastic models to predict energy output, accounting for daily and seasonal variations as well as random weather fluctuations. Hypothetical empirical data are used to simulate the contribution of solar and wind energy to Nigeria's national grid. The study highlights the challenges of integrating renewable energy into the grid, such as variability in energy production and the need for robust storage solutions. The findings shows that mathematical models demonstrate that Nigeria has significant renewable energy potential, with solar irradiance peaking in the dry season and wind energy showing seasonal variability, especially during the Harmattan period. It also indicates that incorporating stochastic elements into deterministic models improves the prediction of solar and wind fluctuations, making the models more realistic. Furthermore renewable energy alone is insufficient for grid stability due to the intermittent nature of solar and wind resources. Hybrid energy solutions, including storage systems, are necessary. Finally there is a need for enhanced infrastructure, data collection, and government policies to facilitate renewable energy integration. This paper contributes to the growing body of knowledge on renewable energy modeling, with practical implications for Nigeria's transition to sustainable energy systems.

Keywords: Grid Stability, Mathematical Modeling, Renewable Energy, Solar Energy, Wind Energy.

Introduction

The transition to renewable energy has become an urgent priority due to the global challenges of climate change and the need for sustainable development. As nations seek alternatives to fossil fuels, Nigeria stands out as a promising candidate for renewable energy adoption, particularly in solar and wind energy, given its abundant natural resources. With an average solar irradiance of 5.5 kWh/m²/day and wind speeds reaching 4–7 m/s in certain regions, the country possesses significant potential for renewable energy generation (Adebayo et al., 2020; Okeke et al., 2021). However, despite these advantages, Nigeria faces substantial obstacles in effectively integrating renewable energy into its national grid, including infrastructural limitations, policy gaps, and grid stability concerns (Olaniyi & Ajayi, 2023).

Mathematical modeling plays a fundamental role in renewable energy planning and optimization, enabling researchers to assess both predictable and uncertain factors influencing energy production. Deterministic models are used to forecast solar irradiance based on the sun's

position and seasonal variations, while stochastic models account for random fluctuations due to weather conditions, such as cloud cover and wind turbulence (Adebayo et al., 2020; Woodruff, 2019). By integrating both approaches, a more comprehensive analysis of renewable energy resources can be achieved, improving grid stability and energy reliability (Charnes & Cooper, 1959; Okeke et al., 2021).

3. Mathematical Modeling in Renewable Energy

Renewable energy modeling aims to predict and optimize energy generation from sustainable sources like solar and wind. Mathematical models are essential in estimating energy outputs under various environmental conditions, enabling effective resource planning and integration into the power grid. For this study, we focus on deterministic and stochastic models, which capture different aspects of renewable energy patterns in Nigeria.

Deterministic Models

Deterministic models operate under the premise that system behaviors are entirely predictable, given specific initial conditions and parameters. In the context of renewable energy, it employs clear-sky models that predict solar radiation based on factors such as geographic location, time, and atmospheric conditions. These models assume ideal conditions without accounting for random atmospheric disturbances. For wind energy, deterministic models typically consider predictable factors like gravitational loading, tower shadow effects, and wind shear. These factors influence the cyclic loads on wind turbine blades, leading to variations in thrust and torque that can be systematically analyzed.

Stochastic Models

Stochastic models incorporate randomness and uncertainties inherent in real-world systems, providing a more realistic representation of renewable energy behaviors. It accounts for unpredictable factors such as cloud cover and atmospheric variability in solar irradiance by introducing random variations into the models, and thereby stimulating the fluctuating nature of solar radiation, leading to more accurate predictions of photovoltaic system performance. It also address the random nature of wind speed and direction considering the probabilistic distribution of wind patterns over time, aiding in the design of turbines that can efficiently operate under varying and unpredictable wind conditions.

Parameters Used in Renewable Energy Models

Several studies have indicated that there are abundant of renewable energy source in Northern Nigeria with approximate solar irradiance of $600W/m^2$ (Sambo, 2009; Iwuoha et al, 2021). Also, (Y. Olotu, A. I. Omoakhalen, R. Ishiekwene , S. K. Abolaji & P.A. Imanogor; 2023) found that the peak solar irradiance is $900W/m^2$. The study of A. B. Muhammad, A. Nasir, M.B. Maina, M. Shuwa, 2020) found that the average wind speed in Maiduguri to be $5m/s$. In the study of (L. F. Buba, N. U. Kura, D. Danlami & J.B. Dakagan, 2018), wind speed can vary and in some areas can be approximately 8m/s.

There is the third parameter that has to do with the grid stability concern and this is modeled by assessing the total renewable energy output relative to demand. The current energy infrastructure in Nigeria is primarily designed to accommodate traditional energy sources, which are more predictable and stable. Integrating renewable energy sources like solar and wind into the electrical grid can influence grid stability, depending on factors such as irradiance levels and wind speeds. (B. Jereb, 2024)

Table 3.1A: Parameters Used in Renewable Energy Models

Parameters	**Solar Energy Model**	**Wind Energy Model**
Average Solar Irradiance	600 W/m^2	N / A
Peak Solar Irradiance	900 W/ m^2 (during the dry season)	N /A
Average Wind Speed	N/A	5 m/s
Peak Wind Speed	N /A	8 m/s (during Harmattan season
Stochastic Variability	Cloud Covered Impact	Wind turbulence and wind fluctuation.

Table 3.1A summarizes the parameters used for modeling solar and wind energy, including deterministic values and stochastic variation.

Table 3.1B: Potential Impacts of Specific Average and Peak Values on Grid Stability

Parameter	Value	Potential Factor on Grid Stability
Average Solar Irradiance	$600W/m^2$	At this level, photovoltaic (PV) systems generate moderate power. Sudden fluctuation due to cloud cover can cause variability in power output, potentially challenging grid stability if not managed with appropriate balancing mechanisms.
Peak Solar Irradiance	$900W/m^2$	High irradiance levels lead to increased PV power generation. Rapid changes such as those caused by cloud movement can introduce variability, necessitating advance forecasting and grid management strategies to maintain stability.
Average Wind Speed	5m/s	Wind turbines typically starting generating power at wind speeds around 3 -5 m/s. Constituent average speed of 5 m/s contribute to stable power output, supporting grid stability.
Peak Wind Speed	8m/s	Wind speed of 8m/s are within the optimal operating range for many turbines, leading to efficient power generation. However, rapid increases or fluctuation in wind speed can cause variability in power output, which may pose challenges for grid stability if not properly managed.

Table 3.1B summarizes the potential impact of specific average and peak values on grid stability.

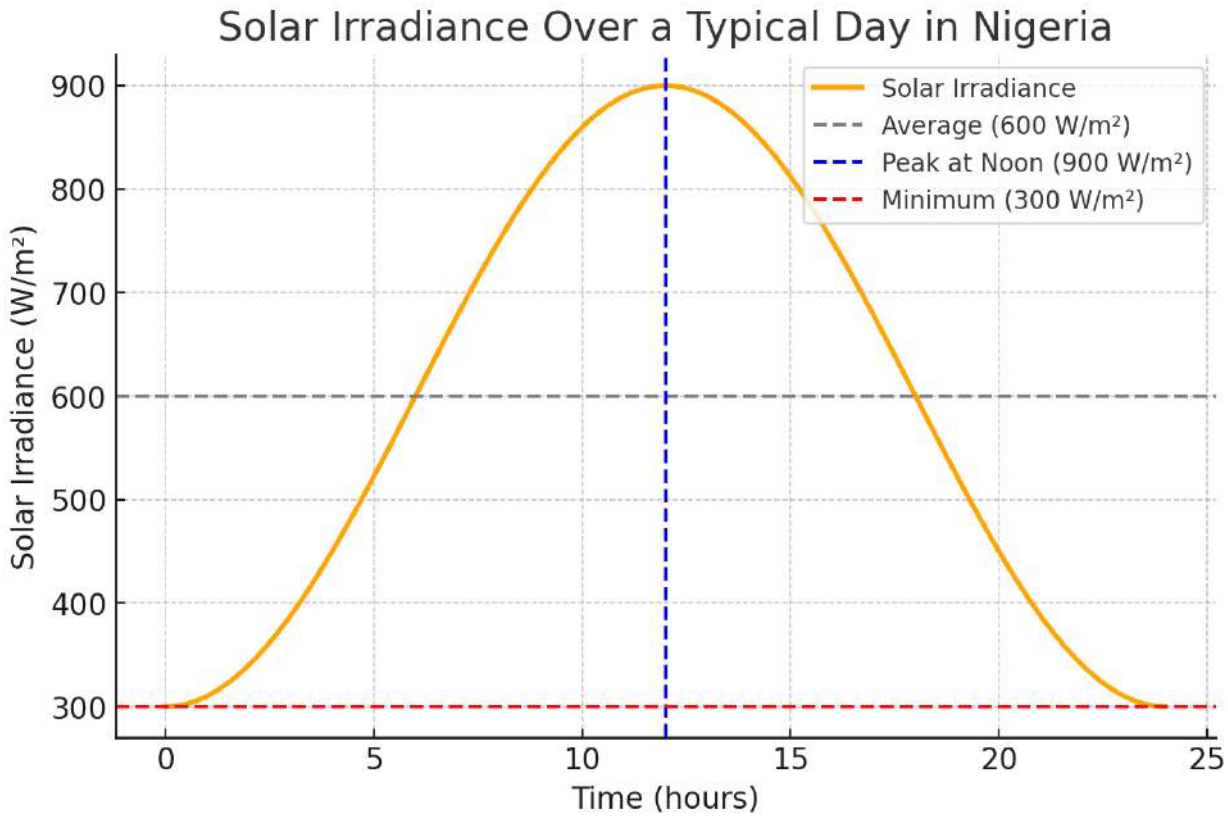

Figure 1. Deterministic And Stochastic Solar Irradiance Over A Typical Day.

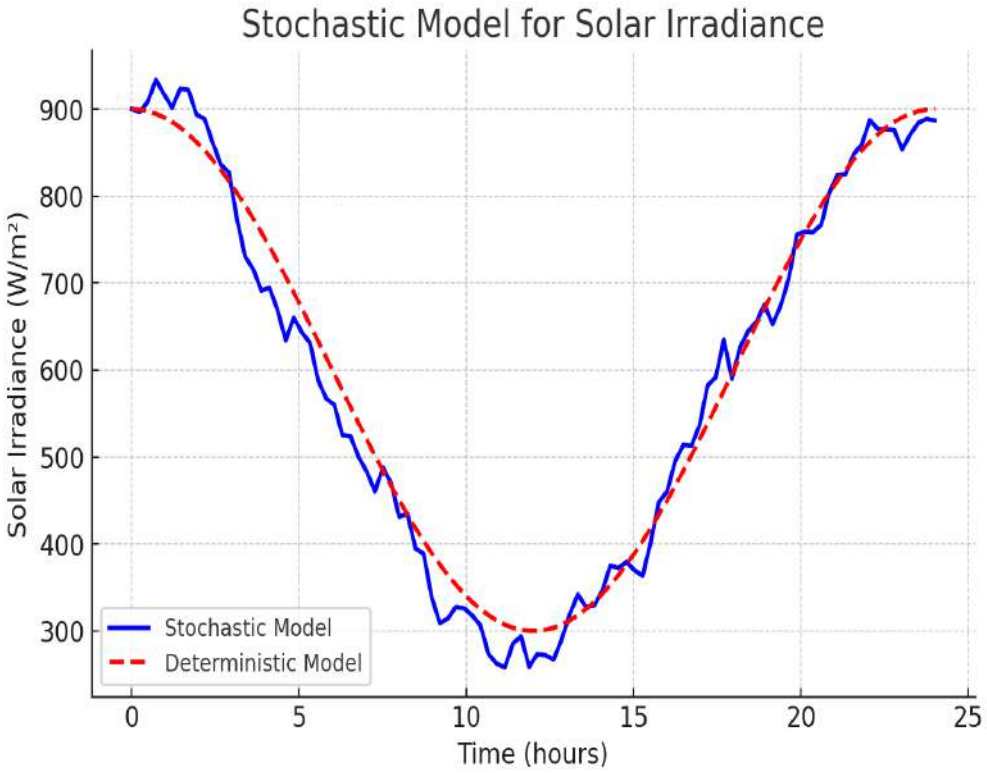

Figure 2. Stochastic Model for Solar Irradiance Output

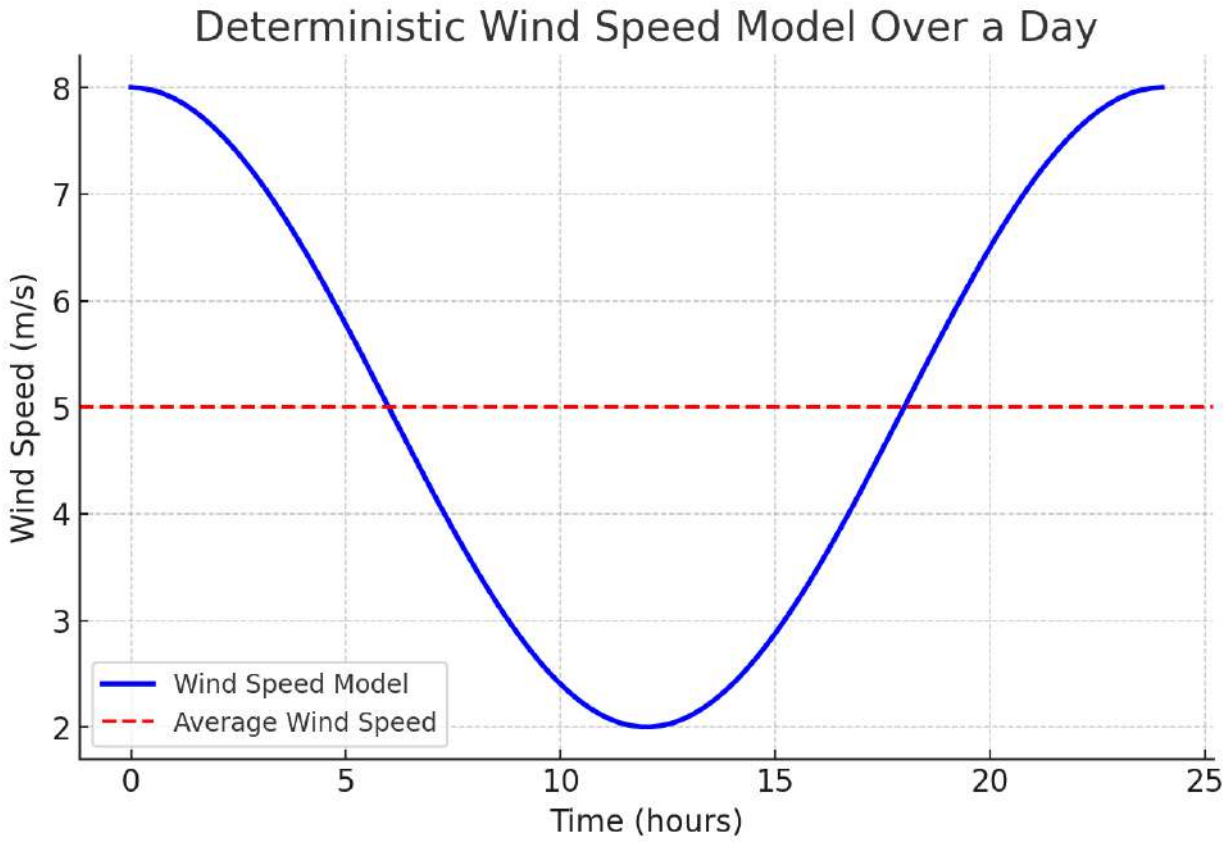

Figure 3: Deterministic Wind Speed over a Day

3.2 Model Equations

This section presents the equations for the models employed in the study:

1. *The Deterministic Model for Solar Irradiance*

The Deterministic Model for Solar Irradiance describes how solar radiation varies predictably over time based on known factors such as the position of the sun and atmospheric conditions. It is typically modeled as:

$$I(t) = I_{avg} + A\cos(\frac{2\pi}{T}(t - t_0))$$

where:

$I(t)$ = Solar irradiance at time (W/m²), I_{avg} = Average solar irradiance (W/m²), A = Amplitude of irradiance variation (W/m²), T = Period of one solar cycle (e.g., 24 hours for daily variations), t_0 = Time of peak irradiance (e.g., solar noon)

This equation accounts for the cyclical nature of solar radiation, where irradiance Increases from sunrise, peaks at solar noon, and decreases toward sunset.

2. *The stochastic model for solar irradiance*

The stochastic model for solar irradiance incorporates random variations to account for unpredictable atmospheric conditions such as cloud cover and dust storms. It is expressed as:

$$I(t) = I_{avg} + A\cos(2\pi ft + \emptyset) + \in (t)$$

where $I(t)$ is the solar irradiance at time t, I_{avg} is the average solar irradiance (e.g., 600 W/m²), A is the amplitude of seasonal fluctuations, f represents the frequency of the daily solar cycle, $\varepsilon(t)$ is a stochastic noise term representing random fluctuations due to atmospheric conditions and $\emptyset$ is phase shift.

This model accounts for both deterministic daily variations and stochastic disturbances, improving the accuracy of solar energy predictions. Let me know if you need further refinements or placement suggestions.

3. *The deterministic model for wind speed*

The deterministic model for wind speed describes the predictable variations in wind velocity over time due to diurnal and seasonal patterns. It is given by:

$$V(t) = V_{avg} + A\cos(2\pi ft + \emptyset)$$

where:

$V(t)$ is the wind speed at time, V_{avg} is the average wind speed (e.g., 5 m/s), A is the amplitude of seasonal or daily fluctuations, f represents the frequency of the wind speed fluctuation and $\emptyset$ is the phase shift.

This model captures the periodic nature of wind speed, such as higher speeds during certain seasons (e.g., Harmattan) and lower speeds during the rainy season.

4. *The stochastic model for wind speed*

The stochastic model for wind speed incorporates random variations to account for turbulence and unpredictable weather fluctuations. It can be expressed as:

$$V(t) = V_{avg} + A\cos(2\pi ft) + \epsilon(t)$$

where:

$V(t)$ is the wind speed at time,

V_{avg} is the average wind speed (e.g., 5 m/s),

A is the amplitude of periodic variations and
f represents the frequency of the wind cycle (daily or seasonal),
$\epsilon(t)$ is a stochastic noise term representing random wind speed fluctuations, typically modeled as a Gaussian white noise process or an autoregressive process (e.g., AR(1)).

The model better reflects real-world wind behavior, where unpredictable gusts and atmospheric disturbances influence wind speed beyond deterministic patterns.

5. *Grid Stability in Renewable Energy Integration*

Grid Stability in Renewable Energy Integration is the Power Balance Equation, which ensures that power generation matches demand while accounting for renewable energy variability and grid dynamics and is given by:

$$P_{gen}(t) + P_{ren}(t) = P_{load}(t) + P_{loss}(t) + \frac{dE(t)}{dt}$$

where:
$P_{gen}(t)$ = Conventional power generation at time; $P_{ren}(t)$ = Renewable power generation (solar, wind, etc.) at time t; $P_{load}(t)$ = Power demand (load) at time t; $P_{loss}(t)$ = Power losses in transmission and distribution; $\frac{dE(t)}{dt}$ = Rate of change of stored energy (from batteries or other storage systems)

Data Analysis and Mathematical Modeling Implementation

This section details the process of analyzing empirical data and implementing mathematical models for renewable energy forecasting in Nigeria. The goal is to use a combination of deterministic and stochastic models to estimate energy potential from solar and wind sources while ensuring grid stability.

Data Collection and Preprocessing: Hypothetical empirical data are generated to represent average solar irradiance and wind speed across different regions of Nigeria and this data includes:

- Solar irradiance data: Collected at regular intervals throughout the day, capturing variations from sunrise to sunset.
- Wind speed data: Measured hourly to account for daily and seasonal changes in wind patterns.
- Grid stability data: Collected from existing energy infrastructure to determine stability thresholds and assess integration potential for renewable energy.

Data preprocessing involves:

- Normalization: Scaling solar irradiance and wind speed data to a common range, which facilitates the modeling of seasonal variations.
- Smoothing techniques: Applying smoothing filters to reduce noise, ensuring that data patterns accurately represent daily and seasonal cycles.
- Interpolation: Filling any gaps in data to create a complete dataset for model calibration.

Results and Discussion

This section present the result (solutions) to the models presented:

1. *Deterministic Model for Solar Irradiance*

$$I(t) = I_{avg} + A\cos(\frac{2\pi}{T}(t - t_0))$$

Given I_{avg} = 600W/m²; $A = 300$ W/m² since solar peak minus solar average is (Amplitude) i.e. 900 -300 = 300 ; T= 24 and hours (daily solar cycle) and t_0 =12 hours (solar noon); the model becomes:

$$I(t) = 600 + 300\cos\frac{2\pi}{24}(t-12))$$

Differentiating with respect to t, we have:

$$\frac{dI}{dt} = 300 \times (-\sin(\frac{\pi}{12}(t-12))) \times \frac{\pi}{12}$$

$$\frac{dI}{dt} = -\frac{300\pi}{12}\sin(\frac{\pi}{12}(t-12))$$

$$\frac{dI}{dt} = -25\pi\ \sin(\frac{\pi}{12}(t-12))$$ and setting $\frac{dI}{dt} = 0$ to obtain the critical point: $\frac{dI}{dt} = -25\pi\ \sin(\frac{\pi}{12}(t-12)) = 0$

$$\sin(\frac{\pi}{12}(t-12)) = 0$$

Since $\sin x = 0\ at\ x = k\pi$ (where k is an integer); $\frac{\pi}{12}(t-12) = k\pi$

$$(t-12) = 12k; t = 12(1+k)$$

For k =0, t =12 hours (solar noon, maximum irradiance; for k = -1, t = 0 hour (midnight, minimum irradiance).

Next, we do maximum and minimum analysis by finding the second derivative:

$$\frac{d^2I}{dt^2} = -25\pi \times \frac{\pi}{12}\cos(\frac{\pi}{12}(t-12))$$

$$\frac{d^2I}{dt^2} = -\frac{25\pi^2}{12}\cos(\frac{\pi}{12}(t-12))$$

At $t = 12\ hour, \cos(0) = 1\ implying\ \frac{d^2I}{dt^2} = \frac{25\pi^2}{12} < 0$ hours,

Thus, $t = 12\ is\ a$ maximum (900 W/m²).

At t = 0 hours, $\cos(-\pi) = -1\ implying\ \frac{d^2I}{dt^2} = \frac{25\pi^2}{12} > 0$

Thus, $t = 0$ is a minimum (300 W/m²). We can from this that:

- Solar irradiance increases from sunrise (600 W/m²) to a peak at noon (900 W/m²).
- It decreases to a minimum (300 W/m²) at midnight. This is clear from figure 1.
- The first derivative confirms the rate of change, while the second derivative verifies max/min points.

2. *The stochastic model for solar irradiance*

The stochastic model for solar irradiance incorporating frequency can be written as:

$$I(t) = I_{avg} + A\cos(2\pi ft + \emptyset) + \in(t)$$

Given, I_{avg} = 600 W/m² (average solar irradiance), A = 300 W/m² (amplitude), $f = \frac{1}{24}$ (daily cycle frequency), $\emptyset$ is the phase shift (assumed 0), $\in(t)$ is a small perturbation representing stochastic fluctuations.

Modeling $\in(t)$ by using a simple autoregressive (AR) noise term

$$\in(t) = \alpha \in(t-1) + \eta(t)$$

where α is a decay factor ($0 \leq \alpha < 1$) to ensure stability, $\eta(t)$ is white noise with mean 0 and small variance σ^2.

To compute specific values, lt's approximate $\in(t)$ with small random variations, say σ = 20 W/m².

- At noon (t =12 hours): $I(12) = 600 + 300\cos(\pi) + \in(12)$ = 300 + $\in(12)$ W/m$\hat{A}^2$
- At Peak Time (t =6 hours): $I(6) = 600 + 300\cos\left(\frac{\pi}{2}\right) + \in(6)$ = 600+$\in$ (6) W/m^2

- At Midday Peak ($t = 0\ or\ t = 24$): $I(0) = 600 + 300\cos(0) + \in(0) = 900 + \in(0)W/ m\hat{A}^2$
- At Midnight (t = 18 hours): $I(18) = 600 + 300\cos\left(\frac{3\pi}{2}\right) + \in(10) = 600 + \in(18)\ \mathrm{W}/m^2$

This implies:

- The stochastic model adds small fluctuations to the deterministic model, representing random variations due to weather effects.
- The term $\in(t)$ can be estimated from real data using an AR(1) process.
- The model maintains the periodic nature of solar irradiance while accounting for real-world variations. This can be illustrated by figure 2.

3. *The Deterministic Model for Wind Speed is typically given by:*

$$V(t) = V_{avg} + A\cos 2\pi ft + \emptyset)$$

Solving for $V(t)$, we substitute hypothetical values for a given location in Northern Nigeria: V_{avg}= 5m/s (average wind speed), A = 3 m/s (assumed amplitude of variation), $f = \frac{1}{24}$ h (one cycle per day), $\emptyset$ =0 (assuming wind speed starts from peak at t =0)

Thus, the wind speed equation becomes: $V(t) = 5 + 3\cos(\frac{2\pi}{24}t)$

To find peak wind speed: $V_{peak} = V_{avg} + A$ = 8m/s.

To find minimum wind speed: $V_{min} = V_{avg} - A$ = 2 m/s. This is illustrated as in figure 3.

4. *The Stochastic Model of Wind Speed*

The stochastic wind speed model is given by:

$V(t) = V_{avg} + A\cos(2\pi ft) + \in(t)$ The term $\in(t)$ accounts for random fluctuations, often modeled as a Gaussian white noise process. Assuming follows a random normal distribution with mean zero and standard deviationσ, we can express the wind speed as:

$$V(t) = V_{avg} + Acos\,(2\pi ft) + \sigma W(t)$$

where $W(t)$ represents a random process (e.g., Brownian motion or Gaussian noise).

For practical implementation, let's assume: $V_{avg} = 5\ m$/s , $A = 2$ m/s, $f = \frac{1}{24}hr$ (daily cycle), $\sigma = 0.5$ m.

Then, over a time range of 24 hours, the solution can be numerically computed.

5. *Grid Stability in Renewable Energy Integration*

$P_{gen}(t) + P_{ren}(t) = P_{load}(t) + P_{loss}(t) + \frac{dE(t)}{dt}$. This is also known as The Power Balance equation.

First, we express Renewable Energy Contributions. Solar and wind power generation can be modeled as follows:

- Solar Power Generation: $P_{solar}(t) = \boldsymbol{\eta_{solar} AI(t)}$

$\boldsymbol{\eta_{solar}}$= Efficiency of solar panels, $\boldsymbol{A}$ = Surface area of solar panels, $\boldsymbol{I(t)}$ = Solar irradiance at time

- Wind Power Generation:

$$P_{wind}(\mathrm{t}) = \frac{1}{2}C_p\rho Av^3$$

C_p= Power coefficient, ρ = Air density, A = Swept area of wind turbine blades, v =Wind speed at time .

Thus, the total renewable energy contribution is:

$$P_{ren}(t) = P_{solar}(t) + P_{wind}(t)$$

Next we express Energy Storage Contribution
The storage system (battery) follows the charge/discharge equation:

$$\frac{dE(t)}{dt} = \boldsymbol{\eta_{bat}} P_{charge} - P_{discharge}$$

where $\boldsymbol{\eta_{bat}}$ = Battery efficiency, P_{charge} = Power used to charge storage and $P_{discharge}$ = Power discharged to the grid

Next we solve for Grid Stability Condition
Substituting all expressions into the main equation:

$$P_{gen}(t) + \boldsymbol{\eta_{solar}} \boldsymbol{AI(t)} + \frac{1}{2} C_p \rho A v^3 = P_{load}(t) + P_{loss}(t) + \boldsymbol{\eta_{bat}} P_{charge}(t) - P_{discharge}(t)$$

Rearrange for the grid stability condition:

$$P_{gen}(t) + P_{ren}(t) - P_{load}(t) - P_{loss}(t) - \boldsymbol{\eta_{solar}} \boldsymbol{P_{charge}}(t) + P_{discharge} = 0$$

This equation ensures that power supply matches demand, with storage compensating for fluctuations. If the left-hand side is positive, excess power is available for storage or grid export; if negative, additional power must be sourced.

Conclusion

This study explored the application of deterministic and stochastic models in analyzing solar irradiance and wind speed for renewable energy integration in Nigeria. The models demonstrated how predictable variations (deterministic components) and random fluctuations (stochastic components) influence energy generation. The findings highlight the feasibility of integrating solar and wind energy into Nigeria's power grid, given the country's substantial renewable energy potential.

However, integrating these energy sources poses significant challenges to grid stability, particularly in terms of power fluctuations, voltage regulation, and frequency stability. The study's grid stability model underscores the need for effective energy management strategies, such as storage systems, demand response mechanisms, and grid reinforcement, to mitigate these challenges.

Overall, the mathematical modeling approach provides a robust framework for optimizing renewable energy integration in Nigeria. Future research should focus on refining these models by incorporating real-time data, advanced optimization techniques, and adaptive control mechanisms to enhance grid stability and ensure sustainable energy supply.

References

Adebayo, T. O., Adegbite, A. O., & Oluwaseun, A. A. (2020). Renewable energy potential in Nigeria: A review of solar and wind resources. Renewable Energy Research Journal, 5(2), 45–61.

Buba, L. F., Kura, N. U., Danlami, D., & Dakagan, J. B. (2018). Wind energy assessment in Northern Nigeria: A case study of Maiduguri. Journal of Energy Systems, 7(1), 88–97.

Charnes, A., & Cooper, W. W. (1959). Chance-constrained programming. Management Science, 6(1), 73–79.

Iwuoha, O. C., Eze, C. C., & Anosike, A. C. (2021). A review of solar energy development in Nigeria: Prospects and challenges. Nigerian Journal of Engineering Research and Development, 18(3), 112–126.

Jereb, B. (2024). Grid stability concerns in renewable energy integration. International Journal of Electrical Power & Energy Systems, 140, 107641.

Muhammad, A. B., Nasir, A., Maina, M. B., & Shuwa, M. (2020). Wind energy resource assessment and utilization in Nigeria. Journal of Renewable Energy Studies, 15(4), 67–79.

Olaniyi, S. A., & Ajayi, O. O. (2023). Renewable energy integration and grid stability: Challenges and solutions for Nigeria. Journal of Energy Policy and Development, 12(2), 199–215.

Olotu, Y., Omoakhalen, A. I., Ishiekwene, R., Abolaji, S. K., & Imanogor, P. A. (2023). Evaluating solar irradiance potential in Nigeria: A regional analysis. African Journal of Sustainable Energy, 10(1), 34–52.

Okeke, C. O., Eneh, E. C., & Onu, M. O. (2021). Mathematical modeling of renewable energy resources: An application to Nigeria's energy sector. Journal of Applied Mathematics and Computation, 9(2), 89–102.

Sambo, A. S. (2009). Strategic developments in renewable energy in Nigeria. International Association for Energy Economics, 4(1), 15–19.

Woodruff, D. L. (2019). Stochastic optimization models in renewable energy systems. Operations Research for Sustainable Energy, 11(4), 201–220.

On the Use of Time Series Model to Investigate the Fluctuation of Bitcoin Prices in Daily Market Activities

Nnaemeka Martin Eze[1,*], Oluchukwu Chukwuemeka Asogwa[2], Christopher Chibuike Charles[3]

[1]Department of Statistics, University of Nigeria, Nsukka, Nigeria
[2]Department of Mathematics & Statistics, Federal University Ndufu Alike, Nigeria
[3]Department of Management Information Systems, Edith Cowan University, Perth Western Australia
[1,*]Corresponding author**:** nnaemeka.eze@unn.edu.ng

Abstract

This study focuses on modeling Bitcoin prices using time series analysis to support investors, traders, and policymakers in making decisions. The data for this study is collected from Yahoo Finance API. The Box-Jenkins methodology is applied to identify the appropriate model. The Autocorrelation Function (ACF) and Partial Autocorrelation Function (PACF) plots exhibit a cut off at lag 1 after first order differencing, suggesting an ARIMA (1, 1, 1) model. Furthermore, Bayesian Information Criterion (BIC) and Akaike Criterion (AIC) are used for model selection, with the ARIMA (4, 1, 2) model identified as the best fit. To assess the adequacy of selected model, the Ljung-Box test is conducted, and the results confirm that the model is statistically adequate. Forecasts are made for 40 days using ARIMA (4, 1, 2). The forecast results showed that there are upward and downward trend within the 40 days. The findings from the forecast have shown that the model can be used for Bitcoin price prediction.

Keyword: Autocorrelation Function, Partial Autocorrelation Function, Autoregressive, Biticoin price, Box-Jenkins, Forecasting, Moving average

1. Introduction

Cryptocurrencies have revolutionised the financial ecosystem, introducing digital assets with the potential to reshape traditional financial systems. Bitcoin, the first cryptocurrency, emerged in 2009 after the creation of the blockchain technology in 2008. Its success made a way for other alternative digital currencies which are known as altcoins (alternative currencies).

The Cryptocurrency Market has had unprecedented growth with a market capitalization of about $2 trillion and growing as at the time of writing this paper, and this alone has drawn the attention of entrepreneurs, investors, regulators and the public at large. A Cryptocurrency, as defined by the Mariam-Webster dictionary, is "any form of currency that only exists digitally, usually has no central issuing or regulating authority, relies on a decentralized system to record transactions and manage the issuance of new units, and uses cryptography to prevent counterfeiting and fraudulent transactions". Crypto currencies have had the media and regulatory bodies watching due to its volatility and unpredictability which is greatly influenced by the market sentiments, lack of regulations, speculations, crypto currency whales and media influence. Prediction of cryptocurrency pieces accurately is crucial for in investors, traders and policy makers to make inform decisions and help mitigate the risks in this dynamic market environment.

Since the cryptocurrency price prediction has garnered significant attention from researchers, investors, and policymakers due to the dynamic and volatile nature of digital asset markets, this study identified that there are so many challenges in cryptocurrency markets today such as risk

management, right decision making, market stability and investor security. These challenges or problems can cause an investor to lose his/her money if it is not properly managed. This study ought to solve the problems by fitting a time series model to daily Bitcoin prices to enable stakeholders and policy makers to make the right policies and decisions. It will also help the investors to invest their money wisely.

The significance of this study on modeling Bitcoin prices using time series analysis is profound for several reasons:

1) **Risk Management:** Cryptocurrency markets are famously volatile. By developing a model to forecast Bitcoin prices, my study helps investors and traders navigate these risks more effectively, offering insights into potential price movements.
2) **Informed Decision-Making:** In the cryptocurrency world, decisions need to be data-driven. My research equips stakeholders and policymakers with accurate forecasts, empowering them to make well-informed choices about trading strategies, investment plans, and regulatory measures.
3) **Timing is Key**: Successful trading often hinges on timing. My model assists traders in identifying the best times to enter or exit the market, potentially improving profitability and minimizing losses.
4) **Regulatory Insights:** Regulators are increasingly interested in cryptocurrencies. My study offers them valuable insights into market dynamics and price trends, aiding in the creation of effective regulatory frameworks to ensure market stability and investor security.
5) **Academic Contribution:** My research contributes to the academic understanding of cryptocurrency price prediction. By applying time series modeling to Bitcoin prices, I expand knowledge in this area, enriching the existing literature.
6) **Practical Applications:** Beyond academia, my findings have practical applications for various cryptocurrency stakeholders, including investors, traders, financial institutions, and policymakers. My model could be integrated into trading algorithms and risk management systems, boosting efficiency and effectiveness in the cryptocurrency market.

This study focuses specifically on Bitcoin (BTC) as the target cryptocurrency for price prediction using historical data of adjusted close prices gotten from yahoo finance API. Bitcoin is the most widely recognized and traded cryptocurrency, making it a suitable choice for analysis. It employs time series models as the primary method for cryptocurrency price prediction. While other cryptocurrencies may exhibit similar price dynamics, their inclusion is outside the scope of this study.

So many methodologies have been explored to forecast cryptocurrency prices accurately, with Auto-regressive Integrated Moving Average (ARIMA) models emerging as popular choice for time series forecasting in financial markets.

Kristoufek (2013) conducted one of the early studies on Bitcoin price prediction using ARIMA models. The author analyzed the historical price data of Bitcoin and applied ARIMA modeling techniques to forecast future price movements. The study found that ARIMA models could capture short-term trends and fluctuations in Bitcoin prices with reasonable accuracy, providing valuable insights for investors and traders.

Cheah and Fry (2015) investigated the Bitcoin basic values and examined whether Bitcoin markets exhibited speculative bubbles. The authors employed ARIMA models to analyze historical price data and assess the deviation of Bitcoin prices from intrinsic value. The study highlighted the potential of ARIMA models in identifying market inefficiencies and speculative bubbles in cryptocurrency markets.

Chen *et al.* (2018) explored the application of ARIMA models in predicting Ethereum (ETH) prices. The authors collected historical price data of Ethereum and evaluated different ARIMA configurations to identify the optimal model for price prediction. The study demonstrated that ARIMA models could effectively capture the seasonal patterns and long-term trends in Ethereum prices, contributing a very much valuable approaches for cryptocurrency market activities for investors and traders.

Overall, the literature review highlights the growing interest in cryptocurrency price prediction using ARIMA models. While more complex machine learning techniques have gained popularity in recent years, ARIMA models remain a reliable and widely used method for forecasting cryptocurrency prices, providing valuable insights for stakeholders in the digital asset ecosystem. While ARIMA models have established themselves as a valuable tool, recent studies highlight their limitations. McNally *et al.* (2018) suggest that GARCH models might outperform ARIMA in capturing the high volatility inherent in cryptocurrencies. Shao *et al.* (2021) explore the growing trend of Deep Learning techniques, suggesting they might offer better accuracy compared to ARIMA models. Several literature reviews offer a broader perspective by comparing ARIMA models with other forecasting techniques. Tsai and Hsu (2018) provide a comprehensive overview of various machine learning techniques used for cryptocurrency price prediction, including ARIMA, Support Vector Machines, and Neural Networks. Yu *et al.* (2021) focus on machine learning techniques used for predicting cryptocurrency transactions, with some discussion on price prediction methods, including ARIMA. These reviews highlight the ongoing development of alternative forecasting techniques and the need for continuous evaluation as the cryptocurrency market evolves.

2. Materials and Methods

2.1 Material

The dataset for this study comprises historical price data of Bitcoin (BTC) obtained from Yahoo Finance API (https://finance.yahoo.com/quote/BTC-USD/history). It spans from April 21, 2020, to March 23, 2024, providing a comprehensive timeframe for analysis and modeling. Yahoo Finance API is a widely used platform for accessing financial data, offering reliable and current information on the price of cryptocurrency, capitalization of market and volumes of trading.

2.2. Methodology

The method used in this study is the Box-Jenkins's method, a systematic approach for identifying, fitting, checking, and applying integrated autoregressive moving average (ARIMA) time series models. This method is particularly suitable for medium to long length time series data.

The Box- Jenkins method involves the iterative application of the following three steps:

1. **Identification:** model identification is performed using plots of the data, autocorrelation, and partial autocorrelation function. Based on these analyses, a suitable ARIMA model is chosen by determining appropriate values for p, d, and q.
   P = order of autoregressive
   d = degree of differencing
   q = order of moving average
2. **Estimation:** The parameters (ϕ) of the selected model are estimated using methods such as maximum likelihood estimation, Yule-Walker equations, and the least square method.
3. **Diagnostic Checking:** The adequacy of the fitted model is assessed analyzing the autocorrelation and partial autocorrelations of the residuals.

The first step in time series analyzing is to examine the stationarity of the dataset by plotting observations against time to identify trends, seasonality, or structural changes. Here we plot the data on the daily report of bitcoin close prices from the yahoo finance API against the corresponding days between the range of April 21, 2020 to March 23, 2024.

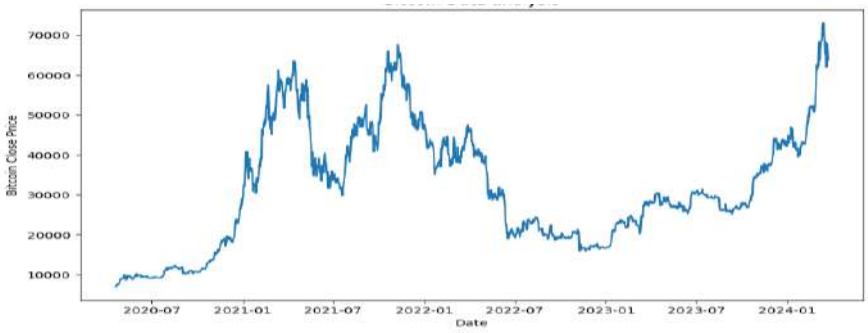

Figure 1: Graph on the Reported Bitcoin close prices against the days of the years

Figure 1 above shows that the data are not stationary; and to confirm non-stationarity, we need to perform the Augmented Dicky Fuller (ADF) test.

Hypothesis:
$\boldsymbol{H_0}$: Data are not stationary
$\boldsymbol{H_1}$: Data are stationary
Test Statistic: $Df_t = \frac{\hat{\gamma}}{SE(\hat{\gamma})}$
$\alpha = 0.05$
Table 1: Test for Stationarity Using ADF (Augmented Dickey Fuller) test

ADF TEST	t-statistic	p-value
BTC data	-1.4165	0.5743

Decision Rule: Reject the null hypothesis if the p-value < α-value; otherwise, do not reject *H*o.
Conclusion: Since p-value = 0.5743 is higher than $\alpha = 0.05$; we fail to reject the null hypothesis and therefore we conclude that the bitcoin close prices is not stationary at $\alpha = 0.05$.
Since the data is non stationary, we apply differencing as it is a common way to deal with non-stationary data.

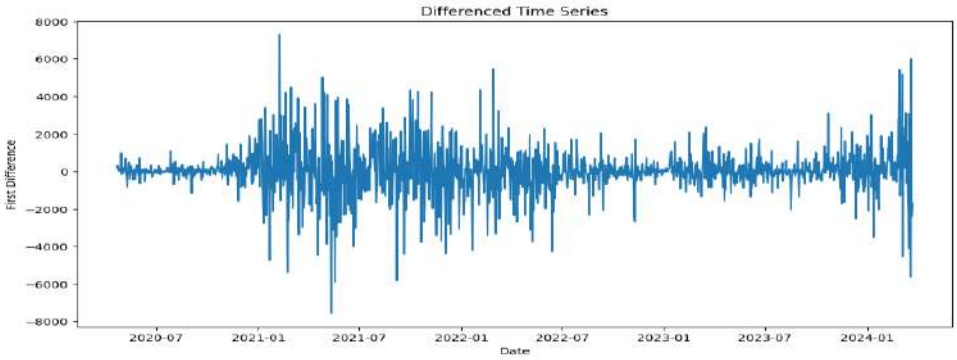

Figure 2: Plot after first order differencing

The plot in Fig 2 shows that after the first differencing the dataset is now stationary.

Moreover, in order to be sure that the first differenced data are stationary, we carried out an empirical test using Augmented Dicker-fuller (ADF) test. Below is the procedure for testing the hypothesis using ADF.

Hypothesis:

$\boldsymbol{H_0}$: Data are not stationary

$\boldsymbol{H_1}$: Data are stationary

Test Statistic: $Df_t = \frac{\hat{\gamma}}{SE(\hat{\gamma})}$

$\alpha = 0.05$

Table 2: Test for stationarity of diffenced data using ADF test

ADF TEST	t-statistic	p-value
BTC data	-11.5941	0.000.

Decision Rule: Reject the null hypothesis if the p-value < α-value; otherwise, do not reject *H*o.

Conclusion: Since p-value = 0.001 is less than α= 0.05; we reject the null hypothesis. Therefore, we conclude that Bitcoin closing prices are stationary at α= 0.05.

2.3. Autoregressive Process

The autoregressive process $\{\mathrm{X}(t), t \in T\}$ is a stochastic model widely used to represent real-life time series data. In an autoregressive model, the current value of the process is expressed as a finite linear combination of its past values.

The model is represented as follows:

$$\mathrm{X}_t = \phi_1 \mathrm{X}_{t-1} + \phi_2 \mathrm{X}_{t-2} + \cdots + \phi_p \mathrm{X}_{t-p} + a_t \quad (1)$$

$$\mathrm{X}_t - \phi_1 \mathrm{X}_{t-1} + \phi_2 \mathrm{X}_{t-2} + \cdots + \phi_p \mathrm{X}_{t-p} = a_t \quad (2)$$

$$\mathrm{X}_t(1 - \phi_1 \mathrm{B} + \phi_2 \mathrm{B}^2 - \cdots - \mathrm{B}^p) = a_t \quad (3)$$

where; $a_t = \phi(\mathrm{B})\mathrm{X}_t$ and $\phi(\mathrm{B}) = 1 - \phi_1 \mathrm{B} + \phi_2 \mathrm{B}^2 - \cdots - \mathrm{B}^p$ is the characteristic polynomial of order p. Here, X_{t-1} represents the previous value of the series. The model can also be written as:

$$\phi(\mathrm{B})\mathrm{X}_t = a_t \quad (4)$$

2.4. The Moving Average Process

In time series analysis, the moving average (MA) model is a common approach for modeling univariate time series data. The MA model assumes that the current value of a series depends linearly on past stochastic error terms. Along with the autoregressive (AR) model, the MA model forms the basis of the more general ARMA and ARIMA models, which have a more complex stochastic structure (Eze *et al.*, 2020).

Unlike the AR model, the finite MA model is always stationary. It is represented as follows:

$$\mathrm{X}_t = a_t - \theta_1 a_{t-1} - \theta_2 a_{t-2} - \cdots - \theta_q a_{t-q} \quad (5)$$

$$\mathrm{X}_t = a_t - \theta_1 \mathrm{B} a_t - \theta_2 \mathrm{B}^2 a_t - \cdots - \theta_q \mathrm{B}^q a_t \quad (6)$$

$$\mathrm{X}_t = \left(1 - \theta_1 \mathrm{B} a_t - \theta_2 \mathrm{B}^2 a_t - \cdots - \theta_q \mathrm{B}^q\right) a_t \quad (7)$$

$\mathrm{X}_t = \theta(\mathrm{B})a_t$; where; $\theta(\mathrm{B}) = 1 - \theta_1 \mathrm{B} a_t - \theta_2 \mathrm{B}^2 a_t - \cdots - \theta_q \mathrm{B}^q$

And is known as the characteristic polynomial of MA of order q. This process is thought of as the output, thought of as the output, X_t from a linear filter with transfer function $\theta(\mathrm{B})$ which the output is a white noise; a_t

2.5. Autoregressive Moving Average (ARMA) Model

To improve the accuracy of time series modeling, both the autoregressive and moving average components can be combined into an ARMA model. The ARMA (p, q) model is defined as:

$$X_t = \phi_1 X_{t-1} + \phi_2 X_{t-2} + \cdots + \phi_p X_{t-p} + a_t - \theta_1 a_{t-1} - \theta_2 a_{t-2} - \cdots - \theta_q a_{t-q} \quad (8)$$

where the ϕ represents the autoregressive parameters, θ represents the moving average parameters, X_t represents the observed series, and a_t is a series of random errors (residuals) assumed to follow a normal distribution (Zhihua *et al.*, 2014).. The Box-Jenkins methodology uses the backshift operator (B) to simplify the notation of time series models. The backward shift operator is defined as: $BX_t = X_{t-1}$ and $B^2 X_t = X_{t-2}$

Using this notation, the ARMA model can be rewritten in a more compact form.

2.6. Autoregressive Integrated Moving Average (ARIMA) Process

The ARIMA (p, d, q) model is an extension of the ARMA model used for non-stationary time series. If a time series is not stationary, it can be transformed into a stationary series by differencing. Mathematically, a time series X_t, follows an ARIMA (p, d, q) process if its dth differenced series $W_t = \overline{V}^d X_t = (1 - B)^d X_t$ is a stationary ARMA (p, q) process.

where; p is the order of the autoregressive model,d is the degree of differencing, and q is order of the moving average model.

3. Results and Discussion

The Box-Jenkins modeling approach is used to analysis the dataset collected from the Yahoo Finance API. The process involves three steps:

1. Model identification
2. Model fitting
3. Model diagnostic

3.0 Identification

As explained earlier, the model is identified using the Autocorrelation Function (ACF) and Partial Autocorrelation Function (PACF). The behaviour of the Autocorrelation and Partial Autocorrelation is examined carefully. Recall that for a model to be identified, the time series must first be stationary (De Gooijer *et al.*, 1985).

Table 3: The theoretical pattern of ACF and PACF

Model	ACF	PACF
AR(p)	Tails off to zero/ decays	Cuts off after lag (p)
MA(q)	Cuts off after lag (q)	Tails off to zero/decays
ARMA (p, q)	Cuts off at lag p	Cuts off at q

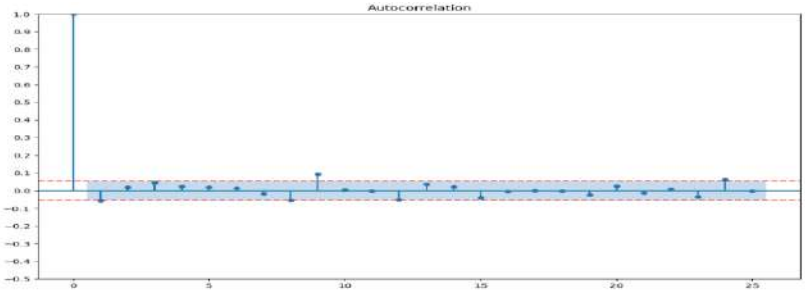

Figure 3: The autocorrelation function plot (ACF)

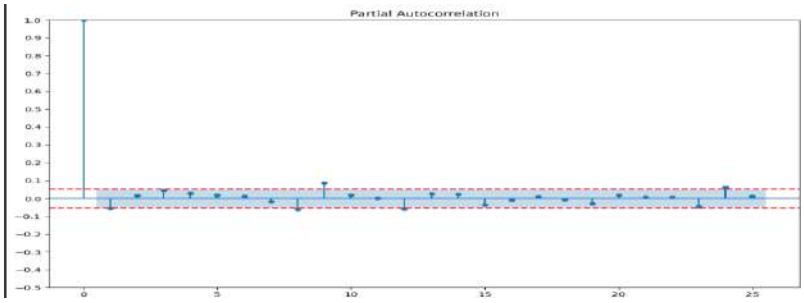

Figure 4: The partial autocorrelation plot (PACF)

The Figure 3 and Figure 4 above are the ACF and PACF plots respectively. The Figure 3 and Figure 4 which are ACF and PACF respectively plots will help us to identify a proper time series model. From the ACF and PACF above, we noticed that both ACF and PACF plots cut off at lag 1 with first order differencing of the data and this suggest ARIMA (1, 1,1).
However, model selection will be done in order to identify the best ARIMA model. This will be done by comparing the following models in Table 4 with the least Bayesian Information Criterion (BIC) and Akaike Criterion (AIC).

Table 4: Model selection using BIC and AIC Criteria

MODEL	AIC	BIC
(1, 1, 1)	24447.8	24488.99
(1, 1, 2)	24449.7	24489.03
(2, 1, 0)	24449.52	24489.58
(2, 1, 1)	24448.14	24489.47
(2, 1, 2)	24449.46	24491.06
(3, 1, 0)	24449.23	24489.56
(3, 1, 1)	24449.78	24495.37
(3, 1, 2)	24447.89	24489.75
(4, 1, 0)	24447.17	24489.77
(4, 1, 1)	24447.73	24489.6
(4, 1, 2)	24446.79	24488.92

From the Table 4, the ARIMA (4, 1, 2) model was selected as the best model because it is the model with the lowest BIC and AIC. Therefore, the suitable model is given as

$$X_t = \phi^1 X_t^{-1} + \phi^2 X_t^{-2} + \phi^3 X_t^{-3} + \phi^4 X_t^{-4} - \theta^1 a_t^{-1} - \theta^2 a_t^{-2} + a_t \quad (9)$$

3.1 Estimation of Parameters in the Model

Having identified the time series model, from the model summary table above it now suffices to estimate the parameters of the identified model.
Given the identified model

$$X_t = \phi^1 X_t^{-1} + \phi^2 X_t^{-2} + \phi^3 X_t^{-3} + \phi^4 X_t^{-4} - \theta^1 a_t^{-1} - \theta^2 a_t^{-2} + a_t \quad (10)$$

Parameter estimates are given in the Table 5

Table 5: Estimation of the parameters of the ARIMA model

	Coefficient	**std err**	**P>|z|**
x1	39.7607	36.074	0.270
ar.L1	-0.3389	0.343	0.323
ar.L2	0.5265	0.232	0.023
ar.L3	0.0883	0.020	0.000
ar.L4	0.0179	0.033	0.590
ma.L1	0.2832	0.344	0.411
ma.L2	-0.5237	0.222	0.018
sigma2	1.529e+06	3.02e+04	0.000

3.2. Diagnostic Checking of the ARIMA (4,1,2)

Here, we use the Ljung-Box Q statistic (Box and Jenkins, 1970; 1976), ACF and PACF of the residuals to check for the adequacy of the model.

Table 6: The ACF and PACF of the residuals

Lag	**ACF**	**PACF**
1	-0.000455985	-0.000456304
2	-0.000774606	-0.000775898
3	-0.000331506	-0.000332911
4	-0.000444035	-0.000446185
5	0.006523332	0.006545289
6	0.001963906	0.001977424
7	-0.027086259	-0.027209039
8	-0.054441547	-0.054807589
9	0.09171369	0.092487596
10	0.010856546	0.010831963
11	-0.005182379	-0.005558965
12	-0.052779478	-0.053605999
13	0.031815504	0.033839537
14	0.020537781	0.019526711
15	-0.036751871	-0.041469649
16	-0.008748064	-0.007415504
17	-0.003811585	0.008344863
18	-0.005729708	-0.013226141
19	-0.022197315	-0.029495679
20	0.022921473	0.020944824
21	-0.013533777	0.001827823
22	0.004509602	-0.000581552
23	-0.033788395	-0.045511259
24	0.057404787	0.064565964
25	0.0001866	0.006108688

The Ljung-Box statistic is defined as;

$Q = n(n+2)\sum_{i=1}^{k}\left(\frac{r_i^2}{n-i}\right) \sim \chi_m^2$

where;
n is the number of observations in the series
k is the largest lag (i.e from i=1,2,3,4,...,25)
r_i is the sample autocorrelation function at lag i of the residual series
Q has approximately the chi-squared distribution with (k-p-d-q) degree of freedom for ARIMA (p, d, q). Q is the Ljung-Box test statistic for checking the adequacy of the model.
m = the (k-p-d-q) degree of freedom of the chi squared distribution

Hypothesis Testing
$\boldsymbol{H_0}$: The model is adequate
$\boldsymbol{H_0}$: The model is not adequate
$\alpha = 0.05$
Test statistic:

Q-statistics=$n(n+2)\sum_{i=1}^{k}\left(\frac{r_i^2}{n-i}\right) \sim \chi_m^2$; p=1; q=0; d=0

Q- statistic = 34.210813

$\chi_m^2 = \chi_{k-p-d-q}^2 = \chi_{25-1-0}^2 = 37.65$

Decision Rule: Reject Ho if Q> χ_m^2; accept if otherwise

Conclusion: Since Q= 34.21 is less than χ_{24-1-0}^2 = 37.65, we do not reject the null hypothesis and therefore conclude that the model is adequate at $\alpha = 0.05$.

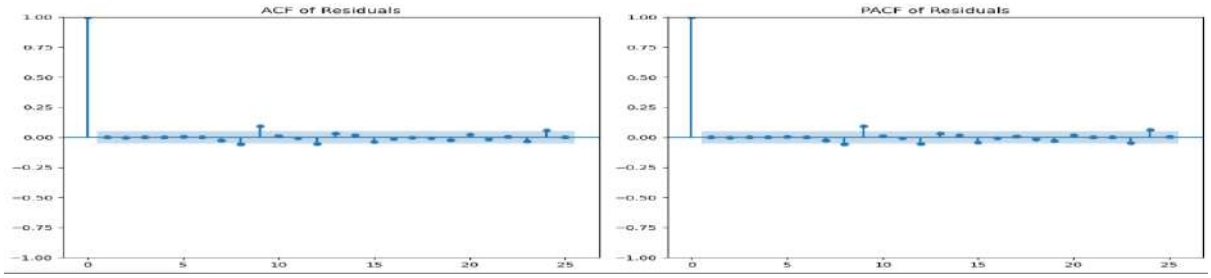

Figure 5: The residuals autocorrelation plot

On careful observation of thes plots in Figure 5, it can be seen that the ACF and PACF of the residuals fall withing 95% confidence interval and that means that the model is adequate.

3.3 . Forecasting

Since the adequacy of the model has been established by diagnostic checking, the model will now be used for forecasting. Now when the predicted values of the identified, estimated and diagnosed models are plotted as a function of time, they represent a relationship called forecast function.

Table 7: Forecasted Bitcoin prices with date

23/03/2024	64130.81032
24/03/2024	63885.57503
25/03/2024	63970.95028
26/03/2024	63838.88314
27/03/2024	63887.7894

28/03/2024	63865.36767
29/03/2024	63990.58976
30/03/2024	63922.0138
31/03/2024	63998.44677
01/04/2024	63999.18455
02/04/2024	63046.36469
03/04/2024	64168.30399
04/04/2024	69119.69772
05/04/2024	64146.93932
06/04/2024	64405.75273
07/04/2024	64226.56154
08/04/2024	64273.22564
09/04/2024	64306.50828
10/04/2024	64351.47103
11/04/2024	64386.50696
12/04/2024	64430.15963
13/04/2024	64466.4568
14/04/2024	64579.11655
15/04/2024	67500.33006
16/04/2024	64588.24434
17/04/2024	64626.1279
18/04/2024	62667.48571
19/04/2024	62557.86125
20/04/2024	62446.80513
21/04/2024	62785.54287
22/04/2024	64826.17952
23/04/2024	64865.18436
24/04/2024	64905.59329
25/04/2024	65044.7953
26/04/2024	64985.03558
27/04/2024	65024.38325
28/04/2024	65064.4987
29/04/2024	65103.95401
30/04/2024	68110.97709
01/05/2024	66100.51196

Table 7 shows forecasted Bitcoin prices with date for 40 days (March 23, 2024 through May 1, 2024). This forecast was made using ARIMA (4, 1, 2) that was selected using BIC and AIC Criteria

(see Table 4). The forecasting results showed that there are cyclical variations or cyclic movements in Bitcoin prices. This implies that the price of Bitcoin moves up and down at any time. The investors and traders need to comprehend the movements of Bitcoin prices before buying and selling take place.

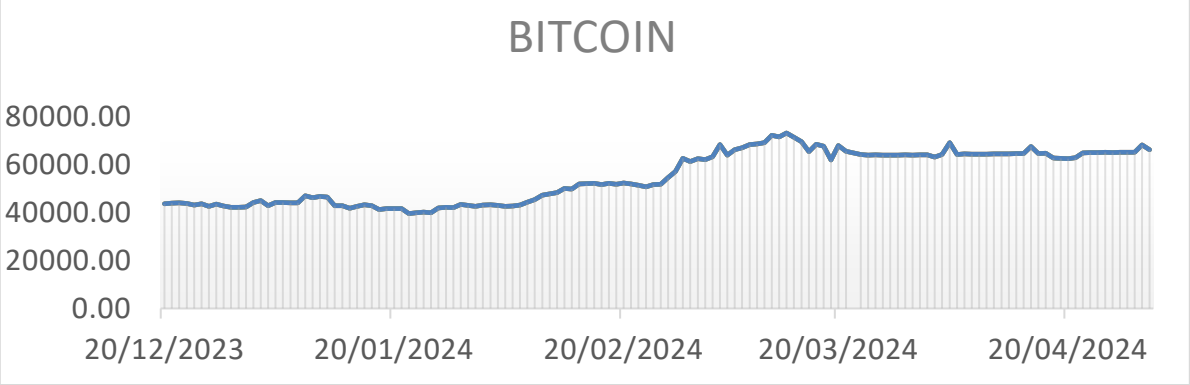

Figure 6: BITCOIN forecasted prices

Figure 6 is a plot for Bitcoin prices forecast. From this Figure 6, it can be seen that there is upward and downward trend in the Bitcoin prices. This trend movement is a confirmation of cyclical variation or cyclic movement in the price of Bitcoin. The understanding of up and down movement of the trend in Bitcoin prices helps people to know when to invest and buy Bitcoin. Hence, this shows that using the ARIMA (4, 1, 2) model, the required forecasts of the Bitcoin prices are possible.

4.1. Summary

In this study, there is a comprehensive analysis of Bitcoin price using Autoregressive Integrated Moving Average (ARIMA) model. The data used in this research are the historical Bitcoin price from April 21, 2020 to March 23, 2024. The dataset was obtained from Yahoo Finance API. The dataset was preprocessed to ensure its suitability for modeling. The analysis was done through the auto ARIMA function from the pmdarima library in python programming language version 3.12. In the course of the analysis, ARIMA model was fitted to the Bitcoin price data. Box and Jenkins approach was used to identify the model. It was observed that both ACF and PACF plots cut off at lag 1 with first order differencing of the data and this proposes ARIMA (1, 1, 1). Moreover, BIC and AIC were used in the model selection and ARIMA (4, 1, 2) was selected as the best model since it has minimum BIC and AIC values. The adequacy of the model was shown under Ljung-Box test. This implies that the residuals have been transformed into white noise and the model is good for prediction. The forecast results from the selected model provided valuable insights into potential price trends and fluctuations, empowering stakeholders to make decisions in the volatile cryptocurrency market.

4.2. Conclusion

In conclusion, the ARIMA model demonstrated its efficacy as a reliable tool for Bitcoin price prediction. By leveraging historical Bitcoin price data and capturing temporal patterns, the ARIMA model was able to generate accurate forecasts. The forecast results will aid the investors, traders, and policymakers in navigating the dynamic cryptocurrency landscape.

However, it's essential to acknowledge the inherent limitations of any predictive model, including ARIMA. While ARIMA excels in capturing linear dependencies and short-term trends, it may

struggle with complex nonlinear relationships and long-term forecasting. Therefore, future research endeavors could explore alternative modeling techniques, such as machine learning algorithms or hybrid models, to enhance prediction accuracy and robustness.

Despite its limitations, the ARIMA model remains a valuable asset in the toolkit of cryptocurrency analysts and enthusiasts. Its simplicity, interpretability, and proven track record make it a popular choice for time series forecasting tasks. As the cryptocurrency market continues to evolve, leveraging advanced analytics and predictive modeling techniques will be crucial for staying ahead of the curve and making informed decisions in this rapidly changing landscape.

References

Box, G. E. P., Jenkins, G. M., Reinsel, G. C., & Ljung, G. M. (2011). *Time series analysis: forecasting and control*. John Wiley & Sons.

Cheah, E. T., & Fry, J. (2015). Speculative bubbles in Bitcoin markets? An empirical investigation into the fundamental value of Bitcoin. *Economics Letters, 130*, 32-36.

Chen, M. K., Páez, F. D., & Trujillo, L. E. (2018). Cryptocurrency price prediction using ARIMA model. In Proceedings of the 2018 IEEE/ACM International Conference on Advances in Social Networks Analysis and Mining (pp. 1407-1410).

Eze, N. M**.**, Asogwa, O. C., Obetta, A. O., Ojide, K. C., Okonkwo, C. I. (2020). A Time Series Analysis of Federal Budgetary Allocations to Education Sector in Nigeria (1970-2018). *American Journal of Applied Mathematics and Statistics, 8(1): 1-8*. DOI:10.12691/ajams-8-1-1

Hayes, A. (2024, April 18). Technical Analysis Explained. Investopedia. Accessed on April 3, 2024. https://www.investopedia.com/terms/t/technicalanalysis.aspx.

McNally, S., Roche, J., & Thomas, A. (2018). Forecasting cryptocurrency returns using a generalized autoregressive conditional heteroscedasticity model. *The North American Journal of Economics and Finance, 47*(1), 104-114.

Shao, J., Yu, H., & Li, X. (2021). Deep learning for cryptocurrency price prediction: *A brief survey. Artificial Intelligence Review, 54*(6), 3727-3760.

SEGAL, M. (2023, January 10). Fundamental Analysis. Investopedia. https://www.investopedia.com/terms/f/fundamentalanalysis.aspx

Tsai, C. F., & Hsu, Y. F. (2018). A literature review on cryptocurrency price prediction using machine learning techniques. *Future Internet, 10*(11), 117.

Yu, H., Li, X., He, H., & Wang, X. (2021). A survey of cryptocurrency transaction prediction using machine learning. IEEE Transactions on Knowledge and Data Engineering.

Box, G. E. P., & Jenkins, G. M. (1976). Time Series Analysis: Forecasting and Control, 2nd ed. San Francisco: Holden Day

Box, George & Jenkins, Gwilym (1970). Time series analysis: Forecasting and control. San Francisco: Holden-Day

De Gooijer, J., Abraham, B., Gould, A., & Robinson, L. (1985). Methods for Determining the Order of an Autoregressive-Moving
Average Process: A Survey. International Statistical Review/Revue Internationale De Statistique, 53(3), 301-329

Zhihua, W., Yongbo, Z., & Huimin, F. (2014). Autoregressive Prediction with Rolling Mechanism for Time Series Forecasting with Small Sample Size.

Modelling Goal Scoring Patterns in the English Premier League (EPL): A Poisson Regression Approach

[1*]L.O. Mashood, [1]E. Alfred, [1]C.L. Ani, [2]T.O. Amuda, [3]Y.A. Bello, [1]J.Y. Anche, and [1]D.T. Aworokun

[1]Department of Statistics, Air Force Institute of Technology, Kaduna, Nigeria
[2]Department of Mathematics, Air Force Institute of Technology, Kaduna, Nigeria
[3]Department of Physics, Air Force Institute of Technology, Kaduna, Nigeria
[1*]Corresponding author: maslaw008@gmail.com

Abstract

This study uses cutting-edge statistical models to improve match outcome predictions as it examines the factors influencing goal scoring in the English Premier League (EPL) from the 2019 to 2023 seasons. Because of its inherent unpredictability, football, a popular sport worldwide, poses special challenges when it comes to result forecasting. The study is to determine the correlation between goal-scoring occurrences and statistical distributions, with a particular focus on the suitability of the alternative regression model and Poisson process. Analysis of data from 1,520 home and away games showed that, according to the Kolmogorov-Smirnov test, the distribution of goals among home teams is Poisson, but the distribution of goals among away teams' deviates, requiring the use of negative binomial regression for accurate modelling. In contrast, shots on target and corners were the factors that influenced the away team goal, which had a significant impact on scoring outcomes, with the most goals scored in January, February, August, and December. The Poisson regression for home goals highlighted important factors like shots on target, corners, total shots, and yellow cards. In addition to improving strategic methods to match outcome forecasting, this research has ramifications for managerial decision-making in both the sport and the betting sector. It also advances predictive analytics in football.

Keywords: Bet, EPL, Football, Gambling, Negative Binomial, Poisson

1. Introduction

One of the most popular games in the world, football or soccer, as it is known in some countries—captivates millions of people with its dramatic moments, especially during crucial goals. One of the most competitive and popular football leagues, the English Premier League (EPL) draws large crowds and has a significant economic impact (Freeman, 2012). Every season, supporters, pundits, and analysts look forward to the results of games, making result prediction an intricate but exciting process that combines statistical analysis, machine learning, and sports knowledge. The Premier League is well known for both its popularity and the unpredictable nature of match results. This uncertainty creates special difficulties in predicting outcomes, especially in figuring out how goal-scoring and statistical distributions relate to one another.

Beyond just sports analytics, the importance of predicting match results is crucial for managerial decisions about player transfers and market valuations (Müller, 2017). In the context of the expanding betting industry, which deals in millions of euros per match, it is critical for bettors who want to make money to understand the factors that influence outcomes. Previous research has emphasized the shortcomings of traditional crowd-sourced valuations, advocating for data-driven approaches to improve accuracy and transparency (Gomes *et al.*, 2016). Additionally, the unpredictable nature of football results has caught the attention of researchers, leading to a plethora of studies on football match predictions, primarily because of the sport's enormous popularity and the difficulty of forecasting results. Haruna (2021) asserts that football match prediction is not only a theoretical endeavour but also a practical requirement for both managers and bettors. Predictions are made more difficult by the game's intrinsic randomness, since some variables, including team dynamics, player skill, and weather, can significantly affect match outcomes (Alten-Ronaess, 2021).

From sophisticated machine learning algorithms to conventional statistical techniques, several approaches have been put forth to improve prediction accuracy. Poisson regression has become a popular technique for goal count prediction because of its applicability to count data (Horvat and Job, 2020). For example, the Poisson approach in conjunction with the Élö–Runyan rating system has shown encouraging accuracy rates in predicting match results (Windarto *et al.*, 2025). Nonetheless, the literature indicates that there are still disagreements about the effectiveness of various models, with many studies arguing that combining multiple statistical methods to better account for the complex nature of football is necessary (Wang, 2023). The Poisson distribution, which models the probability of a given number of events occurring within a fixed interval, has been used extensively in sports analytics (Çelik, 2021). Studies show that the distribution of goals scored in football matches frequently conforms to Poisson assumptions, allowing for more accurate predictions (Azhari *et al.*, 2018). However, issues like overdispersion, in which the variance is greater than the mean, necessitate the use of alternative models, such as negative binomial regression (Palmer *et al.*, 2007; Mashood *et al.*, 2023).

All things considered; the literature emphasizes how crucial it is to use reliable statistical models when analyzing the results of football games. This study aims to improve knowledge of the dynamics within the EPL by investigating the connections between different factors that affect goal scoring and incorporating cutting-edge predictive techniques. In the end, it will provide insightful information for both academic research and real-world applications in sports management and betting. Analysis of goal-scoring trends in the EPL using data from the 2019–2023 seasons is the aim of this study. Specifically, the consistency of goal-scoring with the Poisson process will be confirmed, and several statistical models will be examined for precise forecasts.

2. Materials and Methods

2.1 Data Collection and Pre-processing

This study utilized a secondary dataset comprising match results from the English Premier League (EPL) spanning the 2019 to 2023 seasons. The dataset was sourced from Football-Data.co.uk, which provides comprehensive historical data on football matches, including match outcomes, goals scored, and various match statistics. The total number of observations included in this analysis was 1,520 matches each for home and away matches. The season runs from August to May, with each 20 teams playing 38 matches – two against each other, one home and one away. Before analysis, the dataset underwent thorough pre-processing to ensure its suitability for statistical modelling. This involved the following steps:

a. **Data Cleaning:** Missing values were identified and addressed through imputation or removal, depending on the extent of the missing data. Duplicate entries were also eliminated to maintain data integrity.
b. **Descriptive Analysis:** Summary statistics were computed to assess the distributions of key variables, including goals scored by home and away teams, shots taken, and fouls committed. This allowed for an initial understanding of data patterns and distributions. A frequency table and line plot were generated to visualize the distribution of goals scored. This facilitated the identification of any over-dispersion or under-dispersion in the data, which is critical for selecting appropriate statistical models.

2.2 Statistical Modelling

To analyze goal-scoring patterns, Poisson regression [see equation (1)] was employed as the primary modelling technique. This method is particularly well-suited for count data, where the dependent variable, goals scored follows a Poisson distribution. The Poisson regression model was specified as follows, where λ represents the expected number of goals, and Y is the number of goals scored:

$$P(Y = y) = \frac{e^{-\lambda}\lambda^{y}}{y!}, y = 0,1,2,\ldots \quad (1)$$

Given the potential for over-dispersion in the dataset, negative binomial regression given in equation (2) was also utilized as an alternative modelling approach. This model allows for variance to exceed the mean (over-dispersion), addressing the limitations of the Poisson assumption that the mean equals the variance (equi-dispersion). The negative binomial regression model was formulated as, where λ is the mean count, and ϕ is the dispersion parameter:

$$Y \sim NB(\lambda, \phi)$$

$$P(Y = y) = \frac{\Gamma(\phi + y)}{\Gamma(\phi)\Gamma(y+1)}\left(\frac{\phi}{\phi+\lambda}\right)^{r}\left(1-\frac{\phi}{\phi+\lambda}\right)^{y}, y = 0,1,2,\ldots \quad (2)$$

2.3 Goodness-of-Fit Test and Model Evaluation

The goodness-of-fit of both models was assessed using the Kolmogorov-Smirnov (K-S) test, which compares the empirical distribution of the observed data to the expected Poisson distribution. All statistical analyses were conducted using R Statistical programming (R Core Team, 2023). Statistical significance was set at an alpha level of 0.05 for all tests conducted.

3. Results and Discussion

The analysis of the dataset highlighted major trends in goal scoring across the English Premier League (EPL) from the 2019 to 2023 seasons. The total number of matches evaluated was 3,040, covering both home and away games. Figure 1 shows the trends of goals scored at Full-Time Home Goal (FTHG) and Full-Time Away Goal (FTAG) in all 380 home and away games during the four seasons, for a total of 3,040 games considered for this analysis.

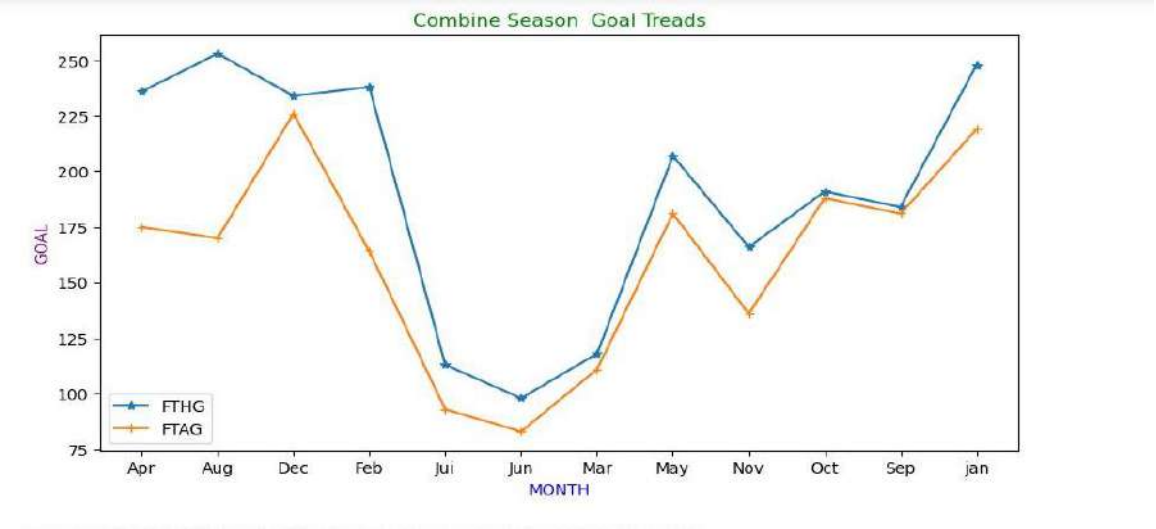

Figure 1: Trend of Full-Time Home and Away Goals Across 2019 to 2023 Seasons

The "Combine Season Goal Trends" Figure 1 shows the monthly goal trends for FTHG and FTAG over four years. Although the FTHG fluctuates throughout the year, August marks a significant surge when home goals hit their highest point, approximately 250. March and November see a sharp decline in the trend, suggesting that fewer goals are scored at home during these months. With distinct peaks and troughs, the FTAG reflects some of the FTHG tendencies. Interestingly, FTAG peaks in December and then falls to a low in March. This implies that as the season comes to a close, away teams can find it difficult to score in the latter months. However, both metrics (FTHG and FTAG) display seasonal changes, demonstrating that goal scoring fluctuates throughout the year. Goal-scoring peaks may correspond with particular times of the season, such the middle of the season, when teams are either doing well or have important games to play. In most months, FTHG seems to be higher than FTAG, suggesting that home teams typically score more goals than away teams. Nonetheless, there are months when away goals increase noticeably, indicating that away clubs might perform well under specific circumstances.

Table 1: Frequency Distribution of Goals Scored

Number of Goals	Home Matches (%)	Away Matches (%)
0	370 (24.34)	480 (31.58)
1	500 (32.89)	498 (32.76)
2	351 (23.09)	311 (20.46)
3	182 (11.97)	153 (10.07)
4	74 (4.87)	52 (3.42)
5	28 (1.84)	20 (1.32)
≥6	15 (0.99)	6 (0.39)
Total	**1520**	**1520**

The most frequent result for both home and away teams, according to the frequency distribution of goals scored, was one goal per game. The 500 games in which home teams scored one goal accounted for roughly 33% of all home games, as indicated in Table 1.

Table 2: Summary Statistics of Goals Scored

Season	Home Goals (Mean ± SD)	Away Goals (Mean ± SD)
2019/2020	1.516 ± 1.559	1.205 ± 1.440
2020/2021	1.353 ± 1.743	1.342 ± 1.581
2021/2022	1.513 ± 1.759	1.305 ± 1.584
2022/2023	1.634 ± 1.218	1.218 ± 1.400

Table 2 displays descriptive statistics for the goals scored by the home and away teams. While away teams scored an average of 1.342 to 1.218 goals throughout the same seasons, home teams scored an average of 1.353 goals in the 2020–2021 season and 1.634 goals in the 2022–2023 season. The fluctuation in goals scored suggests that recent seasons have seen an increase in the number of goals scored at home.

Table 3: Goodness-of-Fit Test Results

Goals Type	P-value
Home Goals	0.0547
Away Goals	0.0366

A Kolmogorov-Smirnov (K-S) test was employed to test for goodness of fit in order to determine if the distribution of goals follows a Poisson distribution, as seen in Table 3. A negative binomial model would be more suitable for away goals, since the K-S test revealed that while away goals had substantial deviations (p-value < 0.05), home goals did not significantly differ from a Poisson distribution (p-value = 0.0547).

Table 4: Regression Models Results

Variables	Poisson		Negative Binomial	
	Estimates	**P-value**	**Estimates**	**P-value**
Intercept	0.0748	0.6518	–0.3197	0.0694
Home team shots	–0.0153	**< 0.05**	–0.0055	0.4801
Home team shot on target	0.2035	**< 0.05**	–0.0148	0.3256
Home team corners	–0.0360	**< 0.05**	0.0098	0.3801
Home team fouls committed	–0.0004	0.9598	–0.0124	0.1553
Home team yellow cards	–0.0777	**< 0.05**	0.0114	0.6396
Home teams' red cards	–0.1669	0.2011	0.0519	0.5961
Away team shots	–0.0094	0.2605	–0.0028	0.7578
Away team shot on target	0.0035	0.8254	0.2140	**< 0.05**
Away team corners	–0.0038	0.7450	–0.0449	**< 0.05**
Away team fouls committed	–0.0090	0.2421	–0.0009	0.9132
Away team yellow cards	–0.0000	0.9978	–0.0006	0.9820
Away teams’ red cards	0.0509	0.5541	–0.1647	0.2821

The outcomes of the Poisson and negative binomial regression models are shown in Table 4. The number of shots, shots on goal, yellow cards, and corners were among the important predictors found in the Poisson regression analysis for home goals. According to the model, a higher number of shots on goal was linked to a higher number of goals scored at home ($p < 0.05$). On the other hand, it was discovered that more corners had a negative correlation with home goals, indicating that more corners could not always result in scoring opportunities. The number of shots, corners, and yellow cards decreased by roughly 2%, 4%, and 8%, respectively, for every goal rise in the home team's score, but the number of shots on goal increased by more than 20%.

For away goals, the negative binomial regression identified significant variables as well, including shots on target and corners ($p < 0.05$) as relevant determinants. The findings showed that the away side's shots on goal rose by almost 21% for every unit rise in the anticipated number of away team goals. The away team's number of corners decreased by 4% for every goal that the away team's

score increased.

4. Conclusion

Using strong statistical techniques, this study offers a thorough examination of goal-scoring trends in the Premier League from the 2019–2023 season, revealing important information about both home and away goal trends. The study successfully tackles the challenges of forecasting match results in a fiercely competitive and dynamic setting by employing both Poisson and negative binomial regression models.

In line with the widely held belief that playing at home gives a team a competitive edge, the results show that home teams generally have greater goal-scoring averages than away teams. The league's increasing competitiveness and tactical innovation are reflected in the trend of rising goal totals in recent seasons, which highlights the necessity for teams to employ aggressive tactics to win. The study also reveals that away goals exhibit over-dispersion, requiring the adoption of alternate modelling techniques to improve prediction accuracy, whilst home goals typically match Poisson distribution assumptions. Important goal-scoring indicators like shots on goal and corners were found to have a significant impact on both home and away goals, underscoring the crucial part offensive strategies play in deciding game results. Shots on target and goals scored have a positive correlation, which emphasizes how crucial offensive qualities are to winning games. On the other hand, the discovered inverse relationship between home goals and corners raises the possibility that merely accruing set-piece opportunities may not result in successful scoring. Teams may be prompted by this discovery to improve their corner tactics to maximize scoring opportunities.

Beyond scholarly research, this study has practical applications for football managers, analysts, and wagerers. By emphasizing the dynamics of goal scoring and the impact of many elements, this study gives stakeholders information based on statistics that can guide their decision-making. As the field of sports analytics develops further, incorporating these discoveries into useful apps might improve betting and team performance tactics. Additionally, bettors can improve their methods by using these prediction models, which will ultimately increase betting market profitability.

In conclusion, this study opens up new research directions while also adding to the corpus of material already available on football analytics. To improve forecasts and broaden knowledge of the complex dynamics of goal scoring in football, future research should include more variables including player data, tactical configurations, and outside variables like the weather. In addition to being an intellectual endeavor, the search for knowledge in this area is essential to improving spectator satisfaction and performance in one of the most popular sports in the world.

References

Alten-Ronæss, J. (2021). *Predictions of Football Results in the Premier League and its Use on the Betting Market* (Master's thesis, NTNU).

Azhari, H.R., Widyaningsih, Y., & Lestari, D. (2018, November). Predicting Final Result of Football Match Using Poisson Regression Model. In *Journal of Physics: Conference Series* (Vol. 1108, No. 1, p. 012066). IOP Publishing. https://doi.org/10.1088/1742-6596/1108/1/012066

Çelik, S. (2021). Predicting the Number of Goals in Football Matches with the Poisson distribution: Example of Spain La Liga. *Scholars Journal of Physics, Mathematics and Statistics*, *8*(8), 133-142. https://doi.org/10.36347/sjpms.2021.v08i08.002

Freeman, K. (2012). Sport as Swaggering: Utilizing Sport as Soft Power. *Sport in Society*, *15*(9), 1260-1274.

Gomes, J., Portela, F., & Santos, M.F. (2016). Pervasive Decision Support to Predict Football Corners and Goals by Means of Data Mining. In *New Advances in Information Systems and Technologies*: *Volume 2* (pp. 547-556). Springer International Publishing.

Haruna, U., Maitama, J.Z., Mohammed, M., & Raj, R.G. (2021, November). Predicting the Outcomes of Football Matches Using Machine Learning Approach. In *International Conference on Informatics and Intelligent Applications* (pp. 92-104). Cham: Springer International Publishing.

Horvat, T., & Job, J. (2020). The Use of Machine Learning in Sport Outcome Prediction: A Review. *Wiley Interdisciplinary Reviews: Data Mining and Knowledge Discovery*, *10*(5), e1380.

Mashood, L.O., Balogun, O.S. and Akingbade, T.J. (2023). *An Application of Count Models to the Number of Antenatal Care Service Visits*. In Handbook of Research on Quality and Competitiveness in the Healthcare Services Sector (pp. 264-281). IGI Global. https://doi.org/10.4018/978-1-6684-8103-5.ch016

Müller, O., Simons, A., & Weinmann, M. (2017). Beyond Crowd Judgments: Data-driven Estimation of Market Value in Association Football. *European Journal of Operational Research, 263*(2), 611-624.

Palmer, A., Losilla, J.M., Vives, J., & Jiménez, R. (2007). Overdispersion in the Poisson Regression Model. *Methodology*, *3*(3), 89-99.

R Core Team. (2023). R: A language and environment for statistical computing. *Foundation for Statistical Computing, Vienna, Austria*.

Wang, W. (2023). The Role of Big Data in Enhancing Sports Performance Analytics. *International IT Journal of Research, ISSN: 3007-6706*, *1*(1), 33-39. https://itjournal.org/index.php/itjournal/article/view/12

Windarto, A.P., Alkhairi, P., & Muslim, J. (2025). Enhancing Premier League Match Outcome Prediction Using Support Vector Machine with Ensemble Techniques: A Comparative Study on Bagging and Boosting. *Jurnal RESTI (Rekayasa Sistem dan Teknologi Informasi)*, *9*(1), 94-103.

Clustering Analysis of Rice Yield Per Hectare Using Data Mining Techniques: Insights from Northeast Nigeria

[1*]Ezra Daniel Dzarma, [2]Ngutor Nyor, [3]Mohammed Jiya and [4]Andrew Saba Gana

[1,2,3]Department of Mathematics, Federal University of Technology, Minna, Nigeria.

[4]Department of Crop Production, Federal University of Technology, Minna, Nigeria.

[*]Email: dzarma2002@gmail.com, +2348088846156

Abstract

This study applied clustering techniques to analyze rice yield data from Northeast Nigeria, identifying five distinct clusters based on yield variations. Using the LQR algorithm in WEKA, the analysis revealed significant differences in productivity, with Cluster 3 achieving the highest mean yield (6107.28 kg/ha) due to advanced technologies and resource optimization, while Cluster 0 recorded the lowest mean yield (3131.32 kg/ha), reflecting limited access to inputs and poor farming practices. The findings highlight the need for tailored interventions, including improved seeds, irrigation systems, and mechanization, to enhance productivity across clusters. This research demonstrates the potential of data mining in agricultural optimization and provides actionable insights for farmers and policymakers to address regional disparities and improve food security.

Keywords: Rice production; Clustering analysis; Agricultural data mining; Northeast Nigeria; Yield variability; LQR algorithm; Sustainable farming practices.

Keywords: Rice production; Clustering analysis; Agricultural data mining; Northeast Nigeria; Yield variability; LQR algorithm; Sustainable farming practices.

1. INTRODUCTION

Rice is a staple food for billions of people worldwide and plays a crucial role in ensuring food security, particularly in developing countries. In Nigeria, rice is both a key dietary staple and a significant agricultural commodity contributing to the economy (FAO, 2018; Ogundele & Okoruwa, 2006). Despite its importance, the productivity of rice farming in Nigeria remains inconsistent, with yields often below global averages. Understanding the factors that influence rice production and identifying patterns in yield data are critical for optimizing agricultural practices and achieving food security goals (Takeshima *et al*., 2013; Ojo *et al*., 2024, Dzarma *et al.,* 2024a).

Data mining techniques, including clustering algorithms, have proven effective in extracting meaningful insights from large datasets across various domains, including agriculture (Han *et al*., 2011; Patil & Kumar, 2012). Clustering is particularly useful in segmenting datasets based on similarities, enabling researchers to identify distinct groups with shared characteristics (Jain, 2010). Tools like WEKA, a widely used machine learning software, offer robust frameworks for implementing clustering techniques and analyzing agricultural data (Hall *et al.*, 2009). This

study employs WEKA and the LQR clustering algorithm to investigate rice yield patterns in Northeast Nigeria, providing a data-driven perspective on productivity trends.

The agricultural landscape of Northeast Nigeria presents unique challenges and opportunities. The region is characterized by varying climatic conditions, soil types, and farming practices, which significantly influence rice yield outcomes (Idu *et al,*, 2013; Nwite *et al*., 2016). By applying clustering analysis to rice yield data, this study aims to uncover patterns that reflect these regional dynamics. The findings offer insights that can inform policy-making, improve resource allocation, and enhance farming practices tailored to specific clusters.

This paper presents the results of clustering analysis applied to rice input-output data from Northeast Nigeria. Five distinct clusters were identified, each with unique yield ranges, means, and distributions. The study's findings contribute to a growing body of literature on the application of data mining in agriculture and provide actionable insights for stakeholders seeking to improve rice productivity in Nigeria.

2. LITERATURE REVIEW

2.1. Rice Production in Nigeria: Trends and Challenges

Rice plays a critical role in Nigeria's agricultural economy and food security framework. Despite significant government initiatives and investments, rice production in Nigeria has not met the rising domestic demand (Takeshima *et al*., 2013; FAO, 2018 Dzarma *et al.,* 2024b). Factors such as climate variability, inadequate infrastructure, limited access to improved seed varieties, and inefficient farming practices contribute to the yield gap (Oluwatusin, 2014; Fadipe *et al.*, 2014). Previous studies have highlighted Northeast Nigeria as a region with significant potential for rice production, but its productivity is hindered by erratic rainfall, poor soil fertility, and socio-political instability (Ahmad *et al.*, 2021;Ogundari, 2014). Understanding regional variations in rice yield is essential for developing tailored solutions.

2.2 Application of Data Mining Techniques in Agriculture

Data mining techniques have emerged as powerful tools for analyzing complex agricultural datasets, enabling the identification of patterns and insights that traditional methods may overlook (Han *et al*., 2011; Patil & Kumar, 2012). Among these techniques, clustering has been widely used to segment agricultural data into meaningful groups based on attributes such as yield, soil type, and climatic conditions. Tools like WEKA provide a user-friendly interface for implementing machine learning algorithms, including clustering methods such as k-means, hierarchical clustering, and LQR clustering (Hall *et al*., 2009). Studies have successfully applied clustering to optimize crop management strategies, assess soil quality, and forecast agricultural outputs (Jain, 2010; Chlingaryan *et al.,* 2018). However, few studies have focused on clustering analyses of rice production data specific to Nigeria.

2.3 Regional Clustering of Agricultural Productivity

Clustering methods are widely recognized for their effectiveness in identifying spatial and temporal variations in agricultural productivity. These methods group similar units based on yield, input characteristics, or other relevant features, enabling targeted interventions that can address specific challenges and optimize resource use (Patil & Kumar, 2012; Jain, 2010). In Northeast Nigeria, where rice production is critical to livelihoods and food security, clustering provides valuable insights into the underlying factors influencing productivity disparities. These factors include input utilization, climatic conditions, soil fertility, and farming practices, which collectively shape yield outcomes (Abdulrahman *et al*., 2015). For example, previous studies in sub-Saharan Africa have demonstrated that clustering can effectively highlight regions where poor irrigation systems are the primary constraint to productivity (Ogunlela & Ogungbile, 2006).

The application of clustering in agricultural analysis is not limited to Nigeria; studies in other developing countries have demonstrated its utility in addressing regional disparities. For instance, research in India used clustering to identify high-potential zones for rice production, leading to targeted interventions that significantly improved productivity (Gopal & Malathi, 2015). Similarly, a study in Indonesia utilized clustering to evaluate the effects of farm management practices on yield stability, highlighting areas where improved techniques could reduce yield variability (Rahman & Wijaya, 2019). Southeast Asia has also benefited from clustering analyses that integrate climatic and soil data to develop precision agriculture systems (Kamilaris *et al*., 2017). These examples highlight the versatility of clustering methods in agricultural contexts, particularly in enhancing decision-making and promoting equitable resource allocation.

Moreover, clustering enables the integration of socio-economic and environmental data, offering a holistic understanding of agricultural systems. By incorporating factors such as market access, labor availability, and crop management practices, clustering can support the development of comprehensive policies that address both productivity and sustainability (Yusuf *et al*., 2021). Research in East Africa has demonstrated that combining clustering with geographic information systems (GIS) provides more precise recommendations for optimizing agricultural land use (Li *et al*., 2021). Similarly, integrating clustering with machine learning algorithms has proven effective in analyzing complex datasets, offering predictive insights for resource management in agriculture (Sarker *et al*., 2021). The growing use of data mining techniques, including clustering, underscores their potential to revolutionize agricultural planning and policy design globally.

3. METHODOLOGY

This study employed a data-driven approach to analyze rice yield data from Northeast Nigeria, utilizing clustering techniques to identify patterns and trends. The methodology consisted of four key stages: data collection, preprocessing, clustering analysis, and interpretation of results.

3.1 Data Collection

Data on rice inputs and outputs were collected from agricultural surveys and local government agricultural offices in Northeast Nigeria. The dataset included key variables such as yield per

hectare, input types (e.g., fertilizers, seeds, labor), and environmental factors. The data represented five states within the region, covering both wet and dry farming seasons over five years. Data collection followed established standards for agricultural surveys to ensure accuracy and representativeness (FAO, 2018; Takeshima *et al*., 2013).

3.2 Data Preprocessing

Before analysis, the data underwent preprocessing to handle missing values, outliers, and inconsistencies. Missing values were addressed using mean imputation for numerical variables, while outliers were identified and treated using Z-score thresholds. Data normalization was applied to scale variables to a uniform range, as clustering algorithms are sensitive to scale variations (Han *et al*., 2011; Jain, 2010).

3.3 Clustering Analysis

The clustering analysis was conducted using the WEKA software, a widely recognized tool for machine learning and data mining (Hall *et al*., 2009). The LQR clustering algorithm was chosen for its efficiency in handling large datasets and its ability to identify clusters with varying densities and distributions (Patil & Kumar, 2012). Key steps included:

Cluster Identification: The optimal number of clusters was determined using the Silhouette Coefficient and Davies-Bouldin Index.

Cluster Assignment: Data points were grouped into clusters based on yield per hectare, with each cluster representing a distinct pattern in productivity.

Cluster Characteristics: The minimum, maximum, and mean yields per hectare were calculated for each cluster to provide descriptive insights.

3.4 Interpretation and Validation

The results of the clustering analysis were interpreted to identify patterns and trends in rice yield. Each cluster was analyzed to determine its unique characteristics, including input utilization and environmental conditions. Validation of the clustering results was performed using cross-validation techniques and comparison with known regional agricultural trends (Abdulrahman *et al.*, 2015; Gopal & Malathi, 2015).

This methodology integrates best practices in data mining and agricultural analysis to provide a robust framework for understanding rice yield variability in Northeast Nigeria. The findings offer actionable insights for policymakers, researchers, and farmers aiming to enhance productivity and resource allocation.

4. RESULTS AND DISCUSSION

The clustering analysis segmented the rice yield data into five distinct clusters as shown in Table 4.1, each representing unique patterns in productivity. The minimum, maximum, and mean yields per hectare within each cluster revealed variations that reflect the influence of input usage, environmental factors, and farming practices.

Table 4.1 Cluster result

	Custer 0	Custer 1	Custer 2	Custer 3	Custer 4
Minimum	200kg	2034kg	3000kg	4188	2000
Maximum	5150kg	7000kg	4000kg	10000	6960
Mean	3131.3195kg	4593.486kg	3600kg	6107.2783	4523.26kg

4.1 Cluster 0: Low-Yield Group

Cluster 0 had a minimum yield of 200 kg/ha and a maximum yield of 5150 kg/ha, with an average yield of 3131.32 kg/ha. This cluster likely represents farms constrained by limited access to high-quality seeds, fertilizers, or irrigation. These findings align with studies indicating that smallholder farmers in Northeast Nigeria often lack sufficient inputs and resources to maximize productivity (Babatunde *et al.*, 2019; Takeshima *et al.*, 2013). Targeted interventions, such as subsidies for fertilizers and improved seed distribution, could enhance yields in this group.

4.2 Cluster 1: Moderate-Yield Group

Cluster 1 reported a minimum yield of 2034 kg/ha and a maximum of 7000 kg/ha, with an average yield of 4593.49 kg/ha. This cluster represents farms achieving moderate yields, possibly due to balanced input utilization and favorable environmental conditions. However, the variability suggests inconsistent access to mechanization or extension services. Studies by Yusuf *et al*. (2021) and Oluwatusin (2014) emphasize the importance of consistent farmer training and support in bridging yield gaps within this category.

4.3 Cluster 2: High-Yield but Narrow Range

Cluster 2 had yields ranging from 3000 kg/ha to 4000 kg/ha, with a mean of 3600 kg/ha. The narrow range indicates a group of farms with relatively standardized practices and conditions. Such homogeneity may result from localized interventions or natural advantages, such as fertile soil or reliable rainfall (Abdulrahman *et al.*, 2015). This cluster demonstrates the potential of replicating successful farming practices across similar regions to boost overall productivity.

4.4 Cluster 3: High-Yield Elite Group

Cluster 3 recorded the highest mean yield of 6107.28 kg/ha, with yields ranging from 4188 kg/ha to 10000 kg/ha. Farms in this cluster likely represent best-practice adopters who have access to modern equipment, efficient irrigation systems, and high-quality inputs. This aligns with findings by Takeshima *et al*. (2013), who noted that farms employing mechanization and advanced technologies in Nigeria achieve significantly higher productivity. Scaling such technologies to other clusters could uplift overall production levels.

4.5 Cluster 4: Diverse-Yield Group

Cluster 4 demonstrated a wide range of yields, from 2000 kg/ha to 6960 kg/ha, with an average of 4523.26 kg/ha. The diversity suggests mixed farming practices and varying levels of input availability. Environmental variability, such as soil fertility and rainfall distribution, likely contributes to this disparity. Studies by Babatunde *et al*. (2019) and FAO (2018) highlight the need for adaptive strategies tailored to local conditions, including climate-resilient farming techniques and soil fertility management.

4.6 Implications of the Results

The clustering analysis underscores the heterogeneous nature of rice farming in Northeast Nigeria. Each cluster represents unique challenges and opportunities for improving productivity. Policy implications include:

Targeted Interventions: Resources should be allocated based on cluster-specific needs, such as inputs for Cluster 0 or mechanization for Cluster 3.

Extension Services: Farmer training programs should focus on disseminating best practices from high-yield clusters (Cluster 3) to lower-performing clusters (Cluster 0 and Cluster 4).

Infrastructure Development: Investment in irrigation systems and access to markets could stabilize and enhance yields across clusters, especially Clusters 1 and 4.

These findings contribute to the growing literature on agricultural data mining and provide actionable insights for policymakers and stakeholders in Nigeria’s rice production sector.

5. CONCLUSION

This study applied clustering analysis to assess rice yield variability in Northeast Nigeria, using WEKA and the LQR algorithm to identify five distinct clusters. The results revealed significant yield disparities, influenced by input use, environmental factors, and farming practices. Clusters 0 and 4, with low-to-moderate yields, require targeted support, such as access to quality inputs and modern farming training. Cluster 3, with the highest yields, highlights the potential of advanced technologies and resource management. The findings stress the importance of region-specific agricultural policies, adaptive strategies, and future research to optimize rice production and food security in Nigeria.

6. RECOMMENDATIONS

Access Government Subsidies: Take advantage of government programs that provide subsidies on fertilizers, seeds, and machinery.

Adopt Digital Solutions: Use mobile applications for weather forecasting, pest management, and market price updates to make informed decisions.

Collaborate with Agricultural NGOs: Partner with non-governmental organizations offering training, inputs, and financial support tailored to rice farming.

REFERENCES

Ahmad, H. A., Lamane, S. A., & S. Zainal, M. (2024). Clustering of rice production in South Sulawesi of January-April 2022 and 2023 period. *Journal of Global Sustainable Agriculture,* 5(1), 1-10. https://doi.org/10.32502/jgsa.v5i1.332

ANwite, J. C., Onunwa, A. O., Igwe, C. A., & Wakatsuki, T. (2016). Sawah rice farming eco-technology options for enhancing sustainable nutrient management and rice production in degraded inland valleys of southeastern Nigeria. *International Journal of Plant & Soil Science,* 9(4), 1–19

Chlingaryan, A., Sukkarieh, S., & Whelan, B. (2018). Machine learning approaches for crop yield prediction and nitrogen status estimation in precision agriculture: A review. *Computers and Electronics in Agriculture*, 151, 61-69.

Dzarma, E. D., Nyor, N., Jiya, M., & Gana, A. S. (2024)a. Rice production goal prioritization in north-east nigeria: the analytic hierarchy process (ahp) approach. *Journal of Economics and Allied Research* Vol. 9, Issue 4, pp.131-141

Dzarma, E. D., Nyor, N., Jiya, M., & Gana, A. S. (2024)b. Optimization of Rice Yield in Gombe State, North-East Nigeria with Machine Learning. *Adeleke University Journal of Engineering and Technology*, 7(2), 065-068.

Fadipe, A. E. A., Amolegbe, K. B., & Afun, O. O. (2014). Food security and university agricultural students' involvement in food production after graduation. *Journal of Research in Forestry, Wildlife and Environmental*, 6(1), 67-80.

FAO (2018). Rice Market Monitor. *Food and Agriculture Organization of the United Nations.*

Han, J., Kamber, M., & Pei, J. (2011). Data Mining: Concepts and Techniques. Elsevier.

Hall, M., Frank, E., Holmes, G., Pfahringer, B., Reutemann, P., & Witten, I. H. (2009). The WEKA data mining software: An update. *ACM SIGKDD Explorations Newsletter.*

Jain, A. K. (2010). Data clustering: 50 years beyond k-means. *Pattern Recognition Letters.*

Kamilaris, A., Kartakoullis, A., & Prenafeta-Boldú, F. X. (2017). A review on the practice of big data analysis in agriculture. Computers and Electronics in Agriculture, 143, 23–37. Doi: https://doi.org/10.1016/j.compag.2017.09.037

Li, X., Zhang, Y., & Wang, X. (2020). Clustering approach to group similar soils for efficient agricultural land use planning. *Agricultural Systems,* 181, 102790. https://doi.org/10.1016/j.agsy.2020.102790

Ogundari, K. (2014). The paradigm of agricultural efficiency and productivity measurement: A survey of recent trends in literature. *AgBioForum*, 17(2), 1–14.

Ogundele, O. O., & Okoruwa, V. O. (2006). Technical efficiency differentials in rice production technologies in Nigeria. *African Economic Research Consortium*.

Idu, E. E., Fadiji, T. O., & Chimdi, A. (2023). Effect of Climate Variability on Rice Production in North-Central, Nigeria from 1980–2020. Direct Research Journal of Agriculture and Food Science, 11(4), 78–89..

Patil, S., & Kumar, M. (2012). Applications of clustering in data mining: A review. I*nternational Journal of Computer Science Issues*, 9(3), 105-110.

Sarker, I. H., Kayes, A. S. M., & Watters, P. (2021). Effectiveness Analysis of Machine Learning Classification Models for Predicting Personalized Context-Aware Smartphone Usage. *Journal of Big Data,* 6(1), 1–28

Takeshima, H., Onyeka, U., & Adeoti, A. (2013). Trends and determinants of rice productivity in Nigeria. *Journal of Agricultural Research*, 8(2), 215-227.

Vector Autoregressive Model and Autoregressive Distributed Lag in the Effectiveness of Monetary Policy in Controlling Inflation in Nigeria

Abdulsalam. A and M. O. Adetutu
Department of Statistics, Federal University of Technology, Minna, Niger State.
Corresponding author's email: abdulsalama631@gmail.com or

Abstract

The research investigated the effectiveness of vector autoregressive model and autoregressive distributed lag in controlling inflation using monetary policy in Nigeria. Secondary quarterly data spanning from 1999Q1 to 2023Q4 with Money Supply, Treasury bills rate, monetary policy rate and exchange rate were adopted as control variables to investigate their relationship with inflation and to assess the dynamic Correlations among instruments used in monetary policy inflation in the Nigeria economy. Long run relationship between the variables were established by co-integration test, stationarity was achieved after first differencing, Ordinary Least Square (OLS) was use to estimate the parameter of the model. The research discovered that exchange rate and money supply has a uni-directional causality with inflation and inflation has a uni-directional relationship with monetary policy rate while exchange rate has a bi-directional relationship with money supply. While the empirical result of vector autoregressive and autoregressive distributed the empirical findings suggest that the monetary policy rate, money supply, and Treasury bill rates have a statistically significant positive effect on inflation in Nigeria. Moreover, exchange rate depreciation is associated with an acceleration in inflationary pressures.. But ARDL give the best result base on the model performance from the analysis using akaike information criterion (AIC). INF AIC = 4.500590, EXG AIC = 8.363651, M2 AIC = 16.88217 which are less than that of VECM. The findings align with the expectations of economic theory. Consequently, the study concludes that money supply, treasury bill rates, monetary policy, and exchange rates significantly influenced inflation during the period examined. Based on this, the study offers the following recommendations: Gradual increases in MPR can reduce demand-pull inflation without causing undue economic disruption and Implement To control the money supply and curb inflationary pressures, the monetary authorities should strengthen the use of open market operations and reserve requirements. Additionally, there is a need to conduct a fresh analysis of the monetary policy rate's effectiveness, as it proved inadequate in managing Inflation dynamics in Nigeria throughout the examined timeframe.

1.0 INTRODUCTION

Economic growth stands as a fundamental policy goal for any government, given its pivotal role in alleviating poverty, fostering employment opportunities, and narrowing the inequality gap (Anowor, 2016). It elevates the general standard of living, facilitates more equitable income distribution, and hastens the provision of essential needs for the majority (Uwakaeme, 2015). Measured With regard to per capita income, economic growth signifies the overall output of the economy output of goods and services produced within a country For a selected year, adjusted for population size(Uwakaeme, 2015). This output is influenced by a nation's The availability of economic resources, along with the scale and expertise of the labor for**ce** level of its labor force,

and the technological efficiency of its capital stock. Thus, the pace of economic growth hinges on the expansion of these resources—both physical and human—as well as improvements in overall productivity (Okwo, 2012).

While monetary policy is widely recognized as a key driver of economic growth and development due to its influence on various economic indicators (Anowor, 2016), the exact role of money in the economy remains a contentious topic among modern economists. Money directly impacts aggregate expenditure by affecting the availability of credit and indirectly through its influence on interest rates. A lower interest rate environment tends to expand the money supply, which often correlates with higher inflation levels (Okwo, 2012). Changes in money demand also alter interest rates, which subsequently influence investment demand—ultimately leading to shifts in national income (Okwo, 2012).

Monetary policy is traditionally viewed as a core tool for economic stabilization. It is employed to regulate the volume, pricing, accessibility, and flow by regulating money and credit to accomplish specific macroeconomic objectives (Obadeyi, 2016). Among the various transmission mechanisms, interest rates are perhaps the most significant. As interest rates climb, the financial burden of loans intensifies. , thereby dampening components of aggregate demand that are sensitive to interest changes. Moreover, rising short-term interest rates lower asset prices, reducing consumption via the wealth effect and discouraging investment through Tobin's q-theory (Ridhwana, 2014).Another notable transmission mechanism is the credit channel, where tighter monetary policy leads to reduced bank lending, thus constraining economic activity. Additionally, Within small, open economies, the exchange rate channel plays a vital role; monetary tightening typically leads to currency appreciation, which can suppress export-driven growth (Ridhwana, 2014).In the case of Nigeria, monetary policy has consistently been a key instrument for achieving macroeconomic goals such as employment generation, economic development, Macroeconomic price steadiness and external payment balance. Yet, despite heightened reliance on monetary interventions, Nigeria continues to grapple with persistent economic challenges. High unemployment, low investment levels, soaring inflation, and exchange rate volatility continue to hamper the country's growth prospects (Nwoko, 2016). These issues are further compounded by a sluggish and erratic growth trajectory, declining productivity, and structural deficiencies, all of which are characteristic of a developing economy burdened by debt and uncertainty.

Empirical studies.

One of the primary macroeconomic goals for policymakers in developing countries is achieving sustainable economic growth, which is typically supported by maintaining low inflation levels. Extensive economic literature, including Fischer (1993), consistently highlights that persistently high inflation rates adversely affect economic growth. Conversely, The correlation between low inflation rates and robust Economic performance has been on the rise shown to have a positive impact. (De Gregorio, 1992), (Khan, 2000).

(Darrat, 1985) An empirical investigation was carried out on inflation levels in Nigeria, Libya, and Saudi Arabia, with a focus on the role of money as a central factor in identifying the sources and forms of inflation within these countries. The analysis revealed that rising money supply, coupled with sluggish growth in real income, is closely linked to increased inflationary pressures in these economies.

Chimobi (2010) This study employed both the cointegration technique and the Granger causality framework to explore the dynamic relationship between inflation and economic growth in Nigeria.

The empirical results revealed no evidence of a long-run cointegrated relationship between the two variables over the period examined. To further substantiate this finding, the Granger causality test was conducted at the second and fourth lag intervals, revealing a unidirectional causality from inflation to economic growth. Based on these results, Chimobi asserted that elevated inflation does not promote economic growth; rather, it exerts a deleterious effect on economic performance.

2.0 MATERIALS AND METHODS

2.1 Materials

A range of software tools will be utilized to clean data, conduct statistical evaluations, and build predictive models. In the preliminary phase, Microsoft Excel 2016 will serve as the platform for organizing the raw data. During this stage, the data will be systematically arranged and sorted to ensure it is properly structured for further analysis. Once the dataset is prepared in Excel, it will then be imported into **Eviews 12 student version**. Eviews will be used for detailed analysis, including stationarity test of the time series data and checking there co-integration the macroeconomics variables will serve as unique identifiers to determine the change in the variables over time of collection. The statistical modeling will employ **a** Vector Autoregressive and Autoregressive Distributed Lag Approach**,** implemented using Eviews libraries.

2.2 Vector Autoregressive model

The Vector Autoregression (VAR) model is developed based on the statistical characteristics of time series data. Every endogenous variable is regressed on its own lags and the lags of all other endogenous variables, thereby generalizing the concept of a univariate autoregressive model to a multivariate framework. This multivariate extension allows for the analysis of multiple time series variables simultaneously. The VAR approach was introduced into the field of economics by C. A. Sims in 1980, which significantly advanced the use of dynamic modeling in economic analysis. The VAR model of order *p*, denoted as VAR(p), is mathematically expressed as follows:

:

$$y_t = \alpha + \sum_{i=1}^{k} \phi_1 y_{t-1} + \sum_{i=1}^{k} \phi_2 y_{t-2} + \ldots + \sum_{i=1}^{k} \phi_p y_{t-p} + u_t \quad (2.1)$$

for t= 1,2, … T

y_t Is the column vector of observation variables at time (t), ϕ_i For i=1, 2 . . . p are fixed (K x K) coefficients for lagged values, α_i is a fixed intercept term, U_t is white noise, P is a positive integer of the lag order, t is the total number of samples.

The above equation can be write as

$$INF_t = \alpha_1 + \sum_{i=1}^{k} \phi_1 INF_{t-1} + \sum_{i=1}^{k} \phi_2 MPR_{t-2} + \sum_{i=1}^{k} \phi_3 EXR_{t-3} + \sum_{i=1}^{k} \phi_4 TBR_{t-4} + \sum_{i=1}^{k} \phi_5 M2_{t-5} + u_{1t} \quad (2.2)$$

$$EXR_t = \alpha_2 + \sum_{i=1}^{k} \phi_1 INF_{t-1} + \sum_{i=1}^{k} \phi_2 INT_{t-2} + \sum_{i=1}^{k} \phi_3 EXR_{t-3} + \sum_{i=1}^{k} \phi_4 TBR_{t-4} + \sum_{i=1}^{k} \phi_5 M2_{t-5} + u_{2t} \quad (2.3)$$

2.3 Autoregressive Distributed Lag Model

The ARDL method is well-suited for estimating Dynamic (short-run) and stable (long-run) interactions, especially when dealing with small sample sizes. It relies on the Ordinary Least Squares (OLS) technique to establish co-integration among variables. (Duasa 2007).

The generalized ARDL (p, q) model is specified as:

$$Y_t = \gamma_o + \sum_{i=1}^{p} \delta_i Y_{t-i} + \sum_{i=0}^{q} \beta_i X_{t-i} + \varepsilon_{it} \quad (2.4)$$

i= 1 … k;

P, q are the optimal lag orders of the observation variables and explanatory variable, Y_t = is a vector of the observation variables at time (t), X_t = are the explanatory variables that are allow to be purely I(0) or I(1) or co-integrated, β and δ = are coefficient, γ = is the constant, ε_{it} = is a vector of the error term or A white noise vector process (where observations are serially uncorrelated or independent).

The above ARDL model is express as follow to illustrate our model ARDL (p,q_1, q_2, q_3, q_4)

$$INF_t = \gamma_o + \sum_{i=1}^{p} \delta_i INF_{t-i} + \sum_{i=0}^{q} \beta_{i1} INT_{t-i} + \sum_{i=0}^{q} \beta_{i2} EXR_{t-i} + \sum_{i=0}^{q} \beta_{i3} TBR_{t-i} + \sum_{i=0}^{q} \beta_{i4} M2_{t-i} + \varepsilon_{it} \quad (2.5)$$

$$EXG_t = \gamma_o + \sum_{i=1}^{p} \delta_i EXG_{t-i} + \sum_{i=0}^{q} \beta_{i1} INT_{t-i} + \sum_{i=0}^{q} \beta_{i2} EXR_{t-i} + \sum_{i=0}^{q} \beta_{i3} TBR_{t-i} + \sum_{i=0}^{q} \beta_{i4} M2_{t-i} + \varepsilon_{it} \quad (2.6)$$

2.4 Lag Selection

To run a VAR and ARDL model there is need to choose the proper lag order with lag length determined through commonly used information criteria, including AIC and the Schwarz Criterion

2.5 Unit Root Test

Before proceeding to the empirical analysis, it is essential to perform pre-estimation diagnostic tests to examine the time series characteristics of the data—particularly through descriptive statistics and unit root testing. This study utilizes the Augmented Dickey-Fuller (ADF) test to assess the stationarity of the selected variables, and it is expressed as follows:

$$\Delta y_t = u + \beta t + \alpha y_{t-1} + \sum_{i=1}^{k} C_t \Delta y_{t-i} + \varepsilon \quad (2.7)$$

2.6 Co-integration Test

Co-integration refers to the presence of a long-term Stable long-term relationship between the time series variables. evidence obtained from the unit root test determines whether the co-integration procedure can be applied, which is only possible if all the variables are either stationary at level or integrated of the same order (i.e., all non-stationary).

it is given as.

$$\Delta Y_t = Y_{t-1} + \sum_{i=1}^{k-1} \Delta Y_{t-1} + \varepsilon_t \quad (2.8)$$

H_0: There is no co-integration among the variables
H_1: There is co-integration among the variables

2.7 ARDL Bound Test of Co-Integration

This ARDL cointegration approach was created by (Pesaran, 1999). This approach offers three key advantages over traditional co-integration methods. Firstly, it does not require that all variables included in the analysis Should be integrated of the same order. This method can be utilized whether the underlying variables are integrated of order I(1), I(0), or a mix of both. For the execution of the bounds test procedure for co-integration, the conditional ARDL model—denoted as ARDL(p, q_1, q_2, q_3, q_4) for a system involving five variables—is specified as follows:

$$lnINF_t = a_{oi} + b_{1i} inINF_{t-i} + b_{2i} lnINT_{t-i} + b_{3i} lnEXR_{t-1} + b_{4i} lnTBR_{t-i} + b_{5i} lnM2_{t-1} + \sum_{i=1}^{p} \delta_i \, lnINF_{t-i} + \sum_{i=0}^{q} \beta_{1i} \, lnINT_{t-i} + \sum_{i=0}^{q} \beta_{2i} \, lnEXR_{t-i} + \sum_{i=0}^{q} \beta_{3i} ln \, TBR_{t-i} + \sum_{i=0}^{q} \beta_{4i} \, lnM2_{t-i} + \varepsilon_{it}$$

If there is co-integration, the error correction model (ECM) representation is specified as;

$$INF_t = \gamma_o + \sum_{i=1}^{p} \delta_i \, INF_{t-i} + \sum_{i=0}^{q} \beta_{i1} \, INT_{t-i} + \sum_{i=0}^{q} \beta_{i2} \, EXR_{t-i} + \sum_{i=0}^{q} \beta_{i3} \, TBR_{t-i} + \sum_{i=0}^{q} \beta_{i4} \, M2_{t-i} + \varphi ECT_{t-1} + \varepsilon_{it}$$

2.8 Granger Causuality

The Granger Causality test is employed to determine whether one variable can be used to forecast another. This test will help identify whether there is a unidirectional, bidirectional, or the lack of any causal connection between monetary policy, inflation, and the other selected variables in the study. The model can be expressed as follows:

$$y_t = \alpha_1 + \sum_{i=1}^{n} \beta i \, x_{t-1} + \sum_{j=1}^{m} \gamma j \, y_{t-1\,j} + e_{1t} \quad (2.9.1)$$

$$x_t = \alpha_2 + \sum_{i=1}^{n} \theta i \, y_{t-1} + \sum_{j=1}^{m} \delta j \, x_{t-1} + e_{2t} \quad (2.9.2)$$

H_0: monetary policy does not granger cause Inflation
H_1: monetary policy granger causes Inflation
Decision Rule: The null hypothesis will be rejected if the p-value is less than 0.1 and the F-statistic exceeds 3.

2.9 Data Source and Description

The data used in this thesis consists of secondary quarterly data extending from the first quarter of 1999 to the fourth quarter of 2023. It was sourced from the Central Bank of Nigeria's 2023 Statistical Bulletin and includes variables such as inflation, monetary rate decisions, Treasury bill yields, the exchange rate, and the money stock for the empirical analysis.

3.0 RESULTS AND DISCUSSIONS

3.1 Descriptive Statistics of the macroeconomic variables

Table 3.1: Descriptive Statistics on the Variables

Metric	EXG	INF	M2	MPR	TBR
Mean	212.7147	12.9248	16635.77	12.9644	12.8176

Median	153.85	12.275	12515	13	13.34
Maximum	843.79	28.15	78831.12	20.5	18.98
Minimum	86.32	0.58	609.0302	6	6.13
Std. Dev.	135.793	5.221976	16521.35	3.375978	3.702234
Probability	0	0.234511	0	0.961667	0.172111
Sum	21271.47	1292.48	1663577	1296.44	1281.76
Sum Sq. Dev.	1825534	2699.634	2.70E+10	1128.325	1356.947
Observations	100	100	100	100	100

3.2 Lag Order Specification

Table 3.2: show the VAR Lag Order Selection

Lag	LogL	LR	FPE	AIC	SC	HQ
0	-2209.800	NA	5.60e+14	48.14783	48.28489	48.20315
1	-1747.222	864.8208	4.14e+10	38.63526	39.45758	38.96715
2	-1679.663	118.9630*	1.65e+10*	37.71006*	39.21765*	38.31853*
3	-1664.999	24.22735	2.09e+10	37.93475	40.12761	38.81981
4	-1648.527	25.42429	2.57e+10	38.12014	40.99827	39.28178
5	-1623.289	36.21076	2.66e+10	38.11497	41.67837	39.55319
6	-1608.669	19.38649	3.53e+10	38.34064	42.58931	40.05544
7	-1585.257	28.50161	3.98e+10	38.37516	43.30910	40.36654
8	-1568.146	18.97181	5.30e+10	38.54664	44.16585	40.81460

* indicates lag order selected by the criterion
LR: sequential modified LR test statistic (each test at 5% level) FPE: Final prediction error
AIC: Akaike information criterion
SC: Schwarz information criterion
HQ: Hannan-Quinn information criterion

According to Akaike information criterion and Schwarz information criterion the model will use two lags for its variables.

3.3 The result of ADF unit root test

Table 3.3: Unit Root Test

	LEVEL		FIRST DIFF		
VARIABLE	**t-stats**	**Prob**	**t-stats**	**Prob**	**ORDER**

EXG	2.91646	1	-6.0225	0.00001	I(1)
INF	-1.6788	0.4387	-7.4465	0.00001	I(1)
M2	1.02806	0.9966	-5.718	0.00001	I(1)
MPR	-1.9003	0.331	-9.42	0.00001	I(1)
TBR	-2.4368	0.1344	-10.487	0.00001	I(1)

3.4 Co-Integration Test

Table 3.4: show the Co-integration test result

Unrestricted Cointegration Rank Test (Trace)

Hypothesized No. of CE(s)	Eigenvalue	Trace Statistic	0.05 Critical Value	Prob.**
None *	0.345139	94.87848	69.81889	0.0002
At most 1 *	0.257244	53.81521	47.85613	0.0124
At most 2	0.149684	24.96862	29.79707	0.1626
At most 3	0.062003	9.240306	15.49471	0.3436
At most 4	0.030769	3.031450	3.841465	0.0817

Trace test indicates 2 cointegrating eqn(s) at the 0.05 level
* denotes rejection of the hypothesis at the 0.05 level
**MacKinnon-Haug-Michelis (1999) p-values

Unrestricted Cointegration Rank Test (Maximum Eigenvalue)

Hypothesized No. of CE(s)	Eigenvalue	Max-Eigen Statistic	0.05 Critical Value	Prob.**
None *	0.345139	41.06327	33.87687	0.0059
At most 1 *	0.257244	28.84659	27.58434	0.0343
At most 2	0.149684	15.72832	21.13162	0.2411
At most 3	0.062003	6.208856	14.26460	0.5865
At most 4	0.030769	3.031450	3.841465	0.0817

Max-eigenvalue test indicates 2 cointegrating eqn(s) at the 0.05 level
* denotes rejection of the hypothesis at the 0.05 level
**MacKinnon-Haug-Michelis (1999) p-values

3.5 Vector Error Correction Model

Table 3.5: Vector Auto Regressive Model

Error Correction:	D(INF)	D(EXG)	D(M2)	D(MPR)	D(TBR)
CointEq1	-0.021238	0.369102	-57.68392	-0.008246	-0.026775
	(0.02194)	(0.14416)	(9.72479)	(0.01125)	(0.01441)
	[-0.96813]	[2.56036]	[-5.93163]	[-0.73320]	[-1.85755]
D(INF(-1))	0.134993	0.240716	-4.963867	0.114383	0.042463
	(0.10174)	(0.66858)	(45.1014)	(0.05216)	(0.06685)
	[1.32685]	[0.36004]	[-0.11006]	[2.19285]	[0.63520]
D(EXG(-1))	0.002876	0.351951	28.94368	-0.004832	-0.004644
	(0.01074)	(0.07061)	(4.76289)	(0.00551)	(0.00706)
	[0.26770]	[4.98478]	[6.07691]	[-0.87723]	[-0.65779]
D(M2(-1))	0.000110	0.017960	-0.240623	6.11E-05	-0.000234
	(0.00025)	(0.00167)	(0.11252)	(0.00013)	(0.00017)
	[0.43508]	[10.7673]	[-2.13844]	[0.46932]	[-1.40563]
D(MPR(-1))	0.062569	1.279104	19.10371	-0.016848	0.009213
	(0.21199)	(1.39310)	(93.9757)	(0.10869)	(0.13929)
	[0.29515]	[0.91817]	[0.20328]	[-0.15501]	[0.06614]
D(TBR(-1))	-0.173367	-2.120320	23.05299	0.050458	-0.040585
	(0.16591)	(1.09030)	(73.5495)	(0.08506)	(0.10902)
	[-1.04494]	[-1.94472]	[0.31344]	[0.59318]	[-0.37228]
C	0.064677	-6.908961	759.7881	-0.013316	0.146572
	(0.32546)	(2.13874)	(144.276)	(0.16686)	(0.21385)
	[0.19873]	[-3.23038]	[5.26622]	[-0.07980]	[0.68540]
R-squared	0.078105	0.677311	0.614542	0.071086	0.048189
Adj. R-squared	0.017321	0.656035	0.589127	0.009839	-0.014567
Sum sq. resids	611.7044	26416.58	1.20E+08	160.7945	264.0985
S.E. equation	2.592687	17.03796	1149.350	1.329275	1.703579
F-statistic	1.284961	31.83418	24.18046	1.160637	0.767874
Log likelihood	-228.7888	-413.2982	-826.0260	-163.3188	-187.6324
Akaike AIC	4.812016	8.577514	17.00053	3.475894	3.972089
Schwarz SC	4.996656	8.762154	17.18517	3.660535	4.156729
Mean dependent	0.181020	7.658571	797.9203	0.005510	-0.035918
S.D. dependent	2.615437	29.05094	1793.076	1.335863	1.691305

VECM

- The error correction terms in the short-run models (e.g., D(INF), D(EXG), etc.) indicate The rate at which deviations from the long-run equilibrium-term equilibrium are corrected.
- For D(INF): The coefficient of CointEq1 is -0.0212, meaning only 2.12% of the disequilibrium is corrected in each period, reflecting a slow adjustment to long-term equilibrium.
- For D(EXG): The coefficient is 0.3691, suggesting that deviations in the exchange rate return to equilibrium more rapidly.
- For D(M2), D(MPR), and D(TBR): Negative coefficients show that these variables also adjust toward the long-term equilibrium, though the rates of adjustment vary.

Short-Run Dynamics:

- The lagged differences (e.g., D(INF(-1))) capture short-term dynamics:

- **D(INF(-1))**: The lag of inflation Shows a positive direction of impact, though not statistically significant its own changes (t-statistic = 1.33).
- **D(EXG(-1))**: Past Variations in the exchange rate significantly impact inflation (t-statistic = 4.98).
- **D(M2(-1))**: The short-term The relationship between money supply and inflation is not statistically significant but it has a notable effect on D(EXG).
- **D(MPR(-1))** and **D(TBR(-1))**: The short-term effects of these variables on inflation are generally insignificant.

•

3.6 ARDL Bounds Tests for Co-integration

Table 3.6 ARDL Bounds Test of co-integration

TEST STATISTIC	VALUE	K
F-statistics	4.692724	4
Critical value Bounds		
Significance	I(O) BOUND	I(1) BOUND
10%	2.2	3.09
5%	2.56	3.49
2.5%	2.88	3.87
1%	3.29	4.37

The result from Table 3.6 shows that the F-statistic value = 16.65744 Is higher than the upper critical bound values (I(1) = 3.09, 3.49, 3.87,4.37) at all the significance levels (10%, 5%, 2.5% and 1%), and thus, it was concluded that there exists a unique long-run relationship among the variables.

3.7 ARDL ERROR CORRECTION MODEL
TABLE 3.7.1 show the result for ARDL ECM for inflation

ECM Regression
Case 2: Restricted Constant and No Trend

Variable	Coefficient	Std. Error	t-Statistic	Prob.
D(INF(-1))	0.310097	0.091879	3.375070	0.0011
CointEq(-1)*	-0.387052	0.071018	-5.450082	0.0000

R-squared	0.252267	Mean dependent var	0.181020
Adjusted R-squared	0.244478	S.D. dependent var	2.615437
S.E. of regression	2.273358	Akaike info criterion	4.500590
Sum squared resid	496.1431	Schwarz criterion	4.553345
Log likelihood	-218.5289	Hannan-Quinn criter.	4.521928
Durbin-Watson stat	2.081149		

ARDL ECM INF (CointEq(-1)):

- The error correction term's coefficient is **-0.3871** ($p < 0.01$), indicating that approximately 38.71% of the deviation from the long-term equilibrium in inflation is corrected in each quarter.
- This is statistically significant, indicating a relatively quick adjustment to equilibrium.
- THE Lagged inflation (D(INF(-1))): Coefficient = **0.3101** ($t = 3.37$), significant positive effect highlights a stronger short-term impact of past inflation on current inflation compared.

Table 3.7.2 show the results for ARDL ECM for Exchange rate

ECM Regression
Case 2: Restricted Constant and No Trend

Variable	Coefficient	Std. Error	t-Statistic	Prob.
D(EXG(-1))	0.377206	0.074601	5.056335	0.0000
D(M2)	0.000353	0.001203	0.293821	0.7696
D(M2(-1))	0.015960	0.001159	13.77222	0.0000
D(MPR)	-2.257491	1.223779	-1.844689	0.0685
D(TBR)	1.671135	0.960069	1.740640	0.0853
D(TBR(-1))	-2.198892	0.942630	-2.332721	0.0220
CointEq(-1)*	-0.195618	0.035935	-5.443665	0.0000

R-squared	0.739442	Mean dependent var	7.658571
Adjusted R-squared	0.722262	S.D. dependent var	29.05094
S.E. of regression	15.31010	Akaike info criterion	8.363651
Sum squared resid	21330.31	Schwarz criterion	8.548292
Log likelihood	-402.8189	Hannan-Quinn criter.	8.438334
Durbin-Watson stat	2.028086		

ARDL ECM EXG (CointEq(-1)):

- Coefficient = **-0.1956**, indicating that about 19.56% Discrepancies from the long-term equilibrium are rectified per quarter.
- This is statistically significant ($t = -5.44$, $p < 0.01$), suggesting a moderate speed of adjustment.

Table 3.7.3 show the results for ARDL ECM for Money supply

ECM Regression
Case 2: Restricted Constant and No Trend

Variable	Coefficient	Std. Error	t-Statistic	Prob.
D(M2(-1))	-0.392758	0.163865	-2.396837	0.0186
D(EXG)	3.138788	6.570196	0.477731	0.6340
D(EXG(-1))	26.88947	4.968620	5.411858	0.0000
CointEq(-1)*	0.066124	0.008944	7.392741	0.0000

R-squared	0.635948	Mean dependent var	797.9203
Adjusted R-squared	0.624329	S.D. dependent var	1793.076
S.E. of regression	1099.012	Akaike info criterion	16.88217
Sum squared resid	1.14E+08	Schwarz criterion	16.98768
Log likelihood	-823.2264	Hannan-Quinn criter.	16.92485
Durbin-Watson stat	2.042113		

ARDL ECM M2 (CointEq(-1)):

- Coefficient = **0.0661**, indicating that approximately 6.61% of the disequilibrium in the money supply is corrected in each quarter.
- This is highly significant ($t = 7.39$, $p < 0.01$), confirming that the system adjusts to the long-term equilibrium, albeit at a slow pace.

3.8 Granger Causality Test
Table 3.8 show the Result for granger causuality

Null Hypothesis:	Obs	F-Statistic	Prob.	Decision
EXG does not Granger Cause INF	98	4.37728	0.0152	Reject
M2 does not Granger Cause EXG	98	60.5539	1.E-17	Reject
EXG does not Granger Cause M2	98	19.2482	1.E-07	Reject
M2 does not Granger Cause INF	98	3.80805	0.0257	Reject
INF does not Granger Cause MPR	98	2.94305	0.0576	Reject

Table 3.8 presents the results of the Granger causality analysis. The findings reveal that we fail to accept the null hypothesis for the following relationships at the 5% significance level: EXG does not Granger Cause INF, M2 does not Granger Cause INF, INF does not Granger Cause MPR, M2 does not Granger Cause EXG, and EXG does not Granger Cause M2. However, the opposite hypotheses cannot be rejected. These results suggest the presence of One-way causal relationships between EXG and INF, M2 and INF, and INF and MPR. a bidirectional between M2 and EXG and EXG and M2.

4.0 CONCLUSIONS

The analysis of monetary policy effect on inflation in Nigeria using VAR and ARDL for our data over the past twenty four years reveal Critical understanding of the dynamics of monetary policy and inflation. The study demonstrated higher monetary policy rates, increased money supply, and

rising Treasury bill rates contribute to higher inflation.in Nigeria. Additionally, depreciation of the exchange rate contributes to inflationary growth. These findings align with the expectations outlined in economic theory. Specifically, the study revealed that; The ARDL ECM results for INF,EXG and M2 as dependent variable indicate The analysis confirms a robust long-run equilibrium relationship between inflation and its core determinants, as evidenced by the statistically significant error correction term, CointEq(−1), with a coefficient of -0.3871 and a p-value of 0.0000. This underscores the economy's tendency to return to long-term stability following short-term disruptions. Focusing on the exchange rate (EXG), the ECM results further reveal that imbalances from the long-term equilibrium are corrected at an average speed of 19.56% per quarter, reinforcing the presence of long-run convergence. In the short run, past movements in the exchange rate exert the policy had A pronounced and statistically validated effect on inflation money supply dynamics, as shown by the large and statistically significant coefficient of 26.88947. These findings collectively highlight the dual role of exchange rate movements in both short-term monetary fluctuations and long-term price stability offering informed recommendations to policy makers focused on maintain macroeconomic balance. The significant positive error correction term CointEq(−1) 0.066124 with a p-value of 0.0000 confirms stable long-run equilibrium relationship and a slow adjustment speed of 6.61% per quarter back to equilibrium.

References

Anowor, O. F. (2016). A reassessment of the impact of monetary policy on economic growth in Nigeria. *Journal of Economics and Sustainable Development,*, 7(9), 120-134. .

Chimobi, O. P. (2010). Relationship between Money, Inflation, and Output in Nigeria. *Research Journal of Social Sciences, 5(4),*, 123-130. .

Darrat, A. F. (1985). Inflatin in Saudi Arabia: An Econometric investigation,. *Journal of Economic Studies, 12,*, 41-51.

De Gregorio, J. (1992). Economic Growth in Latin America. *Journal of Development Economics, 39(1),* , 59-84. .

Fischer, S. (1993.). The Role of Macroeconomic Factors in Growth. *Journal of Monetary Economics, 32(3),* , 485-512. .

Khan, M. S. (2000). Threshold Effects in the Relationship Between Inflation and Growth. *IMF Staff Papers, 47(1),*, 1-21. .

Nwoko, C. N. (2016.). The impact of monetary policy on the economic growth of Nigeria. *African Research Review, 10(3),*, 192-206. .

Obadeyi, J. A. ((2016)). Transmission mechanisms of monetary policy in Nigeria. *Journal of Monetary Economics and Policy Studies*, 5(4) 145-158.

Okwo, I. M. (2012). Evaluation of monetary policy outcomes and its effect on price stability in Nigeria . *Research journal of Finance and Accounting ,3(11),*, 37-47.

Pesaran, M. H. (1999). *An autoregressive distributed lag modelling approach to cointegration analysis. in S.strom(Ed.), Econometrics and Economic Theory in the 20th Century: The Ragnar Frisch centennial Symposium .* Cambridge: Cambridge University Press.

Ridhwana, H. H. (2014). Interest rate effects on economic activity: A theoretical and empirical perspective. *Economic Modelling*, 94-106.

Ridhwana, H. H. (2014). Interest rate effects on economic activity: A theoretical and empirical perspective. *Economic Modelling, 35(1),*, 94-106.

Uwakaeme, O. S. (2015). Theoretical perspectives on the determinants of economic growth. *Journal of Economics and Finance*, 53-62.

Modelling Thermal Radiation Effects on Temperature and Concentration on Magnetohydrodynamic Flow in the Presence of Chemical Reaction in a Porous Medium

[1*]Lawal A. O. Jimoh O.R. and Yusuf S. I.

[1]Department of Mathematics, Federal University of Technology, Minna, Nigeria

Phone : +2348167823987,+2348077808699, +2347069297464

[1*]Corresponding author: [1]azeez.lawal@st.futminna.edu.ng,

Abstract

This study presents a mathematical model that explores the impact of thermal radiation effects on temperature and concentration on magnetohydrodynamic (MHD) flow in the presence of chemical reaction in a porous medium. The governing partial differential equations were non-dimensionalized, transformed to ordinary differential equations using harmonic solution technique and solved using perturbation method. The results which were presented graphically, highlight several key observations. Specifically, an increase in Grashof number, Dufour number, and porosity parameter leads to higher velocity profiles. Furthermore, Radiative parameters are found to reduce the fluid temperature. The findings of this work will be crucial in optimizing processes in areas like combustion, cooling systems and environmental control technology where such complex interactions are prevalent.

Keywords: Dufour number, Grashof number, harmonic solution technique, Magneto-hydrodynamic

1.Introduction

In many scientific, industrial, and environmental applications, natural convection arising from the buoyancy effect produced by density changes in a fluid is one of the key phenomena affecting such cases. Such applications include nuclear waste disposal, catalytic reactors, and energy systems requiring efficient temperature control and security (Riley et al., 2006). Jimoh and Abdullahi (2023) examined the effect of chemical reaction and viscous dissipation in MHD flow over an inclined porous plate for heat and mass transfer. They discovered that an increase in Peclet number, Grashof number, and heat source parameter strengthens velocity and temperature profiles. The internal energy dissipation modified the thermal and concentration boundary layers.

Zubi (2018) examined the conducting fluid and material flow of an to and fro movement flow over a perpendicular Porous medium. He discovered that the fluid velocity rises when the parameters of the interaction species and porous rises, and also rises when the parameters of magnetism reduce.Sandhya *et al*. (2020) investigated how Magnetohydrodynamics flow across a perpendicular flow passage during a chemical reaction is affected by mass and heat transfer. The thermal diffusion influence an perpendicular plate on the flow region have been attempted to be

explained with the aid of the thermal region, interaction species,and heat emission. To solve the dimensional higher derivatives equations, the closed analytical approach was applied. As the Grashof, modified Grashof, and Soret numbers increase, the fluid velocity also increases

3. Model Formulation

In this study, the effects of a variable temperature and concentration inclined moving plate under an external transverse field and flowing through porous medium the unsteady free convection viscous incompressible radiative fluid were investigated. A Cartesian coordinate system is set up, where the x-axis is taken along the plate while the y-axis is taken normal to it. A field of strength B, would act on the system perpendicularly to the plate in the y-direction such that it influences the motion of the electrically conducting fluid. The plate has been inclined with respect to the horizontal by an angle θ, which provides a more realistic representation of practical applications such as geophysical fluid dynamics, industrial heat exchangers, and astrophysical flows. Low magnetic Reynolds numbers give rise to a consideration of induced field being negligible, such that it is the applied field only which acts on the flow.

It is assumed initially that both the fluid and plate are kept at equal temperature $T0$ and concentration $C0$ thereby establishing a thermodynamic equilibrium. For time t>0, the plate is supposed to be accelerated exponentially with a velocity function U(t)in its own plane. At the same time temperature and concentration at the plate surface are assumed to vary linearly with time giving an unsteady thermal and solutal boundary condition. This study also considers a strong chemical reaction that takes part in the fluid species, which affects the concentration profiles as well as diffusion rates. The radiative heat transfer is assumed to consider that the fluid is optically thin gray medium in which no scattering takes place, thus only emission and absorption contributes for the exchange of radiative energy. This gives a special formulation to capture how the combined effects of magnetism, radiation, chemical reaction and porous media would affect temperature, concentration and velocity distribution in an MHD flow system and provides useful insight into engineering and environmental applications.

$$\frac{\partial u^*}{\partial t^*} = g\beta(T^* - T^*_\infty)\cos\gamma + g\beta^*(\mathrm{C}^* - C_\infty{}^*)\cos\gamma + \frac{\nu\partial^2 u^*}{\partial y^{*2}} - \frac{\sigma B_o{}^2 u^*}{\rho} - \frac{\nu u^*}{k_p{}^*} \tag{1}$$

$$\rho c_p \frac{\partial T^*}{\partial t^*} = k\frac{\partial^2 T}{\partial y^{*^2}} - 16a^* T^{*^3}{}_\infty (T^* - T_\infty{}^*) + S^*(T^* - T_\infty{}^*) + \frac{D_m k_T}{c_s c_p}\frac{\partial^2 c^*}{\partial y^{*^2}} \tag{2}$$

$$\frac{\partial \mathrm{C}^*}{\partial t^*} = D_m \frac{\partial^2 c^*}{\partial y^{*^2}} - K_c{}^*(\mathrm{C}^* - C_\infty{}^*) \tag{3}$$

Where,

u^* is the velocity on horizontal component

a^* absorption coefficient

ν static internal friction

u_o is the velocity on fluid,

g constant gravity of the earth,
a is the accelerating parameter,

β is a measure of how much a material's volume increases in response to a change in temperature.,

β^* refers to the measure of how the volume of a substance changes in response to variations in mass transfer processes, particularly when influenced by temperature changes.,

K_p^* is a measure of the medium's ability to allow fluids, such as liquids or gases, to flow through its interconnected pore spaces.,

q_r refers to the rate at which thermal energy is transferred through electromagnetic radiation across a given surface area.,
∞ is incline angle
σ is the heat conducting fluid ,
T^* degree flow

T_∞^* distance degree flow,

K amount of heat energy flow
K_c^* reaction species,
S^* heat source parameter,

C_p heat at constant pressure,

C^* amount of solute presence,

C_∞^* distance solute presence,

D_r is the Dufour number
D_m is the mass diffusivity,
The initial and boundary conditions are given by,

$$\left.\begin{array}{c} u^*(y^*,0)=0, \quad u^*(0,\mathrm{t})=u_o e^{a^* t^*}, \quad u^*(y^*\to\infty,t)\to 0 \\ T^*(y^*,0)=T_\infty{}^*, \quad T^*(0,\mathrm{t})=T_\infty{}^*+\left(\frac{T_w{}^*-T_\infty{}^*}{\nu}\right)u_o{}^2 t^* \quad T^*(y^*\to\infty,t)\to \mathrm{T}_\infty{}^* \\ C^*(y^*,0)=C_\infty{}^* \quad C^*(0,t)=C_\infty{}^*+\left(\frac{C_w{}^*-C_\infty{}^*}{\nu}\right)u_o{}^2 t^* \quad C^*(y^*\to\infty,t)\to C_\infty{}^* \end{array}\right\} \tag{4}$$

Non – dimensionalisation

Equations (1), (2), (3), and (4) are non-dimensionalised using the following dimensionless variables

$$y=\frac{y^* u_o}{\nu}, \quad t=\frac{u_o{}^2 t^*}{\nu}, \quad , \quad \theta=\frac{T^*-T_\infty{}^*}{T_w{}^*-T_\infty{}^*} \quad \phi=\frac{C^*-C_\infty{}^*}{C_w{}^*-C_\infty{}^*}, \qquad u=\frac{u^*}{u_o} \tag{5}$$

After non-dimensionalization, equations (1), (2), (3) and (4) becomes

$$\frac{\partial u}{\partial t}=G_{r\theta}\theta\cos\gamma+G_{m\phi}\phi\cos\gamma+\frac{\partial^2 u}{\partial y^2}-Mu-\frac{u}{K_p} \tag{6}$$

$$\frac{\partial\theta}{\partial t}=\frac{1}{P_r}\frac{\partial^2\theta}{\partial y^2}-\frac{R}{P_r}\theta+S\theta+D_r\frac{\partial^2\phi}{\partial y^2} \tag{7}$$

$$\frac{\partial\phi}{\partial t}=\frac{1}{S_c}\frac{\partial^2\phi}{\partial y^2}-K_c\phi \tag{8}$$

$$\left.\begin{array}{lll} u(\mathrm{y},0)=0, & u(0,t)=e^{at}, & u(\mathrm{y}\to\infty,\mathrm{t})=0 \\ \theta(y,0)=0, & \theta(0,\mathrm{t})=\mathrm{t}, & \theta(y\to\infty,t)=0 \\ \phi(y,0)=0, & \phi(0,t)=t, & \phi(y\to\infty,t)=0 \end{array}\right\} \tag{9}$$

Where,

$$\left.\begin{array}{l} M=\frac{\sigma\beta_o{}^2\nu}{\rho u_o{}^2}, \quad K_c=\frac{\nu K_c{}^*}{u_o{}^2}, \quad G_{r\theta}=\frac{g\beta\nu\left(T^*-T_\infty{}^*\right)}{u_o{}^3} \quad G_{r\phi}=\frac{g\beta\nu\left(C^*-C_\infty{}^*\right)}{u_o{}^3} \\ S_c=\frac{\nu}{D} \quad R=\frac{16a^*\nu^2\sigma T^*{}_\infty}{k u_o{}^2} \quad S=\frac{S^*\nu}{\rho C_p u_o{}^2} \quad K_p=\frac{u_o{}^2 K_p{}^*}{\nu^2} \\ P_r=\frac{\mu C_p}{K} \quad R=\frac{16a^*\sigma^*\nu^2 T_\infty{}^{*3}}{K u_o{}^2} \quad D_r=\frac{D_m k_T\left(C_w{}^*-C_\infty{}^*\right)}{\nu C_s C_p\left(T_w{}^*-T_\infty{}^*\right)} \end{array}\right\} \tag{10}$$

Materials and Methods

The aforementioned equations (6), (7) and (8) are the interconnected partial differential equations

that give an efficient approach to solving them by using harmonic solution method. This method helps in the transformation of PDEs to a system of ordinary differential equations with subsequent analytical solution. The analytical solution will then take the form in which the fluid velocities, temperatures, and concentrations in the area close to the plate are expressed as follows:

$u(y,t)=u(y)e^{iwt}$, $\theta(y,t)=\theta(y)e^{2iwt}$, $\phi(y,t)=\phi(y)e^{iwt}$, (11)

By Substituting equation (11) into equations (6), (7), and (8), the following equations are obtained:

$$\frac{d^2u}{dy^2} - c_1^2 = -G_{r\theta}e^{i\omega t}\theta\cos\gamma - G_{r\phi}\phi\cos\gamma \quad (12)$$

$$\frac{d^2\theta}{dy^2} - c_2^2\theta = -D_rP_re^{-iwt}\frac{d^2\phi}{dy^2} \quad (13)$$

$$\frac{d^2\phi}{dy^2} - c_3^2\phi = 0 \quad (14)$$

Let

Let $c_1 = \sqrt{\left(iw + M + \frac{1}{K_p}\right)}$ (15)

$$c_2 = \sqrt{\left(\frac{R}{P_r} - S + 2iw\right)P_r} \quad (16)$$

$$C_3 = \sqrt{(iw + K_c)S_c} \quad (17)$$

Equations (6), (7), and (8) becomes

$$\left.\begin{aligned} &\frac{d^2u}{dy^2} - c_1^2 = -G_{r\theta}e^{iwt}\theta\cos\gamma - G_{r\theta}\phi\cos\gamma \\ &u(0) = \frac{e^{at}}{e^{iwt}} \quad u(y\to\infty) = 0 \end{aligned}\right\} \quad (18)$$

$$\left.\begin{aligned} &\frac{d^2\theta}{dy^2} - c_2^2\theta = -D_rP_re^{-iwt}\frac{d^2\phi}{dy^2} \\ &\theta(0) = \frac{t}{e^{2iwt}}, \theta(y\to\infty) = 0 \end{aligned}\right\} \quad (19)$$

$$\left.\begin{aligned} &\frac{d^2\phi}{dy^2} - c_3{}^2\phi = 0 \\ &\phi(0) = \frac{t}{e^{iwt}}, \phi(y \to \infty) = 0 \end{aligned}\right\}$$

By applying perturbation method, Let

$$\left.\begin{aligned} u &= u_o + G_{r\theta}u_1 + G^2{}_{r\theta}u_2 + \ldots \\ \theta &= \theta_o + G_{r\theta}\theta_1 + G^2{}_{r\theta}\theta_2 + \ldots \\ \phi &= \phi_o + G_{r\theta}\phi_1 + G^2{}_{r\theta}\phi_2 + \ldots \end{aligned}\right\} \quad (20)$$

By substituting equations (21) into (18), (19) and (20) and equating corresponding terms on both sides, the following equations are obtained:

For order 0, $G_{r\theta}{}^0$: 1,

$$\left.\begin{aligned} &\frac{d^2u_o}{dy^2} - c_1{}^2u_o = 0 \\ &u_o(0) = \frac{e^{at}}{e^{iwt}}, \quad u_o(y \to \infty) = 0 \end{aligned}\right\} \quad (21)$$

$$\left.\begin{aligned} &\frac{d^2\theta_o}{dy^2} - c_2{}^2\theta_o = -D_rP_re^{-iwt}\frac{d^2\phi_o}{dy^2} \\ &\theta_o(0) = \mathrm{te}^{-2iwt}, \quad \theta_o(y \to \infty) = 0 \end{aligned}\right\} \quad (22)$$

$$\left.\begin{aligned} &\frac{d^2\theta_o}{dy^2} - c_2{}^2\theta_o = -D_rP_re^{-iwt}\frac{d^2\phi_o}{dy^2} \\ &\phi_o(0) = te^{-iwt} \quad \phi_o(y \to \infty) = 0 \end{aligned}\right\} \quad (23)$$

For order 1, $G_{r\theta}{}^1$,: $G_{r\theta}$

$$\left.\begin{aligned} &\frac{d^2u_1}{dy^2} - c_1{}^2u_1 = -e^{iwt}\cos\phi\theta_o - \cos\gamma\phi_o \\ &u_1(0) = 0, \quad u_1(y \to \infty) = 0, \end{aligned}\right\} \quad (24)$$

$$\left.\begin{aligned} &\frac{d^2\theta_1}{dy^2} - c_2{}^2\theta_1 = -D_rP_re^{-iwt}\frac{d^2\phi_1}{dy^2} \\ &\theta_1(0) = 0, \quad \theta_1(y \to \infty) = 0, \end{aligned}\right\} \quad (25)$$

$$\left.\begin{aligned} &\frac{d^2\phi_1}{dy^2} - c_3{}^2\phi_1 = 0 \\ &\phi_1(0) = 0, \quad \phi_1(y \to \infty) = 0 \end{aligned}\right\} \tag{26}$$

The boundary value problems (22) to (27) are solved by the method of undetermined coefficients and obtained the following results:

$$u(y) = A_2 e^{-c_1 y} + G_{r\theta}\left(A_9 e^{-c_1 y} + A_{10} e^{-c_2 y} + A_{11} e^{-c_3 y}\right) \tag{28}$$

$$\theta(y) = A_6 e^{-c_2 y} + A_7 e^{-c_3 y} + G_{r\theta}\left(A_{15} e^{c_2 y} + A_{16} e^{-c_3 y}\right) \tag{29}$$

$$\phi(y) = A_4 e^{-c_3 y} + G_{r\theta}\left(A_{13} e^{-c_3 y}\right) \tag{30}$$

The general solution of equations (1), (2) and (3) with the associated boundary and initial conditions (4) is therefore in the form of:

$$\left.u(y,t) = u(y)e^{iwt} \quad \theta(y,t) = \theta(y)\mathrm{e}^{2iwt} \quad \phi(y,t) = \phi e^{iwt}\right\} \tag{31}$$

RESULTS

This part elaborates on the effects of important dimensionless parameters on fluid velocity, temperature distribution, and concentration of species. The Grashof number, thermal interaction species variable, radiation parameter, Schmidt number, Dufour number, porosity parameter, and field parameter were some of the considered parameters.

3.1 Figures

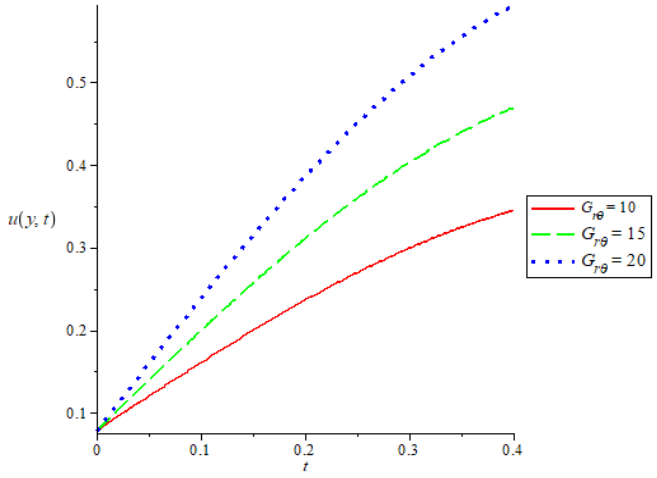

Figure 1 : Graph of Velocity $u(y,t)$ against Time (t) for varies Values of thermal Grashof number $(G_{r\theta})$.

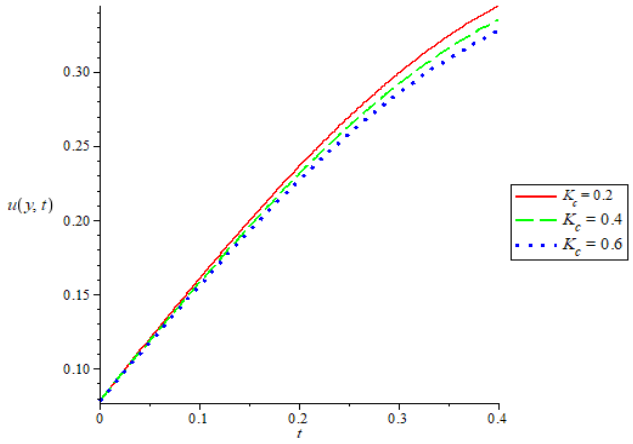

Figure 2 : Diagram of Velocity of the Fluid $u(y,t)$ against time (t) for varies Values of thermal Chemical reaction parameter (K_c).

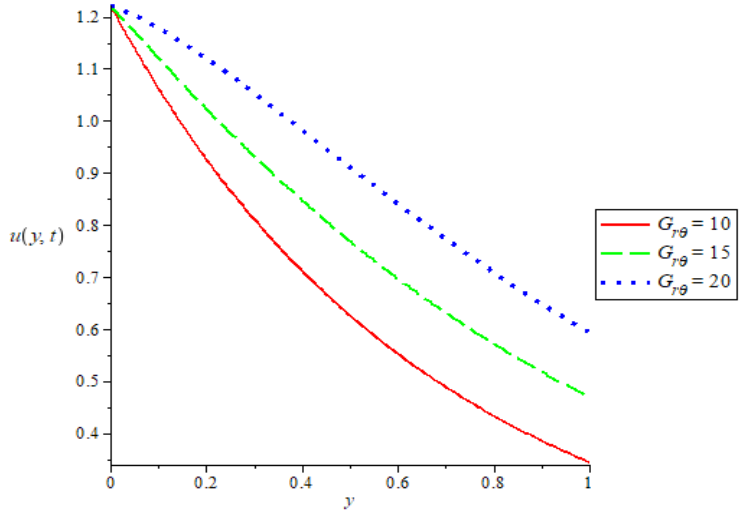

Figure 3 : Graph of Velocity of the Fluid $u(y,t)$ against Distance (y) for Different Values of thermal Grashof Number $(G_{r\theta})$.

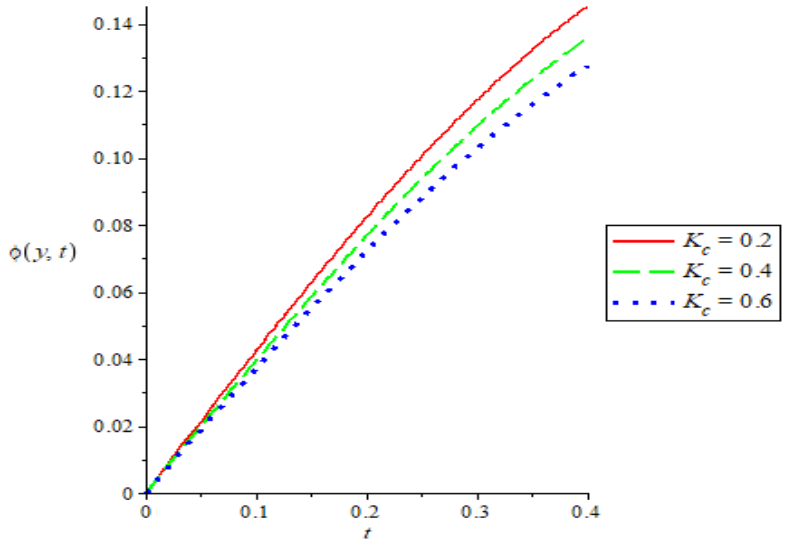

Figure 4 : Graph of Species Concentration $\phi(y,t)$ over Time (t) for Different Values of thermal Chemical reaction parameter (K_c).

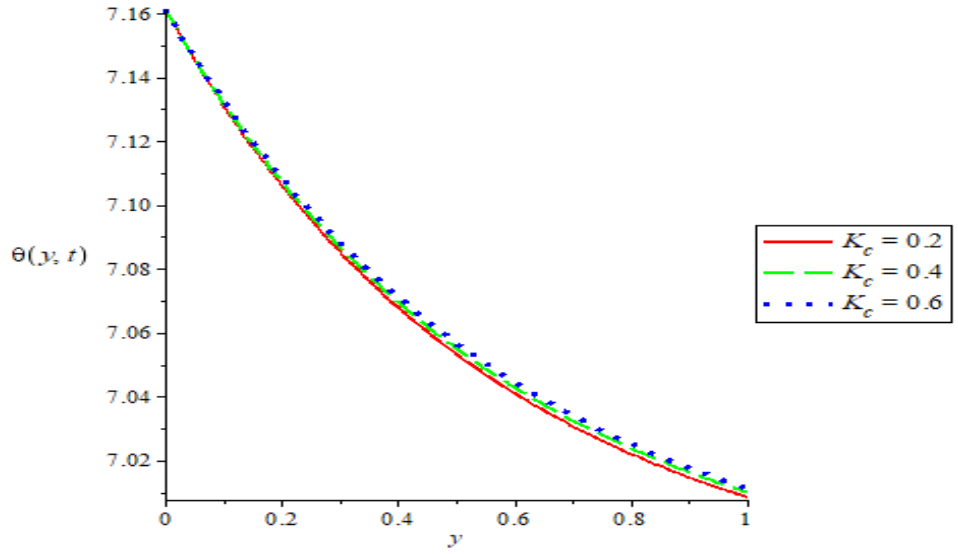

Figure 5 : Graph of Temperature of the Fluid $\theta(y,t)$ against Distance (y) for Different Values of thermal chemical reaction parameter (K_c).

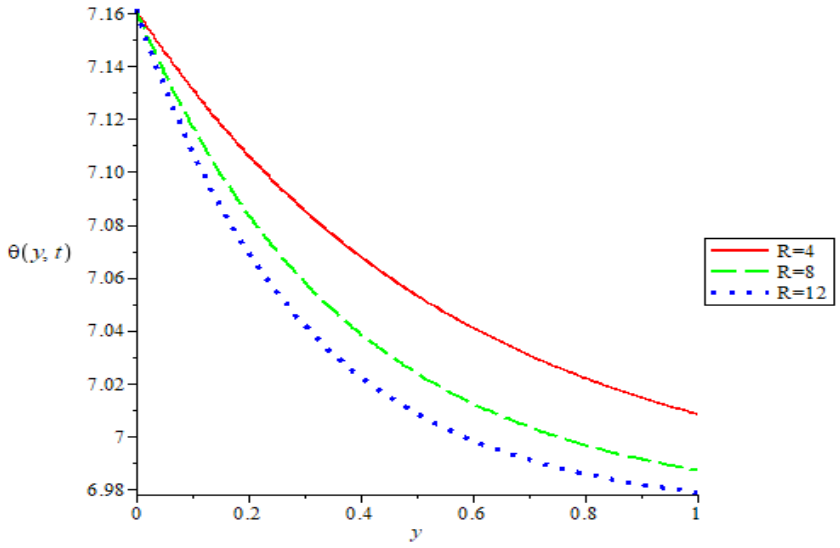

Figure 6 : Graph of Temperature $\theta(y,t)$ against Distance (y) for Different Values of Radiative variables (R).

4. Results and Discussion

Figure 1 shows how the fluid's flow changes on time in relation to thermal Grashof number. It is observed that the velocity of the fluid $u(y,t)$ rises faster with rise in the thermal Grashof number $(G_{r\theta})$ at steady time. Figure 2 show how the fluid's flow changes on time in relation to the thermal chemical reaction parameter. It is observed that the velocity of the fluid $u(y,t)$ reduces with rise in the thermal chemical reaction parameter (K_c).

Figure 3 shows how the heat Grashof Number affects the fluid's velocity as a function of distance. It is observed that the velocity of the fluid $u(y,t)$ rises faster with rise in the thermal Grashof number $(G_{r\theta})$ at steady time. Figure 4 shows the effect of thermal chemical reaction parameter on the concentration of the fluid .It is observed that the species concentration of the fluid $\phi(y,t)$ reduces with rise in the thermal Grashof number $(G_{r\theta})$ at steady time.

Figure 5 shows the effect of thermal chemical reaction parameter (K_c) on the temperature of the fluid $\theta(y,t)$.It is observed that temperature of the fluid $\theta(y,t)$ rises with rise in the thermal

chemical reaction parameter (K_c) at steady time. Figure 6 shows the effect of the radiative parameter (R) on the temperature of the fluid $\theta(y,t)$.It is observed that the temperature of the fluid $\theta(y,t)$ reduces with rise in the thermal chemical reaction parameter (K_c) at steady time.

5. Conclusion

The analysis of mathematical model was studied out to examine how thermal radiation affects the degree of hotness and interaction species profiles in a Magnetohydrodynamic (MHD) flow within a porous material. The harmonic solution method was used to analytically solve the system's coupled, non-linear, dimensionless partial differential equations. Understanding the impact of different dimensionless parameters—which were graphically depicted on the behavior of the system was the main goal of the study. The results of this analysis shed important light on how various parameters affect the temperature distribution, species concentration, and fluid flow over time and space. With possible applications in domains like engineering, environmental science, and industrial processes where such conditions are pertinent, these findings advance our knowledge of heat and mass transport events in MHD flows under the impact of thermal radiation and chemical reactions.

In contrast, components like the Thermal Chemical Reaction, and Grashof number tend to decrease the fluid velocity over time, slowing down the flow; additionally, the Radiative Parameter was found to decrease the fluid's temperature against time, indicating its cooling effect; and finally, the Thermal Chemical Reaction and Schmidt number were observed to lower the species concentration against time, reflecting their impact on the distribution of species concentration in the fluid.

References

Jimoh, O.R. & Abdullahi, D. (2023): Effect of Heat and Mass Transfer on Magneto-Hydrodynamic Flow with Chemical Reaction and viscous energy dissipation past an inclined porous plate**.** *Scientia Africana, Vol. 22 (No. 2), Pp 259-276*

Riley, K. F., Hobson, M. P. & Bence, S. J. (2006). *Mathematical Methods for Physics and Engineers. Third Edition, Cambridge University Press, New York.*

Siti, K.S., Anuar, I.& Loan, P. (2017): Unsteady MHD flow and heat transfer over a shrinking sheet with Ohmic heating. *Chinese journal of physics* Vol. 55, pp 1626-1636.

Zubi, M.A. (2018): MHD heat and mass transfer of an oscillatory flow over a vertical permeable plate in a porous medium with chemical reaction. *Modern Mechanical Engineering 8 (3), 179-191*

Third Refinement of Parametric Reaccelerated Overrelaxation Iterative Method for Linear Algebraic Systems

[*1]Wangwa A., [2]Ndanusa A., and [3]Bako D.U.
[*1,2,3]*Department of Mathematics Federal University of Technology Minna, Niger State*
[*1]Email: wangwaabubakar82@gmail.com

Abstract

The solution of large-scale linear algebraic systems of the form $Ax = b$, is a critical challenge in scientific computing, with iterative methods playing a pivotal role in addressing these systems efficiently. Building upon prior advancements by Isah et. al., 2022 and Vatti et. al., 2020, this study introduces the Third Refinement of the Parametric Reaccelerated Overrelaxation (TRPROR) method, an iterative scheme that synergizes features of Accelerated Overrelaxation (AOR), Parametric Accelerated Overrelaxation (PAOR), and Reaccelerated Overrelaxation (ROR) methods. The refined method optimizes parameter selection to enhance convergence rates and computational efficiency. The goal in all iterative methods for solving linear systems is to minimize the spectral radius to reduce the number of iterations required for convergence. Numerical examples demonstrated the superior efficiency of the TRPROR method compared to the standard AOR, ROR, PAOR, and PROR method.

Keywords: PAOR, PROR, TRPROR, Convergence and Spectral Radius

1. Introduction

Consider the following linear system:

$$Qt = b \tag{1}$$

where $Q \in \mathbb{R}^{n\times n}$, $b \in \mathbb{R}^n$ are given, and $t \in \mathbb{R}^n$ is the unknown. Systems of the form (1) commonly arise in various applications, including linear elasticity, fluid dynamics, and constrained quadratic programming (Varga, 2000). When the coefficient matrix Q in (1) is large and sparse, iterative methods are generally preferred over direct methods (Ndanusa, 2012). To effectively solve (1) using iterative methods, efficient splitting of Q are typically required. For instance, the classical Jacobi and Gauss-Seidel methods involve splitting Q into its diagonal and off-diagonal components.

Over the past few decades, significant advancements have been made in iterative methods for solving partial differential equations resulting in systems like (1). The Jacobi (1884) and Gauss-

Seidel (1874) methods were early examples of such approaches. In 1950, Young introduced the successive over-relaxation (SOR) method, an extrapolated form of the Gauss-Seidel method, which exhibits faster convergence than the Jacobi or Gauss-Seidel methods.

For the numerical solution of (1), the accelerated over-relaxation (AOR) method was introduced by Hadjidimos in 1978. This method generalizes the SOR method by incorporating two parameters, often achieving a better convergence rate than the Jacobi, Gauss-Seidel, or SOR methods in specific cases. Numerous studies have examined sufficient conditions for the convergence of the AOR method, including contributions from Abdullahi and Ndanusa (2020), Ndanusa (2020), Vatti *et al*. (2020), and Isah *et al.* (2022).

To enhance the convergence rate of the AOR method, researchers have proposed the preconditioned AOR (PAOR) method. Authors such as Ndanusa and Adeboye (2012), Wang (2019), Abdullahi and Ndanusa (2020), and Abdullahi *et al.* (2023) have investigated its performance. While Krylov subspace methods Bai, (2000) and Saad (1996) are widely regarded as efficient iterative techniques for solving large, sparse linear systems owing to their cost-effectiveness and ability to leverage matrix sparsity they can be very slow or even fail to converge when the coefficient matrix of (1) is extremely ill-conditioned or highly indefinite.

Vatti *et al.* (2020) introduced two variants of the Accelerated Overrelaxation (AOR) method: the Parametric Accelerated Overrelaxation (PAOR) method and the Reaccelerated Overrelaxation (ROR) method, both designed for consistently ordered matrices. They build on these advancements by further enhancing the convergence properties of the AOR method through the development of a new variant called the Parametric Reaccelerated Overrelaxation (PROR) method. Isah *et al.* (2020) proposed the PROR method, which represents a three-parameter generalization of the Reaccelerated Overrelaxation (ROR) method, further advancing the capabilities of iterative techniques for solving linear systems. The classical AOR, ROR, PAOR and PROR method presented in their work for the solution of equation (1) are given as:

$$AOR = (I - wL)^{-1}\left\{\left[(1-r)I + (r-w)L + rU\right]x^{(n)} + rb\right\} \tag{2}$$

$$PAOR = \left[(1+x)I - wL\right]^{-1}\left\{\left[(1+x-r)I + (r-w)L + rU\right]x^{(n)} + rb\right\}$$

(3)

$$ROR = (I - wL)^{-1}\left\{\left[(1-r+rw)I + (r-w-rw)L + (r-rw)U\right]x^{(n)} + (r-rw)b\right\}$$

(4)

$$PROR = \left[(1+x)I - wL\right]^{-1}\left\{\left[(1+x-r+rw)I + (r-w-rw)L + (r-rw)U\right]x^{(n)} + (r-rw)b\right\}$$

(5)

Assefa and Teklehaymanot (2021) proposed a second refinement of the Accelerated Overrelaxation (AOR) method, which generalizes the method into a two-parameter refinement. Their work also derived optimal parameter values and extended the concept to the K^{th} refinement of accelerated methods. The spectral radius of the iteration matrix and the convergence criteria for the Second Refinement of Accelerated Overrelaxation (SRAOR) method were thoroughly analyzed. Audu (2024) introduces the Third Refinement of Successive Over-Relaxation (TRSOR) and Third Refinement of Accelerated Over-Relaxation (TRAOR) methods to improve the efficiency and convergence of solving linear systems. TRAOR is recommended over TRSOR for applications requiring high efficiency in large-scale linear systems. Many modifications and refinements have been reviewed as in (Ismail *et. al.*, (2023), Vatti *et. al.*, (2018), Eneyew *et. al.*, (2019), Eneyew *et. al.*, (2020), Abdullahi & Muhammad (2021))

The aim of this paper is to introduce an advanced version of the Refined Accelerated Over-Relaxation (RPAOR) method for solving the linear system (1). This new approach, termed the Third Refinement Accelerated Over-Relaxation (TRPAOR) method, includes a discussion on the sufficient conditions necessary for its convergence.

3. Material and Method

a. Derivation of Third Refinement of AOR Method

Considering (1) having the splitting of the form

$$G = D_G - L_G - U_G$$

(6)

Where $D_G = diag(b_{11}, b_{22}, \cdots, b_{nn})$ is the diagonal part of G, $-L_G$ and $-U_G$ the strictly lower and strictly upper parts respectively. If $b_{ii} \neq 0$ for all $i \in \mathbb{N}$ $(i = 1,2, \cdots, n)$, then we can multiply the linear system (1) by ${D_G}^{-1}$, arising therefrom the splitting of the matrix

$$G = I - L - U$$

(7)

where $I = {D_G}^{-1} D_G$, $L = {D_G}^{-1} L_G$ and $U = {D_G}^{-1} U_G$.

Suppose $G = M - N$ is a regular splitting of the coefficient matrix $G = (g_{ij})$, and then the basic iterative method for the solution of system (1) can be expressed in the form

$$t^{(n+1)} = M^{-1} N t^{(k)} + M^{-1} b, \qquad i = 0,1,2, \cdots$$

(8)

where $M^{-1}N$ is known as the iteration matrix of the method. The iteration (8) is known to converge to the exact solution $t = G^{-1} b$ for any initial vector value $t^{(0)} \in \mathbb{R}^n$ if and only if the spectral radius $\rho(M^{-1}N) < 1$. The smaller the spectral radius the faster the convergence speed of the iterative method. The classical AOR iterative method given by

$$t^{(n+1)} = J_{r,\omega} t^{(n)} + (I - wL)^{-1} \omega b \qquad i = 0,1,2, \cdots$$

(9)

The refinement proposed by Vatti, (2018) and Ismail *et. al.*, (2023) is given by;

$$t^{(n+1)} = t^{(k+1)} + r(I - wL)^{-1}(b - Gt^{(k+1)})$$

(10)

Following the pattern of Ismail *et al.*, (2023) The equation (10) can be expressed as;

$$t^{(n+1)} = J_{r,w}^2 t^{(n)} + r(I + J_{r,w} t^{(n)})(I - wL)^{-1} b$$

(11)

The second refinement of (10) is given by

$$t^{(n+1)} = J_{r,w}^3 t^{(n)} + r(I + J_{r,w} t^{(n)} + J_{r,w}^2 t^{(n)})(I - wL)^{-1} b$$

(12)

Substitute (12) into (10) we obtained the Third Refinement of the form;

$$t^{(n+1)} = J_{r,w}^4 t^{(n)} + r(I + J_{r,w} t^{(n)} + J_{r,w}^2 t^{(n)} + J_{r,w}^3 t^{(n)})(I - wL)^{-1} b$$

(13)

The classical and refinement iterative matrix for RAOR, SRAOR, TRAOR is given by

$$\left.\begin{aligned} J_{r,w} &= \left\{(I-wL)^{-1}\left[\left((1-r)I+(r-w)L+rU\right)\right]\right\} \rightarrow AOR \\ J_{r,w}^{2} &= \left\{(I-wL)^{-1}\left[\left((1-r)I+(r-w)L+rU\right)\right]\right\}^{2} \rightarrow RAOR \\ J_{r,w}^{3} &= \left\{(I-wL)^{-1}\left[\left((1-r)I+(r-w)L+rU\right)\right]\right\}^{3} \rightarrow SRAOR \\ J_{r,w}^{4} &= \left\{(I-wL)^{-1}\left[\left((1-r)I+(r-w)L+rU\right)\right]\right\}^{4} \rightarrow TRAOR \end{aligned}\right\}$$

(14)

b. Derivation of Third Refinement of ROR Method

In the same vein, we followed the same pattern from (9) to (13) to obtained the Third refinement of ROR. From (4) and (9) we obtained the refinement of ROR as;

$$t^{(n+1)} = t^{(k+1)} + (r-rw)(I - wL)^{-1}(b - Gt^{(k+1)})$$

(15)

By transforming (15), we have refinement of ROR in (16)

$$t^{(n+1)} = J_{r,w}^{2}t^{(n)} + (r-rw)(I + J_{r,w}t^{(n)})(I-wL)^{-1}b$$

(16)

The Second Refinement of ROR from (16) is given in (17)

$$t^{(n+1)} = J_{r,w}^{3}t^{(n)} + [(I + J_{r,w}t^{(n)} + J_{r,w}^{2}t^{(n)})](r-rw)(I-wL)^{-1}b$$

(17)

Put (17) into (15) we have the Third Refinement of ROR given by

$$t^{(n+1)} = J_{r,w}^{4}t^{(n)} + [I + J_{r,w}t^{(n)} + J_{r,w}^{2}t^{(n)} + J_{r,w}^{3}t^{(n)}](r-rw)(I-wL)^{-1}b$$

(18)

The classical and refinement iterative matrix for ROR, SROR, TROR is given by

$$\left.\begin{aligned} J_{r,w} &= \left\{(I-wL)^{-1}\left[\left((1-r+rw)I+(r-w-rw)L+(r-rw)U\right)\right]\right\} \to ROR \\ J_{r,w}^{2} &= \left\{(I-wL)^{-1}\left[\left((1-r+rw)I+(r-w-rw)L+(r-rw)U\right)\right]\right\}^{2} \to RROR \\ J_{r,w}^{3} &= \left\{(I-wL)^{-1}\left[\left((1-r+rw)I+(r-w-rw)L+(r-rw)U\right)\right]\right\}^{3} \to SROR \\ J_{r,w}^{4} &= \left\{(I-wL)^{-1}\left[\left((1-r+rw)I+(r-w-rw)L+(r-rw)U\right)\right]\right\}^{4} \to TROR \end{aligned}\right\}$$

(14)

The Derivation of Third Refinement of (PAOR & PROR) Method follows the same pattern from (9) to (13) and their iterative matrix expressed in (15) and (16)

$$\left.\begin{aligned} J_{x,r,w} &= \left\{((1+x)I-wL)^{-1}\left[\left((1+x-r)I+(r-w)L+rU\right)\right]\right\} \to PAOR \\ J_{x,r,w}^{2} &= \left\{((1+x)I-wL)^{-1}\left[\left((1+x-r)I+(r-w)L+rU\right)\right]\right\}^{2} \to RPAOR \\ J_{x,r,w}^{3} &= \left\{((1+x)I-wL)^{-1}\left[\left((1+x-r)I+(r-w)L+rU\right)\right]\right\}^{3} \to SRPAOR \\ J_{x,r,w}^{4} &= \left\{((1+x)I-wL)^{-1}\left[\left((1+x-r)I+(r-w)L+rU\right)\right]\right\}^{4} \to TRPAOR \end{aligned}\right\}$$

(15)

$$\left.\begin{aligned} J_{x,r,w} &= \left\{((1+x)I-wL)^{-1}\left[\left((1+x-r+rw)I+(r-w-rw)L+(r-rw)U\right)\right]\right\} \to PROR \\ J_{x,r,w}^{2} &= \left\{((1+x)I-wL)^{-1}\left[\left((1+x-r+rw)I+(r-w-rw)L+(r-rw)U\right)\right]\right\}^{2} \to RPROR \\ J_{x,r,w}^{3} &= \left\{((1+x)I-wL)^{-1}\left[\left((1+x-r+rw)I+(r-w-rw)L+(r-rw)U\right)\right]\right\}^{3} \to SRPROR \\ J_{x,r,w}^{4} &= \left\{((1+x)I-wL)^{-1}\left[\left((1+x-r+rw)I+(r-w-rw)L+(r-rw)U\right)\right]\right\}^{4} \to TRPROR \end{aligned}\right\}$$

(16)

The major concern of these work is the Third Refinement of Parametric Reaccelerated Overrelaxation (TRPROR)

3.1 Convergence of the Methods

Theorem 1

Let G be the coefficient matrix of the linear system $Ax = b$. If $A$is consistently ordered, positive definite and the parameter x, r, w satisfy

$0 < w < 2, \quad 0 < r \leq 1 \qquad x \neq 1$

Then, the iterative matrix J_{TRPROR} has a spectral radius $\rho(J_{TRPROR}) < 1$, ensuring the convergence of the $TRPROR$ method.

Proof:

The $TRPROR$ iterative matrix J is derivates;

$J = [(1 + x)I - wL]^{-1}[(1 + x - r + rw)I + (r - w - rw)L + (r - rw)U].$

(17)

Where L and U are the strictly Lower and Upper triangular parts of A, and I is the identity matrix. For convergence, the spectral radius $\rho(J) = M = max|\lambda| < 1$. Where λ are the eigenvalues of J

If A is positive definite, it guarantees that D (diagonal part of A) is invertible

Consistently ordered matrixes ensure that the splitting $A = D - L - U$ is valid

For $0 < w < 2$ ensures stability, $0 < r \leq 1$ Control reacceleration and avoids divergence

$x \neq -1$ present singularity in $(1 + x)I - wL$.

The refinement ensures; $\rho(J_{TRPROR}) < \rho(J_{PROR}) < 1$

Where $\rho(J_{PROR})$ corresponds to the Parametric Reaccelerated Overrelaxation

Theorem 2

Optimal Parameters

The spectral radius $\rho(J_{TRPROR})$ is minimized for the following optimal parameters.

$w^* = \frac{2(1+x)}{1+\sqrt{1-\mu^*}}$

(18)

Where μ is the eigenvalue of the corresponding Jacobi iteration matrix.

Proof

The spectral radius depends on the eigenvalues λ of (J_{TRPROR}). Using results from PROR (Isah et al., 2023) analysis.

$\lambda = \frac{r\mu^2 w(1-w)}{2(1+x)^2} - \frac{r(1-w)}{(1+x)} + 1$

(19)

To minimize $|\lambda|$, differentiate the above expression with respect to w;

$$\frac{d\lambda}{dw} = \frac{r\mu^2(1-w)}{2(1+x)^2} - \frac{r}{1+x}$$

(20)

Setting $\frac{d\lambda}{dw} = 0$, and solve for w

$$w^* = \frac{2(1+x)}{1+\sqrt{1-\mu^*}}$$

(21)

Substituting w^* back into λ ensures $\rho(J)$ is minimized

4. Result and Discussion

Various numerical test was executed to validate the superiority of the Third Refinement of Reaccelerated Overrelaxation scheme (TRPROR) over AOR, ROR, PAOR and PROR. The criteria for the convergence is that, the spectral radius of iterative matrix must be less than zero

Problem 1. (*Source:* Isah *et al.* (2022))

$$A = \begin{pmatrix} 1 & 0 & \frac{1}{5} & \frac{1}{5} \\ 0 & 1 & -\frac{71}{10} & \frac{113}{10} \\ \frac{16}{5} & \frac{1}{5} & 1 & 0 \\ 2 & \frac{1}{5} & 0 & 1 \end{pmatrix}$$

Problem 2 (*Source:* Wu *et al.* (2007), Abdullahi & Ndanusa (2020))

$$A = \begin{pmatrix} 1 & -1/6 & -1/7 & -1/8 & -1/6 & -1/7 \\ -1/8 & 1 & -1/6 & -1/7 & -1/8 & -1/6 \\ -1/6 & -1/8 & 1 & -1/6 & -1/7 & -1/8 \\ -1/7 & -1/6 & -1/8 & 1 & -1/6 & -1/7 \\ -1/8 & -1/7 & -1/6 & -1/8 & 1 & -1/6 \\ -1/6 & -1/8 & -1/7 & -1/6 & -1/8 & 1 \end{pmatrix}$$

The results for Problem 1 and 2 are performed with Maple 2019 to yield some comparison results. The reduction of spectral radii for the Refinement, Second Refinement and Third Refinement of AOR, ROR, PAOR and PROR when compared to the AOR, ROR, PAOR and PROR proposed by Hadijimos (1981), Vatti *et al.*, (2020) and Isah *et al.*, (2022) scheme are shown in Table 1-8 respectively.

Table 4.1: Comparison of Spectral Radii for Methods

Methods	Choice of Parameters	Spectral Radius
AOR	$r=\frac{14}{3}, w=\frac{5}{3}$	0.7512951780
ROR	$r=\frac{-403}{100}, w=\frac{5}{3}$	0.5689256934
PAOR	$x=\frac{-9}{10}, r=\frac{43}{125}, w=\frac{1}{6}$	0.5842556518
PROR	$x=\frac{-9}{10}, r=\frac{43}{125}, w=\frac{1}{6}$	0.5653710677

$\rho(J_{AOR})<\rho(J_{ROR})<\rho(J_{PAOR})<\rho(J_{PROR})<1$

Table 4.2: Comparison of Spectral Radii for Refinement Methods

Methods	Choice of Parameters	Spectral Radius
RAOR	$r=\frac{14}{3}, w=\frac{5}{3}$	0.5644444444
RROR	$r=\frac{-403}{100}, w=\frac{5}{3}$	0.3236764444
RPAOR	$x=\frac{-9}{10}, r=\frac{43}{125}, w=\frac{1}{6}$	0.3413546667
RPROR	$x=\frac{-9}{10}, r=\frac{43}{125}, w=\frac{1}{6}$	0.3196444444

$\rho(J_{RAOR})<\rho(J_{RROR})<\rho(J_{RPAOR})<\rho(J_{RPROR})<1$

Table 4.3: Comparison of Spectral Radii for Second Refinement Methods

Methods	Choice of Parameters	Spectral Radius
SRAOR	$r=\frac{14}{3}, w=\frac{5}{3}$	0.4240643894
SRROR	$r=\frac{-403}{100}, w=\frac{5}{3}$	0.1841478455

SRPAOR	$x=\frac{-9}{10}, r=\frac{43}{125}, w=\frac{1}{6}$	0.1994383932
SRPROR	$x=\frac{-9}{10}, r=\frac{43}{125}, w=\frac{1}{6}$	0.1807177209

$\rho(J_{SRAOR})<\rho(J_{SRROR})<\rho(J_{SRPAOR})<\rho(J_{SRPROR})<1$

Table 4.4: Comparison of Spectral Radii for Third Refinement Methods

Methods	Choice of Parameters	Spectral Radius
TRAOR	$r=\frac{14}{3}, w=\frac{5}{3}$	0.3185975309
TRROR	$r=\frac{-403}{100}, w=\frac{5}{3}$	0.1047664407
TRPAOR	$x=\frac{-9}{10}, r=\frac{43}{125}, w=\frac{1}{6}$	0.1165230085
TRPROR	$x=\frac{-9}{10}, r=\frac{43}{125}, w=\frac{1}{6}$	0.1021725709

$\rho(J_{TRAOR})<\rho(J_{TRROR})<\rho(J_{TRPAOR})<\rho(J_{TRPROR})<1$

Problem 2

Table 4.5: Comparison of Spectral Radii for Methods

Methods	Choice of Parameters	Spectral Radius
AOR	$r=\frac{1}{7}, w=\frac{1}{5}$	0.8790762378
ROR	$r=\frac{1}{4}, w=\frac{1}{5}$	0.8307398051
PAOR	$x=\frac{-8}{10}, r=\frac{43}{125}, w=\frac{1}{5}$	0.7281216352
PROR	$x=\frac{-8}{10}, r=\frac{43}{125}, w=\frac{1}{5}$	0.6777675433

$\rho(J_{AOR})<\rho(J_{ROR})<\rho(J_{PAOR})<\rho(J_{PROR})<1$

Table 4.6: Comparison of Spectral Radii for Refinement Methods

Methods	Choice of Parameters	Spectral Radius
RAOR	$r=\frac{1}{7}, w=\frac{1}{5}$	0.7727750319

RROR	$r=\frac{1}{4},w=\frac{1}{5}$	0.6901286237
RPAOR	$x=\frac{-8}{10},r=\frac{43}{125},w=\frac{1}{5}$	0.5301611157
RPROR	$x=\frac{-8}{10},r=\frac{43}{125},w=\frac{1}{5}$	0.4593688427

$\rho(J_{RAOR})<\rho(J_{RROR})<\rho(J_{RPAOR})<\rho(J_{RPROR})<1$

Table 4.7: Comparison of Spectral Radii for Second Refinement Methods

Methods	Choice of Parameters	Spectral Radius
SRAOR	$r=\frac{1}{7},w=\frac{1}{5}$	0.6793281677
SRROR	$r=\frac{1}{4},w=\frac{1}{5}$	0.5733173183
SRPAOR	$x=\frac{-8}{10},r=\frac{43}{125},w=\frac{1}{5}$	0.3860217785
SRPROR	$x=\frac{-8}{10},r=\frac{43}{125},w=\frac{1}{5}$	0.3113452920

$\rho(J_{SRAOR})<\rho(J_{SRROR})<\rho(J_{SRPAOR})<\rho(J_{SRPROR})<1$

Table 4.8: Comparison of Spectral Radii for Third Refinement Methods

Methods	Choice of Parameters	Spectral Radius
TRAOR	$r=\frac{1}{7},w=\frac{1}{5}$	0.5971812499
TRROR	$r=\frac{1}{4},w=\frac{1}{5}$	0.4762775172
TRPAOR	$x=\frac{-8}{10},r=\frac{43}{125},w=\frac{1}{5}$	0.2810708086
TRPROR	$x=\frac{-8}{10},r=\frac{43}{125},w=\frac{1}{5}$	0.2110197336

$\rho(J_{TRAOR})<\rho(J_{TRROR})<\rho(J_{TRPAOR})<\rho(J_{TRPROR})<1$

4.1 Discussion of Results

The results from Tables 1 to 8 demonstrate the effectiveness of the Third Refinement of Parametric Reaccelerated Overrelaxation (TRPROR) method in improving convergence rates for solving linear algebraic systems. Initially, the classical methods Accelerated Overrelaxation (AOR), Reaccelerated Overrelaxation (ROR), Parametric Accelerated Overrelaxation (PAOR), and Parametric Reaccelerated Overrelaxation (PROR) exhibited relatively high spectral radii,

indicating slower convergence. Among them, PROR had the lowest spectral radius, suggesting better performance.

With the introduction of refinements, the spectral radii progressively decreased. The first refinement methods (RAOR, RROR, RPAOR, and RPROR) showed notable improvements, with RPROR having the smallest spectral radius. The second refinement methods (SRAOR, SRROR, SRPAOR, and SRPROR) further enhanced convergence, reducing spectral radii even more, with SRPROR leading in efficiency. Finally, the third refinement methods (TRAOR, TRROR, TRPAOR, and TRPROR) achieved the most significant reduction in spectral radii, with TRPROR emerging as the best-performing method.

Overall, the results confirm that iterative refinements effectively enhance convergence by reducing spectral radii. The TRPROR method, with the lowest spectral radius across all test cases, proves to be the most efficient iterative method for solving large-scale linear systems.

5. Conclusion

The spectral radius of an iterative method for solving linear algebraic systems is a critical factor in ensuring convergence, with smaller spectral radii leading to faster convergence. The primary objective of developing new iterative methods is to enhance the convergence performance of existing methods. In this research, we utilized refinement techniques to propose a Third Refinement of the Parametric Reaccelerated Over-Relaxation (TRPROR) method for solving linear systems. Numerical experiments demonstrated that the TRPROR method outperforms the AOR, PAOR, ROR, RAOR, RPAOR, RROR, TRAOR, TRROR, and TRPAOR methods in terms of convergence.

References

Abdullahi, I. and Ndanusa, A. (2020). A new modified preconditioned accelerated overrelaxation (AOR) iterative method for L −matrix linear algebraic systems. Science World Journal, 15(2): 45 – 50.

Assefa, W. L. and Teklehaymanot, A. W. (2021). Second refinement of accelerated over relaxation method for the Solution of Linear System. *Pure and Applied Mathematics Journal*, 10(1): 32-37. doi: 10.11648/j.pamj.20211001.13

Audu, K. J., Oniwinde, M. O., & Essien, J. N. (2024). Enhancing Linear System Solving Through Third Refinement of Successive and Accelerated Over-Relaxation Methods. *Çankaya University Journal of Science and Engineering*, 21(01), 18–32.

Avdelas G. & Hadjidimos, A. (1981). Optimum accelerated overrelaxation method in a special case. Mathematics of computation, 36(153),183-187.

Eneyew, T. K., Awgichew, G., Haile, E. and Abie, G. D. (2019). Second refinement of Jacobi iterative method for solving linear system of equations. *International Journal of Computing Science and Applied Mathematics*, 5(2): 41-47.

Eneyew, T. K., Awgichew, G., Haile, E. and Abie, G. D. (2020). Second refinement of Gauss-Seidel iterative method for solving linear system of equations. *Ethiopian Journal of Science and Technology,* 13(1): 1-15.

Hadjidimos, A. (1978). Accelerated overrelaxation method. *Mathematics of Computation*, (32) 141: 149-157.

Isah, I. O., Ndanusa, A., Shehu, M. D., & Yusuf, A. (2022). Parametric reaccelerated overrelaxation (PROR) method for numerical solution of linear systems. *Science World Journal*, 17(1), 59-64.

Ismaila M., Halidu Muhammad I., & Abdullahi I. (2023). The Improved Preconditioned Accelerated Overrelaxation (AOR) Iterative Method for L −Matrix. Lapai Journal of Applied and Natural Science. LAJANS Vol 8 (1):1-6

Jacobi, C. G. J. (1884). Gessamelte werke. Berlin: G. Reimer. pp 467.

Ndanusa, A. (2020). Convergence of preconditioned Gauss-Seidel iterative method for L −matrices. Communication in Physical Sciences, 6(1): 803 – 808.

Ndanusa, A. and Adeboye, K. R. (2012). Preconditioned SOR iterative methods for L −matrices. American Journal of Computational and Applied Mathematics, 2(6): 300-305.

R. S. Varga, Matrix Iterative Analysis, Springer, Berlin, Germany, 2000.

Seidel, L. (1874). Abh bayer akad wiss. Naturwiss. Kl. 11(3), 81.

Vatti, V. B. K. Sri, R. and Mylapalli, M. S. K. (2018). A refinement of accelerated over relaxation method for the solution of linear systems. *International Journal of Pure and Applied Mathematics*, 118(18): 1571-1577.

Vatti, V. B. K., Rao, G. C. & Pai S. S. (2020). Parametric overrelaxation (PAOR) method. Numerical optimization in Engineering and Sciences, Advances in Intelligent Systems and Computing, 979, 283-288.

Vatti, V. B. K., Rao, G. C. & Pai, S. S. (2020). Reaccelerated overrelaxation (ROR) method. Bulettin of the International Mathematical Virtual Institute, 10(2), 315- 324.

Wang, H. (2019). A preconditioned AOR iterative scheme for systems of linear equations with L-matrices. Open Mathematics, 17: 1764–1773.

Wu, M., Wang, L., Song, Y. (2007). Preconditioned AOR iterative method for linear systems.

Y. Saad, Iterative Methods for Sparse Linear Systems, PWS Publishing, Boston, Mass, USA, 1996.

Young, D. M. (1950). Iterative methods for solving partial difference equations of elliptic type. Doctoral Thesis, Harvard University, Cambridge, MA. pp 74.

Z. Bai, "Sharp error bounds of some Krylov subspace methods for non-Hermitian linear systems," Applied Mathematics and Computation, vol. 109, no. 2-3, pp. 273–285, 2000.

An Iced-Type Model for Disease Control

[1,*]Sahabi Ibrahim Gurjiya and [2]Umar Muhammad Dauda

[1]Department of Mathematics, Sa'adatu Rimi College of Education, Kumbotso Kano

[2]Department of Mathematics, Faculty of Computing & Mathematical Sciences, Kano University of Science & Technology, Wudil, Kano.

[1*]Corresponding author: sahabigurjiya@gmail.com

Abstract

Understanding the pattern or the rate at which diseases spread could help to prepare for an epidemic Situations. Thus, there is need for a reliable model to study the development process of this contemporary issues on the controls of diseases epidemics. This work aims to study the formation of disease organisms via vertex model approach. In particular, we utilize a six-vertex model as a conceptual framework for studying and optimizing factors influencing the prevalence and spread of waterborne diseases. This is due to the fact that, it is a well-known model for the study of crystals with hydrogen bond like H_2O . The primary goal is to explore the pattern formation of disease organisms through the vertex model, employing the statistical approach for patterns identification.

1.0 Introduction

Every natural phenomenon follows a pattern, either obvious or hidden. Waterborne diseases, for example, have transmission patterns that aid in control. Understanding these patterns requires relevant models, such as the logistic model for population growth and decay. This work applies the iced-type or six-vertex model, originally designed to represent the arrangement of H_2O molecules, with oxygen atoms at lattice vertices and hydrogen atoms between adjacent oxygens.

An Iced-type model was first introduced in statistical mechanics by J.C Slater in his paper of (Slater, 1941) and an exact solution was given by Lieb, Elliott to a two-dimensional ice model known as 'square ice', for instance see (Lieb, 1967).

The spread of infectious diseases is influenced by biological, social, and environmental factors (Reich *et al.,* 2019). To study this complexity, scientists use mathematical models that divide populations into compartments, tracking the progression from infection to recovery or death. These models rely on epidemiological parameters (Kermack, 1991) but also involve assumptions that may not always match real-world decision-making needs. Beyond predicting epidemic trends, mathematical models help analyse past outbreaks, validate assumptions, and identify key transmission factors. Studies on household attack rates improve model accuracy and guide policymakers. Experts like Professor Sir Charles Godfray and Professor Jason Leitch stress the importance of modelling in managing epidemics.

Several models have been crucial in disease control. The **SIR model** classifies populations as susceptible (S), infected (I), and recovered (R), while the **SEIR model** adds an exposed (E) group to account for incubation. **Agent-based models** simulate individual interactions, and **metapopulation models** study disease spread across connected groups. These models help assess interventions like vaccination and quarantine.

Despite progress, traditional models have limitations, as they focus on rates of change rather than the structure of disease transmission. An algebraic approach may provide deeper insights but requires refinement. A better understanding of disease propagation should include the interactions of individual disease components. For waterborne diseases, analysing molecular interactions in water (hydrogen and oxygen) could lead to improved control strategies.

2.0. Materials and Methods

2.1 Waterborne diseases modelling

Water is essential but spreads diseases like typhoid, cholera, and diarrhoea when contaminated (Hoeprich *et al*., 1983); (Portier *et al.*, 2010). Typhoid, caused by *Salmonella typhi*, spreads through human waste and survives in water and sewage (Codeco *et al*., 2007). Diarrhoea, often from *E. coli*, is deadly for children due to dehydration, while cholera, caused by *Vibrio cholerae*, leads to severe fluid loss and death if untreated (Codeco *et al*., 2007).

Pathogens enter through water, food, objects, or skin (EU/EEA, 2006–2009). Some bacteria now resist treatment like chlorine. WHO and CDC provide vast epidemiological data. Models help understand disease spread: (Cvjetanovic *et al.* 1971) found sanitation more effective than vaccination. (Tien and Earn, 2013) compared models with and without water compartments. (Robertson *et al.* 2013) studied two populations. (Boots and Sasaki, 1937) introduced a lattice model, and (Codeco *et al.* 2007) developed a seasonal stochastic model.

Our research builds on Boots and Sasaki's model by using a **lattice-weight matrix** to study contamination patterns. (Brascamp 1974) provides further studies on lattice models. Related literature includes (Amol et. al. 2023) and (Charlier, 2021).

2.2. Six-Vertex Model

The model describes the possible states of ice crystals, where hydrogen atoms follow specific configurations (Lieb, 1967). Each vertex represents an intersection of water molecules, with bonding rules dictating their arrangement (Pauling, 1935). The model is named after its six allowed vertex configurations, following the "ice rule," which ensures two bonds point inward and two outward (Baxter, 1982). Mathematically, it is analysed using Boltzmann weights to assign statistical probabilities (Korepin *et al*., 1993).

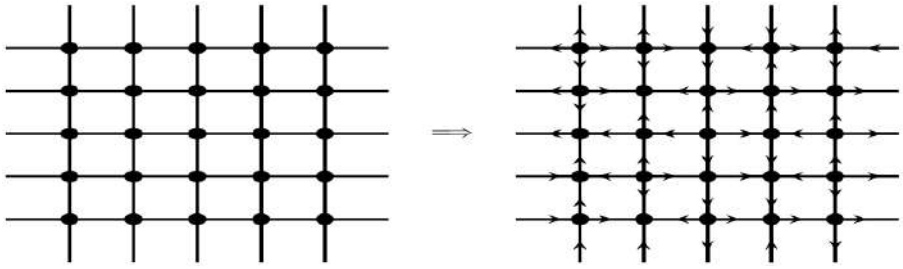

Fig. 2.1: **Left**: *16 square lattices*, **Right**: *a 16 vertex model.*

A square lattice with N^2 vertices is considered (Fig. 2.1), where edges are assigned arrows: ↑ or → as 1, and ↓ or ← as 2. In a 16-vertex lattice (Fig. 2.1, right), each vertex connects to four edges, resulting in six possible configurations (Fig. 2.2). Enforcing equal incoming and outgoing arrows allows only six valid vertex types, with two incoming arrows chosen in $\binom{4}{2} = 6$ ways.

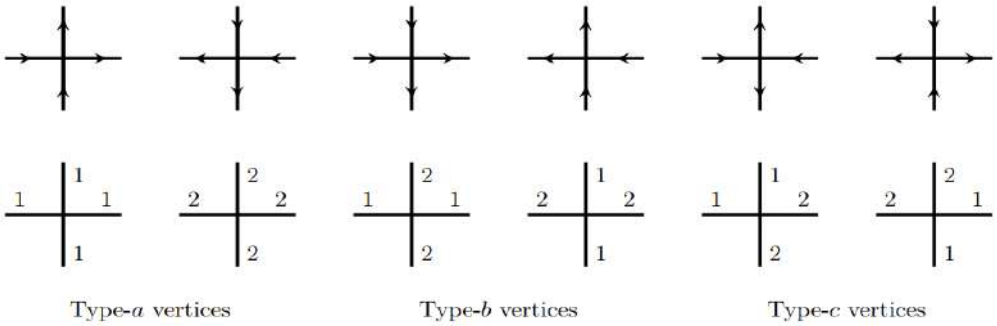

Fig.2.2: Types of the vertices in the upper panel and the corresponding values on the lower panel.

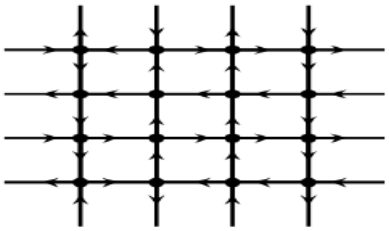

Fig.2.3: The graphical representation of a six-vertex model

2.3 Classical Partition Function with Application.

Let us consider a system of particles consisting of s states with corresponding energy $E(s)$. The associated partition function is defined

$$Z(s) = \sum_{s} \exp(-E(s)/T), \qquad \text{where } T \text{ is the temperature in Joules.}$$

The probability of getting a system in the state s is given by

$$p(s) = \frac{\exp(-E(s)/T)}{Z(s)} = \frac{W(s)}{Z(s)} \tag{2.1}$$

For statistical weight of state s denoted as $W(s) = \exp(-E(s)/T)$.

2.4. Partition Function in Waterborne Disease Control

The partition function is a mathematical tool used in physics to study systems with different possible states. When applied to waterborne disease control, it helps us understand how diseases spread and how interventions like clean water, vaccination, and sanitation can reduce the risk of

infection. This concept connects probabilities, energy levels, and real-world disease control strategies.

In simple terms, a partition function sums up all possible "states" of a system, giving each state a weight based on how likely it is to happen. In waterborne disease control, these states represent groups of people in different health conditions, such as: **susceptible (S)**, **infected (I), recovered (R)**. Each of these states depends on factors like: disease transmission rate (e.g., through contaminated water), recovery rate, interventions.

2.5 Mathematical Form of the Partition Function

Using the partition function (Z) for the classical partition function with $Z(s) = \sum_s \exp(-E(s)/T)$:

$\boldsymbol{E_s}$: represents the "energy" of state s (higher E_s means the state is less favourable).

$\boldsymbol{B = \frac{1}{k \cdot T}}$**:** represents a parameter where T is the level of intervention (e.g., clean water, vaccination), and k is a constant, higher T implies interventions, which make the disease states less likely and lower T implies fewer interventions, which make disease spread more likely.

The probability of being in any state is calculated as: $p(s) = \frac{e^{-\beta E_S}}{Z(s)}$.

The partition function, in this regard, appeared to be a powerful tool for understanding and controlling waterborne diseases. By modelling the probabilities of different health states, it helps predict disease spread, evaluate interventions, and optimize resource use. This approach, facilitates decision-making and could reduce the burden of waterborne diseases in vulnerable communities.

2.4. Real-Life Example

Let's consider a community dealing with a cholera outbreak. People are divided into three groups:

S: 500 people who drink untreated water (high risk of infection).
I: 100 people who are already infected.
R: 400 people who use treated water or have recovered (low risk).

Without Interventions: The corresponding energy of each state (E_s):

E_S =3: susceptible people face high risk (no clean water).
E_I =5: infected people face even higher risk (poor treatment).
E_R =1: recovered people face low risk.

The partition function (Z): This is equivalent to $Z = e^{-3} + e^{-5} + e^{-1} \approx 0.4244$

Probability of Susceptible P(S): $P(s) = \frac{e^{-3}}{Z} = 0.1173$. This is approximately 12% of the population remains susceptible.

Probability of infected P(I): $P(I) = \frac{e^{-5}}{Z} = 0.0158$. Therefore, there is approximately1.5% of the population remains infected.

Probability of Recovered P(R): $P(R) = \frac{e^{-1}}{Z} = 0.8670$**.** This is approximately 87% of the population are recovered or safe.

This shows that without interventions, a small fraction remains infected, but the susceptible group is still significant, risking future outbreaks.

When interventions into account such as supply of clean water and vaccines, reducing E_S and E_I:

New E_S=1: Clean water reduces risk for susceptible people.
New E_I=3: Medical care improves recovery chances for infected people.
E_R remains 1 (low risk for recovered people).

The new partition function becomes: $Z = e^{-1} + e^{3} + e^{-1} \cong 0.79$ and the respective probability of susceptible is $P(s) = \frac{e^{-1}}{Z} = 0.47$. This means approximately 47% of the population remain susceptible, which is much safer than before. Moreover, the probability of the infected $P(I) = 0.063$. This means only about 6.3% of the population remain infected, showing a significant reduction. Again, the corresponding probability of the recovered $P(R) = \frac{e^{-1}}{Z} = 0.47$. This indicates that around 47% of the populations are recovered or safe. This demonstrates that interventions shift the population toward safer states.

In a nutshell, the iced-typed model hinted that, the prediction of disease spread is possible depending on different conditions. And that, optimization of resources such as providing clean water or vaccination to reduce E_S and improving healthcare to reduce E_I would help in the evaluation of the rapid spread and the likelihood of infection of water borne diseases.

Furthermore, there is need for an ultimate and reliable model that models the long-term behaviour of related diseases for proper examination and detection of possible outcomes.

2.6 ICED TYPE MODEL: Waterborne related disease control

Waterborne diseases like cholera, typhoid, and dysentery pose a global threat, especially in areas with poor sanitation. Traditional control methods are often insufficient, necessitating innovative approaches. The six-vertex model, from statistical mechanics, has potentials due to its interesting property, to provide valuable insights for disease prevention and control.

The Six-Vertex Model: A Framework for Analysing Water Networks

The six-vertex model represents systems where each vertex is influenced by its neighbours. In waterborne disease modelling, vertices represent locations in a water network, with connections indicating water flow and contamination spread. Each vertex has six possible states, simulating scenarios like clean water reaching households, contaminated water spreading via damaged pipelines, treated and untreated water interacting at junctions. This model helps identify contamination patterns and optimal intervention points.

One of the key strengths of the six-vertex model is its ability to map how contaminants travel through a water distribution system. For example:

- After heavy rainfall, sewage and industrial waste may enter the water supply. The model can simulate how these pollutants move through the network, identifying high-risk areas where contamination levels are highest. - In rural areas, agricultural runoff can introduce harmful microorganisms into nearby rivers or wells. The model helps visualize how these contaminants spread and affect downstream communities.

This mapping allows public health officials to focus resources on the most vulnerable locations, such as deploying mobile water treatment units or installing protective barriers.

3.0 Model Representation

The proposed Six-Vertex Model describes waterborne disease spread using a grid-based network where: - Each **vertex** represents a water junction. - **Edges** (i, j) represent water flow pathways that can carry contaminants. - **Weight Matrix** W_{ij} assigns contamination severity to each vertex.

- **Probability Matrix** P_{ij} determines the likelihood of contamination at each vertex.

We will model the spread of waterborne diseases using the following terminologies.

Create a weight matrix W_{ij} to represent the contamination severity at each contaminated water junction, generate contamination probability matrix P_{ij}, similar to equation (2.1)

$$P_{ij} = \frac{W_{ij}}{Z} \tag{3.1}$$

to determine the likelihood of the contamination at each vertex (i, j) and to enable targeted water treatment strategies. We normalize the probabilities for a statistical mechanics-based analysis as described.

Then, we construct the Partition function with the W_{ij} defined in equation (3.1) as

$$Z = \sum_{i=1}^{M} \prod_{j=1}^{N} W_{ij} \tag{3.2}$$

which ensures all contamination configurations contribute appropriately to the system state and normalizes the system's probability distribution (3.1). This governs the Markov Chain Monte Carlo (MCMC) process used to model contamination transitions. This process is used to captures realistic spread of contamination. We will use *Markov Chain Monte Carlo* (MCMC) to analyse disease behaviour, as it effectively models state transitions in stochastic systems. The approach involves: Random Sampling: Generating contamination states based on P_{ij} and the transition probabilities.

3.2 Contamination Transition Dynamics

For a given contaminated region, the probability of a neighboring site being infected follows:

$$P_{\text{trans}}(i,j) = \frac{1}{4} P_{ij} \sum_{\text{neighbours}} C_{k,\ell}, \tag{3.3}$$

where: P_{ij} is the contamination probability at site (i,j) defined in (3.1) and $C_{k,\ell}$ represents contamination states of neighboring sites (0: clean, 1: contaminated).

3.3 Treatment and Recovery

Water treatment effectiveness function is introduced with a *removal probability* γ:

$$P_{\text{clean}} = \gamma \cdot C_{ij}, \tag{3.4}$$

where γ (treatment efficiency) determines the probability of decontaminating a contaminated site, where C_{ij} is the contamination state (1 = infected, 0 = clean) in (3.3). Incorporating Water Treatment Effectiveness into the Model would help to study water treatment effectiveness.

Therefore, a treatment matrix T_{ij} is introduced to track the effectiveness of treatment over time where higher T_{ij} signifies better treatment at site (i,j).

That way, we study the (i) contaminated fraction over time; (ii) treatment effectiveness matrix and (iii) rate of contamination spread with vs. without treatment.

4. Results and Discussion

Fixing some of the parameters, such as γ treatment of effectiveness and number of sites and random weight matrices, we give the possible interpretation of the results. In the discussion, it would be clear that for the contamination spread over time, red regions show how contamination propagates while the white regions indicate cleaned water due to treatment.

For the probability matrix, higher values indicate more contamination risk at specific sites. It further helps identify target areas that are in need for urgent treatment. The rate of contamination spread tells us how quickly the disease propagates and guides us to know the effectiveness of intervention offered.

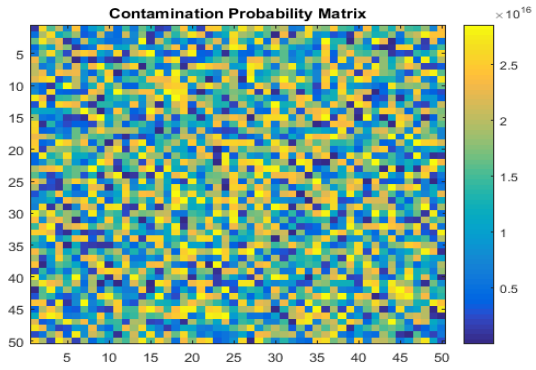

Fig. 4.1. Showing the Contamination areas, where yellowish area indicates highly contamination probability while the bluish areas indicate a low risk of contamination.

Taking $\gamma = 0.25$, representing the 25% of water treatment and random weight-matrix (contamination), we have the following results in the following figures, showing the effectiveness of the water treatment matrix and contamination probability matrix.

The contamination Matrix after time step 4, shown in **Fig. 4.2**, indicates the affected areas and how the spread from a single spot to bigger regions. White areas indicates uncontaminated regions while the red areas indicates total contamination spread.

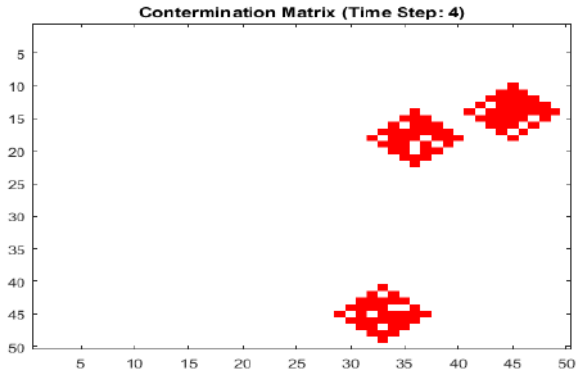

Fig. 4.2. Contamination Matrix.

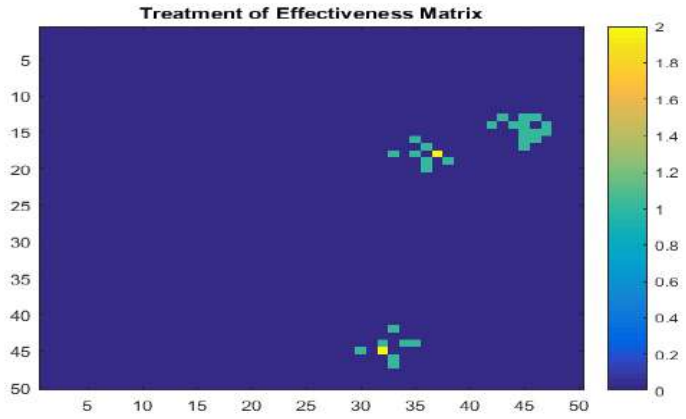

Fig. 4.3. Shows the treatment of effectiveness matrix. The yellowish area indicates higher effectiveness accordingly.

The contamination matrix is shown above with after a time-step of 4 and the corresponding rate of spread of the disease and the effectiveness are shown in the figure below:

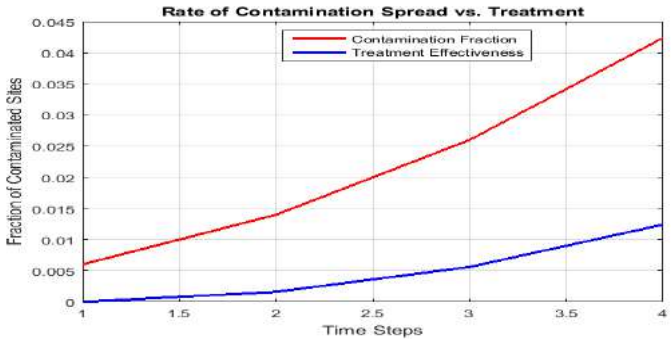

Fig. 4.4. The rate of contamination versus treatment of potential waterborne diseases.

If more time step is allowed, with the same treatment rate $\gamma = 0.25$, the treatment effectiveness rate increase thereby showing significant impact. This is evident from the figures below.

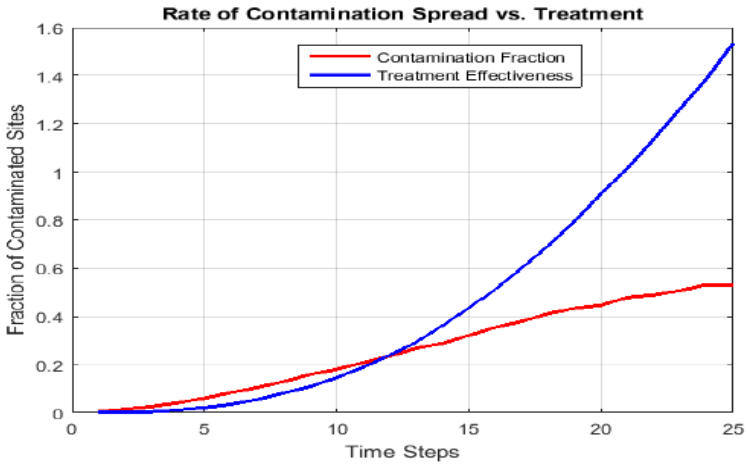

Fig. 4.5. Contamination and treatment effectiveness rates with parameter $\gamma = 0.25$.

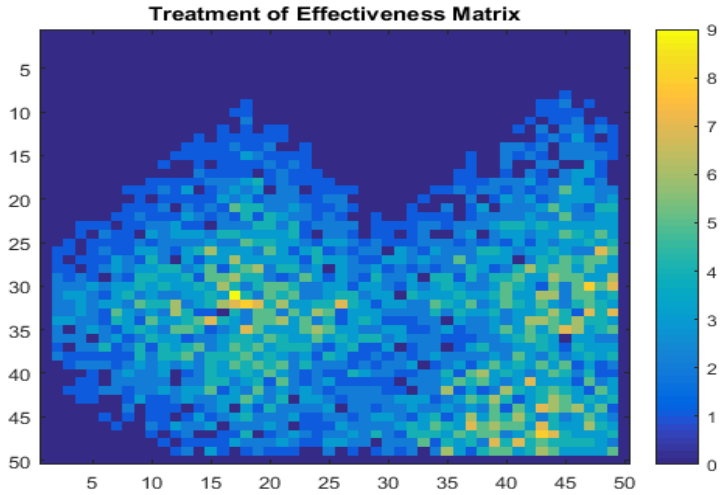

Fig. 4.6. The map showing treatment of effectiveness matrix.

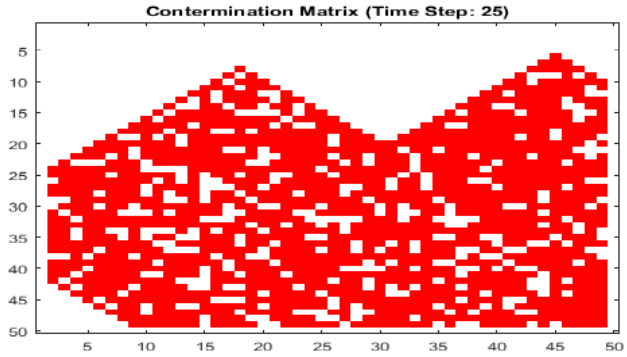

Fig. 4.7. The contamination matrix with $\gamma = 0.25$ after 25 time step;

With the treatment parameter being 100%, the rate of spread and the effect of treatment are shown as follows, respectively, in Fig. 4.8 and Fig. 4.9.

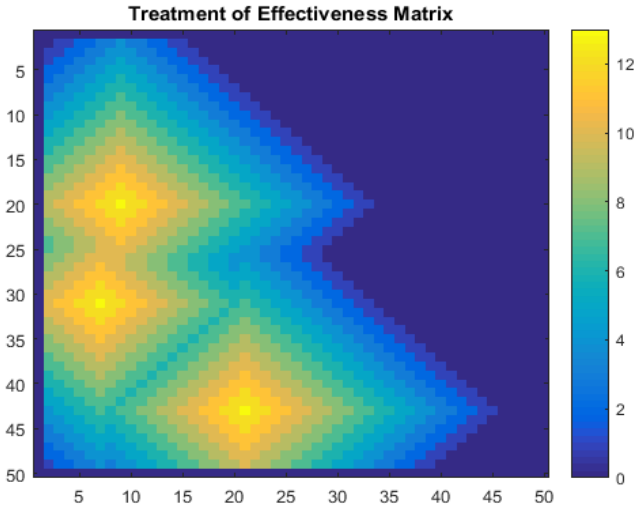

Fig. 4.8. Showing the matrix of effectiveness of treatment with 100% water treatment.

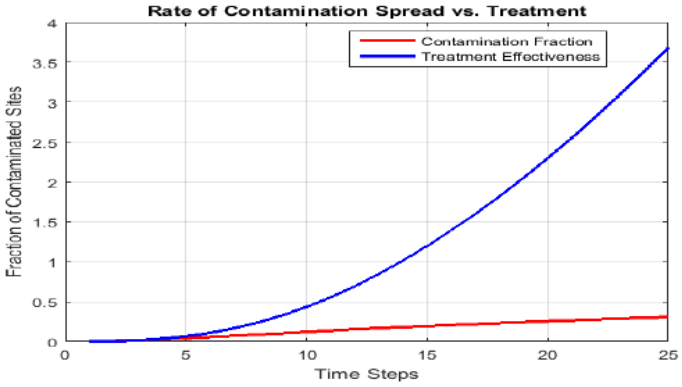

Fig. 4.9. Shows the rate of contamination and effectiveness of treatment with 100% water treatment.

This indicates the 100% water treatment would lead to decrease in the rate of contamination/spread of the diseases.

5. Conclusion

The six-vertex model demonstrates a powerful capability in studying contamination spread and treatment effectiveness for waterborne diseases. Despite using randomly generated weights, the approach shows promising results and, when applied to real-world data, could provide reliable insights.

As global challenges like climate change, population growth, and aging infrastructure intensify, this model offers a crucial tool for ensuring safe water access. By mapping contamination pathways, identifying intervention points, and simulating infrastructure changes, it supports informed decision-making, enhances water system resilience, and contributes to global public health improvements.

References

Amol A., Alexei B., Leonid P. & Michael W. (Jan, 2023). Free Fermion Six Vertex Model: Symmetric Functions and Random Domino Tilings. arXiv:2109.06718v2.

Boots M., Sasaki A. (1938). Small Worlds' and the evolution of virulence: infection occurs locally and at a distance. Proc. The Royal Society. 1999;266:1933-1938.

Brascamp, H. J., Kunz, H., & Wu, F. Y. (1974). Some Rigorous Results for the Vertex Model in Statistical Mechanics. Journal of Mathematical Physics, 15(1), 65–68.

Centres for Disease Control and Prevention. National Centre for Environmental Health: Vessel Sanitation Program. Health Practices on Cruise Ships: Training for Employees Transcript; 2013.

C. Charlier (2021), *Doubly periodic lozenge tilings of a hexagon and matrix valued orthogonal polynomials*, Studies in Applied Mathematics **146** (2021), no. 1, 3{80. arXiv:2001.11095 [math-ph].

Codeco C.T., Lele S., Pascual M., Bouma M., & Ko A.I. (2007). A stochastic model for ecological systems with strong nonlinear response to environmental drivers: application to two water-borne diseases. Journal of the Royal Society Interface. 2007;5:247-252.

Cvjetanovic B, Grab B, Uemura K. Epidemiological model of Typhoid fever and its use in the planning and evaluation of anti-typhoid immunization and sanitation. Bull World Health Organization. 1971;45:53-75. Lieb, E. H. (1967). "Exact solution of the problem of the entropy of two-dimensional ice." Physical Review Letters 18.17 (1967): 692.

Diekmann O, Heesterbeek JAP. Mathematical Epidemiology of Infectious Diseases: Model Building, Analysis and Interpretation. Wiley, New York; 1999.

European Centre for Disease Prevention and Control (ECDC), (2013). *Surveillance of food- and waterborne diseases in the EU/EEA – 2006–2009*. Stockholm: ECDC; 2013.

Hoeprich, P.D. (1983). Infectious Diseases, Third Edition. Harper and Row Publishers; 1983.

Izergin, A.G. (1987) Partition function of the six-vertex model in a finite volume, Sov.Phys. Dokl.32 (1987) 391-418.

Izergin, A.G. & Korepin, V.E. (1981). The quantum inverse scattering method approach to correlation functions, comm.Math.Phys 94.(1981) 67-92.

Kermack W.O., McKendrick A.G. (1991). Contributions to the mathematical theory of epidemics—I. Bull. Math. Biol. 53, 33–55.

Korepin,, V. E. (1982). Calculation of norms of Bethe wave functions, Comm. Math. Phys. 86 (1982) 391-418.

Korepin, V. E., & Zinn-Justin, P. (2000). Thermodynamic Limit of the Six-Vertex Model with Domain Wall Boundary Conditions. Journal of Physics A: Mathematical and General, 33(40), 7053–7066.

Lieb, E. H. (1967). Residual Entropy of Square Ice. Physical Review, 162(1), 162–172.

Nagle, J. F. (1966). Proof of the First-Order Phase Transition in the Slater KDP Model. Communications in Mathematical Physics, 9(4), 283–294.

Pauling, L. (1935). The Structure and Entropy of Ice and of Other Crystals with Some Randomness of Atomic Arrangement. Journal of the American Chemical Society, 57(12), 2680–2684.

Portier CJ, Thigpen Tart K, Carter SR, Dilworth CH, Grambsch AE, Gohlke J, Hess J, Howard SN, Luber G, Lutz JT, Maslak T, Prudent N, Radtke M, Rosenthal JP, Rowles T, Sandifer PA, Scheraga J, Schramm PJ, Strickman D, Trtanj JM, Whung P-Y. A Human Health Perspective On Climate Change: A Report Outlining the Research Needs on the Human Health Effects of Climate Change. Research Triangle Park, NC: Environmental Health Perspectives/National Institute of Environmental Health Sciences; 2010. DOI: 10.1289/ehp.1002272. Available: www.niehs.nih.gov/climaterepo.

Reich N.G. et al. (2019). A collaborative multiyear, multimodel assessment of seasonal influenza forecasting in the United States. Proc. Natl Acad. Sci. 116, 3146–3154. (doi:10.1073/pnas.1812594116).

Robertson SL, Eisenberg MC, Tien JH. Heterogeneity in multiple transmission pathways: modelling the spread of cholera and other waterborne disease in networks with a common water source. Journal of Biological Dynamics. 2013;7(1):254-275. DOI: 10.1080/175137558.2013.853844.

Rys, F. (1963). Über ein zweidimensionales klassisches Konfigurationsmodell. Helvetica Physica Acta, 36(5), 537–552.

Slater, J. C. (1941). Theory of the Transition in KH_2PO_4. Journal of Chemical Physics, 9(1), 16–33.

Tien JH, Earn DJD. Multiple transmission pathways and disease dynamics in a waterborne pathogen model. Bulletin of Mathematical Biology. 2010;72:1506-1533. DOI: 10.1007/s11538-010-9507-6.

Zinn-Justin, Paul. "Six-vertex model with domain wall boundary conditions and one-matrix model." Physical Review E 62.3 (2000): 3411.

Homogenous Markov Chain Model of Dam Water Outflow as a Panacea to Flooding in Nigeria

Mohammed, Abdullahi
Department of Mathematics, Nigerian Army University Biu, Nigeria
.Corresponding author: gbrara1972@gmail.com

Abstract

This paper examine the application of Markov chain model with non-stationary transition probabilities to study the water outflow level of Kainji Dam in the dry and rainy seasons. The results of the model confirm the reality on the phenomenon that the periodic flood is associated with higher water level in terms of the outflow which normally happens at peak rainy seasons. On the other hand, the lower water outflow is occurs mostly during the dry season, the variation of the water outflow have a direct impact on the production of hydroelectric power, periodic flood experienced and availability of other dam resources. Markov chain model could be used as a predictive method for studying reservoir outflow of Kainji Hydro-Dam. These forecasts might be used for the management of the dam resources, preparedness and control of periodic floods being experienced in this era in Nigeria.

Keywords: Markov Chain, Outflow, Kainji Hydro-dam, Dam Resources, Flood

1. Introduction

Dam can be natural or man-made and can be constructed to solve a lot of socio-economic problems which include among others irrigation and electricity generation. A number of related researches have been made on the application of the Markov model to dam dynamics and other areas.

Stochastic models are influential and have been used widely in health care and reservoir management. The Markov chain model has been used to solve numerous dam-related issues. (Akyuz et al., 2012) examined the application of first and second-order Markov chain models to dry and wet periods of annual stream flow records in order to generate a stochastic structure of hydrological droughts. They found that the second-order Markov (MC2) model in general gives results that are in better agreement with simulation results as compared with the first-order (MC1) model. In comparison to the first-order (MC1) model, they discovered that the second-order Markov (MC2) model generally produces results that are more consistent with simulation results.

Sule (1988) used a probabilistic dynamic programming model to calculate the reservoir water release policy for the Shiroro hydroelectric plant. He employed the reservoir storage capacity as the state variable in the simulation, and the model takes into consideration the various potential inflow volumes and their corresponding inflow probabilities to account for the unpredictable character of the inflow process.

The three-state Markov model for both discrete and continuous time for the reservoir elevation has been studied. The model also examined the impact of changing seasonal circumstances. The data collected from the dam was analyzed using the model. The outcome demonstrates that Nigeria's reservoir height varies with the country's dry and wet seasons. It was discovered also that the

reservoir will in the long term, be in high elevation by 49% and 56% in the discrete time and continuous time respectively (Mohammed, 2013).

Rash (2009) investigated the ideal dam reservoir volume using a yield model. They use the yield model for both the water needed for the dam's stream and the water released using the Markov chain method. It was claimed that the yield model's results are reliable for drawing various inferences and that the inflow discharged to the reservoir is at its lowest during critical years.

The system of three connected dams a supply, storage, and capture dam was studied by Paraskevi (2006) using a discrete-time Markov chain. He modeled the system as a discrete time Markov chain with three states, where state one represents the discrete amount of water in the supply dam, state two represents a storage dam, and state three represents the capture dam. He came to the conclusion that the system converges to a steady state. Moran, (1954, 1959) first published his work on the theory of dam storage, motivated by the issues the Snowing Mountain Authority in Australia was facing. He described a method for determining the probability distribution of the volume of water stored in a finite dam with random input and regular demand.
More recently, the situation of two connected dams, a supply Dam and a capture Dam with a regular demand of one unit from the supply Dam and a random input into the capture Dam was studied (Piantadosi, 2004). She modeled a system as a Markov chain and derived a transition probability matrix with a large block structure in order to solve for the invariant state probability vector of the water trapped in the Dams. She then used matrix reduction techniques to reduce the problem's size to one of the supply dam's orders of magnitude.

A Markov steady-state model of the plant was built to determine the probability output of the turbines, and over 200,000 pieces of data about the machines' performance were used to estimate the failure and repair rates for each machine. The Kainji hydropower station, which has seven turbo-alternators, was the base load supply for the Nigerian power grid for many years. The findings indicated that Kaplan turbine (KT) 12 is more likely to fail than any other KT unit in the hydropower plant. The analysis also reveals that 60% of the KT machine units are operating, which is consistent with the output's observed robustness. Additionally, the clusters of probability that define the system state because of the units' varying output capacities demonstrate that the hydropower plant has not operated to its full potential. In addition to fitting observations, the model logically offers a way to examine the results of many potential courses of action to enhance hydropower plant performance (Thomas, 2023).

Given these uncertainties, this paper attempts to develop a Markov chain model that might be applied to quantitatively estimate the dam outflow.

2. Materials and Methods

Study Area and Data Source: The data used in this paper is collected from the Kainji Dam Niger State, Nigeria. Kainji Dam was commissioned in the year 1968 and the dam was constructed primarily for the generation of Hydroelectric power (H E P). The Kainji Lake itself has a surface water level of roughly 1,243 KM^2. With a maximum depth of 12.1Metres. The dam was designed to have a generating capacity of 960 megawatts (MW) (1,290,000hp). However, only eight (8) of its twelve (12) turbines have been put into service, bringing the total power generation down to 760 megawatts (MW) (1,020,000 hp).

Markov Chain: A discrete time Markov chain is the stochastic process $\left(X_n, \quad n=0,1,2,...\right)$ if for each $n=0,1,2,\ldots$

$$P\{X_{n+1}=j_{n+1}/X_0=i_0,\ldots,X_n=i_n\}=P\{X_{n+1}=i_{n+1}/X_n=i_n\}$$

for all possible values of $i_0, i_1,....i_{n-1}, i, j$. We consider only Markov chains with time homogeneous transition probabilities; that is we assume that,

$$P\{X_{n+1}-j/X_n=i\}=P_{ij} \qquad ij\in \mathrm{I}$$

independently of the time parameters n (Ross, 1996).

Formulation of the Model: It has been observed that the typical range of water outflow of Kainji dam that can withstand turbine operation is between 622m^{3}and 1400m^3 levels. Any water excess above 1400m^{3}will cause to opening of spillways for overflows that resulted to flooding. Periodic flooding affects the downstream farming and ecological activities. Therefore, we are interested in utilizing the Markov principle to model this process.

Let's look at the Kainji Dam water outflow as represented by a three-state Markov chain.

STATE1: Lower water outflow (Dam Water Outflow $< <800m^3$)

STATE2: Medium water outflow (Dam Water Outflow between $800m^3$ and $\leq 1400m^3$)

STATE3: High water outflow (Dam Water Outflow $> 1400m^3$)

A possible transition between the states is given in figure 1

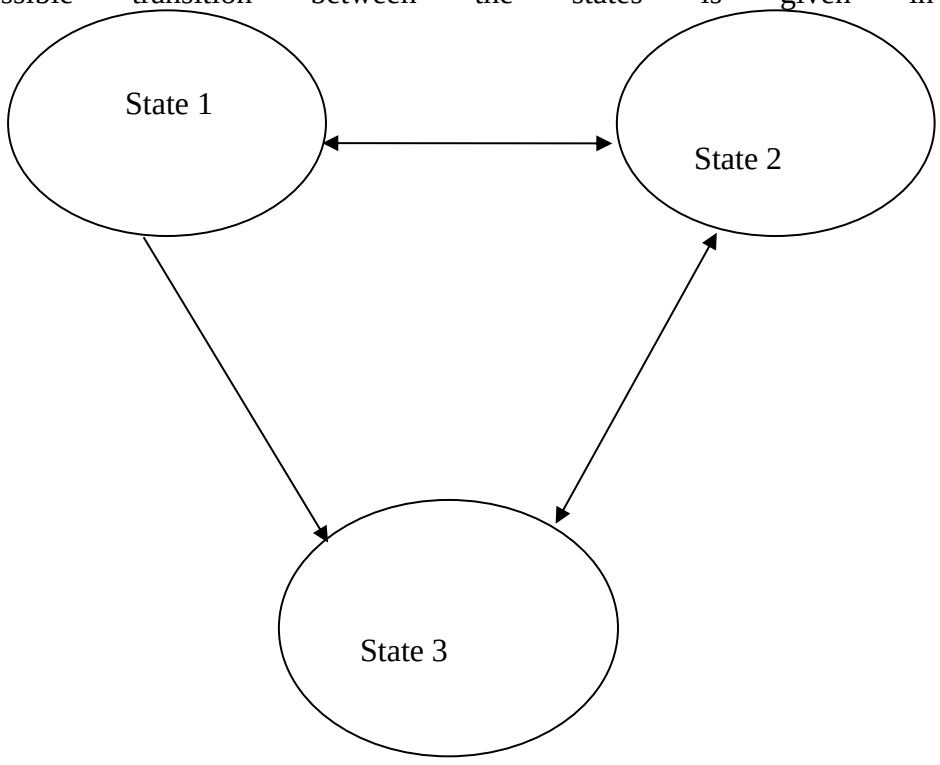

Figure 1: The State Transition Diagram for the Dam Water Outflow

We have thus considered the water outflow at a given time to be a random variable X and a collection of this random variable indexed by time parameter 'n' constitutes a stochastic process, X_n. That is

$$p(X_{n+1} = j \mid X_n = i) = p_{ij} \tag{1}$$

Let P_{ij} be the probability that the water outflow presently in state i will be in j in the subsequent transition. The following matrix P represents the transition probability between states.

$$P = \begin{bmatrix} p_{11} & p_{12} & p_{13} \\ p_{21} & p_{22} & p_{23} \\ 0 & p_{32} & p_{33} \end{bmatrix} \tag{2}$$

Equation (2) is the transition matrix for the water outflow. The above model shall be used to study the data recorded from water outflow of Kainji Dam from year (2014 to 2023).

Let $P_n = \left(P_1^n, P_2^n, P_3^n\right)$ (3)

Indicate the probability of discovering the water outflow in states 1, 2, and 3 over a time n.

Therefore we have

$$P^n = P^{n-1}P \tag{4}$$

In this iteration, we have

$$P^n = P^0 P^n \qquad n = 1, 2, 3 \tag{5}$$

Where P^0 is any starting vector of probabilities

The Limiting State Probabilities: After a sufficiently large period of time the process reaches a steady state. This is the equilibrium probability distribution $\pi = (\pi_1 \quad \pi_2 \quad \pi_3)$ and it is obtained by let $n \to \infty$ in equation (4). Consequently, we've

$$\pi = \pi P \tag{6}$$

and the sum of the component of π must be unity

$$i.e \qquad \sum_{i=1}^{3} \pi_i = 1 \tag{7}$$

The limiting state probabilities for the process will be determined using these last two equations.

Modeling the Seasonal Effect: It is well known that the likely causes and outcome of the water outflow in Kainji Dam changes with the seasons. Two seasons are taken into consideration as transition periods in this paper.

(i) season one (1)

(ii) Season two (2)

Season two (2) spans the months of November through March. In contrast, season one (1) runs from April to October. There are distinct transition count and transition probability matrices for every season (Jain, 1988). Here's how we give these:

M_1 and M_2 are the transition count matrices for dry and raining seasons

P_1 and P_2 are the transition probability matrices for dry and raining seasons.

Let

$$M_k = F_{ij}(k),\ i, j = 1, 2, 3 \text{ and } k = 1, 2 \tag{8}$$

And

$$P_k = P_{ij}(k),\ i, j = 1,2,3\ k = 1, 2 \tag{9}$$

$F_{ij}(k)$ represent the transition count from state i to another state j for the season k

$P_{ij}(k)$ represent the transition probability from state i to another state j for the season k

$$Accordingly,\quad P_{ij}(k) = \frac{F_{ij}(k)}{F_i(k)} \quad k = 1, 2 \text{ and } \quad ij = 1, 2, 3 \tag{10}$$

Where $F_i = \sum_{j=1}^{3} F_{ij}(k)$

Test for Stationarity of the Probability Matrices P_k : To verify for independence of P_k on k, the null hypothesis is stated thus:

$H_0 : P_{ij}(k) = P_{ij}$ for all $i, j = 1,2,3$ and for all k

$H_1 : P_{ij}(k)$ depends on k

The transition count matrix M is given by

$$M = \sum_{k=1}^{2} M_k = (F_{ij}) \tag{11}$$

Where

$$F_{ij} = \sum_{k=1}^{2} F_{ij}(k)$$

The maximum likelihood estimate of the stationary transition probability matrix is

$$P_{ij} = \frac{F_{ij}}{F_i} \tag{12}$$

Where

$$F_i = \sum_{j=1}^{3} F_{ij}(k)$$

The λ, the likelihood ratio criterion is given by

$$\lambda = \prod_{ij=1}^{3} \prod_{k=1}^{2} \left(\frac{p_{ij}}{p_{ij}(k)} \right)^{F_{ij}(k)} \tag{13}$$

$$-2\ln\lambda = \chi^2_{m(m-1)(t-1)} \quad \text{(Bhat, 1984)} \tag{14}$$

Where t is the time parameter and m is the number of states and. We evaluate λ and compute -2lnλ. Next, we compare the critical value of χ^2 with -2lnλ at the α -significant level. It is then decided whether to accept or reject the null hypothesis. With the acceptance of H_0 we have homogenous Markov chain model. The model is represented by a single transition count matrix using equation (11) and $P_{ij}^{,s}$ are estimated from equation (12). Otherwise, we have non homogeneous Markov chain model.

The stochastic matrix P can be written as $P = P_1 P_2$ (15)

and $P_{ij}^{,s}$ are derived from equation (12)

The following is then used to obtain the limiting state probability vector π_1 and π_2 for the two seasons:

$$\pi_1 = \pi_0 p_1 \tag{16}$$

$$\pi_2 = \pi_1 P_2 \tag{17}$$

Where the Equilibrium transition probability matrix p is represented by π_0

3. Results and Discussion

The 10 years monthly data collected from Kainji dam's water outflow is presented in Table 1

Table 1: A Summary for 10 Years Monthly Water Outflow in Cubic Meters of Kainji Dam from 2014 – 2023.

Class interval	state	frequency
Dam Water outflow $<800m^3$	1	5 0
Dam Water outflow between $800m^3$ *and* $1400m^3$	2	62
Dam Water outflow $>1400m^3$	3	8
Total		120

Table 1 presents the summary of monthly water outflow of Kainji dam for the period of ten (10) years, that is from 2014-2023

We provide the following transition count matrices and transition probability matrices using Equations (1) and (2) respectively for the two seasons.

$$M_1 = \begin{bmatrix} 19 & 6 & 0 \\ 9 & 34 & 3 \\ 1 & 1 & 4 \end{bmatrix} \qquad p_1 = \begin{bmatrix} 0.7600 & 0.2400 & 0 \\ 0.1967 & 0.7291 & 0.0652 \\ 0.1667 & 0.1667 & 0.6667 \end{bmatrix} \tag{18}$$

$$M_2 = \begin{bmatrix} 5 & 1 & 1 \\ 0 & 20 & 5 \\ 0 & 7 & 11 \end{bmatrix} \qquad p_2 = \begin{bmatrix} 0.7143 & 0.1429 & 0.1428 \\ 0 & 0.8000 & 0.2000 \\ 0 & 0.3889 & 0.6111 \end{bmatrix} \tag{19}$$

Using Equation (8), we have

$$M = \begin{bmatrix} 24 & 7 & 1 \\ 9 & 54 & 8 \\ 1 & 8 & 15 \end{bmatrix} \qquad p = \begin{bmatrix} 0.7500 & 0.2188 & 0.0312 \\ 0.1268 & 0.7616 & 0.1126 \\ 0.0417 & 0.3333 & 0.6250 \end{bmatrix} \tag{20}$$

Using Equation (13), we have

Therefore $-2In\lambda = 16.187200837$

At 0.05, the critical value is 12.59. The null hypothesis of a constant transition probability matrix is rejected since the computed value of $-2In\lambda$ is higher than the crucial value of χ_6^2 at α significance level. As a result, our Markov chain model is non-homogeneous. Therefore, using

equation (15), we obtain the maximum likelihood estimates of the transition probability matrix, which give us

$$p = \begin{bmatrix} 0.5128 & 0.3119 & 0.1743 \\ 0.1305 & 0.6493 & 0.2212 \\ 0.1111 & 0.4204 & 0.4695 \end{bmatrix} \tag{21}$$

On iteration using Equation (4) we have

$$p^2 = \begin{bmatrix} 0.3232 & 0.4369 & 0.2400 \\ 0.1761 & 0.5550 & 0.2689 \\ 0.1639 & 0.5047 & 0.3314 \end{bmatrix} \tag{22}$$

$$p^9 = \begin{bmatrix} 0.2026 & 0.5169 & 0.2805 \\ 0.2024 & 0.5170 & 0.2806 \\ 0.2024 & 0.5170 & 0.2806 \end{bmatrix} \tag{23}$$

$$p^{23} = \begin{bmatrix} 0.2045 & 0.5170 & 0.2806 \\ 0.2045 & 0.5170 & 0.2806 \\ 0.2045 & 0.5170 & 0.2806 \end{bmatrix} \tag{24}$$

$$p^{23} = \begin{bmatrix} 0.20 & 0.52 & 0.28 \\ 0.20 & 0.52 & 0.28 \\ 0.20 & 0.52 & 0.28 \end{bmatrix} \quad \textit{approximated} \text{ to 2 decimal places} \tag{25}$$

Additionally for $n \geq 23$, we discover that p^n approaches to exactly equation (12); that is, as n increases, the transition probabilities converge and using Equation (4) with $p^0 = \begin{bmatrix} 1 & 0 & 0 \end{bmatrix}$.

$$P = P^0 P^{23} = \begin{bmatrix} 0.20 & 0.52 & 0.28 \\ 0.20 & 0.52 & 0.28 \\ 0.20 & 0.52 & 0.28 \end{bmatrix} = \begin{pmatrix} 0.20 & 0.52 & 0.28 \end{pmatrix} \tag{26}$$

The probability vector for the limiting state is provided by

$$\pi_0 = \pi_0 P = \begin{pmatrix} 0.20 & 0.52 & 0.28 \end{pmatrix} \quad (27)$$

Then, for the two seasons, we have

$$\pi_1 = \pi_0 P_1 = \begin{pmatrix} 0.30 & 0.48 & 0.22 \end{pmatrix} \quad (28)$$

$$\pi_2 = \pi_1 P_2 = \begin{pmatrix} 0.19 & 0.49 & 0.32 \end{pmatrix} \quad (29)$$

Dams and hydrological resources management are critical to power generation in hydropower station such as Kainji hydroelectric power station. This study examines the three state water outflow levels of a dam and in relation to the two seasons of the year using a Markov model with discrete time and discrete states.

The results of the analysis from the empirical data collected on the water outflow of Kainji Dam indicate that the null hypothesis is ultimately rejected based on the value $\left(16.187200837 > 12.59 \right)$ for the test of independence of P_k *on* K . This rejection of the Null hypothesis translates to the non-homogeneity of the Markov chain model where the transition matrix depends on the season. Therefore, we only have transition probabilities for the combined season in additive manner. This finding also demonstrates that the transition probability converges to equilibrium at $n = 23$ on iterations, meaning that as $n \geq 23$ increases, the transition probabilities converge and using equation (2) with $P^0 = \begin{bmatrix} 1 & 0 & 0 \end{bmatrix}$, We find that p^n approaches exactly equation (11).

This also confirms the well-known fact that the courses and outcome of water outflow of Kainji Dam is dependent on the changing patterns of the season. Basically, those threshold percentages were as result of reaching n-step limiting state probabilities and are seemingly dependent on the seasonal climatic change.

The result also shows that a non-stationary transition probability is appropriate. The result indicates that the water outflow shall be 0.20%, 0.52% and 0.28% in lower water outflow, middle water outflow and upper water outflow respectively in the long run. This shows that the water outflow levels stay more in state 2 in about 52% of the time, for the discrete time case. This implies that the water outflow levels shall be in state 2 (i.e middle state) most of the time than in other states some other time. The result also indicates that in the season two (2) the water outflow shall be 19%,

49% and 32% in lower water outflow, middle water outflow and upper water outflow respectively in the long run. This is contrast to the season one (1) with water outflow of about 30%, 48% and 22% in lower water outflow, moderate water outflow and upper water outflow respectively in the long run. The result shows that the water outflow shall be in higher outflow of about 32% in season two (2) and 22% in the season one (1). While in the lower water outflow, we have about 19% in season two (2) and 30% in the season one (1). These shows that higher water outflow is obtained during season two (2) (November to March) of about 49% and 32% in middle water outflow and upper water outflow and lower water outflow is obtained during season (1) (April to October) of about 30%, and 48% in lower water outflow, moderate water outflow The outcome validates the reality on the ground that higher water outflow occurs during season two (2) (November to March). The lower water outflow, on the other hand, occurs mostly during season one (1) (April to October). This prediction could be used in the flood preparedness and awareness as well as management and control of dam resources which majorly helps in power generation to the national grid.

4. Conclusion

A stochastic model to examine and predict monthly water outflow of Kainji dam has been presented. The stochastic model was formulated on the basis of the Markov chain principle. Based on the data collected the results indicate that there shall be a higher water outflow of about 49% and 32% in middle water outflow and upper water outflow during the season two (2) (November to March). The result also indicate that the lower water outflow is obtained during season (1) (April to October) of about 30%, and 48% in lower water outflow, moderate water outflow. These erratic variations in dam water outflow have a significant impact on the amount of hydroelectric power generated by the dam as well as the availability of other dam resources like crop cultivation and freshwater fishing along the dam basins. The model could be used as a predictive device for anticipating the likely flood experienced regularly as a result of water outflow from kainji dam. This prediction can also be utilized for the management of the dam resources.

References

Akyuz, D.E, Bayazit.M.,& Onoz, B. (2012): Markov Chain Models for Hydrological Drought Characteristics, *American Meteorological Society (AMMS) journal*, 13(1) 25-29

Bhat, U. N (1984). Elements of Applied Stochastic Processes, New York: John Wiley

Jain, R.K. (1988). The Use of a Time. Varying Markov Model to Study the Effect of Weather on Asthma. Biomedical Journal, 30, 93-97.

Sule, B.F. (1988). Reservoir Operation Policy for Optimizing Energy Generation at Shiroro Dam, Water Reservoir Management 2 (3) 125-132 .

Mohammed A. (2013): Application of Markov Model to Reservoir Elevation of Shiroro Dam, Unpublished M Tech thesis, Department of Mathematics and Statistics, FUT Minna.

Moran, Moran, P.A.P. (1954). A Probability Theory of Dams and Storage Systems, Australian, Journal of Application Science, 5(1), 45-49

Paraskevi, T. (2006). Calculation of the Steady state Probabilities for a Water Management Problem with Three Connected Dams. University of South Australia.

Piantadosi, J. (2004). Optimal Policies for Storage of Urban Storm Water, Unpublished PHD Thesis, University of South Australia.

Ross, S, M. (1996). *Stochastic Process*, (2nd edition). New York: John Wiley.

Thomas, O. A., Benjamin, J. O., & Mathew, O. O. (2023). A Markov model of generator Performance at the Kainji Hydro-power Station in Nigeria International Journal of Electrical and Computer Engineering (IJECE) Vol. 13, No. 4, August 2023, pp. 3585~3592 ISSN: 2088-8708, DOI: 10.11591/ijece. v13i4. pp3585- 3592

Comparative Analysis of Machine Learning Algorithms for the Detection of Android Applications Malware

Mohammed Lukman[1], Ojeniyi J. A[2], Subairu S. O[3]

[123]Department of Cyber Security Science, Federal University of Technology, Minna, Nigeria

Corresponding author: louqmaan4all@gmail.com

Abstract

With the increasing reliance on Android smartphones and apps, there has been a notable escalation in malware threats targeting this platform. This study addresses the urgent need for effective malware identification by examining and comparing the performance of five machine learning classifiers: Support Vector Machine (SVM), Gradient Boosting (GB), Logistic Regression (LR), K-Nearest Neighbors (KNN), and Naïve Bayes (NB). Two datasets sourced from the Canadian Institute of Cybersecurity were evaluated using the Orange Data Mining tool. Performance was assessed through metrics such as accuracy, precision, recall, and F1-score. Results revealed that Logistic Regression and KNN achieved the highest accuracy (76.9%) on the first dataset, while Gradient Boosting led with a 97.8% accuracy on the second dataset.

Keywords: Algorithm, Android, Classifier, Dataset, Detection, Malware

1.0 **Introduction**

The popularity of Android devices has significantly expanded in recent years, making them attractive targets for cybercriminals. Due to their open-source nature and widespread adoption, Android systems are particularly vulnerable to exploitation. This surge in usage has paralleled an increase in cybersecurity incidents affecting these devices (Gupta et al., 2023).

Cybercriminals often exploit vulnerabilities in mobile applications to gain unauthorized access to sensitive data, perform illicit transactions, or control device functions remotely. In response, the cybersecurity community continues to innovate new malware detection strategies. Among these, machine learning-based detection has gained prominence for its ability to generalize and adapt to novel threats (Haidros et al., 2023; Taher et al., 2023).

To address this growing concern, this research evaluates five widely recognized machine learning algorithms - Support Vector Machine, Gradient Boosting, Logistic Regression, K-Nearest Neighbours and Naïve Bayes - through a comparative analysis aimed at enhancing the accuracy and efficiency of Android malware detection systems.

The key contributions of this paper are summarised as follows:

1. The paper used a large and recent dataset from Canadian Institute of Cybersecurity. the dataset containing 11,598 instances and 470 features encompassing system calls, binders and composite behaviours to capture nuanced malicious patterns.
2. The paper applies feature selection and dimensionality reduction technique known as information gain to identify the most relevant behavioural indicators so as to improve the model performance and interpretability.
3. The performances of different machine learning algorithms were investigated and GB with accuracy of 97.85% has the best performance. This provides practical insights into the effectiveness of the models for real-time malware detection on android platforms.
4. The paper also provides guidance on algorithm selection and feature engineering strategies for deployment in android security solutions.

1.1 **Background and Motivation**

As Android devices continue to dominate the global mobile market, they have simultaneously become prime targets for malicious software. Conventional malware detection systems, such as signature-based techniques, struggle to keep up with the sophisticated evasion methods employed by attackers. In response, the cybersecurity community has turned to machine learning approaches, which offer adaptability and the potential to detect previously unseen malware by analyzing behavioral patterns and system-level interactions.

1.2 **Problem Statement**

Although comprehensive datasets like CICMalDroid 2020 provide detailed behavioral indicators of Android applications, there is a scarcity of comparative research evaluating how different machine learning models perform on such high-dimensional data. This gap limits our understanding of which algorithms are most effective for detecting diverse categories of Android malware.

1.3 **Research Gap**

Existing literatures frequently concentrates on individual algorithms or relies solely on limited data types, such as static features or permission sets. Few studies have conducted a broad evaluation of multiple models using comprehensive behavioral features - like system calls and dynamic logs - which are critical for detecting modern Android threats.

1.4 **Problem Objective**

The objective of this research is to bridge the identified gap by systematically comparing the performance of multiple machine learning algorithms using the CICMalDroid 2020 dataset. This study specifically focuses on assessing how well these models can detect and classify Android malware using detailed behavioral characteristics extracted from real-world application data.

2.0 **Related Work**

Numerous studies have explored the application of machine learning techniques for Android malware detection. Zhou et al. (2023) proposed a method that applies Graph Convolutional Networks (GCNs) to analyze behavioral-level data, demonstrating that representing features in graph form can enhance detection capabilities. Wang et al. (2023) focused on analyzing sequences of system calls and achieved high detection accuracy, underscoring the value of runtime behavior modeling.

Another notable contribution comes from Kumar et al. (2025), who developed a hybrid approach by combining static attributes like permissions with dynamic indicators such as API calls. Their deep learning model showcased the benefits of integrating diverse data sources. Singh et al. (2024) conducted an evaluation of different machine learning classifiers on both static and behavioral datasets, emphasizing the importance of feature selection and performance comparison.

Meanwhile, Chen et al. (2024) explored an alternative strategy by transforming static application features into image data for classification using Convolutional Neural Networks (CNNs). Although this approach differs from behavior-focused models, the concept of structuring complex data for machine learning remains relevant.

3.0 **Methodology**

3.1 *Dataset Description and Collection*

The research utilized the CICMalDroid 2020 dataset, which was developed by the Canadian Institute for Cybersecurity at the University of New Brunswick. This dataset aggregates Android application behavior data from multiple sources, including VirusTotal, MalDozer, Contagio Blog, and the AMD project. Out of 13,077 initial entries, approximately 12% were excluded due to formatting issues. The final dataset consisted of 11,598 labeled instances, categorized as Adware - 1,253, Banking malware - 2,100, SMS malware - 3,904, Riskware - 2,546 and Benign - 1,795. The details of the two datasets used in the study are depicted in Table 1.

Table 1: Description and features of the dataset

Dataset	Dataset 1	Dataset 2
Description	Frequencies of system calls	Frequencies of system calls, binders, and composite behaviors
Features	139	470

3.2 *Environment Description*

All analyses were performed using Orange Data Mining version 3.36.2, a user-friendly, open-source tool for visual data analysis. Orange enables the construction of machine learning workflows through drag-and-drop widgets, making it particularly useful for non-programmatic experimentation. The tool provides built-in support for data preprocessing, model training, evaluation, and visualization, allowing researchers to rapidly test and compare different machine learning approaches. Its graphical interface is especially beneficial for examining performance across multiple classifiers without writing extensive code.

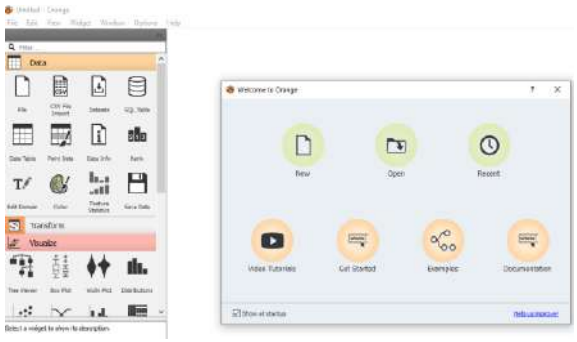

Figure 1: Orange Data Mining User Interface

3.3 *Experimental Procedures*

The experimental process was conducted within the Orange Data Mining environment using the CICMalDroid2020 dataset. After cleaning and formatting the data, the relevant features were loaded via the File widget. Initial preprocessing steps involved addressing missing values and normalizing numerical inputs to ensure uniform scaling across all features. Dimensionality reduction was then applied using feature selection techniques to retain only the most relevant indicators. The dataset was divided into training and testing subsets using a 70:30 split ratio. Each machine learning model was added as a widget and connected to the training dataset. Outputs were evaluated using the "Test & Score" widget, which generated performance metrics for comparison.

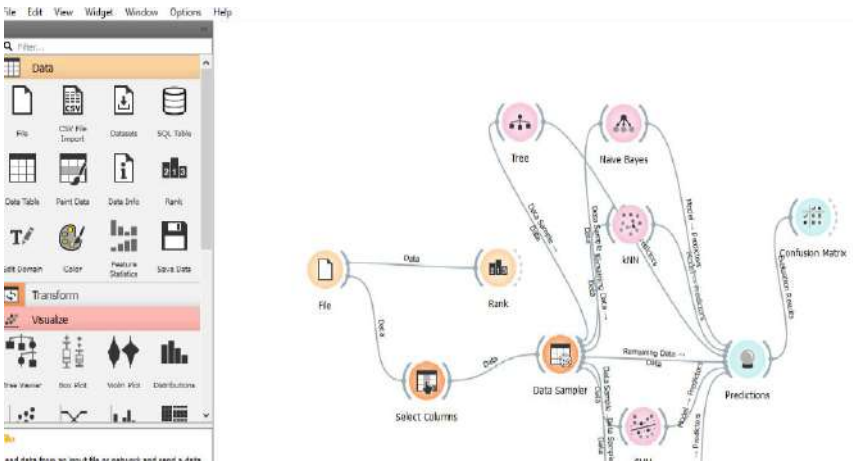

Figure 2: Experimental display of selected classifiers in Orange Environment

3.4 *Performance Evaluation*

Model performance was assessed using four key evaluation metrics commonly employed in classification problems:

a) Accuracy: Represents the proportion of correctly predicted instances out of the total sample size.

$$Accuracy \frac{TP+TN}{TP+FN+TN+FP}$$

b) Recall: Measures the model's ability to correctly identify actual positive cases, minimizing false negatives.

$$Recall = \frac{TP}{TP+FN}$$

c) Precision: Reflects the accuracy of positive predictions by determining how many predicted positives are truly relevant.

$$Precision = \frac{TP}{TP+FP}$$

d) F1-Score: The harmonic mean of precision and recall, offering a balanced evaluation particularly useful when both false positives and false negatives are costly.

$$F1\ Score = \frac{2TP}{2TP+FP+FN}$$

3.5 *Graphical Representation of Methodology*

A visual workflow was constructed to illustrate the experimental pipeline adopted in this study. The process begins with loading both datasets into the Orange Data Mining environment. Each dataset underwent standard preprocessing, followed by a 70:30 train-test split. The models' outputs were evaluated using a unified scoring interface to compare their performance metrics side-by-side. This step-by-step graphical approach in Figure 3 ensured transparency and repeatability of the experimental setup.

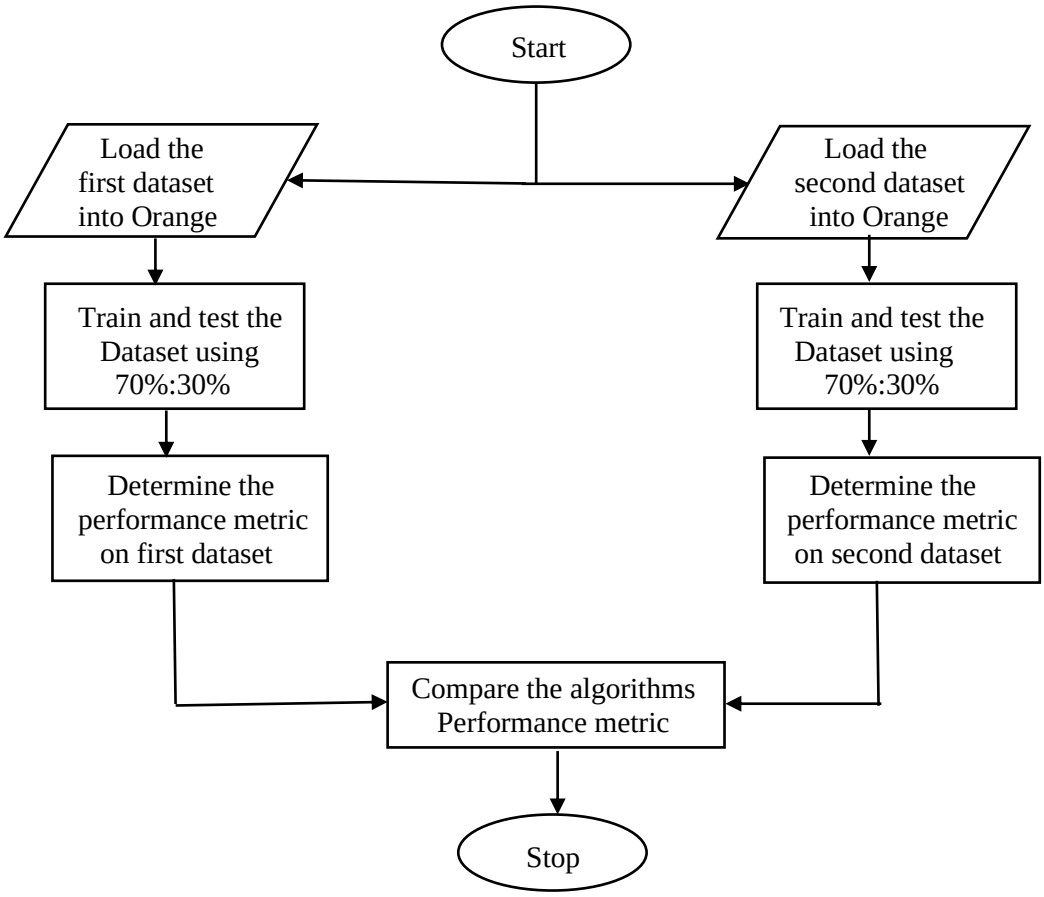

Figure 3: Graphical representation of the methodology

4.0 **Result Discussion**

The results derived from the experimental evaluation are discussed in this section. Each classifier was assessed based on accuracy, precision, recall and F1-score to determine its ability to detect and classify Android malware effectively. The findings provide insight into the

comparative strengths and weaknesses of the models across both datasets, helping to identify the most suitable algorithm for behavioral-based malware detection.

4.1 *Performance Analysis*

On the first dataset, which includes only system call frequency features, both Logistic Regression (LR) and K-Nearest Neighbors (KNN) achieved the highest classification accuracy of 76.9%, along with strong precision and F1-scores. Conversely, Support Vector Machine (SVM) underperformed, with an accuracy of just 53.8% and the lowest precision (29%).

When tested on the second dataset, Gradient Boosting (GB) significantly outperformed all other models with a near-perfect accuracy of 97.8%. Other classifiers, such as LR, KNN, and Naïve Bayes (NB), also showed excellent results, all scoring above 94% in both accuracy and F1-score. These results indicate that the richness of behavioral data, coupled with robust ensemble methods like GB, can dramatically enhance malware detection performance. Table 2 and Table 3 present the performance analysis with dataset 1 and dataset 2 respectively.

Table 2: Performance metric of SVM, GB, LR, KNN and NB on first dataset

ALGORITHM	DATASET 1			
	ACCURACY	PRECISION	RECALL	F1 SCORE
SVM	53.8	29.0	53.8	37.7
GB	61.5	77.6	61.5	52.9
LR	76.9	83.8	76.9	75.1
KNN	76.9	83.8	76.9	75.1
NB	61.5	79.0	61.5	56.5

Table 3: Performance metric of SVM, GB, LR, KNN and NB on second dataset

ALGORITHM	DATASET 2			
	ACCURACY	PRECISION	RECALL	F1 SCORE
SVM	93.3	93.8	93.3	93.2
GB	97.8	97.8	97.8	97.8
LR	97.2	97.3	97.2	97.2
KNN	97.5	97.6	97.5	97.5
NB	94.5	94.9	94.5	94.5

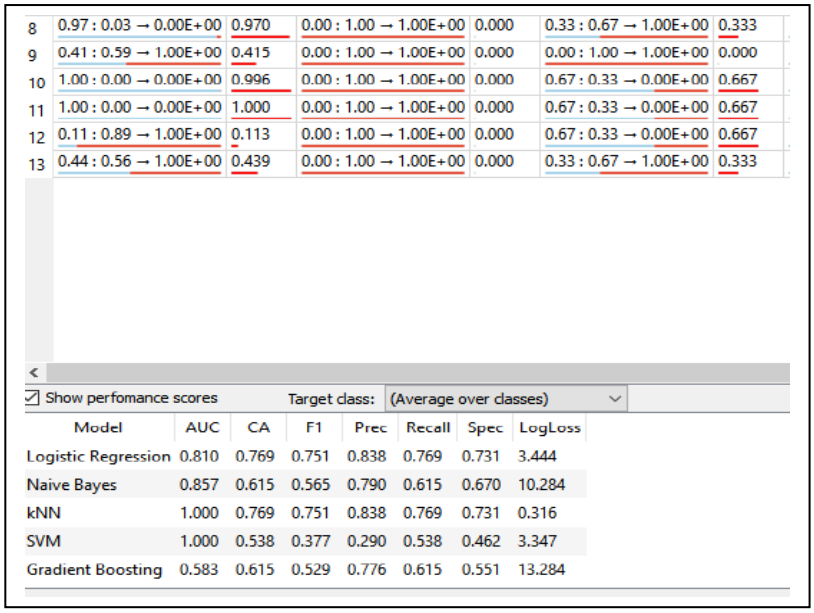

Figure 4: Display of performance metric in the Orange Data Mining Environment

4.2 *Result Comparison*

A comparison between the current study and prior research using the CICMalDroid 2020 dataset reveals that the proposed approach achieved superior performance across all evaluated metrics. As shown in Table 4, the classifiers in this work consistently outperformed their counterparts in earlier studies, particularly in terms of accuracy and F1-score. The enhanced results underscore the effectiveness of the preprocessing strategy, model selection, and inclusion of behavioral features used in this study.

Table 4: Comparison with Previous Work

ACCURACY					
	SVM	GB	LR	KNN	NB
Baseline	83.30%	92.66%	86.71%	88.69%	65.04%
Proposed	93.30%	97.80%	97.20%	97.50%	94.50%
F1 SCORE					
	SVM	GB	LR	KNN	NB
Baseline	83.43%	92.66%	86.71%	88.70%	63.19%
Proposed	93.20%	97.80%	97.20%	97.50%	94.50%

Conclusion

This study conducted a comparative assessment of five widely adopted machine learning classifiers for Android malware detection - Support Vector Machine, K-Nearest Neighbour, Naïve Bayes, Logistic Regression and Gradient Boosting - leveraging the rich behavioral features available in the CICMalDroid 2020 dataset. The evaluation demonstrated that ensemble-based methods, particularly Gradient Boosting, delivered the most accurate results, achieving 97.8% accuracy. The findings affirm the value of behavior-based features in identifying malicious applications and highlight the importance of algorithm selection in achieving optimal performance. While no single model dominated all metrics, the results contribute valuable insights into selecting appropriate models for Android security solutions. The key takeaway is that while choosing an algorithm, practitioners must carefully analyze the properties of their data as well as the needs of their problem domain.

Future Direction

Future research can extend this work by incorporating advanced deep learning models such as Long Short-Term Memory (LSTM) networks, hybrid CNN-LSTM frameworks, or transformer-based architectures, which are well-suited for capturing complex patterns in sequential behavioral data. Moreover, the integration of the proposed models into lightweight, real-time Android security tools could bridge the gap between academic research and practical deployment, enhancing protection for end-users.

References

Gupta, R., Solanki, B. S., Kumar, M., & Murugan, R. (2023). *Intelligent Systems and Applications in Detecting Malware on the Android Phones Based on Golden Jackal Optimized Support Vector Machine*. *11*, 1–7.

Haidros, H., Manzil, R., & Naik, S. M. (2023). Android malware category detection using a novel feature vector - based machine learning model. *Cybersecurity*. https://doi.org/10.1186/s42400-023-00139-y

Taher, F., Alfandi, O., Kfairy, M. Al, Hamadi, H. Al, & Alrabaee, S. (2023). *DroidDetectMW : A Hybrid Intelligent Model for Android Mal- ware Detection*. *May*, 1–20. https://doi.org/10.20944/preprints202305.0333.v1

Zhou, Y., Zhang, X., Liu, Y., Li, W., & Li, K. (2023). Android malware detection based on behavioral-level features using graph convolutional networks. Electronics, 12(23), 4817. https://doi.org/10.3390/electronics12234817

Wang, L., Liu, Y., Xu, Y., & Zhang, T. (2023). A system call-based Android malware detection approach with high precision. Computers & Security, 132, 103236. https://doi.org/10.1016/j.cose.2023.103236

Kumar, R., Singh, A., & Jain, R. (2025). Hybrid Android malware detection and classification using deep learning. International Journal of Information Security and Privacy, 19(1), Article 00783. https://doi.org/10.1007/s44196-025-00783-x

Chen, Y., Zhao, J., Li, Y., & Lin, X. (2024). Visualising static features and classifying Android malware using convolutional neural networks. Applied Sciences, 14(11), 4772. https://doi.org/10.3390/app14114772

Singh, A., Sinha, V., & Yadav, R. (2024). Android malware detection system using machine learning. Proceedings of the 2024 International Conference on Intelligent Computing and Control Systems (ICICCS). https://doi.org/10.1145/3675888.3676049

Mathematical Modelling of Blood Flow and Heat Transfer in the Human Cardiovascular System

[1,2,3,4,5]Salihu, N. O., Aiyesimi, Y. M., Jiya, M., Bolarin, G. A. and Yusuf, A.

[1,2,3,4,5]Department of Mathematics, Federal University of Technology, Minna, Niger State, Nigeria.

[1]*Email: so.nasiru@futminna.edu.ng

Abstract

This work investigates how variations in blood viscosity and thermal conductivity—when influenced by a porous environment and an externally applied magnetic field—affect blood flow and heat distribution within the human circulatory system. The fluid is modelled as flowing through a porous structure, with viscosity assumed to change in relation to hematocrit concentration. Additionally, the thermal conductivity of the blood is treated as temperature-dependent to simulate physiological realism. The unsteady-state governing equations for heat and momentum transfer, considering the flow of an incompressible, laminar, and Newtonian fluid, are addressed using the Generalized Polynomial Approximation Method (GPAM). Solutions were obtained for both velocity and temperature distributions across blood and tissue regions. All mathematical computations were carried out using MAPLE 17, a symbolic computation platform, and the results are displayed through graphical illustrations. The analysis reveals that changes in hematocrit levels, magnetic field strength (quantified by the Hartmann number), the medium's permeability, Reynolds number, and imposed pressure gradients all significantly influence the velocity field of blood. Moreover, temperature responses in both blood and surrounding tissues are heavily affected by variations in Peclet number, pressure gradients, and perfusion mass flow rates. Specifically, it was found that flow velocity reached its peak $\phi(\eta,t)=3.1$ when the condition $\eta=0$ was satisfied. Similarly, the maximum temperature in the blood was observed under the conditions $\eta=0$ and $t=0.5$. A key finding indicates that as the Hartmann number increases (from an unspecified lower to upper bound), the flow velocity approaches zero $\left(\phi(\eta,t)\to 0\right)$, which signifies that the Lorentz force becomes increasingly dominant. This growing electromagnetic resistance effectively slows down the movement of blood, suggesting that magnetic field intensity can serve as a mechanism for regulating arterial blood flow. Additionally, the study found that at a specific temperature ratio $(\alpha=0)$, blood temperature was at its lowest, whereas a higher temperature ratio $(\alpha=-1.0,\ \alpha=1.0)$ led to a pronounced increase in blood temperature. This observation supports the potential use of temperature-dependent thermal conductivity to amplify heat delivery—an advantage in targeted treatments such as cancer hyperthermia. In conclusion, the study demonstrates that external magnetic control and thermally sensitive blood properties can play a pivotal role in managing blood flow dynamics and enhancing therapeutic heat transfer within biological tissues.

Keywords: Artery, Blood Flow, Hematocrit, Magnetic Field, Temperature, Velocity.

1. Introduction

The cardiovascular system plays a vital role in sustaining life by ensuring continuous blood circulation throughout the body. One of its primary responsibilities is to transport oxygen, nutrients, and other essential substances to various tissues, while also facilitating the removal of metabolic waste. Arteries are the primary conduits that transport oxygen-rich blood away from the heart, whereas veins are responsible for returning deoxygenated blood back to the heart for reoxygenation (Tripathi et al., 2017). Venous blood, having delivered oxygen to tissues, becomes oxygen-deficient and enriched with carbon dioxide due to cellular respiration processes (Bessonov et al., 2016). All veins converge into two major vessels—the superior and inferior vena cava—which empty into the right atrium of the heart. From there, the right atrium contracts and directs the blood into the right ventricle. Subsequently, the right ventricle propels this oxygen-depleted blood through the pulmonary arteries into the lungs via the pulmonary trunk. Within the pulmonary capillaries, gas exchange occurs: oxygen from inhaled air is absorbed into the blood, while carbon dioxide is expelled through exhalation (Malatos et al., 2016). Once oxygenated in the lungs, the blood returns to the heart through the pulmonary veins, entering the left atrium. The left atrium then channels it into the left ventricle, which forcefully pumps the oxygen-rich blood into the systemic circulation via the aorta. Through this extensive arterial network, oxygenated blood is distributed across all body tissues to sustain cellular activities and physiological functions. After delivering oxygen and collecting waste products, the blood reenters the venous system and returns to the heart, thus perpetuating the circulatory cycle (Gumez et al., 2017).

A key pathological outcome of arterial obstruction is the escalation in vascular resistance, which significantly diminishes blood flow. This impaired perfusion is a precursor to life-threatening cardiovascular events such as myocardial infarction, ischemic stroke, and chronic circulatory disorders—conditions that remain leading contributors to global mortality (Das et al., 2019). Arterial stenosis, or the narrowing of arteries, disrupts the natural hemodynamic profile, thereby affecting not only mechanical blood transport but also thermal exchange within living tissues. This is particularly evident in peripheral vessels, where tissue temperature is intimately linked to the rate of blood flow (Aiyesimi and Salihu, 2016). A wide range of theoretical and experimental investigations have explored blood flow dynamics and heat transfer in stenosed arteries (Horng et al., 2015). However, many of these studies simplify boundary interactions, often assuming no-slip conditions while focusing solely on the influence of magnetic fields. This approach, although insightful, limits a full understanding of the complex interplay between electromagnetism and blood rheology. Theoretical models frequently treat blood as an electrically conducting fluid to evaluate its response to externally applied magnetic fields (Chen et al., 2006). If blood is considered magneto-responsive due to the presence of iron-containing haemoglobin, magnetic fields could potentially serve as non-invasive tools for modulating hemodynamic parameters such as flow velocity and pressure. This opens up a promising avenue for therapeutic interventions aimed at managing cardiovascular anomalies through targeted magnetic manipulation. Hence, further research into the magneto-hemodynamic behaviour of blood may lead to novel treatments for disorders of the heart and vascular system. Craciunescu and Clegg (2001) conducted a seminal analytical investigation into blood flow through a clogged, tapered artery featuring overlapping stenosis in the presence of an inserted catheter. Recognizing the relevance of cholesterol-induced arterial narrowing, they incorporated a velocity-slip condition at the arterial wall, diverging from traditional no-slip assumptions. Their analysis, based on the approximation of mild stenosis, provided closed-form solutions to the governing fluid dynamics equations. The graphical results

demonstrated that both wall slip and arterial tapering significantly enhanced flow rate, offering insight into the hydrodynamic benefits of geometric divergence and reduced wall adherence.

Further advancing this domain, Ragab et al. (2021) examined blood transport through arteries with multiple stenotic regions, again incorporating velocity-slip conditions. Their study focused on how the stenosis length and shape parameters affect flow resistance and shear stress. From their numerical findings, it was evident that the influence of shape-related variables introduced only marginal deviations in flow behavior, suggesting that slip conditions may play a more critical role than geometrical changes in determining resistance forces within the vessel. In a related study, Khushboo et al. (2017) approached the problem of unsteady blood motion through constricted arteries using a perturbative approximation method. Modeling the non-Newtonian nature of blood via the Bingham plastic fluid framework, their analysis incorporated slip effects at the vessel wall. Key physiological variables such as flow velocity, volumetric flow rate, and wall shear stress were investigated and visually presented. Their results underscored a vital clinical implication: elevated blood viscosity, a known contributor to cardiovascular pathologies, could be mitigated through strategic manipulation of wall slip, offering a potential avenue for therapeutic flow regulation.

Building on these foundational studies, the present research focuses on exploring the coupled effects of spatially varying viscosity and thermal conductivity on blood flow and heat transfer, considering a porous vascular environment subjected to an external magnetic field. This integrated approach aims to provide a more physiologically realistic framework for understanding cardiovascular behavior under complex pathological and therapeutic conditions.

2. Mathematical Formulation

In this study, blood is treated as a homogeneous, viscous, incompressible, and Newtonian fluid. The mathematical formulation of the flow dynamics is based on cylindrical coordinates under the assumption of axial symmetry. The model incorporates spatially varying viscosity and thermal conductivity, accounting for both the thermal behavior of biological tissue and the energy transport mechanisms within the blood vessels. These interactions occur within a porous environment and are influenced by an externally applied magnetic field. The governing equations that describe the unsteady fluid motion and associated heat transfer processes are adapted from the foundational works of Shit and Roy (2017) and Horng et al. (2015), providing a framework for analyzing complex hemodynamic and thermodynamic behavior in magneto-fluidic biological systems.

$$\rho\frac{\partial w}{\partial t}=-\frac{\partial p}{\partial z}+\frac{1}{r}\frac{\partial}{\partial r}\left(r\mu(r)\frac{\partial w}{\partial r}\right)-\sigma B_0^2 w-\frac{\mu(r)}{\bar{k}}w \tag{1}$$

And

$$\rho_t c_t\frac{\partial T_t}{\partial t}=k_t\frac{1}{r}\frac{\partial}{\partial r}\left(r\frac{\partial T_t}{\partial r}\right)+k_t\frac{\partial}{\partial z}\left(\frac{\partial T_t}{\partial z}\right)-W_b c_b\left(T_t-T_a\right)+Q_t\left(r,z,t\right) \tag{2}$$

$$\rho_b c_b\left(\frac{\partial T_b}{\partial t}+w\frac{\partial T_b}{\partial z}\right)=\left(\frac{1}{r}\frac{\partial}{\partial r}\left(k_b r\frac{\partial T_b}{\partial r}\right)+\frac{\partial}{\partial z}\left(k_b\frac{\partial T_b}{\partial z}\right)\right)+Q_b\left(r,z,t\right) \tag{3}$$

Based on Equation (1), the expression describing the spatial variation of blood viscosity is derived using a modified form of Einstein's empirical relation, tailored to capture the influence of hematocrit on fluid behavior.

$$\mu(r) = \mu_0(1 + \beta h(r)) \tag{4}$$

The investigation incorporates an empirical relationship to quantify hematocrit concentration, which serves as a key parameter in characterizing the non-uniformity of blood rheology throughout the analysis.

$$h(r) = H\left(1 - \left(\frac{r}{R_0}\right)^m\right) \tag{5}$$

The external heating rate Q_t in equation (2) and Q_b in equation (3) are defined as:

$$\left.\begin{aligned} Q_t(r,z,t) &= Q_{t0}\,\frac{\pi}{2}\sin\left(\frac{\pi_t}{t_h}\right) \\ Q_b(r,z,t) &= Q_{b0}\,\frac{\pi}{2}\sin\left(\frac{\pi_t}{t_h}\right) \end{aligned}\right\} \tag{6}$$

The blood thermal conductivity on tissue temperature is:

$$k_b = k_{b0}\left(\frac{T_t}{T_a}\right) \tag{7}$$

A no-slip condition is enforced along the inner surface of the vessel wall, ensuring that the fluid velocity matches that of the boundary. The model assumes axial symmetry in the flow field, with the axial velocity prescribed at the centerline of the vessel. Additionally, the vascular segment under consideration is treated as geometrically straight to simplify the analytical framework. The corresponding initial and boundary conditions are defined as follows:

$$\left.\begin{aligned} &w(r,z,0) = 0, \quad \left.\frac{\partial w}{\partial r}\right|_{r=0} = 0, \quad \left.\frac{\partial w}{\partial z}\right|_{r=0} = 0, \quad w(R_0,z,t) = 0, \quad w(r,L,t) = 0 \\ &T_t(r,z,0) = T_a, \quad \left.\frac{\partial T_t}{\partial r}\right|_{r=0} = 0, \quad \left.\frac{\partial T_t}{\partial z}\right|_{r=0} = 0, \quad T_t(R_0,z,t) = T_a, \quad T_t(r,L,t) = T_a \\ &T_b(r,z,0) = T_a, \quad \left.\frac{\partial T_b}{\partial r}\right|_{r=0} = 0, \quad \left.\frac{\partial T_b}{\partial z}\right|_{r=0} = 0, \quad T_b(R_0,z,t) = T_a, \quad T_b(r,L,t) = T_a \end{aligned}\right\} \tag{8}$$

Where z is the axial distance, r is the radial distance, ρ is the density, w is the axial velocity of blood flow, w_0 is the initial axial velocity of blood flow, p is the blood pressure, $\mu(r)$ is the blood viscosity at a radial distance r, $h(r)$ is the hematocrit at a distance r, H is the maximum hematocrit at the center of the artery, μ_0 is the coefficient of viscosity of plasma, R_0 is the radius of a normal arterial segment, β is a constant whose value for blood is equal to 2.5, σ is the electrical conductivity, B_0 is the applied magnetic field strength, k is the permeability of the porous medium, k_t is the thermal conductivity of tissue, k_b is the thermal conductivity of blood, c_t is the specific heat capacity of tissue, c_b is the specific heat capacity of blood, T_t is the tissue temperature, T_b is the blood temperature, T_a is the ambient temperature that is normally assumed to be 37^0C, W_b is the perfusion mass flow rate, $Q_t(r,z,t)$ is the tissue power of heat added axis symmetrically, $Q_b(r,z,t)$ is the blood power of heat added axis symmetrically and L is the length of vessel wall.

For analytical simplification and to generalize the governing system, equations (1) through (8) are reformulated into a dimensionless framework using an appropriate set of non-dimensional transformation variables defined as follows:

$$\left\{\begin{array}{llll} r'=\dfrac{r}{R_0}, & \tau=\dfrac{w_0 t}{R_0}, & z'=\dfrac{z}{L}, & \phi=\dfrac{w}{w_0}, \quad \alpha=\dfrac{T_b}{T_t} \\ \theta=\dfrac{T_t-T_a}{\alpha T_a}, & \psi=\dfrac{T_b-T_a}{\alpha T_a}, & p'=\dfrac{p}{\rho w_0^2} & \end{array}\right\} \tag{9}$$

Dropping primes, the dimensionless equations with their initial and boundary conditions are:

$$\frac{\partial\phi}{\partial\tau}=D+\frac{1}{\mathrm{Re}}\frac{1}{r}\frac{\partial}{\partial r}\left(r\left(1+\beta H\left(1-r^m\right)\right)\frac{\partial\phi}{\partial r}\right)-\frac{M^2}{\mathrm{Re}}\phi-\frac{k_p}{\mathrm{Re}}\left(1+\beta H\left(1-r^m\right)\right)\phi \tag{10}$$

$$\frac{\partial\theta}{\partial\tau}=+\frac{1}{Pe_1}\frac{1}{r}\frac{\partial}{\partial r}\left(r\left(1+\alpha\theta\right)\frac{\partial\theta}{\partial r}\right)+\frac{1}{Pe_2}\frac{\partial}{\partial z}\left(\frac{\partial\theta}{\partial z}\right)-\alpha_1\theta+\gamma_1\frac{\pi}{2}\sin\left(\frac{\pi_t}{t_h}\right) \tag{11}$$

$$\frac{\partial\psi}{\partial\tau}+a\phi\frac{\partial\psi}{\partial z}=\frac{1}{Pe_3}\frac{1}{r}\frac{\partial}{\partial r}\left(r(1+\alpha\theta)\frac{\partial\psi}{\partial r}\right)+\frac{1}{Pe_4}\frac{\partial}{\partial z}\left((1+\alpha\theta)\frac{\partial\theta}{\partial z}\right)+\gamma_2\frac{\pi}{2}\sin\left(\frac{\pi_t}{t_h}\right) \tag{12}$$

$$\left\{\begin{array}{l} \phi(r,\,z,\,0)=0,\ \left.\dfrac{\partial\phi}{\partial r}\right|_{r=0}=0,\ \left.\dfrac{\partial\phi}{\partial z}\right|_{z=0}=0,\ \ \phi(1,\,z,\,t)=0,\ \phi(r,\,1,\,t)=0 \\ \theta(r,\,z,\,0)=0,\ \left.\dfrac{\partial\theta}{\partial r}\right|_{r=0}=0,\ \left.\dfrac{\partial\theta}{\partial z}\right|_{z=0}=0,\ \ \theta(1,\,z,\,t)=0,\ \theta(r,\,1,\,t)=0 \\ \psi(r,\,z,\,0)=0,\ \left.\dfrac{\partial\psi}{\partial r}\right|_{r=0}=0,\ \left.\dfrac{\partial\psi}{\partial z}\right|_{z=0}=0,\ \ \psi(1,\,z,\,t)=0,\ \psi(r,\,1,\,t)=0 \end{array}\right\} \tag{13}$$

3. Method of Solution

Using the transformation $2\eta = r + z$ in equations (10) – (13), after simplifying gives:

$$\frac{\partial \phi}{\partial \tau} = -D + \frac{1}{4\mathrm{Re}}\frac{1}{\varepsilon}\frac{\partial}{\partial \eta}\left(\varepsilon\left(1+\beta H\left(1-\varepsilon^{m}\right)\right)\frac{\partial \phi}{\partial \eta}\right) - \frac{M^{2}}{\mathrm{Re}}\phi - \frac{k_{p}}{\mathrm{Re}}\left(1+\beta H\left(1-\varepsilon^{m}\right)\right)\phi \tag{14}$$

$$\frac{\partial \theta}{\partial \tau} = \frac{1}{4Pe_{1}}\frac{1}{\varepsilon}\frac{\partial}{\partial \eta}\left(\varepsilon\frac{\partial \theta}{\partial \eta}\right) + \frac{1}{4Pe_{2}}\frac{\partial}{\partial \eta}\left(\frac{\partial \theta}{\partial \eta}\right) - \alpha_{1}\theta + \gamma_{1}\frac{\pi}{2}\sin\left(\frac{\pi_{t}}{t_{h}}\right) \tag{15}$$

$$\frac{\partial \psi}{\partial \tau} + \frac{a}{2}\phi\frac{\partial \psi}{\partial \eta} = \frac{1}{4Pe_{3}}\frac{1}{\varepsilon}\frac{\partial}{\partial \eta}\left(\varepsilon\left(1+\alpha\theta\right)\frac{\partial \psi}{\partial \eta}\right) + \frac{1}{4Pe_{4}}\frac{\partial}{\partial \eta}\left(\left(1+\alpha\theta\right)\frac{\partial \psi}{\partial \eta}\right) + \gamma_{2}\frac{\pi}{2}\sin\left(\frac{\pi_{t}}{t_{h}}\right) \tag{16}$$

$$\left.\begin{aligned} &\phi(\eta,0)=0,\ \left.\frac{\partial \phi}{\partial \eta}\right|_{\eta=0}=0,\ \ \phi(1,\tau)=0 \\ &\theta(\eta,0)=0,\ \left.\frac{\partial \theta}{\partial \eta}\right|_{\eta=0}=0,\ \ \theta(1,\tau)=0 \\ &\psi(\eta,0)=0,\ \left.\frac{\partial \psi}{\partial \eta}\right|_{\eta=0}=0,\ \ \psi(1,\tau)=0 \end{aligned}\right\} \tag{17}$$

To obtain solution to equations (14) – (17) using Generalized Polynomial Approximation Method (GPAM) (Olayiwola, 2022) gives:

$$\phi(\eta,t) = \frac{B_{2}}{B_{1}}\left(1-e^{B_{1}t}\right)\left(1-\eta^{2}\right) \tag{18}$$

$$\theta(\eta,t) = \frac{B_{6}}{B_{5}}\left(1-e^{-B_{5}t}\right)\left(1-\eta^{2}\right) \tag{19}$$

$$\psi(\eta,t) = \left.\psi\right|_{\eta=0}\left(1-\eta^{2}\right) \tag{20}$$

Where,

$$B_0 = \begin{pmatrix} \left(\frac{(2-z)^{m+1}}{2(m+1)} - \frac{z^{m+1}}{2(m+1)}\right)\left(\frac{2}{4\mathrm{Re}} + \frac{k_p}{\mathrm{Re}}\right)\beta H - \\ \frac{4(1+\beta H)}{4\mathrm{Re}}\left(\frac{1}{2} + \frac{\ln\left(\frac{z-2}{z}\right)z}{4}\right) - \\ \frac{2M^2}{3\mathrm{Re}} - \frac{2}{3}\frac{k_p}{\mathrm{Re}}(1+\beta H) + \frac{4\beta H}{4\mathrm{Re}}(m+1)\left(\frac{2^{m-1}}{m+1} - \frac{(m-1)2^{m-2}z}{m} + \right) - \\ \frac{k_p}{\mathrm{Re}}\beta H\left(\frac{2^m}{m+3} - \frac{2^{m-1}mz}{m+2} + \frac{2^{m-3}m(m-1)z^2}{(m+1)}\right) \end{pmatrix} \quad (21)$$

$$B_1 = \frac{3}{2}(B_0) \quad (22)$$

$$B_2 = \frac{3D}{2} \quad (23)$$

$$B_3 = 2\left(\frac{1}{4Pe_1}\left(\frac{1}{2} + \frac{\ln\left(\frac{z-2}{z}\right)z}{4}\right) - \frac{\alpha_1}{3}\right) \quad (24)$$

$$B_4 = \gamma_1 \frac{\pi}{2}\sin\left(\frac{\pi_t}{t_h}\right) \quad (25)$$

$$B_5 = \frac{3}{2}\left(\frac{p}{2}(-2+2) + B_3\right) \quad (26)$$

$$B_6 = \frac{3}{2}B_4 \quad (27)$$

$$B_7 = \left(-\frac{2\alpha B_6}{4Pe_3}\left(\frac{\frac{1}{16}ln(-z)z^3 - \frac{1}{4}zln(-z) + \frac{1}{3} - \frac{1}{8}z - \frac{1}{8}z^3 - }{\frac{1}{16}ln(2-z)z^3 + \frac{1}{4}z\ln(2-z)}\right) + \frac{aB_2}{4}\right) \quad (28)$$

$$B_8 = \left(\frac{1}{2} + \frac{\ln\left(\frac{z-2}{z}\right) z}{4} \right) \tag{29}$$

$$B_9 = \gamma_2 \frac{\pi}{2} \sin\left(\frac{\pi_t}{t_h}\right) \tag{30}$$

$$B_{10} = \left(-\frac{q}{2}(-2+2) + B_8 \right) \tag{31}$$

$$B_{11} = \frac{3}{2} B_9 \tag{32}$$

$$\psi\Big|_{\eta=0} = e^{-\frac{3}{2}\left(B_{10}t - \frac{1}{2}B_7 t^2\right)} \left(\sqrt{\frac{\pi}{3B_7}} B_{11} e^{\frac{3}{4}\frac{B_{10}^2}{B_7}} \left(erf\left(\frac{B_{10}}{2}\sqrt{\frac{3}{B_7}} \right) + erf\left(\frac{\sqrt{3}\left(B_7 t - B_{10}\right)}{2\sqrt{B_7}} \right) \right) \right) \tag{33}$$

4. Results and Discussions

To illustrate the dynamics of blood flow and heat transfer within the human cardiovascular system, accounting for both variable viscosity and thermal conductivity, the results are visually represented using MAPLE software. The impact of several influencing parameters on flow velocity, tissue temperature, and blood temperature are systematically analyzed and depicted through graphical representations, highlighting the intricate behavior of the flow and thermal exchange processes under varying conditions.

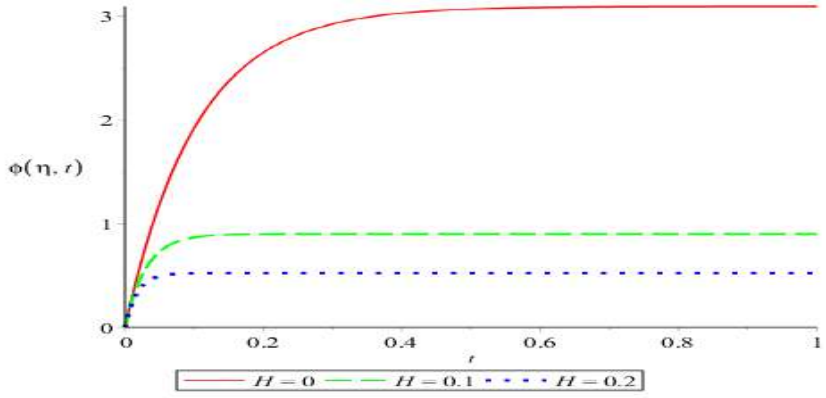

Figure 1: Graph of velocity against time for different values of hematocrit

Figure 1 shows the graph of velocity profile $\phi(\eta,t)$ for different values of hematocrit (H). It is observed that velocity increase and later became steady with time and maximum velocity decreases as values of hematocrit increases.

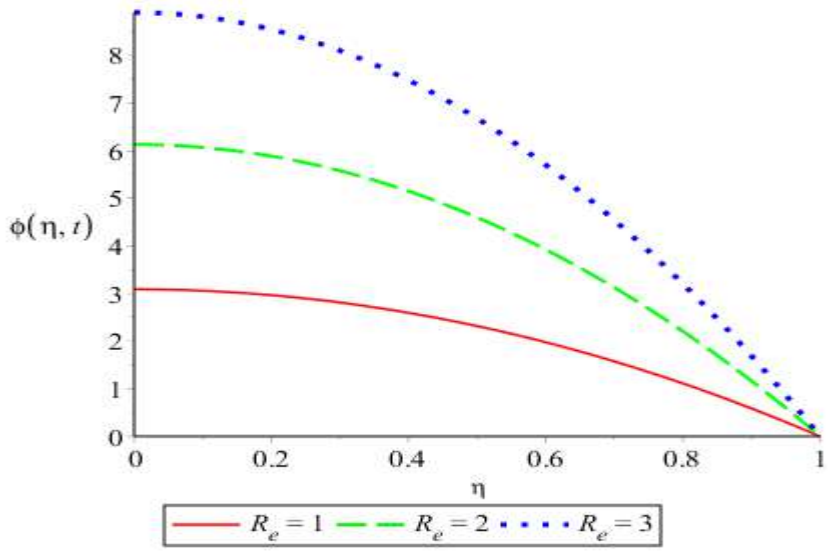

Figure 2: Graph of velocity against distance for different values of Reynolds number

Figure 2 displays the graph of velocity profile $\phi(\eta,t)$ for different values of Reynolds number (R_e). It is observed that velocity decreases along the distance and this velocity increases as Reynolds number increases.

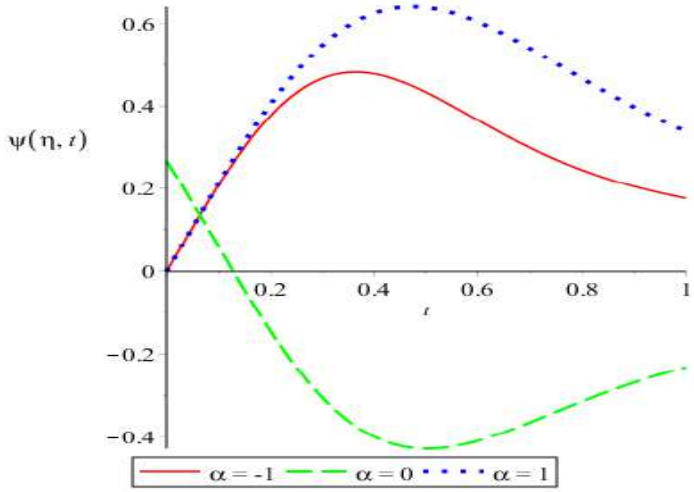

Figure 3: Graph of blood temperature against time for different values of temperatures ratio.

Figure 3 depicts the graph of blood temperature profile $\psi(\eta,t)$ against time for different values of temperature ratio (α). It is observed that we have positive blood temperature profile when $\alpha < 0$ and $\alpha > 0$ while we have negative blood temperature profile when $\alpha = 0$. This by implication means that variable thermal conductivity bring about increase in blood temperature.

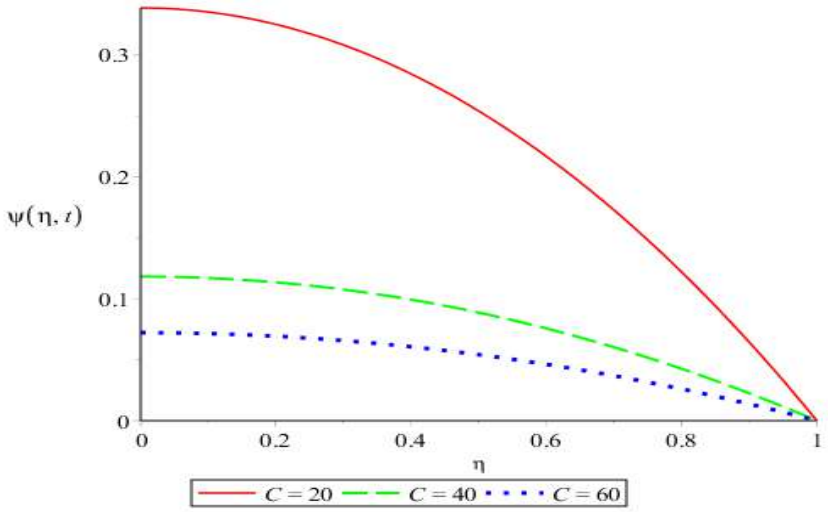

Figure 4: Graph of blood temperature against distance for different values of pressure gradient parameter

Figure 4 shows the graph of blood temperature profile $\psi(\eta,t)$ for different values of pressure gradient parameter (C). It is observed that blood temperature decreases along the distance and this temperature decreases as values of pressure gradient increases.

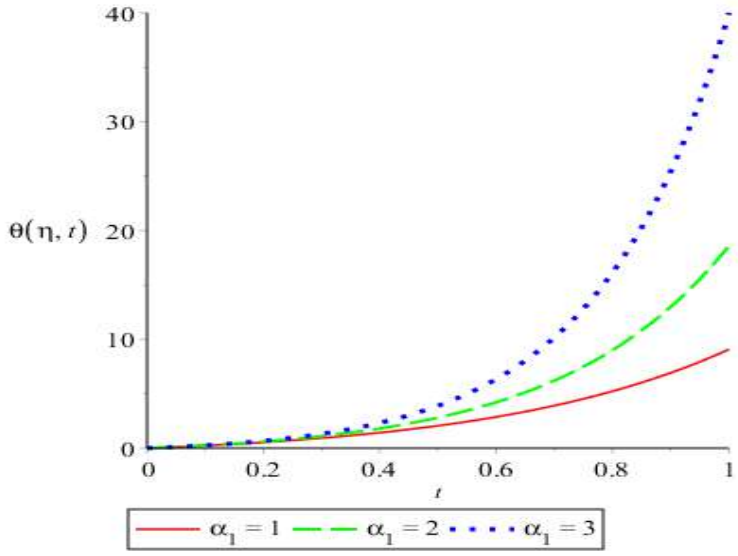

Figure 5: Graph of tissue temperature against time for different values of perfusion mass flow rate.

Figure 5 depicts the graph of tissue temperature profile $\theta(\eta,t)$ for different perfusion mass flow rate (α_1). It is observed that tissue temperature increase with time and maximum temperature increases as perfusion mass flow rate increases.

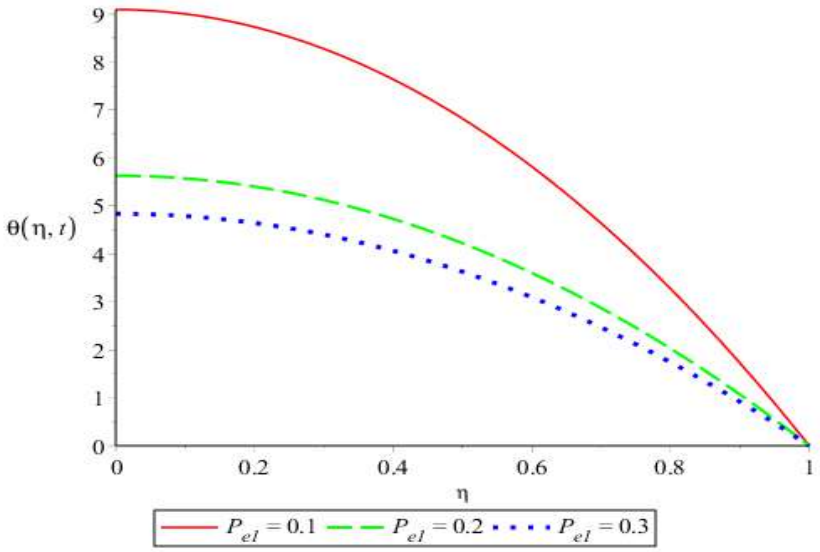

Figure 6: Graph of tissue temperature against distance for different values of Peclet number

Figure 6 shows the graph of tissue temperature profile $\theta(\eta,t)$ for different values of Peclet number (P_{e1}). It is observed that tissue temperature decreases along the distance and this temperature increases as Peclet number increases.

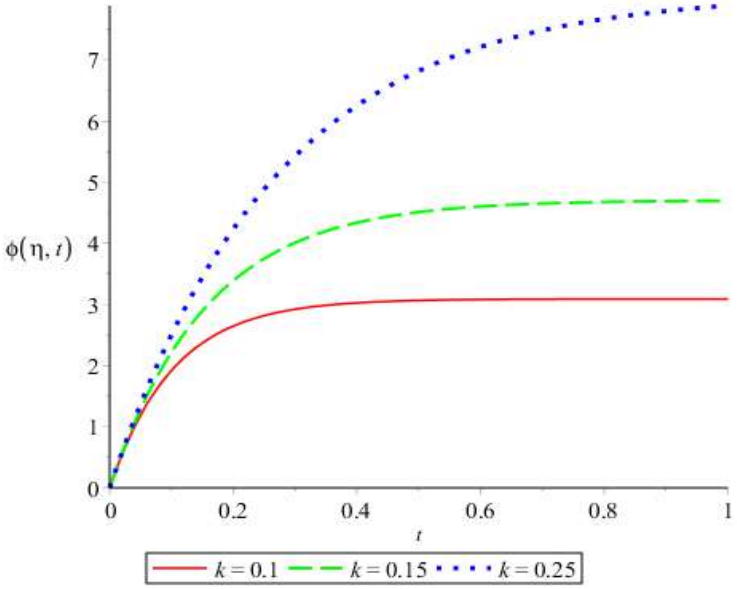

Figure 7: Graph of velocity against time for different values of permeability parameter

Figure 7 shows the graph of velocity profile $\phi(\eta,t)$ for different values of permeability parameter (k). It is observed that velocity increase and later became steady with time and maximum velocity increases as value permeability parameter increases.

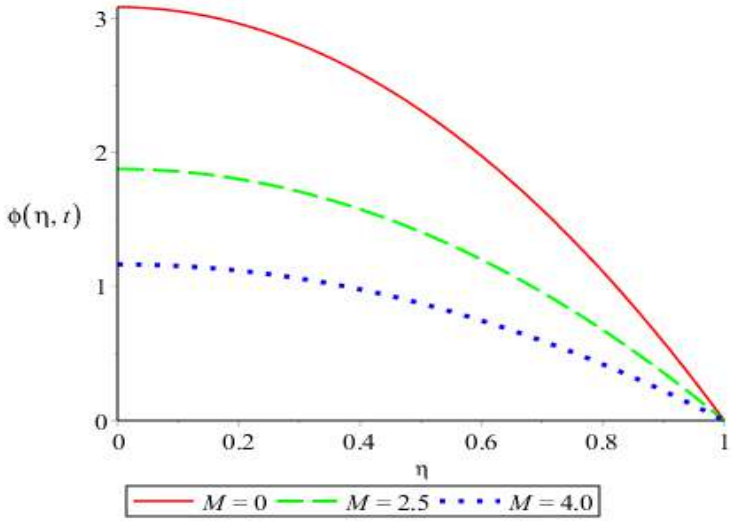

Figure 8: Graph of velocity against distance for different values of Hartmann number

Figure 8 displays the graph of velocity profile $\phi(\eta,t)$ for different values of Hartmann number (M). It is observed that velocity decreases along the distance and this velocity decreases as Hartmann number increases.

5. Conclusion

This theoretical investigation explores the dynamics of blood flow and heat transfer within the human cardiovascular system under the influence of an external magnetic field. In this analysis, both the spatially variable viscosity of blood, which is dependent on hematocrit levels, and the temperature-dependent thermal conductivity of blood are considered, adding complexity to the model. The governing equations are solved analytically using the Generalized Polynomial Approximation Method (GPAM), which provides a robust framework for handling these variations. Key findings from this study reveal several critical insights into the interplay of various physiological and physical factors on blood flow and thermal behaviour. Notably, the Hartmann number, which characterizes the interaction between the magnetic field and blood flow, has a significant inhibitory effect on flow velocity, demonstrating how the magnetic forces contribute to flow retardation. On the other hand, both the Reynolds number and permeability parameter serve to enhance the flow velocity, highlighting their role in facilitating the motion of blood through the vascular system. Furthermore, the Peclet number, which relates to the relative importance of advection and conduction in heat transfer, was found to decrease both blood and tissue temperatures, indicating a stronger dominance of convective heat transfer in the system. The pressure gradient, in contrast, was shown to accelerate flow velocity, while also contributing to a reduction in blood temperature, possibly due to the increased flow rate facilitating heat dissipation. Additionally, hematocrit levels were observed to have a detrimental effect on flow velocity, as higher hematocrit concentrations result in increased blood viscosity, thereby hindering circulation. Conversely, the perfusion mass flow rate was found to have a positive influence on tissue temperature, suggesting that higher blood flow can enhance heat delivery to tissues. Finally, the

variability in blood thermal conductivity was shown to play a significant role in increasing blood temperature, further underscoring the importance of heat transfer properties in the cardiovascular system. These findings provide a comprehensive understanding of how various factors influence both blood flow and thermal regulation within the cardiovascular system, offering valuable insights for future research and potential therapeutic applications.

References

Aiyesimi, Y. M., & Salihu O. N. (2016). Effects of Pollutants and Atmospheric Temperature Rise on Agriculture. *Journal of the Nigerian Association of Mathematical Physics,* 35, 115 – 124.

Bessonov, N., Sequeira, A., Simakov, S., Vassilevskii, Y., &Volpert, V. (2016). Method of Blood Flow Modeling. *Journal of Math. Model Nat. Phenom.*, 11(1), 1-25.

Chen, J., Lu, X. Y., & Wang, W. (2006). Non-Newtonian effects of blood flow on hemodynamic in distal vascular graft anastomoses. *Journal of Biomechanics* 39 (2006), 1983–1995.

Craciunescu, O. I., & Clegg, S. T. (2001). Pulsatile blood flow effects on temperature distribution and heat transfer in rigid vessels. *J BiomechEng*, 123, 500–5005.

Das, P.; Colombo, M., & Prosperi, D. (2019). Recent advances in magnetic fluid hyperthermia for cancer therapy. *Colloids Surf. B Bio interfaces*, 174, 42–55.

Gumez, R. C., Conejero, J. A., & Fernandez, I. G. (2017). Analysis of Blood Flow in One Dimensional Elastic Artery Using Navier-Stokes Conservation Law. arXiv: 1710.06258v2 (physics.flu-dyn) 19 Oct 2017.

Horng, T. L., Lin, W. L., Liauh, C. T., & Shih, T. C. (2015). Effects of pulsatile blood flow in large vessels on thermal dose distribution during thermal therapy. *American Association of Physicists in Medicine*, 34, 1312–1320.

Khushboo, T., Agrawal, A. K., Upadhyay, V., & Harish C. (2017). A Mathematical Study of Two Phase Pulmonary Blood Flow in Artery with Special Special Reference to Tuberculosis. *International Journal of Mathematics and Statistics Invention,* 45, 14 – 22.

Malatos, S., Raptis, A., & Xenos, M. (2016). Advances in Low-Dimensional Mathematical Modeling of the Human Cardiovascular System. *Journal of Hypertension and Management*, 2(2) 2474-3690.

Olayiwola, R. O. (2022). Solving parabolic equations by Olayiwola's generalized polynomial approximation method. *International Journal of Mathematical Analysis and Modelling,* 5(3), 24 – 43.

Ragab, M.; Abouelregal, A. E., Al-Shaibi, H. F., & Mansouri, R.A. (2021). Heat Transfer in Biological Spherical Tissues during Hyperthermia of Magnetoma. *Biology,* 10, 1259.

Shit, G. C., & Roy, M. (2017). Pulsatile flow and heat transfer of a magneto micropolar fluid through a stenosed artery under the influence of body acceleration, *Journal of Mechanics in Medicine and Biology*, 11 (5), 643–661.

Tripathi, K., Agrawal, A. K., Upadhyay, V., & Chandra, H. (2017). A Mathematical Study of Two Phase Pulmonary Blood Flow in Artery with Special Reference to Tuberculosis. *International Journal of Mathematics and Statistics Invention,* 1(5), 14-22.